MATERIALI IN TEHNOLOGIJE

MATERIALS AND TECHNOLOGY

MATER. TEHNOL.
LETNIK VOLUME 51
ŠTEV. NO. 3
STR. P. 351-554
LJUBLJANA SLOVENIJA
MAY-JUNE 2017

ISSN: 1580-2949
UDK: 669+666+678+53

MATERIALI IN TEHNOLOGIJE
MATERIALS AND TECHNOLOGY

3

MATER. TEHNOL. | LETNIK VOLUME 51 | ŠTEV. NO. 3 | STR. P. 351-554 | LJUBLJANA SLOVENIJA | MAY-JUNE 2017

ISSN: 1580-2949
UDK: 669+666+678+53

MATERIALI IN TEHNOLOGIJE / MATERIALS AND TECHNOLOGY *so znanstvena serijska publikacija, ki objavlja izvirne in tudi pregledne znanstvene članke ter tehnične novice, ki obravnavajo teoretična in praktična vprašanja naravoslovnih ved in tehnologije na področjih kovinskih in anorganskih materialov, polimerov, vakuumske tehnike in v zadnjem času tudi nanomaterialov.*

The journal MATERIALI IN TEHNOLOGIJE / MATERIALS AND TECHNOLOGY *is a scientific journal, devoted to original scientific papers, reviewed scientific papers and technical news concerned with the areas of fundamental and applied science and technology. Topics of particular interest include metallic materials, inorganic materials, polymers, vacuum technique and lately nanomaterials.*

Izdajatelj (Published for):
Inštitut za kovinske materiale in tehnologije Ljubljana (IMT)

Soizdajatelji (Associated Publishers):
IMPOL Slovenska Bistrica, METAL Ravne, TALUM Kidričevo

Izdajanje **MATERIALI IN TEHNOLOGIJE** sofinancira: Javna agencija za raziskovalno dejavnost Republike Slovenije (ARRS)
(Journal **MATERIALS AND TECHNOLOGY** is financially supported by Slovenian Research Agency (ARRS))

Glavni in odgovorni urednik (Editor-in-Chief): Paul John McGuiness

Pomočnik glavnega urednika (Associate Editor-in-Chief): Matjaž Godec

Častna glavna urednika (Honorary Editors-in-Chief): Franc Vodopivec, Matjaž Torkar

Članki revije Materiali in tehnologije so indeksirani v/Articles published in Materials and Technology are indexed in: SCIENCE CITATION INDEX EXPANDED, MATERIALS SCIENCE CITATION INDEX® AND JOURNAL CITATION REPORTS/ SCIENCE EDITION.
Po bazi podatkov JCR15 ima Materiali in Tehnologije dejavnik vpliva 0,439. / In JCR15 Database Mater. Tehnol. has an impact factor of 0.439.

Članki objavljeni v periodični publikaciji MATERIALI IN TEHNOLOGIJE so indeksirani v mednarodnih sekundarnih virih: (Articles published in journal are indexed in international secondary periodicals and databases):
- DOAJ (Directory of Open Access Journals)
- Google Scholar
- SCIRUS
- CA SEARCH® – Chemical Abstracts®
- METADEX®
- TEME – Technology and management
- Inside Conferences
- Engineered Materials Abstracts®
- Aluminium Industry Abstracts
- SCOPUS
- Civil Engineering Abstracts
- Ceramic Abstracts/World Ceramic Abstracts
- Corrosion Abstracts
- Mechanical & Transportation Engineering Abstracts
- CSA Aerospace & High Technology Database
- Solid State and Superconductivity Abstracts
- Materials Business File
- Referativnyj žurnal: Metallurgija
- COBIB

Izhajanje: 6 številk letno / **Published:** 6 issues per year
Naročnina / Subscription: 42 EUR – **tujina / abroad:** 85 EUR

Na INTERNET-u je revija MATERIALI IN TEHNOLOGIJE dosegljiva na naslovu (ELECTRONIC ACCESS): http://mit.imt.si

Naslov uredništva (Editorial Address):
MATERIALI IN TEHNOLOGIJE
IMT Ljubljana
Lepi pot 11
1000 Ljubljana, Slovenija
Telefon: +386 1 470 18 60
Telefax: +386 1 470 19 39
Podračun pri UJP št. 01100-6030344339

Elektronska pošta (E-mail): mit@imt.si

Oblikovanje ovitka (Design): Ignac Kofol
Oblikovanje plakata na naslovnici (Poster on the Cover): Ajda Schmidt
Računalniški prelom in tisk (Prepress and Printed by): NONPAREL grafične storitve d.o.o., Medvode
Naklada (Circulation): 400 izvodov/issues

ISSN 1580-2949
UDK 669+666+678+53 MTAEC9, 51(3)353–554(2017)

MATER. TEHNOL.	LETNIK VOLUME 51	ŠTEV. NO. 3	STR. P. 353–554	LJUBLJANA SLOVENIJA	MAJ–JUN. MAY–JUNE 2017

VSEBINA – CONTENTS

PREGLEDNI ČLANEK – REVIEW ARTICLE

IZVIRNI ZNANSTVENI ČLANKI – ORIGINAL SCIENTIFIC ARTICLES

STROKOVNI ČLANKI – PROFESSIONAL ARTICLES

UDK 67.017:621.438:620.1
Review article/Pregledni članek

ISSN 1580-2949
MTAEC9, 51(3)355(2017)

ENERGY-EFFICIENT GAS-TURBINE BLADE-MATERIAL TECHNOLOGY – A REVIEW

TEHNOLOGIJA MATERIALOV LOPATIC ENERGETSKO UČINKOVITIH PLINSKIH TURBIN – PREGLED

Zainul Huda

King Abdulaziz University, Department of Mechanical Engineering, Jeddah 21589, Saudi Arabia
drzainulhuda@hotmail.com

Prejem rokopisa – received: 2015-07-03; sprejem za objavo – accepted for publication: 2016-02-29

doi:10.17222/mit.2015.196

Energy-efficient gas turbines (GTs) with reduced emissions have significantly contributed to sustainable development. However, these advanced engines, operating at turbine inlet temperatures (TITs) as high as 1.600 °C, require the development of highly creep-resistant materials for application in hotter-section components of GTs. This paper first reviews recent advancements in the development of creep-resistant superalloys and their microstructural control, including stable gamma-prime raft structures. Then a comparative analysis of recently developed SC superalloys is presented to enable GT designers to select appropriate materials for hotter energy-efficient GT engines. It is recommended to develop new creep-limited alloys based on the metals with higher melting temperatures (e.g., Mo and Nb alloyed with silicon); these future alloys are proposed as prospective candidates for hotter energy-efficient GTs.

Keywords: energy-efficient gas turbines, gas-turbine blades, turbine inlet temperature, single-crystal superalloys

Energetsko učinkovite plinske turbine (angl. GT) z zmanjšanimi emisijami so močno prispevale pri trajnostnem razvoju. Vendar pa ti napredni stroji, ki delujejo pri temperaturah do 1600 °C v vstopnem delu turbine zahtevajo, za uporabo komponent v vročem delu, razvoj materialov odpornih na lezenje. Članek predstavlja prvi pregled trenutnega napredka pri razvoju na lezenje odpornih superzlitin in kontrolo njihovih mikrostruktur, vključno s stabilno zgradbo gama-prime. Predstavljena je analiza pred kratkim razvitih SC superzlitin, tako da je konstrukterjem GT omogočena izbira primernega materiala za bolj vroče, energijsko učinkovite GT stroje. Predlagan je razvoj novih zlitin z omejenim lezenjem, ki temeljijo na kovinah z višjo temperature tališča (npr. Mo in Nb legiran s silicijem); te bodoče zlitine so predlagane kot perspektivne za bolj vroče, energijsko učinkovite GT.

Ključne besede: energijsko učinkovite plinske turbine, lopatice plinskih turbin, vhodna temperatura turbine, monokristalne superzlitine

1 INTRODUCTION

Modern combined cycle gas-turbine (CCGT) engines require a significant increase of turbine inlet temperatures (TIT) for achieving the maximum efficiency.[1–2] This thermodynamic trend resulted in an increased service temperature, enhanced creep damage and hot-corrosion attack of the hotter-engine materials.[3–4] In particular, the gas-turbine (GT) blades operate under the most arduous conditions of temperature and stress of any component in the engine. Nickel-based superalloys exhibit an excellent high-temperature creep resistance, thermal stability, good tensile strength, long fatigue life, microstructural stability at a high temperature as well as good resistances to oxidation and hot corrosion.[5–6] For these reasons, they are used in the manufacturing of gas turbine hot-section components.[7–8]

In order to enable energy-efficient gas turbines to operate at higher TITs, modern CCGTs including advanced single-crystal (SC) superalloys and special thermal-barrier coatings (TBCs) should be used.[9–10] The thermal efficiency of such advanced engines involving closed-loop steam cooling may reach more than 60 %. The operating temperatures in the first-stage and second-stage SC blades of modern CCGTs lie in ranges of 1300–1500 °C and 1000–1100 °C, respectively. For example, General Electric (GE) Inc., producing USA H turbines, uses SC materials for first-stage blades and vanes that operate at a temperature of 1430 °C. Similarly, first-stage turbine blades of Siemens SGT5-8000H machines are made of specialized high-temperature alloy material to combat the long-term effects of high temperatures at a constant stress (to resist creep deformation).

2 GT-BLADE-MATERIAL TECHNOLOGY

Materials for hot-section components of hotter GT engines are subjected to very hard operating conditions. The GT blades, having their walls only a millimeter thick, whizz around at about 10.000 min^{-1}, while gases pass across their surface at over 1500 °C. The GT-blade-material technology progressed in two fronts:

1) GT-blade alloys,
2) thermal barrier coatings (TBCs).

This progress is reviewed in the following subsections.

Table 1: Chemical compositions of two GT-blade superalloys
Tabela 1: Kemijska sestava dveh superzlitin za lopatice GT

Superalloy	% Cr	% Co	% Ti	% W	%Al	%Ta	% Mo	% Fe	% C	% B	% Cb	% Ni
GTD-111	13.5	9.5	4.75	3.8	3.3	2.7	1.53	0.23	0.09	0.01	-	balance
Allvac® 718 Plus	17.9	9	0.74	1.04	1.5	-	2.68	9.3	0.02	0.003	5.51	balance

2.1 GT-blade-alloy development

It was established in the preceding section that besides the other important alloy characteristics, the high-temperature creep resistance is the primary requirement for the superalloy GT blades of hotter GT engines. The high-temperature creep strength of the superalloy GT blades is ensured by the precipitation of a high volume fraction of fine γ' particles in the material microstructure.[7,11–12] Design principles for developing creep-limited alloys for the hot sections (particularly blades) of gas turbines were reported elsewhere.[10,13]

A number of advanced superalloys have been developed for GT blades during the recent two decades; these include single crystal (SC) superalloys (AM1, Rene N6, MC538, etc), the GTD-111 superalloy, directionally solidified (DS) GTD-111, the Allvac 718Plus superalloy and the like.[14–18] The IN-738 superalloy remained in use for the first-stage blades of GT engines during 1971–1984. However, with the development of the GTD-111 superalloy, IN-738 has now become the stage-2 blade material.[19] A comparative analysis of the performance of various SC alloys is presented in Section 4, whereas the performance of equiaxed superalloys are discussed in the following section.

2.2 TBC developments

Thermal barrier coatings (TBCs) play a significant role in enhancing the energy efficiency since they enable gas turbines to be operated at higher turbine inlet temperatures (*TIT*). A TBC is a multi-layer coating consisting of the top coat (ceramic) and the inner layer (the bond coat) between the ceramic and the substrate.[20–21] Recently, R. Kitazawa et al.[22] have reported that a temperature gradient of 150 °C can be achieved using a ceramic TBC (Y_2O_3-ZrO_2 top coat) on superalloy components.

Research on the TBC (bond coating) of the GT blades at Siemens Inc. resulted in a significant improvement in the long-life reliability of turbine blades.[23] It was reported that adding 1–2 % of rhenium (a rare metal with a high melting temperature and a high density) to a mixture of cobalt, nickel, chromium, aluminum and yttrium (the so-called MCrAlY bond coatings) imbues the complex mixture with extraordinary properties. The rhenium improves the mechanical properties of the protective coating and simultaneously prevents the aluminum from diffusing into the base material. The coating system (300-µm-thick bond coating applied directly on the metal and a thin ceramic layer placed on the top) stops the base material from oxidizing. Without this coating system, the nickel-based alloy in the blade would only survive 4.000 h of operation at the maximum operating temperatures. With the coating, however, the alloy can hold out against the oxygen for more than 25.000 h, longer than power-plant operators require as the minimum.[23]

3 RECENTLY-DEVELOPED EQUI-AXED GT-BLADE SUPERALLOYS

Although a number of superalloys have been developed for GTs, the GTD-111 and the Allvac 718Plus are the two notable equiaxed superalloys developed for the GT-blade application in recent years. The effects of the composition and the heat treatment on the microstructures and performance of the two GT blade superalloys are discussed in the following sub-sections.

3.1 GTD-111 superalloy

The GTD-111 superalloy is employed in manufacturing of the first-stage blades of high-power gas turbines. The chemical composition of the GTD-111 superalloy is presented in **Table 1**. The high aluminum and titanium contents ensure the precipitation of a high volume fraction of the γ' particles in the microstructure promoting a good creep strength.

The GTD-111 superalloy has a multiphase structure consisting of the γ matrix, γ' precipitate, carbide, γ–γ' eutectic and a small amount of deleterious phases (e.g., δ, η, σ, Laves).[15, 16] The superalloy maintains a fairly

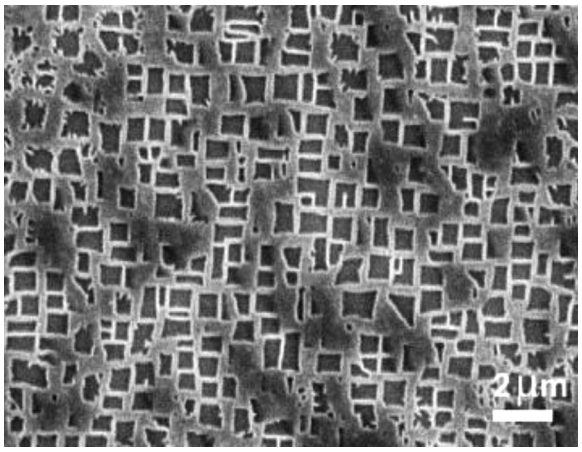

Figure 1: SEM micrograph showing the primary γ' in the heat-treated GTD-111 superalloy[16]
Slika 1: SEM-posnetek primarnih γ' v toplotno obdelani GTD-111 superzlitini[16]

good tensile-yield strength of 780 MPa with a 10 % elongation at 700 °C[24] (**Table 2**). **Figure 1** shows the as-standard heat-treated microstructure of GTD-111.[17]

The alloy obtains its high-temperature creep strength mainly through the γ' precipitates that are present with a volume fraction > 60 %. The primary γ' particles have a cubic shape with the average edge of 0.8 μm. The fine spherical γ' particles precipitated during the aging treatment have the average diameter of ≈0.1 μm. The serrated grain boundaries increase the creep life and creep plasticity.

3.2 Allvac® 718 Plus™ superalloy

Recently, a new *718Plus* nickel-based superalloy has been developed for the application in energy-efficient gas-turbine engines allowing an increase in the TIT to a considerable degree for a high power output. Allvac® 718Plus™ is a novel nickel-based superalloy, designed for heavy-duty applications in energy-efficient gas turbines.[18]

The Allvac® 718Plus™ alloy contains nanometer-sized spherical γ'-phase precipitates ($Ni_3(Al,Ti)$) and plate-shaped δ-phase precipitates (Ni_3Nb) of a micrometer size (**Figure 2**). The chemical composition of the Allvac® 718Plus™ superalloy shows higher chromium (Cr) and molybdenum (Mo) contents as compared to the GTD superalloy (**Table 1**). An exceptional feature in the composition of the Allvac® 718Plus™ alloy is its good columbium (Cb) content (which is absent in the GTD alloy). The high Cb content restricts the coarsening of the γ' particles in the superalloy microstructure ensuring a long-time creep resistance so as to allow an operation of a GT engine at a high temperature for longer periods of time.[7,12] A transmission electron micrograph of the Allvac® 718Plus™ superalloy produced after the aging at 1148 K for 7800 s shows spherical precipitates of the γ' phase in the γ matrix (**Figure 2**). The aging heat treatments of the superalloy lead to the precipitation of intermetallic phases.[18]

ATI Allvac® has excellent tensile properties at 700 °C[25], i.e., σ_y = 1014 MPa and % elongation = 25 (**Table 2**). It has a comparable tensile strength with a 55 °C temperature advantage over the 718 alloy. It has higher tensile and creep strengths than Waspaloy and a comparable thermal stability up to at least 704°C. Because of its good process and metallurgical flexibility, the 718Plus alloy provides opportunities for special processing such as fine-grain, mini-grain and superplastic forming, direct age forging, casting and for large ingot capability.[25]

Table 2: Tensile-yield strength at 700 °C for three typical GT-blade superalloys[14,24]

Tabela 2: Natezna meja plastičnosti pri 700 °C, treh značilnih lopatic iz superzlitine za GT[14,24]

Superalloy	SC superalloy: AMI	GTD-111	Allvac® 718Plus™
Yield strength	1.550 MPa	780 MPa	1014 MPa

4 SINGLE-CRYSTAL GT-BLADE SUPERALLOYS

The use of high-pressure turbine blades made of single-crystal (SC) nickel-based superalloys contributes efficiently to the continuous performance improvement of GT engines in terms of power and thermal efficiency. The employment of directional-solidification (DS) metallurgy enables us to manufacture single-crystal (SC) superalloy GT blades with an increased creep resistance (**Figure 3**).

SC superalloys have a two-phase microstructure consisting of γ' precipitates coherently embedded in the γ-phase matrix as the basic feature (**Figure 4**), which allows the outstanding creep resistance of nickel-based superalloys. **Figure 4** shows a transmission-electron micrograph of a standard heat-treated SC superalloy with

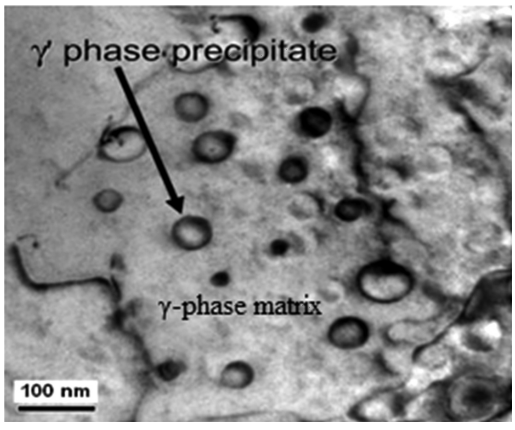

Figure 2: TEM image of superalloy Allvac® 718Plus™ after aging at 1148 K for 7800 s[17]

Slika 2: TEM-posnetek superzlitine Allvac® 718Plus™, po staranju 7800 s na 1148 K[17]

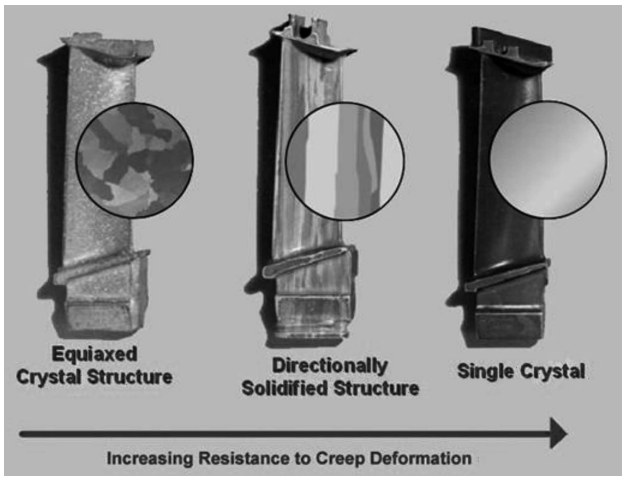

Figure 3: Crystal growth in [001] direction during solidification of a SC-superalloy blade

Slika 3: Rast kristalnih zrn v smeri [001] med strjevanjem lopatice iz SC-superzlitine

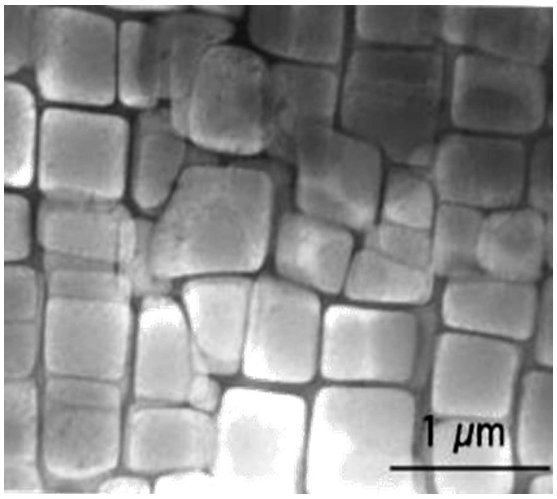

Figure 4: TEM micrograph showing a large volume fraction of cuboidal γ' particles in a γ matrix of a SC superalloy: Ni-9.7Al-1.7Ti-17.1Cr-6.3Co-2.3W % of amount fractions

Slika 4: TEM-posnetek kaže velik delež kockastih delcev γ' v γ osnovi superzlitine: Ni-9.7Al-1.7Ti-17.1Cr-6.3Co-2.3W atomskih %

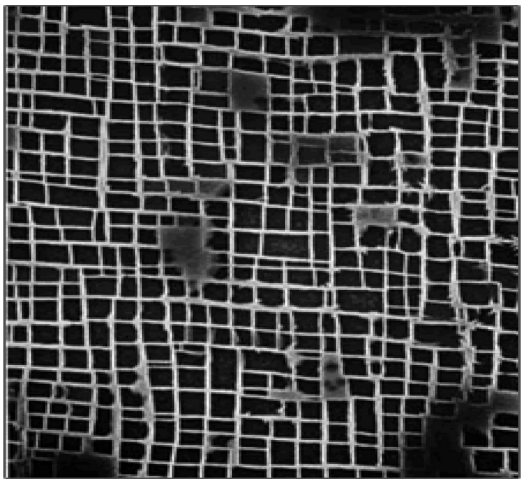

Figure 5: Microstructure of the SC superalloy developed by KEPCO-HITACHI[27]

Slika 5: Mikrostruktura SC-superzlitine razvite pri KEPCO-HITACHI[27]

a composition of Ni-9.7Al-1.7Ti-17.1Cr-6.3Co-2.3W % of the amount fractions. The heat treatment resulted in the precipitation of nano-sized γž precipitates, which are of cuboidal form and oriented with edges parallel to the crystallographic directions. Moreover, they are often ordered into a three-dimensional grid. Mechanical properties of these materials depend strongly on the morphology of the precipitates and, thus, also on the applied heat treatment.

The microstructure of SC superalloys is conventionally studied by transmission electron microscopy (TEM). The advanced-material-characterization technique for SC superalloys involves small-angle neutron scattering (SANS), which yields bulk-averaged information on the parameters (precipitate shape, size, distance between the precipitates and volume fraction) of the microstructure.

4.1 Gamma-prime rafting in SC superalloys

Single-crystal nickel-based superalloys with a large fraction of hardening cuboidal gamma prime (γ') (**Figure 4**), having a negative misfit if the creep is tested under a tensile load along the crystalline direction at a high temperature, can produce a lamellar γ/γ' pattern perpendicular to the loading axis. This drastic change in the morphology of γ' is called rafting.[25] For a long creep life of a SC superalloy, it is important that the rafted γ' structure is stable. R. A. Mackay[27] reported that directional coarsening of γ' began during the primary creep, under certain conditions (at 927–1038 °C) and continued to develop after the onset of the steady-state creep. The length of the rafts increased linearly with the time, up to the plateau region. The thickness of the rafts, however, remained equal to the initial γ' size, at least up through the onset of the tertiary creep, which was reported to be a clear indication of the stability of the finely spaced γ/γ' lamellar structure. It was found that the single crystals with the finest γ' size exhibited the longest creep lives.

4.2 Comparative analysis of energy-efficient SC superalloys

Recently, a new SC Ni-based superalloy has been jointly developed by the Kansai Electric Power Company, Co., Inc. (KEPCO), Nagoya Univ. and Hitachi, Ltd., Japan.[28] This SC superalloy contains Ni, Co, Cr, W, Al, Ti, Ta, Re, Hf, etc. and its microstructure is shown in **Figure 5**.

Figure 5 clearly shows the cuboidal morphology of the γ' precipitates (darker regions) in the γ matrix (brighter regions) of the SC superalloy. Hashizume et al. reported[29] the size of the γ' precipitates to be around 0.4 μm, which is a bit larger than the size reported for GTD-111 (Section 3.1). However, the significant beneficial aspect of the microstructure of KEPCO's SC superalloy, compared to GTD-111, is the absence of grain boundaries. Hence, the microstructure of KEPCO's SC superalloy (**Figure 5**) indicates its high-temperature creep strength, which is also confirmed by the high-temperature capability (>1500 °C) of this superalloy.[28] The chemical compositions of three SC blade superalloys (AM1, Rene-N6 and MC-534) are reported in **Table 2**.

Interesting common features of all the three SC alloys are high W, Al and Ta contents (**Table 2**). Unique features of the MC-534 superalloy are its considerable Re and Ru contents, which impart a remarkable creep resistance to the alloy (**Figure 6**). **Figure 6** shows the tensile-creep behavior of the three SC superalloys (AM1, René N6 and MC-534) at 760 °C/840 MPa; all the three alloy specimens, tested at orientations within 5° of the direction,[30] are compared.

It is clearly evident from the creep curves in Figure 6 that the SC superalloy MC-534 has the lowest creep

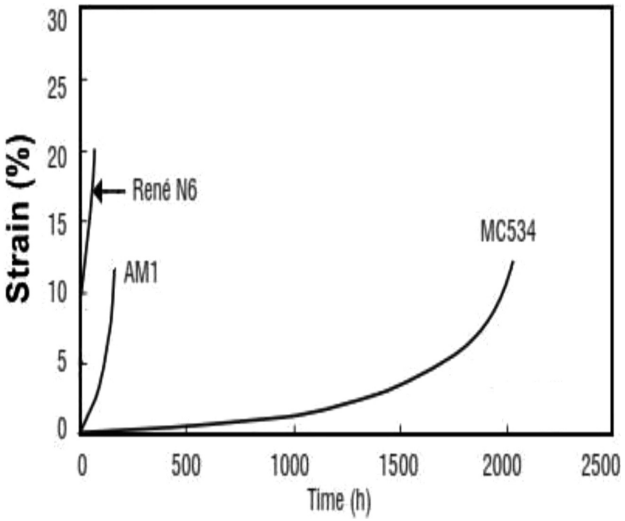

Figure 6: Creep curves at 760 °C/840 MPa for three typical SC superalloys
Slika 6: Krivulje lezenja pri 760 °C/840 MPa treh značilnih SC superzlitin

strain or deformation as compared to the other two SC alloys, attributed to the considerable Re and Ru contents (**Table 3**). However, the creep-rupture life of AM1 was reported to be ten times longer than that of the MC-534 alloy.[14] Although both MA1 and MC-534 alloys have similar γ/γ' microstructures, they widely differ in their chemistries, γ'-precipitate sizes and lattice mismatches. The pronounced and optimum creep-rupture life is observed at 760 °C and 840 MPa, which corresponds to the γ'-precipitate size of 480 nm. The low creep-rupture life of MC-534 can be explained owing to the presence of the deleterious δ phase in the microstructure of the alloy. Additionally, the excellent tensile-yield strength at 700 °C of the SC superalloy AM1, compared to the other competitive GT-blade superalloys, is remarkable (**Table 2**).

5 FUTURE ALLOYS FOR HOTTER GTs

A notable significant development in attaining the world's highest thermal efficiency of GT engines was reported (May, 2011) by Mitsubishi Heavy Industries, Ltd. (MHI), Japan, with respect to achieving the world's highest TIT of 1600 °C with the company's most advanced "J-Series" gas turbine, attaining a gross thermal efficiency of over 60 % – the world's highest level in the CCGT applications.[31] The most advanced J-Series GT uses a SC nickel-based superalloy.

Future GT manufacturers will demand alloys with an excellent high-temperature creep resistance, microstructural stability and castability, along with cost effectiveness. In view of the alloying of advanced SC superalloys with refractories and rare metals (e.g., Co, Cr, W, Ti, Ta, Re, Ru, Hf, etc.) (**Table 3**), the cost of the production has risen significantly. This economic constraint requires research to produce future cost-effective superalloys without significantly sacrificing the long-life reliability. Reed et al. [32] reported on alloy-design rules for the SC superalloys, which allow a very large composition range for just a few ideal compositions to render them cost effective. Another notable development in the production of cost-effective energy-efficient superalloys has recently been made by Hitachi Inc., who reported to reduce the material cost by 1/3 of its previous level by reducing the use of rare metals and by adopting a unique manufacturing (casting) technology, without compromising the high-temperature strength, oxidation resistance, long service life and reliability even in the presence of polycrystalline regions, which form, with high probability, in SC superalloy blades.

The new trend of increasing the Re and Ru contents in recently developed SC alloys requires more research in view of both desirable and undesirable effects of the rare metals on the microstructure and creep behavior of the alloys. F. H. Latief and K. Kakehi[34] reported the effects of the Re content and crystallographic orientation on the creep behavior of aluminized Ni-based SC superalloys. Although an addition of Re was found to be generally effective for the creep-strength improvement of the superalloys, the creep strength was significantly decreased in aluminized specimens due to the change in microstructure under the coating layer caused by the formation of the inter-diffusion zone (IDZ) and substrate-diffusion zone (SDZ). However, the specimens with the {100} side surface showed longer creep-rupture lives than the specimens with the {110} side surface, indicating an anisotropic creep behavior.[34]

A notable development for future superalloys was reported by the researchers, who proposed to control the Cr, Re, and Ru contents for enhancing the creep strength of the SC superalloys.[35–36] An addition of 3 % of the mass fraction of ruthenium (Ru) was found to improve the intermediate temperature/intermediate stress-creep behaviors of the SC Ni-based superalloys; however, the high-temperature creep strength at the intermediate stress was not found to be good.[35] The reduction in the γ' volume fraction upon the addition of Ru appears to be the principal cause of its diminishing strengthening con-

Table 3: Chemical compositions of typical SC superalloys[8,13,17,28]
Tabela 3: Kemijska sestava značilnih SC-superzlitin[8,13,17,28]

Superalloy	% Cr	% Co	% Ti	% W	%Al	%Ta	% Mo	% Fe	% C	% B	% Re	% Ru	% Hf	% Ni
SC: AM1	7.8	6.5	1.1	5.7	5.2	7.9	2	-	-	-	-	-	-	balance
SC: René N6	4.5	12	-	5.7	6	7.5	1.1	-	0.05	0.04	5.3	-	0.15	balance
MC-534	4	-	-	5	5.8	6	4	-	-	-	3	4	0.1	balance

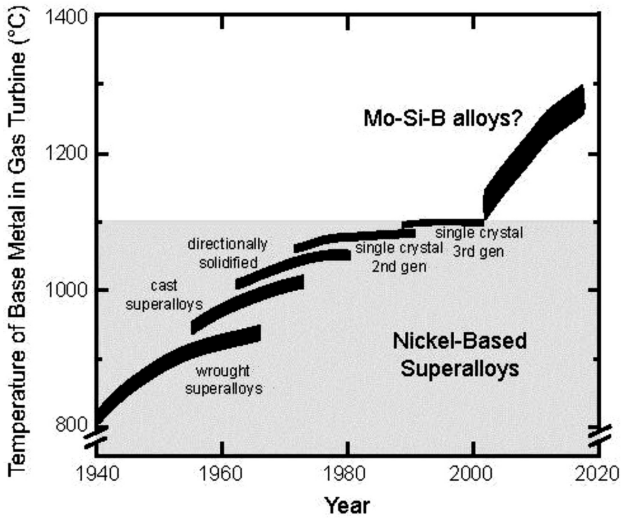

Figure 7: Plot showing the developments in temperature capabilities of superalloys

Slika 7: Diagram prikazuje napredek v temperaturnih zmogljivostih superzlitin

tribution at elevated temperatures. A.-C. Yeh et al.[36] examined the microstructural stability and creep resistance of an advanced SC superalloy, which had high contents of Cr (4.6 % of mass fraction), Re (6.4 % of mass fraction) and Ru (5.0 % of mass fraction).

Experimental results showed that high Re + Ru contents could promote the formation of the hexagonal δ phase at 900 °C; additional Cr and Re could enhance the precipitation of the TCP phase at 1100 °C. Although an increase in the lattice misfit between γ and γ' in the investigated SC superalloy could strengthen the alloy against the creep deformation due to high temperatures ($\geq$1000 °C) and low stresses ($\leq$245 MPa), the microstructural stability remained the same. The tendency to raft should be avoided during the creep at lower temperatures and higher stresses.[36]

Although the advanced alloys used in modern GTs are nickel-based, the tremendous research on the energy-efficient GTs operating at higher TITs (> 1,600 °C) requires the development of new alloys with greater temperature capabilities for future applications. These new alloys should be based on metals with higher melting temperatures (e.g., molybdenum (Mo) and columbium (Cb) alloyed with silicon) that can be prospective candidates for hotter GT engines.[8] This future trend is also evident in **Figure 7**, which illustrates the development of advanced superalloys with respect to the temperature capacity of the alloys since 1940.

Figure 7 not only focuses on nickel-based superalloys for gas-turbine engine applications, but also demonstrates the need for developing new energy-efficient superalloys, such as Mo-based superalloys for achieving further technological gains.

6 CONCLUSIONS AND RECOMMENDATIONS

Having reviewed the recent advances in the GT-blade-material technology, it is recommended to integrate the latest efficiency-improvement techniques with the advanced superalloy technologies to enhance the efficiency and power output in modern industrial gas turbines. Recently developed equiaxed superalloys (e.g., Allvac® 718Plus, GTD-111, etc.) and various SC alloys (with high Re, Ru and Cr contents) should be comparatively analyzed and selected for the hot-section component of a modern GT engine, with the aid of the data presented in the paper. In view of the latest development in the GT technology, which enables an operation at TIT = 1600 °C, it is recommended to develop superalloys based on higher melting temperatures (such as molybdenum-based superalloys) for future CCGT plants with a possibility of operating at TIT > 1600 °C.

7 REFERENCES

[1] I. G. Wright, T. B. Gibbons, Recent Developments in Gas Turbine Materials and Technology and Their Implications for Syngas Firing, International Journal of Hydrogen Energy, (**2007**) 32, 3610–3621, doi:10.1016/j.ijhydene.2006.08.049

[2] P. Jansohn (Ed.), Modern Gas Turbine Systems, 1st Ed., Woodhead Publishing, 2013, 44

[3] C. Kim, Creep damage characterization of Ni-based superalloy by acoustic nonlinearity, Progress in Natural Science Materials International, 22 (**2012**) 4, 303–310, doi:10.1016/j.pnsc.2012.07.005

[4] G. Stein-Brzozowska, D. M. Flórez, J. Maier, G. Scheffknecht, Nickel-base superalloys for ultra-supercritical coal-fired power plants: fireside corrosion, Laboratory studies and power plant exposures, Fuel, 108 (**2013**) 6, 521–533 doi:10.1016/j.fuel.2012.11.081

[5] Z. Huda, T. Zaharinie, S. H. Islam, Effects of annealing parameters on grain growth behavior of Haynes 718 superalloy, International Journal of Physical Science, 30 (**2011**) 6, 7073–7077, doi:10.5897/IJPS11.245

[6] Y. Xingfu, T. Sugui, W. Minggang, Z. Shu, L. Xudong, C. Shusen, Creep behaviors and effect factors of single crystal nickel-base superalloys, Materials Science and Engineering A, 499 (**2009**) 1–2, 352–359, doi:10.1016/j.msea.2008.09.038

[7] Z. Huda, Influence of particle mechanisms on the kinetics of grain growth in a P/M superalloy, Materials Science Forum, 467 (**2004**), 986–990, doi:scientific.net/MSF.467-470.985

[8] W. Maktouf, K. Sai, An investigation of premature fatigue failures of gas turbine blade, Engineering Failure Analysis, 47 Part A, (**2015**) 89–101, doi:10.1016/j.engfailanal.2014.09.015

[9] J. H. Perepezko, The Hotter the Engine, the Better, Science, 326 (**2009**) 5956, 1068–1069, doi:10.1126/science.1179327 (http://science.sciencemag.org/content/326/5956/1068)

[10] Z. Huda, Development of design principles for a creep-limited alloy for turbine blades, Journal of Materials Engineering and Performance, ASM International, 4 (**1995**) 1, 48–53 http://link.springer.com/article/10.1007%2FBF02682704

[11] G. Jianting, The current situation of the application and development of superalloys in the field of energy industry, Acta Metallurgica Sinica, 46 (**2011**) 5, 513–527, doi:10.3724/SP.J.1037.2009.00860 http://www.ams.org.cn/EN/abstract/abstract18812.shtml

[12] R. C. Reed, The Superalloys: Fundamentals and Applications, 2006, Cambridge University Press, UK, 2006

[13] Z. Huda, Development of heat treatment process for a P/M superalloy for turbine blades, Materials and Design, 28 (**2007**) 5, 1664 –1667 doi:10.1016/j.matdes.2006.03.026

[14] P. Caron, O. Lavigne, Recent studies at Onera on superalloys for single-crystal turbine blades, The Onera Journal – Aerospace Lab, 3 (**2011**), 1–14 http://www.aerospacelab-journal.org/al3

[15] S. A. Sajjadi, S. Nategh, A high temperature deformation mechanism map for the high performance Ni-base superalloy GTD-111, Materials Science and Engineering A, 307 (**2001**) 1–2, 158–164, doi:10.1016/S0921-5093(00)01822-0

[16] S. A. Sajjadi, S. Nategh, R. I. L. Guthrie, Study of microstructure and mechanical properties of high performance Ni-base superalloy GTD-111, Materials Science and Engineering A, 325 (**2002**), 484–489, doi:10.1016/S0921-5093(01)01709-9

[17] S. A. Sajjadi, S. M. Zebarjad, R. I. L. Guthrie, M. Isac, Microstructure evolution of high-performance Ni-base superalloy GTD-111 with heat treatment parameters, Journal of Materials Processing Technology, 175 (**2006**) 1–3, 376–381 http://www.journalamme.org/papers_amme03/12157.pdf

[18] G. A. Zickler, R. Schnitzer, R. Radis, R. Hochfellner, R. Schweins, M. Stockinger, H. Leitner, Microstructure and mechanical properties of the superalloy ATI Allvac® 718Plus™, Materials Science and Engineering A, 523 (**2009**) 1–2, 295–303, doi:10.1016/j.msea.2009.06.014

[19] P. W. Schilke, Advanced Gas Turbine Materials and Coatings, GE Energy, NY, USA, 1995 https://powergen.gepower.com/content/dam/gepowerpgdp/global/en_US/documents/technical/ger/ger-3569g-advanced-gas-turbine-materials-coatings.pdf

[20] Z. Huda, Recent advances in energy materials for hot sections of modern gas turbine engines, Proc. ICMME-2012: International Conference on Mechanical and Materials Engineering, held 19–21 Feb, 2012 at Kuala Lumpur, Malaysia, Org. by World Academy of Science, Engineering & Tech., USA, 62, 781–783 http://waset.org/publications/5314/recent-advances-in-energy-materials-for-hot-sections-of-modern-gas-turbine-engines

[21] H. M. Tawancy, A. I. Mohammad, L. M. Al-Hadhrami, H. Dafalla, F. K. Alyousf, On the performance and failure mechanism of thermal barrier coating systems used in gas turbine blade applications: Influence of bond coat/superalloy combination, Engineering Failure Analysis, 57 (**2015**) 1–20, doi:10.1016/j.engfailanal.2015.07.023

[22] R. Kitazawa, M. Tanaka, Y. Kagawa, Y. F. Liu, Damage evolution of [1] TBC system under in-phase thermo-mechanical tests, Materials Science and Engineering B, 173 (**2010**) 1–3, 130–134, doi:10.1016/j.mseb.2009.12.022

[23] SIEMENS Inc., Materials for the Environment – Optimizing Turbine Blades, 2007 (online: http://www.siemens.com/innovation/en/publikation en/publications_pof/pof_fall_2007/materials_for_the_environment/optimizing_turbine_blades.htm)

[24] S. A. Sajjadi, S. M. Zebarjad, Study of fracture mechanism of a nickel-base superalloy at different temperatures, Journal of Achievements in Materials and Manufacturing Engineering, 18 (**2006**) 1–2, 227–230 http://www.journalamme.org/papers_amme06/1247.pdf

[25] R. L. Kennedy, ALLVAC® 718PLUS™ superalloy for the next forty years, in "Superalloys 718, 625, 706 and Derivatives 2005", Edited by E. A. Loria, Publisher: TMS (The Minerals, Metals & Materials Society), USA, 2005 http://www.tms.org/superalloys/10.7449/2005/superalloys_2005_1_14.pdf

[26] N. Tsuno, A. Sato, K. Tanaka, H. Inui, Evolution of raft structure during creep deformation of Ni-based single-crystal superalloy TMS-138, Advanced Materials Research, 278 (**2011**), 19–24, doi:10.4028/www.scientific.net/AMR.278.19 http://www.scientific.net/AMR.278.19

[27] R. A. Mackay, Morphological changes of gamma prime precipitates in nickel-base superalloy single crystals, NTRS (NASA Technical Report Server) # 8/1984, 1984, (Retrieved from online: https://www.researchgate.net/publication/24153495 on February 18, 2016)

[28] R. Hashizume, A. Yoshinari, T. Kiyono, Y. Murata, M. Morinaga, Development of Ni-base SC superalloys for power generation gas turbines, Energy Materials, 2 (**2007**) 1, 5–12 http://www.maneyonline.com/doi/abs/10.1179/174892406X198128

[29] R. Hashizume, A. Yoshinari, T. Kiyono, Y. Murata, M. Morinaga, Development of Ni-base single crystal superalloys for power generation gas turbines, in Superalloys 2004 (Edited by K. A Green, T. M. Pollok, H. Harada, T. E Howson, R. C. Reed, J. J. Schirra, S. Walston), Publisher: TMS (The Minerals, Metals & Materials Society), 2004

[30] F. Diologent, P. Caron, On the creep behavior at 1033 K of new generation single-crystal superalloys, Materials Science and Engineering A, 385 (**2004**) 1–2, 245–257, doi:10.1016/j.msea.2004.07.016

[31] MHI (Mitsubishi Heavy Industries), MHI achieves 1,600°C turbine inlet temperature in test operation of world's highest thermal efficiency "J-Series" gas turbine, MHI News, May 26, 2011, No. 1435 http://www.mhi.co.jp/en/news/story/1105261435.html

[32] R. C. Reed, N. Tao, N. Warnken, Alloy-By-Design: Application to nickel-base single crystal superalloys, Acta Materialia, 57 (**2009**) 19, 5898–5913, doi:10.1016/j.actamat.2009.08.018

[33] Hitachi Technology, 2009–2010, Materials, Components and Others, 69–70 http://www.hitachi.com/rev/archive/2009/__icsFiles/afieldfile/2011/12/05/r2009_technology_mc.pdf

[34] F. H. Latief, K. Kakehi, Effects of Re content and crystallographic orientation on creep behavior of aluminized Ni-base single crystal superalloys, Materials and Design, 49 (**2013**), 485–492, doi:10.1016/j.matdes.2013.01.022

[35] R. A. Hobbs, L. Zhang, C. M. F. Rae, S. Tin, The effect of ruthenium on the intermediate to high temperature creep response of high refractory content single crystal nickel-base superalloys, Materials Science and Engineering A, 489 (**2008**) 1–2, 65–76, doi:10.1016/j.msea.2007.12.045

[36] A-C. Yeh, A. Sato, T. Kobayashi, H. Harada, On the creep and phase stability of advanced Ni-base single-crystal superalloys, Materials Science and Engineering, 490 (**2008**) 1–2, 445–451, doi:10.1016/j.msea.2008.02.008

UDK 519.61/.64:669.35:620.19
Original scientific article/Izvirni znanstveni članek

ISSN 1580-2949
MTAEC9, 51(3)363(2017)

NUMERICAL SIMULATION OF AN EQUILIBRIUM SEGREGATION OF IMPURITIES ON THE GRAIN BOUNDARIES OF COPPER AND ITS ALLOYS

NUMERIČNA SIMULACIJA ENAKOMERNEGA LOČEVANJA NEČISTOČ PRI ZRNATOSTI BAKRA IN NJEGOVIH ZLITIN

Wojciech Ozgowicz

Silesian University of Technology, Faculty of Mechanical Engineering, Konarskiego 18a, 44-100 Gliwice, Poland
wojciech.ozgowicz@polsl.pl

Prejem rokopisa – received: 2014-07-29; sprejem za objavo – accepted for publication: 2016-06-06

doi:10.17222/mit.2014.123

The presented paper deals with a numerical simulation of vacancy diffusion of sulphur, tin and phosphorus atoms to the grain boundary of the structure of copper, type (2D). It was theoretically applied to analysed model alloys of types Cu-S and Cu-Sn, particularly tin bronzes. Its purpose is to verify the obtained experimental results concerning this phenomenon, making use of the Auger method of spectroscopy of electrons (AES). Distinct effects of the segregation of sulphur atoms in the monolayer at the grain boundaries were found as well as an enrichment of the grain boundaries with tin atoms. In addition, the visualization of the simulation revealed a possible formation of stationary clusters of vacancies and segregating atoms on the analysed matrix of the atom structure (2D). The simulated effects of the segregation of S and Sn to the grain boundary, analysed as a function of the number of the cycles of the simulation are characterized by a statistically good repeatability of the results.

Keywords: copper alloys, grain-boundary segregation, diffusion, intercrystalline hot brittleness, mathematical model, numerical simulation

Pričujoče delo predstavlja numerično simulacijo odsotnosti zrn pri difuziji atomov žvepla, kositra in fosforja pri strukturi bakra, tipa 2D. Ta se uporablja za teoretično analiziranje modelov zlitin tipa Cu-S in Cu-Sn, zlasti kositrnih in bronastih. Namen je, da bi pridobljene eksperimentalne rezultate preverili z uporabo AES (Augerjeva elektronska spektroskopija). Ugotovili smo različne učinke tvorjenja ločevanja atomov žvepla v monosloje na mejah zrn pa tudi obogatitev zrn z atomi kositra na mejah zrn. Hkrati pa je vizualizacija simulacije pokazala morebitno nastajanje nepremičnih grozdov praznin in ločevanja atomov v analizirani matriki strukture atomov (2D). Simulirani učinek ločevanja S in Sn do meje zrn, analizirani v odvisnosti od števila ciklov simulacije kaže na značilno statistično dobro ponovljivost rezultatov.

Ključne besede: bakrene zlitine, ločevanje zrnc, difuzija, interkristalna krhkost na vročem, matematični model, numerična simulacija

1 INTRODUCTION

The segregation of admixed or impurity atoms at the boundaries of the grains and on free surfaces proceeds in accordance with two basic mechanisms, viz., equilibrium segregation (ES)[1–3] and non-equilibrium segregation (NES).[4–8] Generally, equilibrium segregation is applied in the course of a diffusive displacement of substituted or interstitial atoms to structurally disturbed interphase surfaces, such as the grain boundaries and free surfaces or to regions of dislocation and stacking faults, causing free energy reduction of the elastic lattice misfit. A reduction of this energy constitutes the driving force of the process ES. Concentrating their attention on metals and binary alloys, M. P. Hondros, E. D. Seah[1] proved that there is a direct relation between the degree of segregation and the temperature of the process, which may be expressed with Equation (1):

$$\frac{C_b}{C_g} = A \exp\left(\frac{E}{kT}\right) \quad (1)$$

where C_b denotes the concentration of the segregating atoms at the grain boundaries, C_g – the concentration of these same atoms in the undisturbed fragments of the structure, A and k – constant values (k – Boltzmann constant) and E – the free energy of segregation, i.e, the reduction of the energy of the segregating atoms in the place of segregation, e.g., at the grain boundary. Usually atoms with a considerable free energy of segregation indicate a much greater differentiation of atomic radiation and electronic structure then the atoms of the matrix.[9]

The quantity of segregation at the grain boundaries, expressed with Equation (1) disregards, however, the dependence of segregation on time and, in the first stage of modelling, this is a considerable shortcoming because the diffusion of the segregating atoms is an essentials element of the ES mechanism. D. McLean[10] defined this dependence even more accurately by taking into account the required accumulation of a monolayer of the segregating atoms, controlled by the diffusion of the atoms in the matrix D_i. This effect is defined with

Equation (2), in which diffusion temperature T appears implicitly as $\alpha = \alpha(T)$:

$$\frac{C_x - C_g}{C_b - C_g} = 1 - \exp\left(\frac{4D_i t}{\alpha^2 d_i^2}\right) erfc\sqrt{\left(\frac{4D_i t}{\alpha^2 d_i^2}\right)} \qquad (2)$$

where: C_s – concentration of the segregating atoms at the grain boundaries in the time t; $\alpha = C_b/C_g$; d_i – potential width of the grain boundary.

Equation (2) permits us to assess the kinetics of the ES phenomenon at the grain boundary and to predict – rather precisely – the duration and temperature of the process, for example the temper brittleness of steel due to the equilibrated segregation of phosphorus.[2]

In recent years much attention has been paid to the mechanism NES, particularly with respect to steel and heat treatment. The theoretical fundamentals concerning this phenomenon were dealt with by K. T. Aust et al.[4] and R. Anthony[5], and later by R. G. Faulkner[3,8] focusing mainly on the developed. The mechanism NES based on the formation of complexes of point defects in the structures of the alloys, mainly of the vacancy-atom type of admixture or impurity, as well as gradients of the concentrations of vacancies in the vicinity of the areas of an intensive elimination of point deffects. Such adsorbents of vacancies are interphase surfaces or grain boundaries and also free surfaces. Non-equilibrium segregations take place in the course of accelerated cooling of the alloy in the conditions of large temperature differences if, for instance, the vacancy-atom pairs of impurity diffuse in the gradients of concentration in the direction of their decreasing concentration. In such conditions the equilibrium concentration of the vacancies and complexes is reduced, and the actual concentration can take place only in the regions of the sink of vacancies.

This process is illustrated quantitatively with the diagram on **Figure 1**. The quantity of NES is characterized by the quotient of concentrations C_b/C_g, and the extent of this effect is expressed by the distance x from the grain boundaries, at which the concentration of impurities attains the lowest level. For the purpose of describing this process quantitatively, it is of essential importance to determine the changes of the curve of the distribution of concentration depending on the time, the temperature and the size of the grains. These parameters can be easily related to the conditions of the heat treatment of the investigated alloys.

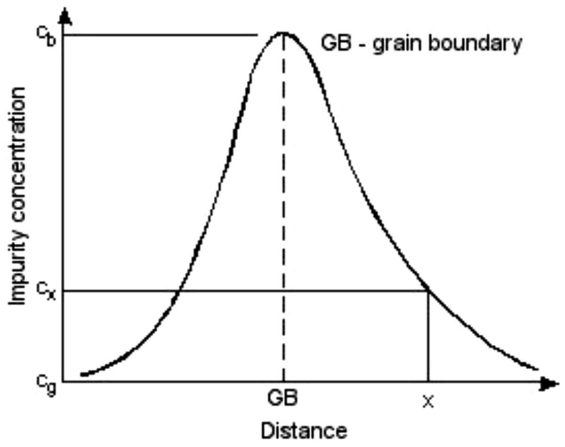

Figure 1: Magnitude and extent of non-equilibrium segregation
Slika 1: Magnituda in obseg neenakomernega ločevanja

An alternative for the description of complex effects in the mechanisms of equilibrium segregation and non-equilibrium segregation by means of phenomenological equations of diffusion is computer aided modelling of these segregations at the grain boundaries of polycrystals, on the atomic scale, applying the method of simulating elementary overshoots of the determined atoms in stable nodal orientations of the structure type (2D).[11–14] In such a case, we move away from the macroscopic phenomena, described by Fick's laws, to the microscopic mechanism of diffusion. However, frequently repeated simulations of individual jumps of diffusion permit us to assess the resulting segregations on the macroscopic scale. In the mathematic model[11] assumed and applied for the computer simulation, the mutual energy concentration between the point defects and grain boundaries were utilized at the atomic level in order to predict the motion of the atoms of impurities, thus resulting in the segregation. The model simulates, in a somewhat simplified way, the vacancy mechanism of the lattice diffusion in metals, particularly the migration of the admixture atoms of impurities and also the vacancies to the grain boundaries, based on an analysis of the effects of the energy in the environment on the respective elements of the lattice, distributed stochastically in the matrix.[15–16] An advantage of this way of modelling is the possibility of simulating complex effects of the processes ES and NES without having to apply equations of the rate of diffusion.

The aim of the investigations was, therefore, to simulate numerically the phenomenon of intercrystalline segregation of the components of alloys and impurities in some selected alloys of copper, particularly tin bronzes, in order to verify the obtained experimental results concerning this phenomenon, making use of the Auger method of spectroscopy of electrons (AES).

2 EXPERIMENTAL PART

2.1 Materials and methods

Experimental investigations were carried out on tin bronzes of the type CuSn6P, resulting from industrial smelting in the firm Trefimetaux (in France), in the form of bars with a diameter of 10 mm, smelted continuously (process Wertli) and with the chemical composition quoted in **Table 1**. Comparative investigations concerning intercrystalline segregation, based on models of high-purity bronzes and bronzes modified with microadditions of rare-earth elements were dealt with earlier.[17,18]

Table 1: Chemical composition of the investigated alloy
Tabela 1: Kemijska sestava preiskovane zlitine

Lp.	Material	Chemical composition, in mass fractions (*w*/%)												
		Sn	P	Cu	Impurities									
					Bi	Pb	Sb	As	S	Fe	Zn	Ni	O_2	
1	Industrial bronze	CuSn6P	6.70	0.42	92.1	0.0100	0.0800	0.0100	0.0250	0.0026	0.0180	0.046	0.030	-
2	Model bronze	CuSn6PM	6.70	0.33	bal.	0.0010	0.0040	0.0002	0.0003	0.0020	0.0060	0.010	0.002	0.0012

Spectrometric investigations were carried out applying the Auger electron spectroscopy technique including the double ionized process of Auger electron emission, using, for this purpose, a spectroscope of the type Riber ASC 2000 (France). Essentially, the Auger emission process requires the excitation of a surface sample with a primary electron beam of 1–10 keV and the detection of the characteristic Auger electrons with peaks well defined in the derivative of the secondary electron energy spectrum. These peaks are specific for the elements, from which the Auger electrons escape. The first process is X-ray fluorescence and the second one is Auger emission. Obviously, none of them can take place at the same initial core hole: thus, they compete. Furthermore, because Auger electrons arrive from depths of about several atom distances, from the point of view of vertical resolution, the technique appears to be an interesting surface analytical tool.

The applied spectrometer was equipped with a cylindrical electrostatic analyser of the energy of the emitted electrons of the type Mac-2 and a scanning electron microscope (SEM) with a spectrometer EDS as well as an electron gun with a high vacuum system, recording the results and controlling the complexity of the entire experiment. An Auger analysis of the energy of electrons was carried out on the surfaces of an intercrystalline fracture of the samples selected at random immediately after having been fractured in the chamber of the spectrometer. Samples with a strain rate of about 10^{-4} s^{-1} were statically stretched in the temperature range of minimum plasticity (DMT – ductility minimum temperature), applying a tensile testing instrument specially designed for the study of fracture surfaces, equipped with a device for resistance heating of the strained samples. Some selected samples were also ionically etched in order to determine the gradient of the chemical composition of the monolayer in the function of the depth of etching from the boundary of the grain.

In order to simulate the process of diffusion of point defects to the grain boundary in the lattice (2D), the mathematical model suggested by Chapman and Faulkner[11] was applied. In this model, the effect of energy was utilized at the level of an atom between the vacancies, the atoms of admixtures or impurities solved in the matrix and the grain boundaries in order to predict the motion of the atoms and the resulting way of segregation. In this model, the atom was assumed to be spherical and the surrounding crystalline lattice elastic, maintaining a constant volume. The interactions of the point effects provide energy driving forces, required to keep up the migration of the segregating atoms to the grain boundaries, and also to create complexes of defects, e.g., divacancies (V_MV_M) or complexes of the vacancy type (V_M) – the admixture atom (F_M), the so-called pair V_MF_M, **Figure 2**.

The applied model assumes a two-dimensional (2D) simulation of the migration of admixture atoms and impurities in the plane (100) of a six-walled lattice with dimensions ($n \times n$) of the atoms, the grain boundary

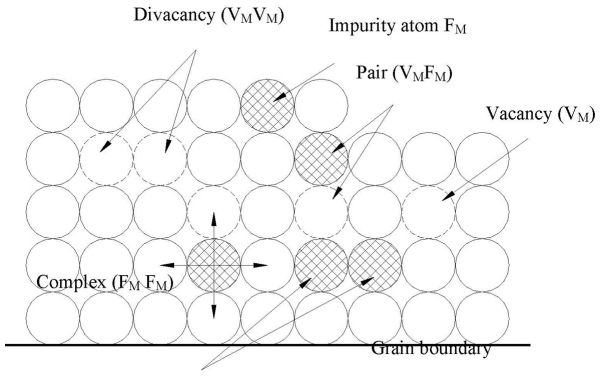

Figure 2: Diagram showing the interaction of lattice defects and possible directions of diffusion jumps simulated with the computer model in a (2D) structure
Slika 2: Diagram inmterakcije napak v mreži in možne smeri difuzijskih skokov, simuliranih z računalniškim modelom v 2D-strukturi

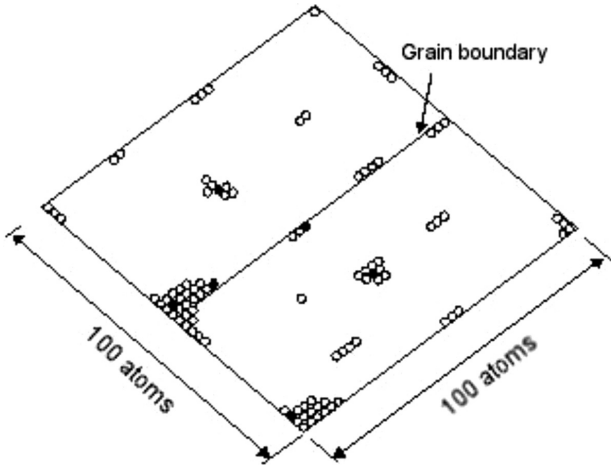

Figure 3: Two-dimensional lattice plane (2D) and grain boundary simulated with the computer model
Slika 3: Dvodimenzionalna mreža 2D in zrna, simulirana z računalniškim modelom

being situated in the centre of the plan, **Figure 3**. The grain boundary concentrates the atoms of impurities and the vacancies, which are annihilated after they have reached them. The point defects are initially distributed in the plane at random with given concentrations of the atoms. The mechanisms of segregation, desegregation and the formation of complexes are simulated based on a dynamic assessment of individual probabilities of a diffusive jump. These probabilities are multiplied by the factor of acceleration W_p in order to shorten the time of numerical calculations. Every cycle of the programme is modelled using W_p 10^{-13} s for the duration of the actual diffusion. Details concerning the model applied to simulate the process of diffusion had been presented in an earlier paper.[19]

3 ANALYSIS OF THE RESULTS

3.1 Results of microfractographic investigations and Auger spectrometric analysis

Industrial tin bronzes of the type CuSn6P, plastically deformed in the range of DMT, display an intercrystalline brittle fracture on microfractographs, **Figure 4**. Intercrystalline cracking, detected on the surfaces of crystalline grains at the boundaries, often run across the pores and defects characteristic for smelted structures. On intercrystalline surfaces, there are often distinct traces of plastic deformation and cavitation, **Figures 4c** and **4d**.

A spectrometric analysis in situ of the fractures of the investigated samples, fractured in the conditions of a high vacuum (UHV) permitted us to reveal the segregation of the admixture atoms and impurities at the grain boundaries, affecting essentially the process of intercrystalline cracking of the investigated tin bronzes. The results of the tests of tin bronze using the AES method and scanning electron microfractography are presented in **Figures 5** and **6**.

Auger emission spectrum recorded on the intercrystalline surfaces of bronze CuSn6P after its fracture in the range of DMT (about 300–600 °C) indicates, besides reference lines (Cu), also distinct lines of tin and sulphur as well as a double line of phosphorus, **Figure 5a**. The atypical shape of the P spectrum of the energy of electrons of the order of 117–120 eV probably results from the specific atomic bond Cu-P. The occurrence of a doublet of this type was proved experimentally in the spectrum of the Cu_3P phase.[17] It was found that both the number of the analysed spectral lines and their intensity depend essentially on the temperature of deformation.[20] It was also found that the tested walls of the fracture are distinctly enriched with Sn, S and P. Ionic etching (Ar^+) of the intercrystalline fractures of the CuSn6P bronze after the stretching in the range of DMT revealed that the S concentration obviously decreases in the course of etching to about 90 min, whereas the concentration of Sn decreases only inconsiderably and the concentration of P

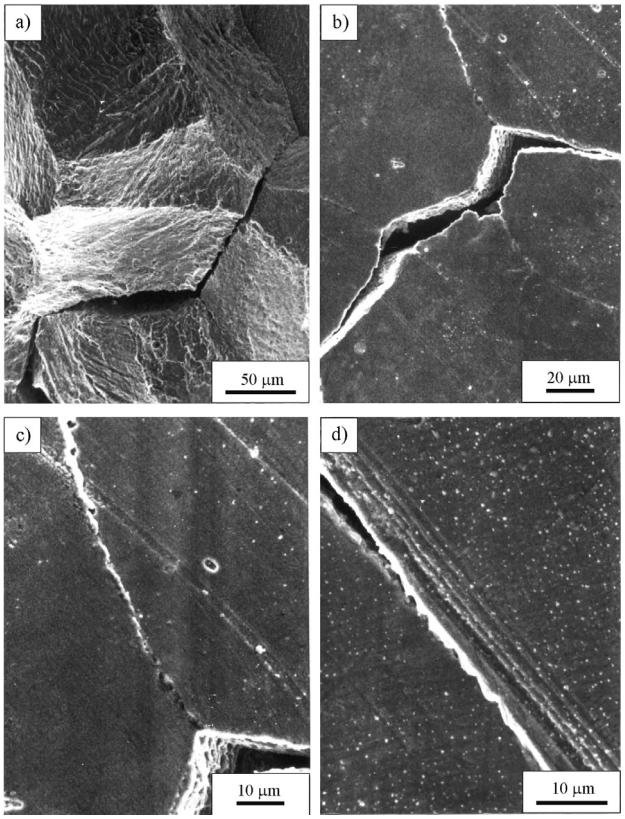

Figure 4: Fractography a) and intercrystalline fissures (b–d) of industrial bronze CuSn6P in the LR state after tensile tests at a strain rate of 10^{-5} s^{-1} and temperature of 400 °C: a) intergranular fracture, b) intercrystalline fissure, c) magnification of b), d) intercrystalline cavitations at the top of the fracture

Slika 4: a) Analiza površine zloma in (b–d) industrijskega brona CuSn6P in LR po nateznih preizkusih pri stopnji obremenitve 10^{-5} s^{-1} in tempreturi 400 °C: a) interkristalni zlom, b) interkristalna razpoka, c) povečava, d) interkristalne razpoke na vrhu zloma

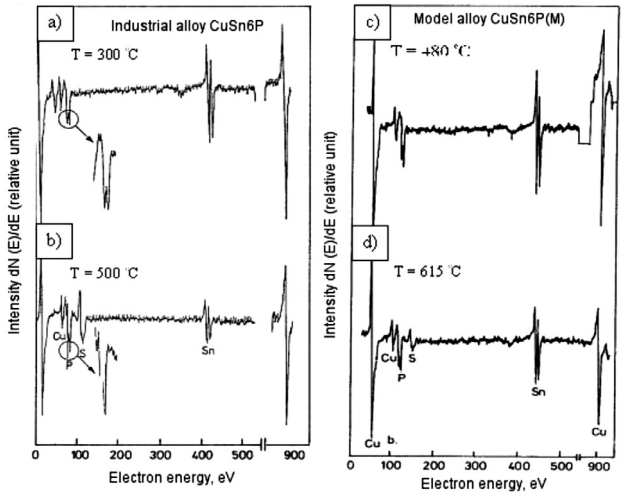

Figure 5: a) Auger spectrum of the intercrystalline fracture surface of industrial bronze CuSn6P and c) model bronze CuSn6P(M) after tensile tests at a) 300°C and c) 480°C

Slika 5: a) Augerjev spekter interkristalne površine zloma pri industrijskem bronu CuSn6P in b) modelu brona CuSn6P(M) po nateznih preizkusih pri a) 300 °C in c) 480 °C

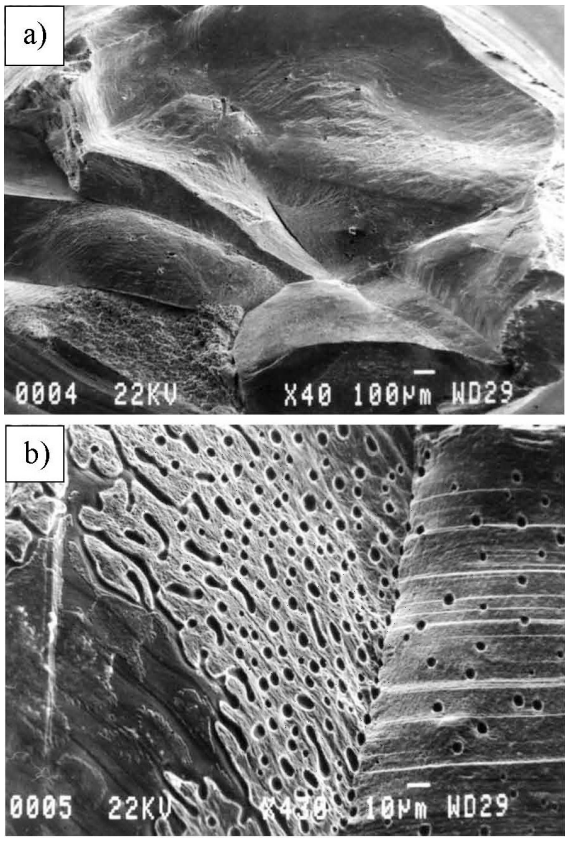

Figure 6: Fractography of industrial bronze CuSn6P analysed with the AES method after tensile tests at the temperature of 300 °C: a) intergranular brittle fracture, b) intergranular fracture with traces of plastic deformations of the surface

Slika 6: Analiza površine zloma pri industrijskem bronu CuSn6P, analiziranem z AES metodo po nateznih preizkusih pri temperaturi 300 °C: a) interkristalni krhki lom, b) interkristalni lom s sledovi plastičnih deformacij površine

practically does not decrease at all, **Figure 7**. The observed changes in the concentration of the components of the alloys (Sn, P) and S in the function of the time of etching prove the occurrence of the segregation of the atoms of these elements at the grain boundaries, probably clustered in monolayers or in the nanometric external layer.

3.2 Results of numerical simulations of the intercrystalline segregation

Numerical simulations of diffusive segregations of admixture atoms and impurities at the grain boundaries of the investigated tin bronze was previously tested with the investigations of the probability of a migration of point defects in (2D) structures. The repeatability of the observed changes in the concentration of the diffusing atoms in the function of the time of simulation was analysed, taking into account the a priori assumed randomness of the process of the model of atomic diffusion.[21] Besides, the operation of this programme was also tested in the case of the model alloys including a Fe-0.75 % amount fraction of B and a Cu-0.75 % amount fraction of Bi.[19]

The simulations of the process of the migration of the atoms of sulphur and vacancies to the grain boundary of the model alloy including a Cu-0.75 % amount fraction of S were performed for the analytically calculated values of the energy of bonding and migration, **Table 2**, and the assumed parameters of the simulation, the temperature of diffusion of 1000 K, the dimensions of the analysed atomic plane of the grains of 100 × 100 atoms, the coefficient of acceleration $W_p = 10^6$ as well as

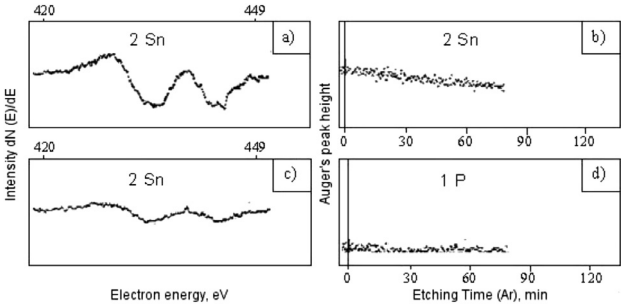

Figure 7: Selective Auger spectrum of tin atoms from the intergranular fracture of bronze CuSn6P after tensile tests at 300 °C: a) before etching, c) after ion-bombardment etching with Ar^+, b) concentration profile of Sn and P and d) as a function of the time of ion etching

Slika 7: Selektivni Augerjev spekter atomov kositra iz imnterkristalnega zloma brona CuSn6P po nateznih preizkusih pri 300 °C a) pred jedkanjem, c) po ionskem jedkanju z Ar^+, b) profil koncentracije Sn in P in d) kot funkcija časa jedkanja

Table 2: Energy of migration and bonding of the lattice defects calculated for the model alloy Cu-0.75 % amount fraction of S

Tabela 2: Energija migracij in povezave mrežnih napak, izračunane za model zlitine Cu-0.75 % atomskih deležev S

Kind of energy	Kind of lattice defect				
	Vacancy (v)	Divacancy (vv)	Impurity atom (i)	Complex biatomic impurity (ii)	Complex vacancy impurity (vi)
Forming energy E_f (eV)	1.49	2.87	1.54	3.03	2.59
Migration energy E_m (eV)	1.49	-	1.54	-	-
Kind of defect	Energy of bonding E_b (eV)				
	Vacancy	Impurity atom	Grain boundary		
Vacancy	0.14	0.34* 0.44	1.49		
Impurity atom	0.34* 0.44	0.1* 0.04	0.2* 0.18		
Grain boundary	1.49	0.2* 0.18	-		

** alternative values adopted to program the simulation*

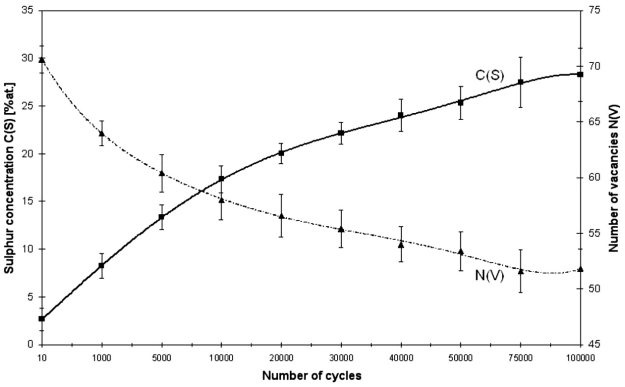

Figure 8: Dependence of the sulphur concentration and number of vacancies on the number of diffusion-simulation cycles concerning the model alloy Cu-0.75 % amount fraction of S and T = 1000 K

Slika 8: Odvisnost koncentracije žvepla in števila zasedenosti pri difuzija-simulacija ciklih za model zlitine Cu-0.75 % atomskih deležev S in T = 1000 K

the volumetric concentration of sulphur and the vacancy in the matrix of the alloy at the level of a 0.75 % amount fraction in the range of up to 100 thousands of iterative cycles.

The results of the simulations are gathered in diagrams on **Figures 8–13**. The analysed mean values of the concentration of sulphur and the number of vacancies in the matrix as a function of the number of cycles of simulations concerning the results of five simulations indicate an intensive increase in the concentration of sulphur in the zone of the grain boundary to about 20 % and in the case of about $2 \cdot 10^4$ cycles with a simultaneously distinctly decreased number of free vacancies in the matrix of the alloy, **Figure 8**.

After the subsequent cycles of iterations (about 10^5) the concentration of sulphur grows to about 25–30 % amount fractions and stabilizes at this level, forming clusters of vacancies and the atoms of sulphur in the

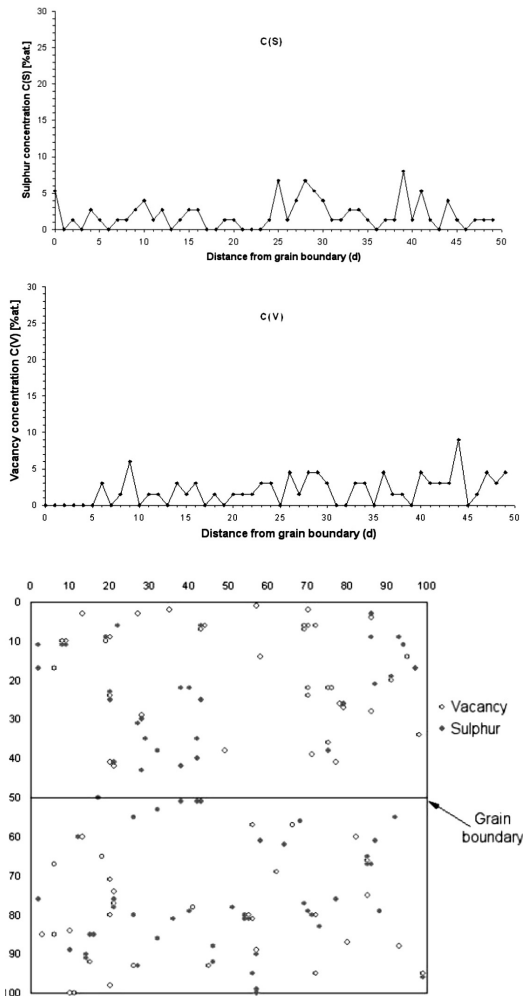

Figure 9: Distribution of sulphur and vacancy concentrations as a function of the distance from the grain boundary concerning the model alloy Cu-0.75 % amount fraction of S and T = 1000 K after a simulation of 10^3 cycles

Slika 9: Porazdelitev žvepla in koncentracija zasedenosti kot funkcija razdalje od mej zrn, model Cu-0.75 % atomskih deležev S in T = 1000 K po simulaciji 10^3 ciklov

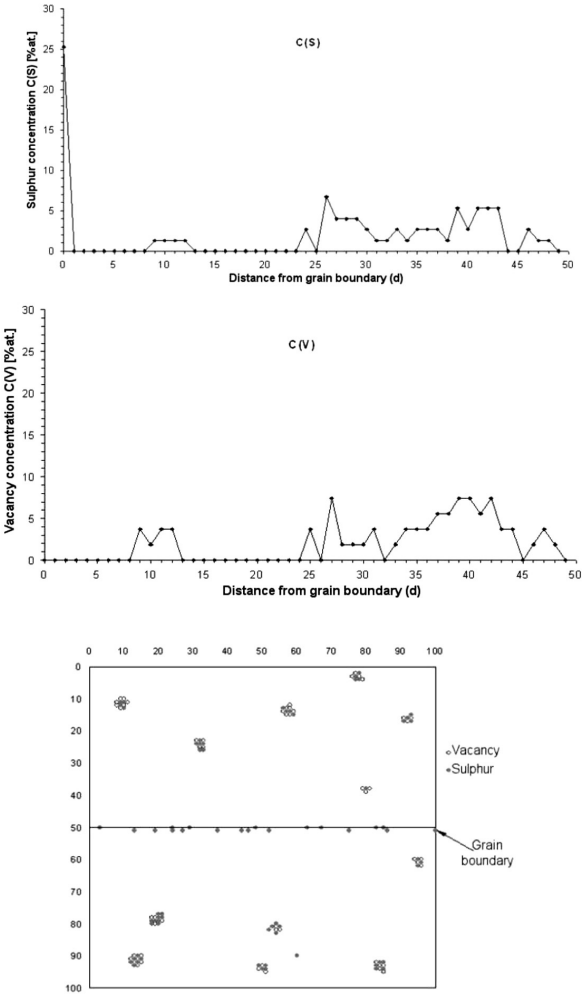

Figure 10: Distribution of sulphur and vacancy concentrations as a function of the distance from the grain boundary concerning the model alloy Cu-0.75 % amount fraction of S and T = 1000 K after a simulation of 10^5 cycles

Slika 10: Porazdelitev žvepla in področja koncentracij pri funkciji razdalje od mej zrn, model Cu-0.75 % atomskih deležev S in T = 1000 K po simulaciji 10^5 ciklov

areas distant from the grain boundary. Such a formation of the C(S) and C(V) concentrations proves the essential role of vacancies in the migration of sulphur atoms towards the grain boundary. The number of vacancies characterizes the amount of their flux in the direction of the grain boundary and the potential connection with the migration of the atoms of sulphur in this direction. The analysis of the kinetics of this process of migration of sulphur to the grain boundary proves that already after about 10^3 cycles of the simulation the concentration of sulphur in the monolayer at the grain boundary attains a value of 5 % amount fraction, **Figure 9**, and after 10^5 cycles – about 25 % amount fraction, **Figure 10**, accompanying the entire annihilation of the vacancies in this zone.

An increased concentration of vacancies to about 5–10 % is also observed in the areas of the matrix distant from the grain boundary by about 30–40 d, which indicates a nucleation of clusters of vacancies with the atoms of sulphur. These clusters may affect the atoms of impurities and free vacancies distributed stochastically in the matrix as additional sinks of defects. Thus, the size and distribution of stable clusters of point defects in the lattice may influence the extent of the resulting segregation of the atoms of sulphur on the grain boundary.

The assumed model simulating the diffusion of vacancies of point defects in the (2D) structure was also applied in the analysis of the influence of some parameters of simulation on the attained concentration of the atoms of sulphur at the grain boundary of the model alloy Cu-0.75 % amount fraction of S, **Figures 11–13**. Among others, it was found that the simulated concentration of sulphur at the grain boundary increases slightly with a decrease in the initial concentration of vacancies in the matrix of the alloy, **Figure 11**. The maximum index of the enrichment of the grain boundary with the atoms of sulphur amounts to about 60 concerning the initial concentration of vacancies of the order of 0.1 % amount fraction and the real time of migration of the atoms is about 10 ms. An increase of the analysed matrix to dimensions of 200 × 200 atoms, **Figure 12**, involves a proportional decrease of the atomic concentration of the atoms of sulphur in the function of the number of cycles, but without any essential qualitative changes in the analysed relation. The number of vacancies changes in a similar way. An evident effect on the simulation is exerted by the temperature of the process of diffusion, **Figure 13**. A drop in the temperature of diffusion by about 100 K results in a nearly twofold decrease in the concentration of the atoms of sulphur at the grain boundary and an inconsiderable change in the number of free vacancies in the matrix of the alloy in the investigated range of iterations.

Simulation of the vacancy diffusion of the atoms of tin to the grain boundary in the analysed model bronze Cu-3 % amount fraction of Sn, **Table 3**, showed that for

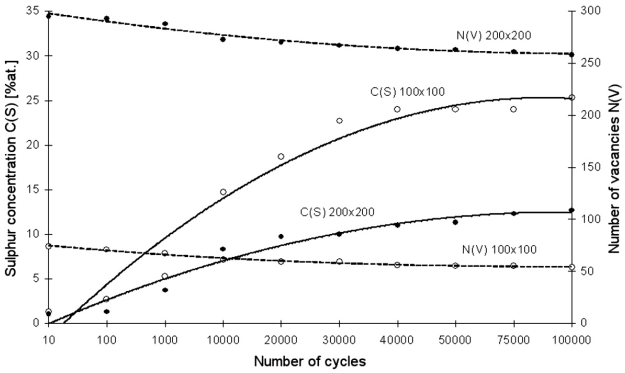

Figure 12: Effect of the size of the atomic plane on the relation between the sulphur concentration and number of vacancies on the number of diffusion-simulation cycles concerning the model alloy Cu-0.75 % amount fraction of S and T = 1000 K

Slika 12: učinek velikosti ravnine atomov na relaciji med koncentracijo žvepla in številom vrzeli na število difuzijsko simulacijskih ciklov pri modelu zlitine Cu-0,75 % atomskega deleža S in temperaturi 1000 K

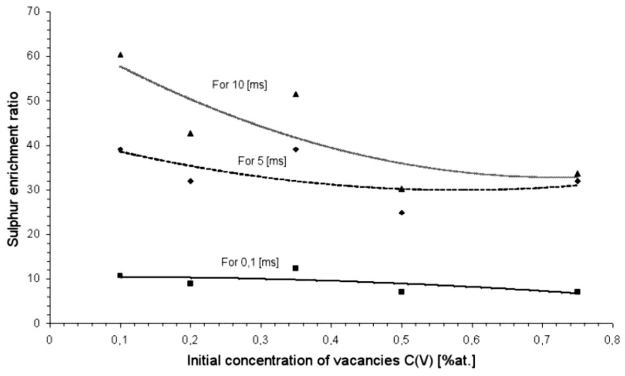

Figure 11: Dependence of the sulphur enrichment ratio at the grain boundary on the initial vacancy concentration in the case of model alloy Cu-0.75 % amount fraction of S and T = 1000 K

Slika 11: Odvisnost razmerja žveplove bogatitve na mejah zrn na začetni koncentraciji v primeru modela zlitine Cu-0,75 % atomskih deležev S in temperaturi 1000 K

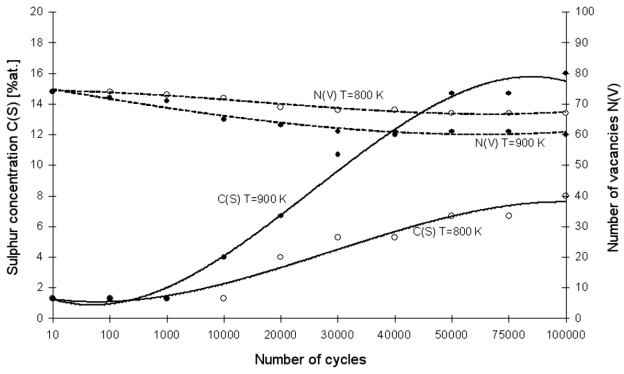

Figure 13: Effect of the diffusion temperature on the relation between the sulphur concentration and number of vacancies on the number of diffusion-simulation cycles concerning the model alloy Cu-0.75 % amount fraction of S and the matrix of 100 × 100 atoms

Slika 13: Učinek difuzije temperature na relacijo med žveplovo koncentracijo in številom vrzeli difuzijsko stimulacijskih ciklov pri modelu zlitine Cu-0,75 % atomskih deležev S in matriki 100 × 100 atomov

Table 3: Energy of migration and bonding of the lattice defects calculated for the model alloy Cu-3 % amount fraction of Sn
Tabela 3: Energija migracij in povezovanja mrežnih pomanjkljivosti za model Cu-3 % atomskih deležev Sn

Kind of energy	Kind of the lattice defect				
	Vacancy (v)	Divacancy (vv)	Impurity atom (i)	Complex biatomic impurity (ii)	Complex vacancy-impurity (vi)
Forming energy E_f (eV)	1.49	2.87	1.65	3.23	4.27
Migration energy E_m (eV)	1.49	-	1.65	-	-
Kind of defect	Energy of bonding E_b (eV)				
	Vacancy	Impurity atom	Grain boundary		
Vacancy	0.14	1.04* 1.13	1.49		
Impurity atom	1.04* 1.13	0.22* 0.07	0.3* 0.28		
Grain boundary	1.49	0.3* 0.28	-		

* *alternative values adopted to program the simulation*

the calculated values of the energy of the effect of point defects the concentration of the atoms of tin at the grain boundary of a (2D) structure increases only slightly with the growing number of iterated cycles, whereas the number of free vacancies in the matrix practically does not change at all, **Figure 14**. After about 10^3 iterated cycles, we can merely observe the effect of the grain boundary as the sink of vacancies without any visible change in the concentration of the atoms of tin in the zone adjacent to the boundary.

A detailed analysis of the changes in the concentration of C(Sn) and C(V) in the function of the distance from the grain boundary permits us to state that, in this stage of simulating the diffusion, we can observe a distinct formation of potential areas of clusters of tin atoms and vacancies. An insignificant enrichment of tin at the grain boundary (about 7 % amount fraction) and an evident localisation of the cluster of (Sn_MV_M) were, however, seen after about 10^5 cycles of the simulation, **Figure 15**.

Computer-aided simulations of lattice diffusion, accomplished on the basis of the newly developed software DYFUZJA, confirmed the possibility of segregations of atoms of S and Sn generated at the grain boundary of the model structure (2D) of the analysed alloys of copper composed of Cu-0.75 % amount fraction of S, **Figures 8–13**, and Cu-3 % amount fraction of Sn, **Figures 14** and **15**. The obtained results coincide, more or less, with the AES experimental results.

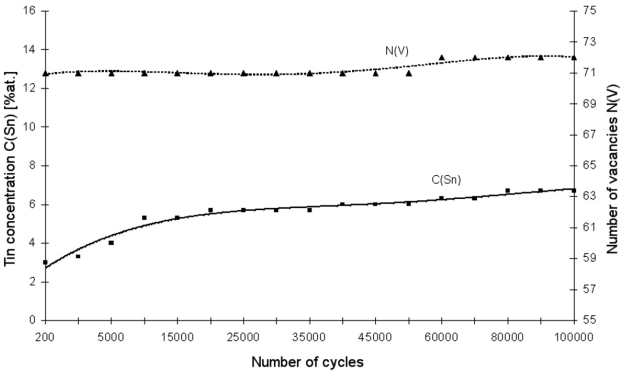

Figure 14: Dependence of the tin concentration and number of vacancies on the number of diffusion-simulation cycles concerning the model bronze Cu-3 % amount fraction of Sn and T = 1000 K

Slika 14: Odvisnost koncentracije kositra in število vrzeli glede na število difuzijskih simulacijskih ciklov glede na model brona Cu-3 % atomskih deležev Sn in T = 1000 K

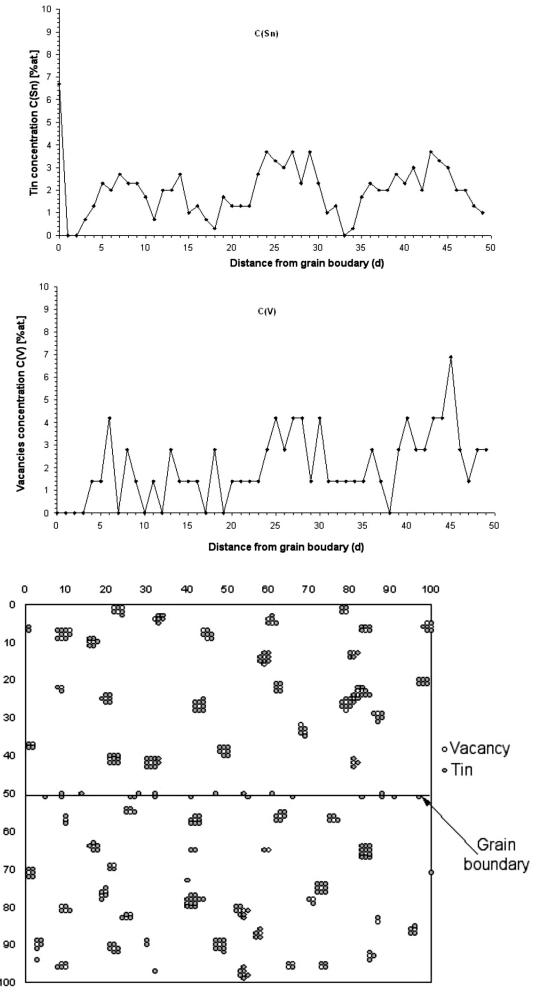

Figure 15: Distribution of tin and vacancy concentrations as a function of the distance from the grain boundary concerning the model bronze Cu-3 % amount fraction of Sn and T = 1000 K after a simulation of 105 cycles

Slika 15: Razpršenost kositra in koncentracije vrzeli kot funkcije razdalj od mej zrn glede na model brona Cu-3 % atomskih deležev Sn in T = 1000 K po simulaciji 150 ciklov

An important problem concerning the attainment of reliable results of a computer-aided simulation of the migration of admixture atoms or impurities to the grain boundary of a (2D) structure is, besides the correctness of the assumed mathematical model, the application of adequate data to the simulative calculations, mainly the physical quantities describing the elements of the computer model and the simulated process. These quantities are usually not available in the literature. The model must take into account the energy of bonding of the point defects with each other (E_b^{didj}), e.g., E_b^{vv}, E_b^{vi}, E_b^{ii} as well as the energy that bonds them with the grain boundary (E_b^{dib}), e.g., E_b^{ib}, E_b^{vb} where d_1, d_2 ... denote the numbers expressing the kind of point defects (vacancies, alloy atoms or impurities) and also the respective energy of migration (E_b^{di}), **Tables 4.2–4.5**. The methods for determining the energy of bonding E_b^{vv}, E_b^{ii} or E_b^{vi} differ considerably from each other, and the obtained results indicate a large scattering of these values[11]. In spite of the fact that the methods of calculations take into account both the elements of the theory of elasticity and the electron factors, as well as the valencies of the formed pairs of distances and the values of their inter-atomic potentials of the Morse type, the degree of accuracy of these methods is still uncertain.

4 CONCLUSION

The results of the performed experimental investigations and the numerical analysis concerning the processes of diffusive intercrystalline segregations in tin bronzes lead to the formulation of the following conclusions:

The Auger spectrometric analysis of the intercrystalline fractures in single-phase tin bronze of the CuSn6P type, stretched in the DMT range, carried out in situ, indicates a segregation of the atoms of S and Sn with various intensities depending mainly on the temperature of deformation.

Computer simulations of the process of lattice vacancy diffusion confirm the variated possibility of the segregation of the atoms of sulphur and tin generated at the grain boundary in the two-dimensional model structure of the theoretically analysed copper alloys with the following composition: Cu-0.75 % amount fraction of S and Cu-3 % amount fraction of Sn. The effect of the segregations in the atomic nanolayer at the grain boundary in the Cu-S system and a merely slight effect of enrichment of this atomic layer of Sn are quite evident in the case of the Cu-Sn composition.

The newly developed programme of computer-aided simulation DYFUZJA, in the actual version, permits us to simulate and visualize the atomic diffusion to the grain boundary of a modelled (2D) structure, taking into account the maximum of four different admixture elements or impurities in the function of the concentration of the investigated elements and vacancies in the matrix of the alloy: the temperature of diffusion, the preliminarily calculated values of the energy of the effects of lattice defects, the size of the atomic plane and the value of the coefficient of acceleration.

The simulated effects of the segregation of atoms to the grain boundary, analysed as a function of the number of the cycles of the simulation are characterized by a statistically good repeatability of the results.

5 REFERENCES

[1] E. D. Hondros, M. P. Seah, Segregation to Interfaces, International Metals Review, 222 (**1977**), 262–301

[2] M. P. Seah, Grain boundary segregation and the *T*–*t* dependence of temper brittleness, Acta Metallurgica, 25 (**1977**) 3, 345–357, doi:10.1016/0001-6160(77)90153-5

[3] R. G. Faulkner, Non-equilibrium grain-boundary segregation in austenitic alloys, Journal of Materials Science, 16 (**1981**), 373–383, 10.1007/BF00738626

[4] K. T. Aust, S. J. Armijo, E. F. Koch, J. A. Westbrook, Vacancy-driven grain boundary segregation, Transactions ASM, 60 (**1967**), 360

[5] R. Anthony, Solute segregation in vacancy gradients generated by sintering and temperature changes, Acta Metallurgica, 17 (**1969**), 603–609, doi:10.1016/0001-6160(69)90120-5

[6] T. M. Williams, A. M. Stoneham, D. R. Harries, The segregation of boron to grain boundaries in solution-treated Type 316 austenitic stainless steel, Metal Science, 10 (**1976**), 14–19, doi:10.1179/030634576790431471

[7] P. Doig, J. Flewitt, Segregation of chromium to prior austenite boundaries during quenching of a 214%Crl%Mo steel, Acta Metallurgica, 29 (**1981**) 11, 1831–1841, doi:10.1016/0001-6160(81)90109-7

[8] R. G. Faulkner, Combined grain boundary equilibrium and non-equilibrium segregation in ferritic/martensitic steels, Acta Metallurgica, 35 (**1987**) 12, 2905–2914, doi:10.1016/0001-6160(87)90289-6

[9] R. Rice, Effect of Hydrogen on Behavior of Materials, Metallurgical Society of AIME, New York, (**1976**), 455–466

[10] D. McLean, Grain boundaries in metals, Oxford Univ. Press, 1957

[11] M. A. V. Chapman, R. G. Faulkner, Computer modelling of grain boundary segregation, Acta Metallurgica, 31 (**1983**), 677–689, doi:10.1016/0001-6160(83)90083-4

[12] C. Waite, R. G. Faulkner, A new computer model of grain boundary segregation, Journal of Materials Science, 25 (**1990**), 649–653, doi:10.1007/BF00714089

[13] R. G. Faulkner, Grain boundary non-equilibrium segregation in steels, Journal de Physique Colloques, 51 (**1990**) C1, 133–138

[14] H. Jiang, R. G. Faulkner, Modelling of grain boundary segregation, precipitation and precipitate-free zones of high strength aluminium alloys – II. Application of the models, Acta Materialia, 44 (**1996**) 5, 1865–1871, doi:10.1016/1359-6454(95)00318-5

[15] S. Mrowec: Theory of diffusion in solid state, PWN, Warsaw (1989)

[16] O. H. Wyatt, D. Dew Hughes, Metals, ceramics and polymers, Cambridge University Press, Cambridge, 1974, ISBN 10: 0521082382, ISBN 13: 9780521082389

[17] W. Ozgowicz, M. Biscondi, High-Temperature Brittleness and Interfacial Segregation in Tin Bronzes, Journal de Physique IV Colloque, 05 (**1995**) C7, 315–320, doi:10.1051/jp4:1995738>.<jpa-00254032>

[18] W. Ozgowicz, Zastosowanie analizy Augera w próbach rozciągania na gorąco miedzi i jej stopów, Materials, mechanical & manufacturing engineering, M3E'2000, Proceedings of the scientific conference, Gliwice, **2000**, 221–226

[19] W. Ozgowicz, E. Kosek, Computer simulation of the diffusive segregation of impurities on the grain boundaries of metallic polycrystals, Archiwum nauki o materiałach, 2 (**2004**), 93–112

[20] W. Ozgowicz, Physico-chemical, structural and mechanical factors of intergranular brittleness of α-bronzes at elevated temperature, Silesian Techn. Univ., Gliwice, Mechanics, Z.145 (2004) (in Polish)

[21] W. Ozgowicz, KBN Report, Nr. 7T08A02517, Silesian Techn. Univ., Gliwice, 2002

UDK 67.017:620.1:621.385.833
Original scientific article/Izvirni znanstveni članek

ISSN 1580-2949
MTAEC9, 51(3)373(2017)

COMPARISON OF HOMOGENIZATION APPROACHES USED FOR THE IDENTIFICATION OF THE MATERIAL PARAMETERS OF UNIDIRECTIONAL COMPOSITES

PRIMERJAVA HOMOGENIZACIJSKIH PRIBLIŽKOV ZA UGOTAVLJANJE PARAMETROV MATERIALA ENOSMERNIH KOMPOZITOV

Hana Srbová, Tomáš Kroupa, Vladimír Lukeš

University of West Bohemia in Pilsen, NTIS – New Technologies for the Information Society, Univerzitní 22, 306 14, Plzeň, Czech Republic
hsrbova@kme.zcu.cz

Prejem rokopisa – received: 2015-07-01; sprejem za objavo – accepted for publication: 2016-06-06

doi:10.17222/mit.2015.177

The paper is aimed at the identification of the material parameters of the constituents of unidirectional long-fiber carbon/epoxy composites. The ratios between the real fiber and the matrix volume of unidirectional fiber composites were identified from the images obtained with scanning electron microscopy (SEM). Fiber and matrix areas were analyzed using Matlab and its image-processing toolbox. Determined volume ratios were used to propose the geometry of a micromechanical representative volume element. An algorithm ensuring an irregular fiber distribution in the representative volume element cross-section and periodicity in the cross-section plane were used. A single-layer representative volume element with a mesh was built in Abaqus/CAE. Experimentally obtained force-elongation dependencies for the tensile tests of the specimens with different fiber orientations were processed and effective moduli were determined. In the first approach, the material parameters of phases were identified using the OptiSlang optimization software and finite-element code Abaqus. A periodically constrained representative volume element was loaded according to the experiments where specimens with different fiber orientations were loaded by tensile force. In the second approach, the SfePy software and asymptotic homogenization were used for the numerical computation on the microscopic scale, resulting in the homogenized material parameters that were afterwards used at the macroscopic level. The optimization function characterized the sum of the differences of the effective moduli and the difference of Poisson's ratios of the whole composite.

Keywords: composite, unidirectional, micro-model, constituents, material parameters, cross-section, homogenization

Namen članka je ugotavljanje materialnih parametrov sestavin epoksi kompozitov z enosmernim dolgimi ogljikovimi vlakni. Razmerje realnih vlaken in volumna osnove kompozitov z usmerjenimi vlakni je bilo določeno iz slik, dobljenih na vrstičnem elektronskem mikroskopu (SEM). Vlakna in področja osnove so bili analizirani s pomočjo Matlaba in njegovega orodja za obdelavo slik. Določena volumska razmerja so bila uporabljena za predlog geometrije reprezentativnih mikromehanskih volumskih elementov. Uporabljen je bil algoritem, ki zagotavlja neenakomerno razporeditev vlaken na preseku reprezentativnega volumskega elementa in periodičnost na ravnini preseka. Plast reprezentativnega volumskega elementa z mrežo, je bila postavljena z Abaqus/CAE. Izvedeni so bili eksperimenti za določanje odvisnosti sila-raztezek pri nateznih preizkušancih z različno orientacijo vlaken in določeni so bili efektivni moduli. V prvem približku so bili ugotavljani materialni parametri faz s pomočjo OptiSlang programske opreme za optimizacijo in kodo končnih elementov Abaqus. Periodično omejen reprezentančni volumski element je bil obremenjen, skladno s preizkusi. Pri čemer so bili vzorci z različno orientacijo vlaken, obremenjeni z natezno silo. Pri drugem približku je uporabljena programska oprema SfePy in asimptotična homogenizacija, za numerične izračune na mikroskopskem nivoju, kar se je odrazilo v homogenih parametrih materiala, ki so bili kasneje uporabljeni na makroskopskem nivoju. Optimizacijska funkcija je karakterizirana z vsoto razlik efektivnega modula in razliko Poissonovega razmerja za celoten kompozit.

Ključne besede: kompozit, enosmernost, mikromodel, sestavine, parametri materiala, presek, homogenizacija

1 INTRODUCTION

The experiments are the main tools and play a dominant role in the characterization of mechanical behavior of materials.[1–4] Nevertheless, in some cases, it is advantageous to support experimental measurements with the knowledge of the behavior of the considered material at the micro- or meso-scale level (low scale).[5–7] A precisely calibrated low-scale model can be helpful in the cases where all the necessary material parameters for a macro-scale model are impossible to be characterized or in the case when the initiation or propagation of the processes observed on the micro-scale are not clear.

Anisotropy and heterogeneity of the inner structure and homogeneity of virtual macro-scale models of composite materials call for low-scale-model processing. The presented paper is aimed at a comparison of two methodologies for the identification of the material parameters of the substituents of unidirectional carbon-epoxy composites. There are several different approaches for homogenization and low-scale modelling, the presented paper deals with two of these. The first approach uses the advantages of commercial software Abaqus 6.14-2 and its wide range of pre- and post-processing tools including the possibility of an automatic model construction using the Python software.[5] The second approach uses

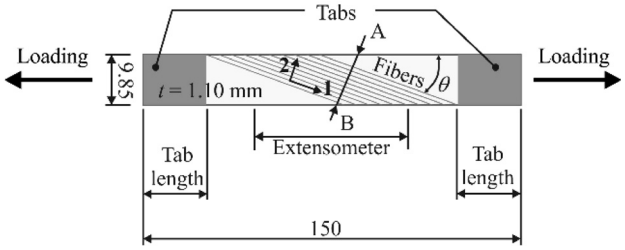

Figure 1: Geometry of coupons (mm), the cross-section (A-B)
Slika 1: Geometrija kuponov (mm), presek A-B)

the well established theory of asymptotic homogenization,[6,7] which is implemented in the SfePy finite-element software.[8–10]

2 SPECIMENS AND THE EXPERIMENTAL PART

Carbon-epoxy unidirectional continuous-fiber composite coupons were subjected to tensile loading. Rectangular specimens (coupons) were cut by a waterjet from a composite plate made of eight equally oriented layers, the so-called prepregs with 40 % of epoxy HexPly 913C with fiber Tenax HTS 5631 cured for 120 minutes at a temperature of 125 °C and a pressure of 6 bar. There were 5 specimens tested for each of the following fiber orientations (10, 20, 30, 40, 50, 60, 70, 80 and 90)° with respect to the loading direction. Only two specimens were successfully tested up to the allowable type of rupture with fiber orientation 0°.

Force-elongation dependencies were obtained using a Zwick Roell/Z050 test machine where force values were estimated by a force cell and the gage area elongation was measured using a uniaxial macro-extensometer. The tested coupons with glass textile (0°) or aluminum tabs (10, 20, 30, 40, 50, 60)° were bonded with high-strength and tough epoxy adhesive Spabond 345. In the case of the specimens with fiber orientations (70, 80 and 90)° a non-bonded emery cloth was used as the interface between the grip and the coupon. The tab configuration summarized in **Table 1** led to the required gage-section tensile failure (**Figure 2**).

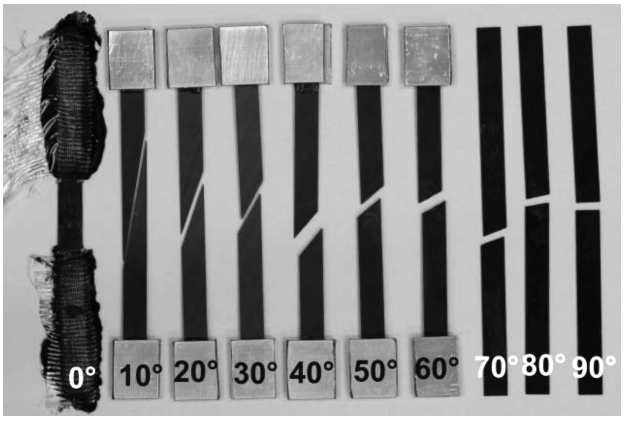

Figure 2: Cracked specimens, the final crack direction is parallel to the fibers for directions 10°–90° and perpendicular for direction 0°
Slika 2: Porušeni vzorci, usmeritev končne razpoke je vzporedna z vlakni za smeri 10°–90° in pravokotna za smer 0°

Table 1: Experiment configuration
Tabela 1: Konfiguracija preizkusov

Fiber orientation (°)	Tab material	Tab length (mm)	Extensometer length (mm)
0	glass textile	60.0	10.0
10, 20, 30, 40, 50, 60	aluminum	25.0	60.0
70, 80, 90	emery cloth	25.0	60.0

3 IDENTIFICATION

Two linear material models were supposed to be calibrated using a combination of finite-element analyses, optimization methods and experiments.[11,12] The targets for the identification process were calculated from the experimental results before the identification process in Python began. The nominal stress was calculated from the applied tensile force F as:

$$\sigma = \frac{F}{A} \tag{1}$$

where A is the cross-section of a non-loaded specimen. The strain was calculated as

$$\varepsilon = \frac{F}{A} \tag{2}$$

Where Δl is the elongation of the gage area (between the arms of the extensometer) and l is the original gage length.

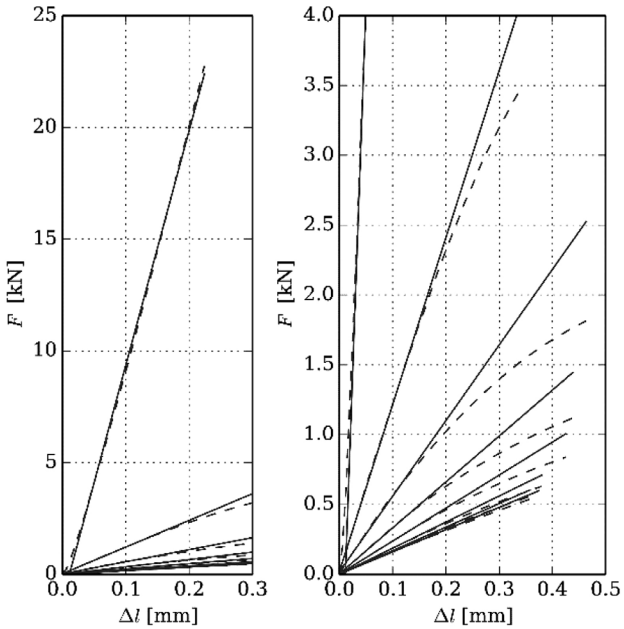

Figure 3: Tensile dependencies (dashed lines) and calculated targets for further identification (solid lines)
Slika 3: Natezne odvisnosti (črtkana linija) in izračunani cilji za nadaljnjo identifikacijo (polna črta)

The target for each tensile test was calculated as least-squares fit of the straight line through the interval of the nominal strain ⟨0, 0.25 %⟩ in the case of the concave dependency of force on elongation (**Figure 3**). The only exceptions are the experimental results with 0° direction of the fibers where the target was calculated as least-squares fit of the straight line through the whole force-elongation dependency (**Figure 3**). The results for 0° fiber orientation are influenced by the uncertainties caused by the penetration of the glass textile by the jaws of the machine at the beginning of the measurement (the loading process).

The tangents k^{E} of the fitted straight lines in the force-elongation diagram for each fiber orientation were taken as the values to be achieved in the numerical model. The only additional condition, which should be met in the model, is that Poisson's ratio v_{12}^{C} of the whole composite should be as close as possible to the value of 0.28 (the measured value and the value obtained from the manufacturer). The residual function r to be minimized in the identification processes, regardless of the used homogenization approach (homogenization using the commercial software Abaqus or asymptotic homogenization performed in SfePy), has the following form:

$$r = \sum_{\theta} \left(1 - \frac{k^{\mathrm{N}}(\theta)}{k^{\mathrm{E}}(\theta)} \right)^2 + \left(1 - \frac{v_{12}^{C}}{0.28} \right)^2 \tag{3}$$

Where θ is the fiber angle (the type of specimen) and k^{N} is the tangent of the numerically obtained results (**Figure 3**). Gradient algorithms implemented in the OptiSLang and Python software were used for the identification.[12]

4 CREATING A REPRESENTATIVE UNIT CELL

The representative volume element with a random distribution of fibers was built with an event-driven algorithm for simulating chaotically colliding billiard balls[13] in Matlab. Each component (a fiber in this case) moves along a straight line until it collides with another component. Events (collisions) are processed in a non-decreasing order of time and interactions are scheduled using pre-integrated equations of the evolutions of the components. In the case of a uniform-component distribution, the evolution space is subdivided into small sectors so that only the components in the neighboring sectors have to be checked to determine the immediate collision and the time for processing the expected event is reduced. The defined fiber volume fraction is ensured with the termination criterion controlled by an increase in the volume fraction of the components.[14]

Periodicity of the volume element is ensured by a component disappearing at a boundary and reappearing at the opposite side (**Figure 4**).

The calculation of the fiber volume fraction was performed in the Matlab software. Digital images obtained with scanning electron microscopy (SEM) were analyzed (**Figure 5**) and the identified fiber volume fraction of the composite material is $V_{\mathrm{f}}^{\mathrm{image}} = 0.59$ The average fiber radius was identified as $R_{\mathrm{f}} = 6.488\ \mu$m. The rectangular area with 15 fibers and dimensions of 28.7334 × 28.7334 μm was discretized in Abaqus/CAE by hexahedral 8-node linear isoparametric elements and wedge 6-node linear isoparametric elements (**Figures 5** and **7**).

The finite-element mesh was built with only one layer of elements in the fiber direction. The fiber direction and loading direction are shown in **Figure 6**.

5 MATERIAL MODELS

The infinitesimal strain theory was considered when proposing the material models. The material model of fibers was linear, transversely isotropic and the behavior in the plane perpendicular to the fiber axis was considered to be isotropic. Five material parameters define this type of material. A material model of the matrix was proposed to be linear isotropic with two parameters necessary for the description of its behavior. The material model can be written in the matrix form as

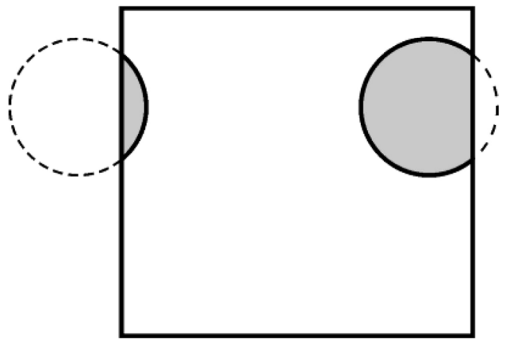

Figure 4: Parts of the fiber at the area boundaries in accordance with periodic boundary conditions

Slika 4: Deli vlakna na področju mej v skladu s pogoji periodičnosti meje

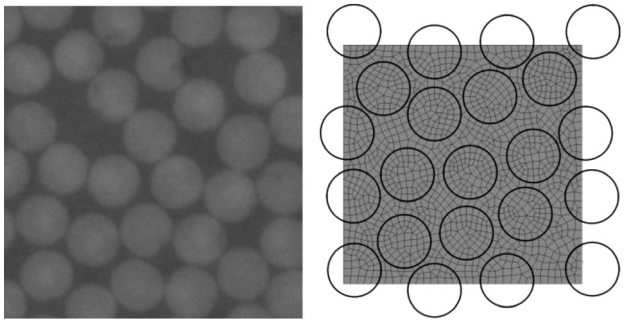

Figure 5: Image of cross-section (A-B) of unidirectional long fiber composite obtained with SEM (left) and unit cell with generated finite elements (right) and depicted fiber edges (black circles)

Slika 5: SEM-posnetek preseka (A-B) enosmernih dolgih vlaken v kompozitu (levo) in enotna celica z ustvarjenimi končnimi elementi (desno) in prikaz robov vlakna (črni krogi)

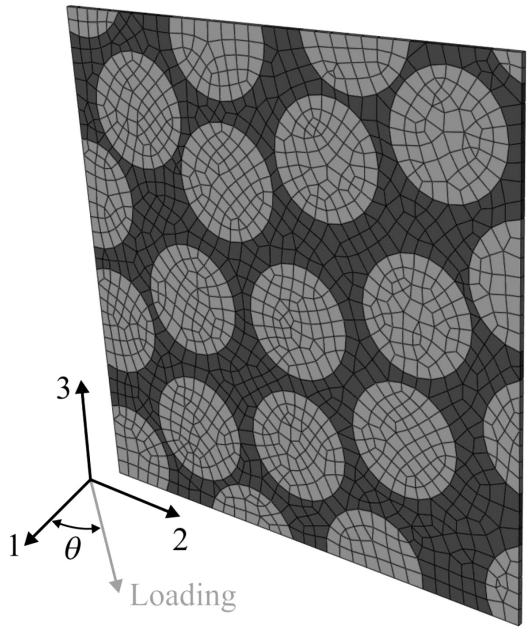

Figure 6: Material principal and loading-force directions
Slika 6: Glavni material in smeri sile obremenitve

$$\begin{bmatrix} \varepsilon_1 \\ \varepsilon_2 \\ \varepsilon_3 \\ \gamma_{12} \\ \gamma_{13} \\ \gamma_{23} \end{bmatrix} = \begin{bmatrix} S_{11} & S_{12} & S_{13} & 0 & 0 & 0 \\ S_{12} & S_{22} & S_{23} & 0 & 0 & 0 \\ S_{13} & S_{23} & S_{33} & 0 & 0 & 0 \\ 0 & 0 & 0 & S_{44} & 0 & 0 \\ 0 & 0 & 0 & 0 & S_{55} & 0 \\ 0 & 0 & 0 & 0 & 0 & S_{66} \end{bmatrix} \cdot \begin{bmatrix} \sigma_1 \\ \sigma_2 \\ \sigma_3 \\ \tau_{12} \\ \tau_{13} \\ \tau_{23} \end{bmatrix} \quad (3)$$

Where ε_i is the normal engineering strain in direction i, γ_{ij} is the engineering shear strain in the ij plane, all being the elements of the strain tensor ε, σ_i is the normal stress in direction i and τ_{ij} is the shear stress in the ij plane, all being the elements of the stress tensor σ. The elements of the compliance matrix S, the elasticity tensor in the inverse shape, are, in the case of isotropic material, as follows in Equation (4):

$$S_{11} = S_{22} = S_{33} = \frac{1}{E}$$
$$S_{12} = S_{13} = S_{23} = -\frac{v}{E} \quad (4)$$
$$S_{44} = S_{55} = S_{66} = \frac{E}{2(1+v)}$$

and in the case of transversely isotropic material in Equation (5):

$$S_{11} = \frac{1}{E_1} \qquad S_{22} = S_{33} = \frac{1}{E_2}$$
$$S_{12} = S_{13} = -\frac{v_{12}}{E_1} \qquad S_{23} = -\frac{v_{23}}{E_2} \quad (5)$$
$$S_{44} = S_{55} = \frac{1}{G_{12}} \qquad S_{66} = \frac{2(1+v_{23})}{E_2}$$

The meanings of the material constants (parameters) of the models mentioned above are given in **Table 2**.

Table 2: Description of material constants
Tabela 2: Opis konstant materiala

Constant	Unit	Meaning
Fibers		
E_1	(Pa)	Young's modulus in the axis direction
E_2	(Pa)	Young's modulus in the radial direction
v_{12}	(-)	Poisson's ratio in the planes parallel to the fiber axis
v_{23}	(-)	Poisson's ratio in the planes perpendicular to the fiber axis. This parameter was defined by the manufacturer.
G_{12}	(Pa)	Shear modulus in the planes parallel to the axis of the fiber
Matrix		
E	(Pa)	Young's modulus
v	(-)	Poisson's ratio

5.1 Micro-model in the commercial software

The geometry of the finite-element model (a micro-model) of the periodically repeated volume (a unit cell) of the unidirectional fiber composite material was created in Abaqus/CAE 6.14-2.

The global coordinate system (xyz) is given by the force direction (x) and the direction perpendicular to the composite surface (z). The local coordinate system (123) is defined by the unit-cell edges where the axis directions correspond to the fiber direction (1) and the directions perpendicular to it (**Figure 7**).

Assuming a uniaxial stress across the whole specimen, the behavior of the material can be simulated by loading the unit cell with the normal stress corresponding to the external tensile force F.

The loading force is represented by stress σ_x obtained with Equation (1) and transformed to the local coordinate system using the following form:

$$\begin{bmatrix} \sigma_1 \\ \sigma_2 \\ \tau_{12} \end{bmatrix} = \begin{bmatrix} \cos^2\theta & \sin^2\theta & 2\sin\theta\cos\theta \\ \sin^2\theta & \cos^2\theta & -2\sin\theta\cos\theta \\ -\sin\theta\cos\theta & \sin\theta\cos\theta & \cos^2\theta - \sin^2\theta \end{bmatrix} \cdot \begin{bmatrix} \sigma_x \\ 0 \\ 0 \end{bmatrix} \quad (6)$$

where θ is the angle of rotation between the local and global coordinate systems, e.g., between the fiber direction and force direction in the experiment.[1,2]

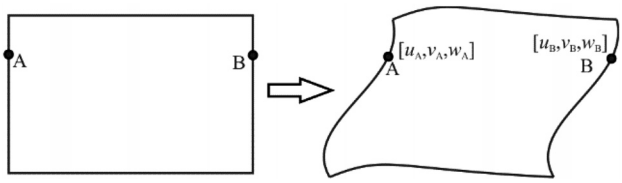

Figure 7: Equivalently deformed opposite boundaries of a heterogeneous unit cell
Slika 7: Ekvivalentno deformirani nasprotni meji heterogene enotne celice

The results of the finite-element analysis (strains) are transformed back to the global coordinate system using the following form:[5]

$$\begin{bmatrix}\varepsilon_x\\ \varepsilon_y\\ \gamma_{xy}\end{bmatrix}=\begin{bmatrix}\cos^2\theta & \sin^2\theta & -\sin\theta\cos\theta\\ \sin^2\theta & \cos^2\theta & \sin\theta\cos\theta\\ 2\sin\theta\cos\theta & -2\sin\theta\cos\theta & \cos^2\theta-\sin^2\theta\end{bmatrix}\cdot\begin{bmatrix}\varepsilon_1\\ \varepsilon_2\\ \gamma_{12}\end{bmatrix} \quad (7)$$

The unit cell must also follow the periodic boundary conditions:[5–7]

$$\begin{aligned}\Delta u &= u_B - u_A\\ \Delta v &= v_B - v_A\\ \Delta w &= w_B - w_A\end{aligned} \quad (8)$$

where Δu, Δv and Δw are the translation differences of the opposing pair of nodes in directions 1, 2 and 3, respectively. These differences must remain constant for all the pairs of the corresponding nodes on opposite sides.[5]

The periodical boundary conditions were implemented in Abaqus/CAE 6.14-2 using equation constraints.

6 ASSYMPTOTIC HOMOGENIZATION

The two-scale asymptotic homogenization method is used to identify the material parameters of the periodic composite structure. The linear elastic medium (occupying domain Ω) whose microstructure can be represented by a periodic (representative) volume element associated with region Y and consists of the matrix part Y_m and fibers Y_f (**Figure 8**). Using the standard method of asymptotic expansion[8] applied to the linear elastic problem, we get a microscopic equation formulated in terms of the characteristic response function and a macroscopic equation that involves the homogenized elasticity parameters.[6,8]

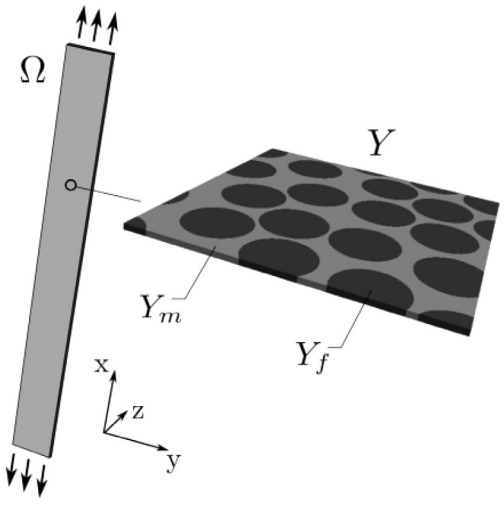

Figure 8: Macroscopic domain Ω and microscopic domain Y (representative volume element) consisting of fibers Y_f and matrix Y_m
Slika 8: Makroskopska domena Ω in mikroskopska domena Y (reprezentativni volumski element), ki sestoji iz vlaken Y_f in osnove Y_m

The problem at the microscopic level can be formulated to find the characteristic response function $\chi^{rs} \in H_{\#}(Y)$ so that:

$$\begin{aligned}&\int_Y D_{ijkl}\varepsilon^y_{kl}(\chi^{rs})\varepsilon^y_{ij}(\omega)\mathrm{d}Y =\\ &\int_Y D_{ijkl}\varepsilon^y_{kl}(\Pi^{rs})\varepsilon^y_{ij}(\omega)\mathrm{d}Y\ \forall\omega \text{ in } H_{\#}(Y)\end{aligned} \quad (9)$$

where $\varepsilon^y(\cdot)$ is the linear strain tensor with respect to the microscopic coordinate y, $\Pi_i^{rs} = y_s\delta_{ri}$, $H_{\#}(Y)$ is the set of Y-periodic functions with the zero average value in Y. The elasticity tensor $D = S^{-1}$ is defined as:

$$\begin{aligned}&D = D(y) =\\ &= \begin{cases} D^f \text{ in } Y_f \text{ (transvers. isotropic fibers)}\\ D^m \text{ in } Y^m \text{ (isotropic matrix)}\end{cases}\end{aligned} \quad (10)$$

The solution of the microscopic equation, which has to be solved with the periodic boundary conditions, is used to evaluate the homogenized elasticity tensor:

$$D^H_{ijkl} = \frac{1}{|Y|}\int_Y D_{pqrs}\varepsilon^y_{rs}(\Pi^{kl}-\chi^{kl})\varepsilon^y_{pq}(\Pi^{ij}-\chi^{ij})\mathrm{d}Y \quad (11)$$

The homogenized (macroscopic) elasticity problem can be expressed with Equation (12):

$$\int_Y D^H_{ijkl}\varepsilon^x_{kl}(\mathbf{u}^0)\varepsilon^y_{ij}(\mathbf{v}^0)\mathrm{d}Y = \int_{\Gamma_t} v_i^0 t_i \mathrm{d}\Gamma \quad (12)$$

which is solved for the unknown macroscopic displacement field $u^0 \in H_0(\Omega)$. The macroscopic linear strain tensor is denoted by $\varepsilon^x(\cdot)$and $H_0(\Omega)$ is the set of admissible displacements with a zero value at a boundary where the Dirichlet conditions are imposed.

The homogenization procedure, i.e., the computation of the microscopic and macroscopic equations, is embedded in an optimization loop in order to find the material parameters of the components constituting the composite structure. The optimization module of SciPy (Python library for scientific computing)[10] and the Python-based finite-element solver SfePy[9] for the numerical solution of the optimization problem are used.

7 COMPARISON OF THE RESULTS

The identified material parameters obtained using both homogenization approaches are in **Table 3**.

Table 3: Identified material parameters
Tabela 3: Opredeljeni parametri materiala

Parameter	Unit	Commercial	Asymptotic
Fibers			
E_1	(GPa)	165.99	162.55
E_2	(GPa)	16.13	18.52
ν_{12}	(-)	0.18	0.16
G_{12}	(GPa)	44.86	45.65
Matrix			
E_m	(GPa)	3.28	3.21
ν_m	(-)	0.43	0.39

Poisson's ratio in plane 23 was considered to be constant, ν_{23} = 0.4. Both methodologies converged to similar values of the identified parameters.

8 CONCLUSION

Both methodologies provide comparable results. The asymptotic homogenization implemented in SfePy exhibits a less time-consuming performance taking into account the whole process of the calculation and pre- and post-processing of the results in each optimization design. Both approaches provide a possibility for an inverse process, calculating the stress distribution at the microscopic level using the macroscopic stress distribution. Nevertheless, commercial software Abaqus 6.14-2 with its ability to apply user subroutines provides (at the present state) a wider range of possibilities for more complicated constitutive relations (e.g., nonlinear elasticity, plasticity, damage).

Acknowledgement

This publication was supported by the project LO1506 of the Czach Ministry of Education, Youth and Sports.

9 REFERENCES

[1] T. Kroupa, V. Laš, R. Zemčík, Improved nonlinear stress–strain relation for carbon–epoxy composites and identification of material parameters, Journal of Composite Materials, 45 (**2011**) 9, 1045–1057, doi:10.1177/0021998310380285

[2] V. Laš, R. Zemčík, Progressive Damage of Unidirectional Composite Panels, Journal of Composite Materials, 42 (**2008**) 1, 25–44, doi:10.1177/0021998307086187

[3] R. Zemčík, R. Kottner, V. Laš, T. Plundrich, Identification of material properties of quasi-unidirectional carbon-epoxy composite using modal analysis, Mater. Tehnol., 43 (**2009**) 5, 257–260

[4] S. Ogihara, K. L. Reifsnider, Characterization of Nonlinear Behavior in Woven Composite Laminates, Applied composite materials, 9 (**2011**), 249–263, doi:10.1023/A:1016069220255

[5] H. Srbová, T. Kroupa, R. Zemčík, Identification of the initial failure and damage of substituents of a unidirectional fiber-reinforced composite using a micromodel, Mater. Tehnol., 48 (**2014**) 4, 549–553

[6] J. Pinho Da-Cruz, J. A. Oliveira, F. Teixeira-Dias, Asymptotic homogenisation in linear elasticity, Part I: Mathematical formulation and finite element modelling, Computational Materials Science, 45 (**2009**), 1073–1080, doi:10.1016/j.commatsci.2009.02.025

[7] J. Pinho Da-Cruz, J. A. Oliveira, F. Teixeira-Dias, Asymptotic homogenisation in linear elasticity, Part II: Finite element procedures and multiscale applications, Computational Materials Science, 45 (**2009**), 1081–1096, doi:10.1016/j.commatsci.2009.01.027

[8] D. Cioranescu, P. Donato, An Introduction to Homogenization, Oxford Lecture Series in Mathematics and its Applications 17, Oxford University Press, 1999

[9] R. Cimrman, SfePy - Write Your Own FE Application, Proceedings of the 6th European Conference on Python in Science (EuroSciPy 2013), (**2014**), 65–70, http://arxiv.org/abs/1404.6391

[10] E. Jones, T. E. Oliphant, P. Peterson et al., SciPy: Open source scientific tools for Python, http://www.scipy.org

[11] K. J. Bathe, Finite element procedures, Prentice Hall, Upper Saddle River, New Jersey 07458, USA, 2007

[12] J. S. Arora, Introduction to Optimum Design, Elsevier, 2012

[13] B. D. Lubachevsky, How to Simulate Billiards and Similar Systems, Journal of Computational Physics, 94 (**1991**) 2, 255–283, doi:10.1016/0021-9991(91)90222-7

[14] H. A. Meier, E. Kuh, P. Steinmann, A Note on the Generation of Periodic Granular Microstructures Based on Grain Size Distributions, International Journal for Numerical and Analytical Methods in Geomechanics, 32 (**2008**), 509–522, doi:10.1002/nag.635

UDK 67.017:625.821.5:681.5.015.42
Original scientific article/Izvirni znanstveni članek

ISSN 1580-2949
MTAEC9, 51(3)379(2017)

STATISTICAL VIEW OF EVALUATING CONCRETE-SURFACE-LAYER PERMEABILITY TESTS IN CONNECTION WITH CHANGES IN CONCRETE FORMULA

STATISTIČNI POGLED NA OCENO PREIZKUSA PREPUSTNOSTI POVRŠINSKE PLASTI BETONA V POVEZAVI S SPREMEMBAMI FORMULE BETONA

Petr Misák, Tomáš Stavař, Iva Rozsypalová, Dalibor Kocáb, Petr Pőssl

Brno University of Technology, Faculty of Civil Engineering, Institute of Building Testing, Veveří 95, 602 00 Brno, Czech Republic
possl.p@fce.vutbr.cz

Prejem rokopisa – received: 2015-07-14; sprejem za objavo – accepted for publication: 2016-06-06

doi:10.17222/mit.2015.223

Concrete is one of the most common building materials and its durability has been observed with increased attention. It can be said that concrete durability is closely connected with permeability and, generally speaking, the quality of its surface layer. Evaluating the quality of the surface layer of concrete is a rather difficult issue that can be addressed in different ways. The authors of this paper focus on three internationally used methods – TPT, GWT and ISAT. The paper sums up the results of the experiment whose goal was to investigate the influence of concrete composition on the outputs of the above-mentioned methods. For the purposes of the experiment, specimens were made using 9 mixtures, which differed only in the amount of cement and plasticiser, i.e., the water/cement ratio. The experiment was designed and evaluated using the statistical methodology DOE (Design of Experiment). Next, the paper discusses a new view of the statistical evaluation of the test results of the methods described above.

Keywords: concrete, permeability, durability, design of experiment

Beton je eden najbolj uporabljanih materialov v gradbeništvu in njegova zdržljivost se proučuje z veliko pozornostjo. Lahko se reče, da je zdržljivost betona tesno povezana s prepustnostjo, na splošno s kvaliteto njegove površinske plasti. Ocena kvalitete površinske plasti betona je precej kompliciranо vprašanje, h kateremu se lahko pristopi na različne načine. Avtorji tega članka se osredotočajo na tri mednarodno priznane metode – TPT, GWT in ISAT. Članek povzema rezultate preizkusa, katerega cilj je bil proučevati vpliv sestave betona na rezultate zgoraj omenjenih metod. Za namene preizkusa so bili vzorci izdelani iz 9 mešanic, ki so se razlikovale samo v količini cementa in plastifikatorja, to je razmerja voda/cement. Preizkusi so bili postavljeni in ocenjeni s statistično metodologijo DOE (angl. Design of Experiment). Nadalje članek obravnava nov pogled na statistično oceno rezultatov preizkusa in zgoraj opisanih metod.

Ključne besede: beton, prepustnost, trajnost, načrtovanje preizkusa

1 INTRODUCTION

The durability of hardened concrete and thus the whole structure greatly depends on the quality and permeability of the surface layer. A low permeability of the surface layer ensures a greater resistance to carbonation and entery of chlorides and other outside intrusions.[1–3] These phenomena cause, among other things, corrosion of the steel reinforcement in concrete and thus its overall degradation.[4,5] It is known that the quality of concrete is determined by the correct composition of fresh concrete and thus by the amount of cement, water and other additives and admixtures.[6,7] There is a large number of rather different methods for determining the quality of a concrete surface layer. In terms of permeability, these methods can be divided into two groups – methods determining the resistance to the penetration of liquids or gases.

The durability of hardened concrete with respect to the quality of its surface layer is being dealt with in the GACR 13-18870S project. One of the goals of the project is the assessment of existing test methodologies for the determination of the surface layer of concrete or the creation of new methodologies. A number of papers have been published within the project, such as [8,9]. Permeability itself is addressed in [10–12].

The research described in this paper summarises an experiment whose goal was to assess the influence of concrete composition on the results of the tests determining the concrete surface layer's permeability, i.e., TPT, GWT and ISAT. For the purposes of the experiment, specimens were made using 9 mixtures, which differed only in the amount of cement and plasticiser, i.e., the water/cement ratio. The experiment was designed and evaluated using the statistical methodology DOE (Design of Experiment). These statistical methods are discussed in greater detail, e.g., in [13].

2 EXPERIMENT PART

2.1 Testing methods

2.1.1 TPT method

A TPT (Torrent Permeability Tester) is suitable for the determination of air permeability of the surface layer and can be used in both laboratory measurements and in-situ. The principle of determining the air permeability of concrete is in creating a vacuum on the surface layer and measuring the flow of air through the concrete into the measurement device over a set period of time. **Table 1**: Evaluation of the concrete cover by means of k_T lists the quality categories of concrete cover as written in [14].

Table 1: Evaluation of concrete cover by means of k_T
Tabela 1: Ocena kvalitete površine betona s pomočjo k_T

Concrete cover quality	index	k_T (× 10^{-6} m^2)
Very bad	5	>10
Bad	4	1.0–10
Medium	3	0.1–1.0
Good	2	0.01–0.1
Very good	1	<0.01

This method is discussed more in [14–18].

2.1.2 ISAT method

The second method used in the experiment, ISAT (Initial Surface Absorption Test), is used for determining the water permeability of the surface layer. Measurement by ISAT is performed exclusively with specimens in a laboratory. The principle of the test is the determination of the rate of water absorption (measured using a calibrated glass capillary) with a concrete cover of known area at a constant water pressure of a 200 mm water column. More can be found in [19–21].

2.1.3 GWT Method

GWT (German Water Permeability Test) is also used for the measurement of concrete cover permeability to water but at constant water pressure of 0.02 MPa. The amount of water absorbed by the surface layer per unit of time is measured. This method can be used in-situ as well as on laboratory specimens.[22]

2.2 Material

The goal of the experiment was to assess the influence of the concrete composition on the results of TPT, ISAT and GWT tests while both the design and the experiment were evaluated using the DOE (Design Of Experiment) method.

The two main factors which were to decisively influence the concrete cover permeability were set to be cement and plasticiser content. The portion of these components in fresh concrete is determining for the amount of water and water/cement ratio as all the mixtures were always designed for S2 or S3 consistency according to [23]. The water/cement ratio was subsequently added into the calculation models as a third factor as the change in water/cement ratio best corresponds to the change of the overall composition of fresh concrete.

Plasticiser was added in 0 %, 50 % and 100 % of the maximum amount recommended by the manufacturer. The amount of cement was increased in the mixture always by approx. 50 kg/m^3 of the concrete. In order to assess the broad spectrum of construction concretes, mixtures were prepared with 4 different contents of cement.

The authors first considered performing the research as a full factorial experiment13 with the factors of the amount of cement and plasticiser, while the amount of cement was represented by four levels and the amount of plasticiser by three. However, some variants of these two factors did not meet the basic technological requirements for the production of concrete and therefore were eliminated from the experiment. The method of evaluation of the experimental results is described in the following sections of this paper.

Table 2: Design of experiment shows the concrete mixture matrix. The horizontal direction shows the amount of plasticiser from zero content to the maximum dose recommended by the manufacturer (100 %). The level of cement amount (vertical) is identified 0–III, while dose 0 corresponds approximately to 255 kg/m^3 of concrete and dose III to 405 kg/m^3 of concrete. The identification of the mixtures then corresponds to the portion of the components. **Table 3:** Composition of the mixtures shows the specific amounts of the components used. All the mixtures use the same aggregate from the same location and the same type of cement from one cement mill.

Table 2: Design of experiment
Tabela 2: Zasnova poskusa

Cement / Plasticiser (%)	**0**	**50**	**100**
0	R	-	-
I	0/1	1/1	-
II	0/2	1/2	2/2
III	0/3	1/3	2/3

Table 3: Composition of the mixtures
Tabela 3: Sestava mešanic

Component	Mixture								
	R	**0/1**	**0/2**	**0/3**	**1/1**	**1/2**	**1/3**	**2/2**	**2/3**
CEM I 42.5 R (kg)	**248**	**308**	**357**	**392**	**295**	**349**	**394**	**338**	**386**
Bratcice 0-4 mm (kg)	953	925	889	826	927	897	846	905	854
Olbramovice 4-8 mm (kg)	173	182	174	195	185	185	192	183	207
Olbramovice 8-16 mm (kg)	675	696	693	669	689	693	684	667	671
Water (kg)	201	203	201	208	177	175	183	176	181
faultPlasti-ciser (kg)	**0**	**0**	**0**	**0**	**0.71**	**0.91**	**0.95**	**1.77**	**2.01**
w/c (-)	**0.75**	**0.61**	**0.53**	**0.50**	**0.55**	**0.46**	**0.43**	**0.48**	**0.44**

Table 4: Properties of fresh concrete
Tabela 4: Lastnosti svežega betona

Property	Mixture								
	R	**0/1**	**0/2**	**0/3**	**1/1**	**1/2**	**1/3**	**2/2**	**2/3**
Density (kg/m^3)	2 250	2 315	2 315	2 290	2 275	2 300	2 300	2 270	2 300
Flow table test (mm)	435	410	385	415	360	350	370	340	330
Slump-test (mm)	110	60	60	110	60	50	60	65	50
Air content (%)	2.8	2.7	2.5	2.5	3.6	2.8	3.2	4.5	3.0

Fresh concrete for the production of specimens was always taken in conditions according to [24]. The properties of the fresh concrete tested according to [23,25–27], are listed in **Table 4**: Properties of fresh concrete.

Beam specimens of size 300 × 300 × 150 mm were made from each mixture. Each specimen was tested three times with TPT and twice with GWT and ISAT. The results of ISAT were recorded at 60 min after the beginning of the test.

3 RESULTS AND DISCUSSION

The authors first performed a statistical analysis of the use of different distributions of probability for the quantities being observed mainly due to a strong absence of symmetry and normality in the test results. The non-normality of k_T (TPT) has been discussed earlier, e.g., in [16]. The test results of the other parameters exhibit a similar statistical behaviour.

In order to test the most suitable distribution of probability, an additional experiment was conducted. The k_T coefficient was determined on 32 specimens of size 300 × 300 × 80 mm using TPT. The measurement was performed in the same conditions in the shortest possible time interval and at a water content of 3.0 % to 3.5 %. TPT was chosen mainly due to time economy.

The results of the tests are represented in the histogram in **Figure 1** TPT result histogram. The most suitable probability distribution was chosen to be the lognormal distribution. This distribution generally appears suitable for a description of the quantities that exhibit high variability and at the same time the results are close to zero. The advantage of the lognormal probability distribution is, among others, the fact that it does not reach negative values. Tests of goodness of fit did not disprove the option of using a lognormal probability distribution in the output of GWT and ISAT.

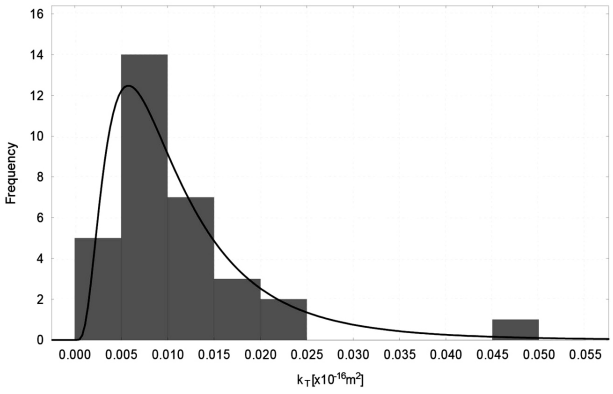

Figure 1: TPT result histogram
Slika 1: Histogram TPT-rezultatov

In **Tables 5** to **7** Measurement results – TPT through 7 show the basic statistical properties of the results of TPT, GWT, and ISAT performed on the above-described concrete mixtures with variable composition. The arithmetic average and the experimental standard deviation s_0 are supplemented with the calculation of 95 % quantiles, which were determined using normal (identified by lower index n0.95) and lognormal (lower index ln0.95) probability distributions. The 95 % quantile was used as the characteristic value of the quantities being observed (amend D of [28]). The value V always identifies coefficient of variation in %. All the values were determined at specimen mass water content within 3–3.5 %, which corresponded to the normal laboratory storage of the specimens.

Table 5: Measurement results – TPT
Tabela 5: Rezultati TPT-meritev

Mixture	k_T (10^{-16} m^2)	s_0 (10^{-16} m^2)	V (%)	$k_{T;ln0.95}$ (10^{-16} m^2)	$k_{T;n0.95}$ (10^{-16} m^2)
R	1.414	0.700	49.5	3.300	2.566
0/1	0.052	0.013	25.0	0.075	0.072
0/2	0.042	0.016	38.1	0.072	0.068
0/3	0.018	0.007	38.9	0.030	0.029
1/1	0.035	0.014	40.0	0.067	0.059
1/2	0.030	0.014	46.7	0.056	0.053
1/3	0.016	0.004	25.0	0.023	0.023
2/2	0.032	0.007	21.9	0.045	0.044
2/3	0.014	0.003	21.4	0.019	0.019

Table 6: Measurement results – GWT
Tabela 6: Rezultati GWT-meritev

Mixture	k_T (10^{-16} m^2)	s_0 (10^{-16} m^2)	V (%)	$k_{T;ln0.95}$ (10^{-16} m^2)	$k_{T;n0.95}$ (10^{-16} m^2)
R	10.70	1.67	15.6	13.70	13.50
0/1	5.21	0.14	2.7	7.88	7.45
0/2	4.60	0.13	2.8	7.02	6.67
0/3	1.20	0.25	20.8	1.73	1.61
1/1	2.13	0.28	13.1	2.62	2.59
1/2	1.78	0.40	22.5	2.51	2.44
1/3	1.24	0.28	22.6	1.78	1.70
2/2	1.43	0.31	21.7	2.04	1.94
2/3	0.59	0.06	10.2	0.70	0.69

In order to determine the influence of the individual factors (water/cement ratio, cement and plasticiser content) on the permeability of the surface layer, the experiment was analysed using DOE. Using the appropriate SW, this method enables an easy identification of such factors that have a significant statistical influence on the quantity being observed.

Table 7: Measurement results – ISAT after 60 min
Tabela 7: Rezultati ISAT-meritev po 60 min

Mixture	f_{60} (mL/m²/s)	s_0 (mL/m²/s)	V (%)	$f_{60;\ ln0.95}$ (mL/m²/s)	$f_{60;\ n0.95}$ (mL/m²/s)
R	0.334	0.061	18.3	0.441	0.434
0/1	0.260	0.024	9.2	0.301	0.299
0/2	0.227	0.027	11.9	0.274	0.271
0/3	0.141	0.008	5.7	0.155	0.155
1/1	0.211	0.042	19.9	0.291	0.281
1/2	0.140	0.007	5.0	0.151	0.151
1/3	0.101	0.012	11.9	0.122	0.121
2/2	0.118	0.006	5.1	0.128	0.128
2/3	0.077	0.023	29.9	0.100	0.098

During multiple factor analysis it is very important not to consider only the individual factors, but also to test their influence at the same time. There are a number of advantages. Especially, it is possible to assess the mutual interactions of the factors and, moreover, to minimise the errors of statistical tests. This paper contains all the effects of the factors as well as their interactions assessed by means of the so-called analysis of variance (ANOVA) on the significance level of 0.05, whose outcomes are subsequently processed into Pareto charts.[13,29]

As mentioned above, the experiment was not designed as a full factorial experiment; all factor options (mixture compositions) were not put to combination. Analytical tools of the so-called central composite design were used as the evaluation apparatus.

The authors used three basic models for the output quantities of TPT, GWT and ISAT. In the first model, all the factors are represented only in the linear form (Equation (1)) and in the second one, in linear and quadratic form (Equation (2)). The third model involves more factor interactions (Equation (3)). For simplicity, in all formulae, factors are represented by x_i and regression coefficients a_i. y represent the output quantity, i.e., k_T or f_{60}:

$$y = a_1 x_1 + a_2 x_2 + a_3 x_3 \quad (1)$$

$$y = a_1 x_1 + a_2 x_1^2 + \ldots + a_5 x_3 + a_6 x_3^2 \quad (2)$$

$$y = a_1 x_1 + \ldots + a_3 x_3 + a_2 x_1^2 + \ldots + a_6 x_3^2 + a_{12} x_1 x_2 + \ldots + a_{23} x_2 x_3 \quad (3)$$

Figures 2a, **2b** and **3** show the outcomes of the analysis of variance of the k_T coefficient (TPT) performed on models according to (1) through (3) as standardised assessments of the effects. A standardised assessment of the effect is in the case of this application test statistic – if it exceeds 0.05 on the level of significance, it can be assumed that the given factor (or interaction of factors) has a statistically significant influence on the output quantity y. Based on this simple linear model (Equation (1) and **Figure 2a**)) all the factors are statistically significant. When introducing the quadratic elements (Equation (2) and **Figure 2b**), the evaluation showed, as the only statistically significant factor, the square of water/cement ratio, which thus

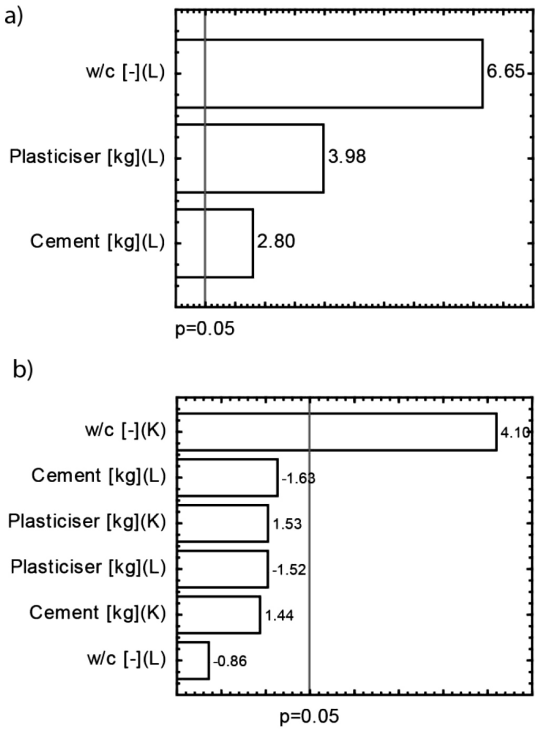

Figure 2: TPT: a) Pareto chart of standardised assessment of effects – linear model, b) Pareto chart of standardised assessment of effects – each effect represented in linear (L) and quadratic (K) form
Slika 2: TPT: a) Pareto diagram standardizirane ocene učinkov – linearni model, b) Pareto diagram standardizirane ocene učinkov – vsak učinek je predstavljen v linearni (L) in kvadratni (K) obliki

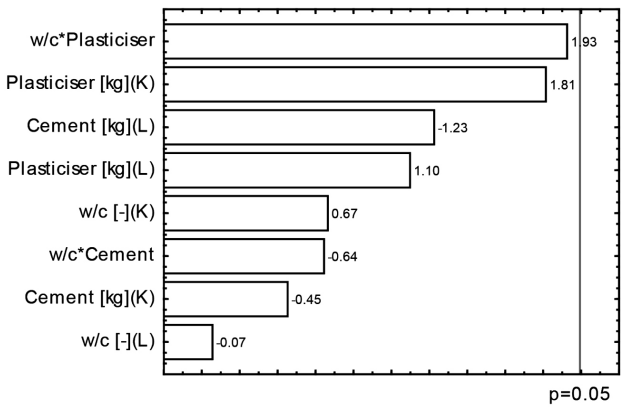

Figure 3: TPT: Pareto chart of standardised assessment of effects – linear (L) as well as quadratic (K) representation of effects and their interaction (*)
Slika 3: TPT: Pareto diagram standardizirane ocene učinkov – linearna (L) kot tudi kvadratna (K) predstavitev učinkov in njihov medsebojni vpliv (*)

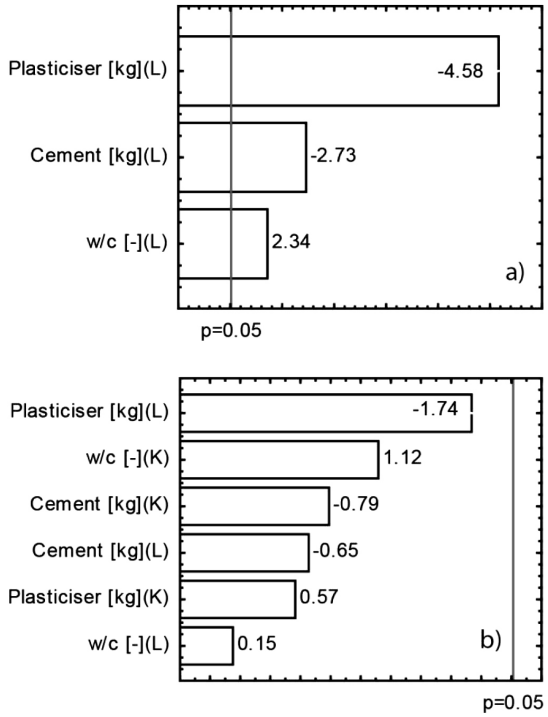

Figure 4: ISAT: a) Pareto chart of standardised assessment of effects – linear model, b) Pareto chart of standardised assessment of effects – each effect represented in linear (L) and quadratic (K) form

Slika 4: ISAT: a) Pareto diagram standardizirane ocene učinkov – linearni model, b) Pareto diagram standardizirane ocene učinkov – vsak učinek je predstavljen v linearni (L) in kvadratni (K) obliki

appears to be the most statistically important factor. The interactions of some of the factors were eliminated from the analysis of the complex model (Equation (3)) because of the clear correlation between them. However, the analysis thus performed did not determine any factor nor combination as being statistically significant.

Based on these calculations it can be said that the permeability of the surface layer of the concrete determined by TPT depends mainly on the water/cement ratio. The analysis of the GWT results arrived at the same results.

In the case of f_{60} measured by means of ISAT, the statistical evaluation is different. The linear model (Equation (1) and **Figure 4a**)) showed the significance of all the factors, much like in the previous cases, however, in different order. According to Equation (2) and **Figure 4b**, no factor or a square of a factor is significant. Only the use of the third model (Equation (3) and **Figure 5**) enabled a better identification of statistically significant factors, which were determined to be mainly water/cement ratio and cement content.

Based on the analyses it can be said that the observed quantities, i.e., TPT, GWT and ISAT outputs, are determined mainly by the water/cement ratio. However, the significance of the water/cement ratio is not statistically large enough for the representation of the other components to be neglected. Nevertheless, the water/cement ratio is very suitable for a simple visualisation of the surface layer permeability values, **Figure 6** through 8. These charts show the results of all the methods using a logarithmic scale. In all cases, the exponential formula was evaluated as best:

$$y = ae^{b\left(\frac{w}{c}\right)} \tag{4}$$

where a and b are the regression coefficients and w/c signifies the water/cement ratio. **Table 8:** Regression coefficients show values of the regression coefficients and the coefficients of determination.

Table 8: Regression coefficients

Tabela 8: Regresijski koeficienti

Method	a	b	R^2
TPT	5E-05	12.705	0.86
GWT	0.343	7.877	0.80
ISAT	0.017	4.223	0.80

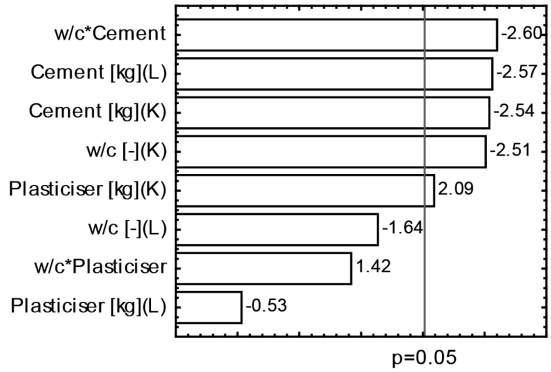

Figure 5: ISAT: Pareto chart of standardised assessment of effects – linear (L) as well as quadratic (K) representation of effects and their interaction (*)

Slika 5: ISAT: a) Pareto diagram standardizirane ocene učinkov – linearna (L) kot tudi kvadratna (K) predstavitev učinkov in njihovega medsebojnega vpliva (*)

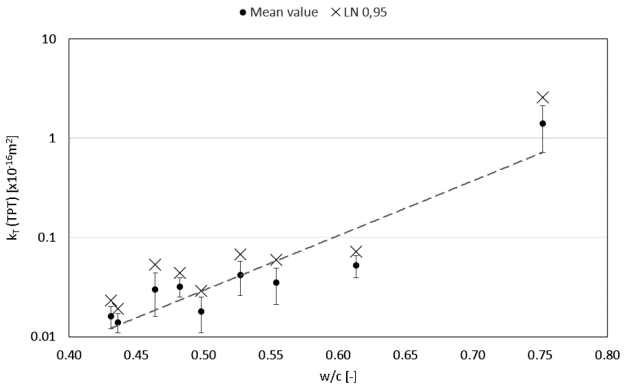

Figure 6: Relationship between w/c ratio and k_T value (TPT method) with standard deviation and characteristic value (lognormal probability distribution)

Slika 6: Odvisnost med w/c razmerjem in vrednostjo k_T (TPT metoda) s standardnim odkolonom in značilno vrednostjo (logaritemska normalna razporeditev verjetnosti)

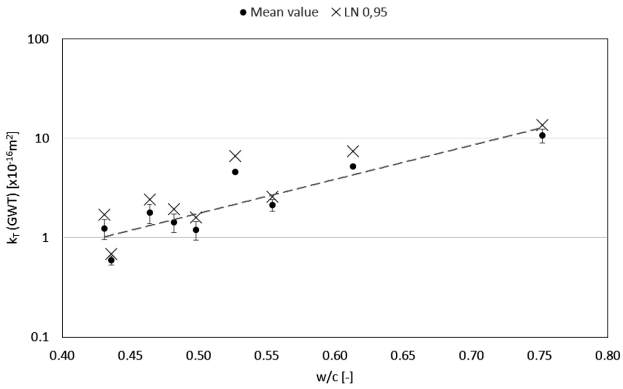

Figure 7: Relationship between *w/c* ratio and k_T value (GWT method) with standard deviation and characteristic value (lognormal probability distribution)

Slika 7: Odvisnost med *w/c* razmerjem in vrednostjo k_T (GWT metoda) s standardnim odklonom in značilno vrednostjo (logaritemska

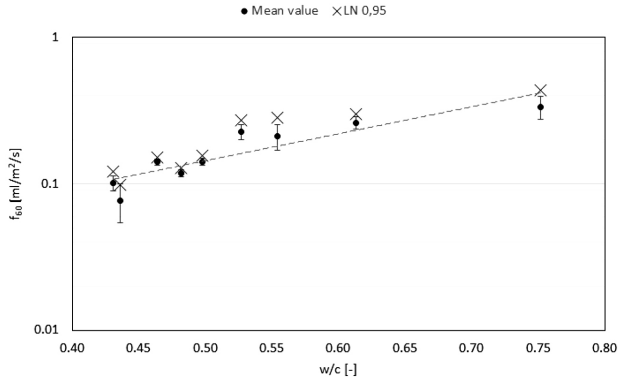

Figure 8: Relationship between *w/c* ratio and f_{60} value (ISAT method) with standard deviation and characteristic value (lognormal probability distribution)

Slika 8: Odvisnost med *w/c* razmerjem in vrednostjo f_{60} (ISAT metoda) s standardnim odklonom in značilno vrednostjo (logaritemska normalna razporeditev verjetnosti)

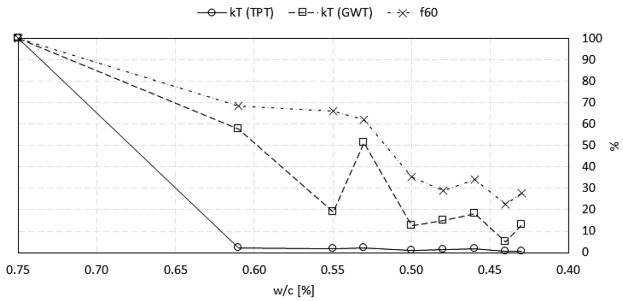

Figure 9: Percentage drop of the results of the observed methods depending on water/cement ratio

Slika 9: Odstotkovno zmanjšanje rezultatov v odvisnosti od razmerja voda/cement

Figure 9 shows the percentage drop of the test results dependent on the water/cement ratio. The results relate to the values measured on the mixture with the highest water/cement ratio, i.e., mixture R. As the chart indicates, the test results of all the methods were able to

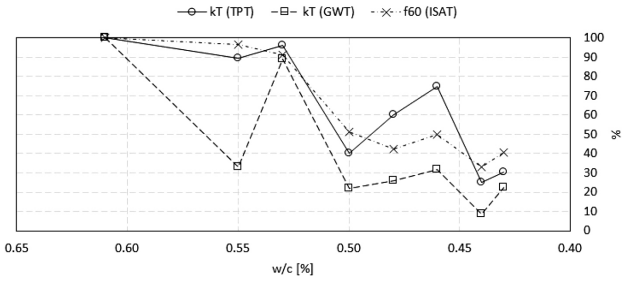

Figure 10: Percentage drop of the results of the observed methods depending on the water/cement ratio without mixture R

Slika 10: Odstotkovno zmanjšanje rezultatov opazovanih metod v odvisnosti od razmerja voda/cement, brez zmesi R

capture the change in the permeability depending on the change in the water/cement ratio (with rare exceptions). **Figure 9** also indicates that the mixture R is not entirely suitable as a reference. In particular, the results of TPT are difficult to distinguish for this setting. **Figure 10** shows the same percentage representation of the results after eliminating mixture R – the reference mixture was chosen to be the mixture with the highest water/cement ratio, i.e., 0/1. **Figure 10** better shows the drop in the permeability of the surface layer depending on the water/cement ratio, especially in the case of the TPT results.

4 CONCLUSIONS

The experiments and their analyses indicate the following:

Given the relatively high variability of the test results (especially in the case of TPT – the lowest coefficient of variation was 21.4 % in concrete identified as 2/3) the more suitable characteristic appears to be the 95 % quantile, as opposed to only the arithmetic average.

The lognormal distribution appears suitable for the evaluation of the results of concrete cover permeability test using TPT, GWT and ISAT. The reason is mainly the limitation of this distribution for negative values. The use of a normal distribution can probably cause a number of problems. As seen in **Table 5**: Measurement results - TPT through 7, the value of the 95 % quantile determined using a normal probability distribution is probably always lower than the value of the 95 % quantile determined using a lognormal distribution. The evaluation of the quality of the concrete cover according to a normal distribution brings higher values.

The authors find it appropriate to slightly adapt the current way of categorising the surface layer of concrete, e.g., according to **Table 1**: Evaluation of concrete cover by means of k_T. A simple categorisation into 5 groups is certainly useful; however, the experiment shows that the limits thus set do not sufficiently capture the significant changes in the concrete composition. The TPT and test result evaluation were first published more than 20 years ago[14] and experiments then performed no longer correspond to the results of contemporary concrete. The

authors believe that a solution to this situation can be the adjustment of existing limits of the categories and performing the categorisation using 95 % quantile instead of the arithmetic average. The introduction of a similar categorisation system would be suitable in the other methods as well.

The water/cement ratio seems to have the most significant influence on the results of the concrete cover permeability tests. However, the significance of the water/cement coefficient is not statistically large enough for the content of the other components to be neglected.

The results of all the methods used in the experiment reacted to a change in the concrete composition with similar trends of concrete cover permeability reduction, especially with respect to its water/cement ratio.

The set of methods called DOE (Design Of Experiment) appears to be a suitable tool for the design and evaluation of similar experiments.

Acknowledgement

This paper was elaborated with the financial support of the Czech Science Foundation project GAČR 13-18870S and European Union's Operational Programme Research and Development for Innovations, No. CZ.1.05/2.1.00/03.0097.

5 REFERENCES

[1] S. Han, W. Park, E. Yang, Evaluation of concrete durability due to carbonation in harbour concrete structures, Construction and Building Materials, 48 (**2013**), 1045–1049, doi:10.1016/j.conbuildmat.2013.07.057

[2] B. Salvoldi, H. Beushausen, M. Alexander, Oxygen permeability of concrete and its relation to carbonation, Construction and Building Materials, 85 (**2015**), 30–37, doi:10.1016/j.conbuildmat.2015.02.019

[3] D. Chopra, R. Siddique, Strength, permeability and microstructure of self-compacting concrete containing rice husk ash, Biosystems Engineering, 130 (**2015**), 72–80, doi:10.1016/j.biosystemseng.2014.12.005

[4] G. Roventi, T. Bellezze, G. Giuliani, C. Conti, Corrosion resistance of galvanized steel reinforcements in carbonated concrete: effect of wet–dry cycles in tap water and in chloride solution on the passivating layer, Cement and Concrete Research, 65 (**2014**), 76–84, doi:10.1016/j.cemconres.2014.07.014

[5] J. Ribeiro, Z. Panossian, S. Selmo, Proposed criterion to assess the electrochemical behavior of carbon steel reinforcements under corrosion in carbonated concrete structures after patch repairs, Construction and Building Materials, 40 (**2013**), 40–49, doi:10.1016/j.conbuildmat.2012.09.097

[6] J. Chen, A. Kwan, Y. Jiang, Adding limestone fines as cement paste replacement to reduce water permeability and sorptivity of concrete, Construction and Building Materials, 56 (**2013**), 87–93, doi:10.1016/j.conbuildmat.2014.01.066

[7] L. Dellinghausen, A. Gastaldini, F. Vanzin, K. Veiga, Total shrinkage, oxygen permeability, and chloride ion penetration in concrete made with white Portland cement and blast-furnace slag, Construction and Building Materials, 37 (**2013**), 652–659, doi:10.1016/j.conbuildmat.2012.07.076

[8] L. Topolář, H. Šimonová, P. Misák, Effect of Concrete Mixture Composition on Acoustic Emission and Fracture Parameters Obtained from Three-Point Bending Test, Advanced Materials Research, 1100 (**2015**), 152–155, doi:10.4028/www.scientific.net/AMR.1100.152

[9] M. Matysík, L. Topolář, P. Daněk, H. Šimonová, T. Vymazal, I. Plšková, An Experimental Study on Acoustic Emission Signals during the Three-Point Bending Fracture Test, Advanced Materials Research, 1000 (**2014**), 281–284, doi:10.4028/www.scientific.net/AMR.1000.281

[10] T. Stavař, M. Stehlík, The Assessment of Durability of Fibre Concretes with Dense Aggregate and Concrete Recyclate from the Results of Permeability and Diffusion Tests, Advanced Materials Research, 1100 (**2015**), 106–111, doi:10.4028/www.scientific.net/AMR.1100.106

[11] M. Stehlík, V. Hermánková, L. Vítek, Opening of microcracks and air permeability in concrete, Journal of Civil Engineering and Management, 21 (**2015**), 177–184, doi:10.3846/13923730.2013.802721

[12] M. Stehlík, Enhancing the durability of concrete made of concrete recyclate by additives and admixtures, Journal of Civil Engineering and Management, 20 (**2014**), 270–279, doi:10.3846/13923730.2013.802708

[13] L. Eriksson, Design of experiments: principles and applications, 3. (**2008**), rev. and enl. ed. Umetrics Academy, Umeå

[14] R. Torrent, A two-chamber vacuum cell for measuring the coefficient of permeability to air of the concrete cover on site, Materials and Structures, 25 (**1992**), 358–365, doi:10.1007/BF02472595

[15] L. Zong, Z. Fei, S. Zhang, Permeability of recycled aggregate concrete containing fly ash and clay brick waste, Journal of Cleaner Production, 70 (**2014**), 175–182, doi:10.1016/j.jclepro.2014.02.040

[16] B. Kucharczyková, P. Misák, T. Vymazal, Determination and evaluation of the air permeability coefficient using Torrent Permeability Tester, Russian Journal of Nondestructive Testing, 46 (**2010**), 226–233, doi:10.1134/S1061830910030113

[17] SN 505 262/1:2003 – Construction en béton –Spécifications complémentaires: Annexe E: "Perméabilité à l'airdans les structures", NS, Switzerland

[18] Recommendation of RILEM TC 189-NEC "Non-destructive evaluation of the concrete cover": Comparative test – Part I, Materials and Structures, 38 (**2005**), 895–906, doi:10.1617/14384

[19] P. Claisse, Surface tests to determine transport properties of concrete – I: the tests, Transport Properties of Concrete, (**2014**), 26, Elsevier

[20] B. Sabir, S. Wild, M. O'Farrell, A water sorptivity test for martar and concrete, Materials and Structures, 31 (**1998**), 568–574, doi:10.1007/BF02481540

[21] BS 1881-122:2011 – Testing concrete. Method for determination of water absorption. BSI, UK

[22] Nondestructive testing of materials and structures: proceedings of NDTMS-2011, (2013), Istanbul, Turkey, May 15–18, 2011. 2 sv.

[23] EN 12350-2:2009 – Testing fresh concrete – Part 2: Slump-test ÚNMZ, Prague

[24] EN 12350-1:2009 Testing fresh concrete – Part 1: Sampling ÚNMZ, Prague

[25] EN 12350-5:2009 Testing fresh concrete – Part 5: Flow table test ÚNMZ, Prague

[26] EN 12350-6:2009 Testing fresh concrete – Part 6: Density ÚNMZ, Prague

[27] EN 12350-7:2009 Testing fresh concrete – Part 7: Air content – Pressure methods ÚNMZ, Prague

[28] EN 1990:2015 Eurocode: Basis of structural design, 2 ed. ÚNMZ, Prague

[29] M. Fritz, P. Berger, Comparing more than two means, Improving the User Experience Through Practical Data Analytics, (**2015**), 163, Elsevier

UDK 666.9-1:66.017
Original scientific article/Izvirni znanstveni članek

ISSN 1580-2949
MTAEC9, 51(3)387(2017)

EXPERIMENTAL DETERMINATION OF THE INFLUENCE OF FRESH CONCRETE'S COMPOSITION ON ITS RESISTANCE TO WATER AND DE-ICING CHEMICALS BY MEANS OF TWO METHODS

UPORABA DVEH METOD ZA EKSPERIMENTALNO DOLOČANJE VPLIVA SESTAVE SVEŽEGA BETONA NA NJEGOVO ODPORNOST NA VODO IN NA KEMIKALIJE ZA PREPREČEVANJE ZMRZOVANJA

Dalibor Kocáb, Tereza Komárková, Monika Králíková, Petr Misák, Bronislava Moravcová

Brno University of Technology, Faculty of Civil Engineering, Department of Building Testing, Veveří 95, 602 00 Brno, Czech Republic
kralikova.m@fce.vutbr.cz

Prejem rokopisa – received: 2015-07-22; sprejem za objavo – accepted for publication: 2016-06-06

doi:10.17222/mit.2015.233

Concrete's durability is currently a frequently discussed topic. The determination of concrete's durability is rather difficult since it depends on a number of factors, out of which the surface-layer quality is very important. One of the options for assessing its quality is the determination of concrete's resistance to water and de-icing chemicals. The testing is based on loading the concrete by cyclic freezing and thawing during the simultaneous action of a thawing solution. The damage to the surface layer manifests itself as scaling, i.e., the loss of small scales from the surface of the material. The resistance of concrete to water and de-icing chemicals can be determined by means of several methods; however, a universal method of evaluation has not yet been established in Europe. The goal of the experiment described here was to assess the influence of fresh concrete's composition on its resistance to water and de-icing chemicals using two different measurement methods (method A and C). A total of 9 fresh concrete mixtures were designed, from which specimens were made. The experiment was created and evaluated using the statistical method DOE (Design of Experiment). Based on the tests performed, it can be stated that a change in the content of cement and plasticiser in fresh concrete is visible in the results of both methods. However, more so in the results for method C, which is generally more sensitive to changes in fresh concrete's composition.

Keywords: concrete, resistance, durability, de-icing chemicals

Zdržljivost betona je pogosto obravnavana tema. Določanje zdržljivosti betona je precej težko, ker je odvisno od številnih faktorjev, med katerimi je pomembna tudi kvaliteta površinske plasti. Ena od opcij določanja njene kvalitete, je določanje odpornosti betona na vodo in na kemikalije proti zmrzovanju. Preizkus temelji na izpostavitvi betona cikličnemu zamrzovanju in odtaljevanju s simultanim delovanjem raztopine za odtaljevanje. Poškodbe površinskega sloja se kažejo kot luščenje površine materiala. Odpornost betona na vodo in kemikalije za raztaljevanje se lahko določi z več metodami; vendar pa univerzalna metoda za oceno tega v Evropi še ni vzpostavljena. Cilj opisanih eksperimentov je bil oceniti vpliv sestavo svežega betona glede na njegovo odpornost na vodo in na kemikalije za raztaljevanje, z uporabo dveh metod (metoda A in C). Skupno je bilo pripravljenih 9 svežih betonskih mešanic iz katerih so bili izdelani vzorci. Eksperimenti so bili postavljeni in izvedeni z uporabo statistične metode DOE (postavitev preizkusa). Na podlagi izvedenih preizkusov se lahko zaključi, da se spremembe v vsebnosti cementa in plastifikatorja v svežem betonu pokažejo pri obeh metodah. Vendar so bolj izrazite pri rezultatih metode C, ki je na splošno bolj občutljiva na spremembe v sestavi svežega betona.

Ključne besede: beton, odpornost, zdržljivost, kemikalije za odtajevanje

1 INTRODUCTION

The surface layer of concrete determines the condition of the structure during its service life, since it is exposed to environmental attack and its parameters show how well it can protect the concrete element and its reinforcement.[1,2] The quality of the surface layer is very important for an assessment of the resistance of the concrete to external attack and especially for the total durability of the concrete.[3] The term surface layer is not yet clearly defined. Generally speaking, it is a layer of approximately 20 mm to 50 mm from the surface, i.e., a concrete cover.[4] The quality of the concrete cover is closely linked with its porosity, which, next to permeability, also influences its other properties.[1] Porosity is influenced mainly by the amount of water needed for cement hydration, air voids produced by inadequate concrete compaction or by air-entrainment (content, size and distribution of air voids), cracks formed during hydration due to volume changes and other factors. [5-7]

The quality of the surface layer together with the porosity of the concrete also determines its resistance to the intrusion of liquids and gases from the environment, i.e., permeability. Permeability is determined, e.g., by TPT [5–8], GWT and ISAT.[9] Other options for assessing the surface layer of concrete are methods for determining the

resistance of cement concrete to water and de-icing chemicals. The damage to concrete due to the action of de-icing chemicals manifests itself as the loss of small pieces of the material's surface; a phenomenon that is defined as scaling.[10] Scaling can also be defined as damage to the surface caused by frost and a salt solution. It must be emphasised that the mechanism of scaling is not analogous to the conventional action of frost that causes ice crystals to form in the internal structure and thus decreases the stiffness and strength. Scaling occurs on the surface, which does not endanger the quality of the material within the concrete body; however, it makes concrete susceptible to water and aggressive agents entering its structure, which puts the overall resistance of the concrete in danger.[10] Previous studies show that the damage to the surface layer of concrete is the most severe when the water contains a particular amount of the dissolved substance (known as pessimum concentration).[11] The pessimum concentration is almost independent of the nature of the dissolved substance (e.g. salt, alcohol, urea – all these act similarly).[12] The damage to the surface layer occurs in the form of small flakes or scales coming loose from the surface.[10] Scaling itself does not occur without free liquid present on the concrete surface (even when the concrete is saturated with water in a dry environment and is exposed to cyclic freezing and thawing). The damage to the concrete surface is greater when the temperature of the loading cycle is lower.[13] The salt concentration in the liquid acting upon the surface is more important than the concentration of salt solutions in the pores of the internal structure of the concrete.[11] The resistance of concrete to freezing and thawing in the presence of de-icing salts is very low; however, it can be significantly increased by the addition of an air-entraining additive.[14] The presence of air-entraining additives reduces the damage to the surface layer of concrete.[12,15–16] However, next to the positive influence on frost resistance, concrete air-entrainment also results in a decrease in the compressive strength; increasing air entrainment by one percent corresponds to a loss of 28-day compressive strength of about 5 %.[17]

Freeze-thaw resistance during the simultaneous action of a solution is described in the European standard CEN/TS 12390-9 [18] (based on the Swedish standard SS 13 72 44[19]). In the Czech Republic, the effect of water containing dissolved salts being frozen and thawed on concrete bodies is addressed in ČSN 73 1326.[20] The action of frost in terms of damage to the internal structure is also dealt with in ČSN 73 1380[21] and the determination of the frost resistance of concrete is in ČSN 73 1322.[22] Other methods worth mentioning are the American standard ASTM C 672/C 672M – 03[23]and the test method CDF according to RILEM, which is a part of the standard.[18]

The aim of the paper is an experimental determination of the influence of fresh concrete composition on its resistance to water and de-icing chemicals. This is done by means of two methods.

2 TEST METHODS

The basic principle of all methods for determining the resistance of concrete to water and de-icing chemicals is in essence the same. The concrete specimens are placed in an environmental chamber with automatic cycling, where they are exposed to the attack of demineralised water or defrosting chemicals for a cyclic alternation of temperatures above and below 0 °C. The differences between these methods are mainly in the required number of cycles, minimum and maximum temperatures, the size of specimens and the area exposed, the direction in which the water and de-icing chemicals act on the specimens and in the interpretation of the obtained result. The testing procedures of the methods for the assessment of the freeze-thaw resistance of concrete are briefly described in the sections below. Only the procedures according to[24] are discussed in greater detail as they are not known internationally.

2.1 Procedure according to CEN/TS 12390-9

This reference test method[18] (hereafter called the scaling method) is based on the Swedish standard.[19] However, it contains some modifications. The test requires four specimens with the dimensions of 50 × 150 × 150 mm cut from four 150-mm concrete cubes. Next, 67 ml of a 3 % NaCl solution is poured onto a sawed face of the specimen (the solution reaches up to 3 mm of the specimen height) and afterwards, the freeze-thaw cycles are initiated – the freezing stage lowers the temperature to (-20±2) °C and during thawing it rises to (+20±4) °C. One cycle takes 24 h. The freeze-thaw resistance is then evaluated by measuring the mass of the material scaled off the specimen surface after 7±1, 14±1, 28±1, 42±1 and 56 freeze-thaw cycles.[18-19]

2.2 Procedure according to ASTM C672 / C672M – 12

This testing method according to[23] is concerned with a determination of the resistance of the horizontal surface layer of concrete exposed to cyclic freezing to the temperature of -18±3 °C and thawing to +23±2 °C in the presence of de-icing chemicals. The test requires a minimum of two specimens at least 75 mm high with the testing surface of a minimum area of 0.045 m^2. Prior to the test, a 4 % $CaCl_2$ solution is poured onto the specimen surface (6 mm layer of the solution). A different solution can also be used if its effect during cyclic temperature loading is being examined. For instance, the authors of [25] used a 3 % solution of NaCl and the authors of [26] used a 4 % solution (NaCl + $CaCl_2$, 7:3). One cycle also takes 24 h. The state of the surface layer is only assessed visually after every 5 cycles, while the test takes 50 cycles in total. The assessment scale is from 0 (no

scaling) to 5 (severe scaling = coarse aggregate is visible throughout the surface).[23]

2.3 Procedure according to the CDF method

This is an alternative method described in [18]. The minimum number of specimens is five and they have the shape of a half-cube. According to the standard[18], the specimens must be made using special moulds. However, in [27] the authors claim that sawing a 150-mm cube into two roughly the same parts is sufficient. The principle of the test is the action of a 3 % NaCl solution on the specimen that is immersed in the solution with its level reaching up to 10±1 mm. The temperature cycles consist of changes between -20±0.5 °C and +20±1 °C twice a day; one cycle takes 12 h. The scales coming loose from the specimens are weighed after 4±1, 6±1, 14±1 and 28±1 freeze-thaw cycles. The test is evaluated by calculating the total amount of material scaled off the test surface after the above-mentioned number of freeze-thaw cycles.[18]

2.4 Procedure according to ČSN 73 1326

The standard ČSN 73 1326[20] is intended for concretes exposed to the action of salt and de-icing chemicals. Despite the fact that it contains three options of performing the test, currently only methods A (automatic cycling I) and C (automatic cycling II) are used. The difference between these two methods is mainly in the direction in which the 3 % NaCl solution acts. In the case of method A, the specimen is immersed in the solution, similarly to the CDF method.[18] In the case of method C, the solution is poured onto the top surface of the specimen, which makes the test similar to the scaling test according to [18] and the method according to [23]. Both methods are discussed in the following sections.

2.4.1 ČSN 73 1326 Method A

The test is performed with three specimens, 150 mm cubes, which are made and cured according to [28,29]. At the age of 28 days, the automatic cycling test is begun where the unmodified top surface of the specimen is tested. The individual specimens are placed into non-corrosive containers, which enable their immersion in a 3 % NaCl solution up to 5±1 mm. The containers also collect the scaled-off material. During thermal loading, the surface of the specimens must be cooled from +20 °C to –15 °C in 45 min to 50 min. It must then be warmed again within the same time and the maximum and minimum temperatures must be maintained for 15 min. One cycle takes approximately 2 h. After every 25th cycle, the mass of the material scaled off the surface of the specimens in a dry state is determined. The resistance of the surface of the cement concrete to water and defrosting chemicals is determined either by the mass of the scaled off material per area in g/m^2 after a certain number of cycles or by the number of cycles necessary for (1000, 2000 or 3000) g/m^2 of concrete to scale off.

2.4.2 ČSN 73 1326 Method C

The basic test specimen is a 50-mm-thick layer cut off from the top surface of a concrete cylinder of diameter 150 mm. The cylinder can be cast or core-drilled from a structure. Each specimen is fitted with a ring so that approximately a 5-mm-thick layer of a 3 % NaCl solution can be poured onto its surface. Afterwards, the specimens are exposed to freeze-thaw cycles with minimum temperatures of -18 °C for 3 h and maximum +5 °C also for 3 h. Thus, one cycle takes 6 h. After every 25th cycle, the particles lost from the tested surface in the dry state are weighed. The resistance of the concrete surface to defrosting chemicals is evaluated according to the D1 criterion (number of cycles necessary for the scale-off to reach 1000 g/m^2) through D5 (number of cycles necessary for scale-off to be 5000 g/m^2).

3 EXPERIMENTAL PART AND MATERIAL

The focus of the project GAČR 13-18870S is the research in concrete durability determined primarily by its surface layer quality. A number of papers have been published within the project, such as [30–34]. This paper describes one of the experiments conducted as part of the project. It involves the experimental assessment of the dependence of the resistance of concrete cover to the attack of water and de-icing chemicals on the amount of cement and plasticiser. The experiment was designed using the DOE (Design Of Experiment) method. [35]

A total of four groups of concretes with different cement contents were made (**Table 1**). They differed in the content of Portland cement CEM I 42.5 R. The concrete mixtures were then modified by the addition of a varied amount of plasticiser. The amount of water was adjusted so that the same workability was maintained. The other components of the fresh concretes were identical throughout the experiment, i.e. the same types of aggregate from the same location and the same type of cement from one cement mill. A large number of specimens were made from each type of concrete, amounting to approximately 0.4 m^3 in total volume. In order to ensure the homogeneity of all the concrete specimens

Table 1: Concrete-mixture identification
Tabela 1: Identifikacija mešanice betona

Mixture		Percentage of plasticiser content relative to the mass of cement in the mixture, in mass fractions (*w*/%)		
		0	0.25	0.50
Amount of cement in 1 m^3 of fresh concrete	250	R	-	-
	300	0/1	1/1	-
	350	0/2	1/2	2/2
	400	0/3	1/3	2/3

Table 2: Composition of the concrete mixtures in 1 m^3 with the real values of amount of the components
Tabela 2: Sestava mešanice betona v 1 m^3, z realno vrednostjo količine komponente

Components per 1 m^3 of fresh concrete		Concrete ID								
		R	0/1	0/2	0/3	1/1	1/2	1/3	2/2	2/3
CEM I 42.5 R (Mokrá) (kg)		248	308	357	392	295	349	394	338	386
Sand (Bratčice) 0-4 (kg)		953	925	889	826	927	897	846	905	854
Aggregate (Olbramovice) 4-8 (kg)		173	182	174	195	185	185	192	183	207
Aggregate (Olbramovice) 8-16 (kg)		675	696	693	669	689	693	684	667	671
Water (kg)	mixing	187	189	188	195	163	162	170	163	168
	in aggregate	14	14	13	13	14	13	13	13	13
	total	201	203	201	208	177	175	183	176	181
Sika ViscoCrete 4035 (kg)		0	0	0	0	0.71	0.91	0.95	1.77	2.01
W/C ratio (w_{mixing}/cement) (-)		0.75	0.61	0.53	0.50	0.55	0.46	0.43	0.44	0.44

throughout their volume, all the concrete mixtures were produced in a concrete mixing tower, which is the cause for the slight differences in the composition of the fresh concretes. For clarity, **Table 2** shows the detailed composition of the fresh concretes and **Table 3** contains the basic properties of the fresh and hardened concretes determined in accordance with the standards of the issue ČSN EN 12350 [28] and ČSN EN 12390 [29].

Table 3: Properties of fresh and hardened concrete
Tabela 3: Lastnosti svežega in strjenega betona

Concrete mixture	Slump test (mm)	Flow table test (mm)	Bulk density of fresh concrete (kg/m^3)	Compressive strength of hardened concrete (N/mm^2)
R	110	440	2 250	21.6
0/1	60	410	2 320	33.3
0/2	60	390	2 320	44.5
0/3	110	420	2 290	55.8
1/1	60	360	2 280	42.8
1/2	50	350	2 300	50.8
1/3	60	370	2 300	56.4
2/2	70	340	2 270	52.2
2/3	50	330	2 300	57.2

Test specimens were made from the mixtures for the purposes of the experiment according to method A and method C.[20] The specimens were cured under water until the time of the tests had arrived. The result of both tests was the average number of cycles necessary for the scaled off material to weigh 1000 g/m^2 and 3000 g/m^2 (i.e., the D1 and D3 coefficients) for each concrete of every mixture. In the case of method C, the D5 coefficient was also determined, i.e., the number of cycles necessary for scale-off amounting to 5000 g/m^2. At the beginning of the experiment, the number of loading cycles was set to be 100 for both methods. In the case of some specimens, the damage was so severe that the specimens were loaded for a lower number of cycles given the high values of scale-off.

4 RESULTS AND DISCUSSION

3 In order to assess the influence of the composition of concrete on the results of tests of its resistance to water and de-icing chemicals, a statistical analysis of the experiment was performed using the techniques of the DOE method. In order to model the dependence of the test results on the input factors, i.e., the components of fresh concretes, three basic models were used: linear, linear with interactions and a model with both a linear and quadratic representation of the factor effects including their mutual interactions. More can be found, e.g., in [35]. During the DOE, the following factors were chosen, which can be assumed to have had an influence on the resistance of the surface layer to defrosting chemicals: the amount of cement and plasticiser, while another factor was added during the evaluation – water/cement (*w/c*) ratio.

4.1 Results for method A

Table 4 contains the results of tests performed using method A described in [20] with all the specimens of all the mixtures being examined. The coefficients being observed were D1 and D3.

Table 4: Evaluation of coefficients D1 and D3 according to method A of [20] for each specimen of each mixture
Tabela 4: Ocena koeficientov D1 in D3 po metodi A [20], za vsak vzorec vsake mešanice

Mixture	**R**	**0/1**	**0/2**	**0/3**	**1/1**	**1/2**	**1/3**	**2/2**	**2/3**
D1 coefficient (number of cycles)	6	13	12	10	9	23	12	32	16
	7	12	12	9	8	24	12	29	13
	4	11	11	10	8	20	15	31	20
Average value of the D1 coefficient	**5**	**12**	**12**	**10**	**9**	**23**	**13**	**31**	**16**
D3 coefficient (number of cycles)	17	27	30	28	26	42	33	60	39
	20	27	27	26	25	43	33	53	33
	11	27	27	29	24	38	37	57	44
Average value of the D3 coefficient	**16**	**27**	**28**	**28**	**25**	**41**	**34**	**57**	**39**

The Pareto analysis of the results of the ANOVA (Analysis of Variance) statistical tests performed on significance level of 0.05 is shown in **Figures 1** and **2**.

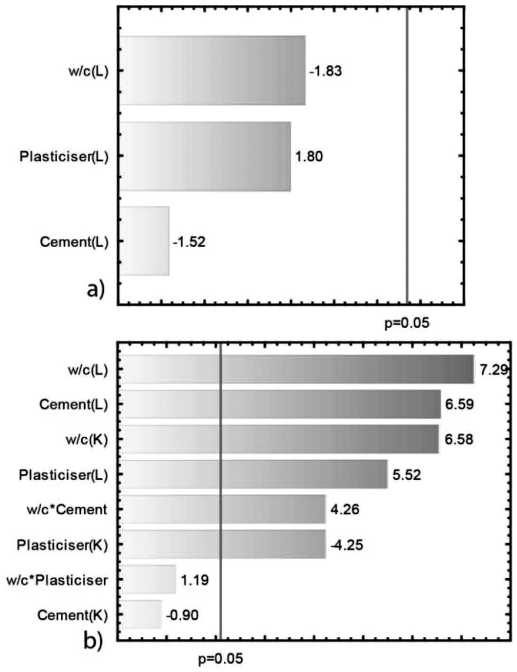

Figure 1: Method A, D1 coefficient: a) Pareto diagram of the standardised assessment of effects – linear model, b) Pareto diagram of the standardised assessment of effects – each effect represented in linear (L) and quadratic form (K)

Slika 1: Metoda A, koeficient D1: a) Pareto diagram standardiziranega ugotavljanja učinkov – linearni model, b) Pareto diagram standardiziranega ugotavljanja učinkov – vsak učinek je predstavljen v linearni (L) in v kvadratni (K) obliki

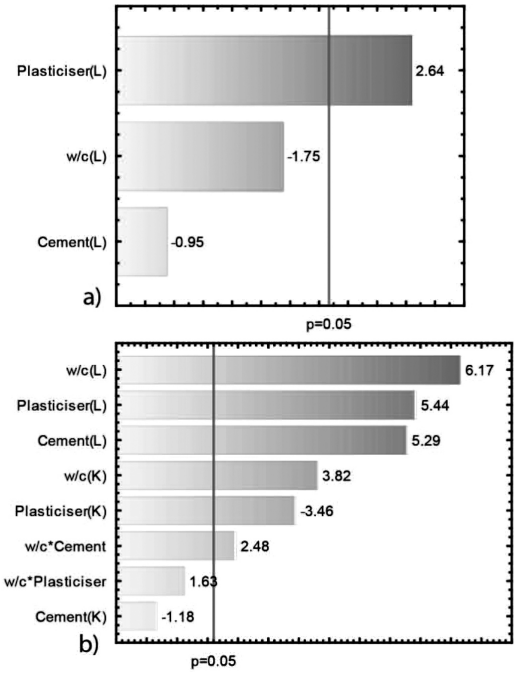

Figure 2: Method A, D3 coefficient: a) Pareto diagram of the standardised assessment of effects – linear model, b) Pareto diagram of the standardised assessment of effects – each effect represented in linear (L) and quadratic form (K)

Slika 2: Metoda A, koeficient D3: a) Pareto diagram standardiziranega ugotavljanja učinkov – linearni model, b) Pareto diagram standardiziranega ugotavljanja učinkov – vsak učinek je predstavljen v linearni (L) in v kvadratni (K) obliki

These statistical tests compared the statistical significances of the standardised assessments of the individual factor effects (*w/c* ratio, cement content and plasticiser content). Generally speaking, it was the statistical influence of concrete composition on test results – i.e., the values of the D1 and D3 coefficients. **Figures 1a** and **2a** show the results of the purely linear model and **Figure 1b** and **2b** show the results of the model with a linear and quadratic representation of effects including mutual interactions.

Based on these results, it appears difficult to analyse the most substantial influence in the composition of concrete on its resistance to de-icing agents using method A. None of the factor effects or their interaction has a more significant influence than any of the others. However, based on the linear model and the complete model with the quadratic representation of all the effects and interactions, it can be said that the slightly more significant factor influencing the value of the D1 coefficient is the w/c ratio. In the case of the D1 and D3 coefficients, the results do not confirm the assumption that higher cement content brings greater resistance of concrete cover to the attack of de-icing chemicals with any plasticiser content. The positive influence of an increase in plasticiser content is more visible in the results in **Table 3**. This fact is confirmed also in [36] which deals with testing by means of CDF, which is in principle identical to method A [20]. The paper [36] contains the results for four types of concrete differing, among others, in the plasticiser content. Compared with the concretes containing additives, the de-icing-chemical resistance of the concrete with no plasticiser was lower by several orders of magnitude. The article [37] describes the same tendency in the behaviour of concretes with a different content of additives in relation to their resistance to water and de-icing chemicals. The results in [37] are supplemented with another parameter, which is the assessment of the influence of air-entrainment on the behaviour of concrete

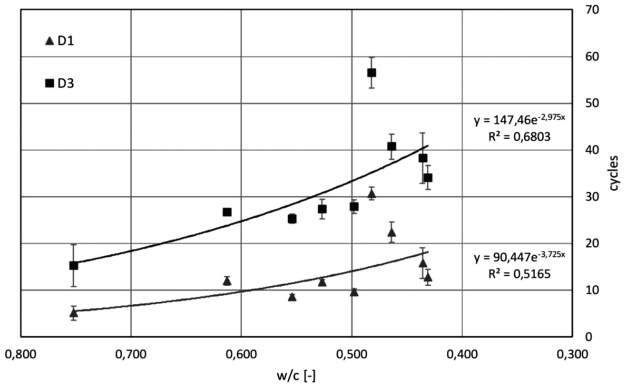

Figure 3: Dependence of average D1 and D3 coefficients according to method A[20] on w/c ratio, including corrected sample standard deviations

Slika 3: Odvisnost povprečja koeficientov D1 in D3 po metodi A[20] na razmerje w/c, z vključenim korigiranim standardnim odstopanjem vzorca

during the CDF test. The issue of the resistance of concrete to water and de-icing chemicals is also discussed in [38], where the matter being tested is the de-icing-chemical resistance of concretes with a different plasticiser content (as well as silica fume and an air-entraining additive). The present issue is also addressed in [39–41].

Figure 3 shows the dependence of the D1 and D3 values on the *w/c* ratio. It is apparent that as the *w/c* ratio is decreased, the resistance of concrete to de-icing agents increases.

4.2 Results for method C

Table 5 contains the results of tests performed using method C described in [20] with all the specimens of all the mixtures being examined. The coefficients being observed were D1, D3 and D5.

Table 5: Evaluation of coefficient D1, D3 and D5 according to method C of [20] for each specimen of each mixture

Tabela 5: Ocena koeficientov D1, D3 in D5 po metodi C [20], za vsak vzorec vsake mešanice

Mixture	R	0/1	0/2	0/3	1/1	1/2	1/3	2/2	2/3
D1 coefficient (number of cycles)	2	2	4	10	4	7	71	25	44
	2	2	4	9	5	7	77	28	36
	2	2	4	8	4	6	83	26	41
Average value of the D1 coefficient	**2**	**2**	**4**	**9**	**4**	**7**	**77**	**27**	**40**
D3 coefficient (number of cycles)	6	5	13	28	11	22	-	42	66
	5	7	12	26	14	20	-	49	61
	6	6	12	23	12	19	-	44	67
Average value of the D3 coefficient	**5**	**6**	**12**	**26**	**13**	**20**	**-**	**45**	**65**
D5 coefficient (number of cycles)	9	9	22	40	19	35	-	58	82
	8	12	20	38	24	33	-	62	78
	9	11	20	37	20	33	-	61	86
Average value of the D5 coefficient	**9**	**10**	**21**	**39**	**21**	**34**	**-**	**61**	**82**

The Pareto analysis of the results of the ANOVA (Analysis of Variance) statistical tests performed on the significance level of 0.05 is shown visually in **Figures 4** through **6**. Two models were chosen for the analysis of the tests performed by means of method C[20] – linear and linear with interactions of the factor effects. Some interactions are in mutual linear combination and were therefore eliminated from the experiment.

Table 5 shows that the results for mixture 1/3 are outliers. After 100 freeze-thaw cycles, the concrete suffered a scale-off corresponding to the D1 coefficient (1000 g/m^2), which indicates a much greater resistance of the surface layer to the action of de-icing chemicals compared with concretes of a similar composition. After a preliminary analysis, these results clearly influenced the overall outcomes. **Figures 4a** and **4b** show the Pareto analysis of the test statistics for the D1 coefficient, which does not correspond to similar results for the D3 and D5 coefficients (**Figures 5** and **6**). After the elimination of the results for mixture 1/3, the Pareto analysis of the D1 coefficient corresponds to the analysis of the D3 and D5 coefficients (**Figures 4c** and **4d**).

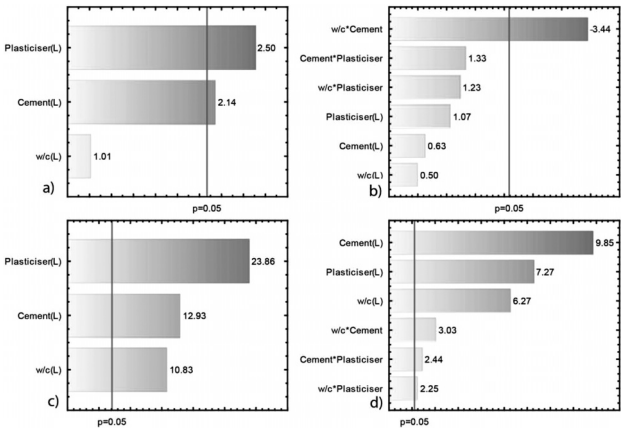

Figure 4: Method C, D1 coefficient: a) Pareto diagram of the standardised assessment of effects – linear model, b) Pareto diagram of the standardised assessment of effects – linear model with interactions, c) Pareto diagram of the standardised assessment of effects – linear model – without results for mixture 1/3, d) Pareto diagram of the standardised assessment of effects – linear model with interactions – without results for mixture 1/3

Slika 4: Metoda C, koeficient D1: a) Pareto diagram standardiziranega ugotavljanja učinkov – linearni model, b) Pareto diagram standardiziranega ugotavljanja učinkov – linearni model z interakcijami, c) Pareto diagram standardiziranega ugotavljanja učinkov – linearni model – brez rezultatov za mešanico 1/3, d) Pareto diagram standardiziranega ugotavljanja učinkov – linearni model z interakcijo – brez rezultatov za mešanico 1/3

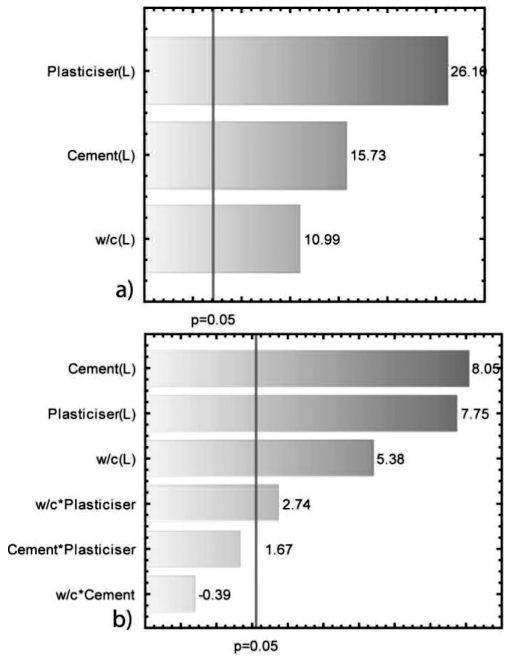

Figure 5: Method C, D3 coefficient: a) Pareto diagram of the standardised assessment of effects – linear model, b) Pareto diagram of the standardised assessment of effects – linear model with interactions

Slika 5: Metoda C, koeficient D3: a) Pareto diagram standardiziranega ugotavljanja učinkov – linearni model, b) Pareto diagram standardiziranega ugotavljanja učinkov – linearni model z interakcijami

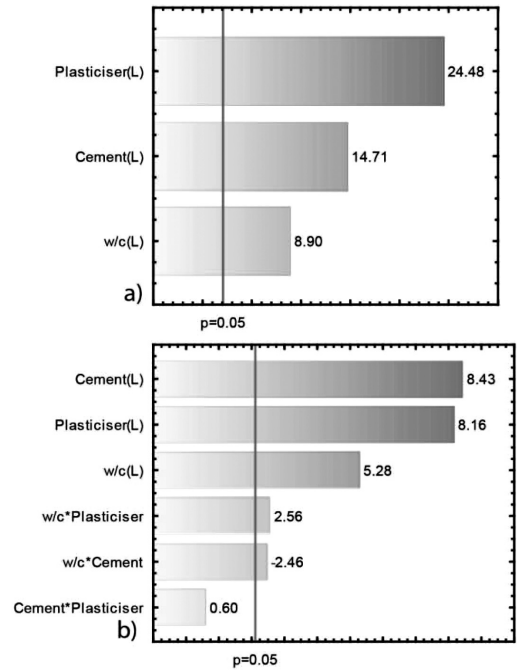

Figure 6: Method C, D5 coefficient: a) Pareto diagram of the standardised assessment of effects – linear model, b) Pareto diagram of the standardised assessment of effects – linear model with interactions

Slika 6: Metoda C, koeficient D5: a) Pareto diagram standardiziranega ugotavljanja učinkov – linearni model, b) Pareto diagram standardiziranega ugotavljanja učinkov – linearni model z interakcijami

Based on the analyses, it can be said that the results of the tests performed using method C from 20 exhibit significant statistical changes, especially in relation to the cement and plasticiser content. **Figure 7** shows the assessment of the D5 coefficient on these two factors with an average *w/c* ratio, which confirms the above-

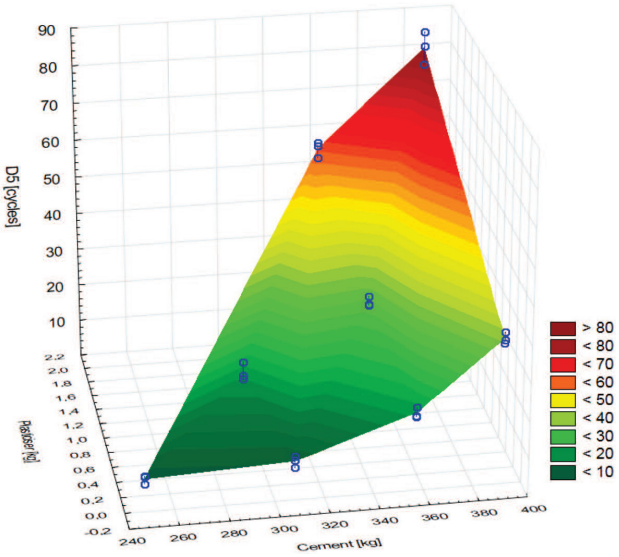

Figure 7: Dependence of the D5 coefficient according to method C [20] on cement and plasticiser content at an average w/c ratio

Slika 7: Odvisnost koeficienta D5 po metodi C [20] od vsebnosti cementa in plastifikatorja pri povprečnem razmerju w/c

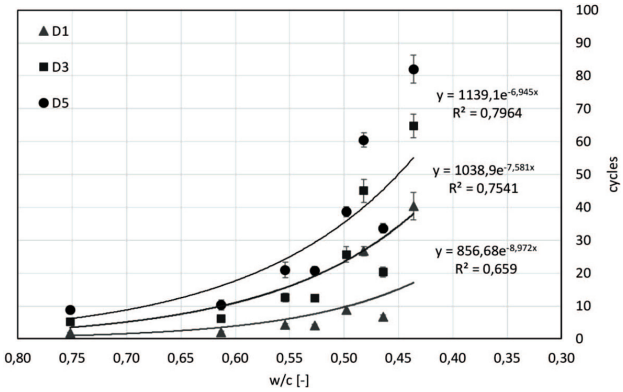

Figure 8: Dependence of the average D1, D3 and D5 coefficients according to method C[20] on the w/c ratio (after the elimination of results for mixture 1/3), including corrected sample standard deviations

Slika 8: Odvisnost povprečja koeficientov D1, D3 in D5 po metodi C[20] od razmerja w/c (po odstranitvi rezultatov za mešanico 1/3), vključujoč korigirana standardna odstopanja vzorca

mentioned findings. **Figure 8** shows, similarly to method A [20], the dependence of the D1, D3 and D5 coefficients on the *w/c* ratio. The test results show the same trends as the previous case; it is, however, necessary to note the high variability of results in relation to the *w/c* ratio.

In [42] the authors discuss, among others, the results of concrete resistance tested by the scaling method according to [18] on concretes of different composition, which is in principle comparable to method C. The test results published in [42] did not show clear tendencies of higher concrete resistance in dependence on increasing plasticiser content in fresh concrete, as opposed to the analysis performed by the authors of this paper. Also, method C is in principle identical to the method in [23], which was used by the authors of the paper [43], where the subject being investigated was how a partial substitution of cement with blast furnace slag (or fly ash) impacts the final resistance of concrete to de-icing chemicals. Next to the finding that the fly ash substantially worsens durability, the authors of [43] arrived at the conclusion that the visual assessment of scale-off is very subjective and it would be appropriate to substitute it with determining the damage to the concrete surface by weighing the scaled-off material. Similarly, the authors of [44] prefer measuring the mass of the scale-off, which corresponds to the experience of this paper's authors as well. The similar issue of determining the resistance of concrete to de-icing chemicals is also addressed in the papers.[45-47]

5 CONCLUSION

The assessment of the durability of concrete through testing its surface layer for damage by de-icing chemicals is very sensitive to a number of factors, whether technological (fresh concrete composition) or test ones (choice of method, means of specimen treatment, etc.), which is confirmed by the conclusions published, e.g., in [37,42,43,45,47]. The results of the experi-

ment described in this paper suggest that the composition of fresh concrete has a demonstrable influence on the resistance of the concrete surface layer to the action of de-icing chemicals. It can be said that performing the laboratory tests using method C^{20}, the coefficients of concrete resistance to de-icing chemicals reach lower values and thus it appears that the surface layer is less durable compared with the case when method A^{20} is used. The reason may be a different direction in which the solution acts upon the specimen (the specimen being immersed vs. the solution being poured onto the specimen), different time of the attack by extreme temperatures, etc. The change in the amount of cement and the amount of plasticiser in fresh concrete is more conclusively visible in the test results according to method C20, which is in principle similar to the scaling methods in [18] and ASTM. [23] The measurement results also indicated a greater sensitivity of method C^{20} to a change in the *w*/*c* ratio of fresh concrete.

Acknowledgement

This paper was written with the financial support of the Czech Science Foundation project GAČR 13-18870S and the European Union's "Operational Programme Research and Development for Innovations", No. CZ.1.05/2.1.00/03.0097.

6 REFERENCES

[1] B. Piwakowski, M. Kaczmarek, P. Safinowski, Evaluation of concrete cover by surface wave technique: Identification procedure, (**2011**), 276–279, doi:10.1063/1.3703188

[2] L. H. R. Lackner, P. Pimienta, F. Meftah, Permeability of concrete under thermal and compressive stress influence; an experimental study, MATEC Web of Conferences, 6 (**2013**), 03007, doi:10.1051/matecconf/20130603007

[3] V. Cnudde, A. Cwirzen, B. Masschaele, P. J. S. Jacobs, Porosity and microstructure characterization of building stones and concretes, Engineering Geology, 103 (**2009**) 3–4, 76–83, doi:10.1016/j.enggeo.2008.06.014

[4] B. Kucharczyková, P. Misák, T. Vymazal, Determination and evaluation of the air permeability coefficient using Torrent Permeability Tester, Russian Journal of Nondestructive Testing, 46 (**2010**) 3, 226–233, doi:10.1134/S1061830910030113

[5] M. Stehlík, V. Hermánková, L. Vítek, Opening of microcracks and air permeability in concrete, Journal of Civil Engineering and Management, 21 (**2015**) 2, 177–184, doi:10.3846/13923730.2013.802721

[6] J. Liu, F. Xing, B. Dong, H. Ma, D. Pan, Study on Surface Permeability of Concrete under Immersion, Materials, 7 (**2014**) 2, 876–886, doi:10.3390/ma7020876

[7] H. Seleem, A. Rashad, B. El-Sabbagh, Durability and strength evaluation of high-performance concrete in marine structures, Construction and Building Materials, 6 (**2010**) 24, 878–884, doi:10.1016/j.conbuildmat.2010.01.013. ISSN 09500618

[8] T. Stavař, M. Stehlík, The Assessment of Durability of Fibre Concretes with Dense Aggregate and Concrete Recyclate from the Results of Permeability and Diffusion Tests, Advanced Materials Research, 1100 (**2015**), 106–111, doi:10.4028/www.scientific.net/AMR.1100.106

[9] M. Stehlík, Enhancing the durability of concrete made of concrete recyclate by additives and admixtures, Journal of Civil Engineering and Management, 2 (**2014**) 20, 270–279, doi:10.3846/13923730.2013.802708

[10] J. Valenza, G. Scherer, A review of salt scaling: I. Phenomenology, Cement and Concrete Research, 37 (**2007**) 7, 1007–1021, doi:10.1016/j.cemconres.2007.03.005

[11] Z. Liu, W. Hansen, Freezing characteristics of air-entrained concrete in the presence of deicing salt, Cement and Concrete Research, 74 (**2015**), 10–18, doi:10.1016/j.cemconres.2015.03.015

[12] J. Valenza, G. Scherer, Mechanism for salt scaling of a cementitious surface, Materials and Structures, 40 (**2007**) 3, 259–268, doi:10.1617/s11527-006-9104-1

[13] Freeze-thaw and de-icing resistance of concrete, Essen: Lund Institute of Technology, 1992

[14] H-S. Shang, T-H Yi, Freeze-Thaw Durability of Air-Entrained Concrete, The Scientific World Journal, (**2013**), 1–6, doi:10.1155/2013/650791. ISSN 1537744x

[15] V. Penttala, Surface and internal deterioration of concrete due to saline and non-saline freeze–thaw loads, Cement and Concrete Research, 36 (**2006**) 5, 921–928, doi:10.1016/j.cemconres.2005.10.007

[16] Z. Sun, G. Scherer, Effect of air voids on salt scaling and internal freezing, Cement and Concrete Research, 40 (**2010**) 2, 260–270, doi:10.1016/j.cemconres.2009.09.027

[17] P-C. Aïtcin, Vysokohodnotný beton. 1. české vyd. Praha: Pro Českou komoru autorizovaných inženýrů a techniků činných ve výstavbě (ČKAIT) a Českou betonářskou společnost vydalo Informační centrum ČKAIT, 2005, Betonové stavitelství

[18] CEN/TS 12390-9, CEN/TS 12390-9 Testing hardened concrete, Freeze-thaw resistance, Scaling, European Committee for Standardization, 2006

[19] Concrete testing – Hardened concrete – Scaling at freezing, Swedish: Swedish Standards Institution, 2005

[20] ČSN 73 1326 Stanovení odolnosti povrchu cementového betonu proti působení vody a chemických rozmrazovacích látek, Praha: Úřad pro normalizaci a měření, 1984

[21] ČSN 73 1380 Zkoušení odolnosti betonu proti zmrazování a rozmrazování - Porušení vnitřní struktury, Praha: Český normalizační institut, 2007

[22] ČSN 73 1322, ČSN 73 1322 Stanovení mrazuvzdornosti betonu, Praha, Úřad pro normalizaci a měření, 1968

[23] Standard Test Method for Scaling Resistance of Concrete Surfaces Exposed to Deicing Chemicals, West Conshohocken, PA: ASTM International, 2012

[24] J. Valenza, G. W. Scherer, A review of salt scaling: II. Mechanisms, Cement and Concrete Research, 37 (**2007**) 7, 1022–1034 doi:10.1016/j.cemconres.2007.03.003

[25] J. Kim, J. H. Moon,J. W. Shim,J. Sim,H. G. Lee, G. Zi, Durability properties of a concrete with waste glass sludge exposed to freeze-and-thaw condition and de-icing salt, Construction and Building Materials, 66 **(2014)**, 398–402, doi:10.1016j.conbuildmat.2014.05.081

[26] BAW Code of Practice: Frost Resistance Tests for Concrete (MFB), Karlsruhe: Bundesanstalt für Wasserbau (BAW), 2012

[27] ČSN EN 12350 Testing of fresh concrete: this standard is the Czech version of the European Standard EN 12350, Praha: ÚNMZ, 2009

[28] ČSN EN 12390 Testing hardened concrete: this standard is the Czech version of the European Standard EN 12390, Praha: ÚNMZ, 2009

[29] H. Šimonová, I. Havlíková, P. Daněk, Z. Keršner, T. Vymazal, The Effect of a Superplasticizer Admixture on the Mechanical Fracture Parameters of Concrete, Mater. Tehnol., 49 (**2015**) 3, 417–421, doi:10.17222/mit.2014.114

[30] H. Šimonová, D. Lehký, Z. Keršner, V. Veselý, J. Macur, Relationships Between Mechanical Fracture and Durability Parameters of Selected Concretes, 39th Solid Mechanics Conference Book of

Abstracts, Warszawa: Institute of Fundamental Technological Research PAN, (2014), 51–52

[31] H. Šimonová, I. Havlíková, P. Daněk , D. Lehký, B. Kucharczyková, Z. Keršner, Study of Influence of Cement Dosage on Mechanical Fracture Parameters of Selected Concretes, In Proc. of the 6 th Int. Conf. on Dynamics of Civil Engineering and Transport Structures and Wind Engineering. Žilina, EDIS publishing house University of Zilina, (**2014**), 291–296

[32] M. Matysík, L. Topolar, P. Daněk, T. Vymazal, I. Plšková, The Effect of Concrete Quality on the Acoustic Emission Parameters during Three-Point Bending Fracture Test, Advanced Materials Research, 897 (**2014**), 149–152, doi:10.4028/www.scientific.net/AMR.897.149

[33] T. Komárková, M. Králíková, P. Kovács, Application of computed tomography in comparison with the standardized methods for determining the permeability of cement-composite structures, Mater. Tehnol., 49 (**2015**) 4, 587–595, doi:10.17222/mit.2014.194

[34] L. Eriksson, N. Kettaneh-Wold, C. Wikström, S. Wold, Design Of Experiments: Principles And Applications. 3. revised and enlarged, Umeå: MKS Umetrics AB, 2008

[35] J. Deja, Freezing and de-icing salt resistance of blast furnace slag concretes. Cement and Concrete Composites, 25 (**2003**) 3, 357–361, doi:10.1016/S0958-9465(02)00052-5

[36] R. Şahin, M. Taşdemir, R. Gül, C. Çelik, Determination of the optimum conditions for de-icing salt scaling resistance of concrete by visual examination and surface scaling, Construction and Building Materials, 24 (**2010**) 3, 353–360, doi:10.1016/j.conbuildmat.2009.08.026

[37] H. Romero, A. Enfedaque, J. Gálvez, M. Casati, Resistencia del hormigón frente a ciclos hielo deshielo medida con técnicas complementarias. Materiales de Construcción, 65 (**2015**) 317, 048–, doi:10.3989/mc.2015.01514

[38] Z. Van, G. F. Wittmann, B. Oh, Durability of strain-hardening cement-based composites (SHCC), Materials and Structures, 45 (**2012**) 10, 1447–1463, doi:10.1617/s11527-012-9845-y

[39] P. A. G. V. Zijl, Gideon, F. H. Wittmann, On Durability of SHCC, Journal of Advanced Concrete Technology, 8 (**2010**) 3, 261–271, doi:10.3151/jact.8.261

[40] J. Zhang, P. C. Taylor, C. Shi, Investigation of approaches for improving interfacial transition zone-related freezing-and-thawing resistance in concrete pavements. ACI Materials Journal, 112 (**2015**) 5, 613–617. doi:10.14359/51687902

[41] T. Rønning, Freeze-Thaw Resistance of Concrete Effect of: Curing Conditions, Moisture Exchange and Materials, Doctoral thesis,Fakultet for ingeniørvitenskap og teknologi Trondheim, 2011

[42] R. M. Ahani, M. R. Nokken, Salt scaling resistance – The effect of curing and pre-saturation, Construction and Building Materials, 26 (**2012**) 1, 558–564, doi:10.1016/j.conbuildmat.2011.06.058

[43] A. Ramezanianpour, M. J. Nadooshan, M. Peydayesh, A. M. Ramezanianpour, Effect of entrained air voids on salt scaling resistance of concrete containing a new composite cement, KSCE Journal of Civil Engineering, 18 (**2014**) 1, 213–219, doi:10.1007/s12205-014-0365-x

[44] A. Ramezanianpour, M. J. Nadooshan, M. Peydayesh, Effect of New Composite Cement Containing Volcanic Ash and Limestone on Mechanical Properties and Salt Scaling Resistance of Concrete, Journal of Materials in Civil Engineering, 25 (**2013**) 11, 1587–1593, doi:10.1061/(ASCE)MT.1943-5533.0000679

[45] M. Pigeon, C. Talbot, J. Marchand a H. Hornain, Surface microstructure and scaling resistance of concrete, Cement and Concrete Research, 26 (**1996**) 10, 1555–1566, doi:10.1016/0008-8846(96)00138-X

[46] E. Houehanou, R. Gagné, M. Jolin, Analysis of the representativeness and relative severity of ASTM C672 and NQ 2621-900 standard procedures in evaluating concrete scaling resistance, Canadian Journal of Civil Engineering, 37 (**2010**) 11, 1471–1482, doi:10.1139/L10-091

UDK 67.017:620.1:621.386.83
Original scientific article/Izvirni znanstveni članek

ISSN 1580-2949
MTAEC9, 51(3)397(2017)

TIME-LAPSE MICRO-TOMOGRAPHY ANALYSIS OF THE DEFORMATION RESPONSE OF A GELLAN-GUM-BASED SCAFFOLD

MIKROTOMOGRAFSKA ANALIZA S ČASOVNIM ZAMIKOM ODZIVA DEFORMACIJE OGRODJA IZ GELANSKEGA GUMIJA

Daniel Kytýř[1,2], Nela Fenclová[1,2], Petr Zlámal[1,2], Ivana Kumpová[2], Tomáš Fíla[1,2], Petr Koudelka[1,2], Ana Gantar[3,4], Sasa Novak[3,4]

[1]Czech Technical University, Faculty of Transportation Sciences, Department of Mechanics and Materials, Konviktská 20, 110 00 Prague 1, Czech Republic
[2]Institute of Theoretical and Applied Mechanics, v.v.i., Academy of Sciences of the Czech Republic, Prosecká 76, 190 00 Prague 9, Czech Republic
[3]Jožef Stefan Institute, Department for Nanostructured Materials, Jamova cesta 39, 1000 Ljubljana, Slovenia
[4]Jožef Stefan International Postgraduate School, Jamova cesta 39, 1000 Ljubljana, Slovenia
kytyr@fd.cvut.cz

Prejem rokopisa – received: 2015-07-27; sprejem za objavo – accepted for publication: 2016-05-20

doi:10.17222/mit.2015.237

The presented work is aimed at a demonstration of modern radiological methods for an investigation of the deformation behaviour of bone scaffolds. Bone scaffold is an artificial structure used for the repairs of trabecular bones damaged by injuries or degenerative diseases. In bone-tissue engineering a proper description of its deformation behaviour is one of the most important characteristics for an assessment of the biocompatibility and bone-integration characteristics of the proposed structure intended to be used as a bone scaffold. According to recent studies bioactive-glass-reinforced gellan-gum (GG-BAG) is a promising material for bone-scaffold production. However, its low specific stiffness and simultaneous low attenuation to X-rays makes both the mechanical and imaging parts of the deformation experiments difficult. As a result a state-of-the-art experimental setup composed of high-precision micro-loading apparatus designed for the X-ray observation of deformation processes and an advanced radiographical device is required for such experiments. Furthermore, the radiographical device has to utilize highly sensitive detectors and corresponding radiation sources with appropriate beam characteristics that provide a high signal-to-noise ratio (*SNR*) during all the measurements. High-resolution time-lapse micro-focus X-ray computed tomography (micro CT) under loading in three different imaging modes was performed to obtain a precise structural and mechanical description of the observed deforming GG-BAG scaffolds. The digital volumetric correlation (DVC) method was applied on reconstructed data from micro CT measurements to evaluate not only the effective mechanical characteristics but also to enable a detailed inspection of the specimens' internal structure, particularly the deformation modes of the individual struts and joints. The calculated volumetric strain fields demonstrate the suitability of such experimental methodology and devices for the assessment of both the microscopic and macroscopic characteristics of the investigated complex GG-BAG microarchitectures.

Keywords: bone scaffold, gellan gum, time-lapse micro CT, digital volume correlation

Predstavljeno delo je namenjeno prikazu sodobnih radioloških metod za preiskave obnašanja deformacije kostno-regenerativnih celičnih ogrodij. Takšno celično ogrodje je tridimenzionalna umetna struktura, ki se uporablja za regeneracijo trabekularne kosti ob poškodbah ali pri degenerativnih boleznih. Pravilen opis obnašanja ogrodja ob deformaciji je eden od pomembnejših faktorjev za določitev biokompatibilnosti ogrodja, in kako se bo to ogrodje vključilo v tkivo, v katerega je vstavljeno. Glede na nedavne študije, je kompozit bioaktivno steklo – gelanski gumi (GG-BAG), obetaven material za pripravo kostno-regenerativnih celičnih ogrodij. Zaradi nizke specifične togosti materiala in slabljenja rentgenskih žarkov, je oteženo zaznavanje deformacije, tako mehansko kot tudi z rentgenskimi žarki. Zaradi zahtevnosti sistema je za tako preizkušanje potrebna posebna naprava, sestavljena iz mikrotlačne naprave z visoko natančnostjo, ki je načrtovana za opazovanje deformacije med slikanjem z rentgenskimi žarki, ter napredne radiografske naprave. V sklopu sistema so potrebni tudi detektorji visoke občutljivosti in ustrezen vir žarčenja, z ustrezno značilnostjo snopa, ki zagotavljajo visoko razmerje med signalom in šumom (angl. *SNR*) med merjenji. Ob kompresiji vzorca je bila izvedena visokoločljivostna mikrofokusna rentgenska računalniška tomografija (angl. micro CT) s časovnim zamikom, v treh različnih načinih slikanja, za pridobitev natančnega konstrukcijskga in mehanskga opisa opaženih deformiracij GG-BAG kostno-regnerativnih celičnih ogrodij. Digitalna volumetrična korelacijska (DVK) metoda je bila uporabljena pri rekonstruiranih podatkih meritev z mikro-CT, za ovrednotenje efektivnih mehanskih karakteristik in tudi za podroben pregled notranje strukture vzorcev ob obremenitvi, zlasti načinov deformacije posameznih opornikov in spojev znotraj celičnega ogrodja. Volumetrično izračunana območja obremenitev prikazujejo ustreznost takšne eksperimentalne metodologije in naprave za določevanje, tako mikroskopskih kot makroskopskih, lastnosti kompleksne mikroarhitekture preiskovanega GG-BAG kompozita.

Ključne besede: celično ogrodje, gelanska guma, mikro-CT s časovnim zamikom, digitalna volumska korelacija

1 INTRODUCTION

To successfully develop an artificial bone scaffold various fundamental requirements have to be fulfilled: i) the provision of normal cellular activity without potential toxicity, ii) the minimization of potential stress shielding effects, iii) the reliable long-term supply of organic/anorganic nutrients and oxygen and iv) the controlled progressive degradation and resorption of the scaffold during healing.[1] Apparently, these requirements also closely comply with the general goals of modern bone-tissue engineering. However, in contrast to established materials for bone-tissue engineering (particularly HAP) the usage of GG-BAG for scaffold production may significantly reduce the potential for complications due to various influences, including donor site morbidity, limited availability, immune rejection and pathogen transfer.[2] Here, the successful application of a GG-BAG-based scaffold allows healing of the bone, even in the case of its partial amputation, supports natural formation of bone tissue according to stress fields and thus full restoration of the bone's primary function – the provision of mechanical support.

High-resolution time-lapse micro-focus X-ray computed tomography (micro CT) is currently the only feasible method for an investigation of volumetric deformation processes of micro-structural materials and specimens during loading.[3] Moreover, due to the very complex, spontaneously synthesized, stochastic scaffold microarchitecture description of its mechanical properties based on the overall characteristics appears to be insufficient. In the presented work a custom-designed experimental setup allowing the performance of mechanical testing during radiographical imaging is employed to evaluate detailed volumetric strain fields in the deforming scaffolds' microstructure using digital volumetric correlation (DVC).[4]

2 MATERIALS AND METHODS

2.1 Bioactive-glass-reinforced gellan-gum scaffolds

The recently proposed bioactive-glass-reinforced gellan-gum (GG-BAG), which is a promising material for bone scaffold fabrication, was used in this study.[5]

Gellan-gum (GG) is a microbial extracted polysaccaride used in the food and pharmaceutical industries.[6,7] GG is composed of repeating units consisting of two D-glucose and one of each L-rhamnose and D-glucuronic acid.[8] Its main advantage is in an ability to form highly porous 3D structures when properly cross-linked and fabricated.[9] In the field of bone regeneration the GG is biocompatible and biodegradable but it doesn't have sufficient mechanical properties to enable successful bone regeneration and it does not promote bone formation. Therefore, GG has to be reinforced by bioactive glass particles (BAG).

BAG is a nano-particulate amorphous material with a chemical composition of 70 n/n % SiO_2 and 30 n/n % CaO and it is prepared by a modified sol-gel method.[10] BAG is a bioactive material and upon biodegradation there are no toxic products left behind. Therefore, BAG particles are very interesting for bone-regeneration applications.

During the production process gellan gum was dissolved in ultra-pure water by heating the solution for 30 °C min at 90 °C. To the hot GG solution a dispersion of BAG was admixed and 0.18 w/w % $CaCl_2$ was added. Kept at high temperatures this mixture was then poured into the required mould and let there to spontaneously jellify. The weight ratio between GG and BAG was 1:1 and the final concentration of $CaCl_2$ was 0.03 w/w % in all samples. Such samples were frozen 12 h at –80 °C and freeze-dried for 3 d in Lio 5 freeze dryer Kambič.[5]

Table 1: Dimensions and weights of the samples subjected to mechanical testing

Tabela 1: Dimenzije in masa vzorcev za mehanske preizkuse

	Specimen 1	Specimen 2	Specimen 3
Weight mg	11.2	10.4	24.7
Width mm	5.95-6.20	5.89-6.28	5.79-6.24
Height mm	6.04-6.08	6.54-6.62	7.93-8.21
BAG	no	no	yes
CT measurement	Photon counting detector, continual loading	Photon counting detector, discrete loading steps	Flat panel detector, discrete loading steps

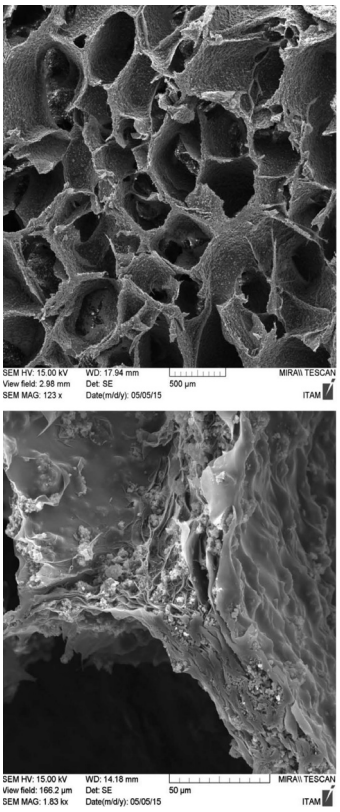

Figure 1: SEM micrograph of the scaffold obtained by scanning electron microscopy

Slika 1: SEM-posnetek celičnega ogrodja

Dimensions and weights of the three scaffolds manufactured from GG are presented in **Table 1**, and details of their microstructure is shown in **Figure 1**.

2.2 Mechanical testing

Compression tests of the GG-BAG samples were performed using a custom-designed uni-axial loading device. The device was designed to be suitable for mechanical testing of materials during continuous observation using X-rays including computed micro-tomography. Therefore, the main frame of the device is made of transparent polymethyl methacrylate tube with a 5.0 mm wall thickness and negligible X-ray attenuation. The loading mechanism consists of a stepper motor, flexible coupling, planetary gear unit P42-25 (Transtecno, Italy) and translation stage with micro-metric screw 7T173-20 (Standa, Lithuania). Such a mechanism is able to stress the specimen with a loading speed of 0.1–20 μm s^{-1} with an experimentally measured movement accuracy of better than 5 μm. The loading procedure is controlled by a GNU/Linux real-time operational system. In the case of scaffold measurements the device was equipped with a high-accuracy load cell and a 50-N load capacity HBM U9C (HBM, Germany).

2.3 Radiographical imaging

X-ray imaging of the compression tests was carried out using a modular X-ray setup with cone-beam tomography arrangement. As the GG-BAG material has very a low attenuation of X-rays three different scanning approaches were employed to find the best settings for the scaffold imaging. Conventional scanning at discrete loading steps using a flat panel detector was selected as a first option. Scanning using a photon counting detector in discrete loading steps was selected as a second option and a continuous fast tomography measurement (without loading steps) using a photon counting detector as a third option. In all cases the X-ray beam was generated by micro-focus X-ray tube with reflection target (XWT-240-SE, X-Ray Worx, Germany) operated at 50 kV, a 500 μA target current and a focal spot size of 5 μm. X-ray images of sample 3 were taken using a large area flat panel scintillating detector (Perkin Elmer XRD 1622 AP, USA) with an effective resolution of 2048 × 2048 px. The setup geometry was adjusted to 1230 mm focus-detector distance and 123 mm focus-object distance. Therefore, planar X-ray images resulted in 10× magnification and a 20 μm pixel size. One highly detailed tomography of the undeformed specimen (1200 projections) and three regular tomography scans (800 projections) at three different loading steps were taken. For scanning of another two samples (sample 1 and sample 2) a modular photon-counting detector consisting of 2×2 TimePIX chips with fast read-out (the ModuPIX detector) and an effective resolution of 1024 × 1024 px was employed. As a photon-counting detector and fast tomography requires an X-ray beam with high intensity the focus-detector distance was reduced to 175.5 mm and the focus-object distance was reduced to 95 mm. Thus, planar X-ray images in the case of imaging using photon counting detector resulted in 1.84× magnification and 30 μm pixel size. Sample 2 was scanned in 6 discrete loading steps. A total of 600 projections were acquired in each tomography measurement. Sample 1 was loaded continuously with 0.1 μm.s^{-1} loading speed and several tomography scans were taken with no time separation. In this case 400 projections were acquired in each tomography and one CT scan lasted approx. 4.5 min. The specimen was compressed by approximately 30 μm displacement during one CT scan (approx. 1 pixel in X-ray images). Linearization of the attenuation range (beam hardening correction) was applied to all the data to reduce the noise and improve the contrast in individual projections.[11] Due to high porosity of the samples and the small thickness of the structural elements (approximately 30 μm), the cone-beam reconstruction algorithm[12] was used to eliminate the distortion of the reconstructed data caused by the divergent nature of the X-ray beam.

The setup for radiographical imaging is shown in **Figure 2**.

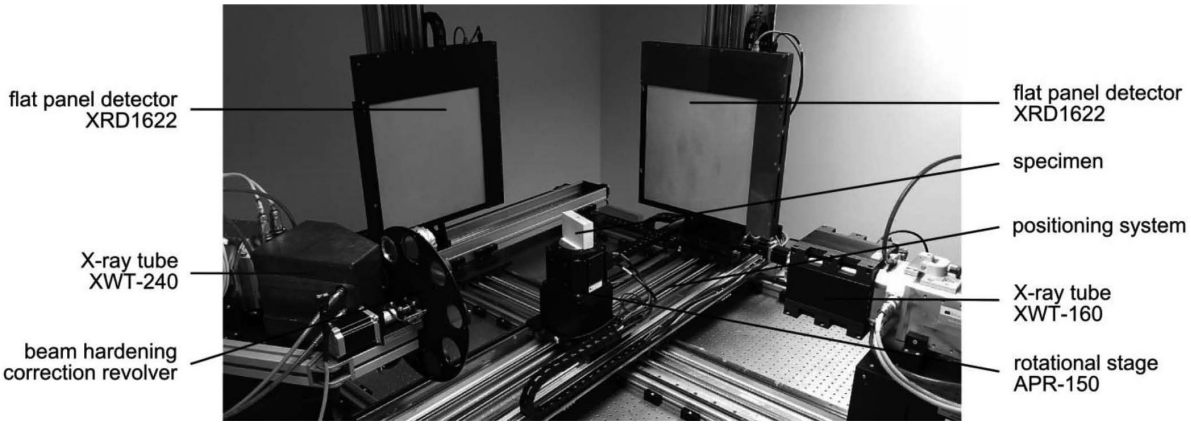

Figure 2: Microtomographical setup arrangement
Slika 2: Mikrotomografski sestav

2.4 Deformation mapping using digital volume correlation

The digital volumetric correlation (DVC) technique is a suitable tool for an evaluation of displacements and strains within the entire volume of the samples. The method makes it possible to track the changes in a sequence of volumetric images and to calculate the displacement of nodes representing the microstructure of the investigated samples. DVC uses the maximisation approach to find the correlation coefficient for the best fit between sub-image data defined around control points established in the reference image data. The correlation coefficient is evaluated by examining the pixel intensity of the image subsets in the corresponding image data and then the deformation mapping function is extracted. To maximise the correlation coefficient a nonlinear optimisation technique and an iterative approach were used. Coefficients of the linear affine transformation between the undeformed and deformed states can be used to establish the components of the displacement vector and the components of the gradient tensor. Then, using the deformation gradient tensor F it is possible to calculate the Green-Lagrangian strain tensor as Equation (1):

$$E = F^T F - I \quad (1)$$

The calculation of the inner deformation of the samples in all the loading states was performed using the custom DVC algorithm implemented in Matlab. Due to the computational complexity only two mutually perpendicular vertical planes passing through the centre of each sample were used for the displacement calculations. It was assumed that the displacement of the nodes in these planes sufficiently describes the deformation behaviour of the whole sample. The initial position of the tracked nodes corresponding to these planes was selected on the basis of detailed voxel model of each sample in the intact state.

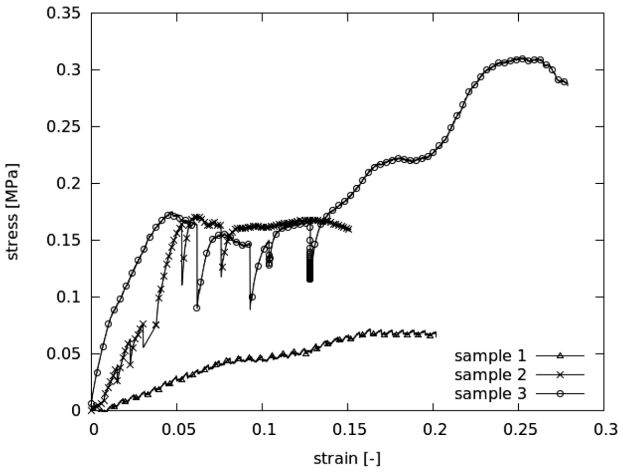

Figure 3: Stress-strain curves of the tested GG-BAG scaffolds

Slika 3: Krivulje obremenitev-deformacija preizkušenih GG-BAG celičnih ogrodij

3 RESULTS AND DISCUSSION

Three samples were subjected to compressive loading using a uni-axial loading device and the deformation behaviour of the inner structure was captured using X-ray imaging technique. Samples 2 and 3 were loaded in several successive phases (between the phases the tomography of sample was performed) while sample 1 was loaded continuously with a 0.1 μm s^{-1} loading speed. Stress-strain curves of these loading tests are shown in **Figure 3**. In the case of samples 2 and 3 it is clearly apparent that considerable relaxation of the samples (sudden decrease in stress value) occurred during the tomographic imaging. On the other hand, the stress-strain curve of sample 1 is not affected by the relaxation process because the tomographic imaging was performed during the loading process and the load applied to the sample was continuously incremented without interruption. The small repetitive decreases of the stress value visible on the stress-strain curve in this case are not a relaxation of the sample but were caused by the technical limitations of the experimental setup. As the loading device is equipped with supply cables the rotation stage with the loading device had to be returned to the initial position and the vibration of the rotation table during the homing sequence caused the micro-movement of the sample.

As expected the stiffness of sample 3 was higher than in case of non-reinforced samples 1 and 2. A mutual comparison of the response of non-reinforced samples 1 and 2 shows large difference of stiffness presumably

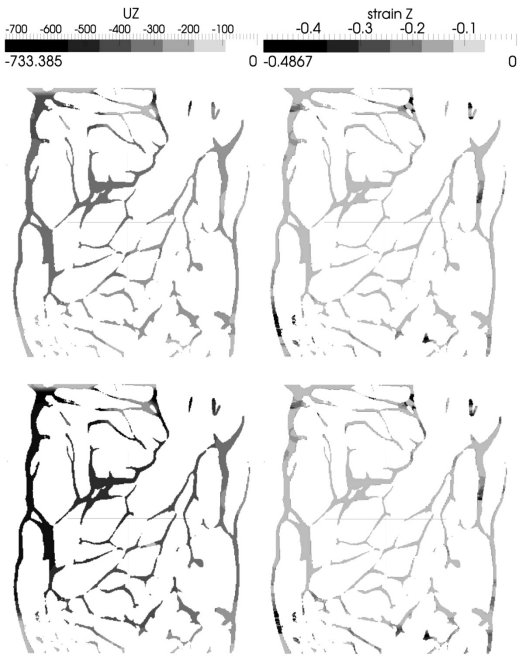

Figure 4: Displacement in z-direction (μm) and Green-Lagrangian strain of the sample 3; 8 % overall deformation; 12 % overall deformation

Slika 4: Premik v z-smeri (μm) in Green-Lagrangianova obremenitev vzorca 3; 8 % celotna deformacija, 12 % celotna deformacija

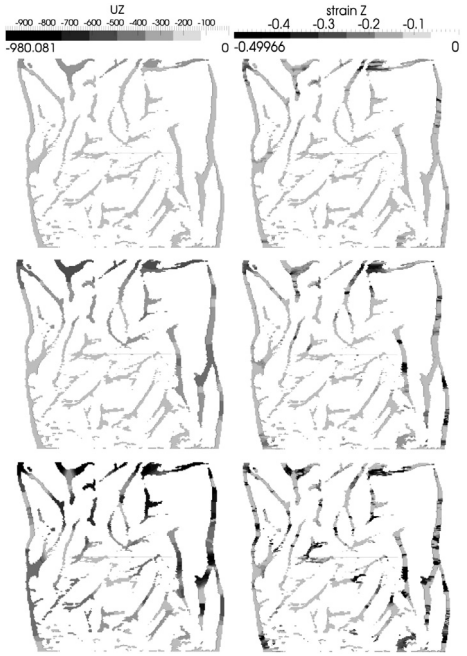

Figure 5: Displacement in z-direction (μm) and Green-Lagrangian strain of the sample 2: 3 % overall deformation (top); 5 % overall deformation; 7 % overall deformation

Slika 5: Premik v z-smeri (μm) in Green-Lagrangianova obremenitev vzorca 2; 3 % celotna deformacija, 5 % celotna deformacija, 7 % celotne deformacije

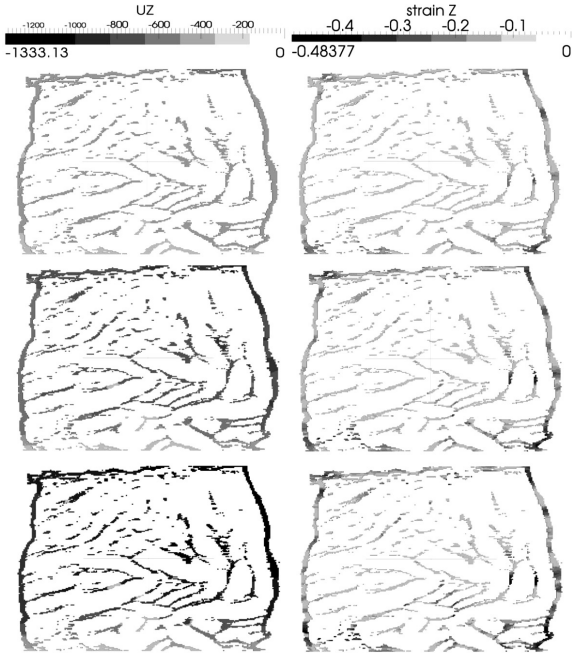

Figure 6: Displacement in z-direction (μm) and Green-Lagrangian strain of the sample 1: 6 % overall deformation; 13 % overall deformation; 20 % overall deformation

Slika 6: Premik v z-smeri (μm) in Green-Lagrangianova obremenitev vzorca 1; 6 % celotna deformacija, 13 % celotna deformacija, 20 % celotne deformacije

caused by the different nature of the spontaneously synthesized inner structure. Because of the complex inner structure of the scaffolds the overall (effective) strain assessed from the movement of the loading platens is not reliable parameter for characterising the deformation behaviour of such a material. Therefore, an advanced strain calculation based on the DVC technique was used in the study.

The DVC algorithm is extensively time-consuming and its computational cost linearly increases with the number of calculated deformation states. For this reason, only the displacement of nodes belonging to two mutually perpendicular vertical planes located in the centre of each sample were used (for sample 3 only one plane was used). These planes (YZ and XZ orientation) included: 14,720 nodes and 19,790 nodes for sample 1; 24,452 nodes and 23,076 nodes for sample 2; 46,728 nodes for sample 3. A larger number of nodes in the case of sample 3 relates to higher resolution of the flat panel detector. During the parallel DVC calculation (4 threads of Intel i7-3820 CPU) the displacement vector of each node in the selected plane through all the loading states was determined. Green-Lagrangian strain of every voxel was evaluated on the basis of displacement vectors of its corresponding nodes. Fields of the vertical displacement and the evaluated strain for one plane of each sample in selected deformation states mapped on the structure of the intact state are shown in **Figures 4** to **6**. The obtained deformation and strain fields show that the DVC technique can be successfully used for a determination of such complex deformation processes. As can be seen from the results the deformation of the samples was not limited only to uni-axial compression, as anticipated, but apparent bending of the samples caused by their complex inner structure, improper boundary conditions and sample geometry was present. Despite our best efforts, it was not possible to manufacture the samples with plan-parallel top and bottom faces. The evaluation of the elastic parts of the resulting stress-strain curves also showed the reason for the lower stiffness of the sample 1 when compared to the sample 2. As can be seen in **Figure 6** the struts of the inner structure of the sample 1 are oriented perpendicularly to the applied load while the struts of the inner structure of sample 2 (**Figure 5**) are mainly oriented in the direction of loading.

4 CONCLUSIONS

In this work the demonstration of modern radiological and computational methods for the investigation of the deformation behaviour of artificial bone scaffolds was shown.

Three samples were loaded using a custom uni-axial compression device and tomographically scanned in three different loading scenarios: i) flat panel scintillating detector with incremental loading steps, ii) fast photon-counting detector with incremental loading steps and iii) fast photon-counting detector with continuous loading. In the case of incrementally applied loading divided into individual steps the relatively large relaxa-

tion of the sample was observed during the tomography scanning. This undesirable relaxation process was eliminated in a scenario with continuous loading, which was made possible by the advantageous characteristics of the single photon-counting detectors, the fast readout speed and very high signal-to-noise ratio. Although the number of tomographic projections during continuous loading was halved compared to other scenarios the reconstructed tomographic data still had sufficient quality for a reliable DVC calculation. This fact clearly demonstrates the suitability of the photon-counting detector for the imaging of samples with a low attenuation of X-rays. Future work will be focused on improvements to the parameters of the compression test with continuously performing tomography using a fast photon-counting detector to obtain precise data for calculation of the mechanical characteristic of scaffold as well as speeding up the measurement.

Acknowledgements

The research was supported by Grant Agency of the Czech Technical University in Prague (grant no. SGS15/225/OHK2/3T/16) and by institutional support RVO: 68378297. The Slovenian Research Agency is acknowledged for its financial support of the PhD study of the co-author, Ms. Ana Gantar (PR-03770).

5 REFERENCES

[1] H. L. M. Bao, E. Y. Teo, M. S. K. Chong, Y. Liu, M. Choolani, J. K. Y. Chan, Advances in Bone Tissue Engineering, Regenerative Medicine and Tissue Engineering, Rijeka, InTech, 2013, doi:10.5772/55916D

[2] A. R. Amini, C. T. Laurencin, S. P. Nukavarapu, Bone Tissue Engineering: Recent Advances and Challenges, Critical reviews in biomedical engineering, 40 (**2012**) 5, 363–408, doi:10.1615/CritRevBiomedEng.v40.i5.10

[3] O. Jirousek, P. Zlamal, D. Kytyr, M. Kroupa, Strain analysis of trabecular bone using time-resolved X-ray microtomography, Nuclear Instruments and Methods in Physics Research Section A: Accelerators, Spectrometers, Detectors and Associated Equipment, 633 (**2011**) 1, 148–151, doi:10.1016/j.nima.2010.06.151

[4] B. K. Bay, Methods and applications of digital volume correlation, The Journal of Strain Analysis for Engineering Design, (**2008**), 43, 745–760, doi:10.1243/03093247JSA436

[5] A. Gantar, L. P. da Silva, J. M. Oliveira, A. P. Marques, V. M. Correlo, S. Novak, R. L. Reis, Nanoparticulate bioactive-glass-reinforced gellan-gum hydrogels for bone-tissue engineering, Materials Science and Engineering C, 43 (**2014**), 27–36, doi:10.1016/j.msec.2014.06.045

[6] D. Hoikhman, Y. Sela, Gellan gum based oral controlled release dosage forms- anovel platform technology for gastric retention. Google Patents, 2006

[7] D. E. Pszczola, Gellan gum wins IFT's food technology industrial achievement award, Food Technology **1993,** 47, 94–6

[8] P.-E. Jansson, B. Lindberg, P. A. Sandford, Structural studies of gellan gum, an extracellular polysaccharide elaborated by Pseudomonas elodea. Carbohydr Res **1983,** 124, 135–9

[9] J. T. Oliveira, L. Martins, R. Picciochi, P. B. Malafaya, R. A. Sousa, N. M. Neves, et al. Gellan gum: a new biomaterial for cartilage tissue engineering applications. Journal of biomedical materials research Part A, **2010**, 93, 852–63

[10] N. Drnovsek, S. Novak, U. Dragin, M. Ceh, M. Gorensek, M. Gradisar, Bioactive glass enhances bone ingrowth into the porous titanium coating on orthopaedic implants. Int Orthop **2012**, 36, 1739–45, doi:10.1007/s00264-012-1520-y

[11] D. Vavrik, J. Jakubek, Radiogram enhancement and linearization using the beam hardening correction method, Nuclear Instruments and Methods in Physics Research Section A: Accelerators, Spectrometers, Detectors and Associated Equipment, 607 (**2009**) 1, 212–214, doi:10.1016/j.nima.2009.03.156

[12] L. A. Feldkamp, L. C. Davis, J. W. Kress, Practical cone-beam algorithm, Journal of the Optical Society of America A, 1 (**1984**) 6, 612–619

UDK 67.017:621.793.7:544.653.23
Original scientific article/Izvirni znanstveni članek

ISSN 1580-2949
MTAEC9, 51(3)403(2017)

THE EFFECT OF CURRENT TYPES ON THE MICROSTRUCTURE AND CORROSION PROPERTIES OF Ni/NANOAl_2O_3 COMPOSITE COATINGS

VPLIV VRSTE TOKA NA MIKROSTRUKTURO IN LASTNOSTI KOROZIJE PREVLEK NA Ni/NANOAl_2O_3 KOMPOZITIH

Beata Kucharska, Agnieszka Krawczynska, Krzysztof Rożniatowski, Joanna Zdunek, Karol Poplawski, Jerzy Robert Sobiecki

Warsaw University of Technology, Woloska 141, 01-407 Warszawa, Poland
b.kucharska@inmat.pw.edu.pl

Prejem rokopisa – received: 2015-12-16; sprejem za objavo – accepted for publication: 2016-09-02

doi:10.17222/mit.2015.347

Nickel matrix composite coatings with a ceramic disperse phase have been widely investigated due to their enhanced properties, such as higher hardness and wear resistance in comparison to pure nickel. This paper describes the research on nickel and nickel-alumina coatings. The coatings were obtained from a Watts bath with the presence of nickel grain-growth inhibitors by DC (direct current), PC (pulse current) and PRC (pulsed reverse current) plating. The study includes the composite coatings of microcrystalline and nanocrystalline Ni matrix and nanometric Al_2O_3 particles. In order to ensure uniform co-embedding of the disperse phase particles with a nickel matrix and producing a stable suspension, mechanical agitation was also used. It was proved in our previous investigations that mechanical agitation is the best way of embedding nano-alumina particles in a nickel matrix. The effect of the electroplating techniques on the microstructure (SEM – scanning electron microscopy, STEM – scanning transmission electron microscopy, XRD – X-ray diffraction, surface profile) of Ni and Ni/Al_2O_3 composite coatings was investigated. In order to evaluate the corrosion resistance of the produced coatings, the corrosion studies were carried out by electrochemical impedance spectroscopy and the potentiodynamic method in a 0.5-M NaCl solution. Bode diagrams obtained by impedance spectroscopy method were established. The equivalent electric circuit and its parameters were determined to interpret impedance spectra. The corrosion current and corrosion potential were determined. Investigations of the corrosion damage to the produced surface layers were performed by scanning microscope techniques. The completed studies have shown that the type of current significantly affects the structure of the nickel and composite coatings, as well as their corrosion properties.

Keywords: nanocomposites, Ni/Al_2O_3 coatings, corrosion resistance, pulse electrodeposition

Matrike nikljevih kompozitnih oblog, razpršenih s keramično fazo, so pogosto raziskovali zaradi njihovih izboljšanih lastnosti, kot na primer zaradi večje trdote in odpornosti proti obrabi, v primerjavi s čistim nikljem. Članek opisuje raziskave na nikljevih in nikelj-aluminijevih premazih. Prevleke so bili narejene iz Watts kopeli s prisotnostjo inhibitorjev rasti zrn niklja s površinsko obdelavo z enosmernim (DC), impulznim (PC) in impulzno-povratnim (PRC) tokom. Študija vključuje mikrokristalne in nanokristalne prevleke kompozitov Ni matrike in nanometrskih Al_2O_3 delcev. Da bi zagotovili enotno delovanje vgrajevanja disperzne faze delcev z matriko Ni in pripravo stabilne suspenzije, je bilo uporabljeno tudi mehansko spodbujanje z mešanjem. Dokazano je bilo, da je mehanska spodbuda najboljši način utrjevanja delcev aluminijevega oksida v Ni matriki. Raziskan je bil učinek tehnik površinske obdelave na mikrostrukturo (SEM – elektronska mikroskopija, STEM – transmisijska elektronska mikroskopija, XRD – rentgenska difrakcija, površinski profil) niklja in Ni/Al_2O_3 kompozita. Da bi ocenili odpornost proti koroziji pri proizvedenih premazih, so bile izvedene študije korozije, ki smo jih izvedli z elektrokemijsko impedančno spektroskopijo in potenciodinamskim postopkom v 0,5 M NaCl raztopini. Vzpostavljeni Bodovi diagrami so bili dobljeni z metodo impedančne spektroskopije. Enakomerni električni krog in njegovi parametri so bili določeni za razlago impedančne spektroskopije. Določena sta bila tok korozije in korozijski potencial. Preiskave korozijskih poškodb proizvedenih površinskih slojev so bile izvedene s tehnikami mikroskopskega skeniranja. Končne preiskave so pokazale, da tip toka pomembno vpliva na strukturi nikljevih in kompozitnih prevlek, tako kot na korozijske lastnosti.

Ključne besede: nanokompoziti, Ni/Al_2O_3 premazi, odpornost proti koroziji, elektrodepozicija

1 INTRODUCTION

The introduction of new materials for transport and industry is mainly aimed at improving the performance characteristics of machine parts and equipment, often working in aggressive environments. Nanocomposite engineering metal coatings are an inspiring material group introduced in the past few years. There are various techniques of producing metallic nanocomposite materials. Electrodeposition is a simple, inexpensive and versatile one, being widely used in industry.[1–4] The structure and properties of composite surface coatings can be designed through a careful selection of the matrix and dispersed phase. Among the wide variety of coatings used for tribological applications, nickel composite coatings with alumina particles appear to have a very promising potential. The size and the amount of the inserted reinforced alumina phase determines the properties of Ni/Al_2O_3 composite coatings.[4,6] Until now, most of the works were carried out using Al_2O_3 microparticles.[2,4,7–10] However, the recent emergence of nanotechnologies has led to scientific and technological interest in the electrodeposition of Ni/Al_2O_3 nanocom-

posite coatings with Al_2O_3 particles smaller than 100 nm, mainly devoted to an increase in the abrasion resistance of material surfaces.[3,5–6,11–12]

These performance characteristics are affected primarily by the process parameters, including the electrolyte composition (e.g., the use of organic growth inhibitors), as well as the type (DC, PC, PRC), amplitude and frequency of the used current. Proper optimization of electrodeposition process of $Ni/_{nm}Al_2O_3$ coatings is faced with the fundamental problem of the agglomeration of particles in the electrolyte, and therefore an insufficient and uneven distribution of nanoparticles in the nickel matrix.[5,6] In the study the effect of the addition of a growth inhibitor and nano-alumina powder disperse phase, as well as the type of current (DC, PC, PRC) on the corrosion properties of nickel and composite Ni/Al_2O_3 coatings were examined.

Hard and wear-resistant Ni/Al_2O_3 coatings should also have good anti-corrosion properties in the environment in which they are operated.[2] The researchers' reports include mainly corrosion rate determination.[3,4,11–15] This allows a good comparison of materials in terms of corrosion resistance, but does not give information about the causes of the corrosion changes and the mechanism of corrosion. Electrochemical impedance spectroscopy can provide significant information regarding the corrosion mechanisms and susceptibility of materials to corrosion in the exposed environment. In the present work the nickel and composite coatings were examined both by the potentiodynamic method (setting the corrosion current, corrosion potential, polarization resistance) as well as electrochemical impedance spectroscopy.

2 EXPERIMENTAL PART

Nickel matrix composite coatings with a dispersed nanometric alumina phase (Aldrich Chemistry) were produced by electrochemical reduction on a copper substrate (75×15×1) mm in a Watts bath modified (or not) with benzoic sulfimide (saccharin) (**Table 1**). For comparison the nickel coatings were also produced with the same process parameters. The electrodeposition process consists of several steps, including preliminary and regular surface preparation (grinding, degreasing, digestion and finally electroplating). The processes were carried out at 45 °C at pH 4.2±0.1 using direct, pulsed and pulse reversed current. The diagram and parameters are shown in **Figure 1**. All the coatings have a thickness of approximately 30 μm, with the exception of the coatings to be examined by STEM technique (150–200 μm), for which the preparation has differed from the conventional procedure (additional application of electrospark cutting, grinding to a thickness of 4 μm and electrochemical polishing). The thickness was estimated using SEM techniques and the study was conducted on metallographic cross-sections. In order to provide the transport of alumina particles into cathode proximate areas, the bath was mechanically stirred at 400 min^{-1}.

Table 1: Bath composition
Tabela 1: Sestava kopeli

Component	Concentration (mol L^{-1})
$NiSO_4 \cdot 6\ H_2O$	1,14
$NiCl_2 \cdot 6\ H_2O$	0,17
H_3BO_3	0,57
Saccharin	0,014
Al_2O_3	0,098

A structure analysis of the alumina powder, the nickel and the nickel-alumina composite coatings was carried out using a Hitachi SU-70 (SEM) and Hitachi HD-2700 (STEM), respectively, scanning and scanning-transmission electron microscopes (both equipped with EDS – energy-dispersive X-ray spectroscopy device).

The phase composition, crystalline size, and residual stresses of the deposits were studied by the XRD technique using Cu-K_α (Philips PW-1830). The surface roughness was measured using a Wyko NT9300 light interference optical microscope.

Examinations and analyses of the corrosive properties of nickel and nickel-alumina coatings were made with the use of potentiostat ATLAS Sollich, AtlasCorr and AtlasLab computer programs. A three-electrode measurement system included a measurement vessel with a saturated calomel electrode (as a reference elec-

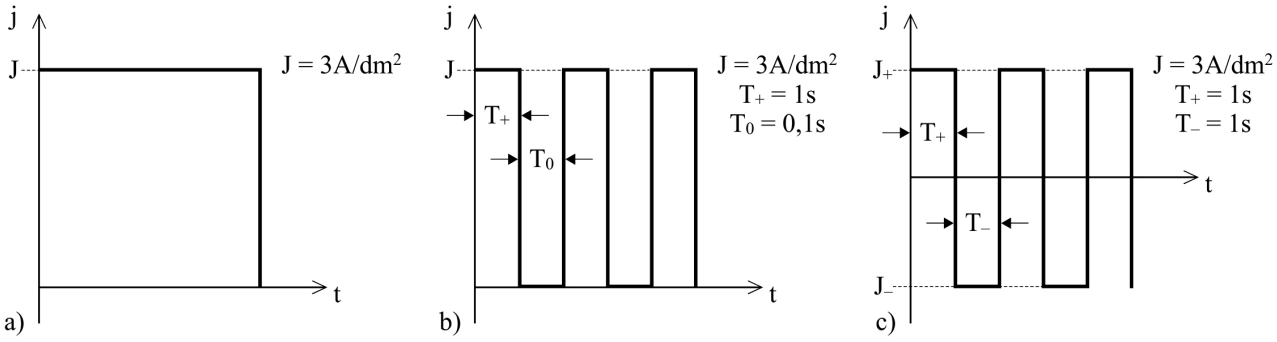

Figure 1: Scheme of impulse current and process parameters: a) DC, b) PC, c) PRC
Slika 1: Shema impulza toka in procesni parametri: a) DC, b) PC, c) PRC

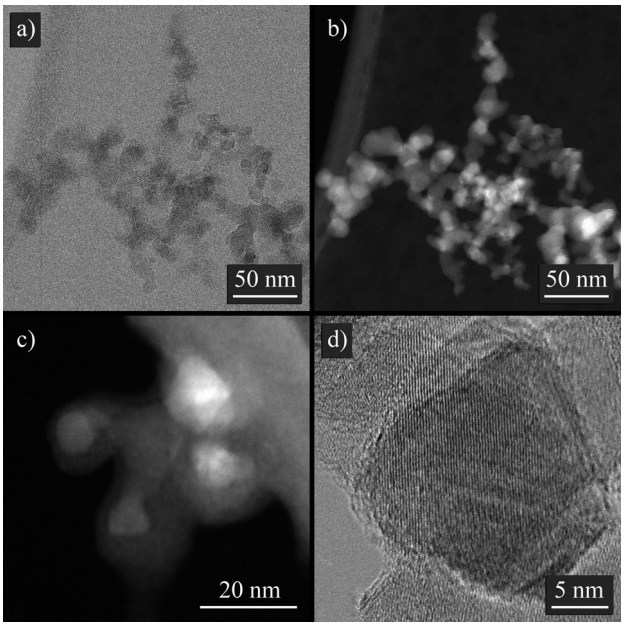

Figure 2: Microstructure of Al_2O_3 powder in: a) bright-field mode, b) Z-contrast mode, c) secondary-electron mode, d) bright-field mode
Slika 2: Mikrostruktura Al_2O_3 prahu: a) svetlo polje, b) Z-kontrast, c) sekundarni elektronski način, d) svetlo polje

trode), platinum mesh (as a counter electrode) and examined coatings (as a working electrode). The corrosion resistance was tested in the 0.5-M NaCl solution at 20 °C. The samples, before corrosive properties examination, were stabilized for 60 min in the target system as an open circuit. Research by electrochemical impedance spectroscopy was carried out in the corrosion potential surroundings in the frequency range 100 kHz to10 MHz of the10 mV amplitude.

The corrosion study was performed using the potentiodynamic method. For determining the polarization curves of the tested materials the measurements started from the potentials having values lower by 200 mV up to the values higher by 200 mV from the predetermined open-circuit potential with the potential scan rate equal to 0.2 mV/s and then up to 500 mV with a scan rate of 0.8 mV/s. The obtained curves were analyzed by the Tafel straight-lines method by keeping the conditions inherent in this method. The surface morphology of the examined materials after potentiodynamic tests was analyzed by scanning electron microscopy.

3 RESULTS AND DISCUSSION

Al_2O_3 powder was used as the dispersed phase in the Ni/Al_2O_3 composite coating formation process. The Al_2O_3 particles are presented in **Figures 2a** and **2b** in bright-field (BF) and Z-contrast modes, respectively. We can estimate from these images that their size is in the nanometric regime and it varies from 5 nm to 25 nm. Furthermore, the particles have the tendency to agglomerate, creating larger **Figures 2a** and 2**b** and smaller agglomerates, consisting of a few particles **(Figure 2c**). Images taken at higher magnifications (**Figure 2d)** showing crystallographic plates demonstrate that at least some of these nanoparticles are crystalline.

All coatings deposited from the basic Watts bath (Ni, Ni/Al_2O_3) have microcrystalline nickel structures (**Figures 3a** to **3f**). In the case of the use of the pulse reverse current the smallest grains are visible in the nickel and composite coatings. In turn the nickel and composite coatings produced in the electrolyte with grain growth inhibitor addition have a nanocrystalline structure

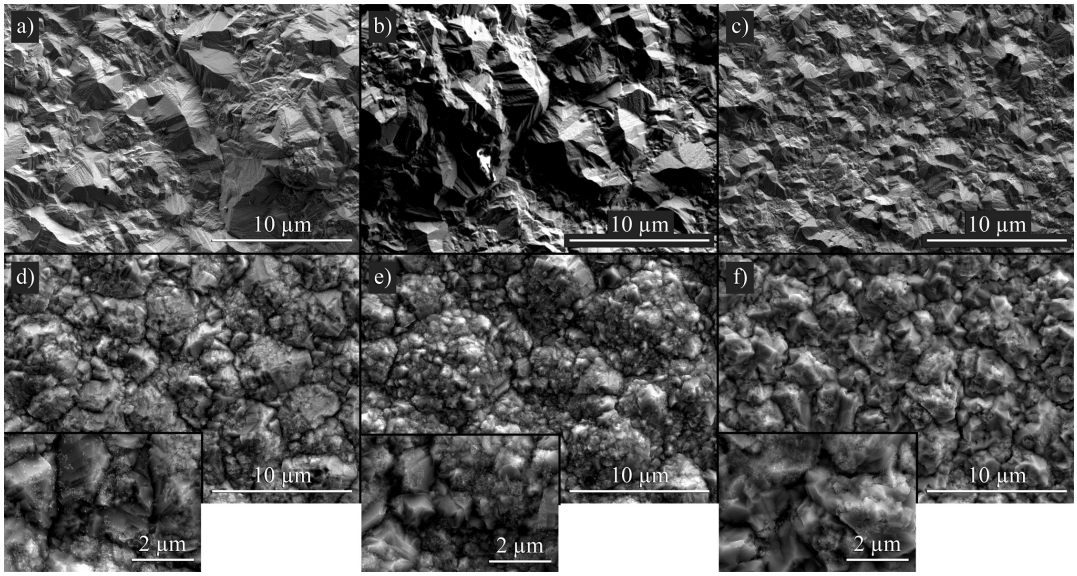

Figure 3: Morphology of microcrystalline coatings: a) nickel (DC), b) nickel (PC), c) nickel (PRC), d) Ni/Al_2O_3 (DC), e) Ni/Al_2O_3 (PC), f) Ni/Al_2O_3 (PRC)
Slika 3: Morfologija mikrokristaliničnih prevlek: a) nikelj (enosmerni tok), b) nikelj (pulzni tok), c) nikelj (impulznopovratni tok), d) Ni/Al_2O_3 (enosmerni tok), e) Ni/Al_2O_3 (pulzni tok), f) Ni/Al_2O_3 (impulznopovratni tok)

(**Figures 4a** to **4f**). The quality of the composite coatings with a nickel matrix and alumina dispersed phase depends on the formation of an appropriate structure with embedded alumina nanoparticles. The Al_2O_3 particles co-deposited in the nickel matrix cause a significant change in the morphology of its surface, as well the microcrystalline Ni matrix, as the nanocrystalline Ni matrix (**Figures 3a** to **3c**). The all $Ni_{\mu m}/Al_2O_3$ have large amounts of embedded disperse phase on its surface, which occurs often as agglomerates. In turn in the case of nanocrystalline composite coatings alumina is better fixed and distributed in the matrix. The nanocomposite coatings deposited with PRC were characterized by the largest surface roughness.

Due to this, one of the coatings was designated to TEM studies. The microstructure of the Ni_{nm}/Al_2O_3 coating obtained in the modified bath with PC was examined by STEM technique (**Figure 5**). The Al_2O_3 particles embedded in the matrix can easily be recognised as they stick out of the surface in **Figure 5a**) taken in SE-mode. Their existence was confirmed by X-ray EDS analysis (**Figure 5d**). In BF-mode (**Figure 5b**) as well as in

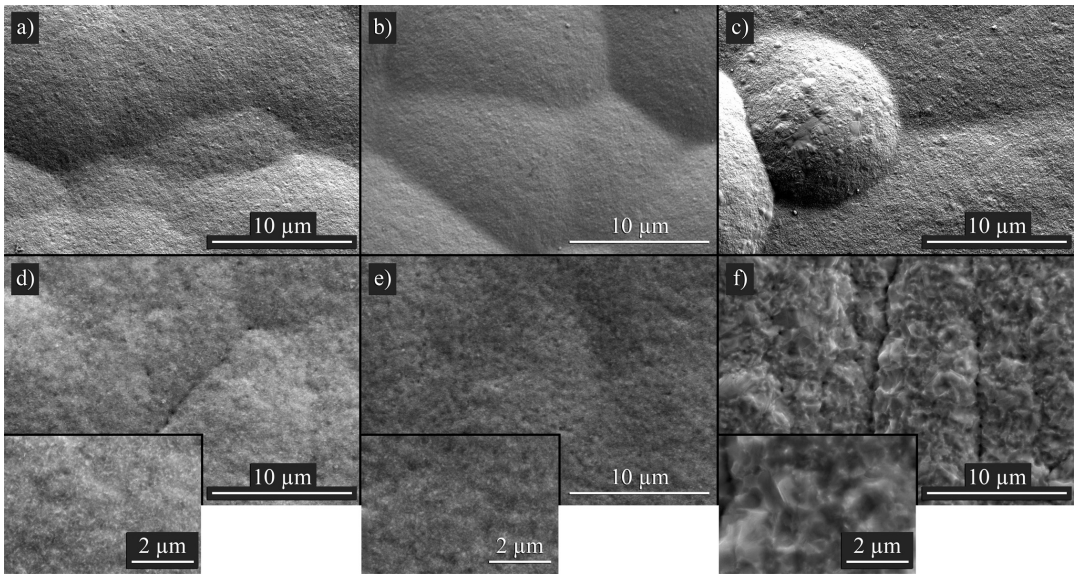

Figure 4: Morphology of nanocrystalline coatings: a) nickel (DC), b) nickel (PC), c) nickel (PRC), d) Ni/Al_2O_3 (DC), e) Ni/Al_2O_3 (PC), f) Ni/Al_2O_3 (PRC)

Slika 4: Morfologija nanokristaliničnih prevlek: a) nikelj (enosmerni tok), b) nikelj (pulzni tok), c) nikelj (impulznopovratni tok), d) Ni/Al_2O_3 (enosmerni tok), e) Ni/Al_2O_3 (pulzni tok), f) Ni/Al_2O_3 (impulznopovratni tok)

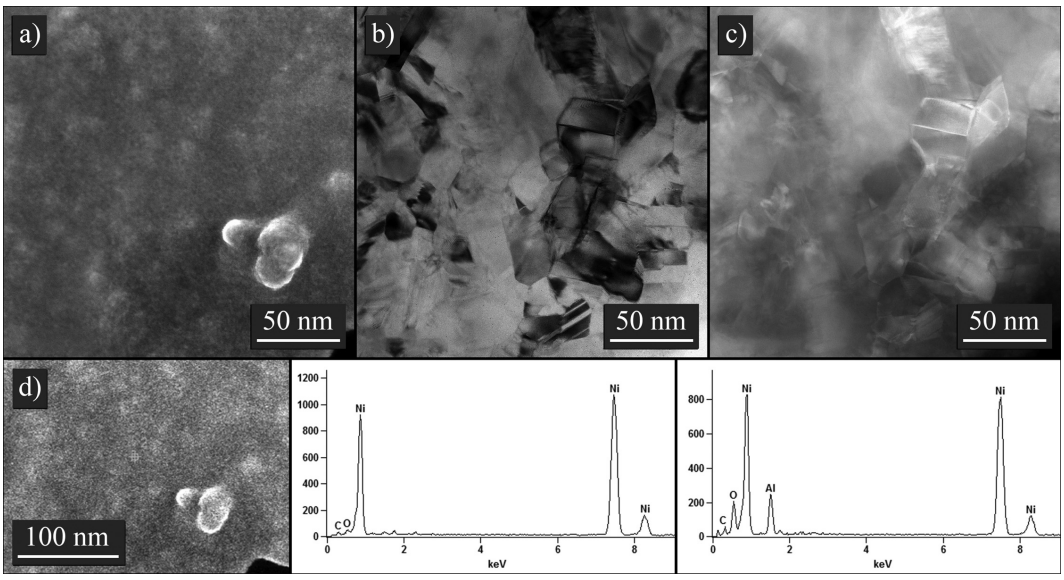

Figure 5: Microstructure and EDS result of Ni/Al_2O_3 coating obtained in the modified bath with PC: a) SE-mode, b) BF-mode, c) Z-contrast mode, d) EDS results

Slika 5: Mikrostruktura in EDS-analiza Ni/Al_2O_3 prevleke, pridobljene v spremenjeni kopeli z impulzivnim tokom (PC): a) SE-način, b) BF-način, c) Z-kontrastni način, d) rezultati EDS-analize

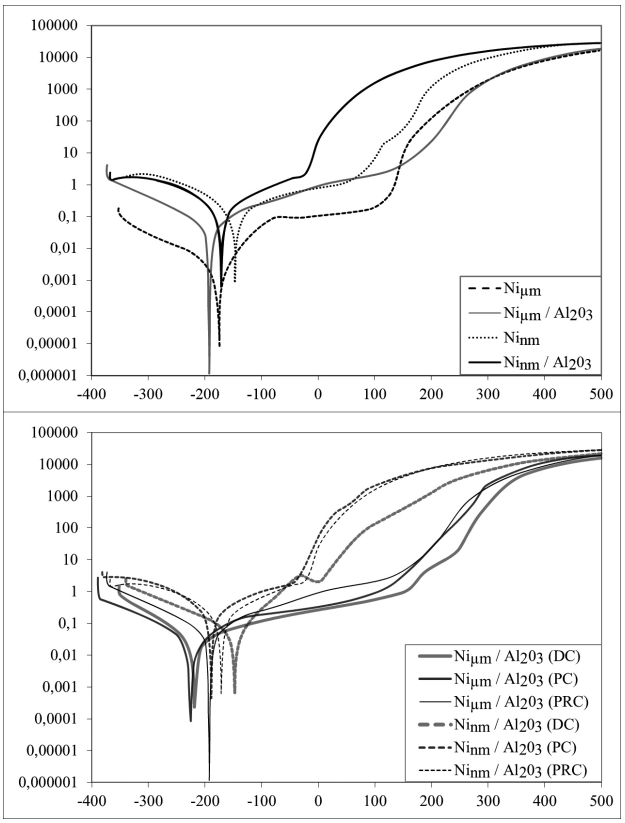

Figure 6: X-ray diffractogram of the nickel and Ni/Al_2O_3 composite coatings produced with DC in a Watts bath and a Watts bath with saccharine additives

Slika 6: XRD-analiza niklja in Al_2O_3 prevlek kompozitov, narejenih z enosmernim tokom in z Watts-ovo kopeljo z dodatki saharina

Z-contrast mode (**Figure 5c**) it is difficult to distinguish them from the matrix. In the matrix grains with an average 30 nm in diameter are present. In most of the grains dislocations can be found. Some of them are divided into sub-grains. Some contain annealing nano-twins.

X-ray analysis was performed to examine the effect of organic additive and the Al_2O_3 powder in the Watts bath on the structure of the nickel and composite coatings produced. The diffraction patterns of the coatings deposited with the DC current are shown in **Figure 6**. All the examined coatings are characterized by a crystalline structure. The profile diffraction lines indicate that the nickel coatings deposited in the base bath have the largest dimensions of the grains (79 nm and 88 nm, as estimated by the Scherrer equation). All the coatings produced with the addition of saccharine have nanocrystalline nickel structures. This is revealed by both the XRD patterns (**Figure 6**) and the images of the microstructure obtained by the SEM (**Figures 3** and **4**).

The diffraction line profiles (**Figure 6**) indicate that the composite coatings are characterized by a smaller dimension of crystallites: 26 nm and 18 nm and by 23nm and 15 nm, respectively, in comparison to micro- and nanocrystalline nickel.

The surface roughness of the examined coatings is shown in **Figures 7** and **8**. It can be seen from the 3D view of the surface profiles that the surface roughness is the highest in the case of the PRC coatings, followed by the DC and finally the PC coatings. The coatings

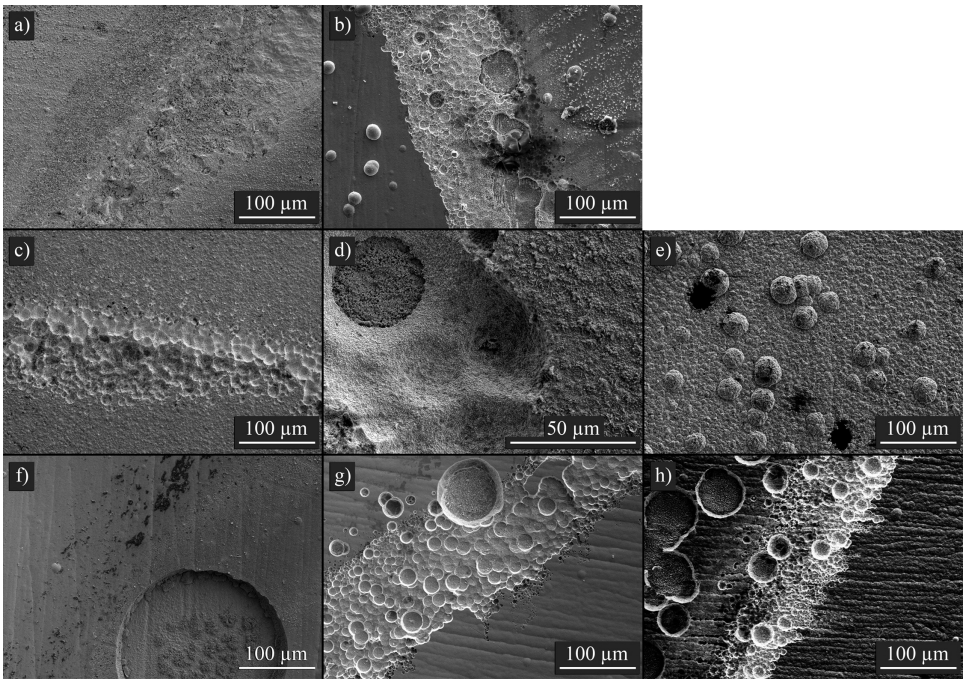

Figure 7: Surface roughness of microcrystalline coatings: a) nickel (DC), b) nickel (PC), c) nickel (PRC), d) Ni/Al_2O_3 (DC), e) Ni/Al_2O_3 (PC), f) Ni/Al_2O_3 (PRC)

Slika 7: Hrapavost površine mikrokristaliničnih prevlek: a) nikelj (enosmerni tok), b) nikelj (pulzni tok), c) nikelj (impulznopovratni tok), d) Ni/Al_2O_3 (enosmerni tok), e) Ni/Al_2O_3 (pulzni tok), f) Ni/Al_2O_3 (impulznopovratni tok)

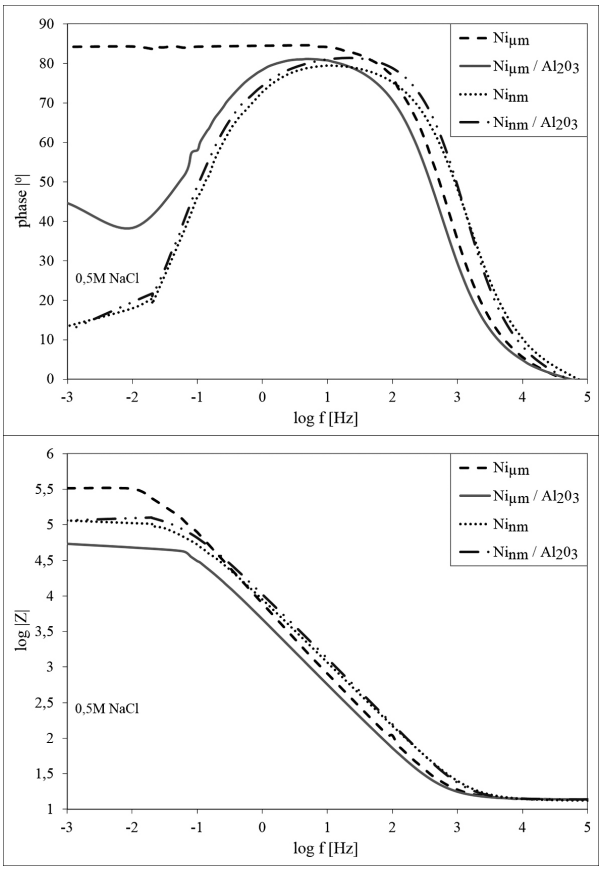

Figure 8: Surface roughness of nanocrystalline coatings: a) nickel (DC), b) nickel (PC), c) nickel (PRC), d) Ni/Al_2O_3 (DC), e) Ni/Al_2O_3 (PC), f) Ni/Al_2O_3 (PRC)

Slika 8: Hrapavost površine nanokristaliničnih prevlek: a) nikelj (enosmerni tok), b) nikelj (pulzni tok), c) nikelj (impulznopovratni tok), d) Ni/Al_2O_3 (enosmerni tok), e) Ni/Al_2O_3 (pulzni tok), f) Ni/Al_2O_3 (impulznopovratni tok)

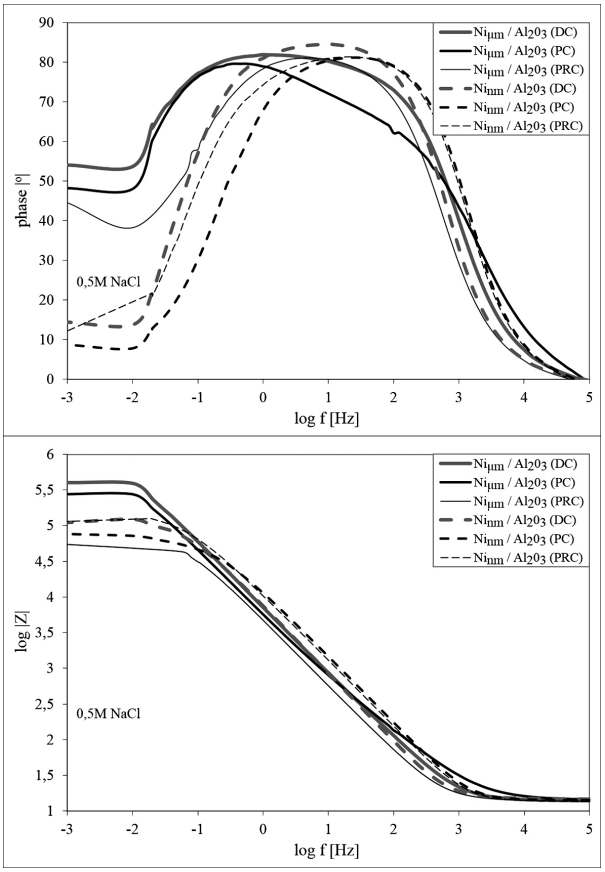

Figure 9: Polarization curves of Ni and Ni/Al_2O_3 coatings deposited with different current parameters

Slika 9: Polarizacijske krivulje niklja in Ni/Al_2O_3 prevlek pri različnih parametrih toka

deposited in the bath without organic additives are characterized by greater roughness (**Figure 7**). In the case of the DC and PRC microcrystalline coatings, the addition of Al_2O_3 makes the surface more irregular, which is visible both in 3D images and from the surface parameter characteristics (**Table 2**).

Table 2: Surface-roughness parameters

Tabela 2: Parametri površinske hrapavosti

		*R*a (nm)	*R*q (nm)	*R*t (nm)
$Ni_{\mu m}$	DC	162	207	1650
	PC	162	206	1520
	PRC	332	423	2930
$Ni_{\mu m}/Al_2O_3$	DC	286	388	3840
	PC	159	213	1870
	PRC	516	672	5120
Ni_{nm}	DC	100	132	1340
	PC	80	103	992
	PRC	141	178	1160
Ni_{nm}/Al_2O_3	DC	112	144	1050
	PC	55	70	525
	PRC	179	229	1970

Table 3: Characteristic parameters obtained as a result of potentiodynamic tests

Tabela 3: Karakteristike parametrov, pridobljene kot rezultat potenciodinamičnih testov

Material	Current	E_{corr} (mV)	i_{corr} (μA cm^{-2})
$Ni_{\mu m}$	PRC	-175	0.013
$Ni_{\mu m}/Al_2O_3$	DC	-218	0.048
	PC	-182	1.25
	PRC	-189	0.062
Ni_{nm}	PRC	-165	0.22
Ni_{nm}/Al_2O_3	DC	-147	0.056
	PC	-186	1.208
	PRC	-172	0.230

The results of the potentiodynamic method examinations are presented at **Figure 9**. The characteristic values are presented in **Table 3**. The potentiodynamic tests revealed that the nickel and composite coatings (with the exception of the composite coatings produced with PC) deposited in the basic Watts bath have good and similar corrosion properties, while the Ni_{nm} and Ni_{nm}/Al_2O_3 coatings obtained in the modified electrolyte (with a nano-nickel matrix) are characterized by increased corrosion potential and current density (**Table 3**).

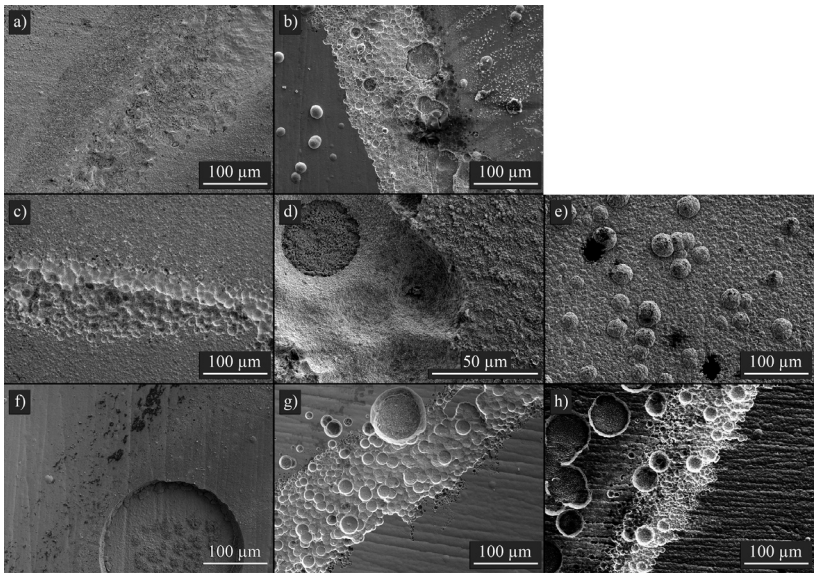

Figure 10: Morphology of the Ni and Ni/Al_2O_3 coatings after corrosion examinations: a) $Ni_{µm,}$ (PRC), b) Ni_{nm} (PRC), c) $Ni_{µm}/Al_2O_3$ (DC), d) $Ni_{µm}/Al_2O_3$ (PC), e) $Ni_{µm}/Al_2O_3$ (PRC), f) Ni_{nm}/Al_2O_3 (DC), g) Ni_{nm}/Al_2O_3 (PC), h) Ni_{nm}/Al_2O_3 (PRC)

Slika 10: Morfologija nikljevih in Ni/Al_2O_3 prevlek po korozijskih pregledih: a) $Ni_{µm,}$ (PRC), b) Ni_{nm} (PRC), c) $Ni_{µm}/Al_2O_3$ (DC), d) $Ni_{µm}/Al_2O_3$ (PC), e) $Ni_{µm}/Al_2O_3$ (PRC), f) Ni_{nm}/Al_2O_3 (DC), g) Ni_{nm}/Al_2O_3 (PC), h) Ni_{nm}/Al_2O_3 (PRC)

Table 4: Electric parameters of corrosion systems and schemes of the equivalent electric circuit for corroded coatings

Tabela 4: Električni parametri korozijskih sistemov in shem ekvivalentnega električnega tokokroga za korodirane prevleke

Material	Current	Electrical equivalent circuit	Electrochemical parameters						
			R_s (Ωcm^2)	R1 ($k\Omega cm^2$)	Y_01 ($\mu Fcm^{-2}s^{(n-1)}$)	n1	R2 ($k\Omega cm^2$)	Y_02 ($Fcm^{-2}s^{(n-1)}$)	n2
$Ni_{µm}$	PRC	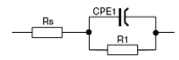	14.0	409	23.0	0.95	—	—	—
$Ni_{µm}/Al_2O_3$	DC	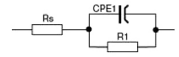	14.2	790	26.2	0.91	—	—	—
	PC	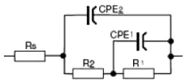	15.1	0.316	21.8	0.86	567	11.8	0.9
	PRC	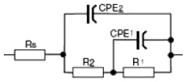	14.0	73.2	39.6	0.91	20.1	215.4	1.3
Ni_{nm}	PRC	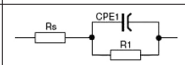	14.3	101	18.8	0.88	—	—	—
Ni_{nm}/Al_2O_3	DC	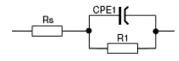	14.9	112	23.8	0.95	—	—	—
	PC	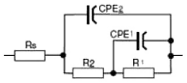	14.3	0.000000049	13.2	0.94	75.6	6.5	0.4
	PRC	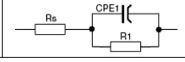	13.5	126	17.5	0.92	—	—	—

Together with an increase of the co-deposited alumina greater etching is visible (**Figure 10**) in comparison with the nickel coatings. Analyses of the electrodeposited nickel and composite coatings after exhibited in corrosion environments have demonstrated a pitting corrosion on the surfaces of the electrodeposited materials, except for the $Ni_{µm}$ and $Ni_{µm}/Al_2O_3$ deposited with PRC. The smallest corrosion degradation of the surface occurs in the case of the microcrystalline coatings (**Figure 10**).

The measured impedance spectra for the nickel and composite coatings deposited at different current parameters in the 0.5-M NaCl are shown as Bode diagrams in **Figures 11** and **12.** The fitting of the spectra obtained during the measurements based on the two equivalent electric circuits (**Table 4**) and enables an evaluation of

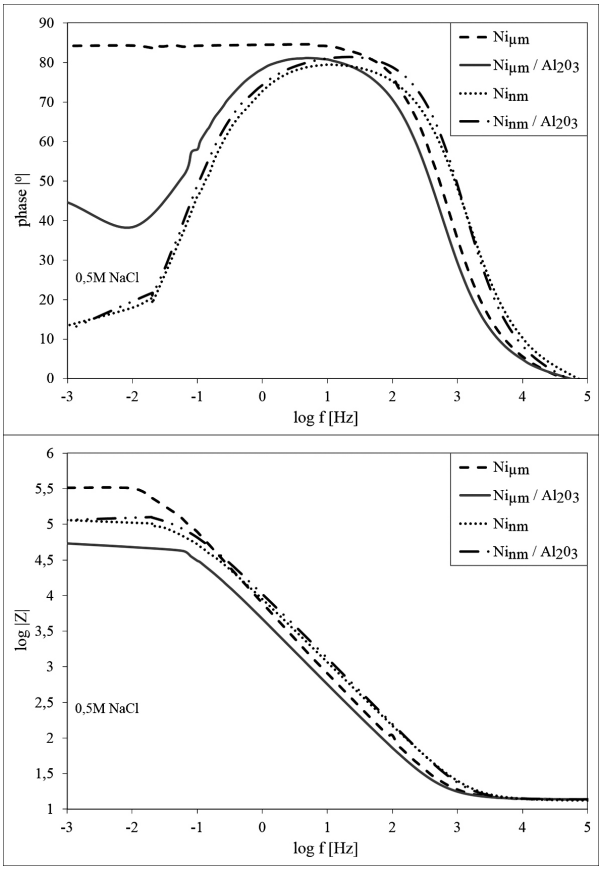

Figure 11: Bode spectra of the Ni and Ni/Al_2O_3 coatings deposited with PRC

Slika 11: Bode spektri Ni in Ni/Al_2O_3 prevlek pridobljenih z PRC

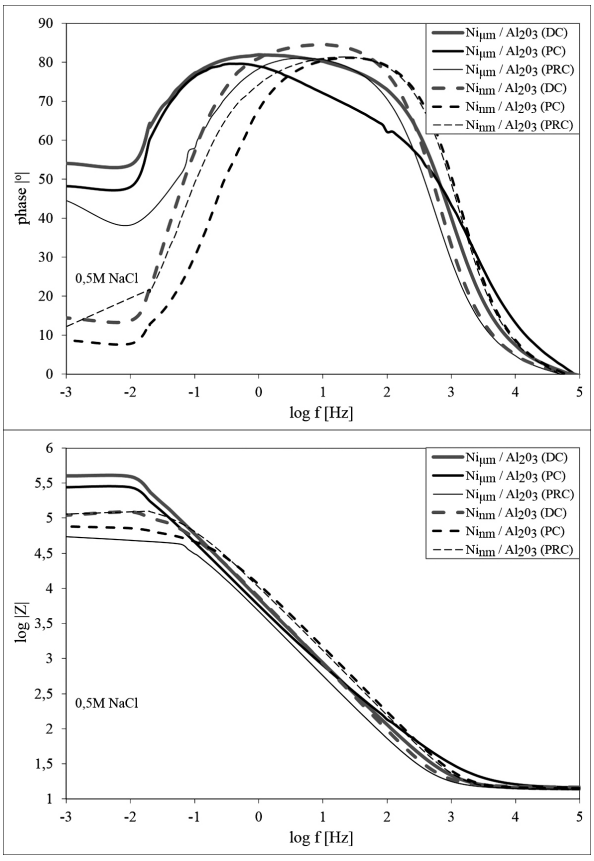

Figure 12: Bode spectra of the Ni/Al_2O_3 coatings deposited with DC, PC and PRC

Slika 12: Bode spektri Ni in Ni/Al_2O_3 prevlek pridobljenih z DC, PC in PRC

the corrosion properties. The equivalent electric circuits represent the process occurring in the corrosion system and allow us to define the parameters of these processes. In the electric models the element R_s reflects the resistance of the corrosion environment. The resistance of the electrolyte was comparable in all cases (**Table 4**). In contrast the element R1 characterizes the rate of corrosion process and it is connected with the resistance of the charge transfer across the interface. The capacity of these coatings reproduces the element $Y_0$1. Two additional elements in the second equivalent electric circuit: capacity of the surface area ($Y_0$2) and the resistance of the electrolyte in the area of the material (R2) are used in the cases of the coatings with higher roughness. The simple equivalent electric circuit (**Table 4**) was used in the case of the micro- and nanocrystalline nickel coatings deposited with PRC and the composite nickel coatings (both micro- and nanocrystalline nickel matrix) deposited with DC. It is related to the different structures of this coatings. For the $Ni_{\mu m}$ and $Ni_{\mu m}/Al_2O_3$ coatings deposited with PRC an increase in the phase-angle maximum is observed at low frequencies in contrast to the nickel and composite coatings with a nano-nickel matrix deposited with PRC (**Figure 11**). The $Ni_{\mu m}/Al_2O_3$ coating deposited with DC has the highest R1 value (790 kΩ cm^2, **Table 4**) and the widest range of maximum phase angle (**Figure 12**). In contrast the micro- and nanocrystalline composite coatings deposited with PC have the lowest R1, which indicates that there are surface-blocking processes.

Based on the analysis of the impedance phase-angle spectra, we found that microcrystalline coatings without Al_2O_3 phase are characterized by the highest corrosion resistance. Impedance phase-angle values have the maximum in a wide frequency range.

The incorporation of the ceramic phase in the microcrystalline nickel matrix results in the presence of boundaries between the embedded particles and the matrix, which is a place of corrosive attack. In particulalr, the Al_2O_3 phase in the case of coatings with microcrystalline matrix is incorporated in the form of several hundred nm agglomerates (**Figure 3d** to **3f**).

From the analysis of the impedance phase-angle spectra, we can also conclude that coatings with nanocrystalline nickel matrix have a decreased corrosion resistance. It is associated with a significantly larger number of grain boundaries, which also take the place of potential corrosive attack. Composite coatings with a nanocrystalline nickel matrix are characterized by

enhanced corrosion resistance compared to nanocrystalline nickel coating (wider range of maximum values of phase angle in the frequency range), which may either be due to the embedding of non-agglomerated, chemically resistant Al_2O_3 (**Figures 4d to 4f**) and the presence of the phase $AlNi_3$ (**Figure 6**).

In the case of coatings produced by the PC current method, a larger amount of built-in Al_2O_3 particles (**Figures 3e** and **4e**) is observed, resulting in a higher amount of interfacial boundary. These connections of the nickel matrix and the nanometric alumina particles are the target of corrosive attacks and therefore it results in the worst possible corrosion resistance.

4 CONCLUSIONS

Composite coatings are characterized by a smaller grain size compared to the pure nickel coatings obtained under the same conditions. Nickel and composite coatings deposited in a bath containing saccharine have a nanometric dimension of the crystallites, as compared to coatings produced in a basic Watts bath. In the case of the Ni_{nm}/Al_2O_3 composite coating, the presence of the $AlNi_3$ phase is also observed.

The surface roughness is the highest in the case of PRC coatings, followed by the DC and lastly the PC coatings. The coatings deposited in the bath with organic additives are characterized by a lower roughness.

Both the nickel and composite coatings deposited in the base Watts bath (microcrystalline coatings) have better corrosion properties in comparison with nanocrystalline coatings. The higher corrosion current and the greater destruction process (especially pitting corrosion) are visible in the case of nanocrystalline coatings.

The composite coatings deposited both in a base Watts bath and modified Watts bath with PC and PRC are characterized by different corrosion properties in comparison with the nickel and composite coatings deposited with DC. They are described by means of an advanced equivalent electric circuit (five-partial circuit).

The best corrosion properties, which are determined, e.g., by the phase-angle maximum and the corrosion destruction of surface, exhibit the $Ni_{\mu m}$ and $Ni_{\mu m}/Al_2O_3$ coatings deposited with PRC. The increase of the phase angle is observed at low frequencies in contrast to nickel and composite coatings with a nano-nickel matrix deposited with PRC.

5 REFERENCES

[1] R. K. Saha, T. I. Khan, Effect of applied current on the electrodeposited Ni-Al_2O_3 composite coatings, Surface and Coatings Technology, 205 (**2010**) 3, 890–895, doi:10.1016/j.surfcoat.2010.08.035

[2] B. Szczygiel, M. Kolodziej, Composite Ni/Al_2O_3 coatings and their corrosion resistance, Electrochimica Acta, 50 (**2005**), 4188–4195

[3] B. Kucharska, A. Brojanowska, K. Popławski, J. R. Sobiecki, Material Science, 21 (**2016**) 1, 31–35, doi:10.5755/j01.ms.22.1.7407

[4] M. Nowak, M. Opyrchal, S. Boczkal, J. Zelechowski, A. Najder, M. Karas, Effect of cathodic current density on microstructure and properties of nickel composite coatings, Archives of Metallurgy and Materials, 59 (**2014**) 1, 323–327, doi: 10.2478/amm-2014-0053

[5] B. Kucharska, K. Popławski, E. Jezierska, D. Oleszak, J. R. Sobiecki, Influence of stirring conditions on Ni/Al_2O_3 nanocomposite coatings, Surface Engineering 32 (**2016**) 7, 457–463, doi:10.1179/1743294414Y.0000000385

[6] H. Gul, F. Kilic, S. Aslan, A. Alp, H. Akbulut, Characteristics of electro-co-deposited Ni–Al_2O_3 nano-particle reinforced metal matrix composite (MMC) coatings, Wear 267 (**2009**) 5–8, 976–990, doi:10.1016/j.wear.2008.12.022

[7] B. Kucharska, J. R. Sobiecki, Microcrystalline and nanocrystalline nickel layers reinforced by Al_2O_3 particles, Composites Theory and Practice, 13 (**2013**) 4, 232–236

[8] L. Chen, L. Wang, Z. Zeng, J. Zhang, Effect of surfactant on the electrodeposition and wear resistance of Ni–Al_2O_3 composite coatings, Materials Science and Engineering, 434 (**2006**) 1–2, 319–325, doi:10.1016/j.msea.2006.06.098

[9] L. Chen, L. Wang, Z. Zeng, T. Xu, Influence of pulse frequency on the microstructure and wear resistance of electrodeposited Ni–Al_2O_3 composite coatings, Surface and Coatings Technology, 201 (**2006**) 3-4, 599–605, doi:10.1016/j.surfcoat.2005.12.008

[10] Y. S. Dong, P. H. Lin, H. X. Wang, Electroplating preparation of Ni–Al_2O_3 graded composite coatings using a rotating cathode, Surface and Coatings Technology, 200 (**2006**) 11, 3633–3636, doi:10.1016/j.surfcoat.2004.11.024

[11] M. Sabri, A. Sarabi, S. Kondelo, The effect of sodium dodecyl sulfate surfactant on the electrodeposition of Ni-alumina composite coatings, Materials Chemistry and Physics, 136 (**2012**) 2-3, 566–569, doi:10.1016/j.matchemphys.2012.07.027

[12] J. Chen, Characteristic of Ni-Al_2O_3 Nanocomposition Coatings, Procedia Engineering, 15 (**2011**), 4414–4418, doi:10.1016/j.proeng.2011.08.829

[13] Q. Feng, T. Li, H. Teng, X. Zhang, Y. Zhang, Ch. Liu, J. Jin, Investigation on the corrosion and oxidation resistance of Ni-Al_2O_3 nano-composite coatings prepared by sediment co-deposition, Metal Finishing, 107 (**2009**) 1, 34–41, doi:10.1016/S0026-0576(09)80007-X

[14] A. Góral, M. Nowak, K. Berent, B. Kania, Influence of current density on microstructure and properties of electrodeposited nickel-alumina composite coatings, Journal of Alloys and Compounds, 615 (**2014**), S406–S410, doi:10.1016/j.jallcom.2014.01.025

[15] C. Zanella, M. Lekka, P. Bonora, Influence of the particle size on the mechanical and electrochemical behaviour of micro- and nano-nickel matrix composite coatings, Journal of Applied Electrochemistry, 39 (**2009**), 31–38, doi: 10.1007/s10800-008-9635-y

UDK 621.78:669.24:661.15'2:621.315.221
Original scientific article/Izvirni znanstveni članek

ISSN 1580-2949
MTAEC9, 51(3)413(2017)

HEAT TREATMENT OF ELECTROLESS Ni-P LAYERS ON AN AUSTENITIC STAINLESS-STEEL SUBSTRATE

TOPLOTNA OBDELAVA KEMIJSKO NANEŠENE PLASTI Ni-P NA PODLAGI IZ AVSTENITNEGA NERJAVNEGA JEKLA

Mauro Maretić, Božo Smoljan, Dario Iljkić

University of Rijeka, Faculty of Engineering, Department of Materials Science and Engineering, Vukovarska 58, Rijeka, Croatia
smoljan@riteh.hr

Prejem rokopisa – received: 2016-01-12; sprejem za objavo – accepted for publication: 2016-06-30

doi:10.17222/mit.2016.010

Properties of electroless deposited nickel-phosphorous coatings on an austenitic stainless-steel substrate were investigated. The main study was focused on the influence of heat treatment on the microhardness and microstructure analysis of electroless Ni-P coatings. A nickel-phosphorous coating was deposited without nickel-strike pre-coating treatment. An electroless Ni-P layer was deposited on a stainless-steel substrate. Sodium hypophosphite was used as the reducing agent. The microstructure and morphology of heat-treated electroless specimens were analyzed with optical and scanning electron microscopy. Adhesivity was estimated with a Vickers indenter. Based on the experimental results, it can be concluded that heat-treated electroless nickel-phosphorous coatings have a higher microhardness than non-heat-treated electroless nickel-phosphorous coatings. An analysis of the Vickers indentation results showed that the proposed electroless process gives satisfactory results.

Keywords: electroless, deposition, coatings, heat treatment, stainless steel, micro-hardness

Preiskovane so bila lastnosti kemijsko nanešene plasti nikelj – fosfor, na podlagi iz avtenitnega nerjavnega jekla. Glavni študij je bil usmerjen na vpliv toplotne obdelave na mikrotrdoto in analizo mikrostrukture kemijsko nanešenega Ni-P nanosa. Nanos nikelj –fosfor je bil nanešen brez predhodnega premaza. Kemijski nanos Ni-P je bil nanešen na osnovo iz nerjavnega jekla. Natrijev hipofosfid je bil uporabljen kot redukcijsko sredstvo. Mikrostruktura in morfologija kemijsko nanešenega vzorca je bila analizirana s svetlobno in z vrstično mikroskopijo. Adhezivnost je bila določena z vtiskovanjem po Vickers piramidi. Na osnovi rezultatov preizkusov je mogoče zaključiti, da ima toplotno obdelan kemijski nanos nikelj – fosfor višjo trdoto kot neobdelan kemijski nanos nikelj – fosfor. Analiza rezultatov Vickers vtiskov je pokazala, da predlagani kemijski postopek daje zadovoljive rezultate.

Ključne besede: brez pomoči električnega toka, nanašanje, nanosi, toplotna obdelava, nerjavno jeklo, mikrotrdota

1 INTRODUCTION

Electroless deposited coatings have a more uniform thickness on complex-shaped objects in comparison to electroplated deposits. This uniform thickness and composition of a coating results in uniform mechanical and physical properties of the surface layer.[1,2,3] Besides, Ni-P coatings deposited with the electroless process can have good anticorrosive properties, wear resistance and high hardness.[4–6] An electroless Ni–P coating has a higher hardness and a better corrosion resistance than the AISI 316 stainless steel.[7]

Since it is very difficult to form a Ni-P deposit on an austenitic stainless-steel substrate using the electroless process, the activation with a weak acid etch, i.e., nickel strike should be applied.[8] Nickel-strike pre-coating treatment makes the Ni-P coating deposition on stainless steel more complicated in comparison to the other similar electroless depositions on other types of steel, aluminium alloys and so on. Ni-P alloy coatings should be heat treated, mainly to increase the hardness of Ni-P alloy coatings; the heat treatment should be applied after the electroless coating process.[8]

Generally, the microstructure of the Ni-P coatings deposited with the electroless process depends on the phosphorous content. Electroless deposited Ni-P coatings are crystalline if the phosphorus content is between 1–5 % mass fraction (low phosphorus). If the content of phosphorous is between 6–9 % mass fraction (medium phosphorous), the Ni-P coatings deposited with the electroless process have mixed, amorphous and crystalline structures. If the content of phosphorous is between 10–13 % mass fraction (high phosphorus), the Ni-P coatings deposited with the electroless process are amorphous.[1,9–12]

To achieve high adhesion, a thorough surface preparation, or a removal of foreign contaminants from the base-metal surface and elimination of mechanically distorted surface layers, resulting in a clean, healthy surface structure, is required.[13] With a prolonged heat treatment, i.e., aging at high temperatures, electroless deposited nickel-phosphorous coatings begin to crystallize and lose their preferable amorphous character.[14] At the same time, a higher hardness of the stainless steel is obtained. As suggested by the authors of reference[14], this effect is probably due to the diffusion of phosphorus from the region near the interface with the substrate. With the prolonged heat treatment at high temperatures, the nickel-phosphide particles conglomerate and the

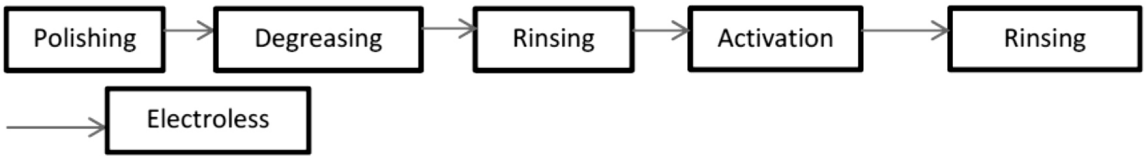

Figure 1: Flow-chart diagram of the electroless process of nickel plating on an austenitic-steel AISI 316 substrate
Slika 1: Potek kemijskega procesa nanašanja niklja na podlago iz avstenitnega nerjavnega jekla AISI 316

matrix of Ni_3P forms due to the continued heating.[14] The hardness of the coating can increase with the appearance of the intermetallic Ni_3P phase and with a higher crystallinity of the nickel-phosphorous coatings.[8–10,15] Moreover, the hardness of the electroless deposited nickel-phosphorous coatings can increase because of the precipitation of the Ni_3P phase.[15] The maximum hardness can be obtained if the phosphorus content is around 4 % mass fraction.[1,9–12]

The application of an appropriate heat treatment of Ni-P coatings deposited with the electroless process can have a significant impact on their hardness.[1–5] The microhardness of Ni-P coatings deposited with the electroless process depends on the heat treatment of the coatings, the content of phosphorus in the coatings and on the contents of other alloying elements in the coatings.[9]

Nickel with an amorphous structure has a lower hardness than nickel with a crystalline structure.[4,10–12,16–28] After the heat treatment, the structure of the coating is more crystalline; moreover, the intermetallic nickel phosphide (Ni_3P) phase appears.[9,10,15] The hardness of coatings can increase with the appearance of the intermetallic Ni_3P phase and a higher crystallinity of nickel-phosphorous coatings.[8–10,15]

The grain size of Ni-P composite coatings deposited with the electroless process can have a significant influence on the hardness.[20]

In this work, the adhesivity related to the optimization of heat-treatment processes was estimated with a Vickers indenter.

2 EXPERIMENTAL PART

In the applied experimental procedure, cylindrical specimens of austenitic steel AISI 316 were used as the substrate. The chemical composition of steel specimens is shown in **Table 1**. The diameter of cylindrical specimens was 8 mm and their length was 50 mm. Before the electroless process, the surfaces of specimens were cleaned to eliminate all types of surface contamination. At first, specimens were mechanically polished using Kemipol T-12, with Al_2O_3 grains of 14 μm. This was followed by degreasing the surfaces of the samples with the cleaning agent UNICLEAN 253, which is composed of silicate, hydroxide and biodegradable surfactants. After that, the substrate surfaces were washed and activated in the activation agent UNICLEAN 675. Additional activation was done with chemical pre-coating treatment. After rinsing, the main electroless-deposition process was applied (**Figure 1**). The electroless nickel-plating process was carried out using a Nikora nickel bath (a registered trademark of Schering AG, Berlin). It is known that the Nikora nickel bath is based on an aqueous solution of sodium hypophosphite. The chemical composition of the electroless plating bath was not studied.

Table 1: Chemical composition of steel substrate
Tabela 1: Kemijska sestava jekla iz podlage

Chemical composition in mass fraction (*w*/%)							
C	Si	Mn	P	S	Cr	Mo	Ni
0.07	0.71	1.36	0.031	0.021	17.1	2.42	11.6

After the electroless processing, some samples were heat treated by aging them at 500 °C for 60 min in an air-furnace atmosphere.[18] Other specimens were not heat treated after the electroless processing. The heat treatment was not longer than 24 h, applied after the electroless processing of the specimens.

Ni-P coating layers of the non-heat-treated samples and heat-treated samples were tested with the microhardness indentation technique. The Vickers microhardness of each sample was determined as the average of five test results obtained with the Vickers tester Struers Duramin 2. A microstructure analysis of the Ni-P coating layers was carried out with an Olympus BX51 optical microscope and scanning electron microscope FEG FEI QUANTA 250 SEM. An X-ray diffraction (XRD) analysis of the heat-treated electroless coating was carried out with a BRUKER AXS D8–Advance instrument and Vertical Theta–Theta goniometer with Co radiation.

3 RESULTS AND DISCUSSION

The obtained microhardness of the non-heat-treated electroless Ni-P coating on the austenitic stainless-steel AISI 316 substrate was 429±17 HV0.01, while the hardness of the heat-treated electroless Ni-P coating was 853±26 HV0.01.

The adhesivity related to the studied electroless process was compared with the adhesivity achieved with the electroless process, in which chemical activation was not applied. The adhesivity was estimated with a Vickers indenter. In **Figure 2**, it can be seen that the delamination of the deposited layer did not appear on the specimen treated with chemical pre-coating.

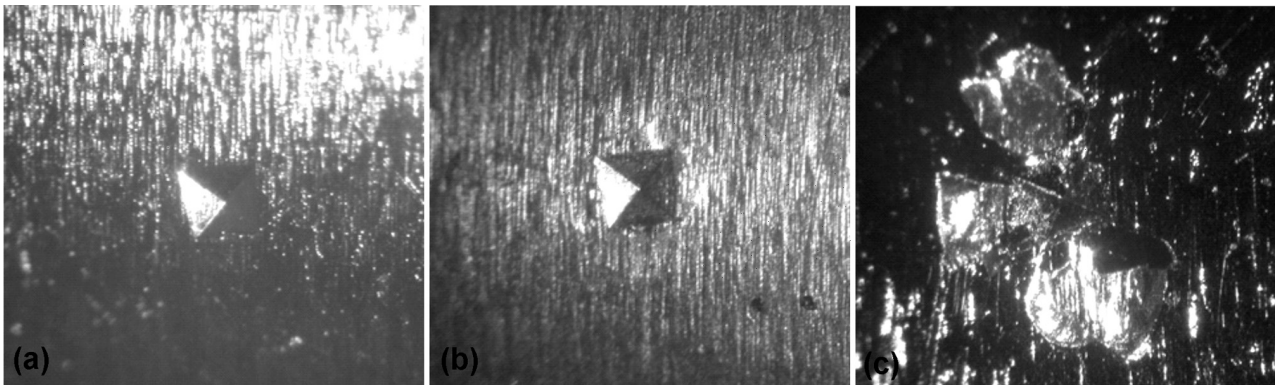

Figure 2: Indentation results for adhesivity of Ni-P electroless coatings, mag. 35:1: a) chemical pre-coating treatment of the surface + electroless coating, b) pre-coating treatment of the surface + electroless coating + aging at 500 °C, c) electroless coating + aging at 500 °C

Slika 2: Rezultati vtiskovanja za adhezivnost kemijskega Ni-P nanosa: 35-kratna povečava: a) kemijska predobdelava površine s kemijskim nanosom, b) kemijska predobdelava površine s kemijskim nanosom in staranjem na 500 °C, c) nanos in staranje na 500 °C

A metallographic analysis of the Ni-P coating layers was performed on the cross-sections of both parts of the samples (**Figure 3**).

From **Figure 3a**, it is evident that the electroless Ni-P coating follows the surface morphology and surface roughness of the substrate. **Figure 3a** shows that the coating exists but shows failures that can be explained with the cracking of the brittle coating during the specimen preparation for the micro-analysis.

The deposited Ni-P coating of a heat-treated specimen is shown in **Figure 3b**. The heat treatment, i.e., the aging of specimens was applied after the main electroless process. No failures in the Ni-P coating were observed on the heat-treated specimens.

No relevant differences between the thicknesses of these two Ni-P coatings were detected. The thickness of the non-heat-treated Ni-P coating is 8.11±0.18 μm while the thickness of the heat-treated Ni-P coating is 7.52±0.18 μm.

The contents of the iron, chromium, nickel and phosphorus of the non-heat-treated sample were evaluated with SEM and EDS mapping. A map of the contents of

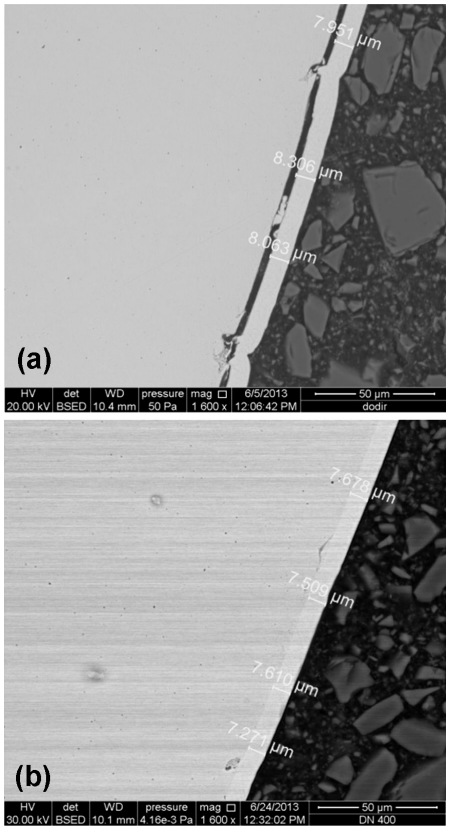

Figure 3: Micrographs of the cross-sections of Ni-P coatings on: a) non-heat-treated austenitic stainless-steel AISI 316 substrate, b) heat-treated austenitic stainless-steel AISI 316 substrate

Slika 3: Posnetka preseka Ni-P nanosa na podlagi iz avstenitnega nerjavnega jekla AISI 316: a) toplotno neobdelano, b) toplotno obdelano

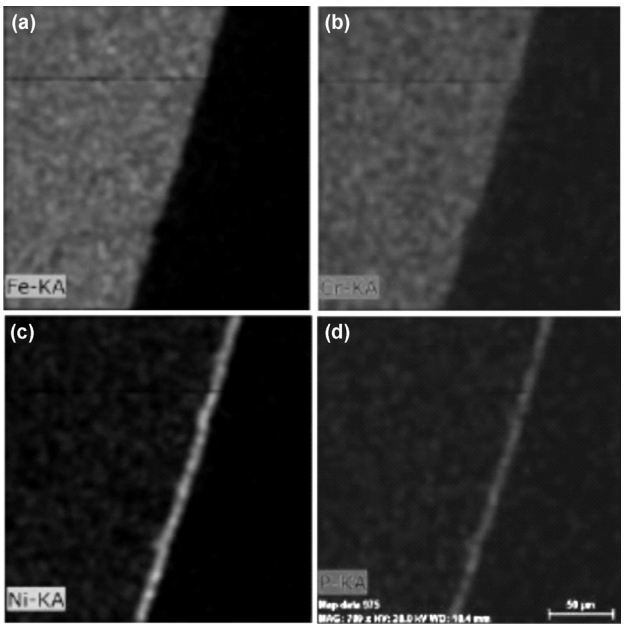

Figure 4: SEM and EDS mapping of the iron, chromium, nickel and phosphorus of the non-heat-treated samples

Slika 4: SEM- in EDS-prikaz razporeditve železa, niklja in fosforja na toplotno neobdelanem vzorcu

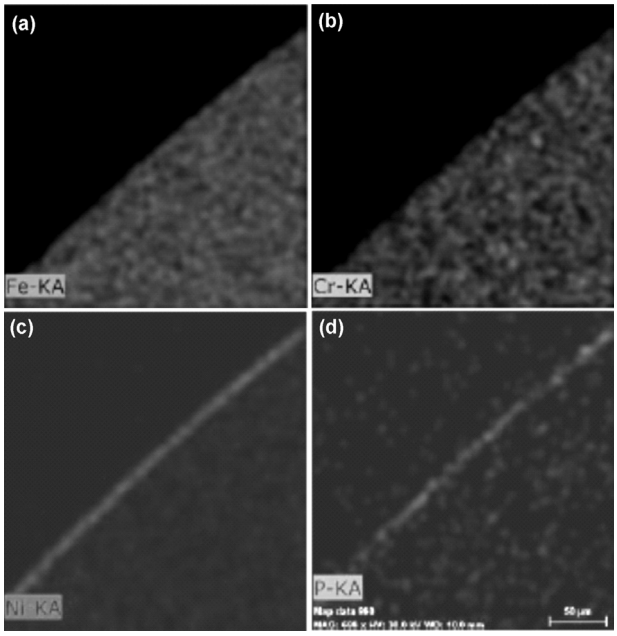

Figure 5: Content of the iron, chromium, nickel and phosphorus present on the cross-sections of Ni-P coatings deposited with the electroless process on austenitic stainless-steel AISI 316 substrate of the heat-treated sample, obtained with SEM and EDS mapping

Slika 5: SEM- in EDS-prikaz razporeditve železa, niklja in fosforja na toplotno obdelanem vzorcu

iron, chromium, nickel and phosphorus is shown in **Figure 4**. It is evident that nickel (**Figure 4c**) and phosphorous (**Figure 4d**) are located in both the coating and the substrate. Iron (**Figure 4a**) and chromium (**Figure 4b**) are located only in the substrate. Phosphorous is uniformly distributed in the Ni-P coating.

SEM and EDS mapping of the contents of the iron, chromium, nickel and phosphorus in the heat-treated samples is shown in **Figure 5**. It is evident that the distribution of chemical elements in the coating and the substrate is similar to the distribution of chemical elements in the non-heat-treated specimen. Nickel (**Figure 5c**) and phosphorous (**Figure 5d**) are found in the coating and in the substrate, but iron (**Figure 5a**) and chromium (**Figure 5b**) are found only in the substrate.

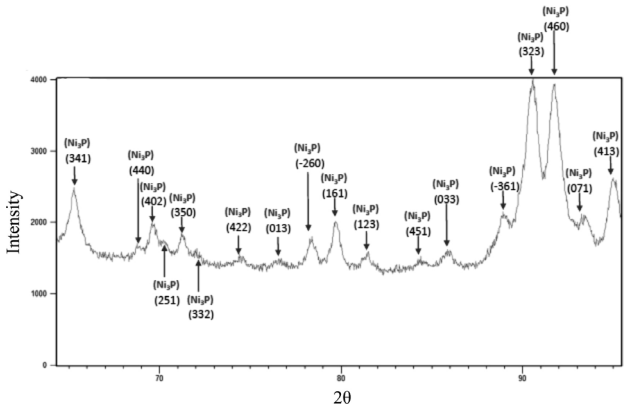

Figure 6: X-ray spectra of the heat-treated electroless nickel-phosphorous coating

Slika 6: Rentgenogram toplotno obdelanega, kemijsko nanešenega nanosa nikelj-fosfor

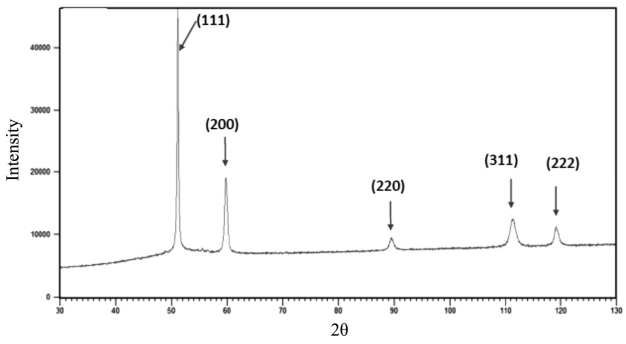

Figure 7: X-ray spectra of the non-heat-treated electroless nickel-phosphorous coating

Slika 7: Rentgenogram toplotno neobdelanega kemijsko nanešenega nanosa nikelj-fosfor

It was found that the heat-treated and non-heat-treated specimens have about 9 % of phosphorous. Distributions of phosphorous in the coatings are similar in both the heat-treated and non-heat-treated specimens, but it is known that the non-heat-treated coating with 9 % of phosphorous has a mixed, amorphous and crystalline structure.[8]

For a more precise definition of a possible mechanism of hardening the coating with heat treatment, a further study of the electroless nickel-phosphorous coatings was done using an X-ray diffraction analysis. The X-ray diffraction analysis was performed on both types of samples, i.e., the heat-treated and non-heat-treated electroless nickel-phosphorous coatings. In **Figure 6,** the results of the X-ray diffraction analysis of a heat-treated electroless coating are shown. It can be seen that the Ni_3P phase is formed in the heat-treated electroless coating. **Figure 7** shows the X-ray diffraction analysis of a non-heat-treated electroless coating. The Ni_3P phase was not formed on the non-heat-treated electroless coating.

4 CONCLUSION

Application of the Ni-P coatings deposited with the electroless process on the austenitic steel AISI 316 was analyzed.

Surfaces of the austenitic-steel AISI 316 substrate were prepared before depositing the Ni-P coatings with the electroless process. The investigated coatings follow the surface morphology of the samples. Uniform Ni-P coatings deposited with the electroless process were formed.

With the X-ray diffraction analysis, it was determined that the Ni_3P phase was formed due to the heat treatment of the samples. At the same time, it was found that a substantial increase in the hardness of an electroless Ni-P

coating is achieved by applying the heat treatment. The thickness of the non-heat-treated Ni-P coating is 8 μm while the thickness of the heat-treated Ni-P coating is 7.5 μm.

Acknowledgement

This work was fully supported by the Croatian Science Foundation under project 5371.

5 REFERENCES

[1] K. Hari Krishnan, S. John, K. N. Srinivasan, J. Praveen, M. Ganesan, P. M. Kavimani, An overall aspect of electroless Ni-P depositions – A review article, Metallurgical and Materials Transactions A, 37 (**2006**) 6, 1917–1926, doi:10.1007/s11661-006-0134-7

[2] Z. C. Shao, Z. Q. Cai, R. Hu, S. Q. Wei, The study of electroless nickel plating directly on magnesium alloy, Surface and Coatings Technology, 249 (**2014**), 42–47, doi:10.1016/j.surfcoat.2014.03.043

[3] Y. Wang, M. Kang, S. W. Jin, X. Q. Fu, X. S. Wang, Electrochemical behaviour in process of electrodeposition Ni–P alloy coating, Surface Engineering, 30 (**2014**) 8, 557–561, doi:http://dx.doi.org/10.1179/1743294414Y.0000000291

[4] T. Y. Soror, Structure and Wear Resistance Properties of Electroless Ni-P Alloy and Ni-P-SiC Composite Coatings, European Chemical Bulletin, 2 (**2013**) 8, 562–567

[5] J. Sudagar, J. Lian, W. Sha, Electroless nickel, alloy, composite and nano coatings – A critical review, Journal of Alloys and Compounds, 571 (**2013**), 183–204, doi:10.1016/j.jallcom.2013.03.107

[6] M. Sajjadnejad, A. Mozafari, H. Omidvar, M. Javanbakht, Preparation and corrosion resistance of pulse electrodeposited Zn and Zn–SiC nanocomposite coatings, Applied Surface Science, 300 (**2014**), 1–7, doi:10.1016/j.apsusc.2013.12.143

[7] Y. H. Wu, T. M. Liu, S. X. Luo, Corrosion characteristics of electroless Ni–P coating in sulfur-bearing solution, Materials and Corrosion, 60 (**2009**) 12, 987–990, doi: 10.1002/maco.200805208

[8] D. W. Baudrand, Electroless Nickel Plating, ASM Handbook, ASM International, Materials Park, OH, 5 (**1994**), 290

[9] R. Taheri, Evaluation of Electroless Nickel-Phosphorus (EN) Coatings, Ph. D. thesis, University of Saskatchewan, 2002

[10] J. N. Balaraju, T. S. N. Sankara Narayanan, S. K. Seshadri, Structure and Phase Transformation Behaviour of Electroless Ni–P Composite Coatings, Materials Research Bulletin, 41 (**2006**) 4, 847–860, doi:10.1016/j.materresbull.2005.09.024

[11] A. A. Zuleta, O. A. Galvis, J. G. Castaño, F. Echeverría, F. J. Bolivar, M. P. Hierro, F. J. Pérez-Trujillo, Preparation and characterization of electroless Ni–P–Fe3O4 composite coatings and evaluation of its high temperature oxidation behavior, Surface & Coatings Technology, 203 (**2009**) 23, 3569–3578, doi:10.1016/j.surfcoat.2009.05.025

[12] P. Sahoo, S. K. Das, Tribology of electroless nickel coatings – A review, Materials and Design, 32 (**2011**) 4, 1760–1775, doi:10.1016/j.matdes.2010.11.013

[13] J. B. Hajdu, Surface Preparation for Electroless Nickel Plating, Electroless Plating, Fundamentals and Applications, American Electroplaters and Surface Finishers Society, Orlando, Fla., 1990, 193–206

[14] The Engineering Properties of Electroless Nickel Coatings, Report, ELNIC Inc., Nashville, TN, 1980, C3–C27

[15] C. Ma, F. Wu, Y. Ning, F. Xia, Y. Liu, Effect of heat treatment on structures and corrosion characteristics of electroless Ni–P–SiC nanocomposite coatings, Ceramics International, 40 (**2014**) 7A, 9279–9284, doi:10.1016/j.ceramint.2014.01.150

[16] L. Ploof, Electroless Nickel Composite Coatings, Advanced Materials & Processes, 166 (**2008**) 5, 36–38

[17] R. Hartung, J. Schmidt, S. Both, Tribologische Nickel-Dispersionsschichten Mit Hexagonalem Bornitrid, Galvanotechnik, 12 (**2008**), 2931–2939

[18] S. Alirezaei, S. M. Monirvaghefi, M. Salehi, A. Saatchi, Effect of Aluminia Content on Surface Morphology and Hardness of Ni-P-Al2O3 (α) Electroless Composite Coatings, Surface and Coating Technology, 184 (**2004**) 2–3, 170–175, doi:10.1016/j.surfcoat.2003.11.013

[19] I. Apachitei, F. D. Tichelaar, J. Duszczyk, L. Katgerman, Solid-State Reaction in Low-Phosphorus Autocatalityc NiP-SiC Coatings, Surface and Coating Technology, 148 (**2001**) 2–3, 284–295, doi:10.1016/S0257-8972(01)01337-8

[20] J. N. Balaraju, K. S. Rajam, Electroless Deposition and Characterization of High Phosphoros Ni-P-Si3N4 Composite Coatings, International Journal of Electrochemical Science, 2 (**2007**)10, 747–761

[21] H. Ma, F. Tian, D. Li, Q. Guo, Study on the Nano-Composite Electroless Coating of Ni-P/Ag, Journal of Alloys and Coumounds, 474 (**2009**) 1–2, 254–267, doi:10.1016/j.jallcom.2008.06.057

[22] J. Novakovic, P. Vassiliou, Kl. Samara, Th. Argyropoulos, Electroless NiP-TiO2 Composite Coatings: Their Production and Properties, Surface & Coatings Technology, 201 (**2006**) 3–4, 895–901, doi:10.1016/j.surfcoat.2006.01.005

[23] Y. H. Cheng, Y. Zou, L. Cheng, W. Liu, Effect of the microstructure on the properties of Ni-P deposits on heat transfer surface, Surface & Coatings Technology, 203 (**2009**) 12, 1559–1564, doi:10.1016/j.surfcoat.2008.10.039

[24] S. Karthikeyan, B. Ramamoorthy, Effect of reducing agent and nano Al2O3 particles on the properties of electroless Ni–P coating, Applied Surface Science, 307 (**2014**), 654–660, doi:10.1016/j.apsusc.2014.04.092

[25] M. Islam, T. Shehbaz, Effect of synthesis conditions and post-deposition treatments on composition and structural morphology of medium-phosphorus electroless Ni–P films, Surface & Coatings Technology, 205 (**2011**) 19, 4397–4400, doi:10.1016/j.surfcoat.2011.03.042

[26] Y. F. Shen, W. Y. Xue, Z. Y. Liu, L. Zuo, Nanoscratching deformation and fracture toughness of electroless Ni–P coatings, Surface & Coatings Technology, 205 (**2010**) 2, 632–640, doi:10.1016/j.surfcoat.2010.07.066

[27] Y. Liu, D. Beckett, D. Hawthorne, Effect of heat treatment, top coatings and conversion coatings on the corrosion properties of black electroless Ni–P films, Applied Surface Science, 257 (**2011**) 9, 4486–4494, doi:10.1016/j.apsusc.2010.12.105

[28] P. Sahoo, Wear behaviour of electroless Ni–P coatings and optimization of process parameters using Taguchi method, Materials and Design, 30 (**2009**) 4, 1341–1349, doi:10.1016/j.matdes.2008.06.031

UDK 669.715:669.295:669.058.67
Original scientific article/Izvirni znanstveni članek

ISSN 1580-2949
MTAEC9, 51(3)419(2017)

CENTRAL COMPOSITE DESIGN ON THE VOLUME OF LASER METAL DEPOSITED Ti6Al4V AND Cu

CENTRALNO NAČRTOVANJE KOMPOZITA NA OSNOVI KOLIČINE LASERSKO NANEŠENE KOVINE Ti6Al4V IN Cu

Mutiu F. Erinosho, Esther Titilayo Akinlabi

University of Johannesburg, Department of Mechanical Engineering Science, Auckland Park Kingsway Campus, 2006 Johannesburg, South Africa
mferinosho@uj.ac.za, mutiuerinosho1@gmail.com

Prejem rokopisa – received: 2016-01-20; sprejem za objavo – accepted for publication: 2016-05-18

doi:10.17222/mit.2016.019

The laser technology process is a pulsating practice in the field of engineering and in all paces of lifespan; since it can travel a longer distance and be focused on a very small bright spot that exceeds the illumination of the sun. This present study reports on the modeling and the prediction of the volume of laser-deposited composites using the central composite design (CCD). Four input factors were put into consideration, which is the laser power, the scanning speed, the powder flow rate and the gas flow rate. Titanium alloy (Ti6Al4V) and copper (Cu) powders were coaxially deposited to form the bulk of a single clad. The factors considered determine the energy density and the melt pool delivered into the substrate and as such, influence the volume of the deposited composite (VDC) that was employed in the response surface methodology (RSM) design. This has been used to predict the actual process parameters for the optimum process setting.

Keywords: laser metal deposition, response surface methodology, central composite design, volume of deposited composite

Postopek laserske tehnologije se uporablja na področju tehnike in na vseh korakih življenjske dobe materialov; saj lahko premaguje velike razdalje in je v obliki zelo majhne svelte točke, ki presega sevanje sonca. Študija predstavlja modeliranje in napovedovanje količine lasersko nanešenega kompozita, z uporabo centralnega načrtovanja kompozita (angl. CCD). Obravnavani so bili štirje vplivni dejavniki: moč laserja, hitrost skeniranja, hitrost toka prahu in hitrost toka plina. Titanova zlitina (Ti6Al4V) in baker (Cu) sta bila koaksialno nanešena in sta tvorila enoten nanos. Obravnavani dejavniki so določali gostoto energije in obseg taline nanešene na podlago in kot taki vplivali na volumen nanešenega kompozita (angl. VDC), ki je bil uporabljen pri načrtovanju metodologije odgovora površine (angl. RSM). To je bilo uporabljeno za napovedovanje dejanskih procesnih parametrov pri optimiranju nastavitev procesa.

Ključne besede: nanašanje kovine z laserjem, metodologija odgovora površine, centralno načrtovanje kompozita, volumen nanešenega kompozita

1 INTRODUCTION

The word laser is an acronym for "Light Amplification by Stimulated Emission of Radiation". In terms of wavelength, a laser device produces intense beams of low-divergence light for electromagnetic radiation ranging from 1 nm to 1000 μm. It is less than 500 nm for ultraviolet and less than 800 nm in visible spectrum, and 200 nm to 400 nm for ultraviolet light. In comparison with photon energy, the wavelength of laser light is of a pure monochromatic type.[1] The laser metal-deposition process produces a metallurgical bonding, which is formed permanently between the clad and the substrate. In applications, a low dilution occurs in one step, with the minimal use of powder; and no form of additional processing is required when this is achieved.[2] The extent of the energy density absorbed by the substrate determines the depth of the melt pool and the volume of the deposited alloy.[3] The material flow rate also has a large effect on the chemical and the mechanical properties of the final deposited clad during laser metal-deposition process.[4,5]

Design of experiment (DOE) has been widely used to minimize the guessing of results and useful for a laboratory experiment to yield a desirable output. It is a problem dependent on a set of experiments; and has been widely used in industries for the development and the optimization of production processes.[6] It is also regarded as a systematic and rigorous approach to engineering problem-solving that applies techniques and principles during the collection stage of data, so as to ensure and arrive at a generally valid, defensible, and a well-aided engineering conclusion, which are carried out under the constraint of a minimal expenditure of engineering runs, time, and money.[7] The first stage in DOE is the planning of the experiment before embarking on the process of testing and data collection. The second stage is the screening test; and this is used to identify the important factors that affect the process parameters under investigation from all the numerous potential factors.[8] Optimization is followed in order to envisage the response values for all the likely factors within the experimental boundary and to locate the optimal experimental point. The next stage is done to ascertain that the approach

used is robust enough to accommodate small alterations in the factor levels.[6] The last stage is the verification of the results and the best-settings validation; and this is achieved by conducting a few follow-up experimental runs to confirm that the process parameters are well conformed.[8] However, the effect of a specific factor can be evaluated at different levels of the other factors; therefore, the results will be reliable over the whole experimental space.[9] The results showed how interconnected factors respond over a wide range of values, without requiring all the possible values to be tested directly. The software fits the response data to mathematical equations; which serve as models to predict what would happen for any given combination of values.[10] A full-factorial design with CCD to investigate the effects of pH and the buffer concentration of catholyte on the performance of two-chamber microbial fuel cell. It was revealed that the maximum power density did not show good manipulation on the fuel cell at a high level of buffer concentration.[11] The relationship between a high sharpness and the configurations of the vortex finder of a hydrocyclone was modeled using the regression method.[12] The production of recycled titanium from acid with the high sharpness was achieved.

A series of predictions have been made in an experiment in order to generate the validity of the result and to optimize the process parameters. In the literature, there are paucities of work on the estimation of the volume of laser-deposited samples. This can be really helpful to determine the bulk measurement of a laser-cladded surface. However, the aim of this work is to apply a full-factorial design and response surface methodology to evaluate and predict the volume of the laser-deposited titanium and copper alloys using the central composite design. The amount of volume generated is proportional and dependent on the laser's energy density and the process parameters employed.

2 EXPERIMENTAL PART

The process model started with several input factors such as the laser power, scanning speed, powder flow rate and gas flow rate that are controlled and varied by the experimenter. One or more outputs are produced as the response, which is assumed to be continuous.[7] The established experimental data are used to derive an empirical model containing the first- and second-order terms linking the outputs and inputs.[13] **Figure 1** shows the general model of a process or system.

The most common empirical models fit to the experimental data take either a linear form or a quadratic form. A linear model with two factors, X_1 and X_2, can be written as Equation (1):

$$Y = \beta_0 + \beta_1 X_1 + \beta_2 X_2 + \beta_{12} X_1 X_2 + \text{Experimental error} \quad (1)$$

From Equation (1), Y represents the response for the given levels of the main effects; X_1 and X_2 and the X_1X_2 term are included to account for a possible interaction effect between X_1 and X_2. The constant β_0 represents the response of Y when both the main effects are 0.

A quadratic model, which is a second-order model, is typically used in response surface DOE with suspected curvature; and it does not include the three-way interaction term, but adds three more terms to the linear model, as illustrated in Equation (2):[13]

$$\beta_{11} X^2_1 + \beta_{22} X^2_2 + \beta_{33} X^2_3 \quad (2)$$

The response surface methodology (RSM) is an efficient statistical tool that has been used successfully in testing the process parameters and their interactive effects.[14,15] In the RSM, the first-order design and the second-order design were adopted; and these are suitable for fitting and checking a first- and second-degree of polynomial. However, in other to allow for the efficient estimation of quadratic terms in the second-order model, a two-level factorial array is adopted,[16] as shown in Equation (3):

$$y = \beta_0 + \sum_{i=1}^{k} \beta_i x_i + \sum_{i=1}^{k} \beta_{ii} x_i^2 \sum_{i=1}^{k-1} + \sum_{j=2}^{k} \beta_{ij} x_i x_j \quad (3)$$

If all the variables are assumed to be measurable, the response surface can be expressed as shown in Equation (4):

$$y = f(x_1, x_2, x_3, x_4, \ldots, x_k) \quad (4)$$

where "y" is the independent variable of the system, and x_i is the dependent variables or factors. $x_1, x_2, x_3, x_4, \ldots, x_k$ are the input factors, which influence the response y; β_0, β_{ii} β_{ij} are the unknown parameters.[17–19]

2.1 Design of experiment

The RSM was implemented in order to analyze the experimental variables, and to provide an average response to the values of the quantitative variables analyzed. The factors from the volume of the deposited Ti6Al4V/Cu composite (VDC) were employed for the RSM design; and these have been used to predict the

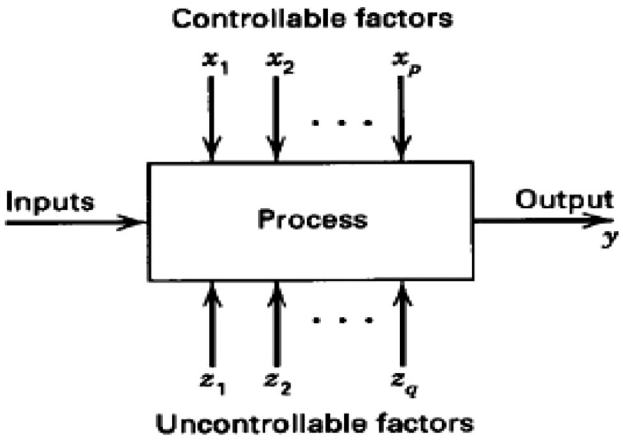

Figure 1: General model of a process or system[9]
Slika 1: Splošni model procesa ali sistema[9]

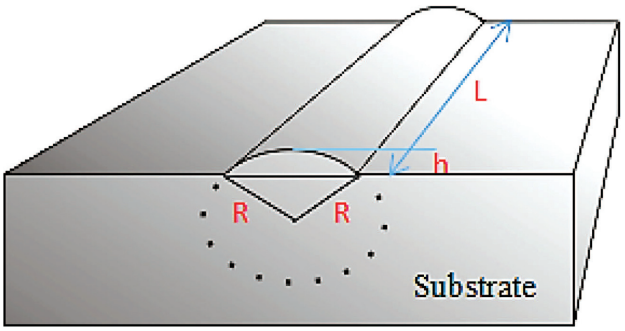

Figure 2: Schematic view of a laser-deposited sample[20]
Slika 2: Shematski prikaz lasersko deponiranega vzorca[20]

actual process parameters that produced the optimum process set-up. **Figure 2** displays a schematic view of a deposited composite showing the track length, track width and the height of the deposit. The schematic is a sample image of the laser-deposited Ti6Al4V/Cu composite, as deposited on the substrate.

The volume of the laser-deposited composite is generated using Equation (5). The full geometry can be obtained elsewhere.[20]

$$V(L,R,h)=L\left[R^2\cos^{-1}\left(\frac{R-h}{R}\right)-(R-h)\left(\frac{W}{2}\right)\right] \quad (5)$$

where L designates the length of the deposit track; W is the deposit width; h is the height of the deposit; R is the radius of the circle and V represents the volume of the deposited composite.

The process parameters were controlled to give reasonable volumes of the deposited samples. The polynomial function is introduced in the RSM design to provide a depiction of how the response is affected by a number of variables over a unit of experimental interest.

The input parameters are the laser power, scanning speed, powder flow rate and the gas flow rate, respectively. In the settings, the low level and high level of the factors are the inputs, as shown in **Table 1**.

Table 1: Input parametric factors for the RMS design
Tabela 1: Vhodni parametri dejavnikov za načrtovanje RMS

Factor	Name	Level	Low Level	High Level
A	Laser power	1.60	0.80	1.60
B	Scanning speed	0.60	0.30	0.90
C	Powder flow rate	2.40	2.40	2.50
D	Gas flow rate	2.95	2.90	3.00

The VDC is studied by using the central composite design (CCD). This is appropriate to fit the quadratic

Table 2: Point-type design layout
Tabela 2: Postavitev točkaste vrste načrtovanja

Number of run	Standard order	Block	Space type	Laser power (kW)	Scanning speed (m/min)	Powder flow rate (min^{-1})	Gas flow rate (l/min)	Volume of deposited composite (mm^3)
1	18	Day 1	Center	1.40	0.40	2.45	2.95	100.54
2	20	Day 1	Center	1.40	0.40	2.45	2.95	100.54
3	11	Day 1	Factorial	1.20	0.50	2.40	3.00	78.68
4	9	Day 1	Factorial	1.20	0.30	2.40	3.00	91.9
5	6	Day 1	Factorial	1.60	0.30	2.50	2.90	147.88
6	13	Day 1	Factorial	1.20	0.30	2.50	3.00	91.90
7	1	Day 1	Factorial	1.20	0.30	2.40	2.90	91.90
8	19	Day 1	Center	1.40	0.40	2.45	2.95	100.54
9	5	Day 1	Factorial	1.20	0.30	2.50	2.90	120.29
10	12	Day 1	Factorial	1.60	0.50	2.40	3.00	104.48
11	3	Day 1	Factorial	1.20	0.50	2.40	2.90	78.68
12	16	Day 1	Factorial	1.60	0.50	2.50	3.00	104.48
13	10	Day 1	Factorial	1.60	0.30	2.40	3.00	111.65
14	17	Day 1	Center	1.40	0.40	2.45	2.95	100.54
15	14	Day 1	Factorial	1.60	0.30	2.50	3.00	147.88
16	4	Day 1	Factorial	1.60	0.50	2.40	2.90	104.48
17	2	Day 1	Factorial	1.60	0.30	2.40	2.90	111.65
18	7	Day 1	Factorial	1.20	0.50	2.50	2.90	78.68
19	8	Day 1	Factorial	1.60	0.50	2.50	2.90	104.48
20	15	Day 1	Factorial	1.20	0.50	2.50	3.00	78.68
21	29	Day 2	Center	1.40	0.40	2.45	2.95	100.54
22	23	Day 2	Axial	1.40	0.20	2.45	2.95	102.76
23	22	Day 2	Axial	1.80	0.40	2.45	2.95	120.76
24	21	Day 2	Axial	1.00	0.40	2.45	2.95	69.38
25	30	Day 2	Center	1.40	0.40	2.45	2.95	100.54
26	28	Day 2	Axial	1.40	0.40	2.45	3.05	100.54
27	26	Day 2	Axial	1.40	0.40	2.55	2.95	100.54
28	27	Day 2	Axial	1.40	0.40	2.45	2.85	100.54
29	24	Day 2	Axial	1.40	0.60	2.45	2.95	97.36
30	25	Day 2	Axial	1.40	0.40	2.35	2.95	98.58

surface. The numerical factors were selected based on the number of factors. The numbers of factors involved are: the laser power, the scanning speed, the powder flow rate, and the gas flow rate. From the CCD formed, a full factorial type was proposed. The number of blockings selected was designated to be run for 2 d, that is d 1 and d 2 are proposed for the experiment. In total, 30 runs were involved for the experiment within the two days. This displays the graphical illustration of the blocks' interpretation in **Table 2**; and the orientation would be much more productive to the impact of the control factors in response to the surface graphics.

The quadratic model used was not aliased, which means there are no fewer independent points in the design model; therefore, the parameters used can be estimated independently. Aliases are calculated, based on the responses selected, and taking into consideration the degree of freedom for the evaluation.

Table 3 illustrates the power at a 5 % alpha level to detect the signal or noise level in this model. The standard error estimates the standard deviation of the parameters; and it is used to calculate a confidence interval around the parameters.

The smaller the standard deviation, the better is the result. In this design, the Variance Inflation Factor (VIF) measures how much the variance of that parameters or model coefficient is inflated by the lack of orthogonality in the design. The VIF in this design follows between 1.0 and 1.05, which is almost ideal. The VIF above 10 indicates some cause for alarm; and this shows that the coefficients are poorly estimated – due to multi-collinearity. The ideal Ri-squared is 0.0, which makes the model a good one. A high Ri-squared specifies that the terms are correlated with each other; and this could possibly lead to poor models. In this design model, the minimum, average and maximum variance mean are 0.159, 0.193 and 0.588, respectively. The average leverage for the 30 runs in the experiment is 0.5333.

3 RESULTS AND DISCUSSION

3.1 Analyses of the responses on the volume of the deposited composites within the CCD

The results of the responses are numerically analyzed after the design evaluation. The resulting values of the VDC were input, based on the output from the number of runs within the design configurations. The design experts offer a full array of response transformation. The responses of the VDC range from the minimum value 69.38 mm^3 and the maximum value 120.29 mm^3. The ratio between the maximum and the minimum values is 1.73. This obtained ratio is less than 3; and the power transformation would consequently have little effect.

In the analysis of the results, a model for the fit summary is suggested. The Sequential Model is formed with the combination of the source, sum of squares, degree of freedom (df), mean square, F value and the p-value. A small F value and a high p-value, which is greater than 0.1, are good for the model. The lowest F value is 0.14; and the highest p-value is 0.9634. These two values fall within the quadratic versus 2 factors interaction (2FI) of the Sequential Model.

However, the model may fit the design points at some point; but it may not be a very good predictor at the other points. Extra design points need to be added, to check the model fit; and these should be beyond those for determining the model coefficients. The variation between the model prediction and the extra points can be compared with the experimental or pure error, to test the lack of fit. The experimental error, or the pure error, is the normal variation within the response when there is a replicate of the experiment. Only one experiment was

Table 3: Power at 5 % alpha level to detect the signal for various standard-deviation values
Tabela 3: Moč na 5 % vsebnosti alfa za zaznavanje signala pri različnih standardnih vrednostih odstopanj

Term	Standard error	VIF	Ri-squared	0.5 Standard deviation	1 Standard deviation	2 Standard deviation
Day 1	0.19	1.00	0.0000			
Day 2						
A	0.20	1.00	0.0000	20.8 %	62.5 %	99.5 %
B	0.20	1.00	0.0000	20.8 %	62.5 %	99.5 %
C	0.20	1.00	0.0000	20.8 %	62.5 %	99.5 %
D	0.20	1.00	0.0000	20.8 %	62.5 %	99.5 %
AB	0.25	1.00	0.0000	15.4 %	46.1 %	96.0 %
AC	0.25	1.00	0.0000	15.4 %	46.1 %	96.0 %
AD	0.25	1.00	0.0000	15.4 %	46.1 %	96.0 %
BC	0.25	1.00	0.0000	15.4 %	46.1 %	96.0 %
BD	0.25	1.00	0.0000	15.4 %	46.1 %	96.0 %
CD	0.25	1.00	0.0000	15.4 %	46.1 %	96.0 %
AČ2	0.19	1.05	0.0476	68.3 %	99.8 %	99.9 %
BČ2	0.19	1.05	0.0476	68.3 %	99.8 %	99.9 %
CČ2	0.19	1.05	0.0476	68.3 %	99.8 %	99.9 %
DČ2	0.19	1.05	0.0476	68.3 %	99.8 %	99.9 %

run in the design space; and the pure error is negligible; since the value of the sum of the square and mean square in the lack of fit test table is zero. The lack of fit tests table compares the residual error with the pure error from replicated design points. Since the pure error is zero, the F value and the Prob > F were not revealed by the model (**Table 4**). The model has an insignificant lack of fit, which shows that it is a good predictor, and a better forecaster of the responses; and this follows the statistical and numerical output.

3.2 Analysis of variance results

The Analysis of Variance (ANOVA) is the statistical approach that partitions the total variation of a dataset into its component parts for the purpose of testing an assumption on the parameters of the certain selected model. The ANOVA is constructed totally on the basis that the factors are fixed, and the design is crossed. **Table 4** depicts the ANOVA for the response surface quadratic model used. The quadratic model is a polynomial model containing the linear and two-factor terms. The sources in the response surface quadratic model include the block, the model, the factors, the residuals, and the lack of fit.

Table 4: Analysis of variance for the response surface quadratic model

Tabela 4: Analiza variance odziva površinsko kvadratnega modela

Source	Sum of squares	Df	Mean square	F Value	p-value Prob > F
Block	74.57	1	74.57		
Model	7528.41	14	537.74	6.92	0.0004
A-Laser power	4505.93	1	4505.93	58.01	< 0.0001
B-Scanning speed	1554.46	1	1554.46	20.01	0.0005
C-Powder flow rate	457.36	1	457.36	5.89	0.0293
D-Gas flow rate	33.58	1	33.58	0.43	0.5215
AB	24.68	1	24.68	0.32	0.5819
AC	121.39	1	121.39	1.56	0.2317
AD	50.37	1	50.37	0.65	0.4341
BC	635.67	1	635.67	8.18	0.0126
BD	50.37	1	50.37	0.65	0.4341
CD	50.37	1	50.37	0.65	0.4341
A^2	12.76	1	12.76	0.16	0.6914
B^2	9.24	1	9.24	0.12	0.7352
C^2	5.60	1	5.60	0.072	0.7923
D^2	13.32	1	13.32	0.17	0.6851
Residual	1087.38	14	77.67		
Lack of fit	1087.38	10	108.74		
Pure error	0.000	4	0.000		
Cor total	8690.36	29			

From the source, the "F-value" of the Model is 6.92; and this infers that the model is significant. There is only a 0.04 % chance that an "F-value" this large could occur due to noise. The values of "Prob > F" less than 0.0500 indicate that the model terms are significant. In other words and as indicated, A, B, C and BC are the significant model terms. Other values greater than 0.1000, indicate that the model terms are not significant.

The values of the R-Squared and the adjusted R-Squared are good; since there values are close to 1. The "Predicted R-Squared" of 0.1082 is not as close to the "Adjusted R-Squared" of 0.7476, as one might normally expect; and the difference is more than 0.2; and this may indicate a large block effect. The "Adequate Precision" measures the signal-to-noise ratio[21] with a value of 11.481, which is desirable for the model; since its ratio is greater than 4. This model can be used to steer and pilot the design space.

The final equation, in terms of the coded factors, is given in the following iteration, as shown in Equation (6):

Volume of Deposited Composites =
99.98+13.70*A-8.05*B+4.37*C-1.18*D-1.24*AB+2.75 *AC+1.77*AD-6.30*BC+1.77*BD-1.77*CB-0.68*A^2 +0.58B^2+0.45*C^2+0.70*D^2 (6)

Equation (6) in the iteration of coded factors can be used to make predictions about the response for given levels of each factor. The coded equation is useful for identifying the relative impact of the factors by comparing the factor coefficients.

3.3 Statistical analysis and the properties of the model

The diagnosis and the statistical properties of the model are presented by normal probability plots. The studentized residuals are used to validate the ANOVA. The normal plot of residuals is a plot of normal percentage probability against the residuals. The data points are linear in the error term, which signifies no problems or difficulties in the data obtained from the probability distribution. **Figure 3** shows the plot of percentage probability versus the externally studentized residual.

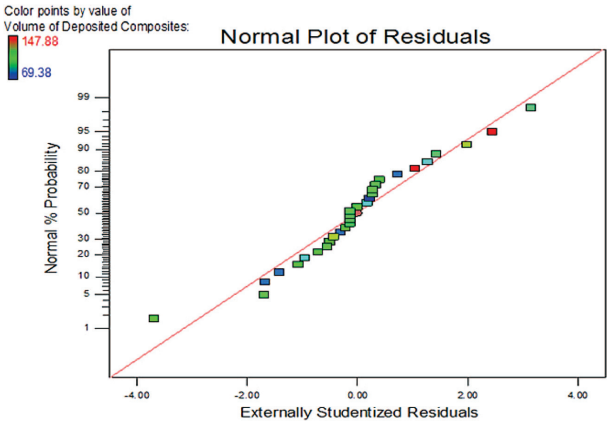

Figure 3: Plot of percentage probability versus the externally studentized residual

Slika 3: Diagram odstotka verjetnosti v primerjavi z zunanje proučevanim ostankom

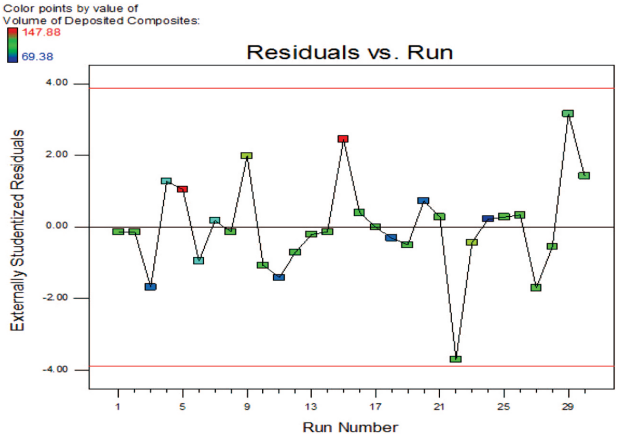

Figure 4: Plot of externally studentized residuals versus experimental run order

Slika 4: Diagram zunanje proučevanega ostanka v odvisnosti od eksperimentalnega poteka

The plot shows the way the actual value deviates from the predicted value. The Design-Expert puts control limits on the externally studentized residuals plot, in order to identify the abnormal runs easily. The externally studentized residual test or outlier t test is applicable when checking whether a run is consistent with the other runs; and is based on the assumption that the chosen model holds. The prediction of the responses at this point is made. In this model, there is no outlier and the responses fit the model, since the value is not greater than 3.5. This can be seen from the residual plots.

Figure 4 represents the plot of residuals versus the experimental run order.

This plot checks for lurking and unobserved variables that may have influenced the response during the experiment. The plot shows a random scatter with a line connecting each point. A consistent trend indicates a time-related variable lurking in the background of the plot. Randomization and blocking provide protection and indemnity for the trends, in order not to tarnish the analysis. The trend from the first run to the thirtieth runs falls between the upper and lower red lines. This proves the assumptions to be established, and most of the green points are found close to the zero point of the externally studentized residuals.

Figure 5 portrays the surface plot of the VDC at varying laser powers and scanning speeds, as well as a constant powder flow rate of 2.45 min^{-1}, and a gas flow rate of 2.95053 L/min, respectively.

From the surface plot, it can be deduced that towards the direction of the laser power, an upward tilt or elevation of the surface plot was observed, as the laser power increases. Their representations indicate that an increase in the laser power leads to an increase in the volume of the composites, as directed by the upward tilt of the surface plot. The reverse is the case for the scanning speed on the same surface plot. Towards the path of the scanning speed, a downward tilt of the surface plot was observed, which indicates that the deposited volume decreases as the scanning speed increases. This phenomenon of the decrease in the volume with an increase in the scanning speed can be attributed

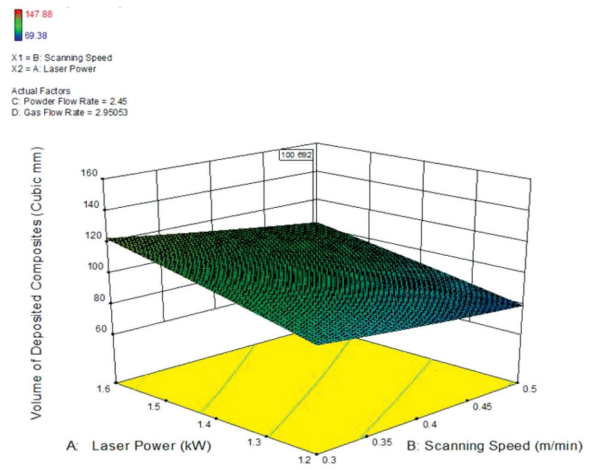

Figure 5: Surface plot of the volume of deposited composites at varying laser powers between 1.2 kW and 1.6 kW, scanning speeds between 0.3 m/min and 0.5 m/min

Slika 5: Površina volumna nanešenih kompozitov pri različnih močeh laserja med 1,2 kW in 1,6 kW, hitrost skeniranja med 0,3 m/min in 0,5 m/min

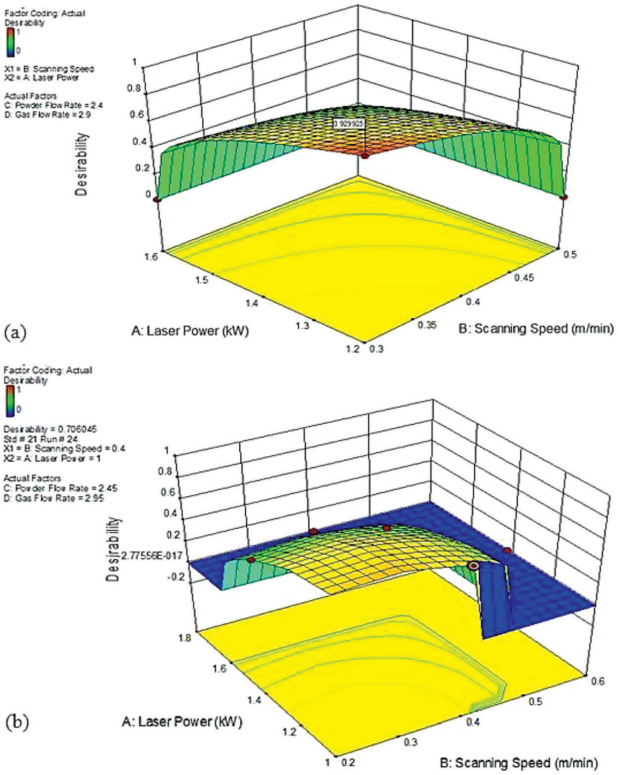

Figure 6: a) Surface plot of the desirability at varying lasers power and scanning speeds, b) surface plot of desirability with a standard order of 21 and run order of 24

Slika 6: a) Zaželjena površina pri različnih močeh laserja in hitrosti skeniranja, b) zaželjena površina z zahtevkom 21 in potekom 24

to the interaction time it takes the powders to be formed on the surface of the substrate. In other words, the faster the speed of the scan, the quicker the time of deposit, and the smaller the deposited volume becomes, and vice versa. For this plot, the powder flow rate and the gas flow rate were kept constant.

The surface plot in **Figures 6a** and **6b** shows a graphical representation and the response optimization of the normal desirability plot and the desirability with a standard order of 21 and a run order of 24 at varying laser powers between 1.2 kW and 1.6 kW, and with a scanning speed between 0.3 m/min and 0.5 m/min.

The contours of the desirability shortened inwardly as the laser power and the scanning speed decrease. This occurrence improves the desirability of achieving the optimal setting. The green and the faint red arcs drawn on the yellow square surface give an indication of the respective desirability. The desirability lies between the laser power of 1.2 kW and 1.4 kW, and the scanning speed lies between 0.3 m/min and 0.42 m/min. The 3D surface plotted ridge and fold are where the desirability can be maintained at a high level over a range of factor levels. The solution is relatively robust to a laser power between 1.6 kW and 1.8 kW, and also robust to the scanning speed between 0.45 m/min and 0.6 m/min. The robustness is indicated by the blue colour, and this shows that the approach used is robust enough to create a small alteration in the factor levels.[6]

3.4 Validation of the experiment

The experiment validation was established to verify the variations between the predicted value by the software and the actual value from the current experiment. This is actually done to validate and confirm the reality of the model. The actual results are almost twice the results predicted by the software. **Figure 7** presents the plot of the actual value against the predicted value of the volume of the deposited composites.

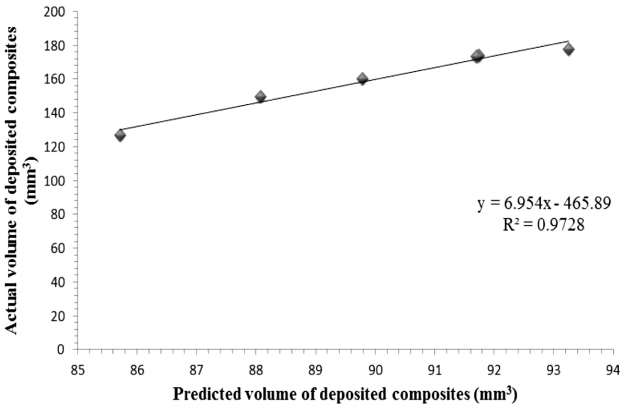

Figure 7: Plot of actual and predicted values for the volume of deposited composites

Slika 7: Prikaz dejanske in napovehanih vrednosti volumna nanešenega kompozita

The plot is a linear regression curve with the independent value of $y = 6.954x - 465.89$. The values of y represent the actual values resulting from the experiment conducted on the selected parameters. The results obtained were approximately two times the predicted VDC. The laser system used for the trial runs and the preliminary studies was different from the laser system used to validate the results. The different laser-system configurations has a strong effect on the result. Also, the heights of the deposit undergoing validation have an influence on the actual results, which in turn affects the area of the segment and the volume of the composites.

4 CONCLUSION

This study discusses the application of RSM and CCD for the modeling and optimization of the effect of some operating variables on the volume of the deposited composite (VDC). It was observed that the cladded volume is directly proportional to the laser power and inversely proportional to the scanning speed. The model has an insignificant lack of fit, which shows that it is a good predictor, and a better forecaster of the responses, and this follows the statistical and numerical outputs. The mathematical model equations were derived for both the dependent variable (response) and the independent variables (input factors) using design expert software 9. The 3D response surface plots, which are simulations from the models, were presented to describe the effect of the process variables on the output volume. The F-value of the model was 6.92, which inferred that the model is significant. The value of the adjusted R-Square was 0.7476 and the adequate precision measures the signal-to-noise ratio with a value of 11.481, which was desirable for the model.

5 REFERENCES

[1] Introduction to Laser Technology, http://www.mellesgriot.com, 12.07.2013

[2] Laser Solutions for Manufacturing, http://www.industrial-lasers.com/articles/print/volume-250/issue-6/features/laser-metal deposition.html, Industrial Pennwell Copyright, 23.08.2013

[3] T. N Baker, Laser surface modification of Ti alloys, Surface Engineering of Light Alloys – Aluminium, Magnesium and Titanium Alloys, Wood-Head Publications, 2010, 398–443

[4] E. Brandl, A. Schoberth, C. Leyens, Materials Science and Engineering, A, 532 (2012) 295-307, doi:10.1016/j.msea.2011.10.095

[5] M. Shukla, R. M. Mahamood, E. T. Akinlabi, S. Pityana, Effect of laser power and powder flow rate on properties of laser metal deposited Ti6Al4V, World Academy of Science, Engineering and Technology, 2012, 71, 1268–1272

[6] L. Eriksson, E. Johansson, N. K. Wold, C. Wikstrom, S. Wold, Design of Experiments, Principles and Applications, (2010), 425

[7] Nist/Sematech, Engineering Statistic handbook, http://www.itl.nist.gov/div898/handbook/pmd/section3/pmd31.htm, 13.07.2014

[8] Reliability Engineering Resources, The eMagazine for the Engineering professionals, http://www.weibull.com/hotwire/issue84/hottopics84.htm, 15.04.2014

[9] D. C. Montgomery, Design and analysis of the experiments, 8th ed, New York, John Wiley & sons, (2001), https://www.academia.edu/30544104/Douglas-C.-Montgomery-Design_and_Analysis_of_Experiments-8th_edition

[10] M. Anderson, Design of Experiment, http://www.eng.auburn.edu/~drmills/mans486/DOE/Fall09/DOE_advantages_indust_examples.pdf, 13.07.2014

[11] S. Madani, R. Gheshlaghi, M. A Mahdavi, M. Sobhani, A. Elkamel, Optimization of the performance of a double-chamber microbial fuel cell through factorial design of experiments and response surface methodology, Fuel, 150 (**2015**), 434–440, doi:10.1016/j.fuel.2015.02.039

[12] B. Tang, Y. Xu, X. Song, Z. Sun, J. Yu, Numerical study on the relationship between high sharpness and configurations of the vortex finder of a hydrocyclone by central composite design, Chemical Engineering Journal, 278 (**2015**), 504–516, doi:10.1016/j.cej.2014.11.022

[13] Nist/Sematech, Engineering Statistic handbook, http://www.itl.nist.gov/div898/handbook/pri/section1/pri11.htm, 13.07.2014

[14] H. M. Hamzah, A. Osman, C. P. Tan, G. F. Mohamad, Carrageenan as an alternative coating for papaya (Carica papaya L. cv. Eksotika), Postharvest Biology and Technology, 75 (**2013**), 142–146, doi:10.1016/j.postharvbio.2012.08.012

[15] K. Murugesan, A. Dhamija, I. H. Nam, Y. M. Kim, Y. S. Chang, Decolourization of reactive black 5 by laccase, Optimization by response surface methodology, Dyes Pigments, 75 (**2007**) 1, 176–84, doi:10.1016/j.dyepig.2006.04.020

[16] G. E. P Box, K. B Wilson, On the Experimental Attainment of Optimum Conditions, Journal of the Royal Statistical Society, B, 13 (**1951**), 1–45

[17] N. Aslan, Y. Cebeci, Application of Box–Behnken design and response surface methodology for modeling of some Turkish coals, Fuel, 86 (**2007**), 90–97, doi:10.1016/j.fuel.2006.06.010

[18] N. Aslan, Application of response surface methodology and central composite rotatable design for modeling the influence of some operating variables of a Multi-Gravity Separator for coal cleaning, Fuel, 86 (**2007**) 5–6, 769–776, doi:10.1016/j.fuel.2006.10.020

[19] N. Aslan, Application of response surface methodology and central composite rotatable design for modeling and optimization of a multi-gravity separator for chromite concentration, Powder Technology, 185(1) (**2008**), 80–86, doi:10.1016/j.powtec.2007.10.002

[20] M. F. Erinosho, E. T. Akinlabi, S. Pityana, Effect of scanning speed and powder flow rate on the evolving properties of laser metal deposited Ti-6Al-4V/Cu composites, International Journal of Surface Science and Engineering, 3 (**2016**), 207–223

[21] G. E. P Box, N. R Darper, Empirical model-building and response surfaces, Wiley, New York, 1987

UDK 621.7.015:669.715:669.295:620.17
Original scientific article/Izvirni znanstveni članek

ISSN 1580-2949
MTAEC9, 51(3)427(2017)

FRICTION-STIR PROCESSING OF A COMPOSITE ALUMINIUM ALLOY (AA 1050) REINFORCED WITH TITANIUM CARBIDE POWDER

UPORABA MEŠANJA S TRENJEM ZA IZDELAVO KOMPOZITA ALUMINIJEVE ZLITINE (AA1050), OJAČANE S TITANOVIM KARBIDOM V PRAHU

Kazeem Oladele Sanusi, Esther Titilayo Akinlabi

University of Johannesburg, Department of Mechanical Science, Auckland Park Kingsway Campus, Johannesburg 2006, South Africa
sanusik@gmail.com

Prejem rokopisa – received: 2016-01-22; sprejem za objavo – accepted for publication: 2016-05-20

doi:10.17222/mit.2016.021

In this study the friction-stir processing (FSP) technique was applied for the development of surface composites of aluminium alloy (AA 1050) reinforced with titanium carbide (TiC) powder of particle size range below 60 μm compressed into the groove. Rotational speeds of 1200 min^{-1} and 1600 min^{-1} and the travel rates of (100, 200 and 300) mm/min were used for the process. This study investigates the effect of processing parameters on the wear-resistance behavior of friction-stir processed Al-TiC composites. This was achieved through microstructural characterization using optical and scanning electron (SEM) microscopes equipped with Oxford energy-dispersion spectrometry (EDS) (Tescan), microhardness profiling and wear resistance tests. From the results, it was found that the processing parameters influenced the distribution of the TiC particles. The microhardness profiling of the processed samples revealed an increase in the hardness value compared to the parent material. The wear-resistance test results confirmed the FSP technique enhanced properties in surface engineering.

Keywords: aluminium alloy, friction-stir processing, microhardness, microstructure, surface composite, TiC

V študiji je bila uporabljena tehnika mešanja s trenjem (angl. FSP) za razvoj površinskih kompozitov iz aluminijeve zlitine (AA 1050), ojačanih s titanovim karbidom (TiC) v prahu, z velikostjo delcev v območju pod 60 μm, stisnjenih v utor. Pri tem postopku so bile uporabljene hitrosti vrtenja 1200 min^{-1} in 1600 min^{-1} in hitrosti pomikanja (100, 200 in 300) mm/min. Študija raziskuje vpliv procesnih parametrov na odpornost kompozitov Al-TiCi proti obrabi s trenjem. Izvedena je bila mikrostrukturna karakterizacija z uporabo svetlobnega in vrstičnega elektronskega mikroskopa (SEM), opremljenega z Oxford energijsko disperzijsko spektrometrijo (EDS) (Tescan), profiliranja mikrotrdote in preizkusa obrabe. Iz rezultatov je bilo ugotovljeno, da so parametri obdelave vplivali na distribucijo TiC delcev. Profiliranje mikrotrdote na vzorcih je pokazalo, da je vrednost trdote povečana v primerjavi z osnovnim materialom. Rezultati testa odpornosti obrabe so potrdili, da FSP-tehnika izboljša lastnosti površine.

Ključne besede: aluminijeve zlitine, tehnika mešanja s trenjem, mikrotrdota, mikrostruktura, površinski kompoziti, TiC

1 INTRODUCTION

Friction-stir processing (FSP) is a newly emerging technology based on the friction-stir welding (FSW) method that allows the near-surface regions of a material to be selectively processed and currently used to enhance the mechanical properties of conventional materials.[1] This process has been applied to microstructural modifications for enhanced mechanical properties through intense plastic deformation using a non-consumable rotating tool that causes material mixing and thermal exposure and results in grain refinement of the material being processed.[2,3] The benefits of the FSP process include significant microstructural refinement, densification, and homogeneity of the processed zone, homogenization of precipitates in various aluminium alloys and composite materials.[4–6] Moreover, the severe plastic deformation (SPD) and material flow in the stirred zone of the FSP can be utilized to achieve surface or bulk alloy modification by the mixing of other elements into the stirred alloys where the stirred material can become a metal matrix composite or an intermetallic alloy with much higher hardness and good wear-resistance properties.[7] Applications of the FSP/FSW are widespread for the aerospace, automotive and the transportation industries. Research studies have been reported on the friction-stir process that grain refinement can be achieved in this way. The microstructure and mechanical behaviour of lightweight materials subjected to the FSW/FSP are being studied extensively, which include the processing of the microstructure amenable to high-strain-rate superplasticity.[8] Y. Kwon et al. produced 1050 aluminium alloy with an ultra-fine grain size through the friction-stir process (FSP). They studied the influence of tool rotation speed on the temperature profile, microstructure and mechanical properties of the friction-stir processed zone (FZ) and they concluded that FSP is very effective in producing an ultra-fine-grained material with excellent mechanical properties.

Aluminium matrix composites (AMCs) reinforced with ceramic particles exhibit high strength, high elastic modulus, and improved resistance to wear, creep and fatigue, which make them promising structural materials for aerospace and automobile industries.[9] These composites can suffer a great loss in ductility and toughness due to the incorporation of non-deformable ceramic reinforcements, which limits their wide applications to a certain extent.[10,11] However, the nature of the technique used to fabricate particle-reinforced metal-matrix composites (MMCs) has been shown to have a significant effect on the product's mechanical properties and hence the applications for which it is suitable.[12–15] Surface-modification techniques such as high-energy laser beam, plasma spraying, cast sinter and electron beam irradiation have been developed over the past two decades to fabricate Surface Metal Matrix Composites (SMMCs).[16–19] It has been shown that friction-stir processing (FSP) can be effectively used to homogenise the particle distribution in Al-based in-situ composites. R. Mishra et al.[12] confirmed the application of FSP technology to fabricate AA5083/SiC SMMC. The incorporation of SiC particles on the surface was successful and bonded well with the matrix. Subsequently, they confirmed FSP as a promising method to fabricate SMMCs.[2] Mahmoud et al. fabricated AA1050/SiC SMMC, their results showed that the distribution of the SiC particles became more homogeneous with an increasing number of passes and with the combination of tool rotational speed and the processing speed resulted in the formation of defects, such as voids and tunnels in the FSP zone.[20] E. R. I. Mahmoud et al.[20] also fabricated AA1050/SiC SMMC and assessed the effect of the tool pin size and profile. From their results, the wear rates of the samples produced with the flat surface tools were higher than that of the samples produced with the round-shaped tools and the samples produced with the square profile pin yielded a finer distribution of the SiC particles.[21] R. Bauri et al.[22] used FSP effectively to homogenise the particle distribution in Al-based in-situ composites. The process was employed on the as-cast composite to uniformly distribute the TiC particles in the Al matrix. The composite was subjected to single- and double-pass FSP and its effect on the microstructure and properties was evaluated. From their results, they confirmed that a single pass of FSP was enough to break the particle segregation from the grain boundaries and improve the distribution and two passes of FSP resulted in complete homogenization and elimination of casting defects. The grain size was also refined after each FSP pass. This led to a significant improvement in the mechanical properties after FSP. A. Kahrizsangi and S. Kashani-Bozorg[23] works on a mild-steel substrate by the introduction of nano-sized TiC powder into the stir zone using four passes of friction stir processing and the TiC clusters were formed after the first pass. Sequential break-up of the clusters and refinement of the matrix grains were caused by subsequent FSP passes. A near-uniform dispersion of nano-sized TiC particles was achieved after the fourth pass. A significant improvement in the wear resistance of the nano-composite layer was observed as compared to that of the as-received substrate and the enhanced properties are attributed to the uniform dispersion of hard nano-sized TiC reinforcements in a matrix of ultra-fine dynamically recrystallized grains. A. Thangarasu et al.[10] fabricated TiC particulates ($\approx$2 μm) and reinforced them with an aluminium matrix composite (AMC) using FSP. The powders were compacted into a groove and a single pass FSP was carried out using a tool rotational speed of 1600 min^{-1} and a processing speed of 60 mm/min. They analysed the microstructure and microhardness of the fabricated AMC and from their results, revealed a uniform distribution of TiC particles which were well bonded to the matrix alloy with an increase in the hardness value of the AMC compared to that of the matrix alloy. E. Akinlabi et al.[3] investigated the effect of the processing parameters on the wear-resistance behaviour of friction-stir processed Al-TiC composites. From their findings it was revealed that an increase in the hardness value, which was a function of the TiC particles incorporated when compared to the parent material and the wear resistance property, was also found to increase as a result of the TiC powder addition. The right combination of the processing parameters was found to improve the wear resistance property of the composites produced. Kurt et al. incorporated SiC particles into the commercially pure aluminium to form particulate surface layers by using friction-stir processing (FSP). The samples were subjected to the various tool rotating and traverse rates with and without SiC powders. Microstructural observations were carried out by employing optical microscopy of the modified surfaces. Mechanical properties like hardness and plate bending were investigated. The results showed that increasing rotating and traverse rate caused a more uniform distribution of the SiC particles. Uygur studied commercially pure (CP) aluminium using the friction stir welding technique (FSW) to weld the specimens. The welding process was carried out by rotating 1500 min^{-1} and by moving 200 mm/min. Under a constant friction force this involved four different shoulder diameters of (20, 25, 30 and 40) mm. During welding, temperature measurements were performed using a non-contact laser thermometer at various parts of the plates from the welding centre outwards. Microscopic and mechanical tests were used to characterize the sample.

In this paper, a further research study was conducted on AA1050 to uniformly distribute the TiC particles into the Al matrix using friction stir processing. The produced composites were investigated through the microstructural evolution, wear resistance behaviour and the hardness distribution. The research study is aimed at providing a better understanding of the materials behaviour

after FSP using different combinations of rotational speeds and travel rates.

2 MATERIALS AND METHODS

In this study, aluminium alloys (AA1050) with rectangular elements with dimensions of (200 × 160 × 3) mm were used for this experiment. The experimental setup showing the clamping fixture and the backing plate system is presented in **Figure 1**. The chemical composition of the aluminium alloy used is presented in **Table 1**. The V-groove of about 5 mm was machined and filled with TiC powder with the aim of strengthening the material. Some 99.5 % TiC with a particle size range below 60 μm ball milled powder with irregular shape was used. The powder was compressed into the groove using a pinless tool across the surface of the material and a second tool, comprising a pin and shoulder, was plunged into the workpiece after compressing the TiC powder. The micrograph of the TiC powder used is shown in **Figure 2**. The tools were machined from H13 tool steel and hardened to 52 HRC. The workpieces were securely clamped on a rigid, smooth, mild-steel backing plate with dimensions of (650 × 265 × 25) mm, to make the material withstand the significant perpendicular and lateral forces developed during the friction-stir process. The weld matrix employed with the processing parameters is presented in **Table 2**. The rotational speeds employed were 1200 min^{-1} and 1600 min^{-1} and the travel rates were (100, 200 and 300) mm/min, both representing the low, medium, and high settings, respectively. **Figure 3** shows a schematic drawing of the V-groove machined into the base metal.

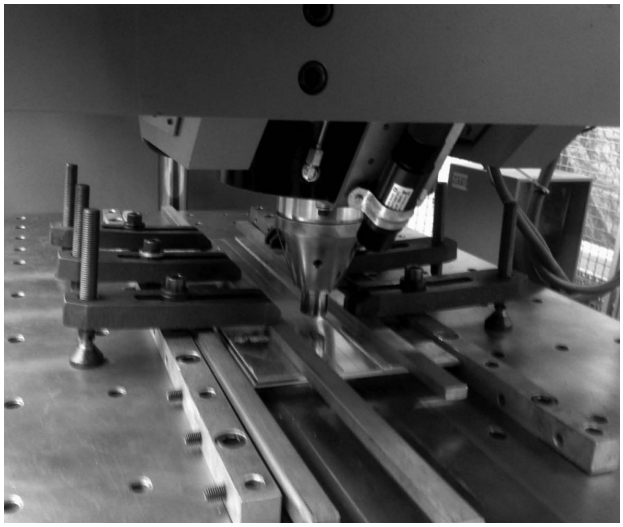

Figure 1: Experimental set up
Slika 1: Experimentalni sestav

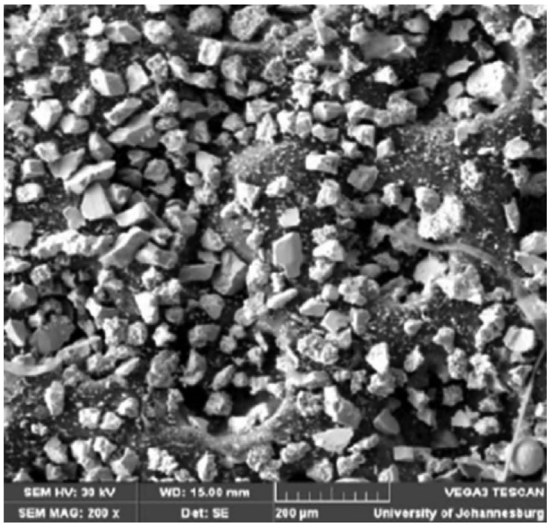

Figure 2: SEM micrograph of the titanium carbide powder
Slika 2: SEM-posnetek prahu titanovega karbida

Table 1: Chemical composition of AA1050
Tabela 1: Kemijska sestava zlitine AA1050

	Al	Si	Fe	Cu	Mn	Mg	Zn	V
AA1050	99.5	0.25	0.4	0.05	0.05	0.05	0.05	0.05

Table 2: Processing-parameters matrix of friction-stir processing
Tabela 2: Matrika procesnih parametrov pri obdelavi mešanja s trenjem

Designation	Spindle speed (min^{-1})	Travel rate (mm/min)
FsP 1200_100	1200	100
FsP 1200_200	1200	200
FsP 1200_300	1200	300
FsP 1600_100	1600	100
FsP 1600_200	1600	200
FsP 1600_300	1600	300

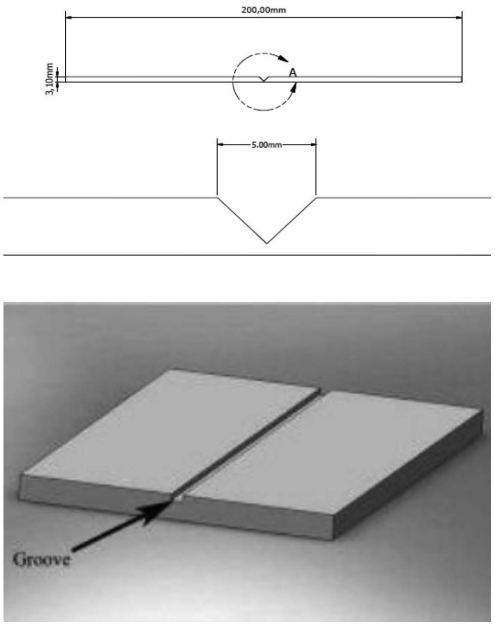

Figure 3: A schematic drawing showing the V-groove machined into the base metal
Slika 3: Shematski prikaz in posnetek klinastega utora v osnovni kovini

All the processed samples and the as-received materials were cut into the required sample sizes with the aid of the water-jet cutting technique for microstructural characterization and microhardness measurements. The processed specimens were examined with a scanning electron microscope (SEM) equipped with Oxford energy-dispersion spectrometry (EDS) (Tescan) were used to characterize the samples. The microhardness measurements were conducted using a Vickers microhardness tester with a diamond indenter using 300 g load and a dwell time of 15 s at the surface of the processed samples and the parent material. The wear tests were evaluated on both the as-received and processed samples using a tribometer (CETRUMT200). The wear resistance test was performed under dry condition using a ball-on-disk arrangement on both the parent material and the materials processed by FSP. The material of the ball is a tungsten carbide of 10 mm diameter and at a load of 25 N with a reciprocating frequency of 20 Hz and for a 2000 m sliding distance.

3 RESULTS AND DISCUSSIONS

3.1 Surface appearance characterisation

Figure 4 shows the upper surface appearances of the samples processed at a rotational speed of 1200 min^{-1} and travel rates of 100 min/min and 300 min/min and **Figure 5** shows the appearance of samples processed at a rotational speed of 1600 min^{-1} and travel rates of 100 min/min and 300 min/min. From the figures, good smooth and quality surfaces were observed after the FSP, the groove is effectively bonded and no defects such as voids and cracks were observed on the surface. **Figure 6** shows the root of sample C at a rotational speed of 1200 min^{-1} and a travel rate of 300 min/min. The root indicates that a thorough stirring was achieved during the FSP.

3.2 Microstructural evolution

Figures 7 and **8** show the SEM micrographs of the distribution of the TiC particles in the AA 1050 aluminium produced at rotational speeds of 1200 min^{-1} and 1600 min^{-1} , respectively. **Figure 7** shows that the grains in the FSP zone of the specimen were refined; this caused a high plastic strain in the stirred zone in which

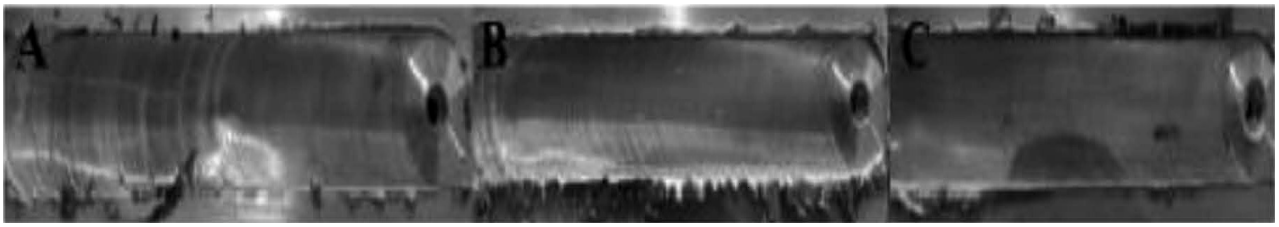

Figure 4: Photograph of samples processed at a rotational speed of 1200 min^{-1} and travel rates of: a)100 mm/min, b) 200 mm/min and c) 300 mm/min

Slika 4: Fotografija vzorcev, obdelanih pri vrtilni hitrosti 1200 min^{-1} in hitrosti pomikanja: a) 100 mm/min, b) 200 mm/min in c) 300 mm/min

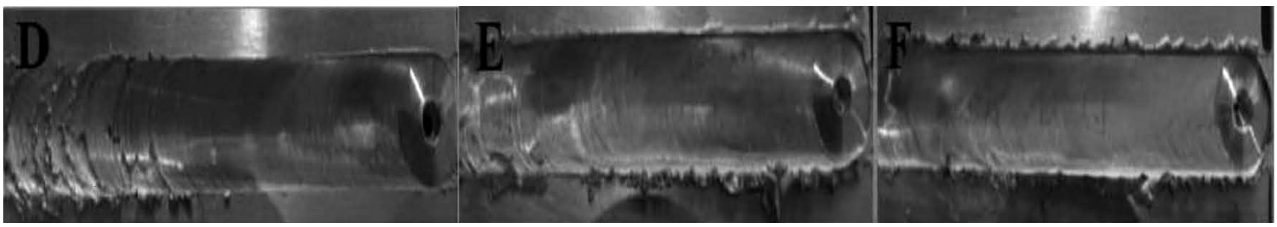

Figure 5: Photograph of samples processed at a rotational speed of 1600 min^{-1} and travel rates of: d)100 mm/min, e) 200 mm/mm and f) 300 mm/min

Slika 5: Fotografija vzorcev obdelanih pri hitrosti vrtenja 1600 min^{-1} pri hitrosti pomikanja: d) 100 mm/min, e) 200 mm/mm in f) 300 mm/min

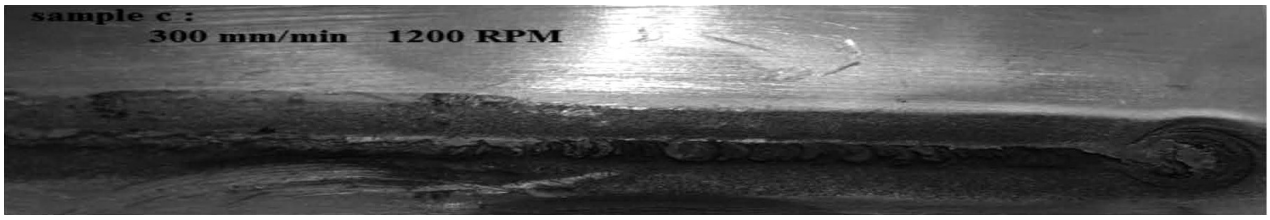

Figure 6: The root of sample C produced at a rotational speed of 1200 min^{-1} and travel rate of 300 mm/min

Slika 6: Koren vzorca C, obdelanega pri hitrosti vrtenja 1200 min^{-1} pri hitrosti pomikanja 300 mm/min

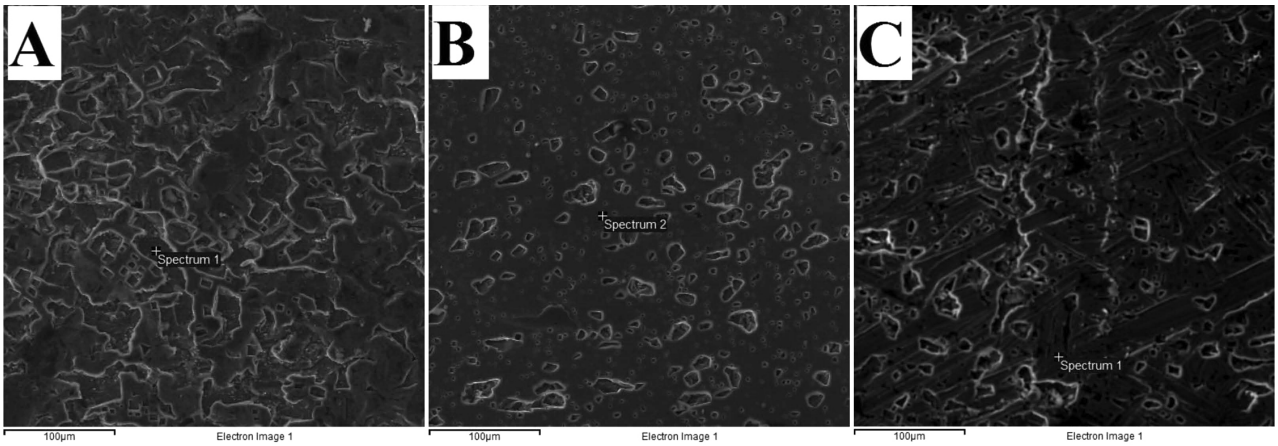

Figure 7: SEM photograph of grains after processing at a rotational speed of 1200 min^{-1} and travel rates of: a) 100 mm/min, b) 200 mm/min, c) 300 mm/min

Slika 7: SEM-posnetek zrn po obdelavi s hitrostjo vrtenja 1200 min^{-1} in hitrostjo pomikanja: a) 100 mm/min, b) 200 mm/min,c) 300 mm/min

severe plastic deformation was introduced into the workpiece through the rotating pin and shoulder, which results in a redistribution of the TiC particles. This can be attributed to the heat generated by the tool rotation speed and the traverse speed that resulted in lots of dilution of the TiC and the Al. A homogenous distribution of the TiC particles is essential to attain higher mechanical properties in the composite of aluminium alloy (AA 1050) and the TiC. The mechanism of grain refinement in AA1050 is that of dynamic recrystallization.[22,24] It was observed in **Figure 7** that the TiC particles were clustered together at a rotational speed of 1200 min^{-1} and a travel rate of 100 min/min compared to the samples produced at travel rates of 200 mm/min and 300 mm/min. This indicates that when the travel is at a slower rate, the TiC particles are not well distributed. It was observed in **Figure 8** that the size of the TiC particles is not uniform throughout the FSP zone. It was observed that some of the TiC particles were clustered in the samples produced at a high rotational speed of 1600 rpm. This can be attributed to the elevated temperature generated by the tool rotation speed and the traverse speed employed, which is in agreement with the published literature, as reported in some work by researchers in aluminium matrix composites.[25–27] Particles other than the TiC and aluminium were also observed in the processed specimens, using energy-dispersive X-ray spectroscopy (EDS).

3.3 Energy-dispersive X-ray spectroscopy (EDS)

Energy-dispersive X-ray spectroscopy (EDS) analysis was conducted to evaluate the morphological features of the debris found in the processed specimens. **Figure 9** shows the EDS of the debris of an FSP specimen processed at rotational speeds of 1200 min^{-1} and 1600 min^{-1}. The EDS pattern, shown in the figures, reveals that some particles are comprised of elements like Si, C, Fe and Ag. The presence of these elements indicates that the debris consist of elements present in the tool as well as in the backing plate (e.g., Fe, C). The figures also reveals that the extent of elements like Si, C, Fe and Ag are

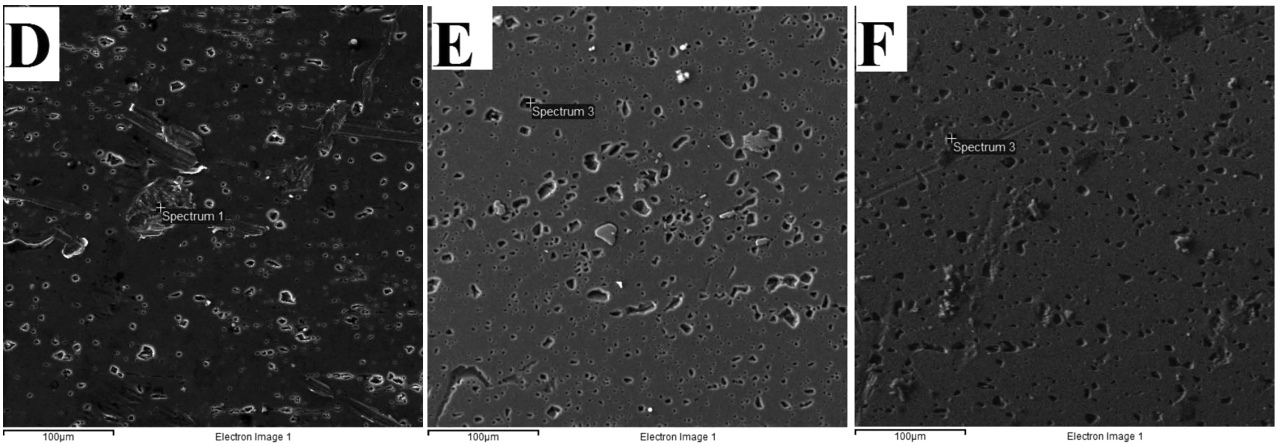

Figure 8: SEM photograph of grains after processing at a rotational speed of 1600 min^{-1} and travel rates of: d) 100 mm/min, e) 200 mm/min, f) 300 mm/min

Slika 8: SEM-posnetek zrn po obdelavi s hitrostjo vrtenja 1600 min^{-1} in hitrostjo pomikanja: d) 100 mm/min, e) 200 mm/min, f) 300 mm/min

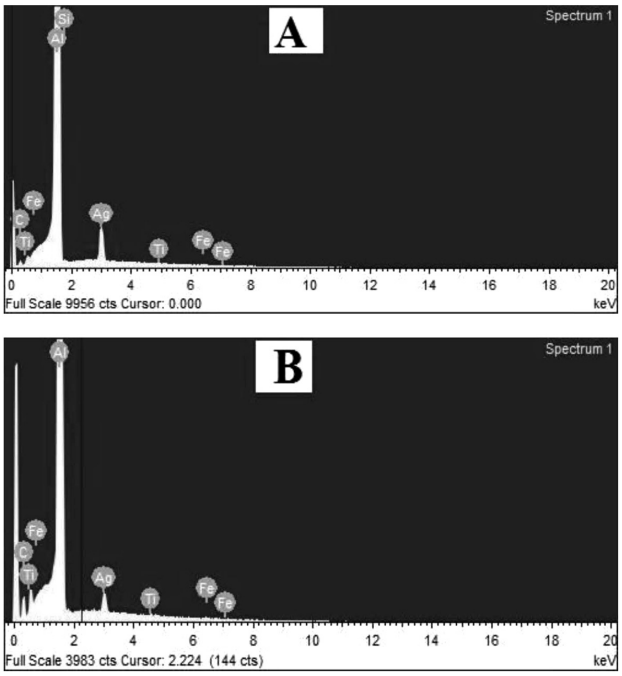

Figure 9: EDS of debris of FSP specimen processed at rotational speed of: a) 1200 min^{-1} and b) 1600 min^{-1}

Slika 9: EDS-zlomnine iz FSP vzorca, obdelanega s hitrostjo vrtenja: a) 1200 min^{-1} in b) 1600 min^{-1}

present in the specimen, which implies that the worn out particles/debris mainly result from the tools/backing plate and/or dissociation of the TiC. However, tool-wear debris is inevitable during FSW/FSP and reported in the FSP specimen layers in a scattered fashion by A. Kahrizsangi and S.vKashani-Bozorg and Y. Wang et. al.[23,28]

3.4 Hardness profiling

Figures 10 and **11** shows the Vickers microhardness of friction-stir processed AA1050 reinforced with TiC powder processed at the rotational speeds of 1200 min^{-1} and 1600 min^{-1}, respectively, at different travel rates of (100, 200 and 300) min^{-1}. The microhardness was measured on the matrices of the parent material and friction-stir processed materials with the lower dashed straight horizontal line indicating the homogeneity of the parent material. The hardness shows a significant improvement of the friction-stir processed material compared to the parent metal. The increase in the hardness can be attributed to the presence of the TiC particles in the matrix of the composite and the grain refinement of the matrix. The hardness across the friction-stir processed zone is not constant and the peak hardness value was observed at the point where the TiC was spotted. The average hardness values of the processed materials and the parent material are shown in **Figure 11**. The average hardness value of the parent materials is 28.9 HV and the average hardness of the processed materials after using 1200) min^{-1} and at (100, 200 and 300) mm/min are (41, 36 and 32) HV, respectively. The hardness results of the processed materials after using 1600 min^{-1} and at (100, 200 and 300) mm/min for processing were (44, 34 and 32) HV, respectively.

3.5 Ultimate tensile strength

D. Tabor[29] has shown that the ratio of ultimate tensile strength (UTS) to the Vickers hardness is related to the strain hardening coefficient. The relation between these parameters was expressed using Equation (1):

$$UTS = \left(\frac{H}{C}\right)(1-n)\left(\frac{12.5n}{1-n}\right)^{n} \quad (1)$$

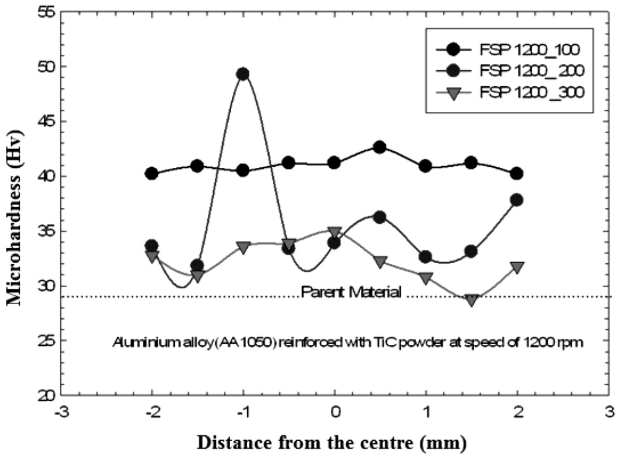

Figure 10: Vickers microhardness of friction-stir processed AA1050 reinforced with TiC powder processed at the rotational speed of 1200 min^{-1} and different travel rates: the lower dashed line shows the parent material's condition

Slika 10: Vickers mikrotrdota predelanega AA1050 z mešanjem, s trenjem in ojačanega s TiC v prahu, obdelanega pri hitrosti vrtenja 1200 min^{-1} in različnih hitrostih premika: spodnja črtkana črta kaže pogoje pri izvorni zlitini

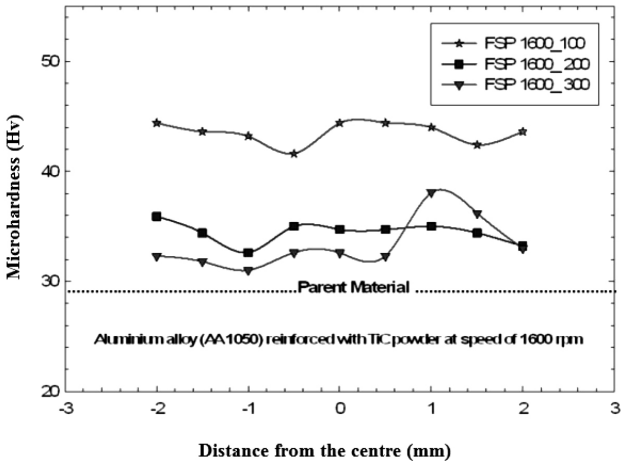

Figure 11: Vickers microhardness of friction-stir processed AA1050 reinforced with TiC powder processed at the rotational speeds of 1600 min^{-1} and different travel rates: the lower dashed line shows the parent material's condition

Slika 11: Vickers mikrotrdota obdelanega AA1050 z mešanjem s trenjem, ojačanega s TiC v prahu, obdelanega pri 1600 min^{-1} in pri različnih hitrostih pomikanja: nižja črtkana črta prikazuje osnovni material

Where *UTS* is the ultimate tensile strength, # is the Vickers hardness, *n* is the strain-hardening coefficient, and *C* is a constant that has a value of 2.9 for mild steels and ~3.0 for copper alloys and aluminium. This relation was further improved by J. R. Cahoon[30] in the form of Equation (2):

$$UTS = \left(\frac{H}{2.9}\right)\left(\frac{n}{0.217}\right)^{n} \quad (2)$$

where *H* is the Vickers hardness and *n* is the strain-hardening coefficient.

Using Equation (2), the UTS were calculated and plotted in **Figure 13**. From **Figure 13** it was observed that the parent material has a lower ultimate tensile strength compared to the materials processed by friction-stir processing reinforced with the TiC powder. It was also observed that the materials processed using rotational speeds of 1200 min^{-1} and 1600 min^{-1} and a travel rate of 100 have higher ultimate tensile strengths compared to the others. The trends in **Figure 13** also correlate with the hardness results in **Figure 12**.

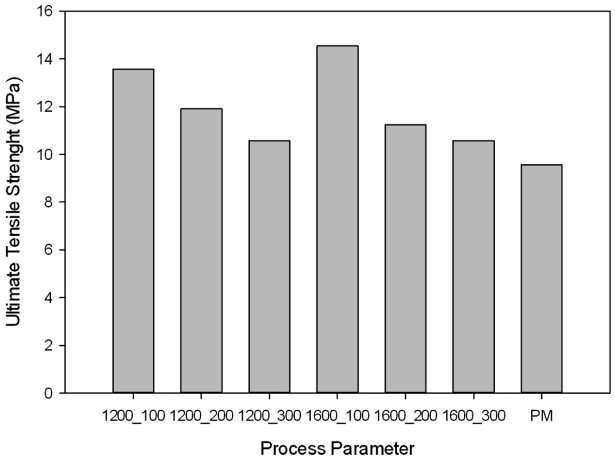

Figure 13: The ultimate tensile strength of parent material and friction-stir processed AA1050 reinforced with TiC powder

Slika 13: Natezna trdnost osnovnega materiala in AA1050 ojačanega s TiC, obdelanega z mešanjem s trenjem

3.6 Wear-volume losses

The wear-volume loss of the samples after the wear test is shown in **Figure 14** as a function of the process parameters for loads of 25 N with a sliding distance of 2000 m. It has been shown theoretically that the mass loss can be estimated using the Archard Equation (3):

$$V = K\frac{SL}{3H} \quad (3)$$

where *V* is the volume worn away during testing, *S* is the total sliding distance, *L* is the normal load, *H* is the hardness of the softer surface, and *K* is a dimensionless wear coefficient specific to the sample under test. It is reasonable to expect from Equation (1) that the materials after FSP will experience a smaller mass loss and it shows in **Figures 9** to **11** that the samples processed by FSP have a higher hardness than the parent material sample, which also shows in **Figure 14** that the samples processed by FSP exhibit a lower mass loss compared to the parent material. Wear resistance is usually better for the MMC than the base metal for all the process parameters. This is due to the fact that the composite surface layer provides better wear resistance and it is harder than the base material.

The dimensional wear coefficient, k, is widely used to compare the wear rates in different classes of materials and is defined by Equation (4):

$$K = \frac{V}{SL} \quad (4)$$

The calculation suggests that under a load of 25 N and at a 2000 m sliding distance, the dimensional wear coefficient for the samples processed and the parent

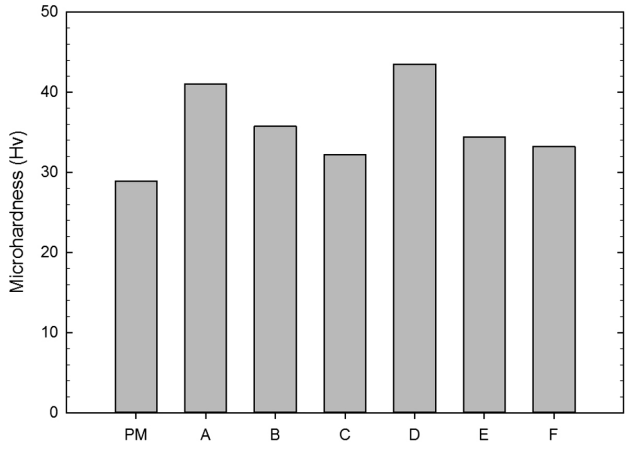

Figure 12: Average microhardness of parent material and friction-stir processed AA1050 reinforced with TiC powder

Slika 12: Povprečna mikrotrdota osnovnega materiala in AA1050, ojačanega s TiC v prahu po obdelavi z mešanjem s trenjem

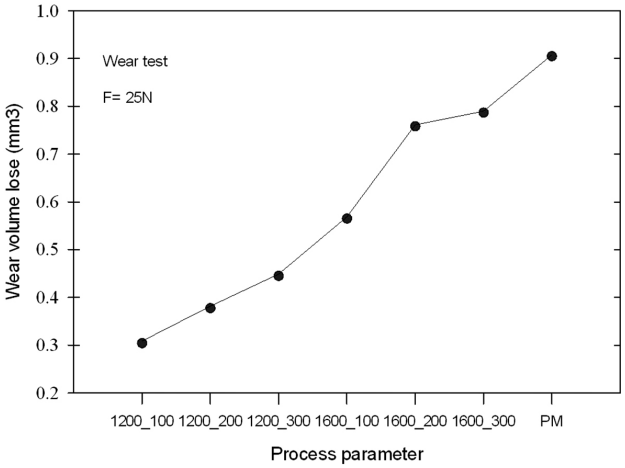

Figure 14: Wear-volume loss of processed samples for different parameters

Slika 14: Volumske izgube pri obrabi vzorcev, obdelanih z različnimi parametri

material are shown in **Table 3**. These results confirm the feasibility of using FSP with larger bulk samples, especially for the optimization of surface properties such as the wear-resistance behaviour.

Table 3: Dimensional wear coefficient
Tabela 3: Koeficient dimenzijske obrabe

Designation	Dimensional wear coefficient ($mm^2\ N^{-1}$)
FsP 1200_100	6.1712×10^{-6}
FsP 1200_200	7.6321×10^{-6}
FsP 1200_300	8.977×10^{-6}
FsP 1600_100	1.378×10^{-5}
FsP 1600_200	1.5227×10^{-5}
FsP 1600_300	1.580×10^{-5}
Parent Material	1.815×10^{-5}

4 CONCLUSION

In the present study, FSP was performed on an aluminium alloy (AA 1050) with TiC powder in order to investigate the evolving microstructural and mechanical properties. A surface composite layer was successfully fabricated on the aluminium sheets and the following conclusions were drawn from the test outcomes:

- The microstructural evolution of the AA1050 during FSP showed that the TiC particles were more uniformly distributed in the AA1050 after FSP using 1200 min^{-1} and at 100 mm/min, while at a high rotational speed of 1600 min^{-1}, it was observed that the TiC particles were clustered in some parts of the stirred zone after the FSP.
- The hardness tests showed an improvement and an enhancement on the integrity of the processed materials due to the improvement in the evolving microstructure.
- The wear-resistance test results confirm the feasibility of using FSP for the optimization of surface properties of the composites produced.

Acknowledgements

The authors gratefully acknowledge the financial support of the National Research Foundation (NRF) South Africa, Faculty of Engineering and the Built Environment, University of Johannesburg, South Africa and the eNtsa Research Group of Nelson Mandela Metropolitan University (NMMU), Port Elizabeth, South Africa, for allowing us to use their facility. The Tertiary Education Support Programme of ESKOM South Africa and the University Research Committee (URC), University of Johannesburg, South Africa are acknowledged for the award of the research funds to support this study.

5 REFERENCES

[1] I. Galvao, A. Loureiro, D. Rodrigues, Influence of process parameters on the mechanical enhancement of copper-DHP by FSP, Advanced Materials Research, 445 (**2012**), 631–636, doi:10.4028/scientific5/AMR.445.631

[2] R. Mishra, M. Mahoney, S. McFadden, N. Mara, A. Mukherjee, High strain rate superplasticity in a friction stir processed 7075 Al alloy, Scripta Materialia, 42 (**2000**) 2, 163–168, doi:10.1016/S1359-6462(99)00329-2

[3] E. Akinlabi, R. Mahamood, S. Akinlabi, E. Ogunmuyiwa, Processing Parameters Influence on Wear Resistance Behaviour of Friction Stir Processed Al-TiC Composites, Advances in Materials Science and Engineering, (**2014**) 11

[4] P. Berbon, W. Bingel, R. Mishra, C. Bampton, M. Mahoney, Friction stir processing: a tool to homogenize nanocomposite aluminum alloys, Scripta Materialia, 44 (**2001**) 1, 61–66, doi:10.1016/S1359-6462(00)00578-9

[5] Z. Ma, R. Mishra, M. Mahoney, Superplastic deformation behaviour of friction stir processed 7075Al alloy, Acta materialia, 50 (**2002**) 17, 4419–4430, doi:10.1016/S1359-6454(02)00278-1

[6] P. Cavalierea, A. Squillace, High temperature deformation of friction stir processed 7075 aluminium alloy, Materials Characterization, 55 (**2005**), 136–142

[7] C. Chuang, J. Huang, P. Hsieh, Using friction stir processing to fabricate MgAlZn intermetallic alloys, Scripta Materialia, 53 (**2005**), 1455–1460, doi:10.1016/j.scriptamat.2005.08.019

[8] Y. Kwon, I. Shigematsu, N. Saito, Production of Ultra-Fine Grained Aluminum Alloy using Friction Stir Process, Materials Transactions, 44 (**2003**) 7, 1343–1350, doi:10.2320/matertrans.44.1343

[9] G. Minak, L. Ceschini, I. Boromei, M. Ponte, Fatigue properties of friction stir welded particulate reinforced aluminium matrix composites, International Journal of Fatigue, 32 (**2010**) 1, 218–226, doi:10.1016/j.ijfatigue.2009.02.018

[10] A. Thangarasu, N. Murugan, I. Dinaharan, S. Vijay, Microstructure and microhardness of AA1050/TiC surface composite fabricated using friction stir processing, Indian Academy of Sciences, 37 (**2012**) 5, 579–586

[11] D. B. Miracle, Metal matrix composites – From science to technological significance.,Composition Science Technology, 65 (**2005**), 2526–2540, doi:10.1016/j.compscitech.2005.05.027

[12] A. Kennedy, S. Wyatt, The effect of processing on the mechanical properties and interfacial strength of aluminium/TiC MMCs, Composites Science and Technology, 60 (**2000**), 307–314, doi:10.1016/S0266-3538(99)00125-6

[13] A. Mortensen, Interfacial phenomena in the solidification processing of metal matrix composites, Material Science Engineering, A135 (**1991**) 1–11, doi:10.1016/0921-5093(91)90527-T

[14] D. Lloyd, H. Lagace, A. McLeod, P. Morris, Microstructural aspects of aluminium-silicon carbide particulate composites produced by a casting method, Material Science Engineering, A 107 (**1989**), 73–80, doi:10.1016/0921-5093(89)90376-6

[15] E. Feest, Interfacial phenomena in metal-matrix composites, Composites, 25 (**1994**) 2, 75–86, doi:10.1016/0010-4361(94)90001-9

[16] O. Verezub, Z. Kálazi, A. Sytcheva, L. Kuzsella, G. Buza, N. Verezub, A. Fedorov, G. Kaptay, Performance of a cutting tool made of steel matrix surface nano-composite produced by in situ laser melt injection technology, Journal of Materials Process Technololgy, 211 (**2011**), 750–758, doi:10.1016/j.jmatprotec.2010.12.009

[17] T. Laha, A. Agarwal, T. McKechnie, S. Seal, Synthesis and characterization of plasma spray formed carbon nanotube reinforced aluminum composite, Materials Science Engineering, A 381 (**2004**), 249–25, doi:10.1016/j.msea.2004.04.014

[18] Y. Wang, X. Zhang, G. Zeng and F. Li, Cast sinter technique for producing iron base surface composites, Materials. Disposition, 21 (**2000**), 447–452

[19] E. Yun, K. Lee, S. Lee, Correlation of microstructure with high-temperature hardness of (TiC,TiN)/Ti–6Al–4V surface composites fabricated by high-energy electron-beam irradiation, Surface Coat Technology, 191 (**2005**), 83–89, doi:10.1016/j.surfcoat.2004.02.040

[20] E. R. I. Mahmoud, K. Ikeuchi, M. Takahashi, Fabrication of SiC particle reinforced composite on aluminium surface by friction stir processing, Science Technology Weld Joining , 13 (**2008**), 607–618, doi:10.1179/136217108X333327

[21] E. R. I. Mahmoud, M. Takahashi, T. Shibayanagi, K. Ikeuchi, Effect of friction stir processing tool probe on fabrication of SiC particle reinforced composite on aluminium surface, Science Technology Weld Joining, 14 (**2009**), 413–425, doi:10.1179/136217109X406974

[22] R. Bauri, D. Yadav, G. Suhas, Effect of friction stir processing (FSP) on microstructure and properties of Al–TiC in situ composite, Materials Science and Engineering A, 528 (**2011**), 4732–4739, doi:10.1016/j.msea.2011.02.085

[23] A. Kahrizsangi, S. Kashani-Bozorg, Microstructure and mechanical properties of steel/TiC nano-composite surface layer produced by friction stir processing, Surface and Coatings Technology, 209 (**2012**), 15–22

[24] D. Yadav, R. Bauri, Nickel particle embedded aluminium matrix composite with high ductility, Materials Letters, 64 (**2010**) 6, 664–667, doi:10.1016/j.matlet.2009.12.030

[25] L. M. Marzoli, A. V. Strombeck, J. F. D. Santos, C. Gambaro, L. M. Volpone, Friction stir welding of an AA6061/Al2O3/20p reinforced alloy, Composite Science Technology, 66 (**2006**), 363–371, doi:10.1016/j.compscitech.2005.04.048

[26] H. Nami, H. Adgi, M. Sharifitabar, H. Shamabadi, Microstructure and mechanical properties of friction stir welded Al/Mg2Si metal matrix cast composite, Materials Description, 32 (**2010**), 976–983

[27] L. Ceschini, I. Boromei, Minak, G, A. Morri, F. Tarterini, Effect of friction stir welding on microstructure, tensile and fatigue properties of the AA7005/10 vol. % Al2O3p composite, Composite Science Technoology, 67 (**2007**), 605–615, doi:10.1016/j.compscitech.2006.07.029

[28] Y. Yu Zhang, Y. Sato, H. Kokawa, S. H. Park, S. Hirano, Stir zone microstructure of commercial purity titanium friction stir welded using pcBN tool, Materials Science and Engineering: A, 488 (**2008**) 1–2, 25–30, doi:10.1016/j.msea.2007.10.062

[29] D. Tabor, The hardness and strength of metals, Journal Institute of Metals, 79 (1951), 1–18

[30] J. R. Cahoon, An improved equation relating hardness to ultimate strength, Metallurgical Transactions, 3 (**1972**) 11, 3040, doi:10.1007/BF02652880

[31] J. F. Archard, Contact and rubbing of flat surfaces, Journal of Applied Physic, 24, (**1953**), 981–988, doi:10.1063/1.1721448

UDK 620.1:67.017:620.17
Original scientific article/Izvirni znanstveni članek

ISSN 1580-2949
MTAEC9, 51(3)437(2017)

USING THE BARKHAUSEN-NOISE ANALYSIS AND METAL-MAGNETIC-MEMORY METHOD FOR MATERIAL CHARACTERISTICS UNDER FATIGUE DAMAGE

UPORABA METODE BARKHAUSNOVEGA HRUPA IN MAGNETNEGA SPOMINA ZA KARAKTERIZACIJO UTRUJENOSTNIH POŠKODB MATERIALA

Kamil Kolařík[1], Jiří Šimeček[1], Antonín Kříž[1], Jiří Čapek[2]

[1]University of West Bohemia, Faculty of Mechanical Engineering, Univerzitení 8, 30100 Plzeň, Czech Republic
[2]Czech Technical University, Faculty of Nuclear Sciences and Physical Engineering, Trojanova 13, 120 00 Prague, Czech Republic
kamil.kolarik@email.cz

Prejem rokopisa – received: 2016-03-30; sprejem za objavo – accepted for publication: 2016-06-09

doi:10.17222/mit.2016.056

The article deals with process monitoring and the subsequent diagnosis of fatigue damage during material testing of steel S355. The study was performed by means of the metal-magnetic-memory method, Barkhausen-noise analysis and X-ray diffraction. This combination could significantly enhance the inspection quality of critical mechanical-unit parts during their lifespan. X-ray diffraction was applied for the description of the state of residual stresses, in combination with the Barkhausen-noise analysis, which allows us to immediately determine the changes in the surface layer resulting from the residual-stress redistribution, hardness and potential microcracks. Additionally, a new unconventional method for the determination of the stress-concentration-zone location and for the detection of material defects and imperfections, the so-called metal-magnetic-memory method, will be introduced.

Keywords: Barkhausen noise, metal-magnetic-memory method, X-ray diffraction, fatigue damage

Članek obravnava proces kontrole, in iz tega naknadno diagnozo utrujenostne poškodbe, med preizkusom materiala, jekla S355. Študija je bila izvedena s pomočjo metode magnetnega spomina kovine, z Barkhausnovo analizo hrupa in z rentgensko difrakcijo. Ta kombinacija lahko občutno izboljša kvaliteto kontrole kritičnih mehanskih komponent med njihovo življenjsko dobo. Rentgenska difrakcija je bila uporabljena za opis stanja zaostalih napetosti, v kombinaciji z analizo Barkhausnovega hrupa, kar omogoča takojšnje določanje sprememb v površinski plasti, kar je posledica prerazporeditve zaostalih napetosti, trdote in potencialnih mikrorazpok. Dodatno bo predstavljena nova neobičajna metoda za določanje področij koncentriranja napetosti ter za odkrivanje napak in nepravilnosti, imenovana metoda magnetnega spomina kovine.

Ključne besede: Barkhausnov hrup, metoda magnetnega spomina kovin, rentgenska difrakcija, utrujenostna poškodba

1 INTRODUCTION

Characteristics of all machine components depend on the final surface quality[1] and surface material layers, namely the residual-stress (RS) distribution and the roughness. These properties involve functionality and durability, especially fatigue life. The surface of an engineering component is a sensitive part, especially because of the interface between the component and the external environment. The surface layers of the material are damaged by the transmitted working load and other degradative effects such as vibrations, radiant energy, chemical influences (rust), etc. In general, it is known that more than 90 % of the operating-part fractures are caused by fatigue.[2]

Material fatigue is a process (a change in mechanical properties, creation of a microcrack net, growth of the maximum crack and workpiece fracture), which gradually deplete the utility properties of a product until a fracture of the workpiece and irreversible damage occur.[3] Currently, the process of crack formation can only be observed if we use non-destructive testing methods such as ultrasonic testing, magnetic particle inspection, industrial radiography and capillary testing. These methods detect only incurred cracks and defects, but they are not able to register the initialization of cracks.[4]

Recently, it was suggested that this drawback could be eliminated with a combination of the Barkhausen-noise analysis (BNA)[5,6] and the metal-magnetic-memory method (MMM).[7,8] Based on different signal inception depths, a combination of these methods can provide a substantial financial reduction thanks to a faster response and cheaper control of a potentially critical point achievement. In addition, for a description of particular surface stages (especially the level of residual stresses in test samples before and after the loading), the mentioned magnetic methods should be supplemented with the results obtained with the X-ray diffraction technique.[9,10]

The principle of the BNA has been known for many years and used in diagnostics of machined layers.[11] The MMM method is based on the magneto-elasticity and magneto-mechanical effect theory.[12,13] Due to the

self-magnetization phenomenon of ferromagnetic materials, during the operation of equipment, the magnetic field is kept down when the work load is off. The residual magnetic field is related to the mechanical stress, that is, the residual magnetic field density *Hp* is characterized by the polarity varying along the normal. Thus, using the MMM testing instrument, the most serious zones of a stress concentration (SZC), defects and metal-structure non-uniformities can be found.[14] Moreover, it does not require special magnetization devices and the tested surface does not require a special treatment. Therefore, the MMM technology has been widely applied to inspect pressure vessels,[15] piping[16] and other equipment in service. The first pilot results of a fatigue-damage analysis obtained with the BNA and MMM methods have been already reported.[17,18]

In the light of these facts, we performed the BNA and MMM testing on the samples of the chosen unalloyed construction steel, monitoring the future fatigue damage even before the initialization of the magistral crack. Subsequently, we compared the obtained results with theoretical predictions and, finally, we discussed the applicability of these methods.

2 SAMPLES UNDER INVESTIGATION

Experimental samples (**Figure 1**) were made from the unalloyed construction steel S355J2G3 with a chemical composition in mass fractions (*w*/%): 0.2C, 0.55Si, 1.6Mn, <0.035P and <0.035S. It is a commonly used material for welded constructions, machine parts and electrical-apparatus parts that are not strained by high temperature. Samples were manufactured from 6-mm thick plates with the water-jet-machining method to avoid a thermal influence and consequent deformation. The surfaces chosen for the analysis were then pre-treated with metallographic papers in a range of 240-400-600-800-1200-2500.

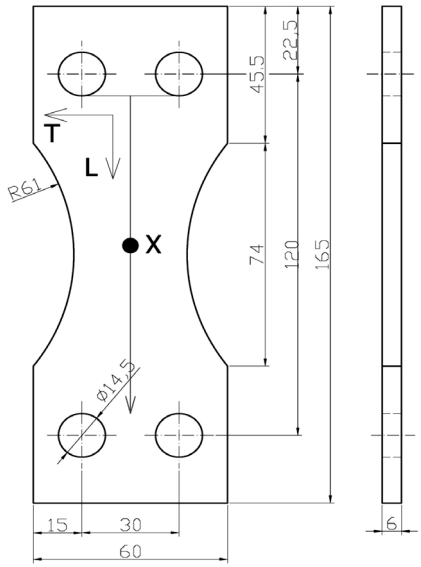

Figure 1: Shape and dimensions of the specimens for fatigue test
Slika 1: Oblika in dimenzije preizkušancev za preizkus utrujanja

In order to restrain the notch effect[19], sample edges were sharpened and, moreover, polished with a diamond paste with the average grain size of 3 μm.

3 EXPERIMENTAL TECHNIQUES

3.1 XRD analysis

XRD measurements were performed with a PROTO iXRD COMBO diffractometer in the ω-goniometer or iso-inclination mode with Cr-$K\alpha$ radiation. The line {211} of the α-Fe phase was measured with interplanar lattice spacings computed from the maxima of Pearson VII functions fitted to Cr-$K\alpha_1$ profiles after the Cr-$K\alpha_2$ stripping carried out with the Rachinger method. The stresses were computed presuming the biaxial state of macroscopic residual stresses (RS) using the Winholtz-Cohen method and X-ray elastic constants $½s_2$ = 5.76 TPa^{-1}, $-s_1$ = 1.25 TPa^{-1}.

3.2 Barkhausen noise analysis

Variations of microstructural changes during the loading were also studied using the micro-magnetic testing method.[20] Magneto-elastic parameter *mp* was chosen as the characteristic of the surface and subsurface layers. This parameter was determined with the root-mean-square method involving all the measured signal amplitudes and it is given in volts. It was calculated for a specified analysis frequency range. The measurements were performed using a commercial unit Stresstech MicroScan 600-1 magneto-elastic analyser with standard sensors, the *S1-138-1501* type for *mp* changes during the fatigue test and the *S1-171-25-11* type for the surface characterization after the crack initialization. The main parameters of the applied method had a sinusoidal shape of the magnetic signal, a magnetic voltage of 3.5 V and a frequency of 75 Hz. The obtained results are the mean values from 10 measurements. The estimation of the penetration depth δ of the excitation signal depends on the used frequency f and the analysed material (permeability μ and conductivity σ), in Equation (1).[21] In practice, a typical expectable effective penetration depth is in a range of up to 20 μm for this experimental arrangement in Equation (1):

$$\delta = \frac{1}{\sqrt{\pi\mu\sigma f}} \tag{1}$$

3.3 MMM method

A TSC-3M-12 instrument was used for the analysis. Probe 1-8E with four sensors was employed.

3.4 Fatigue loading

The bending fatigues tests were performed in a SCHENCK PWYG machine. The loading frequency was 17 Hz. The load ratio was $R = -1$ and the loading force was from 220 MPa to 370 MPa. Cycles were required to initiate cracks.

4 RESULTS AND DISCUSSIONS

Results of the fatigue test after different loads of the samples are given in **Table 1**; they are in accordance with the theoretical presumptions.[22]

Table 1: Results of the fatigue test – the number of cycles to crack initialization

Tabela 1: Rezultati preizkušanja utrujanja – število ciklov do nastanka razpoke

Sample	load (MPa)	number of cycles
1	220	4.518.600 without a crack
2	250	698.500
3	320	600.300
4	330	288.400
5	370	82.000
6	370	67.400

Variations in the magneto-elastic parameters *mp* at three different loads are shown in **Figure 2**.

We can see a similar development of the *mp*-function independently of the load forces. This behaviour should be the subject of further study. Generally, the *mp* development depends on the loading cycles reflecting primarily the changes in the RS. Changes in the

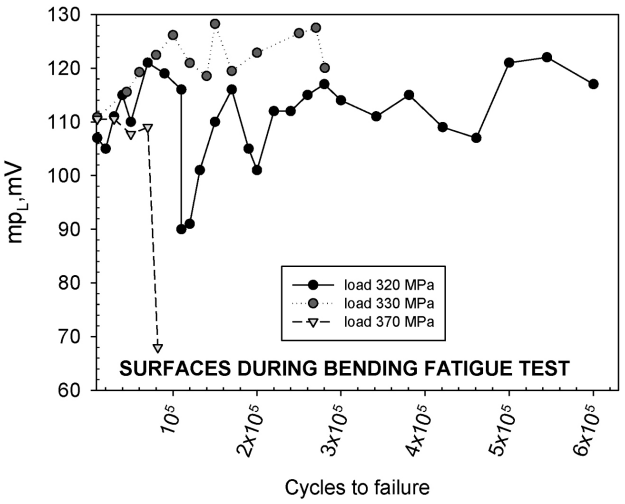

Figure 2: Changes in Barkhausen noise, i.e., parameter *mp*, measured in the middle of a sample (**Figure 1**), marked with "X" symbol, in the direction parallel to the loading axis as a function of the loading cycles of the tested specimens

Slika 2: Spreminjanje Barkausnovega hrupa, to je parameter *mp*, merjen na sredini vzorca (**Slika 1**) označeno z "X" simbolom, v smeri vzporedno z osjo obremenjevanja, v odvisnosti od ciklov obremenjevanja preizkušancev

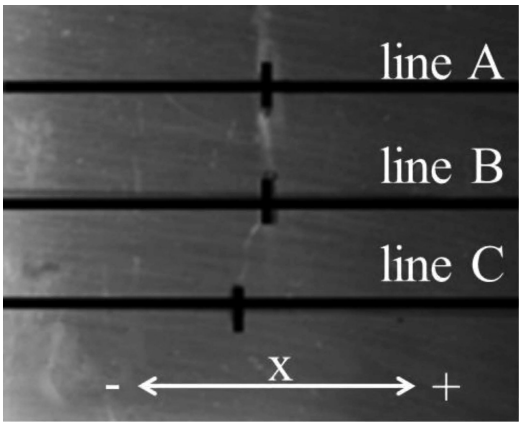

Figure 3: Fatigue crack on the surface of sample 4, the distance between lines is 10 mm

Slika 3: Utrujenostna razpoka na površini vzorca 4, razdalja med linijami je 10 mm

mechanical properties during the loading are determined by the movement of dislocations and their mutual interactions. Dislocation movement is further influenced by the presence of precipitates, foreign particles, grain boundaries, etc. It is, therefore, clear that changes in the configuration and density of dislocations and also changes in the distribution and morphology of other types of obstacles will occur during the cyclic deformation. A greater loading force leads to a higher density of dislocations, 10^{10} to 10^{13} cm^{-2}, resulting in an even more significant drop of *mp*. Moreover, the changes in *mp* reflect the responses of material properties, such as hardening and softening, vacancy concentration and also the mentioned formation of dislocations.

At the start, loading cycles result in a fluctuation of dislocation density, which can be manifested in the changes in the RS as well as in the cyclic softening and hardening of the material.[23] The latter effects influence the domain wall movement, which leads to increases and decreases of *mp* for all the loading forces during the

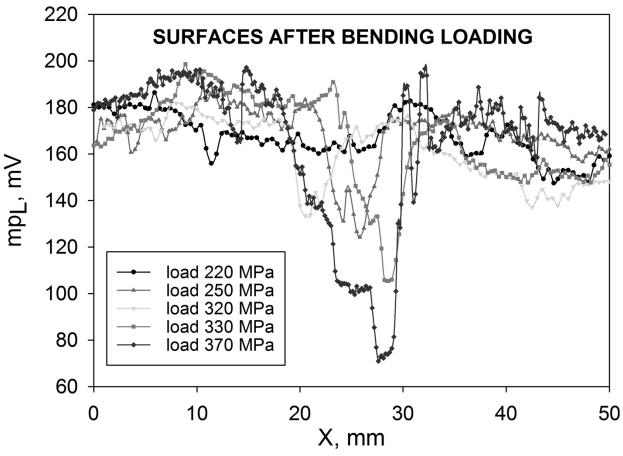

Figure 4: Gradient of *mp* obtained from the area of crack determined with BNA

Slika 4: Gradient *mp* dobljen iz področja razpoke, določene z BNA

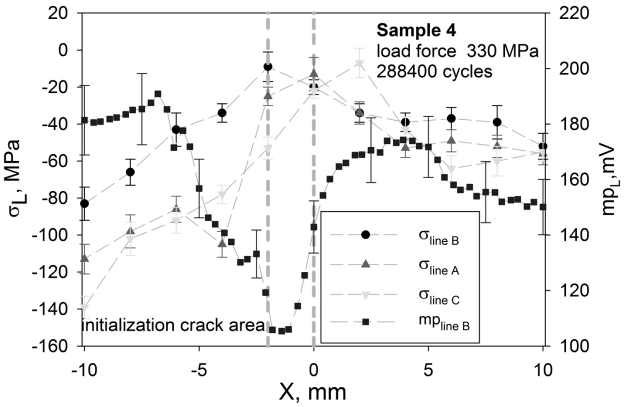

Figure 5: Gradients of RS and *mp* from the area of crack (**Figure 3**) determined with XRD and BNA

Slika 5: Gradient RS in mp iz področja razpoke (**Slika 3**) določena z XRD in BNA

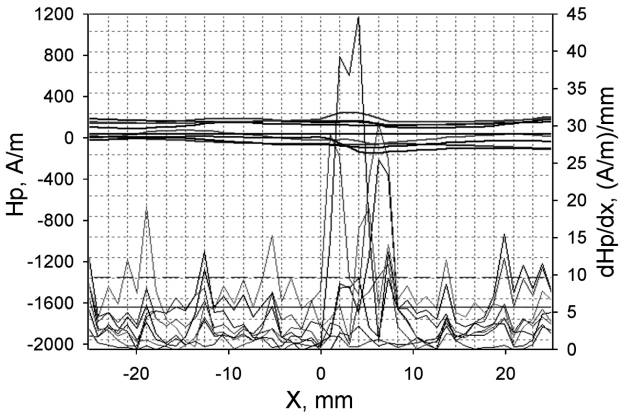

Figure 7: Magnetogram obtained with the MMM method from the surface of sample 4 after the cyclic loading; the lower lines (dHp/dx) are the partial derivation of the measured upper lines (Hp)

Slika 7: Magnetogram, dobljen z MMM metodo iz površine vzorca 4 po cikličnem obremenjevanju, spodnje linije (dHp/dx) so parcialna derivacija izmerjenih zgornjih linij (Hp)

fatigue test. At the end of the fatigue life, *mp* drops rapidly because of the crack growth (**Figures 3** and **4**).

Figure 4 shows the *mp* measured after the cycle loading around the crack area. Because of a high level of plastic deformation and the crack acting as a dielectric, inhomogeneities of the magnetic field and changes in the domain structure of the crack are formed[24], which lead to a decrease of *mp*. From **Figure 4**, it is evident that a higher loading force results in larger deformation zones, a larger amount of cracks and, consequently, in a lower value of *mp*. Because of the crack initialization, the RS starts to relax and it reaches its minimum if the cracks are fully developed, as can be seen in **Figure 5**.

During the cycling loading, dislocations move in the material and can gather, which leads to an accumulation of stress in the given areas. Increasing the stress accumulation results in weak changes of the magnetic field.[18] The final state of this process is an initialization of cracks. These conclusions are consistent with the results presented in **Figures 6** and **7**, where magnetograms of the samples without and with a crack are presented, respectively. In addition, in **Figure 7**, a high value of the magnetic-field gradient (dHp/dx) is evident, which corresponds well with the fatigue-crack presence (**Figure 3**). The physical nature of the gradual dHp/dx increase during the cycling of the analysed surface is related to the secondary domain structure of the ferromagnetic sample. This is produced in the vicinity of defects in the lattice. The increase in the dHp/dx amplitude is associated with an increase in the density of the closing domains compensating the dispersive magnetic field in the vicinity of the accumulating defects during the cycling. The sharp increase in dHp/dx during the cracking is related to the creation of the closing (secondary) domains, which compensate the dispersive field of the new surface, minimizing the magnetostatic energy of the magnetic sample.

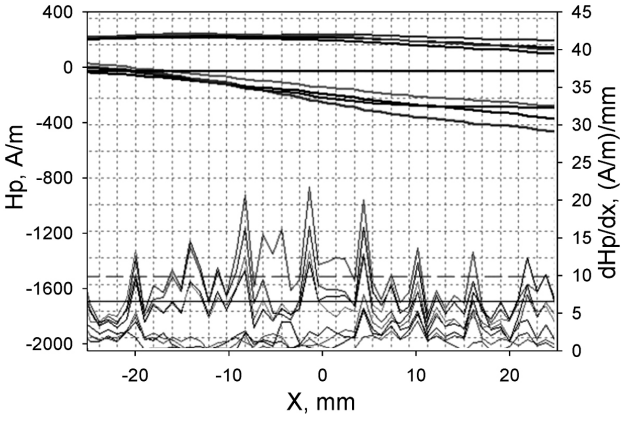

Figure 6: Magnetogram obtained with the MMM method from the surface of sample 1 after the cyclic loading. The lower lines (dHp/dx) are the partial derivation of the measured upper lines (Hp)

Slika 6: Magnetogram, dobljen z MMM metodo iz površine vzorca 1 po cikličnem obremenjevanju. Spodnje linije (dHp/dx) so parcialna derivacija izmerjenih zgornjih linij (HP)

5 CONCLUSIONS

The results of the Barkhausen-noise analysis and metal-magnetic-memory testing correspond well with the established theoretical predictions. Moreover, it was found that

- dependence of the magneto-elastic parameter *mp* on the loading cycles is not monotonous. Nevertheless, mainly before the cracking, it oscillates (**Figure 2**);
- cracks tend towards an inhomogeneous magnetic field of the material (due to the interruptions of the magnetic line of the force), which leads to an *mp* reduction (**Figure 4**). The presence of the cracks causes a relaxation of residual stresses (**Figure 5**).
- using the metal-magnetic-memory method, it should be possible to analyse fatigue damage before the initialization of the magistral crack (**Figures 6** and **7**). On the other hand, it is necessary to know the history of the material.

To summarize, we can conclude that the metal-magnetic-memory technique and Barkhausen-noise analysis are advantageous in certain circumstances, for example, for an in-service inspection of structures with complex geometries.

Acknowledgments

This paper draws on the outcomes of the SGS – 2015 – 016 project: Analysis of Surfaces of Assemblies and Tools by Surface Integrity Method and Impacts on End-Use Properties.

6 REFERENCES

[1] J. P. Davim, Surface integrity in machining, Springer, London 2010, doi:10.1007/978-1-84882-874-2

[2] J. Schijve, Fatigue of structures and materials, Kluwer Academic Publisher, Dordrecht 2001, 513, doi:10.1007/0-306-48396-3

[3] R. G. Govindaraju, A. Strom, D. C. Jiles, S. B. Biner, Evaluation of low-cycle fatigue damage in steel structural components by magnetic measurement technique, Review of Progress in Quantitative Nondestructive Evaluation, New York, 1993, 1839–1846, doi:10.1007/978-1-4615-2848-7_236

[4] M. Witos, M. Zokowski, Passive Magnetic Observer in NDE & SHM Applications, EWSHM-7th European Workshop on Structural Health Monitoring, France, 2014, 213–220

[5] Y. Tomita, K. Hashimoto, N. Osawa, Nondestructive estimation of fatigue damage for steel by Barkhausen noise analysis, NDT & E International, 29 (**1996**) 5, 275–280, doi:10.1016/S0963-8695(96)00030-8

[6] K. Tiitto, Use of Barkhausen noise in fatigue, Nondestructive Testing and Evaluation, 5 (**1989**) 1, 27–37, doi:10.1080/02780898908952952

[7] V. T. Vlasov, A. A. Dubov, Development of theory of ferromagnetic domain structure by the example of iron, Proceedings of the third international conference Diagnostics of equipment and structures with usage of metal magnetic memory, Moscow, 2003

[8] A. A. Dubov, S. M. Kolokolnikov, Method of metal magnetic memory (MMM) and inspection devices: Training handbook, Tisso Co, Moscow 2003, 320

[9] Q. Xin, D. Shu, L. Hui, W. Wei, J. Chen, Magnetic Barkhausen noise, metal magnetic memory testing and estimation of the ship plate welded structure stress, Journal of Nondestructive Evaluation, 31 (**2012**) 1, 80–89, doi:10.1007/s10921-011-0123-7

[10] B. Hu, G. Gan, S. Gongtian, L. Luming, C. Xing, Study on Magnetic Memory Method (MMM) for Fatigue Evaluation, Proc. of 17th World Conference on Nondestructive Testing, China, 2008, 25–28

[11] J. Čížek, M. Neslušan, M. Čilliková, A. Mičietová, O. Melikhova, Modification of steel surfaces induced by turning: non-destructive characterization using Barkhausen noise and positron annihilation, Applied Physics, 47 (**2014**) 44, 445301

[12] A. A. Dubov, A study of metal properties using the method of magnetic memory, Metal Science and Heat Treatment, 39 (**1997**) 9, 401–405, doi:10.1007/BF02469065

[13] A. A. Dubov, Principle features of metal magnetic memory method and inspection tools as compared to known magnetic NDT methods, CINDE Journal, 27 (**2006**) 3, 16–20

[14] X. Hai Yan, X. M. Qiang, Y. Zhijun, Z. Lihong, Stress State Analysis of Failure Blade with MMM Method, Daqing Petroleum Institute China, 2006

[15] O. Stupakov, T. Toshiyuki, K. Kolařík, Barkhausen Noise Testing of Residual Stresses Introduced by Surface Hardening Techniques, Electromagnetic Nondestructive Evaluation (XVII), 39 (**2014**), 288–295, doi:10.3233/978-1-61499-407-7-288

[16] J. W. Wilson, G. Y. Tian, S. Barrans, Residual magnetic field sensing for stress measurement, Sensors and Actuators A: Physical, 135 (**2007**) 2, 381–387, doi:10.1016/j.sna.2006.08.010

[17] G. Pluvinage, Notch effect in fatigue and fracture, Springer, Netherlands 2001, 22, doi:10.1007/978-94-010-0880-8_1

[18] W. A. Theiner, Physical Basis of Micromagnetic Methods and Sensor Systems and their Application Areas, Proceedings of the 1st International Conference on Barkhausen noise and Micromagnetic Testing, Hannover, 1998, 197–218

[19] W. A. Theiner, E. Brinksmeier, E. Stücker, Stress Measurements on Components with Nondestructive Ferromagnetic Methods, Residual Stresses in Science and Technology, 1 (**1987**), 167–174

[20] M. Lindgren, T. Lepistö, Effect of cyclic deformation on Barkhausen noise in a mild steel, NDT & E International, 36 (**2003**) 6, 401–409, doi:10.1016/S0963-8695(03)00031-8

[21] S. Tiitto, R.Säynäjäkangas, Spectral damping in Barkhausen noise, IEEE Transactions on Magnetics, 11 (**1975**) 6, 1666–1672, doi:10.1109/TMAG.1975.1058960

[22] W. Guan, P. Guo, C. Xuedong, Metal Magnetic Memory Testing Technique for Typical Defects in Pressure Vessels and Pipelines, ASME 2015 Pressure Vessels and Piping Conference, American Society of Mechanical Engineers, 2015, doi:10.1115/PVP2015-45826

[23] L. Faturík, L. Trško, S. Hrček, O. Bokůvka, Comparison of Structural Design in High and Ultra-High Cycle Fatigue Regions, Transactions of FAMENA, 38 (**2015**) 4, 1–12

[24] M. Neslušan, J. Majerík, P. Kejzlar, M. Čilliková, A. Mičietová, Barkhausen Noise Emission in Hard Milled Surfaces of Steel C55, Transactions of FAMENA, 39 (**2016**) 4, 55–64

UDK 67.017:669.255:621.762
Original scientific article/Izvirni znanstveni članek

ISSN 1580-2949
MTAEC9, 51(3)443(2017)

INFLUENCE OF ALLOYING ELEMENTS ON THE MECHANICAL PROPERTIES OF A COBALT-BASED ALLOY PRODUCED WITH POWDER METALLURGY

VPLIV LEGIRNIH ELEMENTOV NA MEHANSKE LASTNOSTI OSNOVNE KOBALTOVE ZLITINE, PRIDOBLJENE Z METALURGIJO PRAHOV

Kateřina Nová, Pavel Novák, Drahomír Dvorský

University of Chemistry and Technology, Department of Metals and Corrosion Engineering, Technická 5, 166 28 Prague 6, Czech Republic
novakx@vscht.cz

Prejem rokopisa – received: 2016-03-31; sprejem za objavo – accepted for publication: 2016-07-28

doi:10.17222/mit.2016.054

This work was focused on studying the effect of alloying elements on the mechanical and tribological properties of cobalt alloys. The Co-Cr-Mo alloy has been successfully used for the production of orthopaedic implants thanks to a better wear resistance than that of titanium implants. However, with the development of scientific and technological processes, there is still an ongoing effort to further improve the wear resistance and other properties of cobalt-based alloys. The aim of this research was to find a suitable alloying element, which would increase the wear resistance, while the other characteristics remain unimpaired. When choosing such an element, we have to keep in mind that it has to be non-toxic for the human body. The standard Co-Cr-Mo alloy and Co-Cr-Mo alloy with various alloying elements, specifically Nb, Si, Ti in an amount of 5 % mass fraction, were prepared using mechanical alloying followed by the compacting method called spark-plasma sintering. The influences of the alloying elements on the microstructure as well as mechanical and tribological properties were observed. Based on the obtained results, the Co-Cr-Mo-Nb alloy seems to be most suitable because the addition of niobium greatly improved the wear resistance. However, it is necessary to perform many other tests, especially the tests of corrosion resistance and biocompatibility.

Keywords: cobalt alloy, biomaterial, mechanical properties, wear resistance

Delo je bilo osredotočeno na preučevanje vpliva legirnih elementov na mehanske in tribološke lastnosti kobaltnih zlitin. Co-Cr-Mo zlitina je bila uspešno uporabljena za izdelavo ortopedskih implantantov, zahvaljujoč boljši odpornosti proti obrabi, kot jo nudijo vsadki iz titana. Vendar z razvojem znanstvenih in tehnoloških procesov še vedno potekajo prizadevanja za izboljšanje odpornosti proti obrabi in izboljšanje drugih lastnosti zlitin na osnovi kobalta. Cilj raziskave je bil najti primerno primešani element, ki bi povečal odpornost proti obrabi, medtem ko druge lastnosti ostajajo nedotaknjene. Pri izbiri takega elementa, moramo imeti v mislih, da mora biti nestrupen za človeško telo. Standardna Co-Cr-Mo zlitina in tudi Co-Cr-Mo zlitina z različnimi legirnimi elementi, zlasti Nb, Si, Ti, v 5 % masnem deležu, sta bili pripravljeni s sintranjem. Opažen je bil vpliv legirnih elementov na mikrostrukturo, kot tudi mehanskih in triboloških lastnosti. Na osnovi dobljenih rezultatov se zdi, da je Co-Cr-Mo-Nb zlitina najbolj primerna, saj je dodatek niobija zelo izboljšal odpornost proti obrabi. Vendar pa je potrebno izvesti še številne druge teste, zlasti preizkuse odpornosti proti koroziji in biokompatibilnost.

Ključne besede: kobaltna zlitina, biološki material, mehanske lastnosti, odpornost proti obrabi

1 INTRODUCTION

Metallic materials are very promising for biomedical use and the attention devoted to them is growing. The metallic materials for biomedical application may be biodegradable and non-degradable materials. The most attractive candidates from the second group include titanium and its alloys, cobalt-based alloys as well as stainless steel. Co-based alloys, particularly Co-Cr-Mo and Co-Cr-W, are known under the commercial name of Stellites.[1] Thanks to their excellent resistance to degradation in the oral cavity, they were originally used in medicine for casting dental implants. Over time, cobalt alloys began use as surgical implants. Nowadays, due to a better wear resistance than that of the titanium alloy, they are widely used for the orthopaedic prostheses for the knee, shoulder and hip, and for fracture fixation. These are typical long-term implants. Cobalt endoprostheses are non-magnetic, have suitable mechanical properties, corrosion resistance to the body fluids and also a good biocompatibility with the body´s environment.[2–4]

The mechanical properties of cobalt-based alloys, and of the other metallic materials, are primarily dependent on the chemical composition, microstructure and their manufacturing processes.[5] Pure cobalt exists in two allotropic modifications. While at temperatures below 417 °C, cobalt exhibits a hexagonal close-packed structure, above this temperature, a face-centred cubic one is stable.[5,6] Many properties of the Co-Cr-Mo alloy originate from the crystallographic structure of cobalt. The alloying elements – Cr and Mo – have a solid-solution-strengthening effect. Besides Cr and Mo, the alloy always contains a small amount of carbon, which forms extremely hard carbides in the structure. The size and

distribution of the carbides in the alloy have a significant effect on the mechanical properties and wear resistance.[2,7] Chromium has the highest affinity to carbon, so initially chromium carbide was formed – $Cr_{23}C_6$. The formation of these carbides decreases the content of the unbound chromium applicable to the formation of the passive layer that protects the material against corrosion.[6] Cobalt-based alloys have excellent corrosion resistance mainly due to this thin layer of chromium-based oxide.[8] In literature, there are numerous studies associated with testing the corrosion resistance and biocompatibility of the Co-Cr-Mo alloy for medical applications and even variants with additions of Zr, Cu and N.[9–11] Nitrogen was tested mainly to improve the ductility of the alloy by stabilizing the fcc structure.[11] However, there is a lack of the studies dealing with the improvement of the wear resistance to limit the amount of wear debris in big joints during the lifetime of an implant.

The cobalt alloy – Co-Cr-Mo – for orthopaedic applications is processed mainly by casting, but may also be wrought. The casting method is preferred for complex shaped products. Because the cooling rate is different in each part of the casting, the resulting structure may be coarse and non-homogeneous. Wrought material has better mechanical properties as it has a finer and homogeneous structure without pores.[3] In recent years, powder metallurgy has been commonly used for preparing materials with high purity, exact chemical compositions, desirable structures and porosity. In a material prepared with the powder-metallurgy method, there is always a certain proportion of pores.[12]

Based on the described theory, the following alloying elements were selected: Ti, Si and Nb. It was assumed that they would form carbides (Ti, Nb) or silicides (Si) in the alloy, which would improve the wear resistance as well as the mechanical properties. In this paper, the Co-Cr-Mo alloys with the additions of the above-mentioned alloying elements were prepared with the powder metallurgy using novel two-stage mechanical alloying[13] and spark-plasma sintering. The aim of the work was to develop ultrafine-grained cobalt alloy with improved wear resistance.

2 MATERIALS AND METHODS

The standard Co-Cr-Mo alloy and also the Co-Cr-Mo alloy with various alloying elements, specifically Nb, Si, Ti in an amount of 5 % mass fraction (**Table 1**) were prepared from elemental powders with mechanical alloying under a protective argon atmosphere followed by a spark-plasma-sintering (SPS) compaction. The mechanical alloying, wherein the carbon was added as graphite, was completed in a Retsch PM 100 CM planetary ball mill as a two-stage process, patented by the authors.[13] The first stage, used for the homogenization of the powder mixture, was carried out for 30 min with a rotation speed of 200 min^{-}. In the second stage, devoted to mechanical alloying, the milling time increased to 60 min and the rotational speed to 500 min^{-1}. The method of spark-plasma sintering (SPS) was carried out under the following conditions: 1100 °C, 5 min, 50 MPa.

Table 1: Chemical composition of standard Co-Cr-Mo alloy
Tabela 1: Kemijska sestava standardne Co-Cr-Mo zlitine

	Co (*w*/%)	Cr (*w*/%)	Mo (*w*/%)	C (*w*/%)
Sample	65.75	28.0	6.0	0.25

The phase composition was examined with an X-ray diffraction analysis using a PANalyticalX'Pert Pro diffractometer with a Co anode. The microstructures of the samples were observed after etching with modified Kroll's reagent (5 mL HNO_3 + 10 mL HF + 85 mL H_2O) on a metallographic microscope Olympus PME3 and a TESCAN VEGA 3 LMU scanning electron microscope equipped with an Oxford Instruments X-max 20 mm^2 EDS detector with the Aztec software package. The hardness was measured with the Vickers method on the standard hardness tester with a load of 30 kg (HV30). Each measurement was repeated ten times. The abrasion wear behaviour was evaluated using the pin-on-disk method, where the pin was the tested material and the disk was the P1200 grinding paper. The abrasive distance was 2.5 km and the applied load was 5.8 N. Each sample was weighed before and after the test. The wear rate was calculated from the measured weight loss using Equation (1), where is w – the wear rate (mm^{3}m^{-1}), Δm – the weight loss (g), ρ – the density (g cm^{-1}), l – the abrasive distance (m):

$$W = \frac{\Delta m \cdot 1000}{\rho l} \quad (1)$$

3 RESULTS AND DISCUSSION

The phase composition of an individual alloy was determined with X-ray diffraction. Each alloy type is composed of cobalt with a hexagonal and cubic structure. An increase in the amount of the hcp phase is observable in titanium- and niobium-alloyed materials. On the other hand, silicon lowers the content of hexagonal cobalt (**Table 2**). In addition to cobalt-based solid solutions, the Co-Cr-Mo alloy also contained $Cr_{23}C_6$ carbide and traces of the Co_2C phase. In niobium- and silicon-alloyed materials, NbC carbide and Cr_3Si phase were determined, respectively. When titanium was added, no titanium-based phase appeared, leading to the same phase composition as in the case of the standard Co-Cr-Mo alloy. It implies that titanium was completely dissolved in the Co-based solid solution, or that the amount of the Ti-containing phase was below the detection limit of XRD. The phase composition is shown in **Figure 1**.

Table 2: Weight percentage of individual phases in Co-Cr-Mo-X alloys (determined with XRD)
Tabela 2: Masni delež posameznih faz v Co-Cr-Mr-X zlitinah (določen z XRD-analizo)

Phase	Co-Cr-Mo	Co-Cr-Mo-Nb	Co-Cr-Mo-Si	Co-Cr-Mo-Ti
Co (fcc)	68	59	75	62
Co (hcp)	28	39	18	35
$Cr_{23}C_6$	4	-	-	3
NbC	-	2	-	-
Cr_3Si	-	-	7	-

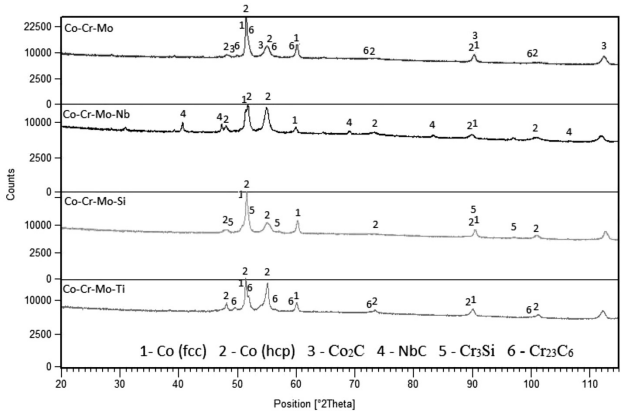

Figure 1: Phase composition
Slika 1: Sestava faze

The differences in the ratio between the hexagonal and cubic cobalt-based solid solutions can be explained with the following theory: niobium forms carbides instead of chromium due to a higher affinity to carbon. Therefore, there is more chromium dissolved in the cobalt-based matrix. According to the Co-Cr binary phase diagram, chromium stabilizes the hcp cobalt.[14] In the case of titanium, the stabilization of the hcp structure is probably due to the similarity of the crystal structure of α-Ti (hcp) and the hexagonal cobalt. The opposite effect of silicon probably occurs due to the formation of chromium silicide (Cr_3Si) instead of the chromium carbide. Therefore, there is more carbon in the matrix. According to the Co-C equilibrium phase diagram[14], carbon is more soluble in the high-temperature cubic modification of cobalt and, therefore, it is able to stabilize it.

Figure 2 shows the microstructures of the samples acquired with an optical microscope. All the alloys are slightly porous (up to 6 area % by image analysis), which is due to the poor compressibility and sinterability of cobalt alloys. All the alloys are composed of a fcc cobalt-based solid solution (darker grey), hcp cobalt (light grey to white) and intermediary phases (carbides or silicide depending on the alloy composition) – dark grey to black. This confirms the results of XRD. It is evident that the microstructure of Co-Cr-Mo is very

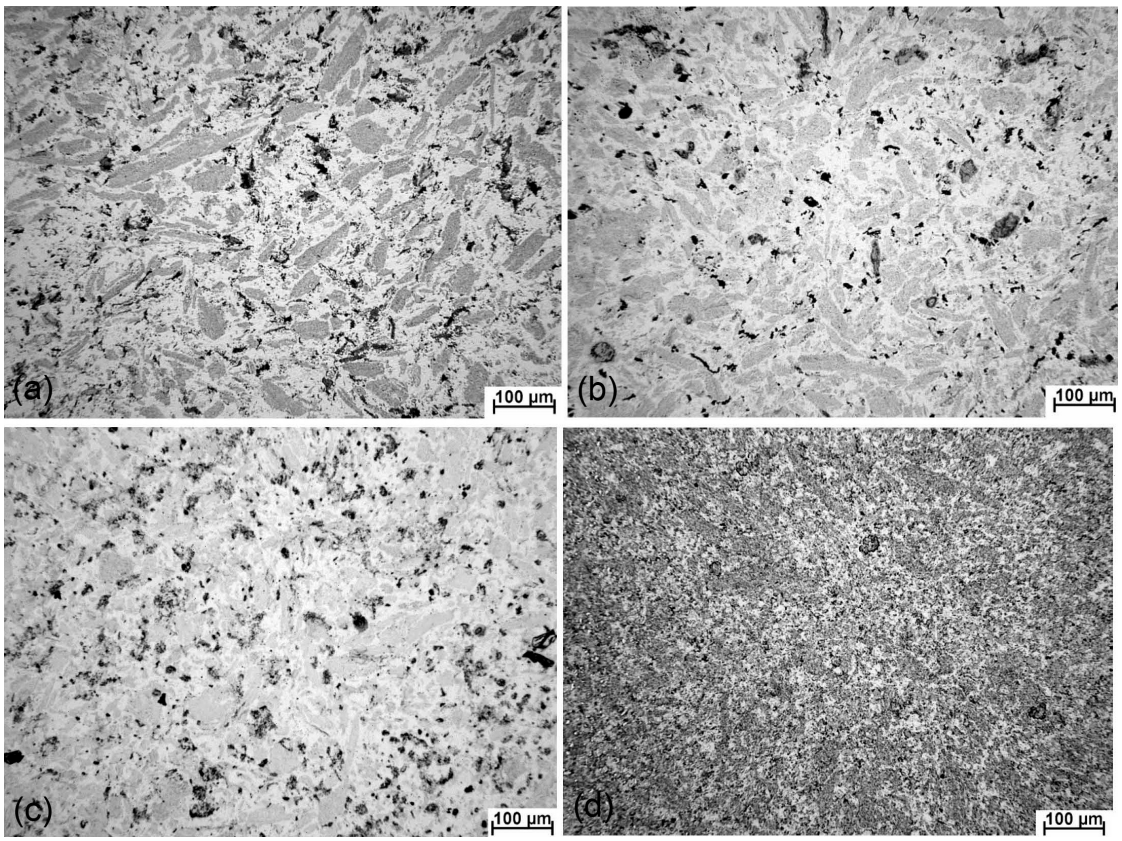

Figure 2: Microstructures of: a) Co-Cr-Mo, b) Co-Cr-Mo-Nb, c) Co-Cr-Mo-Ti and d) Co-Cr-Mo-Si
Slika 2: Mikrostrukture: a) Co-Cr-Mo, b) Co-Cr-Mo-Nb, c) Co-Cr-Mo-Ti in d) Co-Cr-Mo-Si

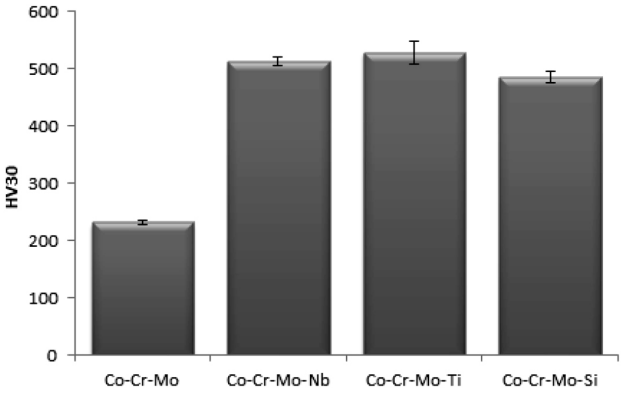

Figure 3: Hardness versus alloy composition
Slika 3: Trdnost v primerjavi s sestavo zlitine

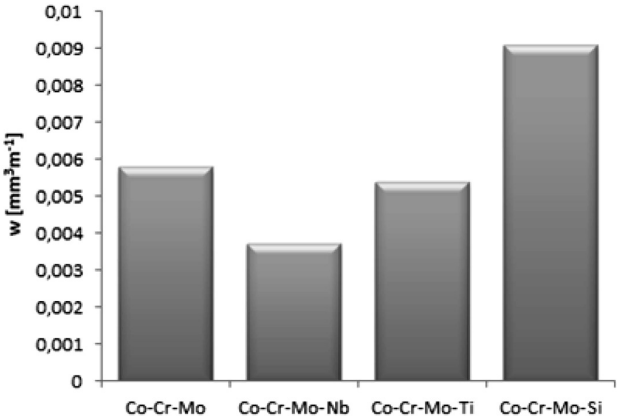

Figure 4: Abrasive-wear rate versus alloy composition
Slika 4: Abrazijska stopnja obrabe v primerjavi s sestavo zlitine

similar to the samples alloyed with titanium and niobium, differing only in the fcc : hcp cobalt ratio. For Co-Cr-Mo-Si, we see a more visible difference in the microstructure, i.e., a significant grain refinement.

The hardness significantly increases with the addition of any alloying element (**Figure 3**). The reason is probably the solid-solution strengthening of the titanium- and silicon-alloyed material, as well as the formation of a dispersed hard phase in the niobium-containing alloy. This was confirmed with the EDS analysis, showing the average content of niobium in the matrix of only 1.6 % mass fraction, while in the titanium- and silicon-alloyed materials, the amounts of titanium and silicon reach 4.9 % mass fraction and 3.9 % mass fraction, respectively (**Table 3**).

Table 3: Average chemical composition of the matrix (in mass fraction (*w*/%), determined with EDS)
Tabela 3: Povprečna kemijska sestava matrice (v masnih deležih (*w*/%), določena z EDS-analizo)

Alloy	Co	Cr	Mo	Ti	Si	Nb
Co-Cr-Mo	65.9	28.0	6.1	-	-	-
Co-Cr-Mo-Nb	64.0	29.3	5.1	-	-	1.6
Co-Cr-Mo-Si	63.1	27.4	5.6	-	3.9	-
Co-Cr-Mo-Ti	62.4	27.3	5.4	4.9	-	-

The results of the test of the wear resistance are presented in **Figure 4**. It is evident that titanium only slightly improved the wear resistance, but the alloying with niobium has a more significant influence. This result corresponded with the previous finding obtained with an XRD analysis, which revealed the presence of dispersed hard niobium carbide in the Nb-alloyed material. It is known that the presence of hard particles improves the wear resistance more than the solid-solution-strengthening effects even though the hardness is comparable. In the case of the Co-Cr-Mo-Si alloy, the wear resistance is much poorer in comparison with the standard Co-Cr-Mo alloy. This can be caused by two possible phenomena – the presence of brittle chromium silicide and the stabilization of the fcc cobalt structure by silicon. The fcc structure exhibits a higher plasticity and, therefore, the material removal is easier.

4 CONCLUSION

The presented results indicate that after the additions of alloying elements – Nb, Si, Ti – in all the cases, the hardness increases. This correlates well with the changes in the phase composition, producing hard phases (NbC) or reinforcing the material mainly with the solid-solution-strengthening effect (Ti, Si). On the other hand, only some of the elements simultaneously improve the abrasive-wear resistance. The measurement of the abrasion resistance was crucial for us because the aim was to specifically improve this property. From this point of view, the alloying with silicon is absolutely unsatisfactory. The best wear resistance was achieved for the Co-Cr-Mo-Nb alloy, wherein the addition of niobium significantly reduced the wear rate. Co-Cr-Mo-Nb thus appears to be the best solution, but it is necessary to perform many more tests, especially the tests of corrosion resistance and biocompatibility.

Acknowledgement

This research was financially supported by the Czech Science Foundation, project No. P108/12/G043.

5 REFERENCES

[1] H. Ö. Gülsoy, Ö. Özgün, S. Bilketay, Powder injection molding of Stellite 6 powder: Sintering, microstructural and mechanical properties, Materials Science and Engineering A, 651 (**2016**), 914–924, doi:10.1016/j.msea.2015.11.058

[2] A. Marti, Cobalt-base alloys used in bone surgery, Injury, 31 (**2000**) 4, D18–D21, doi:10.1016/S0020-1383(00)80018-2

[3] J. Cawley et al., A tribological study of cobalt chromium molybdenum alloys used in metal-on-metal resurfacing hip arthroplasty, Wear, 255 (**2003**) 7–12, 999–1006, doi:10.1016/S0043-1648(03)00046-2

[4] C. Sawangrat et al., Application of Harmonic Struture Design to Biomedical Co-Cr-Mo alloy for Improved Mechanical Properties, Materials Transaction, 55 (**2014**) 1, 99–105, doi:10.2320/matertrans.MA201303

[5] J.-C. Shin et al., Effect of molybdenum on the microstructure and wear resistance of cobalt-base Stellite hardfacting alloys, Surface and Coatings Technology, 166 (**2003**) 2–3, 117–126, doi:10.1016/S0257-8972(02)00853-8

[6] G. Bellefontaine, The corrosion of CoCrMo alloys for biomedical applications, Doctoral dissertation, University of Birmingham, 2010

[7] T. Matković, P. Matković, J. Malina, Effects of Ni and Mo on the microstructure and some other properties of Co-Cr dental alloys, Journal of alloys and compounds, 366 (**2004**) 1–2, 293–297, doi:10.1016/j.jallcom.2003.07.004

[8] R. Zupančič, A. Legat, N. Funduk, Electrochemical and mechanical properties of cobalt-chromium dental alloy joints, Materials and technology, 41 (**2007**) 6, 295–300

[9] P. Stenlund, S. Kurosu, Y. Koizumi, F. Suska, H. Matsumoto, A. Chiba, A. Palmquist, Osseointegration Enhancement by Zr doping of Co-Cr-Mo Implants Fabricated by Electron Beam Melting, Additive Manufacturing, 6 (**2015**), 6–15, doi:10.1016/j.addma.2015.02.002

[10] E. Zhang, C. Liu, A new antibacterial Co-Cr-Mo-Cu alloy: Preparation, biocorrosion, mechanical and antibacterial property, Materials Science and Engineering C, 69 (**2016**), 134–143, doi:10.1016/j.msec.2016.05.028

[11] K. Yamanaka, M. Mori, A. Chiba, Nanoarchitectured Co–Cr–Mo orthopedic implant alloys: Nitrogen-enhanced nanostructural evolution and its effect on phase stability, Acta Biomaterialia, 9 (**2013**), 6259–6267, doi:10.1016/j.actbio.2012.12.013

[12] R. W. Cahn, P. Haasen, E. J. Cramer, Processing of metals and alloys, Materials Science and Technology, 15 (**1991**) 193, doi:10.1002/cite.330640225

[13] P. Novák, CZ Patent 305703, 2014

[14] T. B. Massalski, Binary Alloy Phase Diagrams, ASM, Materials Park, 1990

UDK 620.1:621.791.75:621.791.053
Original scientific article/Izvirni znanstveni članek

ISSN 1580-2949
MTAEC9, 51(3)449(2017)

EFFECT OF THE GMAW METAL-TRANSFER MODE ON THE WELD-METAL STRUCTURE OF HSLA X80

VPLIV NAČINA PRENOSA KOVINE PRI OBLOČNEM VARJENJU V ZAŠČITNEM PLINU (GMAW) NA STRUKTURO ZVARA NA JEKLU HSLA X80

Maja Jurica, Zoran Kožuh, Branko Bauer, Ivica Garašić

University of Zagreb, Faculty of Mechanical Engineering and Naval Architecture, Ivana Lucica 5, 10002 Zagreb, Croatia
branko.bauer@fsb.hr

Prejem rokopisa – received: 2016-04-01; sprejem za objavo – accepted for publication: 2016-06-22

doi:10.17222/mit.2016.057

This paper presents the influence of the metal-transfer mode during GMAW of 10-mm-thick HSLA steel grade X80 on the inclusions and acicular ferrite content in the weld metal. Welding of butt joint specimens was carried out by the conventional short-circuit and CBT metal-transfer mode with different shielding gases and wire feed speeds. An analysis of obtained results showed that the metal-transfer mode affects the weld-metal structure by influencing the acicular ferrite content in relation to the number and size of the inclusions found in the weld metal.

Keywords: GMAW CBT welding, non-metallic inclusions, acicular ferrite, HSLA X80

Članek predstavlja vpliv načina prenosa kovine med obločnim varjenjem v zaščitnem plinu (GMAW), 10 mm debelega visokotrdnostnega malolegiranega (HSLA) jekla vrste X80 na vključke in vsebnost acikularnega ferita v zvaru. Varjenje soležnih vzorcev je bilo izvedeno z običajnim kratkostičnim načinom in s kontroliranim prenosom kovine (CBT) z različnimi zaščitnimi plini in hitrostmi podajanja žice. Analiza dobljenih rezultatov je pokazala, da način prenosa kovine vpliva na strukturo zvara, z vplivanjem na vsebnost acikularnega ferita v povezavi s številom in velikostjo vključkov v kovini zvara.

Ključne besede: GMAW CBT varjenje, nekovinski vključki, acikularni ferit, HSLA X80

1 INTRODUCTION

The HSLA steel grade X80 is more and more in use, but not so much has been investigated on the subject of the influence of the metal transfer on the structure of the weld metal. The most commonly used technology for joining pipeline steels is GMAW, because it results in high productivity and efficiency and also because by changing the welding parameters the metal-transfer mode can easily be modified to achieve different heat inputs. When GMAW with a short-circuit metal-transfer mode is used, the occurrence of spatter is observed. Spatter generates mostly when re-arcing takes place immediately after the short circuit causing additional financial expenses. In order to eliminate spatter, the critical time period, where the molten metal is squeezed by the pinch force effect, the voltage just before re-arcing must be accurately sensed.[1] Following this, the welding current is rapidly decreased immediately after the re-arcing occurs. This causes the molten metal at the tip of the wire to be transferred to the weld pool using only the surface tension, resulting in minimization or even elimination of the spatter generation.[2,3] The modified metal transfer also affects the mechanical properties of the weld metal, which directly depend on the microstructure.[4] Micro-alloyed low-carbon steels with a multiphase microstructure can have a high tensile strength, good toughness and weldability. This combination of properties has led to their application in the manufacturing of large-diameter pipes for gas and oil transportation with significant reductions of wall thickness. Interest in acicular ferrite (AF) formation is motivated by recent evidence that pipeline steels with bainitic microstructure having predominantly AF+MA (martensite–austenite) microstructures that have superior combinations of tensile strength and toughness compared with CB (conventional bainite) + MA microstructures.[5] Acicular ferrite is one of the microstructural constituents that is most commonly observed in the weld deposit of low-alloy steel and is easily differentiated from other constituents by its fine interlocking nature.[6] As follows from **Figure 1**, the ferrite side plate (such as Widmanstätten ferrite or upper bainite) provides preferential crack-propagation paths in austenite grains. This is because the ferrite side plates nucleate at grain boundaries as parallel plates with the same crystallographic orientation. Therefore, the toughness of the steels decreases with an increasing amount of these structures. Alternatively, the acicular ferrite laths nucleate intragranularly at the surface of the inclusions. Then, they have a chaotic crystallographic orientation, resulting in a retardation of the propagation path for a cleavage crack in the metal. Therefore, it can be expected that the steel toughness

increases with an increasing amount of acicular ferrite in the steel.[7]

From the published literature on acicular ferrite in weld metals it is well established that non-metallic inclusions present effective nucleation sites for acicular ferrite and a variety of mechanisms were proposed. Therefore, various authors have discussed the effect of different factors such as: cooling rate in the temperature range 800 °C to 500 °C, chemical composition of the steel, size of the austenite grains, and inclusion parameters on the formation of intragranular acicular ferrite in the weld metal.[5,7–10] However, in real practice it is very difficult, if not impossible, to determine the influence of each of the previously mentioned factors separately.

In the present work, the effect of the metal-transfer mode during GMAW on the formation of non-metallic inclusions as well as acicular ferrite in HSLA X80 steel has been investigated.

2 EXPERIMENTAL PART

The base material used in the experiment was high-strength, low-alloy steel API 5L X80 and the filler material was G 62 4 M Mn3NiCrMo (according to EN ISO 16834) wire, 1.2 mm in diameter. The exact chemical composition of the base and the filler material used in this experiment is shown in **Table 1**.

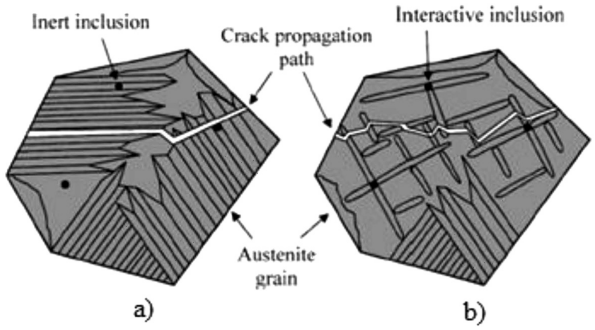

Figure 1: Schematic illustration of propagation path: a) in predominantly ferrite side plate and b) acicular ferrite microstructure[7]
Slika 1: Shematski prikaz poti napredovanja razpoke: a) v pretežno feritni plošči in b) v mikrostrukturi acikularnega ferita[7]

Table 1: Chemical composition of base and filler materials[11]
Tabela 1: Kemijska sestava osnovnega materiala in dodanega materiala[11]

Material	API 5L X80	G 62 4 M Mn3NiCrMo (according to EN ISO 16834)	
Chemical composition in mass fractions, (*w*/%)	C	0.07	0.10
	Si	0.35	0.75
	Mn	1.94	1.65
	P	0.015	-
	S	0.0	-
	Cr	0.15	0.60
	Ni	0.01	0.55
	Mo	0.001	0.30
	Cu	0.01	0.08
	Al	0.027	-

Gas metal arc welding of the specimens was carried out using two different metal-transfer modes: short-circuit (SC) mode and controlled bridge transfer (CBT). During the experiment, three different wire feed speeds were used (4 m/min, 5.5 m/min and 7 m/min).

The maximum wire feed speed was determined by previous experiments as the upper limit where the controlled bridge transfer mode is still stable. Also, the minimum value of the wire feed speed is defined as the speed that does not result in a lack of fusion. The shielding gases used were M21 and C1 according to EN ISO 14175: 2008 standard and a special mixture consisting of 59 % CO_2 and 41 % Ar with the flow set at 18 L/min. The contact tip to work distance (CTWD) was 12 mm, while the welding speed was 25 cm/min. Welding of the filler passes was carried out using the neutral technique. The interpass temperature was controlled with the infrared thermometer to be under 100 °C. Because of a very narrow span of welding parameters which result in good quality root pass (wire feed speed – 3.5 m/min, welding speed – 11.6 cm/min, shielding gas flow – 16 L/min, CTWD – 15 mm, pull technique, short circuit metal transfer mode, heat input – 8.4 kJ/cm), all of the root passes of the specimens were robotically (Almega OTC AX-V6 robot and Varstroj VPS 400 welding power source) welded with the same parameters. Filler passes were welded using the Daihen Varstroj Welbee P500L welding power source and BUG-O Systems MDS 1002 drive system. Sample designations and varied welding parameters are shown in **Table 2**.

Table 2: Sample designation and varied welding parameters
Tabela 2: Oznaka vzorcev in različni parametri varjenja

Sample nr.	Shielding gas CO_2 content, in volume fractions (*X*/%)	Metal transfer mode, CV/CBT	Wire feed speed, m/min
1	18	CV	4
2	18	CBT	4
3	18	CV	5.5
4	18	CBT	5.5
5	18	CV	7
6	18	CBT	7
7	59	CV	4
8	59	CBT	4
9	59	CV	5.5
10	59	CV	5.5
11	59	CV	5.5
12	59	CBT	5.5
13	59	CBT	5.5
14	59	CBT	5.5
15	59	CV	7
16	59	CBT	7
17	100	CV	4
18	100	CBT	4
19	100	CV	5.5
20	100	CBT	5.5
21	100	CV	7
22	100	CBT	7

After welding of the plates, test specimens were prepared in accordance with the EN ISO 15614-1 standard. Later on, specimens were polished and etched in 3 % Nital solution for micrographic analysis and in 7 % Nital solution for macrograph analysis. The exact chemical composition of the inclusions found in the weld metal was analysed by SEM TESCAN VEGA 5136 MM equipped with Oxford EDS detector. Microstructural analysis of the weld metal was observed with an Olympus GX51F-5 inverted light microscope.

All of the gathered data on the microstructure of the weld metal (acicular ferrite content) were statistically analysed with the Design Expert software program. A face-centered central composite design with three factors was used to analyse the influence of the varied factors. In this design the star points (not centered) are at the center of each face of the factorial space, so $\alpha = \pm 1$. Center points were repeated 3 times in order to define the "Pure error" and the curvature of the response surface. According to ANOVA of the results of weld-metal microstructure, categorical factor metal transfer mode (conventional-CV and CBT) is a significant factor with P-value < 0.0001. In order to analyse in detail the influence of the metal-transfer mode as the significant factor, only the results for one shielding gas (C1) are presented and analysed. The reason for analysing this specific shielding gas lies in the fact that it promotes non-axial detachment of the metal droplet, causing more spatter.[11–14] Because the newly developed CBT metal-transfer mode can reduce or even eliminate spatter generation, regardless of the type of shielding gas, 100 % CO_2 shielding gas could be used in short circuit and globular metal transfer parameter range. This type of shielding gas is not typically used when welding HSLA X80, so a detailed analysis of its effect on the weld-metal properties needs to be investigated.

3 RESULTS

3.1 Chemical composition and size distribution of non-metallic inclusions in the weld metal

Inclusions of varying size and type were examined and the results in **Table 3** present the average values of all the inclusions analysed per one test specimen. The results indicate that the analysed inclusions are rich in oxygen, silicon, manganese and aluminium with a small amount in titanium and sulphur. The smallest inclusions were observed in sample 17, which was welded with a wire feed speed of 4 m/min and a short-circuit metal-transfer mode. The chemical compositions of these inclusions are in relation to the diameter – it can be seen that the mass percentage of all the chemical elements are at the lowest values in comparison to the other inclusions. It can also be noticed that in the samples 17 and 18 no titanium was observed. In samples 19 and 21, which were welded with higher wire feed speeds (5.5 m/min and 7 m/min) and short-circuit mode, no chromium was found. All the other alloying elements are noticed to be in a positive linear dependence with the diameter of the observed inclusions (with the growth of the inclusions also the growth of the mass percentage of all the elements is observed). Taking into account the fact that carbon, iron and chromium are constituent elements of the base and filler metal, the observed inclusion can be characterized as complex Si-, Mn- and Al-oxides.

The average values of the size distribution of the observed non-metallic inclusions are also presented in **Table 3**. It can be seen that the average diameter of the inclusions varied in the range from 0.51 μm to 1.12 μm. The smallest inclusions are noticed in sample 1 (welded with 4 m/min wire feed speed and short-circuit, metal-transfer mode) and the largest inclusions are observed in sample 19 (welded with 5.5 m/min wire feed speed and short-circuit transfer mode), as can be seen in **Figure 2**. Comparing the chemical composition with the size distribution of the observed inclusions it can be seen that the diameter of inclusions containing chromium is smaller when welding with the short-circuit metal-transfer mode (compared to the CBT metal-transfer mode) and larger when no chromium is found. Samples welded with the globular metal-transfer mode (samples 19 and 21) show significant difference in inclusion size (increase in size is over 100 %) to the sample (Sample 17) welded with short-circuit metal-transfer mode.

3.2 Microstructure of the weld metal

The microstructure analysis of the weld metal is given in **Table 4**. The obtained results show the area fraction of acicular ferrite and also of inclusions. Minimum acicular content of 60.2 % and minimum content of

Table 3: Chemical composition and size distribution of the observed inclusions (samples 17-22)
Tabela 3: Kemijska sestava in razporeditev velikosti opaženih vključkov (vzorci 17 – 22)

Sample	$\bar{d}_i$ μm	Chemical composition, in mass fractions (*w*/ %)								
		C	O	Al	Si	S	Cr	Ti	Mn	Fe
17	0.51	5.49	7.06	0.22	3.55	0.43	0.47	-	6.30	77.00
18	0.88	6.80	10.51	0.33	4.48	0.71	0.69	-	6.38	71.25
19	1.12	7.27	19.10	0.95	6.93	0.66	-	0.18	10.68	54.05
20	0.93	7.10	13.61	0.92	5.96	0.43	0.48	0.17	11.48	60.90
21	1.01	9.73	18.57	0.31	6.55	0.68	-	0.32	12.39	51.23
22	0.87	8.50	12.40	0.34	5.04	0.61	0.46	0.22	11.13	61.48

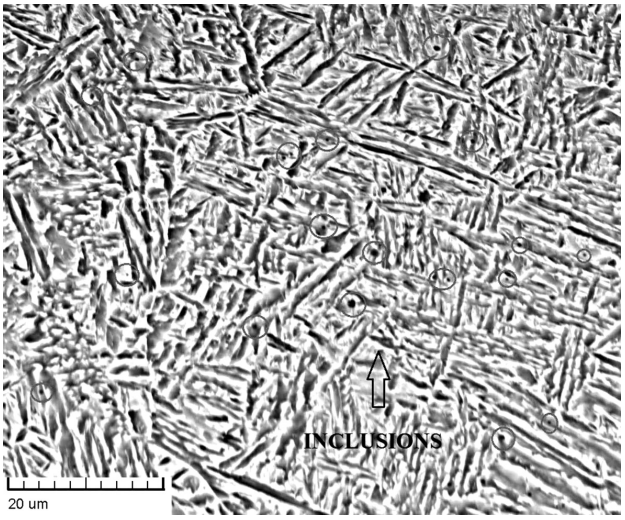

Figure 2: SEM micrograph of the sample 19
Slika 2: SEM-posnetek vzorca 19

inclusions of 1.3 % is achieved in sample 18 (**Figure 3**), which was welded with the CBT metal-transfer mode and a wire-feed speed of 4 m/min. Also, the maximum values of the area fraction for both acicular ferrite (74.9 %) and inclusions (2.1 %) were observed in the same sample, sample 21 (which was welded with globular transfer mode and 7 m/min wire feed speed). From these results it can be clearly seen that the area fraction of acicular ferrite is closely related to the area fraction of inclusions - higher content of inclusion results in a higher content of acicular ferrite. The biggest difference in the obtained results between the CBT and globular transfer mode is observed in samples 19 and 20. From **Table 4** it can be seen that the area fraction of the acicular ferrite is in sample 19 16 % larger than in sample 20. Similarly, the area fraction of inclusions is in sample 19 larger by 36 % than in sample 20. Comparing the results of the area fraction of the acicular ferrite and the inclusion diameter no direct dependence could be observed.

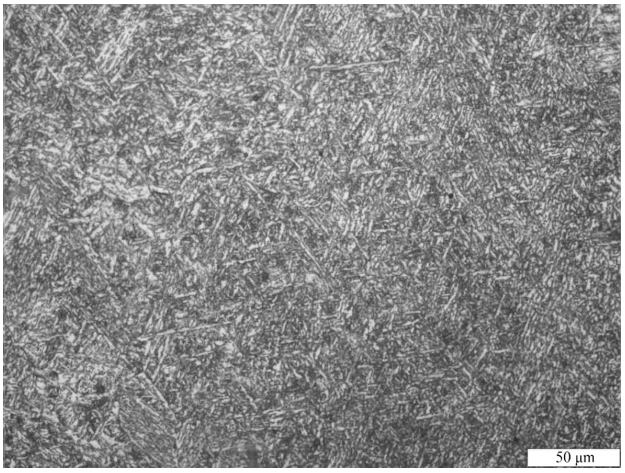

Figure 3: Weld-metal microstructure with predominantly acicular ferrite (sample 21)
Slika 3: Mikrostruktura zvara s prevladujočim acikularnim feritom (vzorec 21)

Table 4: Microstructure analysis – area fraction of acicular ferrite and non-metallic inclusions
Tabela 4: Analiza mikrostrukture – delež površine acikularnega ferita in nekovinskih vključkov

Sample	Area fraction of acicular ferrite, %	Area fraction of non-metallic inclusions, %
17	68.2	1.6
18	60.2	1.3
19	72.3	1.9
20	62.5	1.4
21	74.9	2.1
22	66.7	1.6

4 DISCUSSION

Among other steel deoxidants, Al is the most commonly used alloying element added for fully killed steel. Therefore, the simple Al_2O_3 oxides are often found in different steel grades, but are not considered to be an effective nucleant for AF. But, in steels containing Mn and which have been deoxidized by Al, more complex manganese-oxide inclusion evolve, which then become effective nucleation sites for AF.[7] Unlike simple Al-oxides, various Ti-oxides are very efficient nuclei for the formation of AF.

Some of the complex oxides can also nucleate AF. More specifically, the observed aluminium-manganese silicates nucleate AF. Their effectiveness can be explained with their highest thermal expansion difference from iron (in comparison with other observed inclusions) resulting in the largest thermal stresses.[7] Among the observed inclusions, in addition to oxides, some sulphides (MnS) were also found. Pure MnS inclusions, unlike some oxides, are not active nucleants for AF, because they are incoherent in austenite.[15] Complex oxy-sulphides and multi-phase inclusions observed in analysed specimens are very often stated as nucleants for AF. The factors that positively influence the nucleation of AF are: low mismatch strain between the inclusions and ferrite; positive thermal strains in the surrounding matrix (due to large difference in thermal coefficients for inclusion and matrix) and the formation of Mn-depleted zone in the matrix near the MnS inclusion. Because simple inclusions affect the nucleation of the AF with only one of the mentioned factors, they present less active nucleants for AF compared to the complex inclusions. According to [16], inclusions consist of an oxide core, which is formed during the primary deoxidation stage. The chemical composition of deoxidation products can vary within wide limits, depending on the relative activities of aluminium, titanium, silicone, manganese and oxygen in the weld metal. Except for the MnS spotted in the observed inclusions in the experiment, the surface of the oxides can be partially covered by TiN.

The precipitation of these phases occurs after the completion of the weld-metal deoxidation, probably during solidification, where the reactions are favoured by solute enrichment in the interdendritic liquid.

Regarding the frequency of the occurrence of the observed inclusions, it can be concluded that a smaller amount of inclusions appeared in the samples welded with the CBT metal-transfer mode, resulting in a microstructure with a smaller area fraction of acicular ferrite. The larger acicular ferrite content in the weld metal welded with the natural metal-transfer mode could be explained by the thermal stresses that occur during the welding. Namely, during CBT welding a smaller heat input is introduced to the metal, resulting in smaller thermal stresses, which negatively influence the nucleation of the acicular ferrite. When welding with a higher heat input (conventional metal transfer mode), because of the large difference in the thermal coefficients for the inclusion and austenite matrix, the nucleation of acicular ferrite is more stimulated. Besides the area fraction of inclusions in the weld metal, which has proven to influence the content of acicular ferrite, the size of the inclusion has also been observed to have a great influence, as can be seen from **Table 3** and **Table 4**. These results indicate the critical size of the particles for the heterogeneous nucleation of acicular ferrite to be around 1 μm, which is in accordance with previous investigations of other authors.[6,7] This is a critical value because of the fact that the energy barrier to heterogeneous nucleation of ferrite at inclusions decreases significantly with an increased inclusion diameter in the range from 0 to 1 μm. This is due to the increasing of the particle surface area. However, it follows from[7] that the value of this energy barrier for particles with diameters larger than about 1 μm decreases only slightly with a further increase in the inclusion size. Therefore, it is expected that a further increase of the diameter of the inclusions over 1 μm does not result in a greater possibility of ferrite nucleation on an inclusion surface.

5 CONCLUSIONS

Based on the results obtained in this study, the following main conclusions can be drawn:

- The diameter of the observed inclusions is in direct correlation with its chemical composition,
- Samples welded with CBT metal-transfer mode resulted in weld metals with a smaller amount of inclusions, resulting in a smaller area fraction of acicular ferrite,
- Samples welded with the globular metal-transfer mode resulted in a larger inclusion size to the one welded with short-circuit, metal-transfer mode.

6 REFERENCES

[1] T. Era, A. Ide, T. Uezono, T. Ueyama, Y. Hirata, Controlled bridge transfer (CBT) gas metal arc process for steel sheet joining; Welding International, 27 (**2009**) 4, 268–273, doi:10.1179/136217109X-406965

[2] T. Era, T. Ueyama, M. Brooks, Welding steel sheet with a modified short circuiting process, Welding Journal, 87/12 (**2008**), 28–33

[3] J. I. Achebo, Complex Behavior of Forces Influencing Molten Weld Metal Flow based on Static Force Balance Theory; Physics Procedia, 25 (**2012**), 317–324, doi:10.1016/j.phpro.2012.03.090

[4] Y. J. Oh, S. Y. Lee, J. S. Byun, J. H. Shim, Y. W. Cho, Non-metallic inclusions and acicular ferrite in low carbon steel, Materials Transactions, JIM, 40/12 (**2000**), 1663–1669, doi:10.2320/matertrans1989.41.1663

[5] E. V. Morales, R. A. Silva, I. S. Bott, S. Paciornik, Strengthening mechanisms in a pipeline microalloyed steel with a complex microstructure, Materials Science & Engineering A, 585 (**2013**), 253–260, doi:10.1016/j.msea.2013.07.060

[6] T. K. Lee, H. J. Kim, B. Y. Kang, S. K. Hwang, Effect of inclusion size on the nucleation of acicular ferrite in welds, ISIJ International, 40 (**2000**), 1260–1268, doi:10.2355/isijinternational.40.1260

[7] D. S. Sarma, A. V. Karasev, P. G. Jönsson, On the role of non-metallic inclusions in the nucleation of acicular ferrite in steels, ISIJ International, 49/7 (**2009**), 1063–1074, doi:10.2355/isijinternational.49.1063

[8] S. Terashima, H. K. D. H. Bhadeshia, Size distribution of oxides and toughness of steel weld metals, Science and technology of welding and joining, 11/5 (**2006**), 580–582, doi:10.1179/174329306X120868

[9] H. K. Sung, S. Y. Shin, W. Cha, K. Oh, S. Lee, N. J. Kim, Effects of acicular ferrite on charpy impact properties in heat affected zones of oxide-containing API X80 linepipe steels, Materials science and engineering A 528 (**2011**), 3350–335, doi:10.1016/j.msea.2011.01.031

[10] S.S. Babu, H.K.D.H. Bhadeshia, Mechanism of the transition from bainite to acicular ferrite, Material transactions, JIM, 32/8 (**1991**), 679–688, doi:10.2320/matertrans1989.32.679

[11] M. Jurica, Utjecaj zaštitnoga plina i načina prijenosa metala na svojstva zavarenoga spoja čelika X80, Doktorski rad, Fakultet strojarstva i brodogradnje, (2015), Zagreb

[12] J. Rykała, T. Pfeifer, Influence of the technological conditions of welding using the MIG/MAG method on metal transfer in the welding arc, Welding International, 28/12 (**2014**), 931–940, doi:10.1080/09507116.2012.753233

[13] Y. Ogino, Y. Hirata, A. B. Murphy, Numerical simulation of GMAW process using Ar and an Ar–CO_2 gas mixture, Welding in the World, 60/2 (**2016**), 345–353, doi:10.1007/s40194-015-0287-3

[14] Y.-R. Wong, S.-F. Ling, An investigation of dynamical metal transfer in GMAW-Effects of argon shielding gas, Journal of Materials Processing Technology, 214/1 (**2014**), 106–111, doi:10.1016/j.jmatprotec.2013.08.003

[15] T. Furuhara, J. Yamaguchi, N. Sugita, G. Miyamoto, T. Maki, Nucleation of proeutectoid ferrite on complex precipitates in austenite, ISIJ International, 43/10 (**2003**), 1630–1639, doi:10.2355/isijinternational.43.1630

[16] J. E. Ramirez, Characterization of High-Strength Steel Weld Metals: Chemical Composition, Microstructure, and Nonmetallic Inclusions, Welding journal, 87 (**2008**), 65–75

UDK 67.017:620.1:669.14.018.8
Original scientific article/Izvirni znanstveni članek

ISSN 1580-2949
MTAEC9, 51(3)455(2017)

INFLUENCE OF STAINLESS-STEEL WIRE MESH ON THE MECHANICAL BEHAVIOUR IN A GLASS-FIBRE-REINFORCED EPOXY COMPOSITE

VPLIV ŽIČNE MREŽE IZ NERJAVNEGA JEKLA NA OBNAŠANJE EPOKSI KOMPOZITA, OJAČANEGA S STEKLENIMI VLAKNI

Munisamy Sakthivel[1], Subramani Vijayakumar[2]

[1]Adhiyamaan College of Engineering, Department of Mechanical Engineering, Hosur, 635109 Tamilnadu, India
[2]University College of Engineering, Department of Mechanical Engineering, Kanchipuram, 631 552 Tamilnadu, India
metalsakthi@gmail.com

Prejem rokopisa – received: 2016-04-16; sprejem za objavo – accepted for publication: 2016-05-18

doi:10.17222/mit.2016.063

This work covers the fabrication and investigation of the mechanical behaviour of a glass-fibre-reinforced polymer (GFRP) composite embedded with a stainless-steel wire mesh (SSWM) layer. This work takes the hybridising approach in improving the mechanical properties of GFRP through the incorporation of SSWM into the laminates. The structure of the composite is such that the SSWM was placed in the top, middle and bottom of the GFRP. The laminates are fabricated using the hand-layup method with a 40 % weight fractions of epoxy resin, 50 % weight fractions of woven glass fibre and the remainder being SSWM. The mechanical characteristics of the composites are obtained using tensile, flexural, inter delamination and drop weight impact tests. In addition to that, a morphological investigation is made utilizing a scanning electron microscope (SEM). The test outcome demonstrates that the introduction of SSWM leads to far better mechanical properties than GFRP and SSWM in the middle layer has a superior strength compared to other laminates.

Keywords: glass fibre reinforced polymer, stainless-steel wire mesh, mechanical tests, ultimate strength, SEM

Delo obravnava izdelavo in preiskavo mehanskih lastnosti polimera, ojačanega s steklenimi vlakni (angl. GFRP) v katerem je vgrajena ploskovna žična mreža iz nerjavnega jekla (angl. SSWM). To delo predstavlja hibridiziran približek za izboljšanje mehanskih lastnosti GFRP z vgraditvijo SSWM v laminate. Kompozit je sestavljen tako, da je bila SSWM nameščena zgoraj, v sredini in spodaj. Laminati so izdelani z ročnim polaganjem 40 masnimi % epoksi smole, 50 masnimi % tkanine iz steklenih vlaken, ostalo pa je SSWM. Mehanske lastnosti kompozitov so določene z nateznim in z upogibnim preizkusom, z razslojevanjem in z udarno žilavostjo. Dodatno k temu je izvedena tudi morfološka preiskava s pomočjo vrstičnega elektronskega mikroskopa (SEM). Rezultati preizkusov kažejo, da vstavitev SSWM bolj izboljša mehanske lastnosti kot GFRP, SSWM v sredini pa izboljša trdnost v primerjavi z ostalimi laminati.

Ključne besede: steklena vlakna, jeklo ojačano s polimeri, ploskovna žična mreža iz nerjavnega jekla, mehanski preizkusi, natezna trdnost, SEM

1 INTRODUCTION

A composite material is a heterogeneous material that is formed by the combination of two or more materials in order to obtain the favourable characteristics of each. Polymer matrix composite materials are made of fibres embedded in a polymer matrix, also known as fibre-reinforced polymers (FRPs).[1] The fibre is usually made of carbon, glass, aramid and graphite.[2] The polymer is mostly made of polyester, epoxy, vinyl ester and phenol formaldehyde resins. However, the most commonly used fibre is woven glass fibre that was initially developed for strand off insulator for electrical wiring fibre forming capabilities and is now used almost exclusively as the reinforcing phase in the matrix. Woven roving is available in a variety of weaves, width, weights and finishes to suit a broad range of applications.[3,4]

Composites made with woven glass fibre are finding application in a variety of engineering fields due to their low cost, low weight, high stiffness and corrosion resistance. Fibre-reinforced polymers (FRPs) are utilized to fortify the auxiliary individuals, even after they have been seriously damaged. Woven glass fibre improves the impact resistance, toughness and energy absorption for the composite. The vicinity of woven glass fibre tends to expand the disintegration wear rate of the composite. The Young's modulus can be enhanced by increasing the volume of fibre in the composite.[5,6]

Though the glass fibre has vital mechanical properties but still the other fibres such as carbon fibre, aramid fibre, ceramic fibre, provide better mechanical properties compared to the glass fibre. The major drawback of these fibres is high cost and less abundance. In day-to-day life, the trend is to obtain the high strength material at low cost. So some modification must be made to improve the mechanical properties of glass-fibre-reinforced polymer (GFRP). Numerous methods have been employed such as matrix toughening, fibre hybridising and many more.[7–9] The major drawback of hybrid FRPs strengthening is the high cost of the different FRPs materials. The FRPs have some drawbacks such as while fitting as

well as joining applications in the fibrous environment it will not withstand total failure load. This leads to delamination and fibre damage.[10] Minimising the uses of metallic inserts in the fibrous environment can increase the entire failure loads, which prevent continuous fibre cut off.[11,12] To stabilise the fibre structure, drilling a hole before riveting the wire mesh is used as reinforcement material to minimise the wear of fibre in polymer matrix. Between two FRP layers amid the shaping operation, the open metallic structure is infiltrated by the polymers, and hence, the metallic structure is completely embedded in the polymer matrix.[13,14]

The GFRP laminate composites are layered materials based on a stacked arrangement of SSWM and fibre-reinforced epoxy resin. The SSWM is introduced at the top, middle and bottom of the laminate. The main objective of this work is to investigate the effects of the SSWM layer in the glass-fibre-reinforced epoxy composite under mechanical testing such as tensile test, flexural test, inter delamination test and drop weight impact test. A micrograph of the fractured specimen is analysed using a scanning electron microscope (SEM).

2 EXPERIMENTAL PART

2.1 Materials

The most commonly used reinforcement in polymer composites is glass fibre due to its toughness, energy absorption and strength. In this work stainless steel mesh and woven glass fibre are used as the reinforcement. Epoxy (LY556) resin with hardener (HY951) was used as the matrix material. The SSWM enhances the cracking behaviour and energy-absorption capability, also the epoxy resin coating provides good corrosion resistance of the wire mesh. Also SSWM maintained constant weight percentage to achieve the same weight as in plain GFRP. The matrix material and woven glass fibre were purchased from Covai seenu brothers ltd, Coimbatore. The properties of the stainless-steel mesh and the woven glass fibre are illustrated in **Table 1**.

Table 1: Properties of stainless-steel wire mesh and woven glass fibre
Tabela 1: Lastnosti žične mreže iz nerjavnega jekla in tkanine iz steklenih vlaken

Reinforcement material	Tensile strength (MPa)	Yield strength (MPa)	Density g/cm^3	Diameter of wire (mm)	Width between wires (mm)
Stainless steel (SS304)	620	275	8.0	0.5	1.6
Woven glass fibre	500	170	2.54	-	-

2.2 Fabrication of composites

The hand layup technique is used for preparing composite laminates. Before use, the woven AISI 304 SSWM is cleaned in an alkaline soap bath and is followed by a rinse in deionized water and allowed to dry in air. Then the flat mould surface is taken and cleaned thoroughly to avoid any foreign particles. A releasing agent (wax) was properly spread over a flat mould for easy removal of the composite. A thin layer of resin and hardener mixture in the ratio 10:1 is applied to the mould surface. Then woven glass fibre is placed over the thin layer of resin and filled with epoxy resin-hardener mixture. Then, by using the roller, the resin is rolled to remove the entrapped air and to ensure uniform spreading of the mixture. After each layer, a mixture of resin and hardener is rolled over and allowed to dry. In this way, several layers of woven glass fibre are placed, one over the other, and the same steps are repeated until the required thickness was obtained. Finally, the pre-processed SSWM is placed over the laminate evenly, and resin-hardener mixture with woven glass fibre is applied on the stainless-steel mesh and is allowed to cure. A weight of 8–10 kg is placed over the laminate and left undisturbed for a curing period of 4–5 h. Ensure the thickness of all the laminates that must be kept the same way as 3.2 mm for mechanical testing. The weight fraction of woven glass fibre is 50 % of mass fractions, the epoxy resin is 40 % of mass fractions, and the SSWM is 10 % of mass fractions.

3 COMPOSITES TESTING

3.1 Tensile test

The specimens for conducting the tensile test in four categories such as Plain GFRP, Top mesh GFRP, Middle mesh GFRP and Bottom mesh GFRP are prepared according to ASTM D638 standards. The top and bottom mesh is the same geometry, but the test is conducted for both individually to obtain a clear load-bearing capability. The test is performed in a universal testing machine (UTM) at room temperature. The specimen is held between the grippers of the UTM, and the load is applied gradually and the corresponding deflections are recorded. The load is applied incessantly until the specimen breaks and the corresponding break load is noted.

3.2 Flexural test

The flexural test specimens are cut according to the ASTM D790 standard. The test is carried out in the UTM by placing the specimen on the two vertical supports. The load is applied transversely to the middle of the laminate until the specimen bends and fractures. Then the corresponding fracture load is noted and the graph is generated.

3.3 Inter delamination

The specimen is prepared according to ASTM D5528 standards. A delamination or interfaced crack is a crack that initiates and grows between the different plies of a composite. Delamination is a kind of failure in which the

layers detach, resulting in a loss of strength. It is an internal mode of failure. The specimen is held between two vertical supports. The transverse load is applied until the fracture occurs. The corresponding fracture load is noted. The internal cracks are viewed through the macro images to identify their interfacial cracks.

3.4 Drop weight impact test

A vertical drop weight impact-testing machine is employed to perform the above test. For the drop-weight impact test the specimens are cut according to ASTM D7136 standard. The impactor guide mechanism releases an impactor of mass 2–5 kg at the desired height. A hemispherical tub is placed on the specimen that allows the material to attain the peak force and produces the shortest contact duration. The diameter of the tub is about 25.4 mm. The laminate is impacted to produce damage and the resulting damaged area is captured through the macro images.

The above mechanical tests are performed in five replicates for each combination, and the average values are determined.

4 RESULTS AND DISCUSSION

4.1 Tensile properties

The tensile test is conducted on the fabricated composite specimen using the UTM. The values of the mechanical properties, such as break load, elongation and ultimate tensile strength, are shown in **Table 2**. The stress vs. strain graph is shown in **Figure 1**. **Figure 1** shows that stress increases linearly with the strain for all the composites. Generally, the epoxy resin behaves like brittle materials when the fibre (SSWM, glass fibre) is loaded in the epoxy resin that behaves like ductile materials, which are shown in the stress-strain curve.[15] For all the combinations, the stress and strain decrease after a particular point exhibiting ductile properties. For all the laminates, the stress and strain decrease after a particular point exhibiting ductile properties.

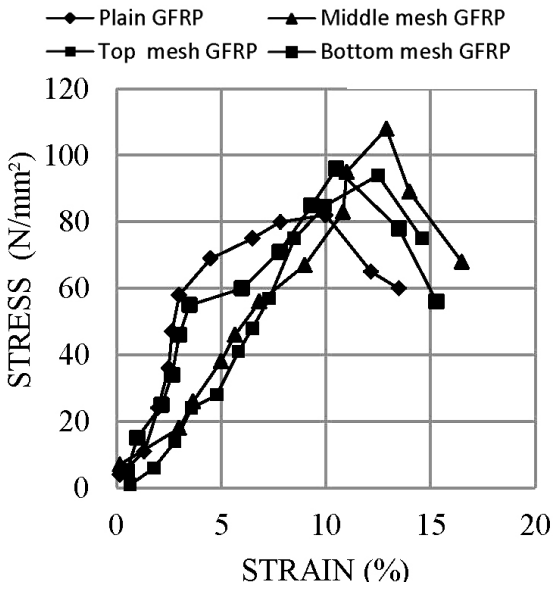

Figure 1: Stress vs. strain curve for tensile test
Slika 1: Krivulja napetost-raztezek pri nateznem preizkusu

The first crack and ultimate load were generally improved with the increasing number of wire mesh layers. This is attributed to the fact that additional wire mesh provides more resistance to an increasing load and restraint of micro-cracks propagation. The overall results of the first cracks and failure load demonstrate the advantage of using wire mesh as an external method for enhancing the strength and the first crack. The first crack was delayed much better than the other enhancing techniques, such as internal steel fibres.[16]

Table 2: Tensile properties of GFRP-SSWM
Tabela 2: Natezne lastnosti GFRP-SSWM

Laminate	Ultimate breaking load (N)	Ultimate tensile strength (N/mm²)	Elongation (%)
Plain	1100	86	13.667
Top	2900	95	14.900
Middle	3600	110	16.833
Bottom	3500	99	15.500

The enhancement in the tensile strength is predominant in GFRP-SSWM laminate where the strength of GFRP improves from 86 MPa to 110 MPa when the SSWM is introduced in the middle of the laminate. In contrast, the elongation of GFRP-SSWM at the middle layer exhibits 1.23 times that of the plain GFRP, 1.09 times that of top layers and 1.13 times that of the bottom layer. Similarly, the ultimate strength of GFRP-SSWM at the middle layer is 1.28 times that of plain GFRP, 1.105 times that of the top layers and 1.151 times that of the bottom layer.

The tensile-test result shows that the performance of the GFRP-SSWM at the middle layer is higher than the other laminates. This signifies that the tensile properties of the GFRP improve with the inclusion of a stainless-steel mesh in the middle of the laminate. The incorporation of SSWM layer into the epoxy matrix had a considerable effect on its tensile properties. The SSWM impregnated into the epoxy matrix, which improves the efficiency of the composites and prevents cracking in the cured product.

4.2 Flexural properties

The flexural properties together with the break load and the displacement of the composite are tabulated in **Table 3**. The flexural test is carried out in the state of stress experienced by the specimens can be extremely perplexing and several failure modes can occur, in particular fibre buckling and delamination. The harm zone so nucleated can cause longitudinal splitting, leading to premature failure of the composite laminate,

thus preventing higher stresses in the outermost fibres to be reached. This event is less critical in glass-fibre laminates because glass fibres show lower modulus and higher elongation at the break.[17] The loading phases of the specimens can be explained as follows. The first phase represents the elastic behaviour where there is no crack in the tension face and the specimen maintains its full flexural stiffness and rigidity. The load increases linearly with the deflection. The second phase corresponds to the initiation of cracks and reduction in the load and deflection. In this phase, the bending stiffness of the specimen reduced. The final phase includes the failure of wire mesh–epoxy composite and the fracture of the specimen.[14]

Table 3: Flexural properties of GFRP-SSWM
Tabela 3: Upogibne lastnosti GFRP-SSWM

Laminate	Breaking load (N)	Flexural strength (N/mm^2)
Plain	310	75
Top	480	80
Middle	520	95
Bottom	430	85

It is understood from **Table 3** that the result of the GFRP-SSWM at the middle layer is higher than that of all the other laminates. It was found that GFRP-SSWM at the middle layer has a higher ultimate breaking load than that of the other laminates. The ultimate strength of the GFRP-SSWM at the middle layer is higher than all the other laminates. The ultimate strength of GFRP-SSWM at the middle layer is 1.266 times that of the plain GFRP (1.067 times that of the top layer and 1.133 times that of the bottom layer). From these discussions, it is observed that GFRP-SSWM at the middle layer has more flexural strength compared to all the laminates.

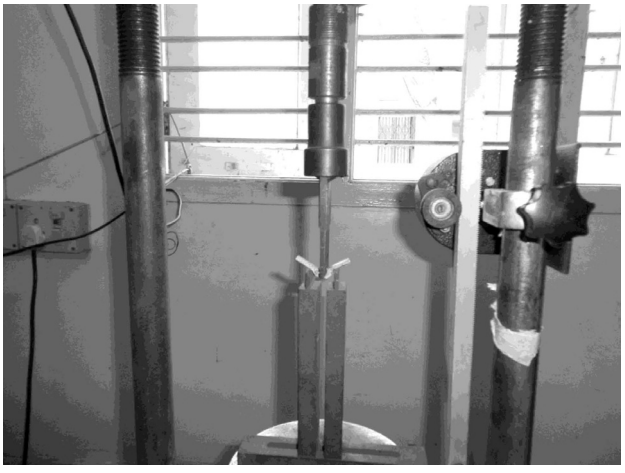

Figure 2: Inter-delamination test arrangement
Slika 2: Naprava za preizkus razslojevanja

4.3 Inter-delamination test

Delamination is one of the modes of failure in composite laminate materials. Delamination is caused in a laminated composite due to fatigue stress. The various properties such as breaking load and the ultimate strength of the inter-delamination test are tabulated in **Table 4**. The inter-delamination test arrangement is shown in **Figure 2**.

Table 4: Inter delamination properties of GFRP-SSWM
Tabela 4: Lastnosti razslojevanja GFRP-SSWM

Laminate	Ultimate breaking load (N)	Ultimate strength (N/mm^2)
Plain	140	20
Top	155	30
Middle	180	36
Bottom	170	32

The maximum load is higher for the GFRP laminate with SSWM at the middle of the layer since it bears more load than all the other laminates. The load is increased from elastic region the SSWM resist more load as well as the load transfer being even throughout the composites because of the open metallic inserts.

It is clear from **Table 4** that the ultimate breaking load of GFRP-SSWM at the middle layer is 1.286 times than that of plain GFRP (1.107 times than that of the top layer and 1.214 times than that of the bottom layer). Similarly, the ultimate strength of GFRP-SSWM at the middle layer is two times that of the plain GFRP (1.125 times that of the top layer and 1.5 times of bottom layer of the laminate). A macro image of the inter-delamination test specimens is shown in **Figure 3**.

From the results it is clear that the sequence of this SSWM increases the load-bearing capacity with a reduction of the weight and also improving the strength. With the proper sequence of materials and its varying properties the fracture and failure of laminates has been reduced. It is concluded that the GFRP at middle layer (SSWM) shows good results under the inter-delamination test compared to the other laminates.

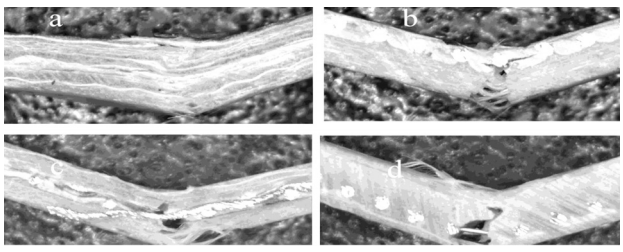

Figure 3: Macro image of inter delamination test specimens: a) plain GFRP laminate, b) top mesh GFRP laminate c) middle mesh GFRP laminate and d) bottom mesh GFRP laminate
Slika 3: Makroposnetek preizkusa notranjega razslojevanja: a) GFRP laminat, b) GFRP laminat z mrežo zgoraj, c) GFRP laminat z mrežo v sredini in d) GFRP laminat z mrežo spodaj

4.4 Drop-weight impact test

The drop-weight impact test is used to determine the impact energy absorption capacity of the laminates. This impact characterization is essential for applications in the aeronautical and mechanical fields where crash aspects represent a key point. **Figure 4** shows the result of the plain and hybrid laminate after the impact of a body of mass 2.5 kg at a height of 1 m. The circle indicates that the damage is due to the drop-weight impact test.

Figure 4a illustrates the plain GFRP laminate that displays fibre and matrix crushing on the impact side with multilevel delamination through the thickness and finally tensile and buckling failure on the back surface.

Figure 4b reveals the GFRP-SSWM at the top layer of the laminate, where it displays modest evidence of crushing in the mesh region where the tough combination of the mesh reinforced epoxy absorbs much of the energy and the remaining energy is crushed in the fibre-matrix combination. The application of force to the laminate helps the stainless-steel mesh absorb the initial energy. The remaining energy will crush the fibre matrix combination. So the laminates are crushed less than the plain GFRP.

Similarly, **Figure 4c** shows that the GFRP-SSWM at the middle layer of the laminate, the impact energy is absorbed by a fibre matrix combination. So it absorbs a small amount of impact energy and then it faces the mesh reinforced epoxy and the remaining energy is absorbed in the middle layer itself. So the damage occurs in the GFRP-SSWM at the middle layer that is almost less when compared to all the other laminates.

Figure 4d shows that GFRP-SSWM at the bottom layer of the laminate displays the fibre matrix crushing till the bottom of the laminate and then it faces the mesh-reinforced epoxy. The 3/4th of the laminate is crushed when the initial impact energy is applied to the laminate. When the force is applied on the laminate almost all the impact energy is absorbed by the fibre matrix combination and the remaining amount of energy is impacted on the stainless-steel mesh. It is seen that these laminates are crushed more than the top layered mesh laminate but lesser than the plain GFRP.

4.5 Morphological analysis

The morphological analyses of the tested specimen were performed utilizing an SEM. The fractured specimens from the tensile and flexural tesst are examined utilizing SEM. The interfacial adhesion between the matrix and the fibre is clearly seen from the SEM images. The SSWM is visible in **Figure 5** that are in the top, middle and bottom layers. An almost culminate infiltration into the wire meshes and merge between the woven glass fibre and the metal mesh reinforced epoxy could be achieved. There is no unsettling influence of the fibre structure close to the wires, as found in **Figure 5a**.

Figure 5b shows that there is no distinctive damage to the fibre or matrix. However, transversal fibre cracks

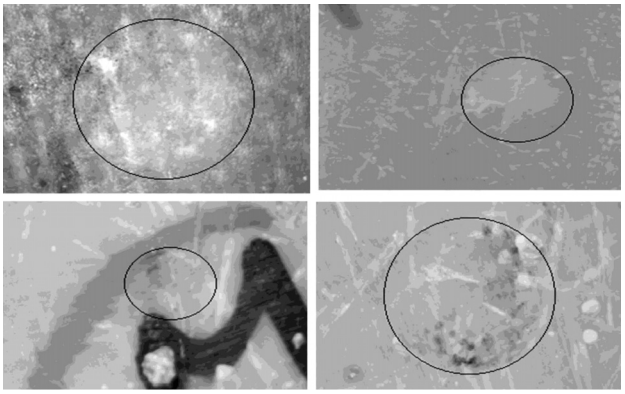

Figure 4: Macro image of drop-weight impact test specimens: a) plain GFRP laminate, b) top mesh GFRP laminate, c) middle mesh GFRP laminate and d) bottom mesh GFRP laminate

Slika 4: Makroposnetek vzorca pri udarnem preizkusu: a) GFRP-laminat, b) GFRP-laminat z mrežo zgoraj, c) GFRP-laminat z mrežo v sredini in d) GFRP-laminat z mrežo spodaj

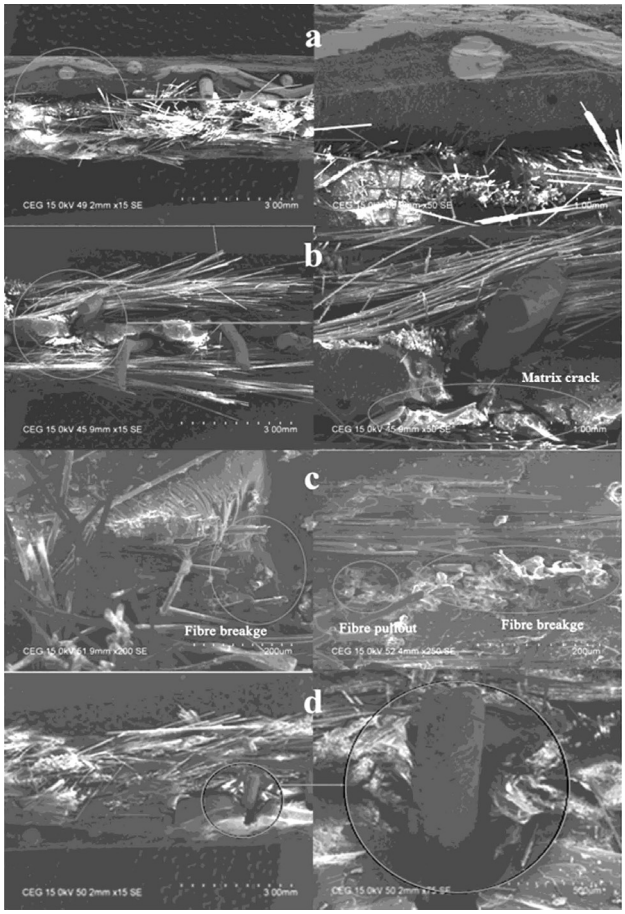

Figure 5: SEM images GFRP-SSWM laminate composites: a) top mesh GFRP laminate, b) middle mesh GFRP laminate, c) plain mesh GFRP laminate and d) bottom mesh GFRP composite

Slika 5: SEM-posnetek GFRP-SSWM laminatnega kompozita: a) GFRP-laminat z mrežo zgoraj, b) GFRP-laminat z mrežo v sredini, c) GFRP-laminat z običajno mrežo in d) GFRP-laminat mrežo spodaj

can be detected where the disturbance of the fibre structure is high, and the fibres surround the wire very closely. This implies the fibres are seriously bent during a flexural load.

The SSWM in the middle layer is clearly visible in **Figure 5b**. A microcrack is formed, initiated and propagated through the matrix, and when it arrives at an interface, it continues along the interface up to the fracture of the fibre. After the fibre fractures, the crack propagates through the matrix and then moves to the next interface, this process continues until there is a complete fracture. The SSWM layer withstands the tensile load, which pulls the SSWM and matrix cracks.

Both fibre breakage and pullout are clearly visible in **Figure 5c**, where it is evident that the strength is lower compared to the other laminates. It is found that the fibres in the region of the loading region are more prone to damage. The strain values of the fibre in this region might have diminished and that leads to fibre pull-out.

A typical crater at the wire of the composite produced with a tensile force and also an interface debonding between the wire and the matrix is observed in **Figure 5d**. It also shows that the fibre/matrix interface of adjacent fabric layers. **Figure 5d** the circles illustrate the process-induced damage. The circle indicates a high tensile load as a result of a wire-induced distortion to the fibre structure at the maximum tensile force. Due to a purely elastic deformation at maximum force, a subsequent discharge leads to the elastic reshaping of the wire mesh. This leads to the debonding that occurs at the fibre/matrix interface.

5 CONCLUSIONS

The influence of a stainless-steel wire mesh layer on the mechanical behaviour of GFRP was investigated. From the above test results, the following conclusions are drawn:

- The ultimate strength and breaking load of GFRP-SSWM at the middle layer is 110MPa and 3600 N, respectively, which is higher than that of all the other laminates.
- From the tensile test, the percentage elongation of GFRP-SSWM in the middle layer is 16.83 %, which is higher than that of all the other laminates.
- In the flexural test, it is clear that GFRP-SSWM at the middle layer has an ultimate stress and breaking load of 95 MPa and 520 N, respectively, which is higher than that of the other composites.
- In the inter-delamination test, a breaking load of 180 N and ultimate strength of 36 MPa were obtained for GFRP-SSWM at the middle layer, which is found to be greater than the other laminates.
- Similarly, in the drop-weight impact test, more impact energy is absorbed by the GFRP-SSWM at the middle layer that is higher and has less impression on the laminate compared to the other laminates.
- The treatment of the metallic surface may also contribute to an improvement of the wire/matrix interface. From this morphology study, it is evident that SSWM is a reinforcement material in the epoxy matrix.
- It was found that the GFRP- SSWM at the middle layer provides better results compared to the other laminates. Hence, the introduction of stainless-steel mesh in the middle layer improves the mechanical properties of GFRP.

6 REFERENCES

[1] B. D. Agarwal, L. J. Broutman, Analysis and performance of fibre composites, 2nd ed., John Wiley& Sons, 1990

[2] C. Soutis, Carbon fibre reinforced plastics in aircraft construction, Materials Science and Engineering, A, 412 (**2005**), 1–2, 171–176, doi:10.1016/j.msea.2005.08.064

[3] K. Friedrich, Z. Lu, A. M. Hager, Recent advances in polymer composites tribology, Wear, 190 (**1996**) 2, 139–144, doi:10.1016/0043-1648(96)80012-3

[4] P. B. Mody, T.W. Chou, K. Friedrich, Effect of testing conditions and microstructure on the sliding wear of graphite fibre/PEEK matrix composites, Journal of Materials Science, 23 (**1988**) 12, 4319–4330

[5] S. Carmisciano, I. M. De Rosa, F. Sarassini, A. Tamburrano, Basalt woven fibre reinforced vinyl ester composites: Flexural and electrical properties, Materials and Design, 32 (**2011**) 1, 337–342, doi:10.1016/j.matdes.2010.06.042

[6] T. Wittek, T. Tanimoto, Mechanical properties and fire retardance of bi-directional reinforced composite based on biodegradable starch resin and basalt fibres, Express Polymer Letter, 2 (**2008**) 11, 810–822, doi:10.3144/expresspolymlett.2008.94

[7] G. R. Villanueva, W. J. Cantwell, The high-velocity impact response of composite and FML-reinforced sandwich structures, Composite Science and Technology, 64 (**2004**) 1, 35–54, doi:10.1016/S0266-3538(03)00197-0

[8] A. Asundi, Y. N. Choi Alta, Fibre-metal laminates an advanced material for future aircraft, Journal of Materials Processing Technology, 63 (**1997**) 1–3, 384–394. doi:10.1016/S0924-0136(96)02652-0

[9] J. J. C. Remmers, R. D. Borst, Delamination Buckling of fibre–metal laminates, Composite Science and Technology, 6 (**2001**) 15, 2207–2213, doi:10.1016/S0266-3538(01)00114-2

[10] P. P. Camacho, C. M. L.Tavanas, R. De Oliveiro, A. T. Mangues, A. J. M. Fesseiro, Increasing the efficiency of composite single shear lap joints using bonded inserts, Composites Part B: Engineering, 36 (**2005**) 5, 372–383, doi:10.1016/j.compositesb.2005.01.007

[11] L. Fratini, V. F. Ruisi, Self-piercing riveting for aluminium alloys-composite hybrid joints, The International Journal of Advanced Manufacturing Technology, 43 (**2009**), 61–66, doi:10.1007/s00170-008-1690-3

[12] Z. Huang, S. Sugiyama, J. Yaragimoto, Hybrid joining the process for carbon fibre reinforced thermosetting plastic and thin metallic sheets by chemical bonding and plastic deformation, Journal of Materials Processing Technology, 213 (**2013**), 1864–1874, doi:10.1016/j.jmatprotec.2013.04.015

[13] H. Hasselbruch, A.Von Hehl, H. W. Zoch, Properties and failure behaviour of hybrid wire mesh/carbon fibre reinforced thermoplastic composites under quasi-static tensile load, Materials and Design, 66 (**2015**), 429–436, doi:10.1016/j.matdes.2014.07.032

[14] M. I. Ismail, Q. Payam Shafigh, Md. Zamin Jumaat, A. Ibrahim Abdull, Z. Ibrahim,U. Johnson Alengaram, The use of wire mesh–epoxy composite for enhancing the flexural performance of concrete beams, Materials and Design, 60 (**2014**) 11, 250–259, doi:10.1016/j.matdes.2014.03.075

[15] V. S. Sreenivasan, D. Ravindran,V. Manikandan, R. Narayanasamy, Mechanical properties of randomly oriented short Sansevieria cylindrica fibre/polyester composites, Materials and Design, 32 (**2011**) 4, 2444–2455, doi:10.1016/j.matdes.2010.11.042

[16] D. Soulioti, N. Barkoula, A. Paipetis, T. Matikas, Effects of fibre geometry and volume fraction on the flexural behaviour of steel-fibre reinforced concrete, Strain, 47 (**2011**) 1, 535–541, 10.1111/j.1475-1305.2009.00652.x

[17] M. I. Okereke, Flexural response of polypropylene/ E-glass fibre reinforced unidirectional composites, Composites Part B: Engineering, 89 (**2016**), 388–396. doi:10.1016/j.compositesb. 2016.01.007

UDK 621.73.042:669.715:620.172.21
Original scientific article/Izvirni znanstveni članek

ISSN 1580-2949
MTAEC9, 51(3)463(2017)

LOAD DETERMINATION BY ANALYSING THE STRESS STATE FOR THE OPEN-DIE FORGING OF THE ALUMINIUM ALLOY AlMgSi0.5

DOLOČANJE OBREMENITVE Z ANALIZO NAPETOSTNEGA STANJA PRI PROSTEM KOVANJU ALUMINIJEVE ZLITINE AlMgSi0,5

Mileta Janjić, Milan Vukčević, Nikola Šibalić, Sreten Savićević

University of Montenegro, Faculty of Mechanical Engineering, Cetinjska 2, 81000 Podgorica, Montenegro
mileta@ac.me

Prejem rokopisa – received: 2016-05-19; sprejem za objavo – accepted for publication: 2016-06-03

doi:10.17222/mit.2016.092

This paper deals with the stress state for the open-die forging of a staggered axial-symmetric specimen of the aluminium alloy AlMgSi0.5. The experimental-theoretical method of visioplasticity, adjusted for the process of open-die forging, consisted of five steps. The basic equations of the plasticity theory, i.e., balance equation, conditions of a plastic flow and Levy-Mises equations are applied. The basic partial differential equations of visioplasticity are obtained theoretically, while the displacement of points of the meridian cross-section, which represents the basis for its solution, can be experimentally obtained. The deformation force is calculated on the basis of the obtained results and is compared to the experimental values.

Keywords: visioplasticity, strain rate, stress, deformation force, displacement, tensor

Članek obravnava napetostno stanje pri prostem kovanju stopničastega osnosimetričnega vzorca iz aluminijeve zlitine AlMgSi0,5. Eksperimentalno-teoretična metoda, prilagojena postopku prostega kovanja, je setavljena iz petih korakov. Uporabljena je bila osnovna enačba teorije plastičnosti: ravnotežna enačba, pogoji plastičnega tečenja in Levy-Misesove enačbe. Osnovna parcialna diferencialna enačba vizioplastičnosti je dobljena teoretično, medtem ko se premik meridiana prečnega preseka, kar predstavlja osnovo za njeno rešitev, lahko dobi eksperimentalno. Sila deformacije je izračunana na osnovi dobljenih rezultatov in je primerjana z eksperimentalno dobljenimi vrednostmi.

Ključne besede: vizioplastičnost, raztezek, trgalna hitrost, napetost, sila deformacije, premik, tenzor

1 INTRODUCTION

The use of numerical methods for the deformation parameters' calculation is constantly being enhanced by the increment of simplicity of usage, the development of advanced software, reducing the time for the preparation of input data and obtaining of a wide spectrum of output information. Beside this, the questions asking whether the entry data were correctly taken and are the obtained results valid always are being raised.[1,2] For this purpose, it is necessary to develop or adapt the experimental–theoretical methods serving to verify the numerically obtained results.[1,3] There were many attempts by several authors to determine the stress state for a volumetric deformation, such as setting of a mesh at the specimen's cross-section before the deformation and a comparison with a deformed mesh,[4–6] determination of a deformed image of the cross-section after the deformation process,[7,8] use of the Upper Bound Elemental Technique (UBET),[9] etc.

One of the methods for the determination of the stress state is the visioplasticity method.[10,11] This is an experimental–theoretical method based on the known kinematic parameters of the deformation process. This method enables the analysis of plane and axial-symmetric problems in the processing by deformation. The method uses the basic equations of the theory of plasticity: balance equations, conditions of a plastic flow and equations by Levy-Mises.

The procedure of the calculation of the tensor stress components by the visioplasticity method can be divided into five steps:

- Deformation of the specimen and preparation for the reading of point displacements of the meridian cross-section,
- Determination of the strain tensor components,
- Determination of the strain rate tensor components,
- Solution of the basic equation for visioplasticity,
- Determinations of stress tensor components.

There are three different variants of this method. The differences are conditioned by the deformation processes and the manner of the experimental determination of displacements of points of a specimen's cross-section. This paper presents the originally adjusted method of visioplasticity, adjusted to open-die forging.

2 THEORETICAL BASICS

2.1 Stresses

The stress tensor for an axial-symmetrical problem has the following shape: ($\tau_{r\theta} = \tau_{\theta z} = 0$):[12]

$$T_\sigma = \begin{vmatrix} \sigma_r & 0 & \tau_{rz} \\ 0 & \sigma_\theta & 0 \\ \tau_{rz} & 0 & \sigma_z \end{vmatrix} \quad (1)$$

and the balance equations are:

$$\left.\begin{aligned} \frac{\partial \sigma_r}{\partial r} + \frac{\partial \tau_{rz}}{\partial z} + \frac{\sigma_r - \sigma_\theta}{r} = 0 \\ \frac{\partial \tau_{rz}}{\partial r} + \frac{\partial \sigma_z}{\partial z} + \frac{\tau_{rz}}{r} = 0 \end{aligned}\right\} \quad (2)$$

The effective stress [42,67] is:

$$\sigma_e = \frac{1}{\sqrt{2}} \sqrt{(\sigma_r - \sigma_\theta)^2 + (\sigma_\theta - \sigma_r)^2 + (\sigma_r - \sigma_z)^2 + 6\tau_{rz}^2} \quad (3)$$

and the average normal stress is equal to:

$$\sigma_a = \frac{1}{3}\left(\sigma_r + \sigma_\theta + \sigma_z\right) \quad (4)$$

The stress intensity has major importance in the theory of plastic flow because on the basis of the biggest deformation energy spent for the shape change, an elementary part changes from the elastic into plastic state when the stress intensity reaches the boundary value. From (3), it follows that:

$$(\sigma_r - \sigma_\theta)^2 + (\sigma_\theta - \sigma_r)^2 + (\sigma_r - \sigma_z)^2 + 6\tau_{rz}^2 = 2\sigma_e^2 \quad (5)$$

which represents the condition of plastic flow for an axial-symmetric stress state.

2.2 Strain

There is no displacement in the tangential direction for the axial-symmetric state and the changes of two other displacements in this direction are:[12]

$$u_\theta = 0, \quad \frac{\partial u_r}{\partial \theta} = 0, \quad \frac{\partial u_z}{\partial \theta} = 0 \quad (6)$$

The stress tensor for the axial-symmetric deformation state is:

$$T_\varepsilon = \begin{vmatrix} \varepsilon_r & 0 & \frac{1}{2}\gamma_{rz} \\ 0 & \varepsilon_\theta & 0 \\ \frac{1}{2}\gamma_{rz} & 0 & \varepsilon_z \end{vmatrix} \quad (7)$$

The components of the strain tensor are:

$$\left.\begin{aligned} \varepsilon_r = \frac{\partial u_r}{\partial r} \quad \gamma_{r\theta} = 0 \\ \varepsilon_\theta = \frac{u_r}{r} \quad \gamma_{\theta z} = 0 \\ \varepsilon_z = \frac{\partial u_z}{\partial z} \quad \gamma_{rz} = \frac{\partial u_r}{\partial z} + \frac{\partial u_z}{\partial r} \end{aligned}\right\} \quad (8)$$

The effective strain is:

$$\varepsilon_e = \frac{\sqrt{2}}{3} \sqrt{(\varepsilon_r - \varepsilon_\theta)^2 + (\varepsilon_\theta - \varepsilon_z)^2 + (\varepsilon_r - \varepsilon_z)^2 + 3/2\gamma_{rz}^2} \quad (9)$$

2.3 Strain rates

Analogously with the previous tensor, the tensor of strain rates for the axial-symmetric state is:[12]

$$T_{\dot\varepsilon} = \begin{vmatrix} \dot\varepsilon_x & \frac{1}{2}\dot\gamma_{xy} & \frac{1}{2}\dot\gamma_{xz} \\ \frac{1}{2}\dot\gamma_{xy} & \dot\varepsilon_y & \frac{1}{2}\dot\gamma_{yz} \\ \frac{1}{2}\dot\gamma_{xz} & \frac{1}{2}\dot\gamma_{yz} & \dot\varepsilon_z \end{vmatrix} \quad (10)$$

The components of the strain-rate tensor in a cylindrical coordinate system, on the basis of [8], are:

$$\left.\begin{aligned} \dot\varepsilon_r = \frac{\partial v_r}{\partial r} \quad \dot\gamma_{r\theta} = 0 \\ \dot\varepsilon_\theta = \frac{v_r}{r} \quad \dot\gamma_{\theta z} = 0 \\ \dot\varepsilon_z = \frac{\partial v_z}{\partial z} \quad \dot\gamma_{zr} = \frac{\partial v_r}{\partial z} + \frac{\partial v_z}{\partial r} \end{aligned}\right\} \quad (11)$$

The effective strain rate is:

$$\dot\varepsilon_e = \frac{\sqrt{2}}{3} \sqrt{(\dot\varepsilon_r - \dot\varepsilon_\theta)^2 + (\dot\varepsilon_\theta - \dot\varepsilon_z)^2 + (\dot\varepsilon_r - \dot\varepsilon_z)^2 + 3/2\dot\gamma_{rz}^2} \quad (12)$$

In the cylindrical coordinate system for the axial-symmetric state, the equations by Levy-Mises are as follows:

$$\left.\begin{aligned} \dot\varepsilon_z = \lambda'(\sigma_z - \sigma_{sr}) = \frac{\partial v_z}{\partial z} \\ \dot\varepsilon_\theta = \lambda'(\sigma_\theta - \sigma_{sr}) = \frac{v_r}{r} \\ \dot\varepsilon_r = \lambda'(\sigma_r - \sigma_{sr}) = \frac{\partial v_r}{\partial r} \\ \dot\gamma_{rz} = 2\lambda'\tau_{rz} = \frac{\partial v_r}{\partial z} + \frac{\partial v_z}{\partial r} \end{aligned}\right\} \quad (13)$$

The coefficient of proportionality of λ' in [13] is:

$$\lambda' = \frac{3}{2}\frac{\dot\varepsilon_e}{\sigma_e} \quad (14)$$

3 EQUATION OF VISIOPLASTICITY

By combining of first two equations from Equation (13) the following can be written:

$$\dot\varepsilon_z - \dot\varepsilon_r = \lambda'(\sigma_z - \sigma_r) \quad (15)$$

which gives the following:

$$\sigma_z = \frac{\dot\varepsilon_z - \dot\varepsilon_r}{\lambda'} + \sigma_r \quad (16)$$

By differentiating the above equation with respect to r for constant z and θ we obtain the following:

$$\frac{\partial \sigma_z}{\partial r} = \frac{\partial \sigma_r}{\partial r} + \frac{\partial}{\partial r} \cdot \left(\frac{\dot{\varepsilon}_z - \dot{\varepsilon}_r}{\lambda'} \right) \tag{17}$$

From the first system balance equation (2) we obtain the following:

$$\frac{\partial \sigma_r}{\partial r} = -\frac{\sigma_r - \sigma_\theta}{r} - \frac{\partial \tau_{zr}}{\partial z} \tag{18}$$

while from the second and third equations the relation of the stress and strain rates of the system can be obtained (13):

$$\begin{aligned} \sigma_r &= \frac{\dot{\varepsilon}_r}{\lambda'} - \sigma_{sr} \\ \sigma_\theta &= \frac{\dot{\varepsilon}_\theta}{\lambda'} - \sigma_{sr} \end{aligned} \tag{19}$$

Substituting (19) into (17) we obtain:

$$\frac{\partial \sigma_r}{\partial r} = \left(\frac{\dot{\varepsilon}_\theta - \dot{\varepsilon}_r}{\lambda' r} \right) - \frac{\partial \tau_{sr}}{\partial z} \tag{20}$$

If the above expression is replaced into equation (17) we obtain the following expression:

$$\frac{\partial \sigma_z}{\partial r} = -\frac{\dot{\varepsilon}_z - \dot{\varepsilon}_\theta}{\lambda'} - \frac{\partial \tau_{zr}}{\partial z} + \frac{\partial}{\partial r} \left(\frac{\dot{\varepsilon}_z - \dot{\varepsilon}_r}{\lambda'} \right) \tag{21}$$

Since from the fourth equation of the Levy-Mises system (13):

$$\tau = -\frac{\dot{\gamma}_{rz}}{2\lambda'} \tag{22}$$

then equation (21) takes the following shape:

$$\frac{\partial \sigma_z}{\partial r} = \frac{\partial}{\partial r} \left(\frac{\dot{\varepsilon}_z - \dot{\varepsilon}_r}{\lambda'} \right) - \frac{\dot{\varepsilon}_z - \dot{\varepsilon}_\theta}{\lambda' r} - \frac{\partial}{\partial z} \left(\frac{\dot{\gamma}_r}{2\lambda'} \right) \tag{23}$$

Substituting Equation (14) for λ' into equation (23) we obtain:

$$\frac{\partial \sigma_z}{\partial r} = \frac{2}{3} \sigma_e \frac{\partial}{\partial r} \left(\frac{\dot{\varepsilon}_z - \dot{\varepsilon}_r}{\dot{\varepsilon}_e} \right) - \frac{\dot{\varepsilon}_r - \dot{\varepsilon}_\theta}{r \dot{\varepsilon}_e} - \frac{1}{2} \frac{\partial}{\partial z} \left(\frac{\dot{\gamma}_{zr}}{\dot{\varepsilon}_e} \right) \tag{24}$$

Equation (24) represents the gradient of an axial stress, which depends on the strain rates and the effective stress at every point of the deformation zone. This is the basic equation of visioplasticity.

The components of the strain rates and the effective stress are determined experimentally so as to, using the defined mathematical operations via Equation (24), obtain the value of an axial stress in the relevant points of a deformable body volume. The only point where the axial stress cannot be determined is for $r = 0$, because Equation (24) becomes undefined. However, because of the process symmetry at this point, the following applies:

$$\frac{\partial \sigma_z}{\partial r} = 0 \tag{25}$$

From the above it can be seen that the problem of determining the axial component of stress in the process of the axial-symmetric deformation is reduced to the problem of determining the components of the strain rates, the effective stress and the effective strain in the deformation zone.

With knowledge of the axial stress at each point of body volume, it is easy to obtain other components of the stress using the Levy-Mises equations (13):

$$\begin{aligned} \sigma_r &= \sigma_z + \frac{2}{3} \sigma_e \left(\frac{\dot{\varepsilon}_r - \dot{\varepsilon}_z}{\dot{\varepsilon}_e} \right) \\ \sigma_\theta &= \sigma_z + \frac{2}{3} \sigma_e \left(\frac{\dot{\varepsilon}_\theta - \dot{\varepsilon}_z}{\dot{\varepsilon}_e} \right) \\ \tau_{rs} &= \frac{\sigma_e}{3} \frac{\dot{\gamma}_{rz}}{\dot{\varepsilon}_e} \end{aligned} \tag{26}$$

4 STUDY TOPIC

The research was carried out in laboratory conditions, which were adjusted to be as similar as possible to the manufacturing conditions.[7,8]

The staggered axial-symmetric processing body with two levels of height from upper and one level on the lower partition plane is adopted (**Figure 1**).

Aluminium alloy AlMgSi0.5, the chemical composition of which is given in **Table 1,** is used as a test material.

Table 1: Chemical composition AlMgSi0.5 in mass fractions (*w*/%)
Tabela 1: Kemijska sestava AlMgSi0,5, v masnih odstotkih (*w*/%)

Fe	Si	Ti	Cu	Zn	V	Cr	Mn	Mg	Ni
0.207	0.477	0.01	0.09	0.068	0.004	0.01	0.1	0.493	0.02

The testing is carried out at the hot processing temperature: T = 440 °C. The deformation is accomplished with a constant velocity: v = 2 mm/s. Graphite grease is used for the lubrication.

The experiment is carried out on the machine for the static testing with a hydraulic drive.

The upper and lower dies are used as tools (**Figure 1**), located in a slideway, which ensures their coaxiality

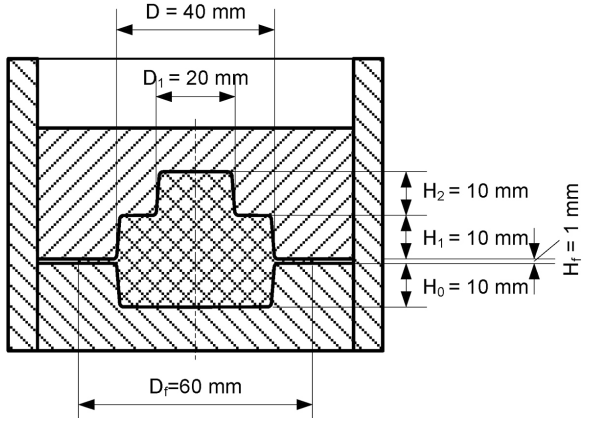

Figure 1: System: tools workpiece
Slika 1: Sistem: orodje-obdelovanec

and has the role of a chamber for the maintenance of a constant temperature. The slideway is heated together with the die and the specimens.

The dies are made of tool steel for work in hot state designated by X38CrMoV-5-1.[13]

The specimen dimensions are: $\varnothing\, d_0 \times h_0 = 33{\times}33{,}94$ mm. The specimen's height is calculated from the condition of volume constancy.

5 DETERMINATION OF THE STRESS STATE

5.1 Determination of kinematic field using the specimen volume

The basis for the determination of a stress state using the visioplasticity method is the familiarity of the kinematic field. Two kinds of process can be differentiated:[10]

- stationary (drawing, milling, direct extrusion),
- non-stationary (opposite extrusion, squeezing in open dies).

For stationary processes, it is characteristic that the elements of the kinematic and stress fields in one unmovable point of space where the process is carried out are independent of time. Therefore, the kinematic field can be determined experimentally in any time (phase). Also, the duration of the phase is also not important under the assumption of the constant strain rate. For the non-stationary processes, the kinematic and stress fields in one unmovable space point where the deformation is carried out, are changed over time. In such a processes, the analyses of one defined increment of deformation cannot give an image about the kinematic and stress field for the entire process time, but only for the observed increment. Therefore, it is necessary to determine the interval (phase) at the end of which the stress state can be determined in the specimen volume.

The determination of the kinematic field necessary for solving the basic equation of visioplasticity (24) is carried out experimentally. It is possible to determine the components of the displacement velocities on the basis of the measured values of the displacements of the meridian cross-section points according to [7, 8]:

$$\left.\begin{aligned} v_r &= \frac{\Delta u_r}{\Delta t} \\ v_z &= \frac{\Delta u_z}{\Delta t} \end{aligned}\right\} \tag{27}$$

The constant deformation state is the assumption for such a method of determination.

The displacements of the points in the radial and axial directions are determined on the basis of known numerical value coordinates of the mesh nodes (**Figure 2**):

$$\left.\begin{aligned} u_r &= r - r_0 \\ u_z &= z - z_0 \end{aligned}\right\} \tag{28}$$

where:

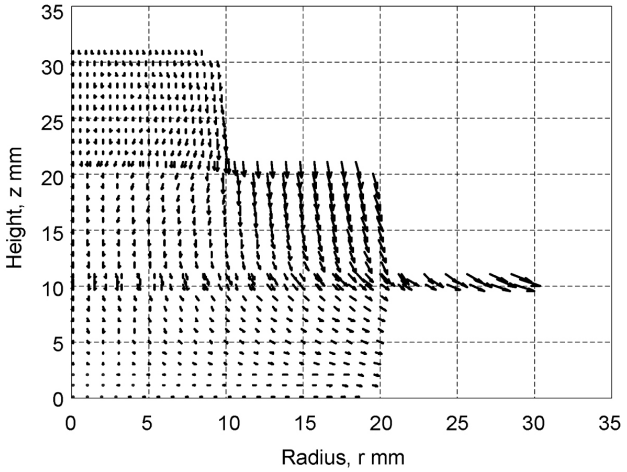

Figure 2: Displacements of cross-section points of the deformed mesh
Slika 2: Premiki točk preseka v deformirani mreži

u_r, u_z are the displacements in radial and axial directions at the end of the process,

r, z are the coordinates of node points at the end of the process,

r_0, z_0 are the coordinates of node points at the start of the process.

In this way it is possible to determine the partial derivations of displacements using the radius, serving to obtain the deformation values.[8,9]

The determination of the displacement velocity represents the basis of the kinematic analysis. Since the deformation process in an open die is a non-stationary process, the displacement velocities are determined on the basis of the displacements of points at the start and at the end of a finite interval of the deformation at the end of the deformation process, under the assumption of a constant deformation velocity. This interval must be small enough to represent the true state of the displacement velocities, but not too small so as to avoid the impact of the anisotropy of deformation. Based on the preliminary experiments, it was proved that the optimal interval of deformation at the end of the process for the increment of a tool step of $\Delta z = 2$ mm.[14]

At the beginning of the adopted interval, it was necessary to determine the deformed mesh of the specimen's radial cross-section. The deformation process is stopped at the flash height of $h_f = 3$ mm. The process of preparation of the specimen's cross-section, and the measurement of the lines of the deformed mesh is the same as for the determination of the deformations.

On the basis of the known values of the nodal point coordinates in the deformed and non-deformed mesh at the start of the observed interval, the displacements of the points in the radial and axial directions are determined:

$$\left.\begin{aligned} u_{ra} &= r_a - r_0 \\ u_{za} &= z_a - z_0 \end{aligned}\right\} \tag{29}$$

where:

u_{ra}, u_{za} are the displacements in the radial and axial directions at the start of the observed deformation interval, and r_a, z_a are the coordinates of the nodal points at the start of the observed deformation interval.

The increase of the displacements in the nodal points of the deformed mesh is calculated as the difference in the displacements at the end and the start of the observed interval:

$$\left.\begin{aligned}\Delta u_{ra} &= u_r - u_{ra} = r - r_a = \Delta r\\ \Delta u_z &= u_z - u_{za} = z - z_a = \Delta z\end{aligned}\right\} \tag{30}$$

where: Δu_r, Δu_z are the increments of displacements in radial and axial direction, and Δr, Δz are the increments of the coordinates.

Having in mind that the deformation velocity is constant at v = 2 mm/s, and for the adopted tool step increment Δz = 2 mm the time increment is:

$$\Delta t = \frac{\Delta z}{v}\, s \tag{31}$$

It is possible to determine the components of the displacement velocity (27) on the basis of the values of the displacements of nodal points in the deformed mesh of the meridian cross-section (**Figure 3**):

$$\left.\begin{aligned}v_r &= \frac{\Delta u_r}{\Delta t} = \frac{\Delta r}{\Delta t}\\ v_z &= \frac{\Delta u_z}{\Delta t} = \frac{\Delta z}{\Delta t}\end{aligned}\right\} \tag{32}$$

where: v_r, v_z are the displacement velocities in the radial and axial directions.

Using the knowledge of the kinematic field, i.e., the distribution of displacement velocities, it is possible to determine the displacement velocities for the points of the meridian cross-section according to [11], while the effective strain rate is determined using Equation (12). The partial derivations are determined for the small enough values Δr, Δz and Δt on the basis of the following Equations (33), (34) and (35):

$$\frac{\partial v_r}{\partial r} = \frac{\Delta v_r}{\Delta r} \tag{33}$$

$$\frac{\partial v_z}{\partial z} = \frac{\Delta v_z}{\Delta z} \tag{34}$$

$$\frac{\partial v_r}{\partial z} + \frac{\partial v_z}{\partial r} = \frac{\Delta v_r}{\Delta z}\frac{\Delta v_z}{\Delta z} \tag{35}$$

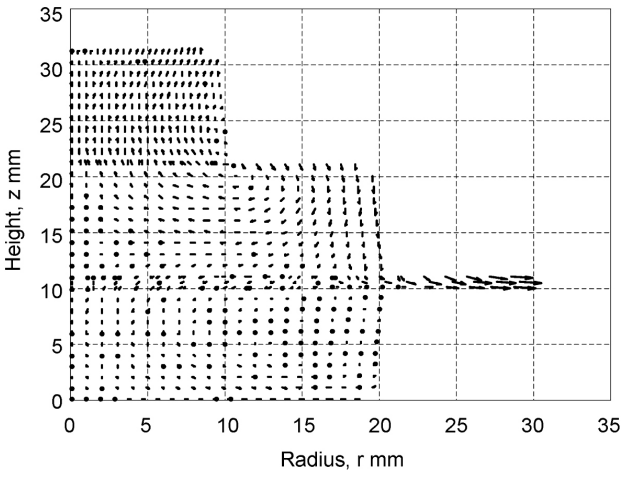

Figure 3: Vectors of the displacement velocities at certain points of the cross-section

Slika 3: Vektorji hitrosti premika določenih točk na preseku

5.2 Determination of the stress components

The distribution of an axial stress σ_z in planes z = const. is obtained by the integration of the basic visioplasticity Equation (24):

$$\sigma_z = \int_0^r \frac{2}{3}\sigma_e \left[\frac{\partial}{\partial r}\left(\frac{\dot\varepsilon_z - \dot\varepsilon_r}{\dot\varepsilon_e}\right) - \left(\frac{\dot\varepsilon_r - \dot\varepsilon_\theta}{r\dot\varepsilon_e}\right) - \frac{1}{2}\frac{\partial}{\partial z}\left(\frac{\dot\gamma_{zr}}{\dot\varepsilon_e}\right)\right] \mathrm{d}r + C_1 \tag{36}$$

To obtain the absolute values of the axial stresses, it is necessary to determine the integral constant C_1. From the first equation of the system (26) it is necessary to obtain an expression for an axial stress at each point of the deformation zone as in the following Equation (37):

$$\sigma_z = \sigma_r - \frac{2}{3}\sigma_e\left(\frac{\dot\varepsilon_r - \dot\varepsilon_z}{\dot\varepsilon_e}\right) \tag{37}$$

The radial stress σ_r is not known for the complete deformation zone, but in the free area in the flash cross-section it is equal to zero, which means that the axial stress can be determined in that cross-section. If the first term from Equation (36) for a axial stress is designated with $\Delta\sigma_z$, the following Equation (38) can be written:

$$\sigma_z = \Delta\sigma_z + C_1 \tag{38}$$

The integral constant at the point of the free area at the end of the flash can be obtained in the following way:

$$C_1 = \sigma_z\Big|_{\left(\substack{z=z_f\\ r=r_f}\right)} - \Delta\sigma_z\Big|_{\left(\substack{z=z_f\\ r=r_f}\right)} \tag{39}$$

On the basis of known values σ_z, the values of other components of the stress tensor can be obtained from Equation (26).

5.3 Solving the basic visioplasticity equation

The method is based on a calculation of the axial stress component σ_z by solving the basic visioplasticity Equation (24), where the main problem is the determination of integral constant C_1 (Equation (36)). Having in mind that the integration of the visioplasticity equation is done with a radius, the value of the axial stress component at one point of radius r for a particular value of the height y must be known in order to determine the integral constant C_1. The only points where it is possible

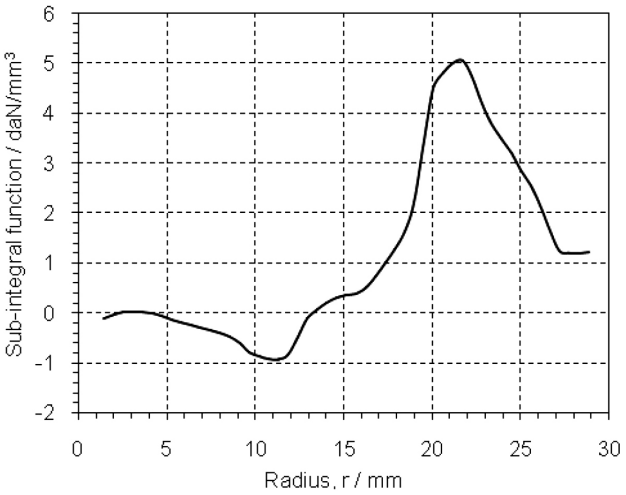

Figure 4: Sub-integral function of the visioplasticity equation for the cross-section of the partition plane

Slika 4: Podintegralna funkcija enačbe vizioplastičnosti na preseku delilne ravnine

to determine the value of the axial stress component are the points for the maximum values of the radius on the flash level (**Figure 1**). These values are determined on the basis (37) form the condition that the radial stress component in these points is equal to zero: $\sigma_r = 0$. Other deformation kinematic parameters are known, where the effective stress is determined from the corresponding curved strengthening for the value of the effective strain.

The value of the sub-integral function of Equation (36) is known because all the strain and kinematic parameters and the effective stress are known, and they are presented in **Figure 4**. Using the integration of this function on r, the indefinite integral given in **Figure 5** is obtained, and the integral constant is determined in a previously described way.

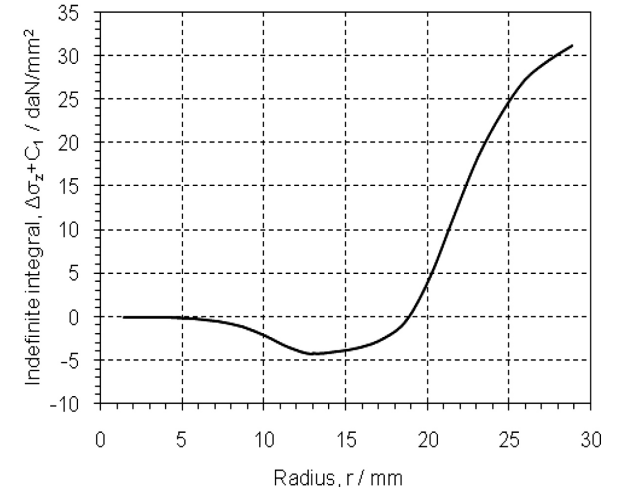

Figure 5: Undefined integral of the visioplasticity equation $\Delta\sigma_z + C_1$ at the cross-section of the partition plane

Slika 5: Nedoločeni integral enačbe vizioplastičnosti $\Delta\sigma_z + C_1$ na preseku delilne ravnine

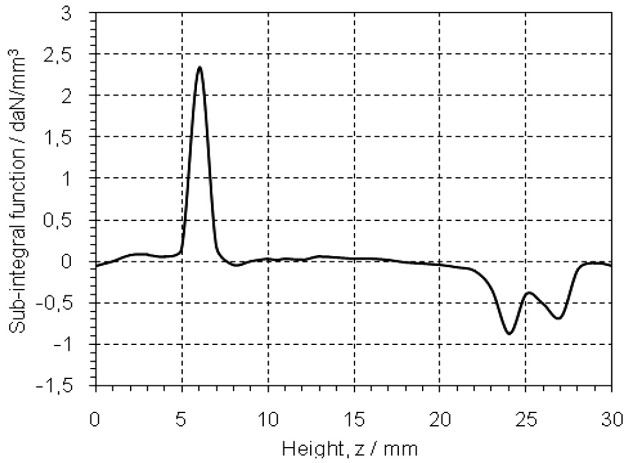

Figure 6: Sub-integral function of the second equation for the specimen's axis

Slika 6: Podintegralna funkcija druge enačbe za os vzorca

The integral constant is impossible to determine because of the unknown radial stress at other points. For this reason, on the basis of the system balance Equation (2), it follows that:

$$\sigma_z = \int_0^z \left(\frac{\partial \tau_{rz}}{\partial r} + \frac{\tau_{rz}}{r} \right) dz + C_2 \tag{40}$$

If the first term of the previous expression is marked with $\Delta\sigma_{z0}$, then the following can be written:

$$\sigma_z \Big|_{\left(\substack{z=z_f \\ r=0}\right)} = \Delta\sigma_z \Big|_{\left(\substack{z=z_f \\ r=0}\right)} + C_2 \tag{41}$$

and so:

$$C_2 = \sigma_z \Big|_{\left(\substack{z=z_f \\ r=0}\right)} - \Delta\sigma_{z0} \Big|_{\left(\substack{z=z_f \\ r=0}\right)} \tag{42}$$

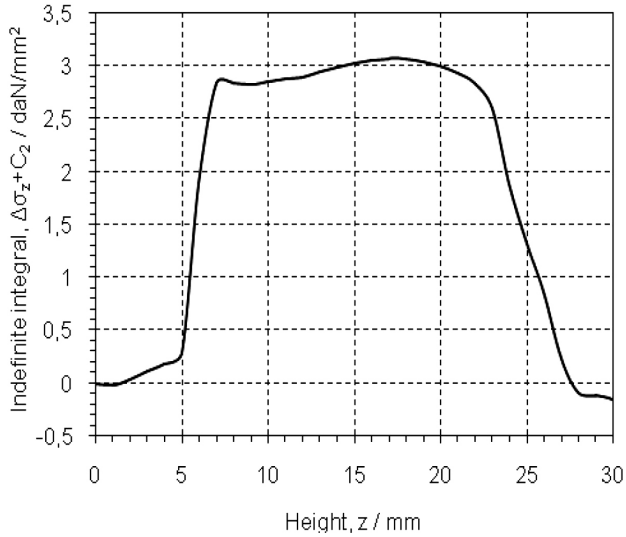

Figure 7: Indefinite integral of the second balance equation $\Delta\sigma_{z0} + C_2$ in the specimen's axis

Slika 7: Nedoločni integral druge ravnotežne enačbe $\Delta\sigma_{z0} + C_2$ na osi vzorca

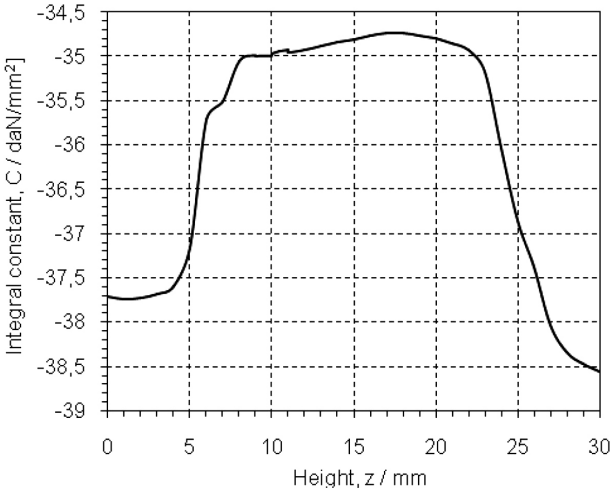

Figure 8: Integral constant C as a function of the height z
Slika 8: Konstanta integrala C v funkciji višine z

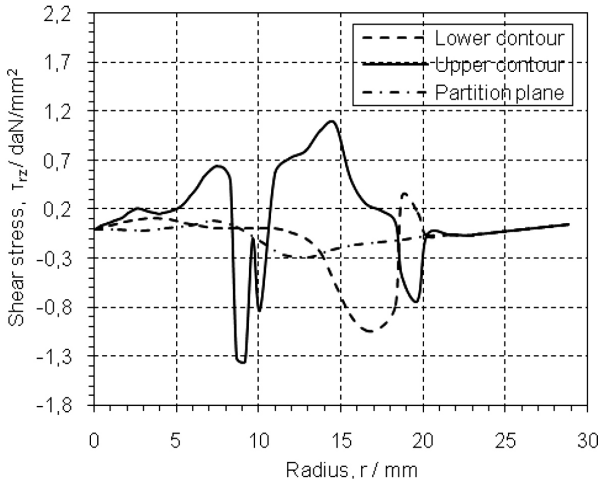

Figure 10: Shear stress τ_{rz}
Slika 10: Strižna napetost τ_{rz}

In this way, all the values of the axial stress component in the axis of the specimen's symmetry are obtained, i.e., r = 0 mm, which actually represents the possibility for a determination of the integral constant for all the values of the height z.

The values of the sub-integral function (40) as a function of the height are given at **Figure 6**, and the values of indefinite integral for r = 0 mm in **Figure 7**.

The integral constant is determined on the basis of:

$$\sigma_z\Big|_{\left(\substack{z\\r=0}\right)} = \Delta\sigma_z\Big|_{\left(\substack{z\\r=0}\right)} + C \tag{43}$$

and so:

$$C = \sigma_z\Big|_{\left(\substack{z\\r=0}\right)} - \Delta\sigma_{z0}\Big|_{\left(\substack{z\\r=0}\right)} \tag{44}$$

which is graphically represented in **Figure 8** as a function of the height z.

The values of the normal stress at all the points of the specimen's meridian cross-section are obtained in the previously described way, and other tensor components are determined on the basis of relations (26). The values of the axial and shear stress using the upper and lower contour of the specimen's contour, and in the cross-section of the partition plane, are given in **Figure 9** and **Figure 10**.

MATLAB has developed the program for a determination of all the stress parameters for the specimen's cross-section using the visioplasticity method, all numerical integrations and for the determination of the integral constants. As the entry data, besides the curve of strengthening and the geometrical parameters, the program uses the output results from the strain and kinematic analyses.

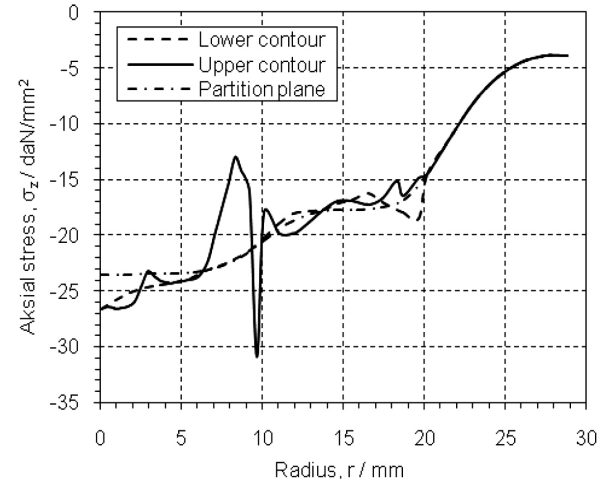

Figure 9: Axial stress σ_z
Slika 9: Napetost v osi σ_z

6 DEFORMATION FORCE

The familiarity with the stress state in the specimen's meridian plane enables the determination of deformation force. Also, this value, in a relatively simple way, can be experimentally measured with a high accuracy and can be used for an estimation of the accuracy of the stress deformation analysis. In this case it is the z-axis direction and the stress components that are the axial and shear stress. The deformation force is calculated as a sum of the integrals using the area of change of the mentioned stress components:[12]

$$F_m = \int_A \sigma_z \, \mathrm{d}A + \int_A \tau_{rz} \, \mathrm{d}A \tag{45}$$

Figure 11 presents the experimentally obtained deformation forces during the process and the values of the forces at the end of the deformation process calculated using the visioplasticity method on the basis of the determined stress state for the upper contour, the lower contour and the cross-section of the partition plane. On the basis of the law of static balance of a body, the forces obtained for the upper and lower die should be the same; however, certain deflections emerge because of

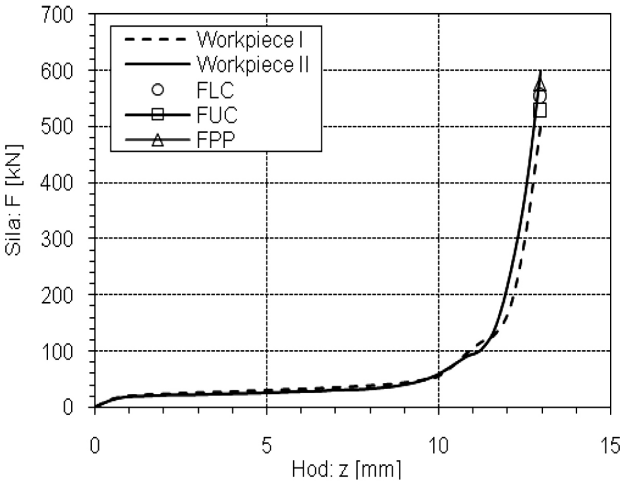

Figure 11: Deformation forces as a function of motion
Slika 11: Sile deformacije v odvisnosti od premika

the calculation errors. These deflections are relatively small, which indicates that the forces are determined with a satisfactory accuracy.

7 CONCLUSION

This paper deals with the stress state for the open-die forging process for an axial-symmetric specimen made of the aluminium alloy AlMgSi0.5. The originally adjusted, experimental–theoretical visioplasticity method for the open-die forging.

The visioplasticity method consists of five steps. Using the basic equations of the plasticity theory, i.e., balance equation, condition of plastic flow, and Levy-Mises equation, enables the obtaining of the basic visioplasticity equation. The starting basis is made of experimentally determined displacements of the points of the meridian cross-section.

When solving the basic visioplasticity equation, the determination of the integral constant represents the main problem. It is calculated for the cross-section of the partition plane because an axial stress is known at the free end of the flash and it is equal to the flow stress. Then the axial stress along the specimen axis and integral constant on the basis of the known axial stress in the cross-section of partition plane and z axis. After this, an axial stress in all cross-sections is determined, and the integral constants on the basis of known values of the stress along the z axis.

The deformation force, as the sum of the integrals for the area of normal and shear stress for the upper contour, the lower contour and the cross-section of the partition plane, is obtained on the basis of the obtained results. The obtained values are: F_u = 529 kN, F_l = 555 kN, F_p = 576 kN. The experimentally measured values at the end of the deformation process are: F_I = 500.66 kN in F_{II} = 600.35 kN. The deflections of the experimental values are in range of 16.61 %, and for the calculated values on the basis of the stress state obtained by the visioplasticity method 8.16 %, and they are between the minimum and maximum experimental values of the experimental values of the deformation force at the end of the process.

It can be concluded that the adapted visioplasticity model for the determination of the stress state for the open-die forging gives the results that overlap well with the experimental results, so that it can be applied to other families of axial-symmetry specimens made of different materials.

Acknowledgements

This work was carried out as a part of the research on the project: RTPPIMS&NS, number: 01-376, funded by The Ministry of Science of Montenegro.

APPENDIX

T_σ stress tensor
σ_r radial normal stress
σ_z axial normal stress
σ_θ tangential normal stress
τ_{rz} radial-axial shear stress
σ_e axial normal stress
σ_a average normal stress
u_r radial displacement
u_z axial displacement
u_θ tangential displacement
T_ε strain tensor
ε_r radial normal strain
ε_z axial normal strain
ε_θ tangential normal strain
γ_{rz} radial-axial shear strain
ε_e effective strain
$T_{\dot\varepsilon}$ strain rate tensor
$\dot\varepsilon_r$ radial strain rate
$\dot\varepsilon_z$ axial strain rate
$\dot\varepsilon_\theta$ tangential strain rate
$\dot\gamma_{rz}$ radial-axial strain rate
$\dot\gamma_\theta$ effective strain rate
λ' coefficient of proportionality
T temperature
v deformation velocity
d_0 diameter of specimen
h_0 height of specimen
D basic diameter of workpiece
D_1 diameter of second degree of workpiece
D_f diameter of flash
h_f height of flash
H_0 height of lower degree under the partition plane of workpiece
H_1 height of first degree above the partition plane of workpiece
H_2 height of second degree above the partition plane of workpiece
v_r radial displacement velocity

v_z axial displacement velocity
u_r radial displacement
u_z axial displacement
r radial coordinate
z axial coordinate
r_0 radial coordinate at the start of the deformation process
z_0 axial coordinate at the start of the deformation process
Δr radial increment
Δz axial increment
Δt time increment
u_{ra} radial displacement at the start of the observed deformation interval
u_{za} axial displacement at the start of the observed deformation interval
r_a radial coordinate at the start of the observed deformation interval
z_a axial coordinate at the start of the observed deformation interval
Δu_r radial increment of displacement
Δu_z axial increment of displacement
C, C_1, C_2 integral constants
F_m maximum deformation force
F_u deformation force for the upper contour of the workpiece
F_1 deformation force for the lower contour of the workpiece
Fp deformation force for the partition plane of workpiece
FI experimental measured deformation force for workpiece I
FII experimental measured deformation force for workpiece II

8 REFERENCES

[1] V. Mandic, D. Adamovic, Z. Jurkovic, M. Stefanovic, M. Zivkovic, S. Ranđelovic, T. Marinkovic, Numerical FE Modelling of the Ironing Process of Aluminium Alloy and its Experimental Verification, Transactions of FAMENA, 34 (**2010**) 4, 59–69

[2] P. Harley, I. Pillinger, Numerical simulation of the forging process, Computer Methods in Applied Mechanics and Engineering, 195 (**2006**) 48–49, 6676–6690, doi:10.1016/j.cma.2005.03.013

[3] V. Mandic, Physical and numerical modeling of deformation processing, University of Kragujevac - Faculty of Engineering Sciences, 2012, 27

[4] J. Danckert, T. Wanheim, The use of a square grid as an alternative to a cirkular grid in the determination of strains, Journal of Mechanical Working Technology, 3 (**1979**), 5–15, doi:10.1016/0378-3804(79)90028-7

[5] S. Alexandrov, An analysis of the Axisymmetric Compression of Viscous Materials, Journal of Material Processing Technology, 105 (**2000**) 3, 278–283, doi:10.1016/S0924-0136(00)00652-X

[6] R. Sowerby, E. Chu, J. L. Duncan, Determination of large strains in metal forming, Journal of Strain Analysis, 17 (**1982**) 2, 95–101

[7] M. Janjic, M. Vukcevic, N. Sibalic: Strain modelling at axi-symmetrical deformation process in open dies, Proc. of the 11th International Research/Expert Conference: Trends in the Development of Machinery and Associated Technology, Hammamet, 2007, 115–118

[8] M. Janjic, S. Savicevic, M. Vukcevic, N. Sibalic: Experimental discretization for determination of strain state. http://www.mech-ing.com/journal/Archive/2013/10/41_Janjic_mtm13.pdf, 01.10.2013

[9] M. Vukcevic, M. Janjic, V. Domazetovic: The influence of geometrical parameters in deforming of axys-symmetric workpieces in open dies, Proc. of the XXVI JUPITER Conference, Belgrade, 2000, 3.117–3.122

[10] M. Plancak, Stress-strain state in the processes of cold extrusion steel, Faculty of Technical Sciences, Novi Sad, 1984, 33

[11] L. Gusel, R. Rudolf, B. Kosec, Analysis of a strain rate field in cold formed material using the visioplasticity method, Metalurgija, 48 (**2009**) 2, 103–107

[11] B. Musafia, Applied theory of plasticity, University of Sarajevo, 1973, 13

[13] M. Plancak, D. Vilotic, Dies and tools for metal forming, Faculty of Technical Sciences, Novi Sad, 2011, 171

[14] M. Janjic, S. Savicevic, N. Sibalic: Analysis of kinematic state parameters by simulation and experimental method Proc. of the 16th International Research/Expert Conference: Trends in the Development of Machinery and Associated Technology, Dubai, 2012, 535–538

UDK 621.793:621.793.7:669.018
Original scientific article/Izvirni znanstveni članek

ISSN 1580-2949
MTAEC9, 51(3)473(2017)

INFLUENCE OF SCANNING SPEED ON THE INTERMETALLIC PRODUCED IN-SITU IN LASER-METAL-DEPOSITED TiC/Ti6Al4V COMPOSITE

VPLIV HITROSTI SKENIRANJA NA INTERMETALNO ZLITINO IZDELANO IN-SITU Z LASERSKO DEPOZICIJO TiC/Ti6Al4V KOMPOZITA

Rasheedat Modupe Mahamood[1,2], Esther Titilayo Akinlabi[1]

[1]University of Johannesburg, Department of Mechanical Engineering Science, Auckland Park, Kingsway Campus, Johannesburg 2006, South Africa
[2]University of Ilorin, Department of Mechanical Engineering, Tanke road 23400003, Nigeria
mahamoodmr2009@gmail.com

Prejem rokopisa – received: 2016-05-29; sprejem za objavo – accepted for publication: 2016-06-28

doi:10.17222/mit.2016.096

The effect of scanning speed on titanium aluminide Ti_3Al produced in-situ during laser metal deposited TiC/Ti6Al4V has been investigated and its effect on the microhardness and wear-resistance properties has been studied. In this study, the titanium alloy Ti6Al4V (an important aerospace alloy) was deposited in combination with titanium carbide TiC using a laser metal deposition process. The laser power was maintained at 3.2 kW throughout the deposition process. The powder flow rate and the gas flow rate were also kept at constant values of 2.88 g/min and 2 l/min, respectively. The scanning speed was varied between 0.015 and 0.105 m/s, and the influence of the scanning speed on the titanium aluminide (Ti_3Al) produced in-situ was studied, and its effect on the wear resistance behaviour was also investigated. The study revealed that as the scanning speed was initially increased, the Ti_3Al produced in-situ was found to increase and the wear resistance was found to improve. As the scanning speed was further increased beyond 0.06 m/s, the Ti_3Al produced and the wear resistance were found to decrease.

Keywords: laser metal deposition process, microhardness, microstructure, titanium alloy, Ti_3Al, wear resistance

Preiskovan je bil vpliv hitrosti skeniranja na in-situ nastanek titanovega aluminida – Ti3Al, izdelanega med lasersko depozicijo TiC/Ti6Al4V ter proučevan je bil njen vpliv na mikrotrdoto in obrabne lastnosti. V tej študiji je bila titanova zlitina –Ti6Al4V (pomembna zlitina za letalstvo), nanešena v kombinaciji s titanovim karbidom – TiC, s pomočjo postopka laserskega nanašanja. Med postopkom nanašanja je bila vzdrževana moč laserja pri 3,2 kW. Hitrosti toka prahu in toka plina sta bili zadržani pri konstantnih vrednostih 2,88 g/min in 2 l/min. Hitrost skeniranja se je spreminjala med 0,015 in 0,105 m/s. Študiran je bil vpliv hitrosti skeniranja na in-situ nastanek titanovega aluminide (Ti_3Al) ter njen vpliv na obnašanje pri obrabi. Študija je odkrila, da je začetno povečanje hitrosti skeniranja povečalo in-situ nastajanje Ti_3Al, povečala se je tudi odpornost proti obrabi. Pri nadaljnjem povečevanju hitrosti skeniranja nad 0,06 m/s, je bilo ugotovljeno zmanjšanje nastajanja Ti_3Al in zmanjšanje odpornosti proti obrabi.

Ključne besede: postopek nanašanja kovine z laserjem, mikrotrdota, mikrostruktura, titanova zlitina, Ti_3Al, odpornost proti obrabi

1 INTRODUCTION

Ti6Al4V is widely used in industry because of its good combination of properties, such as high specific strength, low density and good corrosion resistance. However, Ti6Al4V has a poor wear-resistance property owing to its chemical behaviour that tends to reduce its further application.[1,2] The surface property of the material can be modified in order to improve its wear resistance property. Different surface-treatment methods have been applied to titanium alloys in order to improve their wear-resistance property in the literature, such as physical vapour deposition, chemical vapour deposition and sol-gel methods.[3,4] The laser metal deposition (LMD) process, an additive manufacturing technique, is the most advantageous of all the methods. This is because a complex shaped part can be produced with the desired surface properties directly from the three-dimensional (3D) computer-aided-design (CAD) model of the part by adding material layer by layer.[5] LMD also has the flexibility to handle more than one material simultaneously, thereby making it possible to make a part with composite or functionally graded materials.

An intermetallic compound of Ti_3Al has been found to have several advantages, such as higher elastic modulus, lower density, better mechanical properties at elevated temperatures and higher oxidation resistance because it forms a surface-passivated alumina layer.[1] The intermetallic-matrix composites (IMCs) with ceramic particles are also found to possess higher specific strength, improved toughness, and high-temperature strength retention.[6,7] A lot of studies have been conducted in the literature on intermetallic compound reinforced ceramic composite as a result of the improved properties they offer.[8–10] In this work, a composite of TiC/Ti6Al4V was produced and Ti_3Al was formed

in-situ. The effect of scanning speed on the quantity of the Ti_3Al formed in-situ was studied and its influence on the microhardness and the wear-resistance properties was investigated in detail and reported.

2 EXPERIMENTAL PART

The powders used in this study are titanium alloy Ti6Al4V power of 99.6 % purity, supplied by VSMPO-AVISMA Corporation, Russia and TiC powder of 99.5 % purity and it was supplied by F. J. Brodmann and Co., L. L. C. Louisiana. The substrate material used is a 99.6 % pure Ti6Al4V, (72 × 72 × 5) mm sheet. The chemical compositions of the powders and the substrate are listed in **Table 1**. The TiC powder is of particle size range below 60 μm and the Ti6Al4V powder is of particle size range between 150 μm and 200 μm. The substrate was sandblasted and then degreased using acetone before the deposition processes: this is to improve the laser-energy absorption. A Kuka robot was used for the laser metal deposition experiment. The 4.0-kW Nd-YAG laser (Rofin Sinar) was attached to the robot's end effector with two coaxial powder-delivery nozzles. The experimental set-up also consists of a glove box, a table and a two-hoppers powder feeder. The experimental set-up is shown in **Figure 1**. The two powders were put in a separate hopper of the powder feeder and the powder flow rates were set to give 50 W % of TiC powder and 50 W % Ti6Al4V powder for the composite. Multiple tracks were produced at 50 % overlap. The laser power was set at 3.2 kW and maintained at that value throughout the deposition process. The powder flow rate and the gas flow rate were set and kept at constant values of 2.88 g/min and 2 L/min respectively. The scanning speeds were varied between 0.015 and 0.105 m/s. Argon gas was used to keep the oxygen level in the glove box below 10 ppm during the deposition process to prevent the atmospheric oxygen and nitrogen from contaminating the deposits. The laser metal deposition process was achieved by feeding the powders through the coaxial nozzles into the melt pool that was created on the substrate using the laser beam that forms the composite after the solidification of the melt pool. See **Figure 2** for the schematic of the laser metal deposition process.

Scanning electron microscopy (SEM), X-ray energy-dispersive spectroscopy (EDS) analysis, and X-ray diffraction (XRD) were used for the microstructures and phase analyses of the deposited samples respectively. Samples for the SEM and microhardness were sectioned laterally, mounted in hot resin, ground and polished using the standard metallographic techniques according to the ASTM E3 – 11, standard.[11] The SEM samples were etched using Kroll's reagent. The Kroll's reagent consists of 100 mL of water with 2 mL of hydrofluoric acid and 4 mL of nitric acid. The microhardness measurements were conducted using a Vickers indenter under a 300-g load and a dwell time of 15 s according to the ASTM E384 – 11e1 (2011) standard.[12] The wear tests were performed under dry conditions (no lubrication) using a ball-on-disk arrangement on a Cert tribotester. A Tungsten Carbide ball of 10 mm diameter was used at a load of 25 N, reciprocating frequency of 20 Hz and at a sliding distance of 2000 mm. The wear test was

Figure 1: Experimental set-up
Slika 1: Eksperimentalni sestav

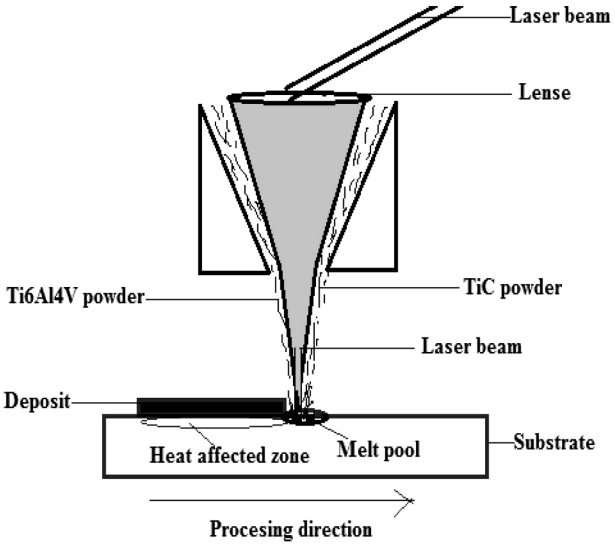

Figure 2: The schematic diagram of laser metal deposition process[14]
Slika 2: Shematski prikaz postopka laserskega nanašanja kovine[14]

performed according to the ASTM G133 – 05(2010) standard.[13] The schematical diagram of the laser metal deposition process is based on R. M. Mahamood et al.[14]

Table 1: Chemical composition of the Ti6Al4V substrate, Ti6Al4V powder and TiC powder

Tabela 1: Kemijska sestava podlage iz Ti6Al4V, Ti6Al4V prahu in TiC prahu Ti6Al4V substrate

Element	Al	V	Fe	C	N_2	H_2	O_2	Ti
w/%	6.42	3.91	0.19	0.008	0.006	0.004	0.155	balance

Ti6Al4V powder

Element	Al	V	Fe	C	N_2	H_2	O_2	Ti
w/%	6.20	3.90	0.18	0.008	0.005	0.005	0.150	balance

TiC Powder

Element	C	O_2	N_2	Fe	Al	Na	Ti
w/%	19.5	0.28	0.4	0.045	0.03	0.026	balance

3 RESULTS AND DISCUSSION

The morphologies of the Ti6Al4V and TiC powders are shown in **Figures 3a** and **3b** respectively. The micrograph of the Ti6Al4V substrate is shown in **Figure 3c**. The Ti6Al4V powder is characterized by spherically shaped powder particles, which is typical of a gas-atomized powder.[15] Spherically shaped, gas-atomized powder is more favoured in the laser metal deposition process because of its improved absorption of the laser rays.[15] The TiC powder is a ball-milled powder with an irregular shape, which is the characteristics of any ball-milled powder. The Ti6Al4V substrate is characterized by alpha (light contrast) and beta (dark contrast) phases, as shown in **Figure 3c**.

The results of the intermetallic of Ti_3Al (in percentage), the average Vickers hardness number and the wear-volume loss are presented in **Table 2**.

Table 2: Results

Tabela 2: Rezultati

Sample designation	Scanning speed (m/s)	Ti_3Al (%)	Average Vickers hardness number	Wear volume (mm^3)
A	0.015	5	386	0.098
B	0.025	6	390	0.082
C	0.035	8	420	0.08
D	0.045	12	448	0.07
E	0.055	13	449	0.061
F	0.065	15	460	0.058
G	0.075	12	469	0.071
H	0.085	10	475	0.086
I	0.095	5	489	0.082
J	0.105	4	498	0.1
Substrate	0	0	300	0.178

The graph of the Ti_3Al intermetallic against the scanning speed is shown in **Figure 4a**. The graph of the average Vickers hardness against the scanning speed is shown in **Figure 4b**. The wear volume is plotted against the scanning speed and is shown in **Figure 4c**. The combined graph of the Ti_3Al intermetallic and the wear volume is shown in **Figure 4d**. The Ti_3Al intermetallic

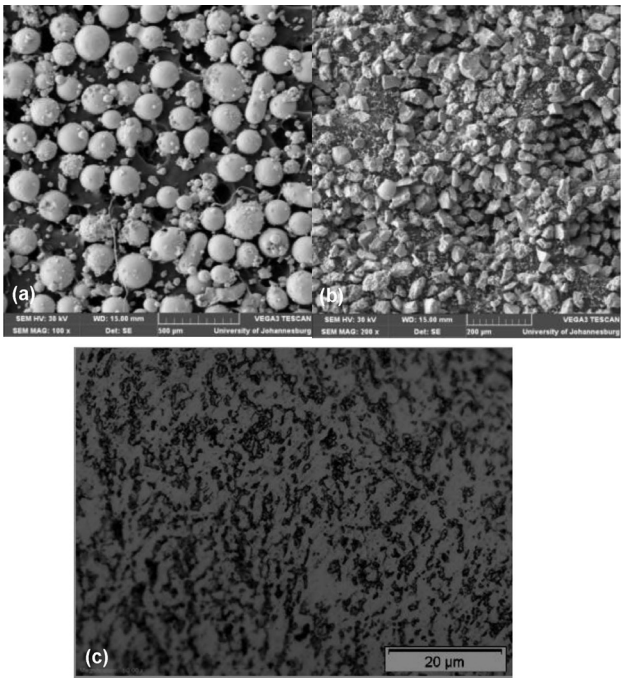

Figure 3: a) Morphology of the Ti6Al4V powder, b) morphology of the TiC powder, c) micrograph of the Ti6Al4V substrate

Slika 3: a) Morfologija prahu Ti6Al4V, b) morfologija prahu TiC, c) mikrostruktura podlage iz Ti6Al4V

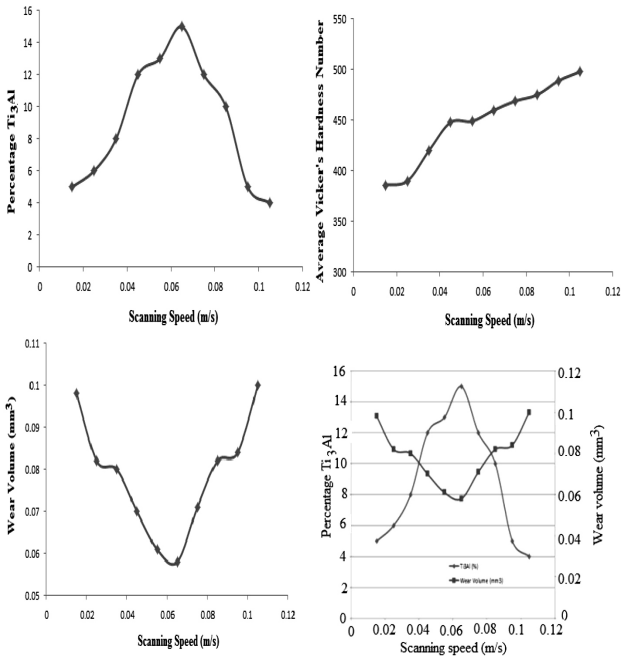

Figure 4: Graph of scanning speed and: a) percentage Ti_3Al, b) average Vickers hardness, c) wear volume, d) percentage Ti_3Al and wear volume

Slika 4: Diagrami odvisnosti hitrosti skeniranja in: a) odstotka Ti3Al, b) povprečne trdote po Vickersu, c) volumna obrabe, d) odstotka Ti_3Al in volumna obrabe

was found to increase as the scanning speed was initially increased. The maximum Ti_3Al intermetallic was seen at a scanning speed of 0.065 m/s with a value of 15 %. As the scanning speed was increased beyond 0.065 m/s, the Ti_3Al intermetallic was seen to start decreasing. Our earlier study also revealed that as the scanning speed was increased, the wear resistance was found to be increased and then decrease as the scanning speed was further increased. The reason for this was attributed to the unmelted carbide (UMC) particles, whose size and quantity were found to be responsible for the wear behaviour of the laser metal deposited TiC/Ti6Al4V composite.[16] The present investigation shows that it was not only the unmelted carbide particles that were responsible for the wear-resistance behaviour, the Ti_3Al intermetallic formed also contributed to it. The XRD analysis (**Figure 5**) revealed that the Ti_3Al intermetallic was changing with the change in the scanning speed, and it is also found to have an effect on the wear-resistance behaviour, as shown in **Figure 4a**. The higher quantity of Ti_3Al intermetallic was seen to improve the wear resistance behaviour of the TiC/Ti6Al4V composites. The Ti_3Al intermetallic is formed as a result of the solid-state phase transformation of the primary α phase structure at a low scanning speed. At a low scanning speed, the laser material interaction time is longer and the melt pool created is larger, thereby causing the solidification and cooling time to be longer and thus allowing a small quantity of the Ti_3Al to be formed. As the scanning speed was increased, the laser material interaction time was reduced and the melt pool produced is smaller. This promotes the rapid solidification and the cooling rate of the melt pool that favours a larger quantity of Ti_3Al being formed. As the scanning speed was further increased beyond 0.065 m/s, the percentage Ti_3Al was found to be reduced. This may be because of improper melting of the TiC powder at these higher scanning speeds. If the scanning speed is too large, the laser material interaction time will be very short and this may result in improper melting of the powders. Also, because the melt pools created at such high scanning speeds are very small, this will result in the formation of a small quantity of the Ti_3Al intermetallic. Since intermetallic compounds are produced from the solid-state reaction of the solidified melted powders and if the quantity of the melted powder is reduced as a result of high scanning speeds, it follows that the quantity of the Ti_3Al intermetallic formed will be reduced. On the other hand, the microhardness was found to continue to increase as the scanning speed was increased, as shown in **Figure 4b**. This is because of the insufficient melting of the TiC powder particles as a result of the low laser material interaction time that resulted in the production of larger unmelted carbide particles. The increase in the microhardness values even at much higher scanning speeds may be as a result of these unmelted carbide particles. The large particles of the unmelted TiC carbide are detrimental to the wear-resistance properties and that is why the wear resistance properties are found to be reducing as the scanning speed was increased beyond 0.065 m/s. The large unmelted TiC particles cause damage to the

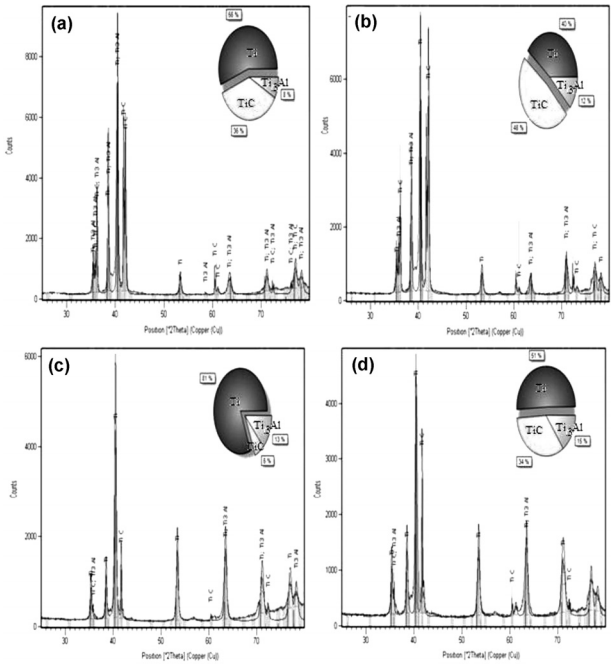

Figure 5: The XRD analysis of the sample at the scanning speed of: a) 0.035 m/s, b) 0.045 m/s, c) 0.055 m/s, d) 0.065 m/s

Slika 5: Rentgenogram vzorca pri hitrosti skeniranja: a) 0,035 m/s, b) 0,045 m/s, c) 0,055 m/s in d) 0,065 m/s

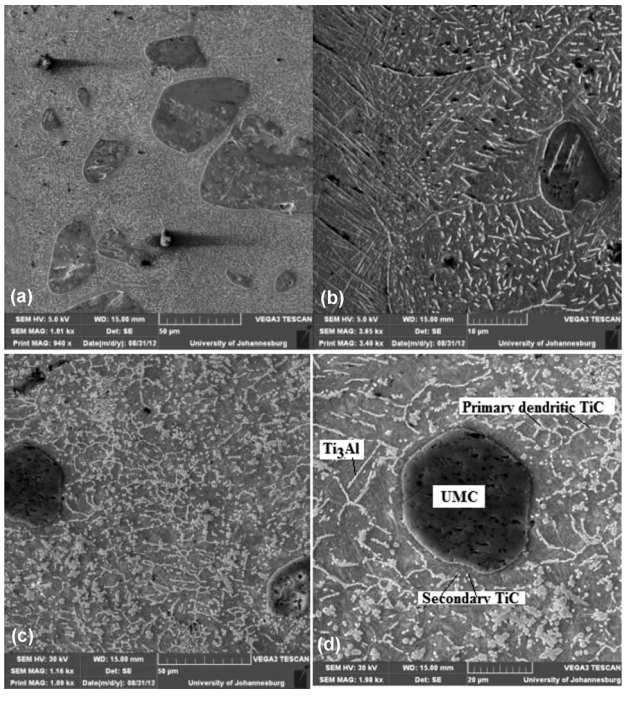

Figure 6: SEM micrograph of the sample at: a) 0.025 m/s, b) higher magnification of sample in a), c) 0.065 m/s, d) higher magnification of sample in c)

Slika 6: SEM-posnetek vzorca pri: a) 0,025 m/s, b) vzorec a) pri večji povečavi, c) 0,065 m/s, d) vzorec c) pri večji povečavi

sliding surface as a result of the cutting and tearing actions of these large unmelted TiC particles during the rubbing actions.

Also, as shown in a previous study, as the scanning speed was increased, the size and the quantity of the unmelted TiC particles also increased, which formed a powder lubricant that inhibits the wear action as the sliding action progresses.[16] The Ti_3Al also mimics the behaviour of the unmelted carbide action as it is also hard and brittle, which also forms a powder lubricant as the sliding wear action continues, due to rubbing and grinding of the Ti_3Al and the unmelted carbide particles (**Figue 6**) as the wear action continues. The particle size of these Ti_3Al intermetallic and the smaller unmelted TiC carbide particles are reduced in size as they are rubbed against one another during the wear experiment. This unmelted TiC and the Ti_3Al intermetallic particles were ground by the rubbing surfaces of the deposited sample and the tungsten carbide ball to form fine powder. The fine powder now forms a protective layer between the rubbing surfaces, which prevents the two surfaces from being in contact, thereby forming a powdery lubricant between the two surfaces and thus, reducing the wear action.

The wear track of the parent material is shown in **Figure 7a**. It is characterized by parallel ploughing grooves, as shown in **Figure 7a**, and their formation is as a result of the combination of abrasive wear, adhesive wear and plastic deformation.[16] The wear tracks of the samples at 0.015 m/s are shown in **Figure 7b**, while that of the sample at a scanning speed of 0.065 m/s is shown in **Figure 7c** and the wear track of the sample at the scanning speed of 0.105 m/s is shown in **Figure 7d**. At a low scanning speed, the UMC and the Ti_3Al seen in the microstructure are less than those seen at the higher scanning speed. Both the UMC and the Ti_3Al serve as reinforcement in the composite. The smaller number of these reinforcements does not really improve the wear resistance because they are serving as a third-body wear mechanism that results in cutting of the surfaces in sliding motion, as seen in **Figure 7b**. The size of the UMC is smaller at a scanning speed of 0.065 m/s when compared to those seen at higher scanning speeds. Also, the quantities of the UMC are more than those seen at a lower scanning speed, where most of the TiC powder is completely melted. The quantity of the Ti_3Al is also more at the scanning speed of 0.065 m/s, thereby resulting in improved wear-resistance behaviour (**Figure 7c**). This is because the UMC particles and the Ti_3Al are ground into finer powder as the sliding action progresses because they are hard and brittle. The powder they form serves as a protective layer (and as powder lubricant), which tends to reduce the wear action of the two surfaces in the sliding motion. The size of the UMC particles seen at the scanning speed of 0.105 m/s is larger than those seen at the lower scanning speed because of the lower laser material interaction time at the higher scanning speed. There was not enough time to melt the surfaces of the TiC powder particles at the higher scanning speed, thereby leaving behind larger UMC TiC particles. Also, the quantity of the UMC TiC particles as well as the Ti_3Al intermetallic is fewer than those seen at the scanning speed of 0.065 m/s. These large UMC TiC particles cause cracking of the surfaces in the sliding motion, thereby escalating the wear action as shown in **Figure 7d**.

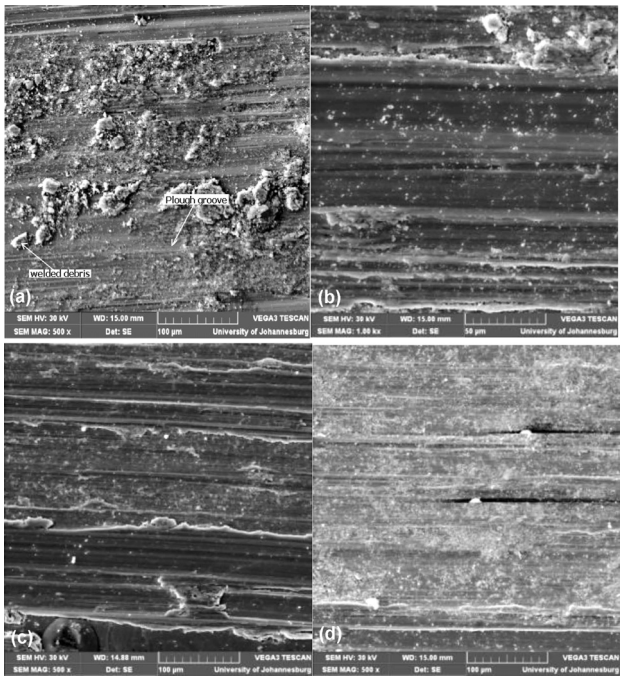

Figure 7: SEM micrograph of the wear track of the: a) substrate[16], b) sample at the scanning speed of 0.015 m/s, c) sample at the scanning speed of 0.065 m/s, d) sample at the scanning speed of 0.105 m/s

Slika 7: SEM-posnetek sledi obrabe na: a) podlagi[16], b) vzorec pri hitrosti skeniranja 0,015 m/s, c) vzorec pri hitrosti skeniranja 0,065 m/s, d) vzorec pri hitrosti skeniranja 0,105 m/s

4 CONCLUSION

A study of the influence of the scanning speed on an Ti_3Al intermetallic produced in-situ during a laser metal deposition process has been conducted. The scanning speed was varied between 0.015 m/s and 0.105 m/s. The evolving microstructures were studied; microhardness and wear test were also performed. The effect of the quantity of the Ti_3Al on the wear-resistance property was investigated. Qualitative metallographic analyses of the microstructures confirmed that during the solidification and cooling processes of the deposited samples, the Ti6Al4V and the TiC powders were transformed into various phases, including the intermetallic phase of Ti_3Al. Also, the secondary phase of Ti_3Al is formed in-situ by chemical reactions between the Ti6Al4V and the TiC. The intensive phase transformations that occurred, during the solidification and cooling down process, resulted in the various quantities of the Ti_3Al

produced, which was found to initially increase as the scanning speed was increased and then reduce as the scanning speed was further increased. The wear test conducted revealed that the wear-resistance property initially increased as the scanning speed was increased and then decreased as the scanning speed was increased beyond 0.065 m/s. Also, the maximum Ti_3Al observed also occurred at the same scanning speed and it was found to be 15%. It can be concluded that, the optimum scanning speed for the best wear-resistance performance of the laser metal deposited Ti6Al4V and TiC composite is 0.065 m/s for the set of other processing parameters considered in this study.

Acknowledgments

This work is supported by L'Oreal UNESCO for Women in Science and the University of Johannesburg Research Council.

5 REFERENCES

[1] C. H. J. Hager, J. H. Sanders, S. Sharma, Unlubricated gross slip fretting wear of metallic plasma-sprayed coatings for Ti6Al4V surfaces, Wear, 3/4 (**2008**) 265, 439–451

[2] W. Pang, H. C. Man, T. M. Yue, Laser surface coating of Mo–WC metal matrix composite on Ti6Al4V alloy, Materials Science and Engineering A, 1/2 (**2005**) 390, 144–153

[3] F. Variola, J. H. Yi, L. Richert, J. D. Jwues, F. Rosei, A. Nanci, Tailoring the surface properties of Ti6Al4V by controlled chemical oxidation, Biomaterials, 10 (**2008**) 29, 1285–1298

[4] M. M. Silva, M. Ueda, L. Pichon, H. Reuther, C. M. Lepienski, Surface modification of Ti6Al4V alloy by PIII at high temperatures: Effects of plasma potential, Nuclear Instruments and Methods in Physics Research B, 1/2 (**2007**) 257, 722–726

[5] J. Scott, N. Gupta, C. Wember, S. Newsom, T. Wohlers, T. Caffrey, Additive manufacturing: status and opportunities, Science and Technology Policy Institute, (2012), https://www.ida.org/stpi/occasionalpapers/papers/AM3D_33012_Final.pdf

[6] C. Li-Fang, Z. Yong-Zhong, S. Li-Kai, Microstructure and formation mechanism of titanium matrix composites coating on Ti-6Al-4V by laser cladding, Rare Metals, 4 (**2007**) 26, 342–346

[7] J. D. Majumdar, I. Manna, A. Kumar, Direct laser cladding of Co on Ti-6Al-4V with a compositionally graded interface, Journal of Materials Processing Technology, 209 (**2009**), 2237–2243

[8] R. Mahmoodian, M. A. Hassan, M. Hamdi, R. Yahya, R.G. Rahbari, In situ TiC–Fe–Al2O3–TiAl/Ti3Al composite coating processing using centrifugal assisted combustion synthesis, Composites Part B: Engineering, 59 (**2014**), 279–28

[9] Z. Liu, X. Zhang, F. Xuan, Z. Wang, S. Tu, Effect of laser power on the microstructure and mechanical properties of TiN/Ti_3Al composite coatings on Ti6Al4V, Chinese Journal of Mechanical Engineering , 26 (**2013**) 4, 714–721

[10] B. G. Guo, J. S. Zhou, S. T. Zhang, H. D. Zho, Y. P. Pu, J. M. Chen, Microstructure and tribological properties of in situ synthesized TiN/Ti3Al intermetallic matrix composite coatings on titanium by laser cladding and laser nitriding. Mater Science Engineering A, 480 (**2008**), 404–10

[11] E3–11 (2011). Standard Guide for Preparation of Metallographic Specimens, ASTM international Book of Standards, vol. 03.01

[12] ASTM E384 – 11e1, 2011, Standard Test Method for Knoop and Vickers Hardness of Materials, ASTM International Book of Standards, vol. 03.01

[13] ASTM G133 – 05, 2010, Standard Test Method for Linearly Reciprocating Ball-on-Flat Sliding Wear, ASTM International Book of Standards, vol. 03.02

[14] R. M. Mahamood, E. T. Akinlabi, M. Shukla, S. Pityana, Characterization of Laser Deposited Ti6A4V/TiC Composite. Lasers in Engineering, 29 (**2014**) 3–4, 197–213

[15] C. T. Schade, T. F. Murphy, Chris Walton, Development Of Atomized Powders for Additive Manufacturing, Powder Metallurgy Word Congress, (2014). Accessed on 2nd July 2014 available at: http://www.gkn.com/hoeganaes/media/Tech%20Library/Schade-Atomized%20Powders%20for%20Additive%20Manufacturing%20%281%29.pdf

[16] R. M. Mahamood, E. T. Akinlabi, M. Shukla and S. Pityana, Scanning Velocity Influence on Microstructure, Microhardness and Wear Resistance Performance on Laser Deposited Ti6Al4V/TiC Composite, Materials and Design, 50 (**2013**), 656–666

UDK 69.059.7:69.01:624.011.1
Original scientific article/Izvirni znanstveni članek

ISSN 1580-2949
MTAEC9, 51(3)479(2017)

METODA REKONSTRUKCIJE ZIDANIH STAVB Z NOTRANJIM JEDROM IZ KRIŽNO LEPLJENIH LESENIH PLOŠČ

RECONSTRUCTION OF MASONRY BUILDINGS WITH AN INNER CORE MADE OF CROSS-LAMINATED TIMBER PANELS

Andrej Štrukelj[2], Aleš Perjet[1], Erika Kozem Šilih[2]

[1]2BUILD4U, Tacenska cesta 125E, 1000 Ljubljana, Slovenija
[2]Univerza v Mariboru, Fakulteta za gradbeništvo, prometno inženirstvo in arhitekturo, Katedra za gradbene konstrukcije, Smetanova 17, 2000 Maribor
andrej.strukelj@um.si

Prejem rokopisa – received: 2016-06-14; sprejem za objavo – accepted for publication: 2016-06-29

doi:10.17222/mit.2016.107

Članek opisuje tehnologijo izvedbe nove metode rekonstrukcije starih, potresno neodpornih, zidanih stavb, in sicer na način, da v notranjost zidanih stavb vstavimo novo sekundarno leseno konstrukcijo iz križno lepljenih lesenih masivnih plošč (kot notranje jedro stavbe) in jo ustrezno spojimo s staro, primarno zidano, konstrukcijo. S tem načinom utrdimo prvotno potresno neodporno zidano konstrukcijo z novo leseno konstrukcijo, ki prevzame celotno potresno obremenitev. V članku je na vzorčnem primeru zidane stavbe predstavljena tehnologija izvedbe konstrukcijskih ukrepov in računska analiza. Z izračuni smo dokazali možnost utrditve zidane stavbe z ustreznim spajanjem z novim notranjim lesenim jedrom in doprinos izvedenega posega z gradbeno-fizikalnega vidika.

Ključne besede: rekonstrukcija, zidane stavbe, križno lepljene lesene konstrukcije

The article describes the technology of performing a new reconstruction method for old seismically unsafe masonry buildings in such a way that a new secondary timber construction made of cross-laminated massive timber panels (as the inner core of the building) is embedded in the interior of the masonry buildings and appropriately connected to the old primary masonry construction. With this method the primary, seismically unsafe masonry construction is retrofit with the new timber construction, which resists the entire seismic load. In the article the calculation analysis and the technology of performing construction measures are presented on a case-study masonry building. With a numerical study we have shown the possibility of strengthening an existing building by connecting it with the new inner core as well as the contribution of the intervention to the building-physics aspects.

Keywords: reconstruction, masonry buildings, cross laminated timber panels

1 UVOD

Na splošno lahko ugotovimo, da je zaradi nekakovostne gradnje ali neustreznega vzdrževanja stanje posameznih vrst obstoječih zgradb v Sloveniji, predvsem stanovanjskih, relativno slabo.[1] Takšni objekti zaradi energetske neučinkovitosti povzročajo škodo zaradi onesnaževanja okolja, obenem pa zaradi potresno neodporne gradnje predstavljajo grožnjo za življenje ljudi.[1] Tipičen primer potresno neodporne stanovanjske zgradbe je večetažna nearmirana zidana konstrukcija, zgrajena v obdobju od leta 1920 do 1965. Takšnih naj bi bilo v Sloveniji skoraj 30 % celotnega stanovanjskega fonda. Ko k temu prištejmo še zidane stavbe iz starejših obdobij, kamor spada večina stavb kulturne dediščine, se omenjeni delež takšnih konstrukcij precej poveča.[2] Pri rekonstrukciji takšnih objektov pa se lahko srečamo z zahtevo, da se ne dovoljujejo posegi v zunanji izgled objekta (spomeniškovarstvene zahteve). Pri mnogih tradicionalnih metodah protipotresnih rekonstrukcij stavb je vprašljiva ohranitev zunanjega prvotnega izgleda stavbe. Te metode lahko obenem tudi narekujejo ukrepe, ki še dodatno obremenijo staro konstrukcijo, kar pomeni, da moramo zaradi protipotresnih posegov povečati nosilnost vsem konstrukcijskim elementom vse do temeljev,[2] v zgradbo pa se dovede dodatna vlaga (armiranobetonski ometi, armiranobetonski estrihi, injektiranje ipd.), kar povzroča slabe klimatske pogoje v zgradbi. Ko se srečamo s pogojem, da obstoječih starih konstrukcij ne smemo dodatno obremeniti (npr. zaradi slabih temeljev) ali da moramo upoštevati spomeniškovarstvene zahteve po ohranitvi zunanjega izgleda stavbe, lahko rekonstrukcijo stavbe izvedemo z novim jedrom iz masivnih križno lepljenih (X-lam, CLT) lesenih plošč, ki se uporabljajo za gradnjo sodobnih, tudi večnadstropnih lesenih zgradb. X-lam plošče uvrščamo med masivne konstrukcije, enako kot opečne ali betonske konstrukcije,[3] vendar pa so bistveno lažje in bolj enostavne za montažo, obenem pa so sposobne prenašati velike obremenitve. Zaradi križno orientiranih lamel lahko te plošče obremenitev prenašajo v dveh pravokotnih smereh, kar omogoča, da se uporabljajo kot ploskovni nosilni elementi konstrukcije.[4] Ob ustrezni povezavi stenskih in stropnih plošč v celotno konstrukcijo z veznimi sredstvi lahko dosežemo, da plošče, ki se uporabljajo za stenske elemente, prevzamejo veliko horizontalno obremenitev tako v ravnini stene kot pravokotno nanjo, s čimer zagotovimo odlično potresno odpornost zgradbe. X-lam plošče so zaradi

lepljenih stikov med posameznimi lamelami zelo toge v svoji ravnini. Pri prenosu potresne obtežbe se tako večina deformacij izvede v veznih sredstvih, tj. jeklenih kotnikih, vijakih in žebljih.[5–7]

2 METODA REKONSTRUKCIJE

2.1 Opis tehnologije izvedbe konstrukcijskih in nekonstrukcijskih ukrepov

Novo metodo rekonstrukcije potresno neodporne zidane stavbe izvedemo na način, da v njeno notranjost vstavimo jedro iz X-lam plošč s ciljem, da bo nova konstrukcija prenašala vse obtežbe in bo nudila podporo prvotnemu obstoječemu zidovju v primeru potresne obremenitve. Tako dodatno ne obremenjujemo obstoječih konstrukcij, niti ne posegamo v zunanji izgled stavbe.

Prikaz tehnologije in numerično študijo izvedemo na vzorčnem primeru objekta stare zidane stavbe pravilne oblike, simetrične na obe glavni osi, tlorisnih dimenzij X = 10 m in Y = 8 m, etažnosti P + 1 in skupne višine zidov (brez strešja) 5,64 m. Stavba je bila pred rekonstrukcijo stenasta konstrukcija škatlastega tipa. Temelji so bili kamniti, nosilno zidovje je bilo nearmirano, zidano iz polne opeke običajnega formata in malte, debelina zidov je 38 cm. Stropne konstrukcije so bile lesene, sestavljene iz stropnikov, za katere so bili narejeni utori v zidovju. Ostrešje je bilo leseno, pokrito z opečno kritino. Stavba je do sedaj samostojno prenašala lastno in koristno obtežbo.

Stari zidani stavbi najprej odstranimo dotrajane konstrukcijske elemente (streho, vmesne strope, vmesno zidovje, itd.) in izdelamo med zunanjimi zidovi, ki jih ohranimo, novo talno temeljno AB ploščo. Na nivoju etaž, na notranji strani zidovja, izdelamo po celotni dolžini obodnega zidu AB vez. V notranjost stavbe nato tik ob obstoječem zidovju na AB temeljno ploščo vstavimo, po etažah, novo nosilno jedro iz križno lepljenih masivnih lesenih plošč ter ustrezno medsebojno povežemo stare in nove konstrukcije. X-lam obodne stenske plošče in vmesne X-lam stene sidramo v talno AB ploščo s pomočjo kovinskih kotnikov, ki jih pritrdimo stransko na X-lam stenske plošče z obročastimi žeblji, navzdol v AB ploščo pa s sidrnimi vijaki za beton. Vrsto kovinskih kotnikov in razdaljo med njimi določimo s statičnim izračunom v nadaljevanju. Tako postavljene nove X-lam stene sedaj prenašajo prevzete obtežbe na novo izvedeno talno AB temeljno ploščo. Na nivoju etaž, kjer imamo pripravljeno AB vez, s pomočjo kovinskih kotnikov povežemo obstoječe zunanje zidovje z medetažnimi X-lam ploščami novega lesenega jedra. Kotnike pritrdimo v X-lam plošče z obročastimi žeblji, v obstoječe zidove pa v zato predhodno pripravljeno AB vez s sidrnimi vijaki za beton. Takšna izdelava novega nosilnega jedra iz X-lam plošč, ki so znane po svoji veliki togosti in dobrem prenašanju potresnih obremenitev,[3] lahko sedaj zagotavlja obstoječi stari konstrukciji stabilnost pri potresni obremenitvi. Predvsem pomembna je izvedba ustreznih detajlov, s katerimi bomo zagotovili ustrezno medsebojno povezanost stare in nove konstrukcije, predvsem na etažnih višinah, posledično pa sodelovanje starih in novih elementov konstrukcijskih sklopov in zagotovitev sistema togih šip v ravnini stropov. Rekonstrukcijo objekta na vrhu zaključimo z novo strešno konstrukcijo, s kritino, ki jo postavimo neposredno na novo X-lam nosilno konstrukcijo. Na tak način obstoječih starih konstrukcij dodatno ne obremenjujemo,

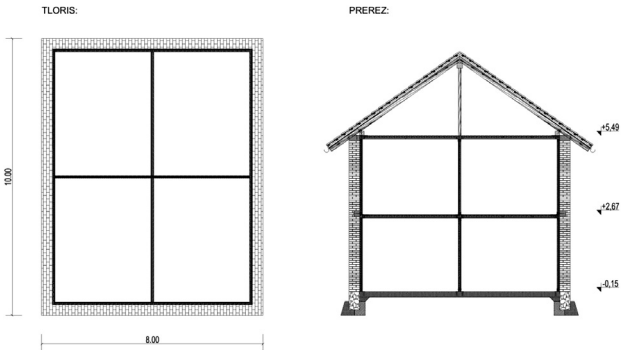

Slika 1: Tloris in prerez rekonstruiranega vzorčnega objekta
Figure 1: Ground and cross-section of the case-study building

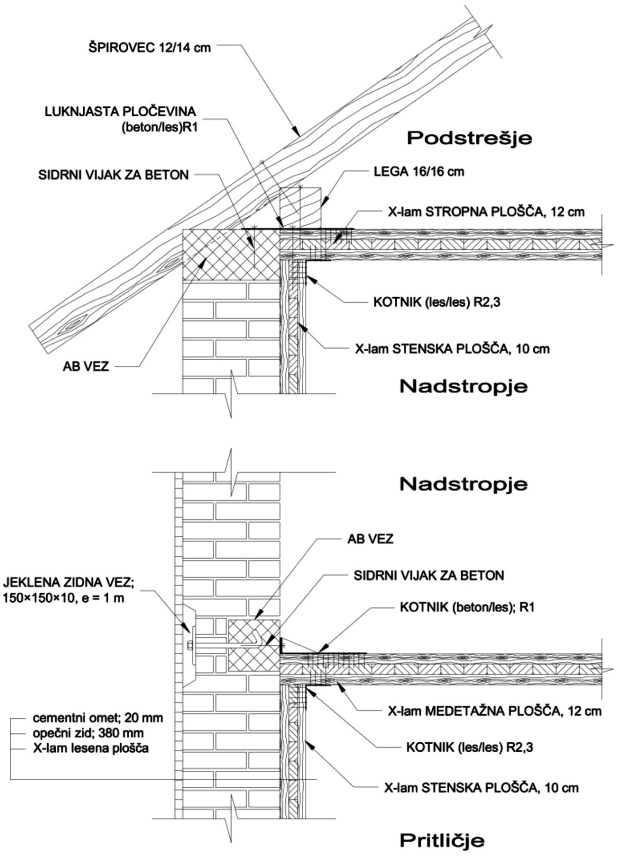

Slika 2: Sidranje zunanjega opečnega zidu na X-lam stropno ploščo na nivoju podstrešja in etaže
Figure 2: Anchoring of the outer brick wall onto the X-lam ceiling panel at the level of the attic and 1st floor

niti z njo ne posegamo v zunanji izgled stavbe, znotraj objekta pa dobimo novo pomlajeno notranjost stavbe.

Gradbeno-fizikalne zahteve pa rešujemo s sanacijskimi ukrepi, s katerimi izboljšamo bivalno ugodje, varčujemo z energijo in s tem varujemo okolje. Konstrukcijo saniramo na način, da preprečimo prehode zunanje vlage v notranjost stavbe, namestimo toplotno izolacijo na zunanje obodne stene (v našem primeru na notranji strani), na tla proti terenu in na vrhnjo stropno ploščo.

2.2 Potresna analiza z metodo vodoravnih sil

Za določitev potresnih sil, delujočih na rekonstruiran objekt, uporabimo poenostavljeno metodo analize s spektrom odziva, ki je znana tudi pod imenom metoda z vodoravnimi silami.[8] Po tej metodi v računski analizi potresno obtežbo predpostavimo kot linijsko obtežbo na nivoju vsake etaže, ki jo izračunamo glede na višino in število etaž objekta ter največjo strižno silo (angl. base shear) ob vpetju konstrukcije v temelje.

2.2.1 Potresna nosilnost X-lam jedra

Najprej izračunamo celotno potresno silo, ki deluje na rekonstruiran objekt (**Slika 1**), pri čemer upoštevamo skupaj mase starih opečnih zidov in nove (lesene) konstrukcije objekta, ki sta medsebojno povezana na nivoju etaž. Na podlagi teh potresnih sil dimenzioniramo spojne elemente, ki medsebojno povezujejo konstrukcijo iz X-lam plošč. Tako mora sedaj v primeru potresa nova X-lam konstrukcija prevzeti tudi potresno obtežbo inercije mase starih zidov.

Vrednost faktorja obnašanja (q), za X-lam plošče, upoštevamo v skladu s priporočili standarda SIST EN 1998-1:2006[8] (v nadaljevanju EC8) za lepljene plošče, ki znaša q = 2. Podatki preizkusa potresnega obnašanja trinadstropne stavbe iz projekta SOFIE[3] so sicer pokazali, da bi bil lahko faktor obnašanja takšne stavbe tudi 3, vendar v našem primeru prevzamemo bolj konservativno predpostavko. Za vzorčni objekt predpostavimo tla tipa C (S = 1.15, T_B = 0.2 s, T_C = 0.6 s, T_D = 2 s), nihajni čas konstrukcije izračunamo z Enačbo (1) 4.6 iz standarda EC8:

$$T_1 = C_t \times H^{3/4} = 0{,}18 \text{ s} \quad (1)$$

Vrednost projektnega spektra (**Slika 3**) za naš nihajni čas znaša $S_d(T_1)$ = 3,36 m/s^2.

Skupno efektivno maso za posamezno etažo določimo z upoštevanjem prispevka mas konstrukcij na nivojih etaž, tj. deleži zunanjih opečnih zidov, AB vezi, X-lam stenskih plošč z oblogami, X-lam medetažnih plošč z estrihi ter strehe. Efektivna masa konstrukcije nad pritličjem znaša 90 ton, konstrukcije nad nadstropjem pa 53,4 tone.

Celotno potresno prečno silo izračunamo z Enačbo (2) 4.5 iz EC8:

$$F_{\text{b, celotna, X, Y}} = 481{,}76 \text{ kN} \quad (2)$$

Po višini konstrukcije razporedimo potresne sile z Enačbo (3) 4.11 iz EC8:

$$\begin{aligned} F_{\text{prit, X, Y}} &= 220{,}47 \text{ kN}; \\ F_{\text{nad, X, Y}} &= 261{,}29 \text{ kN} \end{aligned} \quad (3)$$

Upoštevamo še vpliv naključne torzije s pomočjo Enačbe (4) 4.12 iz EC8, iz česar sledi povečanje učinka vpliva vodoravnih potresnih sil:

$$\begin{aligned} F_{\text{b, celotna, X, Y}} &= 770{,}82 \text{ kN}; \\ F_{\text{prit, X, Y}} &= 352{,}75 \text{ kN}; \\ F_{\text{nad, X, Y}} &= 418{,}06 \text{ kN} \end{aligned} \quad (4)$$

Za preverjanje mejnega stanja nosilnosti X-lam masivne konstrukcije (njenih kovinskih spojnih elementov nameščenih na spojih med stenami in ploščami) moramo izpolniti pogoj, da je projektna vrednost učinka vpliva pri projektni potresni kombinaciji manjša ali kvečjemu enaka odgovarjajoči projektni nosilnosti kovinskega spojnega elementa. Projektna nosilnost kovin-

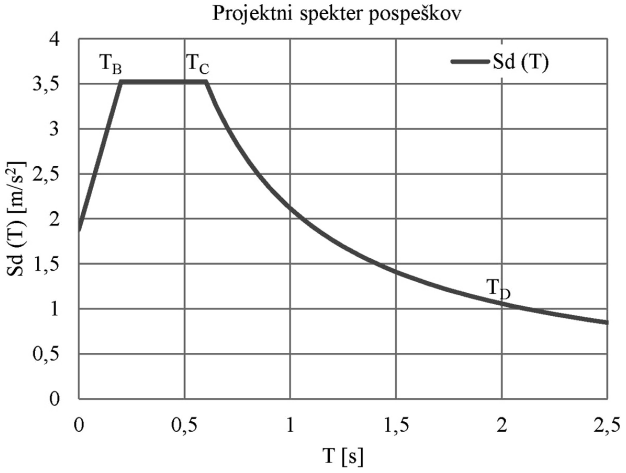

Slika 3: Projektni spekter za X-lam konstrukcijo (q = 2, dušenje 5 %)
Figure 3: Project spectrum for the X-lam construction (q = 2, 5 % damping)

Slika 4: Sidranje X-lam stenskih plošč s kotniki za prevzem strižnih obremenitev na spoju beton/les[9]
Figure 4: Anchoring of X-lam wall panels with steel angular brackets for the transfer of shear load in the concrete-timber joint[9]

skega spojnega elementa se računa po pravilih, ki veljajo za uporabljen material (uporabljajo se karakteristične vrednosti lastnosti materiala f_k in parcialni faktorji varnosti γ_m). Za spojne elemente na vzorčnem primeru bomo uporabili tipske kotnike (**Slika 4**) podjetja Rothoblaas.[9] Ko dimenzioniramo spojne elemente za prevzem potresne obremenitve med križno lepljenimi lesenimi stenskimi in stropnimi ploščami, računamo s kotniki za prenos strižnih sil. Ker imamo precej dolge stene in nizko zgradbo, do dvižnih sil v vogalih sten načeloma ne prihaja.

Dolžine sidranja X-lam sten izračunamo ob dejstvu, da imamo v vsaki smeri zgradbe 3 linije enako dolgih sten (**Slika 1**). Srednji steni, ki sta dostopni z obeh strani, lahko tako z vsake strani tudi sidramo, do zunanjih parov sten pa lahko dostopamo le z ene strani. Zato v račun v vsaki smeri vzamemo 4 efektivne dolžinske linije sten (enačba (5)):

$$\begin{aligned} L_{\text{sten, X}} &= 4 \times 9{,}04 \text{ m}; \\ L_{\text{sten, Y}} &= 4 \times 7{,}04 \text{ m} \end{aligned} \tag{5}$$

Izračunamo strižne sile po tekočem metru v posamezni etaži. Kasneje bomo izračunali, koliko kotnikov potrebujemo v smereh X in Y.

Potresne sile na tekoči meter sten na koti vpetja v pritličju (spoj talne AB plošče in X-lam stenskih plošč pritličja) so:

$$F'_{\text{b, X}} = \frac{F_{\text{b, celotna, X, Y}}}{L_{\text{sten, X}}} = 21{,}31 \frac{\text{kN}}{\text{m}} \tag{6}$$

$$F'_{\text{b, Y}} = \frac{F_{\text{b, celotna, X, Y}}}{L_{\text{sten, Y}}} = 27{,}37 \frac{\text{kN}}{\text{m}} \tag{7}$$

Za prevzem sil izberemo kotnik TITAN TCN 200 za obremenitve na polnih stenah, ki ga na tem nivoju etaže pritrjujemo navzdol v AB talno ploščo s kemijskim sidrom tipa AB1 M12 × 103 in stransko v les z žeblji LBA ϕ4 × 60. Sile na vrhu sten so tako rekoč enake kot na dnu sten, vendar tu izberemo drugačen kotnik, tj. WBR90, ki ga na tem nivoju etaže pritrjujemo navzgor in stransko v les z žeblji LBA ϕ4 × 60.

Potresne sile na tekoči meter stene na koti nadstropja spodaj (spoj medetažne X-lam plošče in X-lam sten nadstropja) in na vrhu nadstropja (spoj X-lam stropne plošče in X-lam sten nadstropja) pa so:

$$F'_{\text{b, nad, X}} = \frac{F_{\text{b, nad, X, Y}}}{L_{\text{sten, X}}} = 11{,}56 \frac{\text{kN}}{\text{m}} \tag{8}$$

$$F'_{\text{b, nad, Y}} = \frac{F_{\text{b, nad, X, Y}}}{L_{\text{sten, Y}}} = 14{,}84 \frac{\text{kN}}{\text{m}} \tag{9}$$

V obeh primerih:

$$F_{\text{2/a, nad, spod, X}} = \frac{F_{\text{nad, X}}}{L_{\text{CLT, stenaX}} \times 4} = 11{,}56 \frac{\text{kN}}{\text{m}}$$

$$F_{\text{2/3, nad, spod, Y}} = \frac{F_{\text{nad, Y}}}{L_{\text{CLT, stenaY}} \times 4} = 14{,}84 \frac{\text{kN}}{\text{m}}$$

izberemo kotnik WBR90, ki ga na tem nivoju etaže pritrjujemo navzdol in stransko v les z žeblji LBA ϕ4 × 60.

Potrebne razdalje med posameznimi spojnimi sredstvi (L_{kotnik}) v smeri X in Y so izračunane kot razmerje med projektnimi vrednostmi odpornosti spojnih sredstev in strižnimi silami, delujočih po tekočem metru objekta v smereh *X* in *Y* (**Tabela 1**). Projektne vrednosti odpornosti spojnih sredstev (R_d) se izračunajo iz lastnosti spojnih sredstev za posamezne načine pritrjevanja.

2.2.2 Potresno sidranje starih zidov v X-lam jedro

S pomočjo iste metode izračunamo potresne sile, ki jih povzroči masa zunanjih opečnih zidov, povezanih na nivoju etaž na notranje jedro iz križno lepljenih lesenih masivnih plošč. V tem primeru dimenzioniramo spojne elemente, potrebne za vpetje zunanjih opečnih zidov na notranje leseno jedro, ki bodo preprečili porušitev starih zidov izven svoje ravnine (**Slika 2**). Pri izračunu potresnih sil, ki jih povzročajo stari zidovi na konstrukcijo, bomo predpostavili faktor obnašanja q = 1, ker ne pričakujemo disipiranja energije v spojih med starimi zidovi in novo konstrukcijo. Računamo z elastičnim spektrom odziva, njegova vrednost za izračunan primer znaša $S_d(T_1)$ = 6,53 m/s^2.

Skupna efektivna masa za posamezno etažo je določena z upoštevanjem prispevka mas zunanjih opečnih zidov in AB vezi na nivojih etaž, (deleži zunanjih opečnih zidov in AB vezi). Za zunanje opečne zidove, ki jih sidramo na koti etaže znaša 66,8 t, za zidove, ki jih sidramo na vrhu prvega nadstropja pa 34,1 t.

Celotna potresna prečna sila, ki jo povzroči opečni zid, z upoštevanjem vpliva naključne torzije, znaša $F_{\text{b,zid,X,Y}}$ = 1065,17 kN. Silo razdelimo še po višini, tako dobimo silo, ki deluje nad pritličjem $F_{\text{zid,prit,X,Y}}$ = 519,46 kN ter silo, ki deluje nad nadstropjem $F_{\text{zid,nad,X,Y}}$ = 545,71 kN; $F_{\text{zid,pritX,Y}}$ = 516,40 kN; $F_{\text{zid,nad,X,Y}}$ = 542,51 kN.

Opečne zidove lahko sidramo le v zunanjo konturo lesenega jedra. Proporcionalni delež sile, ki deluje na

Tabela 1: Raster veznih sredstev za X-lam jedro
Table 1: The spacing of fasteners in the X-lam core

Nivo pritrditve	Kotnik (X-lam)	Način pritrditve	R_d (kN)	$F'_{b,x}$ (kN/m)	$F'_{b,Y}$ (kN/m)	$L_{\text{kotnik,X}}$ (m)	$L_{\text{kotnik,Y}}$ (m)
pritličje spodaj	TCN 200	beton/les	20,2	21,31	27,37	0,95	0,74
pritličje zgoraj	WBR 90	les/les	9,02	21,31	27,37	0,42	0,33
nadstropje spodaj	WBR 90	les/les	9,02	11,56	14,84	0,78	0,61
nadstropje zgoraj	WBR 90	les/les	9,02	11,56	14,84	0,78	0,61

leseno jedro v smeri izven svoje ravnine, dobimo tako, da delimo celotno potresno silo v etaži s celotno dolžino oboda zgradbe. Celotna dolžina sidranja znaša:

$$L_{\text{zid,tot}} = 2 \times 9{,}24 \text{ m} + 2 \times 7{,}24 \text{ m} = 32{,}96 \text{ m} \quad (10)$$

Izračunamo natezne sile (F_1) po tekočem metru v posamezni etaži, na podlagi katerih bomo določili, koliko kotnikov potrebujemo v smereh *X* in *Y*.

Na koti nadstropja (spoj medetažne lesene plošče in zunanjih opečnih zidov) znaša sila:

$$F'_{1,\text{nad}} = \frac{F_{\text{zid,prit,X,Y}}}{L_{\text{zid,tot}}} = 15{,}76 \frac{\text{kN}}{\text{m}} \quad (11)$$

Predpostavimo, da je opečni zid v svoji ravnini sposoben prenesti silo lastne inercije sam. Izberemo kotnik WHT340 za natezni spoj les/beton, ki ga na tem nivoju etaže pritrjujemo stransko s kemijskim sidralom tipa VINYLPRO 1×M16×160 v AB vez in navzdol z žeblji LBA ϕ4 × 60 v les.

Na koti podstrešja (spoj medetažne lesene plošče in zunanjih opečnih zidov) pa je sila:

$$F'_{1,\text{podd}} = \frac{F_{\text{zid,nad,X,Y}}}{L_{\text{zid,tot}}} = 16{,}56 \frac{\text{kN}}{\text{m}} \quad (12)$$

Izberemo luknjane plošče WHT 440 za natezni spoj les/beton, ki ga na tem nivoju etaže pritrjujemo navzdol v AB vez s kemijskim sidralom tipa VINYLPRO M16x190 in navzdol v les z žeblji LBA ϕ4 × 60. Razdalje med veznimi sredstvi so podane v **Tabeli 2**.

Tabela 2: Raster veznih sredstev za pritrjevanje starega zidu v X-lam jedro

Table 2: The spacing of fasteners for attaching the old masonry wall to the X-lam core

Nivo pritrditve	Kotnik (zid)	Način pritrditve	R_d (kN)	$F_{1,X,Y}$ (kN/m)	$L_{\text{kotnik,zid,XY}}$ (m)
nadstropje	WHT340	beton/les	36,02	15,76	2,28
podstrešje	WHT440	beton/les	22,58	16,56	1,36

3 REZULTATI IN DISKUSIJA

3.1 Rekonstrukcija

Potresno obremenitev mora v rekonstruiranem objektu prevzeti novo vstavljena konstrukcija iz X-lam plošč, oziroma spojna sredstva (kovinski kotnik), ki povezujejo elemente X-lam konstrukcije (stenske in medetažne plošče). Za zagotovitev nosilnosti X-lam konstrukcije ob delovanju potresnih sil potrebujemo zadostno število spojnih sredstev, ki bodo prevzele obremenitev. Prav tako potrebujemo za zagotovitev stabilnosti zunanjih opečnih zidov proti prevrnitvi izven svoje ravnine zadostno število spojnih sredstev (kovinski kotniki, luknjane plošče), ki povezujejo novo X-lam konstrukcijo s starimi zidovi na nivoju etaž. Z numerično študijo smo dokazali, da je možno potresne sile za dvoetažni objekt prevzeti s standardnimi veznimi sredstvi na relativno enostaven način.

3.2 Energetska sanacija

Z novo izvedeno sekundarno konstrukcijo v notranjosti objekta, s katero potresno zavarujemo staro zidovje, prepolovimo toplotno prehodnost na zidnem konstrukcijskem sklopu že brez dodajanja toplotne izolacije. Uporabljamo namreč dokaj izolativen material (masivne lesene plošče), kar samo po sebi zmanjša prehod skozi rekonstruiran konstrukcijski sklop. Medsebojni primerjavi toplotnih prehodnosti skozi zidni konstrukcijski sklop smo izračunali s programom "U-Wert Rechner".[10] Toplotna prevodnost za zunanji ovoj konstrukcije znaša 1,19 W/m^{2}K za prvoten ter 0,57 W/m^{2}K za rekonstruiran objekt.

3.3 Parametrična študija

V študiji obravnavamo tri vzorčne primere po novi metodi rekonstruiranih objektov enakih tlorisnih dimenzij 8×10 m in etažne višine 2,82 m. Parameter, ki ga v študiji spreminjamo, je etažnost objektov, ki jo spreminjamo od ene do treh etaž. Ostalih parametrov v tej študiji ne spreminjamo.

Ob zviševanju števila etaž objektov se potresna sila ob vpetju močno povečuje, kar je logična posledica delovanja večje celotne mase objekta z več etažami. Vrednosti potresnih sil nato proti vrhu naših vzorčnih primerov objekta v vsaki etaži padajo, saj je bila v osnovi naša predpostavka, da so vzorčni primeri objektov pravilni po višini in se masa postopoma zmanjšuje od temeljev proti vrhu. Med vzorčnima primeroma objekta "P" in "P + 1" je precejšnja razlika v silah, ker smo pri izvedbi vzorčnega primera objekta "P" še pred t. i. platojem projektnega spektra pospeškov, z vzorčnim primerom objekta "P + 1" pa smo že v platoju projektnega spektra pospeškov, kjer se generirajo tudi največje sile. Obenem pa vidimo, da pri vzorčnem primeru objekta "P + 2" razmerje velikosti skupne potresne sile in lastne teže objekta (**Slika 5**) pade. Če bi parametrično študijo pri enakih pogojih nadaljevali (na primer "P + 3" itd.), bi to razmerje še nadalje padalo, ker bi se vse bolj oddaljevali od platoja spektra pospeškov in bi normirana potresna obremenitev padala. Predvide-

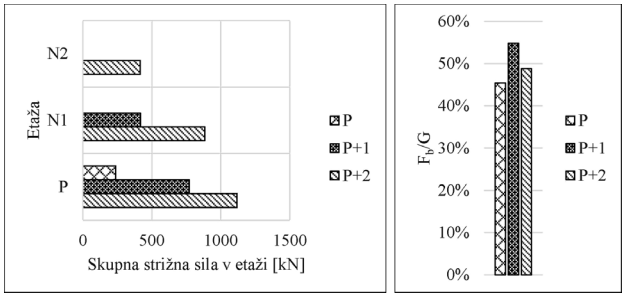

Slika 5: Prikaz velikosti skupnih potresnih strižnih sil, ki delujejo po posameznih etažah in razmerja med celotno potresno silo in skupnimi lastnimi težami vzorčnih objektov

Figure 5: Total seismic shear forces in each floor and the ratios between the total seismic force and self-weights of case-study buildings

vamo lahko torej, da se stroški rekonstruiranja (na uporabno površino) po novi metodi na račun veznih sredstev ne bi nujno linearno bistveno povečevali, pri rekonstrukcijah večetažnih stavb. Obenem pa moramo pri rekonstrukcijah upoštevati tudi dejstvo, da so stroški pripravljalnih in zemeljskih del, ureditve odvodnjavanj v okolici objekta, rekonstrukcije in sanacije vdora zunanje vode v objekt itd. (torej vsa dela do kote + 0,00 m) skoraj enaki za manj etažne kot za večetažne stavbe, kar vpliva na končno ceno rekonstrukcije po enoti rekonstruirane površine.

3.4 Stroškovna ocena

Za izvedbo rekonstrukcije po novi metodi protipotresne utrditve zidane stavbe bi celotni ocenjeni stroški investicije izvedbe takšne rekonstrukcije (vključeni stroški izvedbe konstrukcijskih ukrepov, sanacijskih ukrepov in izvedbe novih instalacij) znašali okoli 820 EUR/m^2 neto. Primerjava zgolj stroškov konstrukcijskih ukrepov po novi tehnologiji v primerjavi z eno od tradicionalnih metod rekonstrukcije protipotresne utrditve zidanih stavb je sledeča:

Rekonstrukcija s stabilizacijo zidane stavbe z notranjim jedrom iz križno lepljenih lesenih plošč: 346 EUR/m^2 (strošek vključuje že novo streho in delno toplotno izolirane zunanje stene zaradi uporabe izolativnega materiala).

Rekonstrukcija obstoječih zidov zidane stavbe z oblaganjem z armiranimi ometi in izvedba utrditvenih armiranobetonskih estrihov: 348 EUR/m^2.

Primerjava pokaže, da gre v osnovi za praktično enake stroške, vendar pa nova metoda ugodno vpliva tudi na energetski vidik zaradi uporabe bolj izolativnega materiala. To pomeni, da gre pri celotni investiciji vsekakor za ugodnejšo tehnologijo v primerjavi z ostalimi.

4 ZAKLJUČEK

Nova tehnologija izvedbe X-lam notranjega jedra kot sekundarnega nosilnega konstrukcijskega sistema v notranjosti obstoječe zidane stavbe, ki zahteva pravilno in smiselno izvedbo posameznih detajlov spojitve stare in nove konstrukcije po posameznih etažah, predstavlja učinkovit sistem protipotresne rekonstrukcije primarne stare potresno neodporne stavbe in zvišuje obstoječi konstrukciji stabilnost pri potresni obremenitvi. Rekonstrukcijo lahko izvedemo brez večjih posegov v zunanji izgled objekta (v primeru stavbe pod spomeniškim varstvom) ter ne predstavlja dodatnih obremenitev za obstoječe stare konstrukcije. Računsko smo dokazali, da lahko z ustrezno izvedenimi načini spajanj starih in novih konstrukcijskih elementov prevzamemo potresno obremenitev, ki bi delovala na tako rekonstruiran objekt. Ob izvedbi rekonstrukcijskega posega se izboljšajo tudi energetski pogoji v stavbi, ker oblagamo obstoječe staro toplotno prehodno zidovje z novim toplotno izolativnim materialom (masivnimi lesenimi ploščami), kar samo po sebi zmanjša prehod toplote skozi rekonstruiran konstrukcijski sklop. Stroškovna analiza ne pokaže bistvenih razlik v primerjavi s konvencionalnimi metodami potresne rekonstrukcije, vendar sistem zaradi svoje večfunkcionalnosti predstavlja bolj racionalno investicijo, saj ob enakem strošku omogoča celovito prenovo objektov.

5 LITERATURA

[1] G. Černe, I. Janežič, Uvod, Sanacija in rekonstrukcija zgradb: Zbornik referatov Gradbeni inštitut ZRMK, Ljubljana 1999, 5–7

[2] S. Gostič, A. Mezgec, R. Žarnić, Protipotresne utrditve zidanih konstrukcij s CFRP kompoziti, Gradbenik, 3 (**2005**), 37–41

[3] S. Gagnon, C. Pirvu, CLT handbook: Cross – laminated timber, Canadian ed., FPInnovations, Québec 2011

[4] K. Štraus, Analiza dinamičnega odziva 7-etažne lesene masivne konstrukcije na potresni mizi, FGG, Ljubljana 2008

[5] J. Jančar, B. Dujič, Primerjava lesenih masivnih panelov sestavljenih iz različno križno spojenih lesenih struktur, 33. Zborovanje gradbenih konstruktorjev Slovenije, Bled 2011

[6] B. Dujič, R. Žarnić, M. Kitek Kuzman, Vrednotenje potresne odpornosti lesene gradnje, Gradnja z lesom - izziv in priložnost za Slovenijo, Univerza v Ljubljani, Biotehniška fakulteta, Oddelek za lesarstvo, Ljubljana 2009, 176–180

[7] I. Sustersic, M. Fragiacomo, B. Dujic, Seismic Analysis of Cross-Laminated Multistory Timber Buildings Using Code-Prescribed Methods: Influence of Panel Size, Connection Ductility, and Schematization. Journal of Structural Engineering, 142 (**2016**) 4, doi: 10.1061/(ASCE)ST.1943-541X.0001344

[8] SIST EN 1998-1: 2006, Evrokod 8: Projektiranje potresnoodpornih konstrukcij – 1. del: Splošna pravila, potresni vplivi in pravila za stavbe, Slovenski inštitut za standardizacijo, Ljubljana, 2006

[9] Plošče in spojniki za les, Katalog podjetja Rohtoblaas, http://www.rothoblaas.com/en/si/catalogues/fastening-systems.html, 30. 3. 2016

[10] Računalniški program U-wert Rechner, https://www.u-wert.net/, 23. 3. 2016

UDK 621.78:621.77:669.15
Original scientific article/Izvirni znanstveni članek

ISSN 1580-2949
MTAEC9, 51(3)485(2017)

IMPROVING OF HOT WORKABILITY AND EXPANDING THE TEMPERATURE RANGE OF SAFE HOT WORKING FOR M35 HIGH-SPEED STEEL

IZBOLJŠANJE VROČE PREOBLIKOVALNOSTI IN RAZŠIRITEV TEMPERATURNEGA INTERVALA VARNEGA PREOBLIKOVANJA V VROČEM ZA HITROREZNO JEKLO M35

Iztok Peruš[1], Milan Terčelj[1], Matjaž Godec[2], Goran Kugler[1]

[1]University of Ljubljana, Faculty of Natural Science and Engineering, 12 Aškerčeva street, 1000 Ljubljana, Slovenia
[2]Institute of Metals and Technology, Lepi pot 11, 1000 Ljubljana, Slovenia
goran.kugler@omm.ntf.uni.lj.si

Prejem rokopisa – received: 2016-07-12; sprejem za objavo – accepted for publication: 2016-08-31

doi:10.17222/mit.2016.150

Increasing the hot workability and expanding the temperature working range for M35 high-speed steel (HSS) by industrial hot rolling as well as by hot compression tests have been studied and achieved. The types of carbides for as-cast as well as for wrought states were revealed by EBSD and the optimal soaking temperatures for both microstructural states were assessed. The soaking temperature had a decisive influence on the characteristics of carbides that lead to improving the intrinsic hot workability as well as to considerably expanding the temperature range of safe hot working down to 850 °C. The apparent activation energy for hot working which amounts 639 kJ/mol as well as constants of the hyperbolic sine constitutive equation for extended temperature range have been calculated. Industrial practice confirms the laboratory results.

Keywords: M35 HSS, hot workability, carbides, EBSD, activation energy

Na osnovi vročega valjanja v industrijskih razmerah ter s tlačnimi preizkusi v vročem smo študirali in izboljšali vročo preoblikovalnost hitroreznega orodnega jekla M35 ter razširili temperaturni interval varnega preoblikovanja. Na osnovi posebej zasnovane metodologije, smo ocenili optimalno temperaturo žarjenja pred vročim preoblikovanjem, s pomočjo EBSD, pa smo določili tipe karbidov tako za predelano, kot tudi za lito stanje obravnavanega jekla. Temperatura žarjenja pred preoblikovanjem močno vpliva na značilnosti karbidov in posledično na vročo preoblikovalnost ter temperaturni interval varnega preoblikovanja. Na osnovi izmerjenih krivulj tečenja so bili za razširjen temperaturni interval izračunani parametri sinus hiperbolične konstitucijske zveze ter navidezna aktivacijska za deformacijo, ki znaša 639 kJ/mol. Rezultati laboratorijskih testiranj so bili uporabljeni in potrjeni v industrijski praksi.

Ključne besede: hitrorezno jeklo M35, vroča preoblikovalnost, karbidi, EBSD, aktivacijska energija

1 INTRODUCTION

In order to increase the economy of tool-steels production, both the improvement of their intrinsic hot deformability and the extension of temperature range of safe hot working are required. An improvement of the intrinsic hot workability of tool steels is related to the characteristics of carbides[1–4] that on the other hand have a large influence on the mechanical properties of tool steels that are used for the manufacture of various tools and dies usually subjected to high mechanical, temperature, chemical and tribological loads.[5–7] Referring to the scientific literature, it is known that initial deformations at upper temperature limit, as well as final deformations at lower temperature limit of hot working range, are characterized by considerably decreased hot deformability in comparison to temperatures within the mentioned range.[1–4,8–13] The decreased hot deformability at the upper limit is attributed to the characteristics of carbides, i.e., to their type, size, shape, size- and/or spatial- distributions, fraction, melting point of eutectic carbides and/or other phases, etc. Also at lower temperature limit characteristics of carbides (i.e., with additionally precipitated secondary carbides) are responsible for pore deformability, where this is related also with the effect of a decreased recrystallization rate. Moreover, the characteristics of the carbides are also influenced by the casting temperature and solidification rate.[3,14–23] The appearance of cracks on areas that are most exposed during thermo-mechanical processing are thus related to similar conditions as described above for both limits of the safe hot working range. These areas are in combination with increased tensile strains additionally subjected to accelerated heating and/or cooling.[24] Some recently published works[3–4] reported that by proper selection of the process parameters prior to hot deformation the increase of hot deformability can be achieved.

In the present study we report about the increase of the hot workability of M35 high-speed steel (HSS) which is used for making severely stressed drills, milling cutters, formed tools, tap drills and cold forming tools, where an increased toughness is required. So far a temperature of 900 °C was considered as the lowest

temperature for the safe hot working of HSS. But market demands for increasing the mechanical properties as well as for lowering the dimensions of semi-products (also below Φ = 14 mm) consequently requires hot rolling at lower final temperatures down to 850 °C. Therefore, the aims of our research were to: (i) study the possibility of extension of hot working range based on optimal selection of appropriate soaking temperature, (ii) to improve the microstructure of final rolled profile, (iii) to determine the main characteristics of the carbides, and (iv) to determine the activation energy for hot working considering an extended temperature range.

2 EXPERIMENTAL PART

The chemical composition in mass fractions (*w*/%) of the studied M35 HSS was: 0.92C, 0.28Si, 0.35Mn, 4.52Co, 4.11Cr, 4.94Mo, 2,03V, 6.35W, 0.021P and 0.012S. Besides industrial hot rolling of ingot and billet, three types of laboratory hot compression tests for M35 HSS were conducted. For these tests cylindrical specimens with dimensions of Φ10 × 15 mm were cut from as-cast ingot and from a square billet, i.e., in the wrought state. The first type of (i) hot compression tests carried out on Gleeble 1500D is related to assessment of an optimal soaking temperature for as-cast and wrought initial microstructural states, respectively, using a special procedure developed by T. Večko Pirtovšek et al.[4] To determine the optimal soaking temperature or upper temperature limit of safe hot-working specimens were soaked for 2 h at selected temperature (beginning at 1200 °C) and then compressed at this temperature up to true strain of 0.9 using constant strain rate of 1 s^{-1}. The upper safe hot-working temperature is then selected as the highest temperature where no macro cracks on the surface of the deformed specimens appeared as well as appropriate microstructure, i.e., no oversized carbides and grains, in the deformed specimen was obtained. To determine the optimal lower safe hot working temperature, samples were soaked on determined high limit and then cooled to low deformation temperature (at first to 900 °C, considered appropriate in industrial practice) and compressed up to true strain of 0.9 using constant strain rate of 1 s^{-1}. If there were no cracks on the sample surface, temperature was lowered for 10 °C and procedure repeated until cracks were noticed on the deformed surface. A safe lower hot deformation limit is then last low deformation temperature without cracks on the sample surface. Using this procedure also appropriate microstructure in compressed samples should be obtained, i.e., carbides growth during soaking should be minimal, etc. The detailed description of the procedure is given in [4].

The second type of (ii) hot compression tests is similar to first type, i.e., including soaking at selected temperature (beginning at 1200 °C), which was followed by cooling and hot compression at a selected lower temperature. In this way the influence of the soaking temperature on the shifting of upper limit of temperature range of safe hot working was studied.

Furthermore, in order to study the mechanical and microstructural response on impaired deformation conditions, especially at lower temperatures, a third type (iii) of hot compression tests were carried out, i.e., compression in strain rates range 0.001–10 s^{-1} and temperature range 1150 °C to 850 °C. During compression testing the samples were heated with a rate of 3° C/s to the soaking temperature and holding there for 10 min, which was then followed by cooling to the deformation temperature with 2 °C/s and holding on deformation temperature for 10 min. After deformation the samples were quenched with water. The flow curves were determined by considering the temperature compensation[1] for higher strain rates. The microstructure and the precipitation of carbides on deformed and quenched samples have been studied and the apparent activation energy for hot working for an extended temperature range was calculated.

Optical microscopy (OM, Carl Zeiss AXIO Imager.A1m) and a field-emission scanning electron microscope (FE SEM JEOL 6500F) in combination with the attached energy-dispersive spectroscopy (EDS, INCA x-SIGHT LN_2) and HKL Nordlys II electron backscatter diffraction (EBSD) camera using Channel5 software analytical tools were applied for observation of the microstructure and determination of the type of carbides. The SEM was operated at 15 kV and a 1.5-nA current for the EDS spot and map analysis as well as for EBSD spot analysis, with a tilting angle of 70°. Individual diffraction patterns were obtained with 4×4 binning and using 5–7 bands. For EDS analysis only 15 kV was used to get small analysing volume; however, it was estimated to be approximately 1 μm^3. Therefore, measuring compositions of carbides we get also information from the matrix and thus the iron amounts in the carbides are much higher as it is. Also, the carbon in carbides is increased due to carbon build up under the electron beam.

3 RESULTS AND DISCUSSION

3.1 Initial microstructure

In **Figure 1a** the initial as-cast microstructures with details in **Figure 1b** and denoted spots for EBSD analysis for M35 HSS are presented. The microstructures consist of martensite, primary, eutectic as well as secondary carbides. In **Figure 2c** a Kikuchi pattern for spot 2 (i.e., eutectic carbides) is given that reveals M_2C (Mo_2C – Space group 60, Pbcn, Laue group 3 mmm) type of carbides. Similar result was obtained also for spots 1 and 4, while for spots 3 and 5 MC (VC - Space group 225, F m-3m, Laue group 11 m-3m) type of carbides were revealed. Analysis of the distribution of Mo, W, V, Cr reveals that eutectic carbides (spots 1, 2 and 4) are mainly composed of Mo (**Figure 1d**) as well as of W.

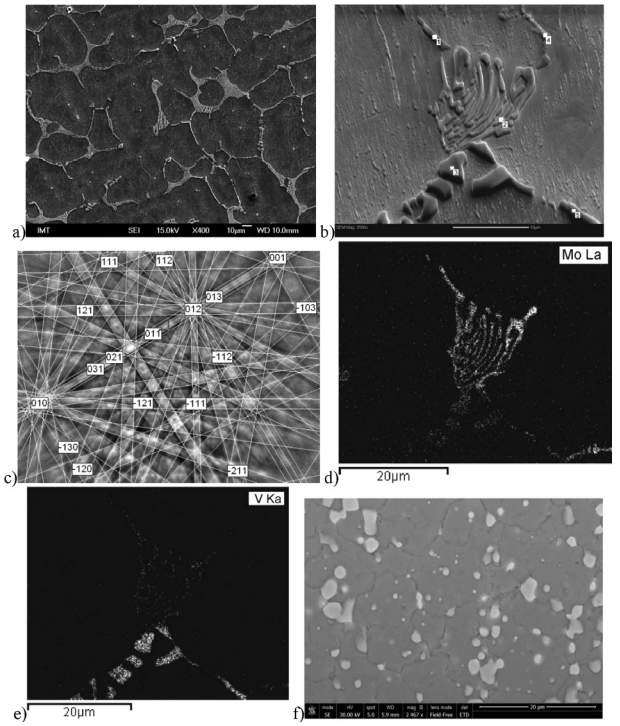

Figure 1: a) Initial microstructure of as-cast specimen from ingot with detail and b) denotes spots for EBSD and c) EDS analysis Kikuchi pattern for spot 2 (M_2C type of carbides), d) distribution of Mo, e) distribution of V and f) wrought microstructure

Slika 1: a) Začetna mikrostruktura litega stanja za vzorce vzete iz ingota z detajlom in b) označena mesta za EBSD in c) EDS-analiza Kikuchijevih vzorcev za točko 2 (M_2C tip karbidov), d) porazdelitev Mo, e) porazdelitev V in f) predelana mikrostruktura

On the other hand, the primary carbides (spots 3 and 5) are mainly composed of V (**Figure 1e**). Analysis of chemical composition on spots denoted in **Figure 2b** as well as type of carbides is given in **Table 1**. Thus eutectic carbides are M_2C type, while the primary carbides are of MC type. The wrought microstructure is given in **Figure 1f**. From this figure it is visible that the eutectic carbides are broken down and the size of grains is decreased in comparison to the microstructure given in **Figure 1a**.

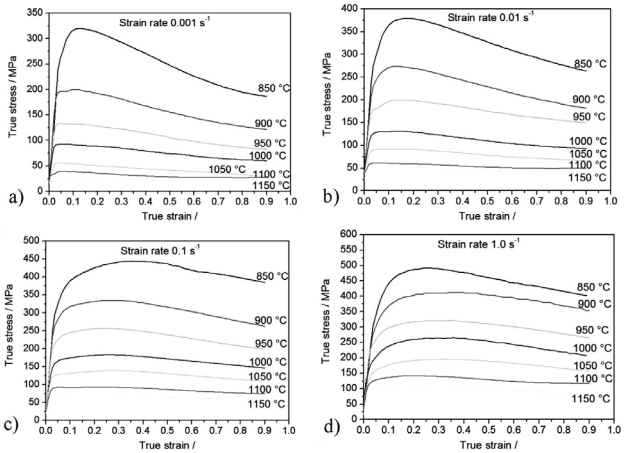

Figure 2: Flow curves for M35 HSS for temperature range 850–1150 °C and different strain rates: a) for strain rate of 0.001 s^{-1}, b) for strain rate 0.01 s^{-1}, c) for strain rate 0.1 s^{-1}, d) strain rate of 1 s^{-1}, wrought state

Slika 2: Krivulje tečenja za hitrorezno jeklo M35 v temperaturnem območju 850–1150 °C pri različnih hitrostih deformacije: a) 0.001 s^{-1}, b) 0.01 s^{-1}, c) 0.1 s^{-1}, d) 1 s^{-1}; predelano stanje

Table 1: Average chemical compositions of the analysed carbides on spots denoted in **Figure 1b** in mass fractions, (*w*/%)

Tabela 1: Povprečna kemijska sestava analiziranih karbidov na mestih, ki so označena na **Sliki 1b**, v masnih deležih, (*w*/%)

	C	V	Cr	Fe	Co	Mo	W	Type
Spots 1,2,4	8.9	9.2	5.1	6.1	-	35.4	35.5	M_2C
Spots 3,5	15.3	37.6	3.3	6.7	-	17.0	20.1	MC

3.2 Obtained optimal soaking temperatures and flow curves

Using the procedure developed[4] the optimal soaking temperatures for as-cast and for wrought states were assessed to be 1150 °C and 1160 °C, respectively. This enables safe hot working within the temperature range between assessed optimal soaking temperature and 850 °C. Our study also revealed, i.e., using the second type of hot compression tests, that by using higher soaking temperature (e.g., 1200 °C), at upper temperature limit of safe hot working is lower by about 20 °C, while the lower temperature limit is about 50 °C higher. Furthermore, it was found that at optimal soaking temperatures determined in the present work and soaking time of 2h, the carbides did not exhibit extensive growth. In **Figures 2a** to **2d** flow curves (i.e., the wrought state) for the temperature range 1150–850 °C and strain rate range 0.001–1.0 s^{-1} are given. Achieving the peak values with an increasing of the strain rate and decreasing of the temperature suggests that dynamic recrystallization has taken place during the hot deformation, which was also confirmed by the inspection of the microstructures.

The strain-rate and temperature dependences of the peak stress were determined using the hyperbolic sine Equation (1)[25]:

$$Z = \dot{\varepsilon} \cdot \exp\left(\frac{Q}{RT}\right) = A(\sin \alpha\sigma)^n \qquad (1)$$

where Z is the Zener-Hollomon parameter, R is the gas constant, Q is the apparent activation energy for hot working, and A, n and α are constants. The activation energies as well as the constants in this Equation (1) were determined using the procedure developed by G. Kugler et al.[26] The values of all constants and activation energy are given **Figure 3a**. Thus the apparent activation energy for hot deformation amounts to 639 kJ/mol. That is slightly higher in comparison to values found in literature for other HSSs. Namely, C. A. Imbert et al.[2] obtained a value for the activation energy of 455 kJ/mol for M2 HSS, while J. Liu et al.[1] obtained values of 467 and 654 kJ/mol for the upper and lower temperature ranges, respectively, for T1 HSS. The comparison

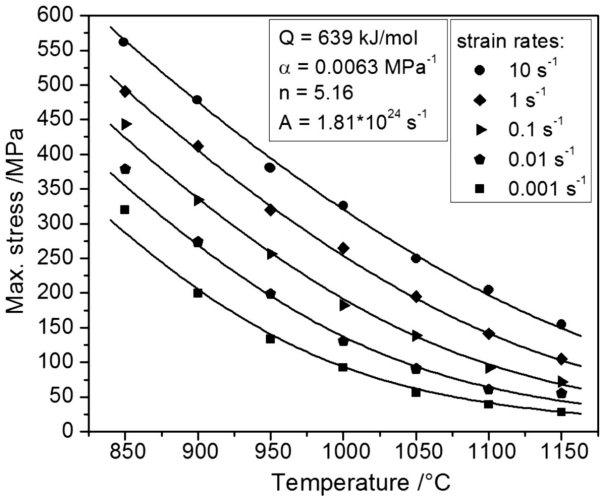

Figure 3: Comparison between measured and calculated peak values of the flow curves at different temperatures and strain rates

Slika 3: Primerjava med izmerjenimi in izračunanimi vrednostmi za maksimalne napetosti tečenja pri različnih temperaturah in hitrostih deformacije

between the measured and calculated peak stresses is given in **Figure 3**, where very good agreement was obtained. A slight deviation can be observed at 850 °C for the lowest strain rate, i.e., 0.001 s^{-1}, which can be attributed to an increased precipitation of secondary carbides (**Figure 4a**) under these thermo-mechanical conditions. Furthermore, more intensive precipitation of the secondary carbides begins at temperatures below 1050 °C, while above it precipitation was almost not observed (**Figure 4b** for the deformation temperature of 1100 °C).

Since for both microstructural states in the deformation chain, i.e., ingot hot rolling as well as billet deformation, soakings were carried out at previous assessed appropriate temperatures, small sized carbides were expected in all the specimens deformed at 850 °C. Namely, soaking at the appropriate temperature does not lead to oversized carbides.[4] Soakings before the deformation of the ingot (as-cast state) were carried out at 1150 °C, while for a billet (wrought state) this temperature was 1160 °C. Very similar microstructures for strain rates of 0.01 s^{-1} and above (for strain rate of 0.01 s^{-1}, **Figure 5a**) at a deformation temperature of 850 °C were obtained. From **Figure 5a** it can be further visible that small sized carbides are mainly below 3 μm, which also indicates good mechanical properties for the further application of the M35 HSS. At deformations at higher temperatures, i.e., 1050 °C, slightly increased coarsening of carbides can be observed at lower strain rates (**Figure 5b**) in comparison to higher strain rates, i.e., 1 s^{-1}

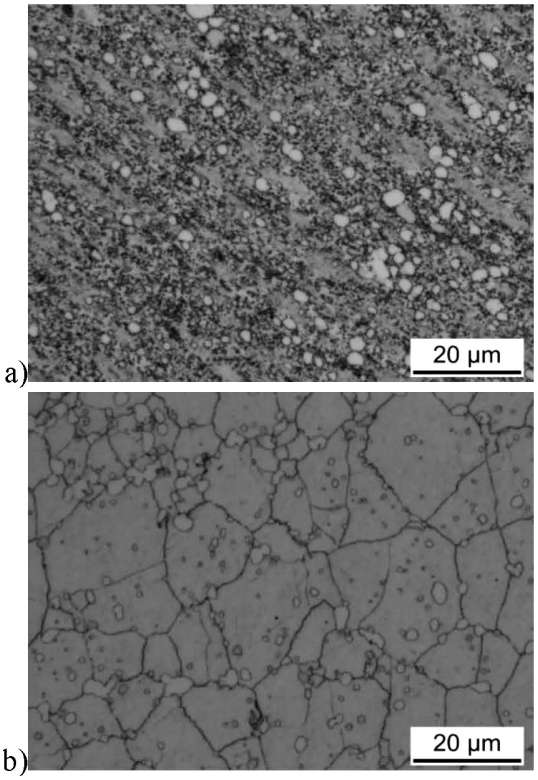

Figure 4: Precipitation of secondary carbides at lower strain rates; intensive precipitation at lower temperatures (850 °C) and decreased precipitation at higher temperatures (1100 °C)

Slika 4: Izločanje sekundarnih karbidov pri nižjih hitrostih deformacije; intenzivno izločanje pri nižjih temperaturah (850 °C) ter manj intenzivno izločanje pri višjih temperaturah (1100 °C)

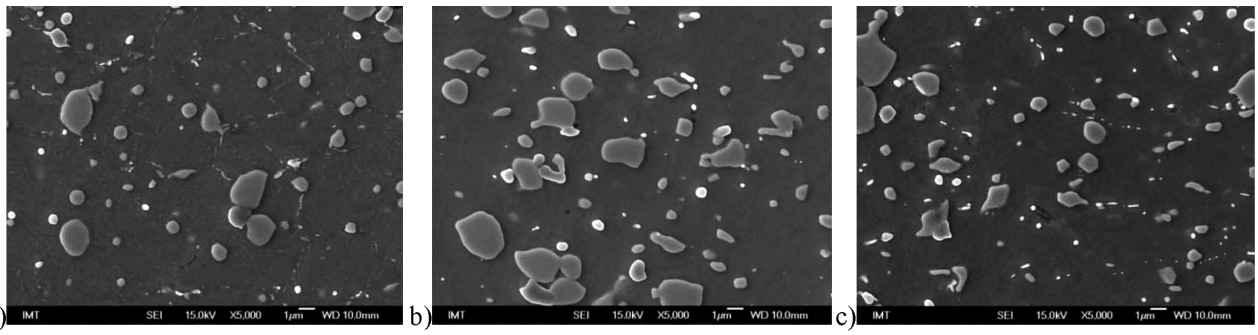

Figure 5: SEI micrographs for compressed specimens at different temperatures and strain rates: a) 850 °C and strain rate of 0.01s^{-1}, b) 1050 °C and strain rate of 0.01 s^{-1}, c) 1050 °C and strain rate of 1 s^{-1}

Slika 5: SEI mikrostrukture za tlačno deformiran vzorec pri različnih temperaturah in hitrostih deformacije: a) 850 °C in hitrost deformacije 0.01s^{-1}, b) 1050 °C in hitrost deformacije 0.01 s^{-1}, c) 1050 °C in hitrost deformacije 1 s^{-1}

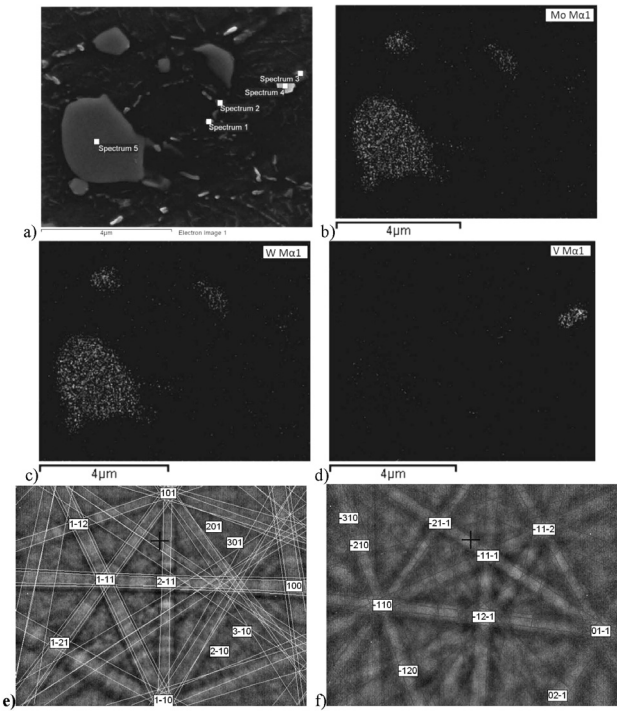

Figure 6: SEI image of carbides distribution with denoted spots for: a) chemical and EBSD analysis on deformed sample, b) distribution of Mo, c) distribution of W and d) distribution of V, e) Kikuchi pattern for M_6C type (spectrum 5) and for: f) MC type of carbides (spectrum 4) deformation temperature 850 °C

Slika 6: SEI slika prostorske porazdelitve karbidov z označenimi mesti za: a) kemijsko in EBSD analizo vzorcev deformiranih pri temperaturi 850 °C, b) porazdelitev Mo, c) porazdelitev W in d) porazdelitev V, e) Kikuchijevi vzorci za M6C tip karbidov (spekter 5) in za: f) MC tip karbidov (spekter 4)

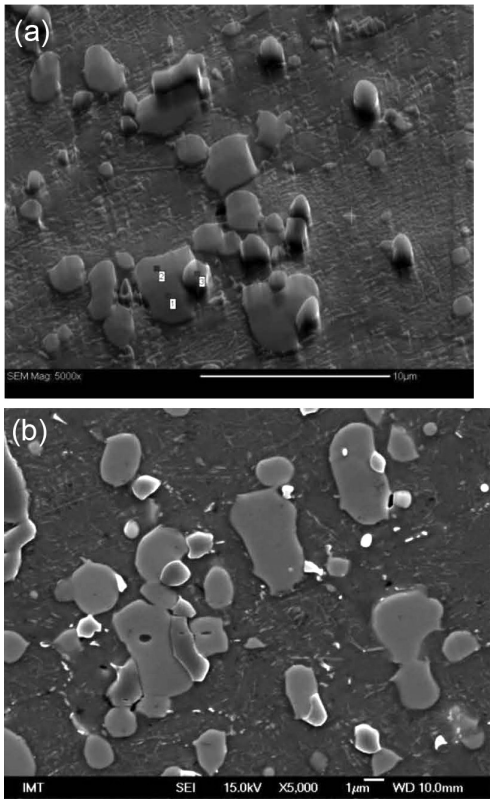

Figure 7: Coalescence of carbides of different types (a-b)

Slika 7: Koalescenca različnih tipov karbidov (a-b)

(**Figure 5c**). This can be attributed to the more time that is available for an increase of their size.

For samples deformed at 850 °C the analyses of the chemical compositions of the carbides were carried out together with the determination of their types. These results are shown in **Figure 6** and **Table 2**. Typical image of presented carbides in the matrix with denoted points for chemical analysis is shown in **Figure 6a**. Analysis of spectrum 5 reveals that Mo (19.2 %) and W (36.7 %) are the main elements in carbides with relative increased size that is further confirmed in **Figures 6b** to **6c**, where distributions of both elements, respectively, are presented. The amount of V in this case is relatively low, i.e., 2.97 %. On the other hand, an analysis of spectrums 3 and 4 revealed that in these carbides V, i.e., 26.21 % and 20.28 %, respectively, and Mo, i.e., 11.3 and 10.4 %, respectively, and W, i.e., 14.8 % and 13.7 %, respectively, are the most important carbide-forming elements. The distribution of V on these spots is given in **Figure 6d**. The amounts of Fe for spectrums 3 and 4 were 28.7 % and 31.8 %, while for spectrums 1 and 2 these values were 92.9 and 67.1 %, respectively, but with much lower amounts of V, Mo and W in comparison to spectrums 3 and 5. Thus, on spots 1–2 the amounts of these elements were 5.7 and 2.6 %, 5.8 and 6.4 %, and 7.1 and 7.4 %, i.e., for V, Mo and W, respectively. The analysis further revealed that the carbide on spectrum 5 refers to the M_6C type (Kikuchi pattern given on **Figure 6e**), on spectrums 1, 3 and 4 to MC type (Kikuchi pattern given on **Figure 6f**), while on spectrum 2, this refers to the $M_{23}C_6$ type. From the distribution of the chemical elements in the carbides it can be concluded that increased sized carbides refer to M_6C type. A comparison of the results related to the carbides for as-cast state

Table 2: Chemical composition in mass fractions, (*w*/%) on denoted spots given in **Figure 5a**

Tabela 2: Kemijska sestava v masnih deležih, (*w*/%), na označenih mestih, ki so podana na **Sliki 5a**

	C	V	Cr	Fe	Co	Mo	W	Type	Type
Spectrum 1	10.3	5.7	4.1	62.9	4.2	5.8	7.1	MC	VC
Spectrum 2	7.7	2.6	3.9	67.1	4.8	6.4	7.4	$M_{23}C_6$	$Cr_{23}C_6$
Spectrum 3	12.4	26.2	3.9	29.7	1.8	11.3	14.8	MC	VC
Spectrum 4	14.4	20.3	3.6	31.8	2.1	10.4	13.7	MC	VC
Spectrum 5	7.4	3.0	2.7	28.7	2.4	19.2	36.7	M_6C	Fe_3W_3C

(**Figure 1** and **Table 1**), where M_2C and MC types of carbides were found, with those for deformed state (**Table 2**), where three types of carbides, i.e. M_6C, MC and $M_{23}C_6$, were revealed, implies that M_2C type of carbides were transformed into M_6C and MC types.[4] The occurrence of the $M_{23}C_6$ type in the wrought microstructure can be attributed to the precipitation of secondary carbides.

Here, it is worth to mention that also the coalescence (unification) of different types of carbides was observed in the sample deformed at 850 °C, i.e., predominately M_6C type (**Figure 7a**, spots 1-2) and MC type (**Figure 7a**, spot 3). This can be seen in **Figures 7a** to **b**. Thus in the final microstructure of M35 HSS very complex carbides are presented. Industrial practice[3] confirms our laboratory results that are related to improving the hot deformability, expanded range of safe hot deformation and size of carbides.

4 CONCLUSIONS

To increase the hot workability of M35 HSS industrial hot rolling and hot compression tests were carried out, which was supported with an analysis of the microstructure. From the obtained results the following conclusions can be derived:

- The appropriate soaking temperature depends on the initial microstructural state of M35 HSS, where for as-cast state this value is slightly lower in comparison to the wrought state, i.e., 1150 and 1160 °C, respectively.
- The selection of the appropriate soaking temperature has a decisive influence on the characteristics of carbides, on the hot workability, and on expanding the temperature range for safe hot working, i.e., at its upper and lower limits. In consequence, this influences the mechanical properties of the final product. The selection of the appropriate soaking temperature for both microstructural states in process chain of hot rolling led to a decreased size of the carbides in final product, i.e., approximately 3 μm. Safe hot rolling up to temperatures around 850 °C is thus assured, which enable hot rolling of profiles with smaller cross-sections.
- M_2C and MC types of carbides were found in as-cast microstructure.
- M_6C, MC and $M_{23}C_6$ types of carbides were found in the final microstructures of compressed samples that deformed at 850 °C. Carbides of type M_6C as largest carbides reached a size of around 3 μm. W and Mo are the main carbide-forming elements in these types of carbides. Smaller-sized carbides refer to the MC type where V is the main carbide-forming element.
- Unification of different types of carbides takes place, i.e., predominately M_6C and MC, which results in very complex compositions of carbides.
- The calculated apparent activation energy for hot working amounts to 639 kJ/mol.

5 REFERENCES

[1] J. Liu, H. Chang, R. Wu, T.Y. Hsu, X. Ruan, Investigation on hot deformation behaviour of AISI T1 high-speed steel, Materials Characterization, 45 (**2000**), 175–186, doi:10.1016/S1044-5803(00)00071-1

[2] C. A. C. Imbert, H. J. McQueen, Hot ductility of tool steels, Canadian Metallurgical Quarterly, 40 (**2001**), 235–244, doi:10.1179/000844301794388461

[3] T. Večko Pirtovšek, G. Kugler, M. Godec, M. Terčelj, Three important points that relate to improving the hot workability of ledeburitic tool steels, Metallurgical and Materials Transactions A, 43 (**2012**) 10, 3797–808, doi:10.1007/s11661-012-1195-4

[4] T. Večko Pirtovšek, G. Kugler, M. Godec, M. Terčelj, Microstructural characterization during the hot deformation of 1.17C-11.3Cr-1.48V-2.24W-1.35Mo ledeburitic tool steel, Materials Characterization, 62 (**2011**) 2, 189–197, doi:10.1016/j.matchar.2010.11.016

[5] T. Pepelnjak, B. Barišič, Analysis and elimination of the stretcher strains on TH415 tinplate rings in the stamping process, Journal of Materials Processing Technology,186 (**2007**), 111–119, doi:10.1016/j.jmatprotec.2006.12.025

[6] D. Klobčar, J. Tušek, B. Taljat, Thermal fatigue of materials for die-casting tooling, Materials Science and Engineering A, 472 (**2008**), 198–207, doi:10.1016/j.msea.2007.03.025

[7] J. Rech, P. J. Arrazola, C. Claudin, C. Courbon, F. Pusavec, J. Kopac, Characterisation of friction and heat partition coefficients at the tool-work material interface in cutting, CIRP Annals – Manufacturing Technology, 62 (**2013**) 1, 79–82, doi:10.1016/j.cirp.2013.03.099

[8] F. Yan, H. Shi, B. Jin, J. Fan, Z. Xu, Microstructure evolution during hot rolling and heat treatment of the spray formed Vanadis 4 cold work steel, Materials Characterization, 59 (**2008**), 1007–1014, doi:10.1016/j.matchar.2007.08.012

[9] T. Večko Pirtovšek, G. Kugler, M. Terčelj, The behaviour of the carbides of ledeburitic AISI D2 tool steel during multiple hot deformation cycles, Materials Characterization, 83 (**2013**), 97–108, doi:10.1016/j.matchar.2013.06.008

[10] R. Milovic, D. Manojlovic, M. Andjelic and D. Drobnjak, Hot workability of M2 type High-speed steel, Steel Research, 63 (**1992**), 78–84

[11] C. Rodenburg, M. Kryzanowski, J. H. Beynon, W. M. Rainforth, Hot workability of spray-formed AISI M3:2 high speed steel, Materials Science and Engineering A, 386 (**2004**), 420–427, doi:10.1016/j.msea.2004.07.056

[12] Z. Bin, S. Yu, C. Yun, C. Zhen-shan, Breakdown Behavior of Eutectic carbide in High Speed Steel During Hot compression, Journal of Iron and Steel Research, International, 18 (**2011**)1, 41–48, doi:10.1016/S1006-706X(11)60009-5

[13] A. Akbarzadeh, S. Naghdy, Hot workability of a high carbon high chromium tool steel, Materials & Design, 46 (**2013**), 654–659, doi:10.1016/j.matdes.2012.10.055

[14] H. Kim, J. Y. Kang, D. Son, T. H. Lee, K. M. Cho, Evolution of carbides in cold-work tool steels, Materials Characterization, 107 (**2015**), 376–385, doi:10.1016/j.matchar.2015.08.001

[15] M. R. Ghomashchi, C. M. Sellars, Microstructural Changes in As-cast M2 Grade High Speed Steel during Hot Forging, Metallurgical Transactions A, 24A (**1993**) 2171–2179, doi:10.1007/BF02648591

[16] J. Gontarev, M. Doberšek, J. Medved, P. Mrvar, Solidification of hipereutectoid high speed steel for rolls, Metalurgija 50 (**2011**) 1, 29–32

[17] W.Shizhong, Z. Jinhua, X. Liujie, L. Rui, Effects of carbon on microstructures and properties of high vanadium high-speed steel, Materials and Design, 27 (**2006**), 58–63, doi:10.1016/j.matdes.2004.09.027

[18] M. A. Hidzadameh, M. Meratian, A. Saatchi, Effect of cerium and lanthanum on the microstructure and mechanical properties of AISID2 tool steel, Materials Science & Engineering A, 571 (**2013**), 193–198, doi:10.1016/j.msea.2013.01.074

[19] K. C. Hwang, S. Lee, H. C. Lee, Effect of alloying elements on microstructure and fracture properties of cast high speed steel rolls, Part I: Microstructural analysis, Materials Science and Engineering A, 254 (**1998**), 282–295, doi:10.1016/S0921-5093(98)00626-1

[20] V. Vitry, S. Nardone, J. P. Breyer, M. Sinnaeve, F. Delaunois, Microstructure of two centrifugal cast high speed steels for hot strip mills applications, Materials and Design, 34 (**2012**), 372–378, doi:10.1016/j.matdes.2011.07.041

[21] H. Di, X. Zhang, G. Wang, X. Liu, Spheroidizing kinetics of eutectic carbide in the twin roll-casting of M2 high speed steel, Journal of Materials Processing Technology, 166 (**2005**), 359–363, doi:10.1016/j.jmatprotec.2004.07.085

[22] M. R. Ghomashchi: Quantitative microstructural analysys of M2 grade high speed steel during high temperature treatment, Acta Materialia, 46 (**1998**) 14, 5207–5220, doi:10.1016/S1359-6454(98)00110-4

[23] P. Ding, G. Shi, S. Zhou, As-cast Carbides in High-Speed Steels, Metallurgical Transactions A, 24 (**1993**), 1265–1271, doi:10.1007/BF02668195

[24] T. Inoue, F. Yin, Y. Kimura, Strain Distribution and microstructural evaluation in multi-pass warm calibre rolling, Materials Sciences and Engineering A, 466 (**2007**) 1–2, 114–122, doi:10.1016/j.msea.2007.02.098

[25] J. J. Jonas, C. M. Sellars, W. J. M. Tegart, Strength and structure under hot working conditions, Metall. Rev., 130 (**1969**), 1–24, doi:10.1179/mtlr.1969.14.1.1

[26] G. Kugler, M. Knap, H. Palkowski, R. Turk, Estimation of activation energy for calculating the hot workability properties of metals, Metalurgija, 43 (**2004**) 4, 267–272

UDK 67.017:622.785:621.365.46
Original scientific article/Izvirni znanstveni članek

ISSN 1580-2949
MTAEC9, 51(3)493(2017)

DEFORMATION AND IMPROVEMENT OF THE IR TRANSMISSION OF SINGLE-CRYSTAL SILICON BY DIRECT CURRENT HEATING

DEFORMACIJA IN IZBOLJŠANJE IR PRENOSA MONOKRISTALNEGA SILICIJA Z ENOSMERNIM TOKOM

Kiyotaka Miura[1], Yasuhiko Shimotsuma[1], Masaaki Sakakura[2], Shunsuke Gunji[1], Taiki Sakamoto[1], Kohei Morishita[3], Satoru Hachinohe[4]

[1]Kyoto University, Graduate School of Engineering, Department of Material Chemistry, Kyoto 615-8510, Japan
[2]Kyoto University, Hitachi Zosen Collaborative Research Division, Kyoto 615-8520, Japan
[3]Kyoto University, Graduate School of Engineering, Materials Science and Engineering, Kyoto 606-8501, Japan
[4]Proud INC., 6-9 Fudanotsuji, 2-chome, Higashi-Omi-shi, Shiga 527-0024, Japan
miura2@func.mc.kyoto-u.ac.jp

Prejem rokopisa – received: 2016-07-14; sprejem za objavo – accepted for publication: 2016-08-02

doi:10.17222/mit.2016.158

We confirmed that the deformation occurred at about 800 °C when CZ-Si was pressure and heat treated by a pulse-heating-method, spark plasma sintering (SPS), while at the same time, the absorption peak of silicon single crystal produced using the Czochralski process (CZ-Si), which was a major issue for infrared transparent material in the vicinity of 9 μm, was also confirmed to have been reduced within a short time. The absorption coefficient in the vicinity of 9 μm, which was derived from the interstitial oxygen, decreased the most at 800 °C, and the absorption derived from the stretching mode of Si–O observed in the vicinity of 9.7 μm reached its maximum at 800 °C. This is considered to have been due to the migration of interstitial oxygen via clusters to change the material into amorphous SiO_2. It was confirmed that the impact of the applied pressure direction was relative to crystal orientation on the peak of 9 μm. It was also found that the deformation was the maximum from the (110) plane, that the change in absorption coefficients before and after deformation was the largest, and that the relationship turned out to be (110)> (100)> (111). The dislocation lines in the sample after the deformation of the (100) plane were observed using EBSD, and the polarization dependencies of transmittance in the infrared region were measured for the planes parallel and perpendicular to the applied pressure.

Keywords: silicon, spark plasma sintering, infrared transparent material, interstitial oxygen, molding

Potrdili smo, da se je deformacija zgodila pri okoli 800 °C, ko je bila CZ-Si tlačno in toplotno obdelana s pulzno toplotno metodo sintranja z iskrečo plazmo (angl. SPS), medtem ko je bil hkrati dosežen absorpcijski vrh silicijevega monokristala z uporabo Czochralskijevega postopka (CZ-Si), pri katerem je glavno težavo predstavljal infrardeči prosojni material pri približno 9 μm, saj je bil zmanjšan v zelo kratkem času. Absorpcijski koeficient pri približno 9 μm, ki je bil pridobljen iz intersticijskega kisika, se je najbolj znižal pri 800 °C in opazili smo absorpcijo, ki je izhajala iz raztezka Si-O, in je v bližini 9,7 μm pri 800 °C dosegla svoj maksimum. Iz tega izhaja, da je bil zaradi migracije intersticijskega kisika preko skupin material spremenjen v amorfni SiO_2. Potrdili smo, da je bil vpliv povezan z uporabo smeri tlaka, v primerjavi s kristalno orientacijo na področju 9 μm. Ugotovljeno je bilo tudi, da je bila deformacija največja na (110) ravnini in da je sprememba koeficientov absorpcije, pred in po deformaciji, največja ter da se je pokazalo razmerje (110)> (100)> (111). Opazili smo premikanje linije v vzorcu po deformaciji (100), ravnine so bile opazovane z uporabo EBSD ter z uporabo polarizacije odvisnosti od prepustnosti v infrardečem območju, ki smo jo izmerili v ravnini vzporedno in pravokotno glede na tlak.

Ključne besede: silicij, sintranje z iskrečo plazmo, infrardeči prozorni material, intersticijski kisik, modeliranje

1 INTRODUCTION

Pyroelectric infrared sensors, commonly used in motion sensors and similar devices, are required to efficiently detect infrared radiation with a wavelength of approximately 9 μm. Silicon produced using the Czochralski process (CZ Silicon), can be obtained at low prices, but can only be used for IR rays in a relatively narrow band (around 1.2–6 μm) since the oxygen eluted from the quartz crucible is trapped in the crystal, which results in the presence of absorption near 9 μm that arises from interstitial oxygen.[1–3] Silicon can be produced as either a single-crystalline form by the Czochralski (CZ) crystal-growth process or the float zone (FZ) method. FZ silicon is grown without a quartz crucible and is thus almost completely oxygen-free, making the absorption of 9 μm much less pronounced, but FZ silicon is expensive. If this absorption band at 9 μm is improved, the wavelength range of infrared transparent windows or lenses of CZ silicon crystal may possibly be expanded. It is known that the absorption band at 9 μm due to interstitial oxygen can be reduced by a long heat treatment (for several to several dozen hours) because of the conversion of Si into SiO_x ($x \leq 2$).[4–6] In addition, silicon, which is naturally brittle owing to its covalent character, easily cracks under a small load. Thus, the conventional process used to obtain a specific lens shape is expensive. Moreover, it is difficult to shape aspherical lenses, which are ideal and highly efficient shapes for focusing. To

solve these problems, a silicon lens fabricated by hot pressing has been investigated.[7] However, in hot pressing, single-crystal silicon is pressed at 1405 °C, just below the silicon's melting temperature. Therefore, the dislocation density is large. As a result, the transmittance is reduced to 10–20 %. When the sample is recrystallized, the dislocation density is reduced, and the transmittance is restored to about 40 %. However, a heat treatment is required after hot pressing.[7]

We have recently succeeded in manufacturing a silicon lens at around 800 °C, (roughly 600 °C lower than the temperature for hot pressing) by direct current heating using a spark plasma sintering (SPS) system. Furthermore, we confirmed that the interstitial oxygen decreased in a short time by adding pressure with direct current heating. The aims of the present study are to 1) provide a silicon material for an infrared transmitting member that secures transmittance for infrared of wavelength around 9 μm and can be used for a wide range of wavelengths and 2) provide an infrared transmitting member made of the silicon material.

2 EXPERIMENTAL PART

Single-crystal silicon (Φ6 × 4mm) grown by the Czochralski process was used as the starting material. The samples have 100, 110, and 111 planes perpendicular to the axis of pressing. The samples were heated to the desired temperature under a uniaxial compressive pressure in a carbon die with an inside diameter of 15 mm by the SPS system (LABOX-125, Spark Plasma Sintering System, Sinter Land, Japan). The SPS system is made up of a uniaxial press, punch electrodes, vacuum chamber, direct current (DC) pulse generator and position, temperature, and pressure measuring units. The temperature was increased from 700 °C to 1100 °C. The heating rate was 100 °C/min from room temperature to the desired temperature. The sample temperature was controlled by adjusting the pulse duration, current and voltage, and measured on the silicon surface directly by a radiation thermometer. The uniaxial pressure was changed between 0.1 kN and 8 kN. The pressure rising rate was changed between 0.05 kN/min and 2 kN/min. After the samples had been heated to the pre-set temperature under a uniaxial compressive pressure of 0.4 kN, the pressure was increased to the pre-set pressure while keeping the temperature the same. In the heat/press deformation of the plasma sintering system (SPS) in this study, when the temperature of silicon reached about 400 °C, there was a change in electrical resistance, which confirmed the start of direct power supply to the interior of silicon. After being cut into 1-mm-thick chunks, the specimens were mirror polished and then used for infrared transmission measurements.

Infrared transmission was measured in the range of 2–12 μm at room temperature by FT-IR to determine the absorption coefficient. In addition, to compare the differences between a plane perpendicular and a plane parallel to the axis of the pressure, the polarization dependence of the infrared transmission spectrum was investigated using a holographic wire grid polarizer. The crystal orientation and the distribution of dislocations for the CZ silicon crystal after transformation were also characterized by electron backscatter diffraction (EBSD).

3 RESULTS AND DISCUSSION

Figure 1 shows a photograph and the IR absorption spectra of the CZ silicon that was compressed by changing the temperature at a pressure of 4 kN perpendicular to a plane of silicon (100). The absorption coefficient around 9 μm, derived from the interstitial oxygen decreases to its minimum at 800 °C, and then increased as the temperature rose from 900 °C to 1100 °C. In contrast, the absorption derived from the Si-O stretching mode observed around 9.7 μm was at its maximum at 800 °C. This is because the interstitial oxygen had moved and changed to amorphous Silica SiO_2 over the cluster (SiO_4). It is well known that interstitial oxygen is transformed into oxygen precipitation and into amorphous SiO_2 by heat treatment over a long

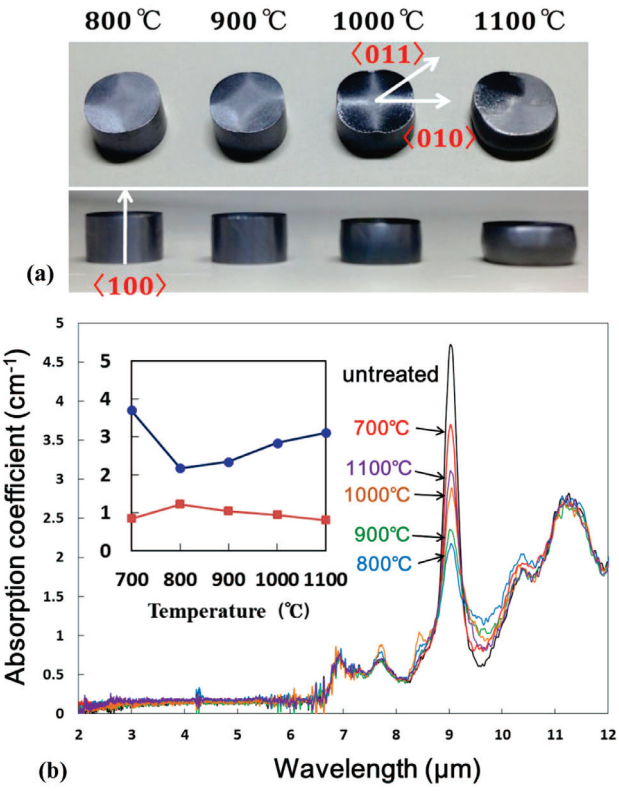

Figure 1: a) Image and b) IR absorption spectra of CZ silicon obtained by changing the temperature reached by applying a pressure (4 kN) perpendicular to a plane of silicon (100)

Slika 1: a) Slika in b) IR spektri absorpcije CZ silikona, pridobljenega s spreminjanjem temperature, dosežene z dodajanjem tlaka (4 kN) pravokotno na površino silikona (100)

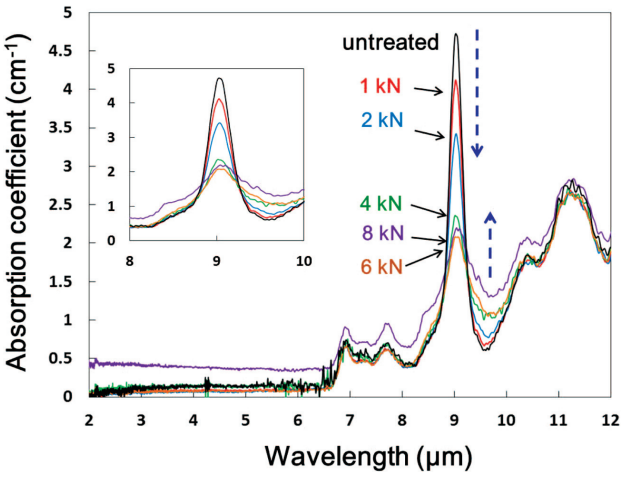

Figure 2: IR absorption spectra of CZ silicon obtained by changing the ultimate pressure at 900 °C

Slika 2: IR absorpcija spektrov CZ silikona, pridobljenega s spreminjanjem končnega tlaka pri 900 °C

time.[8,9] The reason for the maximum reduction of interstitial oxygen at 800 °C is controlled oxygen diffusion.[10,11] We also found that in the high-temperature region beyond 800 °C, the super-saturation of the SiO_2 that formed was reduced and the process of crystal growth from nucleation did not progress further. In addition, SiO_2 that had segregated once in the low-temperature region, decomposed again. Therefore, the optimum temperature of the decreasing absorption band at 9 μm is estimated to be 800 °C.

Similarly, when the ultimate pressure is changed, the 9 μm absorption decreased proportionately with the pressure, and it was confirmed that the pressure at the time of deformation, greatly contributes to the movement of interstitial oxygen. **Figure 2** shows the IR spectrum of the samples pressed at 1, 2, 4, 6, and 8 kN by fixing the temperature at 900 °C. The absorption band at 9 μm decreases in proportion to increasing loads, except for the 8 kN load. This result indicates that the precipitation of SiO_2 clusters or particles is increased by dislocations due to high pressure. In contrast, the absorption band at 9 μm

Figure 3: A silicon single-crystal lens obtained from a CZ silicon disk (Φ22 × 4 mm) by molding at around 800 °C (actual sample temperature), which is about 600 °C lower than the melting temperature, by using an SPS system

Slika 3: Silikonski monokristalni leči, pridobljeni iz CZ silikonskega diska (Φ22 × 4 mm) z dolivanjem na okoli 800 °C (dejanska temperatura vzorca), ki je za 600 °C nižja kot talilna temperatura, pri uporabi SPS-sistema

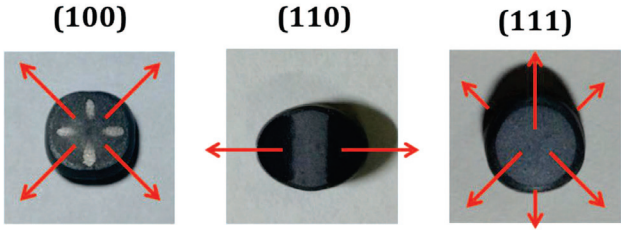

Figure 4: Shape difference of samples obtained by pressure perpendicular to the pressing axis on 100, 110, and 111 planes at 1000 °C and 4 kN

Slika 4: Različne oblike vzorcev, pridobljene s tlakom pravokotno s potisno osjo na 100, 110 in 111 pri 1000 °C in 4 kN

of the sample that is pressed at 8 kN tends to increase. The crack of the surface of this sample is observed using an optical microscope. This result indicates that the crack generates the light scattering.

From these results, it is clear that deformation due to pressure is used with heat treatment for the diffusion of interstitial oxygen. Thus, the pressing in optimum conditions can be expected to be applied for an infrared transmission lens because not only are the samples molded but also the absorption property at 9 μm is improved. An example succeeded in manufacturing a silicon single crystal lens at around 800 °C (actual sample temperature) is shown **Figure 3**, which is about 600 °C lower than the molding temperature for the hot-pressing method,[6] by using an SPS system.

In order to determine the impact of the applied pressure direction relative to crystal orientation on the peak of 9 μm, each sample was prepared and placed so that the crystalline planes were perpendicular to the pressing axis on the 100, 110 and 111 planes. **Figure 4** and **Table 1** show the obtained results. It was found that the deformation was a maximum from the (110) plane, that the change in absorption coefficients before and after deformation was the largest, and that the relationship turned out to be (110)> (100)> (111). During the deformation of the (110) plane, the transformation was parallel to the axis of the applied pressure, while, in the case of the deformation of the (100) plane, due to mutual intersection of slip planes, the interaction due to slip planes became larger and the change was smaller when compared to the (110) plane. In the (111) plane, the change was small because the slip plane is perpendicular to the loading axis.

Table 1: Absorption coefficient difference at 9 μm and deformation amount of height for samples in **Figure 4**

Tabela 1: Koeficient absorpcije – razlika pri 9 μm in deformacijska količina višine za vzorce na **Sliki 4**

Crystal plane	Absorption coefficient difference at 9.0 μm (cm^{-1})	Deformation amount (mm)
(100)	2.37	0.28
(110)	2.68	0.44
(111)	1.55	0.12

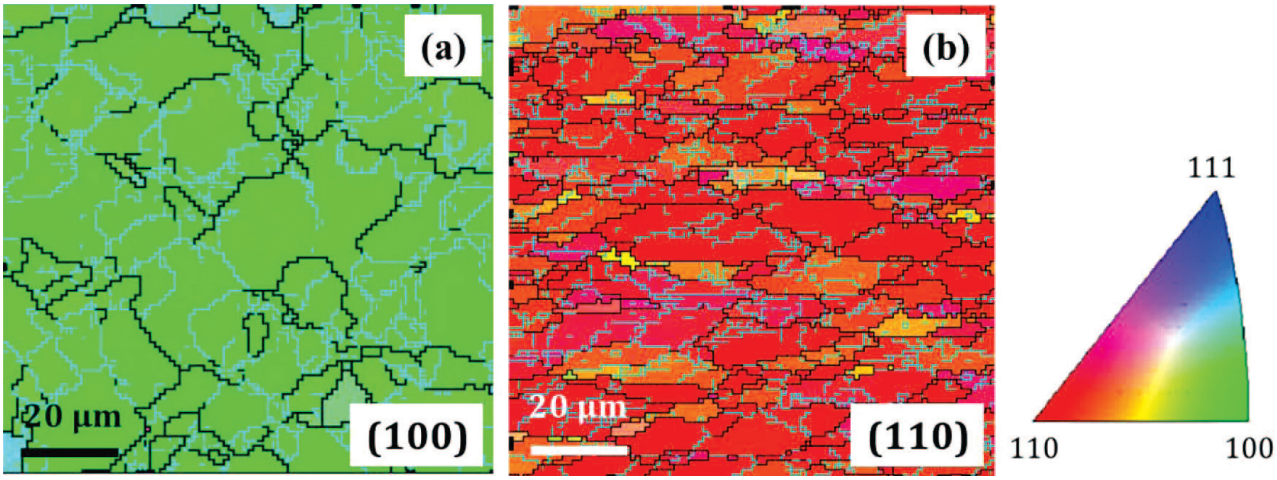

Figure 5: Dislocation lines in samples after the deformation of (100) plane observed using electron backscatter diffraction (EBSD): a) perpendicular and b) parallel to the applied pressure

Slika 5: Dislokacijske linije v vzorcih po deformaciji (100), izmerjene z uporabo EBSD: a) pravokotno in b) paralelno glede na uporabljeni tlak

The dislocation lines in the sample after the deformation of the (100) plane were observed using EBSD and the results are shown in **Figure 5a** and **5b**.

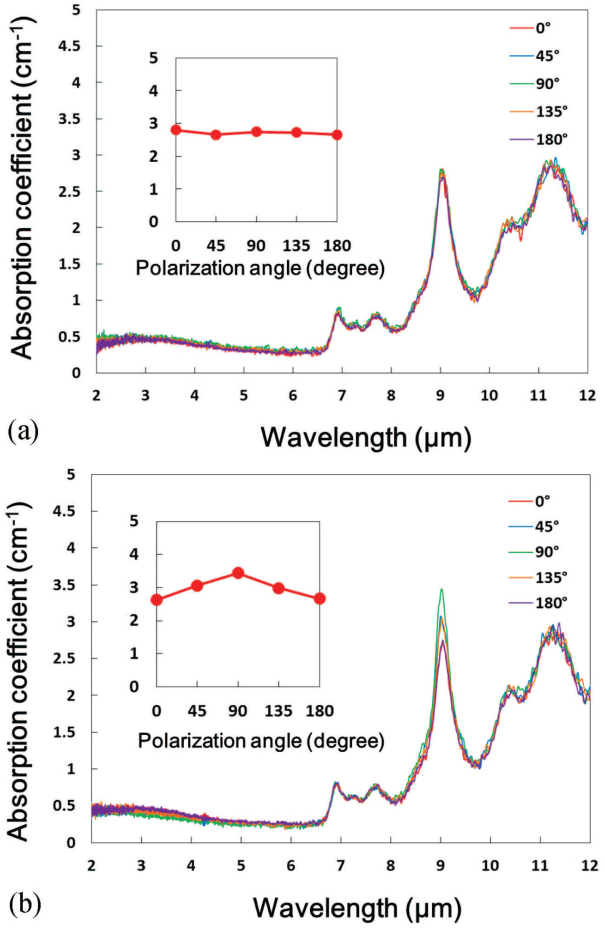

Figure 6: Polarization dependence of absorption in the infrared region obtained for samples in **Figures 5a** and **5b**

Slika 6: Polarizacijska odvisnost na infrardečem področju, pridobljena za vzorce iz **Slike 5a** in **5b**

As seen in **Figure 5a**, where the plane is perpendicular to the applied pressure, the dislocation lines enter randomly, while in **Figure 5b**, where the plane is parallel to the applied pressure, the dislocations lines are oriented horizontally. Then, the polarization dependencies of absorption in the infrared region were measured for each case. The changes in IR absorption spectra are shown in **Figure 6a** and **6b**. In the sample in **Figure 5a**, no polarization dependency was observed, while in the sample of **Figure 5b**, where the transition lines are horizontally oriented, polarization dependency was observed in the absorption of 9 µm. Interstitial oxygen is known to move through the central position of Si-Si bond along the (110) planes[12] and as a result, we can say that the interstitial oxygen segregated along the loading axis towards the dislocation lines. It can be predicted that in the pressure temperature region (700–1100 °C), the carrier density must have increased due to the flow of direct current in the silicon, and due to the weakening of covalent bonds, a metal-like deformation with weak orientation was formed. This indicates that the dislocation lines in **Figure 5a** and **5b** do not originate from the crystal structure and that the impact of the axis of the applied pressure is reflected in a much larger way.

4 CONCLUSION

We have shown that deformation occurred at 800 °C and 6 kN when CZ-Si was pressure and heat treated by direct current heating using the SPS system, while at the same time, the absorption peak of CZ-Si, which had been a major issue for the infrared transparent material in the vicinity of 9 µm, was also confirmed to have been reduced within a short time. It was also found that the deformation was the maximum from the (110) plane, that the change in absorption coefficients before and after molding was the largest, and that the relationship turned

out to be (110)> (100)> (111). Furthermore, we have shown that a silicon lens could be molded at around 800 °C, which is about 600 °C lower than the melting temperature, by using an SPS system. Although further studies are required for elucidating the detailed mechanism behind low-temperature deformation, we can expect that single-crystal silicon formation can be realized at low temperatures of 800–900 °C and that this technique where the interstitial oxygen absorption is reduced in a short period of time at the same time as formation, can be applied in the making of infrared transmission windows and lenses.

5 REFERENCES

[1] F. A. Johnson, Lattice absorption bands in silicon, Proc. of Phys. Soc., 73 (**1959**), 265–272, doi:org/10.1088/0370-1328/73/2/315

[2] S. Sadamitsu, S. Umeno, Y. Koike, M. Hourai, S. Sumita, T. Shigematsu, Dependence of the grown-in defect distribution on growth rates in czochralski silicon, Jpn. J. Appl. Phys., 32 (**1993**), 3675–3681, doi:org/10.1143/JJAP.32.3675

[3] K. Krishnan, In defects in silicon, Material Research Society Symposium Proc., 83–9 (**1983**), 285–292

[4] P. Gaworzewski, E. Hild, F. G. Kirscht, L. Vecsernyés, Infrared spedtroscopical and TEM investigations of oxygen precipitation in silicon crhystals with medium and high oxygen concentrations, Phys. Stat. Sol. (a), 85 (**1984**), 133–147, doi:10.1002/pssa.2210850116

[5] K. Tempelhoff, F. Spiegelberg, R. Gleichmann, D. Wruck, Precipitation of oxygen in dislocation-free silicon, Phys. Stat. Sol. (a), 56 (**1979**), 213–223, doi:10.1002/pssa.2210560123

[6] W. A. Tiller, S. Hahn, F. A. Ponce, Thermodynamic and kinetic considerations on the equilibrium shape for thermally induced microdefects in czochralski silicon, J. Appl. Phys., 59 (**1986**), 3255, doi:10.1063/1.336908

[7] K. Morishita, K. Nakajima, T. Fujii, M. Shiinoki, Near-net shaping of single-crystal silicon for optical lens by one-shot pressing at temperature just below silicon melting point and its demonstration of optical properties, Appl. Phys. Express, 4 (**2011**), 106501, doi:10.1143/APEX.4.106501

[8] V. E. Gusakov, General model of diffusion of interstitial oxygen in silicon and germanium crystals, Solid State Phenomena, 108–109 (**2005**), 413–418, doi:10.4028/www.scientific.net/SSP.108-109.413

[9] I. Yonenaga, K. Sumino, Influence of oxygen precipitation along dislocation on the strength of silicon crystals, J. Appl. Phys., 80 (**1996**) 2, 734–738, doi:10.1063/1.362881

[10] K. H. Yang, H. F. Kappert, G. H. Schwuttke, Minority carrier lifetime in annealed silicon crystals containing oxygen, Phys. Stat. Sol. (a), 50 (**1978**), 221–235, doi:10.1002/pssa.2210500126

[11] K. Wada, N. Inoue, Growth kinetics of oxide precipitates in czochralski silicon, J. Cryst. Growth, 71 (**1985**), 111–117, doi:10.1016/0022-0248(85)90050-8

[12] I. Yonenaga, K. Nakajima, Dislocation dynamics in bending deformation of Si, Key. Eng. Mater., 508 (**2012**), 357–360, doi:10.4028/www.scientific.net/KEM.508.357

UDK 669.24:669.15:621.793
Original scientific article/Izvirni znanstveni članek

ISSN 1580-2949
MTAEC9, 51(3)499(2017)

Ni-Fe ALLOY THIN FILMS FOR AMR SENSORS

TANKE PLASTI ZLITINE Ni–Fe ZA IZDELAVO AMR-SENZORJEV

Marijan Maček[1], Alen Oblak[2]

[1]University of Ljubljana, Faculty of Electrical Engineering, Tržaška 25, 1000 Ljubljana, Slovenia
[2]LEK, Verovškova 57, 1000 Ljubljana, Slovenia
marijan.macek@fe.uni-lj.si

Prejem rokopisa – received: 2016-07-15; sprejem za objavo – accepted for publication: 2016-09-19

doi:10.17222/mit.2016.203

Ni-Fe alloy films deposited in sputtering apparatus and the subsequent AMR sensor fabrication were successfully developed. The results on test devices are comparable to the commercially available device with AMR as measured on the standard multipole magnetic tape.

Keywords: Ni-Fe alloy, AMR, sputtering

Razvit je bil postopek naprševanja in kasnejše obdelave tankih plasti zlitine Ni-Fe, potrebnih za izdelavo senzorjev AMR. Rezultati testnih uporov, merjenih na standardnem, mnogopolnem magnetnem traku, so primerljivi s komercialnimi senzorji.

Ključne besede: zlitina Ni-Fe, AMR, naprševanje

1 INTRODUCTION

Magnetoresistance (MR) is a phenomenon that reflects the effect of an external magnetic field on the resistance change of certain materials. Among known MR the anisotropic magnetoresistance phenomenon (AMR) is widely used in the field of position sensors and encoders due to its robustness compared to optical ones. The AMR effect arises from spin–orbital coupling and therefore depends on the angle θ between the magnetic moment M and the current j.[1] Therefore, resistivity ρ is a function of θ and can be written as in Equation (1), where the symbols $\perp$ and $\|$ denote the perpendicular and parallel components:

$$\rho = \rho\| \sin^2 \theta + \rho\perp \cos^2 \theta \quad (1)$$

The response, i.e., the difference between both components of resistivity, of AMR sensors strongly depends on the soft ferromagnetic material properties. A very common choice are Ni_xFe_{1-x} alloys, known under commercial name Ni–Fe alloy with typical concentration x close to 0.8. The properties of thin layers however depend on the deposition parameters (pressure, temperature, deposition rate, applied magnetic field), subsequent annealing and of course on the layer thickness. Conditions should be set in such a way as to obtain a highly oriented crystalline structure. In the absence of an external field during the film's deposition the correct deposition condition leads usually to the (111) preferred orientation of film with the easy axis of magnetisation perpendicular to the surface. For other orientations of the easy axis, an external magnetic field of 5–15 kA/m during deposition or subsequent annealing is essential.

In our work we concentrate the efforts in order to sputter deposit thin films of Ni–Fe from a $Ni_{80}Fe_{20}$ target without an external magnetic field. Therefore, we are limited in variation of deposition parameters (power P and Ar pressure p_{Ar}), which influence the deposition rate and the chemical constitution[1] of the deposited films and on to the effects of subsequent annealing at temperatures from 150 °C to above 400 °C in forming gas (10 % H_2 in N_2).

2 EXPERIMENTAL PART

Thin Ni–Fe films were deposited onto 500-nm-thick thermally grown SiO_2 on 100-mm Si test wafers. The depositions were performed in Perkin Elmer Sputtering Model 2400 apparatus working at a base pressure below 1.3×10^{-4} Pa from a $Ni_{80}Fe_{20}$ target. The pressure of the Ar during the sputtering was set to 1.1 Pa as first results suggest that higher pressures give unsatisfactory results. The Ni–Fe alloy films were usually deposited onto a buffer layer in order to promote preferential (111) crystallite orientation. A very common buffer is Ta, but $(Ni_{0.81}Fe_{0.19})_{0.66}Cr_{0.34}$ layer[2] gives better results. We tried to simulate the NiFeCr depositing thin layer of Cr/NiFe/Cr in the way to reach preferred ratio between Cr and Ni–Fe alloy.

The resistors were defined by the so-called lift-off process since with standard positive PR process and subsequent etching in Ni etchant the minimum dimension could not be kept in the desired limits. For test resistors devices with two different geometries LxW (500×25 μm^2, 150×3 μm^2) from the laboratory test vehicles. After the finished "lift-off" step test and device

wafers were annealed in quartz tube in forming gas (10 % H_2 in N_2) atmosphere at different temperatures 200–420 °C. The device wafers were finished by the standard double metal process with the highest temperature 350 °C during inter-metal dielectric deposition.

The properties of the AMR layers were analyzed on test samples by XRD analysis and magnetic measurements by a Lake Shore 7307 vibrating-sample magnetometer. On the same test wafers sheet resistance and surface roughness were measured after different annealing steps. The sheet resistance was measured by a 4–point probe and roughness by a laser scanning microscope.

The AMR measurements of the resistors were made in a measured magnetic field of permanent magnet or multipole magnetic tape with periodic magnetization as used for standard applications with 2λ = 4 mm. The results on the tape were also compared to the results of single resistor from commercial AMR encoder bridge structure.

3 RESULTS AND DISCUSSION

The AMR effect is inversely proportional to the thickness, but unfortunately the coercivity H_c limits the lower thickness to about 50 nm.[1] The layer thickness t can be calculated from the measured sheet resistance R_{sh} and the known resistivity ρ, $t = \rho/R_{sh}$. Unfortunately, in thin films the resistivity depends on its thickness and structure as modeled by [3]. The accepted values are 123±30 nΩm,[4] but H. Faltin[5] observed even 196 nΩm for 120-nm-thick films deposited onto Si. Not at least, within the fixed geometry the resistivity of single resistor of about 1 kΩ is the optimum one. Therefore, an optimum R_{sh} is between 5 Ω/sq and 10 Ω/sq.

To characterize the AMR films their sheet resistance R_{sh} was measured after different processing steps, and after isochronal (30 min) annealing in forming gas. The results are shown in **Figure 1**. There is a rapid change in R_{sh} for the samples deposited without a buffer layer. The layers deposited onto the buffer exhibit a moderate reduction in the resistivity up to the annealing at 350 °C, which is also the highest temperature in the process. Generally speaking, samples without buffer, and samples deposited with lower power have a higher R_{sh}. Since the sputtering energy $P.t$ was set to 17 kJ the difference is in the layer structure. The final R_{sh} was 8–12 Ω/sq, close to our demands for an AMR sensor. Annealing at 400 °C and 420 °C does not significantly change the resistance, but microscopic investigations show unwanted changes in the structure of the film and an increase in the surface roughness S_{ra} from 10–20 nm to over 50 nm, especially for films deposited without a buffer.

The reduction of R_{sh} after annealing at 350 °C indicates strong changes in the crystal structure of the Ni–Fe alloy layer. The XRD analysis in **Figure 2** shows changes in the preferred (111) orientation after annealing up to 350 °C. Annealing at higher temperatures has no effect on the orientation of the crystallites. In the XRD pattern a weak (200) Cr peak is also observed as well a strong (400) Si. Obviously our presumption for buffer layers does not work. In any case, the Cr buffer has some beneficial effects on the surface roughness and it significantly reduces the sheet resistivity of at least the annealed samples.

The magnetic properties of the deposited AMR layers are shown in next **Figure 3**. From rather rough plot we can see a distinctive difference between the plots for easy axis of magnetization (full circles), perpendicular orientation of magnetic field to the surface and hard axis (open circles), lying parallel to the surface. From this plot the coercivity H_c is estimated to be 5kA/m. Since these are the very first experiments, the effects of pro-

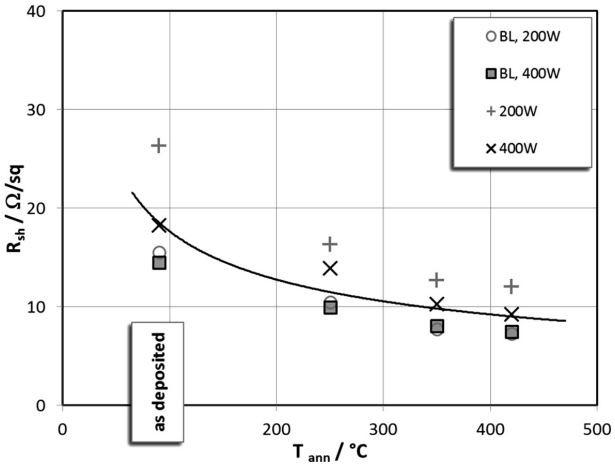

Figure 1: R_{sh} measured after the deposition and isochronal annealing in forming gas; crosses denote sheet resistances for films deposited without buffer layer

Slika 1: Plastna upornost R_{pl} po nanosu in izokronalnih popuščanjih v tvornem plinu; križi predstavljajo plastne upornosti filmov, nanesenih brez vmesne plasti

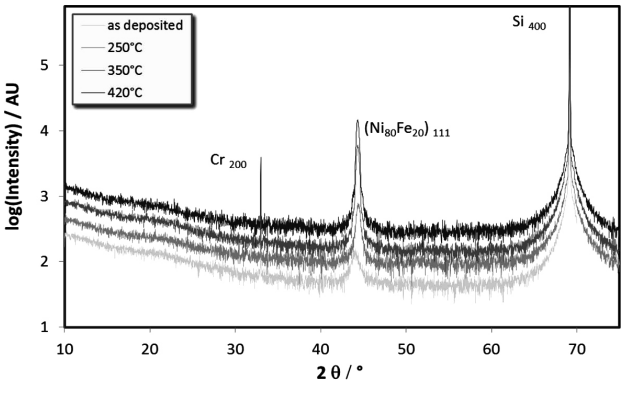

Figure 2: XRD pattern for a layer deposited onto buffer layer at 400 W and pressure 1.1 Pa after deposition and isochronal annealing at (250, 350 and 420) °C

Slika 2: XRD-vzorec plasti, nanesene pri 400 W in tlaku 1.1 Pa na vmesno plast po nanosu in izokronalnih popuščanjih na (250, 350 in 420) °C

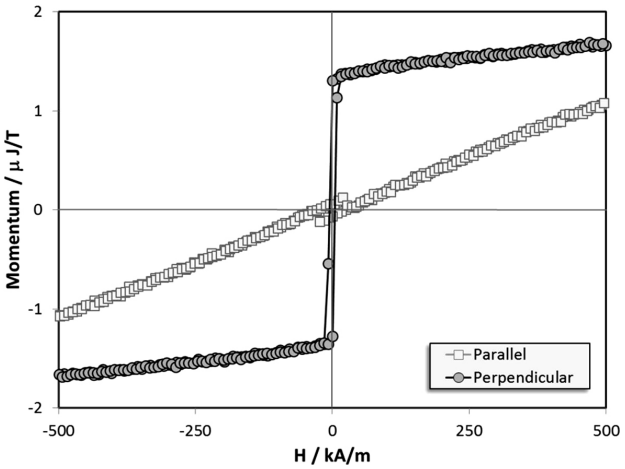

Figure 3: Magnetization curve for sample deposited with 400 W at 1.1 Pa, directly onto thermally grown SiO_2 and annealed at 420 °C for 30 min

Slika 3: Krivulja magnetizacije za vzorec nanesen pri 400 W in tlaku 1.1 Pa, direktno na termičen SiO_2 in popuščano 30 min na 420 °C

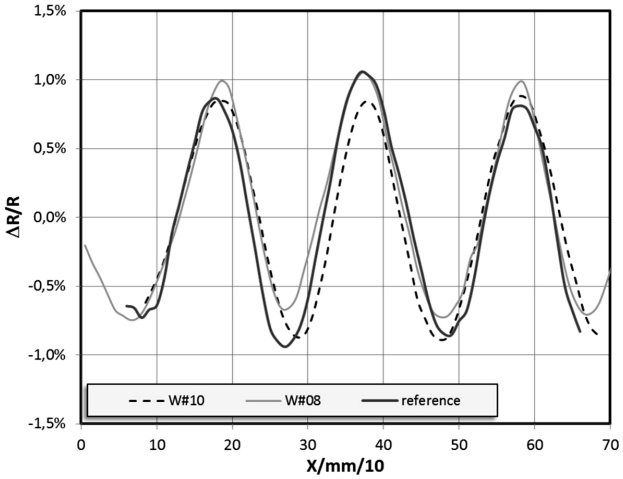

Figure 4: A typical response $\Delta R/R_{avg}$ of 2 test resistors and commercial reference to position over periodic multipole magnetic field with 2λ = 4 mm at a distance of 1.5 mm

Slika 4: Tipična krivulja odziva $\Delta R/R_{avg}$ 2 testnih uporov in komercialne reference na pomik nad periodično spreminjajočim magnetnim

cessing parameters on to magnetic properties and the structure revealed by XRD of soft ferromagnetic layers have not been studied yet.

The first experimental AMR resistors show promising results. In **Figure 4** the responses $\Delta R/R_{avg}$ of the two test resistors LxW = 500×25 μm with slight differences in the processing (W#10 without buffer, W#08 with buffer layer) and a commercial AMR encoder are shown. The measurements were performed on a commercially available multipole magnetic tape with 2λ = 4 mm in steps of 0.1 mm and at a distance of 1.5 mm above the tape with a manual manipulator in all cases. From **Figure 4** it is clear that there is no significant difference between both test samples, but their responses (~1.7 %) are somewhat lower than that on the commercial (~1.9 %) sensors.

4 CONCLUSIONS

The first AMR resistors were successfully fabricated by sputtering of Ni–Fe alloy $Ni_{80}Fe_{20}$ in a Perkin Elmer apparatus and the necessary process steps for the subsequent annealing and fabrication of the resistors with predefined geometries with minimum dimensions W = 3 μm were established.

The results from tests of the AMR resistors were comparable to the commercial one and encourages us to proceed with the development of extrapolators of custom design.

Acknowledgment

The authors acknowledge RLS company and especially director Mr. J. Novak and their employees Mrs. D. Domanjko and Mr. M. Janežič for support and encouraging during the first steps of AMR material process research and work on the design of the test encoder. Authors acknowledge dr. S. Gyergyek and dr. M. Spreitzer of the Jozef Stefan Institut, Ljubljana, for magnetic properties and XRD measurements.

5 REFERENCES

[1] A. V. Svalov, R. Aseguinolaza, A. Garcia-Arribas, I. Orue, J. M. Barandiaran, J. Alonso, M. L. Fernández-Gubieda, G. V. Kurlyandskaya, Structure and Magnetic Properties of Thin Ni–Fe alloy Films Near the Transcritical State, IEEE Trans Magn, 46 (**2010**) 2, 333–336

[2] W. Y. Lee, M. F. Toney, D. Mauri, P. Tameerug, E. Allen, High Magnetoresistance Permalloy Films Trough Growth on Seed layers of $(Ni_{0.81}Fe_{0.19})_{1-x}Cr_x$, IEEE Trans. Magn., 36 (**2000**) 1, 381–387

[3] P. Wismann, K. Muller, Surface Physics, Springer-Verlag, Berlin 1975

[4] A. C. Reilly, W. Park, R. Slater, B. Ouaglal, R. Loloee, W. P. Pratt Jr., J. Bass, Perpendicular Giant magnetoresistance of $Co_{91}Fe_9$/Cu Exchange-Biased Spin-Valves: A Further Test of the Unified Picture, JMMM, 195 (**1999**), L269–L274

[5] H. A. Faltin, The Magnetic and Electrical Properties of Ni–Fe alloy-Carbon Thin Film Multilayers, thesis College of William and Mary, Virginia, USA 2000

UDK 620.1:621.7.019.1:621.184.3
Original scientific article/Izvirni znanstveni članek

ISSN 1580-2949
MTAEC9, 51(3)503(2017)

ROOT-CAUSE ANALYSIS OF SUPERHEATER-TUBE FAILURE

ANALIZA GLAVNEGA VZROKA NAPAKE CEVI PRI PREGREVALNIKU

Martin Naď, Jiří Buzík, Tomáš Létal, Pavel Lošák

Brno University of Technology, Faculty of Mechanical Engineering, Institute of Process Engineering, Technicka 2, 616 69 Brno, Czech Republic
nad@fme.vutbr.cz

Prejem rokopisa – received: 2016-07-15; sprejem za objavo – accepted for publication: 2016-09-15

doi:10.17222/mit.2016.204

Superheater-tube failure is listed among the major causes of a fossil-fuel-fired boiler outage. Therefore, it is necessary not only to identify and repair it in the case of failure but also to eliminate the root cause of this problem. As there may be multiple reasons of failure in exposed equipment such as a superheater, a thorough investigation of more than one probable cause is usually required. This article focuses on a failure analysis of a boiler located in a chemical plant. After a leak was discovered, several cracks on the superheater tubes were identified as its main cause. It was necessary to assess the extent of the damage, detect the root cause and propose corrective actions. Two problematic locations with cracks were identified during the visual inspection: the first was on the superheater-tube bends and the other was the weld joint between the superheater and the transition pipe. As the first step, the material-microstructure and composition analyses of the tubes in these critical locations were carried out. Even though small weaknesses were found in the microstructure, the main cause of the tube failure was not identified. As the next probable cause, thermal-dilatation stresses were investigated using the finite-element analysis (angl. FEA). The support system, consisting of fixed and spring supports, as well as the compensator were included in the analysis that confirmed the thermal-dilatation stresses as the major cause of the failure. Based on the results, a new technical solution for the supports was suggested and verified with the FEA.

Keywords: corrosion, weldment cracks, superheater supports, thermal dilatation

Napaka cevi pregrevalnika je znana kot ena najpogostejših napak pri kotlu na fosilna goriva. Zato jo je treba, ne le prepoznati in v primeru okvare popraviti, pač pa tudi v splošnem odpraviti vzrok za njen nastanek. V tako izpostavljenem elementu kot je pregrevalnik, je za tovrstno napako lahko več vzrokov, zato je za ugotovitev le-teh, potrebna temeljita preiskava. Članek je osredotočen na analize okvar kotla, ki se nahaja v kemični tovarni. Potem, ko so odkrili puščanje, je bilo na pregrevalnih ceveh več razpok, ki so bile opredeljene kot glavni vzrok. Treba je bilo oceniti obseg škode, odkriti vzrok in predlagati ukrepe za popravilo. Med vizualnim pregledom sta bili ugotovljeni dve problematični lokaciji z razpokami. Prva na zavojih cevi pregrevalnika in druga v spoju zvara med pregrevalnikom in prehodno cevjo. Najprej je bila izvedena analiza mikrostrukture materiala in analiza sestave cevi na kritičnih mestih. Čeprav so bile ugotovljene pomanjkljivosti v mikrostrukturi, glavni vzrok napake cevi ni bil ugotovljen. Naslednji možni vzrok bi lahko bila termodilatacijska napetost, ki je bila raziskovana z uporabo analize končnih elementov (FEA). Sistem za podporo, ki je sestavljen iz fiksnih in podpornih vzmeti pa tudi kompenzator, so bili vključeni v analizo, ki je potrdila, da je toplotna dilatacijska napetost glavni vzrok napake. Na podlagi rezultatov je bila predlagana nova tehnična rešitev "podpor", ki jo je potrdila tudi FEA.

Ključne besede: korozija, razpoke pri zvarih, pregrevalnik, termodilatacija

1 INTRODUCTION

Boilers are common parts of many process units. Since their life expectancy can be counted by decades (usually 200,000 working hours), some minor or bigger problems are inevitable. Regular inspections are carried out after some time to find problematic areas and establish corrective actions to prevent failure. The boiler life expectancy may vary based on the material used, working conditions, boiler operation history, etc. One of the most exposed boiler parts is the superheater, which is one of the crucial heat-exchanger types among the heat-exchanger applications. Its main advantage is the reduction of fuel consumption, but it is also susceptible to various types of damage such as creep, deflection, damage caused by environmental influences and mechanical loads.

According to D. R. H. Jones[1], the superheater is the most commonly damaged part of a boiler, thus regular inspections are necessary to check its condition. The main damage reasons can be divided into three major categories:

- Mechanical – caused by a higher stress and strain at a specific location (deflection, cracks, weldment damage);
- Corrosion – material-structure deformation due to various corrosion mechanisms;
- Erosion – damage caused by the particles in the medium flow.

H. Othman[2] faced a similar problem of superheater-tube deformation and cracks near the weldments. He found that the main factor causing the problems was the temperature of 520 °C, which caused temperature dilatations. As soon as the supports did not allow compensation of dilatation stresses, deformation and cracks of the pipes occurred.

2 BOILER DESCRIPTION

The analyzed boiler located in the chemical power plant has been in operation for a long time under various conditions, which differed from the original design conditions. Therefore, regular inspections of critical areas were necessary. Boiler design parameters are: a steam production of 50 t/h, the nominal pressure of superheated steam of 3.8 MPa and the nominal temperature of superheated steam of 375^{+15}_{-10} °C. The boiler consists of several crucial parts. The article is focused only on superheaters (referred to as P1 and P2) and the U-shaped transition pipe between them. During one of the inspections, cracks and perforations were revealed in the area of weldments near the inlet chamber of superheater P2 as well as cracks and leakage on the superheater-P2 pipe bend.

2.1 Description of superheaters

The construction of these superheaters is classic, widely used all over the world. Both of them are similar, having the same dimensions and being situated one above the other. The output chamber of superheater P1 is connected with the input chamber of superheater P2 by the U-shaped transition pipe. Each superheater has 9 pipes in 4 rows (a total of 36 pipes), which go through the membrane wall, with which they are connected by a seal-weld joint (**Figure 1**).

The presented article is focused on superheater P2, which was exposed to a medium with a temperature of 335 °C and a pressure of 4.0 MPa (**Figure 2**). Another crucial part is in the U-shaped transition pipe where cooling water is sprayed to achieve the required steam properties.

2.2 Description of the supports

Superheater collectors are supported by two fixed strap iron profiles (**Figure 2**).

The U-shaped transition pipe has spring supports on three locations (**Figure 3**). Two of them are at the upper part with displacements of 15 mm and 23 mm and one at the bottom part with a displacement of 75 mm.

Figure 1: Part of superheater P1 and the membrane wall
Slika 1: Del super grelca-pregrevalnika P1 in stena membrane

Figure 2: Support of the superheater collector
Slika 2: Del zbiralnika v pregrevalniku

2.3 Damaged areas

As mentioned, there are two main problematic areas. One of them includes the crack and the leakage on the superheater-P2 pipe bend (**Figure 4**).

Another problem was the crack near the weld on the superheater collector with the U-shaped transition pipe (**Figure 5**). This problematic part had been repaired several times in the past, which can be seen in the figure.

The structure of the material was expected to be one of the possible root causes of the damage, mainly the dislocations in the structure. Critical imperfections may have been developed not only during the equipment operation but even during its manufacture. In the following step, two samples from the damaged areas were taken for a metallurgical analysis to prove the dislocation presence. The conformity with the declared chemical composition and mechanical properties of material 1.0405 were tested. A spectrometric analysis was per-

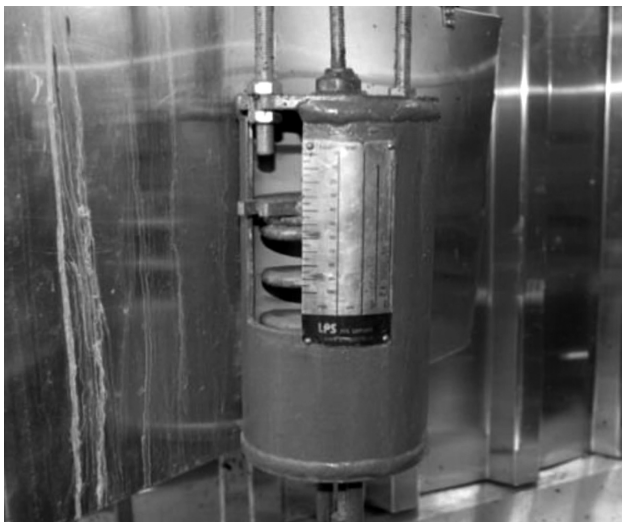

Figure 3: Spring support of the transition pipe
Slika 3: Vzmet v pretočni cevi

Figure 4: Leakage on superheater-P2 pipe bend
Slika 4: Puščanje na P2 pregrevalniku na krivini cevi

Figure 5: Crack near weld on the superheater-P2 collector metallurgical analysis
Slika 5: Razpoka blizu zvara na pregrevalniku P2 metalurška analiza zbiralnika

formed (Method – 12-MTL-5.4/07 program Fe-10) as well as a tensile test (Method – ČSN EN ISO 6892-1B). The tests proved that all the values were within the limits.[3]

The first sample was taken from the pipe-bend area because the visual inspection revealed a horizontal crack (length 25 mm) on the pipe bend. This kind of crack cannot have been caused by the bending process. However, the manufacturing process should have influenced the material structure by lowering its corrosion resistance. The purity results of the analyses proved the material to be of a very good quality.

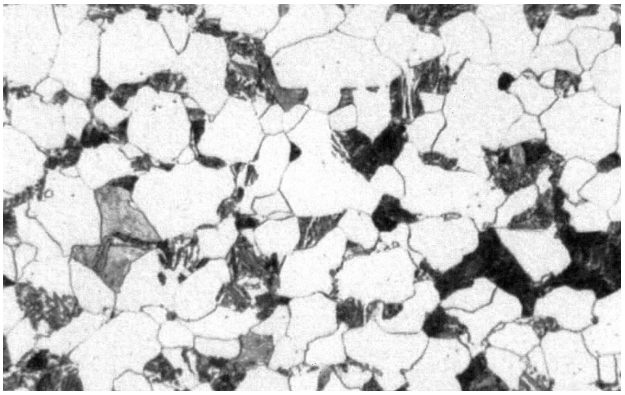

Figure 6: Micrograph of the basic material (500× zoom, etched with Nital)[3]
Slika 6: Posnetek osnovnega materiala (500× povečava, jedkano z Nitalom)[3]

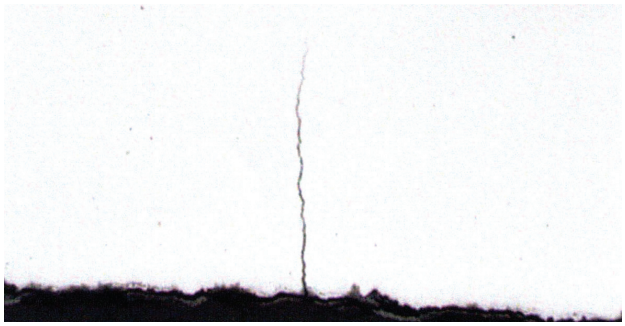

Figure 7: Crack located on the inner surface of the pipe (50× zoom)[3]
Slika 7: Razpoka, locirana na notranjostipovršine cevi (50× povečava)[3]

Afterwards, the corrosion that was found on both surfaces of the pipe was examined. Pitting and small sharp projections were found on the inside. Some of the pits already had a character of small cracks (**Figure 7**), caused by a combination of corrosion and stress. Based on these findings, it was expected that the cracks had started on the outside of the pipe, in the area where the material was weakened by the small cracks from the inner side. Stress and the medium flow might be important during the process of crack growth and will be further examined.

The second tested sample was taken from the area where the collector is welded to the U-shaped transition pipe. The crack goes through the whole weld and is divided into two branches in the middle of the cross-section (**Figure 8**). The crack is open mainly in the middle part and even with the microscope analyses, the direction of the crack formation could not be determined.

There were no defects found either in the material structure or in terms of material properties that would directly influence the crack formation. Only some small

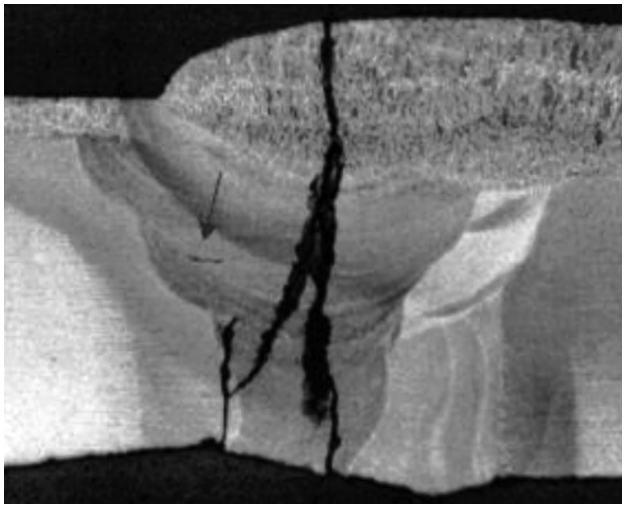

Figure 8: Weld macrosection with the crack (5× zoom)[3]
Slika 8: Prerez zvara z razpoko (5× povečava)[3]

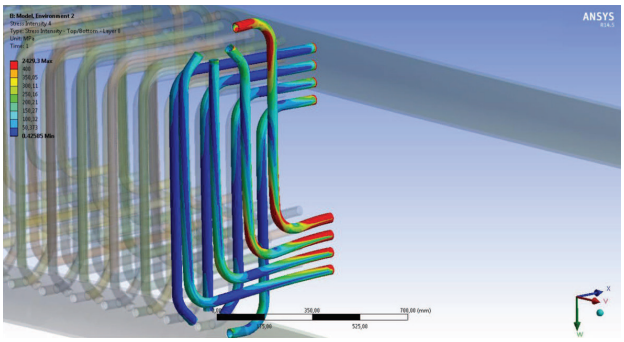

Figure 9: Stress intensity for bent pipes
Slika 9: Intenzivnost napetosti na zvite/zavoje cevi

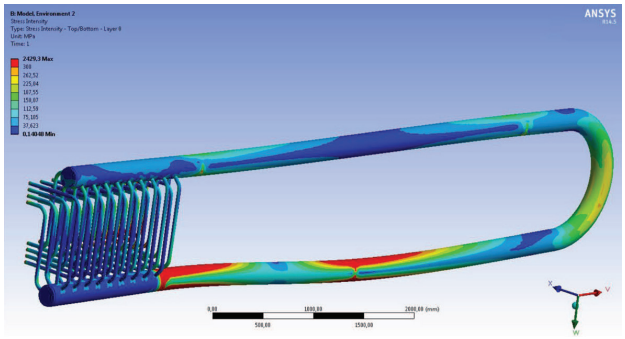

Figure 10: Stress intensity for the whole computational model
Slika 10: Intenzivnost napetosti za celoten model

defects were found (see the black arrow in **Figure 8**). As mentioned above, this weld was repaired several times in the past so it was obvious that there was some problem with the equipment geometry (e.g., supports locations), stress and temperature dilatation.

To fully understand the root cause of the crack formation, stress analyses were carried out.

2.4 FEM analyses

As the material analysis did not show the root cause of the problem, finite-element analyses were used. A shell model of the two collectors (one from each superheater) connected by the U-shaped transition pipe was prepared in SolidWorks. For the analyses, we used computational program ANSYS® Academic Research, Release 14.5.

2.5 Mathematical model preparation

Steady-state thermal analyses and their combination with static structural analyses were performed. At first, the model geometry was imported from SolidWorks to ANSYS Workbench and material properties were set up for material 1.0405. In the next step, a computation mesh, which had approximately 150,000 elements, was created.

2.6 Simulation of current conditions

After preparing a sufficient mesh, appropriate boundary conditions (BCs) were set up. These included the standard earth gravity (g = 9,8066 m/s^2), fixed supports (at the place where the collector pipes were connected to the membrane wall and also at the places of collector supports), the internal pressure, the temperature and displacements (at the place where three spring supports were located). The last three BCs varied based on the analysis type. Two load cases were considered:

Design conditions:

First, an analysis based on design parameters was performed. The internal pressure (4.01 MPa) was applied to all the surfaces as well as the temperature (334 °C). Spring supports were replaced with a direction displacement, which prevented the movement in the vertical direction. Although the stress value was slightly higher in the area of pipe bends, it was not high enough to initiate a crack formation.

Operational conditions:

To examine the problematic areas, it was necessary to apply operational conditions. Therefore, to all the surfaces, the internal pressure (p = 3,61 MPa) and two different temperatures were applied because, as mentioned above, there is a part of the U-shaped transition pipe where the cooling water is sprayed. This was the part where the temperature varied. The first temperature (T_{max} = 332 °C) was used for one collector with pipes and the second temperature (T_{min} = 278 °C) was used for the second collector and the part of the U-shaped transition pipe. At first, all the other BCs remained unchanged but the stresses still were not high enough. This is why one of the BCs was changed and the spring supports were simulated with the exact values of the direction displacement (as mentioned before, these included 15 mm, 23 mm and 75 mm). The results of this analysis were identical to our problem and they confirmed our expectations that the problematic parts of this construction are the spring supports.

As can be seen on **Figure 9**, the stress intensity is crucial in the pipe bends, the exact location where the crack and leakage were discovered.

An improper use of the supports was confirmed by a higher stress intensity at the second problematic location including the collector and the U-shaped transition-pipe weld joint (**Figure 10**).

Based on these results, it was obvious that the problematic parts were the supports. They allow higher values of the total displacement of the U-shaped transition pipe that induce higher moments and stresses. Also, there is one support at the bottom part, witch behaves like the center of rotation; thus, an additional stress is induced. The other crucial elements were the fixed supports of the collectors, located too close to the weld-joint location.

2.7 Support modification

In order to avoid financial losses caused by repeated shutdowns and repairs, multiple corrective measures were proposed. The modification of the supports, which led to a stress reduction at the crucial areas, was performed. It was achieved by increasing the spring stiffness, which influenced the BC displacement. Due to this modification, each displacement was reduced by almost a half of the previous value (10 mm, 20 mm and 35 mm). Unfortunately, the results proved that the stress intensity decreases insufficiently and the spring modification is not sufficient to fix the problem. Another improvement could take the form of minimizing the displacements or removing the bottom support, identified as problematic. This would lead to a further decrease in the stress levels in the critical areas. However, these analyses are not included in the article.

3 CONCLUSIONS

The paper focused on superheater damage. Cracks and leakage were found in several crucial areas; thus, material and FEM analyses were carried out. The analyses proved that the main cause of the problems was an inappropriate support of the U-shaped transition pipe. The problem was caused by a vertical displacement and also by the spring-support location, combined with the fixed supports of the collectors near the weld location. Due to the surface stresses induced in the problematic areas, this place is the most ideal for a crack formation based on shape discontinuities, heat treatment and material discontinuities. Based on the analysis results, a reduction of the support displacements and a change in their location form the easiest and fastest way to prevent increased values of the stresses and further crack formation and propagation.

Acknowledgement

The authors gratefully acknowledge the financial support provided by the Technology Agency of the Czech Republic within the research project No. TA13401000 "Waste-to-Energy (WtE) Competence Centre".

4 REFERENCES

[1] D. R. H. Jones, Creep failures of overheated boiler, superheater and reformer tubes, Engineering Failure Analysis, 11 (**2004**), 873–893, doi:10.1016/j.engfailanal.2004.03.001

[2] H. Othman, J. Purbolaksono, B. Ahmad, Failure investigation on deformed superheater tubes, Engineering Failure Analysis, 16 (**2009**), 329–339, doi:10.1016/j.engfailanal.2008.05.023

[3] J. Štemberk, M. Halaš, Materiálový rozbor vzorků přehříváku kotle K2, NDT servis s.r.o., 2014

UDK 67.017:661.728.7:661.8'071.4
Original scientific article/Izvirni znanstveni članek

ISSN 1580-2949
MTAEC9, 51(3)509(2017)

VPLIV DODATKA NANOFIBRILIRANE CELULOZE NA MEHANSKE LASTNOSTI POLI(3-HIDROKSIBUTIRATA)

THE IMPACT OF THE NANOFIBRILLATED-CELLULOSE ADDITION ON THE MECHANICAL PROPERTIES OF POLY(3-HYDROXYBUTYRATE)

Vesna Žepič[1], Erika Švara Fabjan[2], Ida Poljanšek[3], Primož Oven[3]

[1]TECOS – Razvojni center orodjarstva Slovenije, Kidričeva 25, 3000 Celje, Slovenija
[2]ZAG – Zavod za gradbeništvo Slovenije, Dimičeva 12, 1000 Ljubljana, Slovenija
[3]Univerza v Ljubljani, Biotehniška fakulteta, Oddelek za lesarstvo, Jamnikarjeva 101, 1000 Ljubljana, Slovenija
vesna.zepic@tecos.si

Prejem rokopisa – received: 2016-07-15; sprejem za objavo – accepted for publication: 2016-09-20

doi:10.17222/mit.2016.192

Namen prispevka temelji na inovativnem postopku izdelave nanokompozitov na osnovi poli(3-hidroksibutirata) (PHB) in nanofibrilirane celuloze (NFC). Raziskovalno delo obravnava pripravo koncentratnih mešanic PHB-prahu in NFC v vodni raztopini za tehnologijo ekstruzijskega mešanja. Ekstrudat koncentrirane mešanice PHB/NFC je bil nato uporabljen kot dodatek h granulirani obliki PHB pri pripravi brizganih vzorcev z različnimi utežnimi deleži NFC. V prispevku so podane določene omejitve pri predelavi tovrstnih materialov in predlagane uporabne rešitve za njihovo optimiziranje. Morfološke lastnosti nanokompozitnih komponent smo raziskali z elektronsko mikroskopijo (FE-SEM), mehanske lastnosti pa z nateznim preizkusom. Morfološka preiskava koncentratnih mešanic je razkrila prepleteno sestavo celuloznih nanofibril in polimernih kroglic, pri čemer se posamezne fibrile prepletajo v obliki širših pramenov in ustvarjajo videz zamrežene strukture znotraj polimerne komponente. Mikroskopski posnetki nanokompozitnih mešanic in izboljšane mehanske lastnosti izhodnih materialov potrjujejo, da je adhezivni stik med matrično in ojačitveno komponento dosežen, porazdelitev celuloznih nanofibril po polimerni osnovi pa homogena. Nanokompoziti z visokimi utežnimi deleži NFC (10 % utežnega deleža) dosegajo pomembno večje vrednosti modula elastičnosti (E_t = 1720 MPa) in raztezka pri pretrgu (ε_b = 3,1 %) ter prenesejo višje pretržne napetosti (σ_M = 26 MPa) v primerjavi z referenčnim polimernim vzorcem (E_t = 1340 MPa; ε_b = 2,4 %; σ_M = 20 MPa). Rezultati študije dokazujejo, da je ob pravilni predpripravi polimernih mešanic in optimizaciji tehnologije ekstruzijske predelave, mogoče izdelati trdne in žilave materiale, pri čemer delež ojačitvene faze narekuje stopnjo izboljšave končnih lastnosti biopolimerne osnove.

Ključne besede: nanofibrilirana celuloza, poli(3-hidroksibutirat), morfologija, mehanske lastnosti, ekstruzija, tehnologija brizganja

In this paper a novel processing route for nanocomposites, based on (3-hydroxybutyrate) (PHB) and nanofibrillated cellulose (NFC), is presented. To obtain a uniform dispersion of the reinforcing filler, a PHB powder was first dispersed in water, mixed with an NFC aqueous suspension and then freeze dried to eliminate the water phase from the ensuing system. The dried batch was then extruded and added to the granulated PHB in different weight proportions. Nanocomposites with various NFC contents were subsequently produced with the injection-moulding technology. The processing limits and feasible solutions for their optimization are thoroughly described within this work. Morphological properties were investigated with FE-SEM, while mechanical properties were determined via a tensile test. SEM images showed that the PHB powder can be effectively incorporated into the mesh of cellulose nanofibrils, as clearly evident by the interlaced structure of individual fibrils with the average lateral dimensions of 69±14 nm. Improved mechanical properties and SEM observations confirmed a good interfacial adhesion and uniform distribution of the reinforcing component. Compared to the unfilled matrix (E_t = 1340 MPa; σ_M = 20 MPa; ε_b = 2.4 %), an escalating trend in Young's modulus (E_t = 1720 MPa) and tensile strength (σ_M = 26 MPa), along with decisively improved values of the elongation at break (ε_b = 3.1 %), were observed for the nanocomposites with the highest content of NFC. According to the results presented, strong and tough nanocomposites can be produced via extrusion moulding, whereby the proportion of the reinforcing phase dictates the final material performances.

Keywords: nanofibrillated cellulose, poly(3-hydroxybutyrate), morphology, mechanical properties, extrusion, injection moulding

1 UVOD

Sintetični polimeri so vsestransko uporabni materiali, brez katerih si naš vsakdanjik težko predstavljamo. Ena njihovih glavnih slabosti je dolgotrajen proces razgradnje, druga pa pridobivanje, ki temelji na neobnovljivih surovinskih virih. Poleg raziskav o možnostih recikliranja odpadnih plastičnih mas se v zadnjem času raziskave vse intenzivneje usmerjajo v razvoj biopolimernih materialov, ki bi zmanjšali škodljive učinke na okolje in znižali našo odvisnost od ekonomsko nestabilnih naftnih derivatov. Tržno uspešen in v svetu vedno bolj prodoren biopolimer je polimlečna ali polilaktična kislina (PLA), proizvedena s fermentacijo ogljikovih hidratov.[1] Druga pomembna skupina biorazgradljivih polimerov so polihidroksialkanoati (PHA), sintetizirani preko bakterijsko vodenih fermentacijskih postopkov.[2] Najbolj znana oblika PHA polimerov z nizko molsko maso je poli(3-hidroksibutirat).[3] Obe skupini razgradljivih polimerov imata visok tržni potencial na področju bioplastike, vendar nekatere njihove lastnosti, kot so krhkost, nizka temperaturna odpornost, visoka paroprepustnost in nizka viskoznost za nadaljnjo predelavo,[4] omejujejo njihovo

širšo uporabo. Ena izmed rešitev za izboljšanje teh lastnosti je vgradnja nano-ojačitvenih elementov z ugodnim razmerjem med njihovo dolžino in premerom. Dober primer takih dodatkov so celulozne nanofibrile oz. nanofibrilirana celuloza (NFC), navadno pridobljena iz celuloze lesa, ki po fizikalnih, kemičnih in mehanskih lastnostih daleč presega lastnosti makroceluloznih vlaken.[5] Modul elastičnosti celuloznih nanofibril je teoretično višji od jekla in dosega vrednosti blizu 137 GPa.[6] Natezna trdnost NFC je približno 10 GPa, koeficient termičnega raztezka pa je nizek in dosega vrednosti blizu $2{,}6 \cdot 10^{-6}$ K^{-1}.[7–10] Ker so mehanske lastnosti celuloznih nanofibril primerljive z lastnostmi drugih inženirskih materialov (steklena, aramidna, kevlar vlakna),[5] so primerna ojačitvena sredstva za utrjevanje najrazličnejših polimernih osnov.

Priprava biopolimernih nanokompozitov, osnovanih na celuloznih nanofibrilah ali nanokristalih temelji na vlivanju organske raztopine in nadaljnji evaporaciji topila [11] ali na metodi ekstruzijskega mešanja, pri kateri mora biti ojačitveni element v obliki suhe snovi – navadno prahu.[12] V prvem primeru pridobimo transparentne filmske strukture z navadno izboljšanimi bariernimi in mehanskimi lastnostmi.[11,13] Možnosti uporabe nanokompozitov, izdelanih po drugem postopku predelave so precej bolj raznolike, ker jih je mogoče oblikovati v najrazličnejše profile oziroma končne izdelke. Po drugi strani je izdelava nanokompozitov s tehnologijo ekstruzije veliko bolj zapletena kot pri tehnologiji vlivanja in trenutno predstavlja številne izzive na raziskovalnem področju. Znanstvenih študij, v katerih bi bila opisana uspešna študija s področja ekstrudiranja celuloznih bionanokompozitov, je relativno malo.[12,14–17] Pri ekstruzijskem postopku se soočamo s problematiko nehomogene porazdelitve ojačitvene faze po polimerni osnovi, kar poslabša kakovost in trajnost nastalih materialov.[12–17] Pomembno omejitev uporabe NFC v takšnih sistemih predstavlja medij shranjevanja, ki je voda, in hidrofilna površina NFC, zaradi katere jo težko dispergiramo v medijih nepolarnega značaja.[5] Mešanje NFC in polimerov različnega izvora je zato v večini primerov omejeno na vodna ali polarna okolja,[17] tehnologije predelave pa na laboratorijsko merilo.[13–14] Z namenom izdelave bionanokompozitov ojačanih z NFC v industrijskem merilu, smo pripravo kompozitnih mešanic prilagodili ekstruzijskemu mešanju liofiliziranih koncentratnih mešanic PHB prahu in celuloznih nanofibril ter nadaljnji predelavi s tehnologijo brizganja. Predelovalne, morfološke in mehanske lastnosti nanokompozitnih materialov smo ovrednotili v odvisnosti od različnih utežnih razmerij NFC.

2 MATERIALI IN METODE

2.1 Nanofibrilirana celuloza (NFC)

Vodna suspenzija celuloznih nanofibril (1.6 utežnih %) je bila pridobljena iz CBBP (Centre for Biocomposite and Biomaterial Processing), Univerza v Torontu, Kanada. Po podatkih proizvajalca je povprečni premer fibril med 25 nm in 70 nm, njihova dolžina pa presega velikostno območje 1 mikrometra. Končni produkt je bil izdelan z večkrat ponovljenimi postopki fibrilacije beljenih celuloznih vlaken lesa iglavcev. Po kemični sestavi NFC vsebuje 91 % celuloze, 8,7 % hemiceluloze in manj kot 0,3 % lignina.

2.2 Poli(3-hidroksibutirat) (PHB)

V raziskavo smo vključili dve različni obliki poli(3-hidroksibutirata): prva v obliki granul pod tržnim imenom Biomer®P226, druga pa v obliki prahu kot izhodni produkt bakterijsko vodenih fermentacijskih postopkov. Oba materiala sta bila pridobljena iz podjetja Biomer®biopolyesters, Krailling, Nemčija. Po podatkih proizvajalca, granulirana oblika PHB, Biomer®226, lahko vsebuje do 20 utežnih % različnih aditivnih sredstev za stabilizacijo končnega produkta, katerih identiteta ni javno dostopna.

2.3 Priprava PHB/NFC nanokompozitov

Nanokompozite z utežnim deležem NFC v višini (2, 4, 6, 8 in 10) %, smo pripravili na osnovi PHB/NFC koncentratov in granulirane oblike biopolimerne osnove, PHB®P226. Za pripravo koncentratnih mešanic ali "masterbach" komponent smo uporabili PHB v obliki prahu in NFC v vodni suspenziji. Biopolimerni prah, dispergiran v destilirani vodi, smo mešali z vodno suspenzijo nanofibril v utežnem razmerju 85/15. Pripravljen disperzni sistem smo zamrznili v tekočem dušiku in ga sušili 72 h s postopkom liofilizacije (LyoQuest freeze dryer, Telstar) pri tlačnih pogojih – 0,040 mbar, temperaturi pladnjev – 22 °C in temperaturi kondenzatorja –50 °C. Sušen koncentrat smo nato ekstrudirali z dvopolžnim laboratorijskim ekstruderjem HAAKE™ MiniLab II (Thermo Scientific) pri delovni temperaturi 180 °C in hitrostjo vrtenja polžev 40 obratov/min. Ekstruzijsko predelane materiale smo nato granulirali in jih mešali s komponento PHB®P226. Pripravili smo pet različnih sestav kompozitnega materiala v odvisnosti od dodatka ojačitvene komponente NFC (**Tabela 1**). Za referenčni vzorec smo pripravili mešanico ekstrudiranega prahu PHB in granulirane komponente PHB®P226 v utežnem razmerju 15/85. Kompozitne mešanice PHB/NFC /PHB®P226 smo sušili 15 h v laboratorijskem sušilniku pri 80 °C, nato pa jih ekstrudirali pri delovni temperaturi 180 °C, zadrževalnim časom taline 10 min ter hitrostjo vrtenja polžev 40 obratov/min. Talino predelanega materiala smo brizgali s povezano enoto HAAKE™ MiniJet v standardno orodje za izdelavo nateznih preizkušancev tipa 1BA. Temperaturo brizganja smo nastavili na 185 °C, temperaturo orodja na 45 °C, tlak brizganja je bil 500 b, čas cikla in čas ohlajevanja pa 5 s oziroma 10 s. Izdelane preizkušance smo 7 dni klimatizirali pri 23 °C in 50 % vlažnosti, kot določa standard ISO 527-2.

Tabela 1: Končna sestava PHB®P226/PHB mešanic glede na dodani utežni delež NFC

Table 1: Final compositions of PHB®P226/PHB blends with respect to the weight ratio of NFC

Oznaka vzorca	PHB	NFC	PHB®P226	Razmerje komponent
PHB/PHB®P226	1,35 g	–	7,65 g	15/85
PHB/NFC/ PHB®P226_2	1,17 g	0,18 g	7,65 g	13/2/85
PHB/NFC/ PHB®P226_4	0,99 g	0,36 g	7,65 g	11/4/85
PHB/NFC/ PHB®P226_6	0,81 g	0,54 g	7,65 g	9/6/85
PHB/NFC/ PHB®P226_8	0,63 g	0,72 g	7,65 g	7/8/85
PHB/NFC/ PHB®P226_10	0,45 g	0,90 g	7,65 g	5/10/85

2.4 Elektronska vrstična mikroskopija z delovanjem na poljsko emisijo (FE-SEM)

Morfološke lastnosti nanokompozitnih komponent, NFC in PHB, smo opisali s pomočjo FE-SEM mikroskopa (Zeiss ULTRA plus, Nemčija) pri različnih povečavah. Pospeševalne napetosti (EHT) so variirale v območju od 1 kV do 3 kV, razdalja snemanja je bila med 3 mm in 3.5 mm Vsi testni vzorci so bili prevlečeni s tanko plastjo ogljika s pomočjo naparjevalne naprave BAL – TEC/SCD 500.

2.5 Mehanske lastnosti nanokompozitnih sistemov

Mehanske lastnosti referenčnega vzorca in nanokompozitov z različnimi utežnimi dodatki NFC so bile določene preko nateznega preizkusa na trgalnem stroju Zwick/Roell Z005. Natezni modul (E_t), trdnost (σ_M) in raztezek pri pretrgu (ε_b) je bil za preiskane materiale določen na 30 mm razdalji med čeljustmi, pri hitrosti obremenjevanja 5 mm/min. Za vsako končno sestavo je bilo testiranih najmanj pet preizkušancev.

3 REZULTATI Z RAZPRAVO

3.1 Ekstruzijsko mešanje nanokompozitnih zmesi in predelava s tehnologijo brizganja

Ko smo dispergirali PHB prah v vodni suspenziji celuloznih nanofibril, je nastala stabilna zmes (**Slika 1**). Po sušenju te mešanice z zamrzovanjem (liofilizacijo) so nastali lahki, porozni in krhki kosmi (**Slika 1**). Tehnološka predelava takega materiala je zahtevna, predvsem zaradi velike prostornine sušenega produkta in njegove občutljivosti na vlago. Pri procesu ekstruzijskega mešanja smo z izklopom funkcije zadrževalnega časa, z izbiro ročnega doziranja ter visokimi obrati vrtenja polžev, pretok taline vodili kontinuirano, pri čemer je bila poraba operativne energije stroja nižja, temperaturna degradacija materiala pa zaradi kratkega zadrževalnega časa izključena. Ekstrudat v obliki traku (**Slika 1**) smo v nadaljnjih postopkih predelave granulirali in ga uporabili

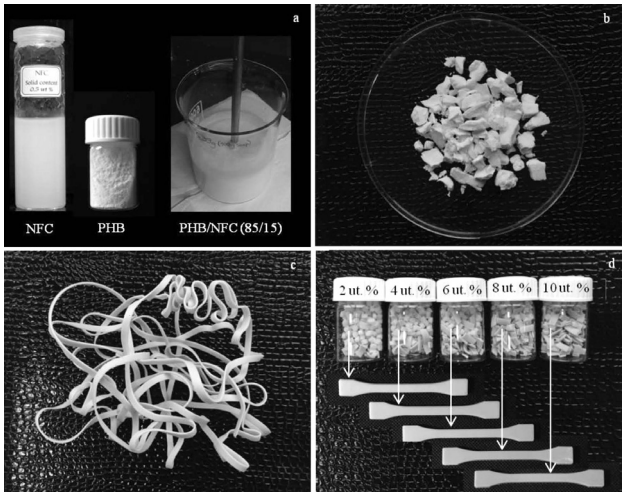

Slika 1: Priprava nanokompozitnih mešanic: a) sestavne komponente masterbatch sistemov: vodna suspenzija NFC, PHB v obliki prahu in disperzni sistem PHB/NFC, b) liofiliziran produkt PHB/NFC, c) ekstrudat liofilizirane mešanice PHB/NFC in d) nanokompozitne mešanice PHB/NFC/PHB®P226 in brizgani testni preizkušanci z različnim vsebnostnim deležem NFC

Figure 1: Preparation of the nanocomposite blends: a) constituent components of the masterbatch blends: an aqueous suspension of NFC, PHB in the powder form and a dispersed aqueous system of PHB/NFC, b) freeze-dried product of PHB/NFC, c) extrudate of the lyophilized PHB/NFC blend, d) nanocomposite blends of PHB/NFC/ PHB®P226 and injection-moulded test specimens with various contents of NFC

kot dodatek granulirani obliki PHB (PHB®P226). Pri iterativni predelavi večkomponentnih sestav je za homogeno porazdelitev materialnih komponent potrebno zagotoviti dovolj dolg obratovalni čas ekstruzijskega mešanja. Ob upoštevanju združevanja treh različnih materialnih komponent, t.im. PHB, NFC in PHB®P226, ter želji po enakomerni porazdelitvi nanofibril, je bil čas cikličnega ekstruzijskega mešanja podaljšan na 10 min. Z ozirom na kakovost površine izhodnih brizganih produktov (**Slika 1**) smo ugotovili, da mora biti temperatura orodja sorazmerno visoka, četudi se cikel predelave s tem časovno podaljša.

3.2 Morfološka analiza nanokompozitnih komponent

Morfološka preiskava nanofibrilirane celuloze v vodni suspenziji in njene sušene različice, pridobljene s postopkom liofilizacije, kaže na nekatere pomembne razlike v površinski strukturi fibrilarnih entitet. Pri izvorni obliki NFC so razvidne dolge in tanke fibrile s povprečnimi premeri od 20 nm do 60 nm (**Slika 2**), medtem ko je morfološka površina sušenega vzorca sestavljena iz plastno urejenih fibril, ki se prepletajo v obliki širših pramenov in ustvarjajo videz zamrežene površine (**Slika 2**). Njihove prečne dimenzije so relativno velike (1,2 μm), dosegajo pa tudi sub-mikronske (35 nm) vrednosti. Povečane premere celuloznih nanofibril v suhem stanju je mogoče pripisati tvorbi dodatnih vodikovih vezi med postopkom liofilizacije,[18–20] ki se pojavi selektivno med stično razporejenimi fibrilami.[21]

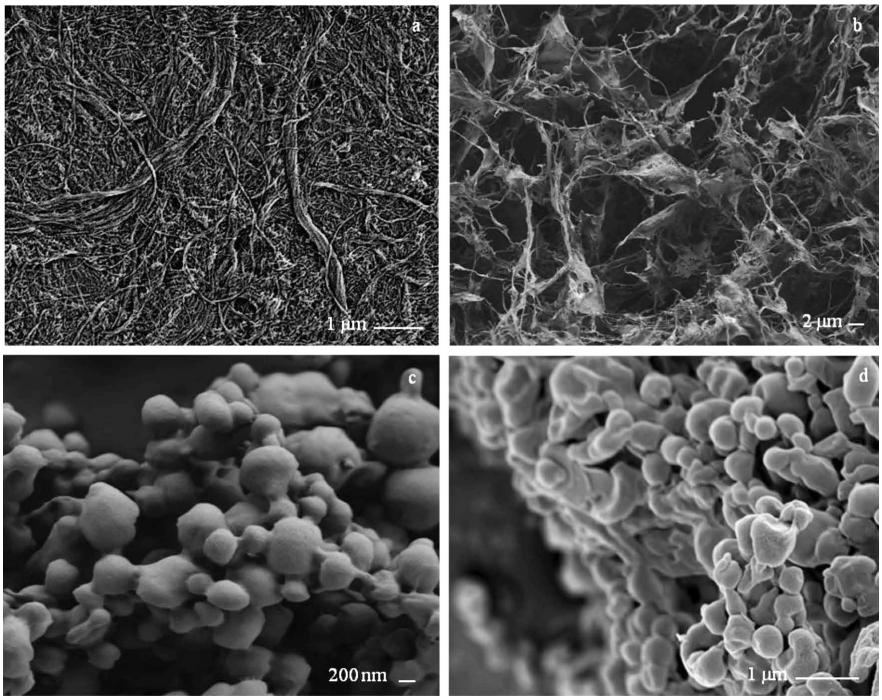

Slika 2: Nanokompozitne komponente: a) vodna suspenzija NFC, b) sušena oblika NFC, pridobljena s postopkom liofilizacije, c) PHB v obliki prahu in d) liofiliziran produkt PHB prahu dispergiranega v vodnem mediju

Figure 2: Nanocomposite components: a) NFC aqueous suspension, b) freeze-dried NFC, c) PHB in the powder form, d) freeze-dried product of the PHB powder dispersed in an aqueous medium

Fenomen nanofibrilarne agregacije, ki je posledica intra- in intermolekularne tvorbe vodikovih vezi, opisujemo z izrazom hornifikacija.[18]

Morfologija PHB prahu predstavlja delce skoraj pravilnih sferičnih oblik, povprečne velikosti 0,5 µm (**Slika 2**). Sprememba v morfologiji površine liofiliziranega PHB vzorca je zanemarljiva (**Slika 2**), opazna je le nekoliko bolj sprijeta sestava sferičnih polimernih struktur.

Mešanica PHB/NFC v utežnem razmerju 85/15, ki smo jo pridobili po sušenju z zamrzovanjem je prikazana na **Sliki 3** pri različnih mikroskopskih povečavah. Sušena oblika koncentrirane mešanice sestoji iz sferičnih delcev polimera, ujetih v mreži prepletenih nanofibril s povprečnimi prečnimi dimenzijami 69±14 nm. Te so v večini individualno razporejene po polimerni osnovi, na nekaterih mestih pa ostajajo v agregirani obliki zaradi pojava hornifikacije, ki nastopi med postopkom sušenja.

3.2 Mehanske lastnosti nanokompozitnih vzorcev

Vpliv dodatka PHB/NFC v različnih utežnih razmerjih na mehanske lastnosti matrične osnove PHB®P226 smo določili na osnovi nateznega preizkusa in primerjali z vrednostmi mehanskih parametrov (E_t, σ_M in ε_b) referenčnega vzorca PHB/PHB®P226. Reprezentativne krivulje preiskovanih materialov so v odvisnosti od napetosti (σ) in raztega (ε) prikazane na **Sliki 4**, povprečne vrednosti mehanskih parametrov s standardno deviacijo pa so zbrane v **Tabeli 2**.

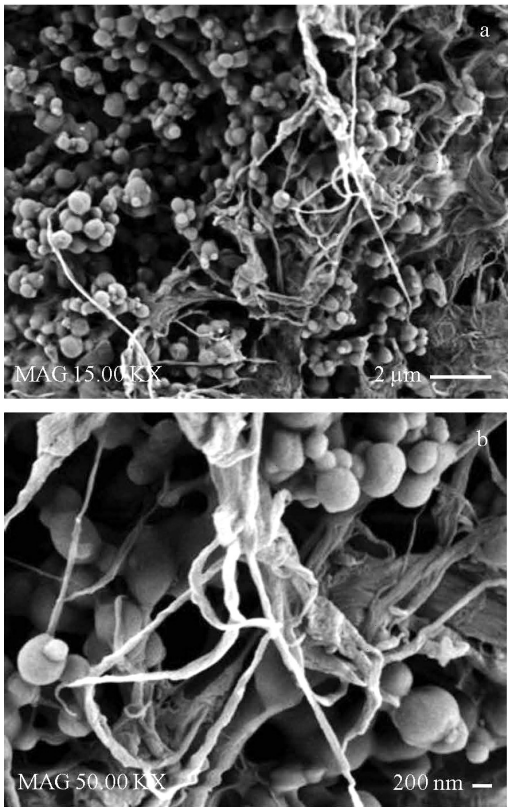

Slika 3: Koncentrirane mešanice PHB/NFC (85/15): a) pri 15.000-kratni mikroskopski povečavi in b) pri 50.000-kratni mikroskopski povečavi

Figure 3: PHB/NFC masterbatch mixtures (85/15): a) 15.000×, b) 50.000× magnification

Tabela 2: Mehanske lastnosti kompozitnih vzorcev glede na dodani utežni delež NFC

Table 2: Mechanical properties of the resulting composites with various contents of NFC

Vzorec	Natezni modul (E_t)	Natezna trdnost (σ_M)	Raztezek pri pretrgu (ε_b)
	MPa	MPa	%
PHB/NFC/ PHB®P226	1340 ± 90	20 ± 1	2,4 ± 1,0
PHB/NFC/ PHB®P226_2	1330 ± 30	22 ± 1	3,3 ± 0,2
PHB/NFC/ PHB®P226_4	1380 ± 30	22 ± 0,4	3,4 ± 0,3
PHB/NFC/ PHB®P226_6	1470 ± 20	23 ± 1	3,1 ± 0,2
PHB/NFC/ PHB®P226_8	1520 ± 50	24 ± 0,4	3,1 ± 0,3
PHB/NFC/ PHB®P226_10	1720 ± 40	26 ± 1	3,1 ± 0,5

Glede na potek σ–ε krivulj preiskanih vzorcev je razvidno, da dodatek NFC v splošnem izboljša mehanske lastnosti referenčnega vzorca PHB/PHB®P226, stopnja opisane spremembe pa je odvisna od utežnega razmerja ojačitvene komponente (**Slika 4**). Višji je utežni delež NFC v končni sestavi vzorca, višji so parametri elastične deformacije (E_t), trdnosti (σ_M) in raztezka (ε_b) nanokompozitnih materialov. Dodatek NFC v višini 2 % in 4 % vpliva na rahlo povišanje elastičnega modula (iz 1340 MPa na 1380 MPa) in natezne trdnosti (iz 20 MPa na približno 22 MPa), medtem ko so spremembe v vrednostih raztezka pri pretrgu bistveno bolj izrazite saj se z dodatkom celuloznih nanofibril v višini 10 utežnih % izboljša za skoraj 40 %. Ob povišanih deležih NFC elastični modul in natezna trdnost nanokompozitnih vzorcev naraščata (Preglednica 2), vrednosti za raztezek pri pretrgu pa se postopoma znižujejo, vendar še vedno ostajajo nad izmerjenimi vrednostmi za referenčni vzorec. Najvišje vrednosti izmerjenih mehanskih parametrov smo zabeležili pri nanokompozitih z dodanim deležem ojačitve v višini 10 %, pri čemer se modul elastičnosti in natezna trdnost zvišata za približno 28,5 % in 30 %, raztezek pri pretrgu pa za 28 %.

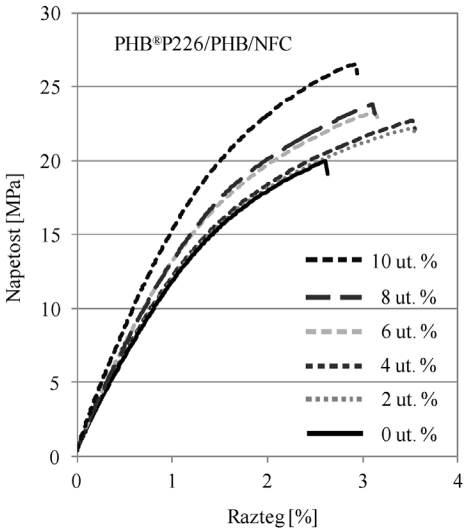

Slika 4: Krivulje odnosa napetost-raztezek kompozitnih vzorcev glede na variabilni utežni delež NFC

Figure 4: Stress-strain curves of the resulting composites with various contents of NFC

Glede na izsledke dosedanjih znanstvenih študij o spajanju tovrstnih materialov je navedba take izboljšave mehanskih lastnosti izjemno redka. Navadno izboljšan modul elastičnosti in večjo natezno trdnost spremlja manjši pretržni raztezek,[12,14–16] kar prispeva k povečani krhkosti izhodnih materialov. Delno izboljšanje ali celo poslabšanje mehanskih lastnosti nanokompozitnih formulacij z dodano komponento NFC se največkrat pripisuje njeni težnji k agregaciji med postopkom ekstruzijskega mešanja in nehomogeni porazdelitvi ojačitvene faze po polimerni osnovi.[12–16,19] Rezultati mehanske analize nanokompozitov izdelanih v tej študiji, pa v nasprotju s temi trditvami kažejo, da dodatek celuloznih nanofibril v obliki liofiliziranega koncentrata vodi do pridobitve ne le trdnih in togih, ampak tudi žilavih materialov. Mehanske lastnosti nanokompozitnih sistemov so odvisne od združljivosti medfaznih komponent, porazdelitve ojačitvene faze in njene morfološke oblike. Sklepamo, da s predhodnim postopkom mešanja polimernega prahu in nanofibril v vodnem mediju dosežemo koloidno stabilnost disperznega sistema in homogeno porazdelitev nanofibril po polimerni osnovi. Ta se glede na rezultate morfološke preiskave vzorcev ohrani skozi postopek liofilizacije in nadaljnjo ekstruzijsko pripravo nanokompozitov ter pomembno vpliva na izboljšanje mehanskih lastnosti izhodnih produktov.

4 SKLEPNE UGOTOVITVE

V prispevku je podan inovativni postopek izdelave nanokompozitov na osnovi koncentrirane mešanice biopolimernega prahu in celuloznih nanofibril z visokim utežnim deležem. Ker je opisana tehnologija prenosljiva na industrijski predelovalni obrat je še posebno zanimiva z vidika tržno usmerjenih aplikacij za tovrstne materiale in širjenja njihovih proizvodnih kapacitet. Z optimizacijo priprave koncentratnih nanokompozitnih mešanic in ustreznim utežnim deležem NFC v končni materialni formulaciji smo dokazali, da je z izbrano metodo tehnološke predelave ekstruzije in brizganja mogoče izdelati trdne, toge in žilave materiale, pri čemer delež ojačitvene faze narekuje stopnjo izboljšave mehanskih lastnosti biopolimerne osnove. Višji je delež dodanih celuloznih nanofibril v končni sestavi vzorca, višje so izmerjene vrednosti mehanskih parametrov. V primerjavi z referenčnim vzorcem imajo nanokompoziti z dodatkom 10 utežnih % NFC za okoli 30 % višji modul elastičnosti in prenesejo za približno 6 MPa višjo pretržno napetost. Pri vseh nanokompozitih smo zabeležili tudi pomembno višje vrednosti raztezka pri pretrgu, torej lahko sklepamo, da je adhezivni spoj med matrično in ojačitveno fazo dosežen, porazdelitev nanofibril pa homogena, kar

potrjujejo tudi mikroskopske preiskave nanokompozitnih mešanic.

PHB kompoziti ojačani z naravnimi vlakni kot so bambusova,[22] lesna ali kenaf vlakna[23] beležijo bistveno nižje vrednosti natezne trdnosti in raztezka pri pretrgu kot jih izkazujejo nanokompoziti izdelani v tej študiji. Natezno trdnost PHB kompozitov ojačanih z bambusovimi vlakni[22] je mogoče preseči za dvakratno vrednost že pri zelo nizkih utežnih deležih NFC (2 utežna %), medtem ko se raztezne lastnosti PHB osnove z dodatkom celuloznih nanofibril izboljšajo za več kot 400 % v primerjavi z dobljenimi vrednostmi raztezka za PHB kompozite na osnovi naravnih vlaken.[22,23] Z izdelavo nanokompozitov na osnovi liofiliziranih koncentratnih mešanic PHB/NFC smo dokazali, da lahko izhodni produkti dosegajo izboljšane mehanske lastnosti že ob zelo nizkem utežnem dodatku nano ojačitvenega elementa in tako predstavljajo zanimivo alternativo konvencionalnim mikro- ali makrobiokompozitnim materialom ter sintetičnim polimerom s steklenimi ali karbonsko osnovanimi polnili.

5 ZAHVALA

Avtorji se zahvaljujejo Javni agenciji za raziskovalno dejavnost Republike Slovenije za finančno podporo v okviru programske skupine P4-0015. Zahvala gre prav tako Agenciji SPIRIT Slovenija za delno finančno podporo v okviru Evropskega socialnega sklada Evropske Unije, v okviru katere je nastal del te raziskave.

6 LITERATURA

[1] D. Garlotta, A literature Review of Poly(Lactic Acid), Journal of Polymers and the Environment, 9 (**2001**) 63–84, doi:10.1023/A:1020200822435

[2] P. M. Visakh, Polyhydroxyalkanoates (PHAs), their Blends, Composites and Nanocomposites: State of the Art, New Challenges and Opportunities, Polyhydroxyalkanoate (PHA) Based Blends, Composites and Nanocomposites, (**2014**) 1–17, doi:10.1039/9781782622314-00001

[3] K. Van de Velde, P. Kiekens, Biopolymers: overview of several properties and consequences on their applications, Polymer Testing, 21 (**2002**), 433–442, doi:10.1016/S0142-9418(01)00107-6

[4] C. Winkworth-Smith, T. J. Foster, General Overview of Biopolymers: Structure, Properties, and Applications, Handbook of Biopolymer-Based Materials: From Blends and Composites to Gels and Complex Networks (eds S. Thomas, D. Durand, C. Chassenieux and P. Jyotishkumar), 2013, Wiley-VCH Verlag GmbH & Co. KGaA, Weinheim, Germany, doi:10.1002/9783527652457.ch2

[5] S. J. Eichhorn, A. Dufresne, M. Aranguren, N. E. Marcovich, J. R. Capadona, S. J. Rowa, C. Weder, W. Thielemans, M. Roman, S. Renneckar, W. Gindl, S. Veigel, J. Keckes, H. Yano, K. Abe, M. Nogi, A. N. Nakagaito, A. Mangalam, J. Simonsen, A. S. Benight, A. Bismarck, L. A. Berglund, T. Peijs, Review: current international research into cellulose nanofibres and nanocomposites, Journal of Material Science, 45 (**2010**) 1, 1–33, doi:10.1007/s10853-009-3874-0

[6] W. J. Orts, J. Shey, S. H. Imam, G. M. Glenn, M. E. Guttman, J. F. Revol, Application of cellulose microfibrils in polymer nanocomposites, Journal of Polymers and the Environment, 13 (**2005**) 4, 301–306, doi:10.1007/s10924-005-5514-3

[7] K. Tashiro, M. Kobayashi, Theoretical evaluation of three-dimensional elastic contacts of native and regenerated celluloses: role of hydrogen bonds, Polymer, 32 (**1991**), 1516–1526, doi:10.1016/0032-3861(91)90435-L

[8] S. J. Eichhorn, R. J. Young, The Young's modulus of a microcrystalline cellulose, Cellulose, 8 (**2003**), 197–207, doi:10.1023/A:1013181804540

[9] A. Šturcova, G. R. Davies, S. J. Eichorn, Elastic modulus of stress-transfer properties of tunicate cellulose whiskers, Biomacromolecules, 6 (**2005**), 1055–1061, doi:10.1021/bm049291k

[10] S. Iwamoto, W. Kai, A. Isogai, T. Iwata, Elastic modulus of single cellulose microfibrils from tunicate measured by atomic force microscopy, Biomacromolecules, 10 (**2009**), 2571–2576, doi:10.1021/bm900520n

[11] M. Sanchez-Garcia, J. M. Lagaron, On the use of plant cellulose nanowhiskers to enhance the barrier properties of polylactic acid, Cellulose, 17 (**2010**), 987–1004, doi:10.1007/s10570-010-9430-x

[12] K. Oksman, A. P. Mathew, D. Bondeson, I. Kvien, Manufacturing process of cellulose whiskers/polylactic acid nanocomposites, Composite Science Technology, 66 (**2006**), 2776–2784, doi:10.1016/j.compscitech.2006.03.002

[13] M. Bulota, K. Kreitsmann, M. Hughes, J. Paltakari, Acetylated microfibrillated cellulose as a toughening agent in poly(lactic acid), J App Polym Sci, 126 (**2012**), 448–457, doi:10.1002/app.36787

[14] M. Jonoobi, A. P. Mathew, M. M. Abdi, M. Davoodi Makinejad, K. Oksman, A comparison of modified and unmodified cellulose nanofiber reinforced polylactic acid (PLA) prepared by twin screw extrusion, Polymer Environment, 20 (**2012**), 991–997, doi:10.1007/s10924-012-0503-9

[15] Y. Srithep, T. Ellingham, J. Peng, R. Sabo, C. Clemons, L. S. Turng, S. Pilla, Melt compounding of poly(3-hydroxybutyrate-co-3-hydroxyvalerate)/nanofibrillated cellulose nanocomposites, Polymer Degradation and Stability, 98 (**2013**), 1439–1449, doi:10.1016/j.polymdegradstab.2013.05.006

[16] M. Jonoobi, J. Harun, A. P. Mathew, K. Oksman, Mechanical properties of cellulose nano-fiber (CNF) prepared by twin screw extrusion, Composite Science and Technology, 70 (**2010**), 1742–1747, doi:10.1016/j.compscitech.2010.07.005

[17] G. Siqueira, J. Bras, A. Dufresne, Cellulosic bionanocomposites: A review of Preparation, Properties and Applications, Polymer, 2 (**2010**), 728–765, doi:10.3390/polym2040728

[18] A. M. Scallan, The structure of the cell wall of wood – A consequence of anisotropic inter-microfibrillar bonding, Wood Science, 6 (**1974**) 3, 226–271

[19] V. Žepič, I. Poljanšek, P. Oven, M. Čop, COST-FP1105: Properties of PLA films reinforced with unmodified and acetylated freeze dried nanofibrillated cellulose Holzforschung, 70 (**2016**) 12, 1125–1134

[20] V. Žepič, I. Poljanšek, P. Oven, Š. A. Sever, A. Hančič, Effect of drying pretreatment on the acetylation of nanofibrillated cellulose, Bioresources, 10 (**2015**) 4, 8148–8167

[21] V. Žepič, E. Š. Fabjan, M. Kasunič, R. C. Korošec, A. Hančič, P. Oven, L. Perše, I. Poljanšek, Morphological, thermal, and structural aspects of dried and redispersed nanofibrillated cellulose (NFC), Holzforschung, 68 (**2014**) 6, 657–667, doi:10.1515/hf-2013-0132

[22] R. Krishnaprasad, N. R. Veena, H. J. Maria, R. Rajan, M. Skrifvars, K. Joseph, Mechanical and Thermal Properties of Bamboo Microfibril Reinforced Polyhydroxybutyrate Biocomposites, J Polym Environ, 17 (**2009**) 2, 109–114, doi:109. doi:10.1007/s10924-009-0127-x

[23] S. Kuciel, A. Liber-Knec, Biocomposites based on PHB filled with wood or kenaf fibers, Polimery, 3 (**2011**), 218–223

UDK 67.017:620.17:669.13
Original scientific article/Izvirni znanstveni članek

ISSN 1580-2949
MTAEC9, 51(3)515(2017)

CHARACTERISTICS OF THE THERMAL FATIGUE RESISTANCE FOR 3.1C, 0.8Si, 0.9Mn, 1.7Cr, 4.5Ni AND 0.3Mo ICDP CAST IRON ROLL AT 600 °C

ZNAČILNOSTI ODPORNOSTI ZLITIN LITEGA ŽELEZA ZA VALJE 3.1C, 0.8Si, 0.9Mn, 1.7Cr, 4.5Ni IN 0.3Mo NA ICDP TERMIČNO UTRUJANJE PRI 600 °C

Milan Terčelj[1], Peter Fajfar[1], Matjaž Godec[2], Goran Kugler[1]

[1]University of Ljubljana, Faculty of Natural Science and Engineering, 12 Aškerčeva street, 1000 Ljubljana, Slovenia
[2]Institute of Metals and Technology, Lepi pot 11, 1000 Ljubljana, Slovenia
Goran.Kugler@omm.ntf.uni-lj.si

Prejem rokopisa – received: 2016-08-23; sprejem za objavo – accepted for publication: 2016-08-31

doi:10.17222/mit.2016.259

Using a new test rig the characteristics related to the thermal fatigue resistance for ICDP (Indefinite Chill Double Pour) cast iron for hot working rolls was investigated. Tests were carried out at 600 °C to obtain the characteristics of cracks at (500, 1000 and 1500) cycles. For comparative purposes, additionally a test at 500 °C was carried out. The average length of all the cracks, their density, average length of five longest cracks and relevant microstructural characteristics for the mentioned cycles were determined. It was found that the cracks initiation and their growth are related to the cracking and spalling of the carbides, shape of graphite, distribution of carbides and graphite particles, oxidation, etc. The obtained results contribute to a better understanding of the thermal cracking of selected roll cast iron. Based on these results the suggestions for improving the thermal fatigue resistance for the cast iron roll are given.

Keywords: roll cast iron, thermal fatigue, cementite, graphite, cracks

Novo razvita naprava je bila uporabljena za raziskave lastnosti ICDP litega železa, ki so povezane z odpornostjo na termično utrujanjem. Značilnosti razpok so bile določene po (500, 1000 in 1500) ciklih, pri 600 °C. Za primerjavo je bilo izvedenih nekaj testiranj tudi pri 500 °C. Na osnovi rezultatov testiranj je bilo za vsako število ciklov določena povprečna dolžina vseh dobljenih razpok, njihova gostota, povprečna dolžina petih najdaljših razpok, vključno z ostalimi relevantnimi mikrostrukturnimi značilnostmi. Rezultati so pokazali, da sta nukleacija in rast razpok tesno povezana s pokanjem in drobljenjem karbidov, z geometrijo grafita, z volumsko porazdelitvijo karbidov ter grafitnih delcev, z oksidacijo, itd. Rezultati prispevajo k boljšemu razumevanju termičnega pokanja izbranega materiala za valje. Na osnovi predstavljenih rezultatov so podani predlogi za izboljšanje odpornosti litega železa za valje na termično utrujanje.

Ključne besede: lito železo za valje, termično utrujanje, cementit, grafit, razpoke

1 INTRODUCTION

Dies used in hot-working applications like die casting, rolling, forging and hot extrusion are exposed to high thermal, mechanical, tribological and chemical loads. The occurrence of different damage, i.e., cracks, fracture, plastic deformation and wear, are a consequence of the different magnitudes of the mentioned loads as well as their different mutual ratios, materials properties, etc.[1–7] Thus, in the case of cyclical subjection to high temperatures, i.e., the heating of rolls (also above 600 °C) and their water cooling, these conditions lead to the occurrence of cracking on the die's surface, which appears in the shape of a crack network that consequently results in spalling of the die material that further leads to a deterioration of the surface finish of the workpiece. In hot-working rolls the thermal stresses are usually comparable or even larger than the mechanical stresses.[3–10]

To increase the die's service time it is important and also the common task for both die designers as well as for producers of die steels, to shift the occurrence of cracks to later times and to decrease their growth rate. Hot working rolls are usually alloyed with Cr, V, Mo, W, and after solidification process they are heat treated accordingly. Furthermore, with optimization of the chemical composition and the process parameters of the roll production improved microstructure with better thermal fatigue resistance for each individual application can be achieved. In relation to the desired microstructural properties it is important to achieve (i) appropriate type, size, amount, shape, distribution, etc. of carbides, (ii) amount, size and shape of graphite particles, (iii) grain size, etc. Thus, regarding the specific application the appropriate combination of mechanical (ductility, yield strength, toughness, hardness, etc.), thermal, microstructural properties as well as oxidation resistance should be engineered.[3–17]

Several research works related to thermal fatigue resistance of die materials (i.e. steels, cast irons) were carried out where reasons for initiation and growth of cracks at hot working dies (forging, die casting)[17–30] and hot working rolls [3–6,9,31–34] were investigated using various

laboratory tests. However, detailed knowledge about the influence of the stress state, the temperature and the oxidation on the initiation and propagation of thermal cracks in hot working applications is still lacking. Each of the applied laboratory tests has some advantages and disadvantages from the point of view of achieving of test conditions and their controllability. Thus, the accuracy of achieving the prescribed test temperature and subsequent cooling rate are key factors that influence the quality of the obtained laboratory results and consequently also on an explanation of the crack initiation and their growth.[19–27]

In this work the thermal fatigue resistance of Indefinite Chilled Double Poured (ICDP) cast iron for rolls at two different temperatures was studied using a new test rig with specially prepared test samples. The resistance to thermal fatigue at three different numbers of heating-cooling cycles were evaluated by measuring the average length of cracks, their density, average length of five largest cracks and the relevant microstructures. The initiation and growth of the cracks were evaluated and explained. Some suggestions for improvement of thermal fatigue resistance for the used cast iron roll are given.

2 EXPERIMENTAL PART

2.1 ICDP cast iron

ICDP cast iron with the chemical composition given in **Table** 1 was used for thermal fatigue testing. From the table it is clear that there is an increased content of C (above 3 %) as well as for Si, Mn, Cr, Mo in comparison to the usual constructional steels and almost 4.5 %Ni. Thus, due to high content of carbon as well as the presence of carbide-forming elements, i.e., Cr, Mo and V, this indicates the presence of carbides and graphite in the microstructure.

Table 1: Chemical composition of used cast iron in mass fraction, (*w*/%)

Tabela 1: Kemijska sestava uporabljenega litega železa v masnih deležih, (*w*/%)

C	Si	Mn	Cr	Ni	Mo	V	W	Nb
3.11	0.84	0.86	1.71	4.45	0.30	0.13	0.01	0.01

2.2 Applied thermal fatigue test and conditions of testing

The shape of the samples and the applied thermal fatigue tests are shown in **Figures 1a** and **1b**, respectively. Hollow specimen is on both sides tightly clamped between two copper anvils which are placed in the working cells of a Gleeble 1500D thermo-mechanical simulator. On the middle of 12 mm working length of samples thermocouple wires of type K are welded, while water and air inlet as well as their outlet from samples are enabled by tubes fixed on its both lateral sides. Heating of the specimen and its cooling by water and air

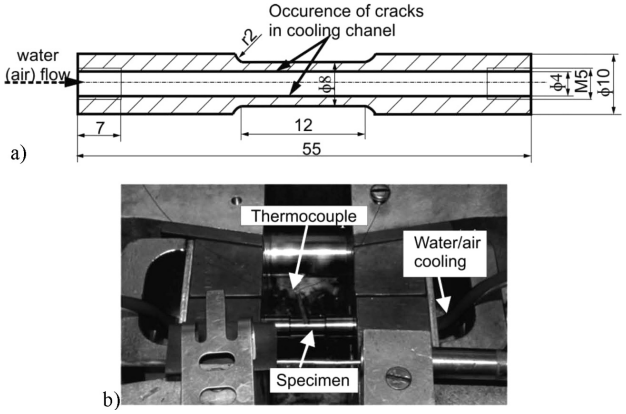

Figure 1: a) Used sample for thermal fatigue test and b) tight clamped sample between two cooper anvils in working cells of the Gleeble 1500D

Slika 1: a) Vzorec za testiranje termičnega utrujanja, b) tesno vpetje med dvoje čeljusti iz bakra v delovni celici naprave Gleeble 1500D

that flow through hollow specimen is computer guided, whereas constant testing conditions, i.e., achieving of constant heating to test temperature and specimen internal cooling, are ensured (**Figure 2**). Regarding the program the specimens were heated to a selected temperature in 3 s, which was followed by water cooling and emptying of specimen by air flow. Thus, the temperature gradient and consequently the stress gradient on the internal surface of the specimen is achieved. On this area (**Figure 1a**) the occurrence of cracks is expected. A maximum selected test temperature was 600 °C and for comparative reason also test at 500 °C was carried out. At test temperature of 600 °C cracks were observed and measured after 500, 1000 and 1500 thermal cooling cycles, while at 500 °C this was done after 1000 cycles (**Table 2**). After a selected number of cycles the working lengths of samples were cut in radial as well as in the axial directions. Characterization of the cracks was focused within area of 8 mm length of the central working dimension of samples. The cracks were characterized by (i) mean length of all cracks, (ii) density of cracks, i.e.,

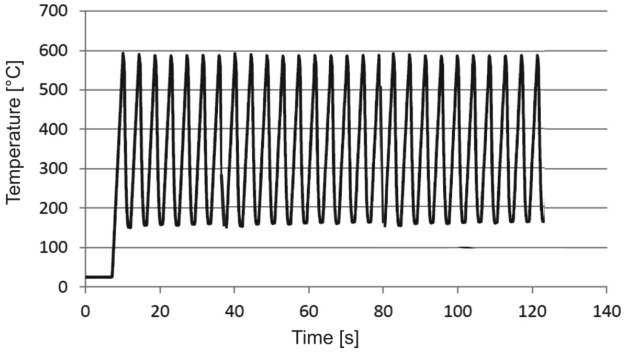

Figure 2: Measured time courses of temperature on outside surface of test specimen

Slika 2: Izmerjeni časovni potek temperature na zunanji površini vzorca za testiranje

average number of cracks per length of 1mm, and (iii) average length of the 5 longest cracks.

Table 2: Test conditions
Tabela 2: Pogoji testiranja

Test temperature	No. of cycles
500 °C	1000
600 °C	500, 1000, 1500

2.3 Characterization of cracks, carbides and microstructure

Optical microscopy (OM, Carl Zeiss AXIO Imager. A1m) and a field-emission scanning electron microscope (FE SEM JEOL 6500F) in combination with the attached Energy-Dispersive Spectroscopy (EDS, INCA x-SIGHT LN2 with INCA ENERGY 450 software) analytical tool were applied for observations of microstructure, i.e., determination of main constituents (graphite, cementite (carbides), etc.), characterization of cracks, etc. Furthermore, the amount of cementite (carbides) as well as of graphite particles regarding to size, distribution and shape were determined. Thus by means of automatic image analysis the form, distribution, and size of graphite nodes were classified according to the EN ISO 945 standard. The specimens used in optical microscopy were etched with 3 % Nital reagent.

3 RESULTS

3.1 Characterization of initial microstructure of cast iron

The obtained microstructure of the initial material at room temperature is presented in **Figure 3a** (OM) with details in **Figure 3b** as well as in **Figure 3c** (BEI) with mapping for C in **Figure 3d**. As can be seen the microstructure consists of martensite, retained austenite, carbides (cementite), graphite and also MnS inclusions. The results of the EDS analyses, which served for clear distinction between cementite and graphite, are given in **Table 3**. In general, cementite contains a considerably smaller amount of C in comparison to graphite. Thus, in cementite (carbides) besides C and Fe also main carbide-forming elements, i.e., Cr, Mo and V, as well as Co and Ni were found. The relative lower obtained values for C contents in cementite and graphite can be attributed to the detection depth of EDS analyses, whereas in our case this exceeded the depth of the interface between both relevant constituents and matrix, i.e., the matrix was also partly included in the analyses that apparently detected lower C contents. Furthermore, it also known that EDS analysis for light elements is not a very accurate method. A SEI image of the initial microstructure is given in **Figure 3c,** while the distribution of carbon is given in **Figure 3d**. Thus, also by this graphite particles and cementite can be clearly distinguished. Note that the obtained microstructure is very similar to the microstructure found in 45 for cast iron for rolls with similar chemical composition.

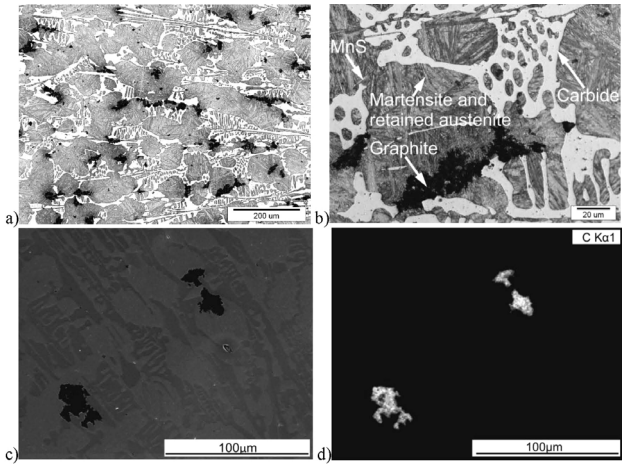

Figure 3: a) Initial microstructure (OM) of used cast iron with b) detail, c) BEI image showing carbides and graphite and d) corresponding X-ray image (mapping) of C distribution
Slika 3: Začetna mikrostruktura (OM) uporabljenega litega železa; a) z detajlom, b) slika BEI, ki prikazuje karbide in grafit, c) pripadajoča XRD slika (mapiranje), d) porazdelitev ogljika

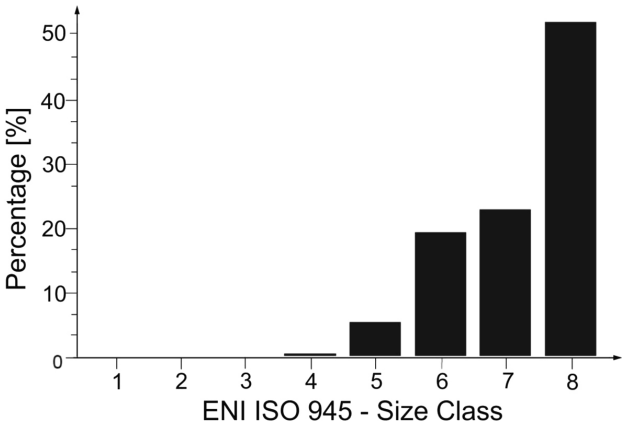

Figure 4: Percentage of graphite particles regarding their size
Slika 4: Delež grafitnih delcev v povezavi z njihovo velikostjo

Table 3: EDS analyse of chemical elements in carbides, graphite and martensite of used cast iron in mass fractions, (*w*/%)
Tabela 3: EDS-analiza kemičnih elementov v karbidih, grafitu ter martenzitu za uporabljeno lito železo v masnih deležih, (*w*/%)

	C	Si	Mn	Cr	Mo	V	Co	Ni	Fe	O	Al	Imp.
Carbides	5.7		0.9	3.6	0.3	0.3	1.3	1.8	91.4			rest
Graphite	93.9	-	-	-	-	-	-	-	6.1	-	-	-
Martensite	2.5	1.2	0.6	0.5	-	-	-	5.4	89.7	-	-	rest

The percentage of graphite and carbides in the microstructure amounted approximately 4.9 % and 29.5 %, respectively, where the nodularity of the graphite was 0.34. Using automatic image analysis, the form, distribution, and size of graphite nodes were classified according to the EN ISO 945 standard. The majority (almost 60 %) of the graphite particles were of Form II (crab or spiky) or (15 %) of Form III (vermicular) (**Figure 4**). More than half of all the graphite particles were smaller than 15 μm, equivalent to size class 8 (**Figure 4**).

3.2 Characterization of cracks growth

As mentioned above the obtained characteristics of cracks refer to the length of 8 mm in central working length of the samples. Numbers of cracks for different class length of cracks in dependence on number of cycles and for test temperature of 600 °C are given in **Figure 5**. As can be seen, in general, the number of cracks decreases with increasing of class length for all numbers of cycles. Thus, for the class length of cracks up to 100 μm the number of cracks amounts about 70 for all number of cycles, at class length range 100–200 μm this value amounts slightly below 20, while at class length range 200–300 μm the number of cracks is in the range 3–6. With further increasing of class length range the number of cracks decreases, thus in class length range 800–900 μm only one crack for thermal cycle 1000 and 1500, respectively, were obtained.

For the comparison at 1000 cycles and 500 °C the number of cracks are up to class length range of 300 μm, approximately by about 20 % lower in comparison to the test temperature of 600 °C and the same number of thermal cycles. Furthermore, the longest cracks at test temperature of 500 °C and 1000 thermal cycles were about 500 μm.

From **Figure 6a** it is clear that at test temperature of 600 °C the average lengths of all the cracks increases with the number of cycles. Thus, after 500 thermal

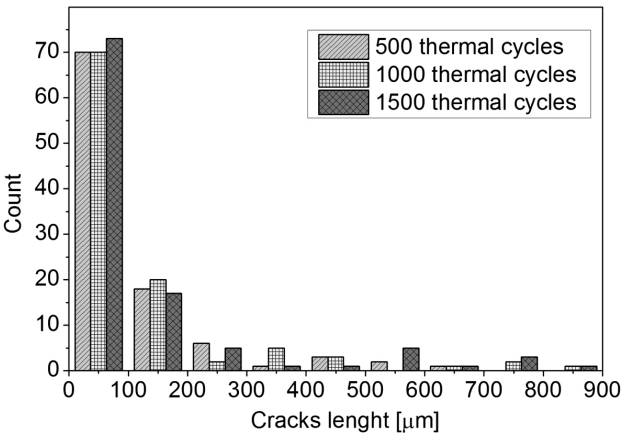

Figure 5: Distribution of crack number related to class length and in dependence on number of thermal cycles and test temperature

Slika 5: Porazdelitev števila razpok v povezavi z razredom dolžin v odvisnosti od števila termičnih ciklov ter temperature testiranja

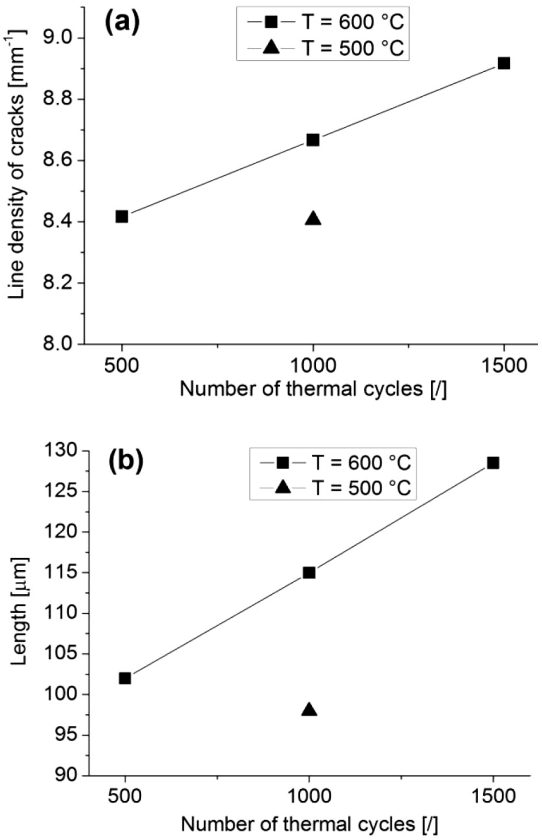

Figure 6: a) Average lengths of all cracks and b) cracks density in dependence of the number of thermal cycles and test temperature

Slika 6: a) Povprečna velikost vseh razpok b) in gostota razpok kot funkcija števila termičnih ciklov in temperature testiranja

cycles the average crack length amounts to 102 μm, at 1000 cycles, 115 μm and at 1500 cycles, 127 μm. For comparative test conditions, i.e., 500 °C and 1000 cycles, the average crack length amounted to 97 μm. As expected, this value is lower in comparison to the one obtained for a temperature of 600 °C for the same thermal cycles. Similar relationships were also obtained for the crack density, which is shown in **Figure 6b**. Thus at the test temperature of 500 °C and 1000 cycles the density of cracks was 8.4 cracks/mm, i.e., lower in comparison to the test temperature of 600 °C and the same number of cycles where this value was 8.7 cracks/mm. At 500 cycles and the same temperature this value is slightly lower, i.e., 8.4 cracks/mm, while at 1500 cycles it is slightly higher, i.e., 8.9 cracks/mm, regarding to 1000 cycles. Therefore, the density of the cracks increases only slightly with the increasing number of cycles and decreases with lower test temperature. The lower density of cracks at the lower temperature can be attributed to the lower stresses on the tested surface layer.

Also, the average length of the five longest cracks at test temperature of 600 °C increases with the number of cycles (**Figure 7**). Thus, this value is 570 μm at 500 cycles, 700 μm at 1000 cycles and 840 μm at 1500

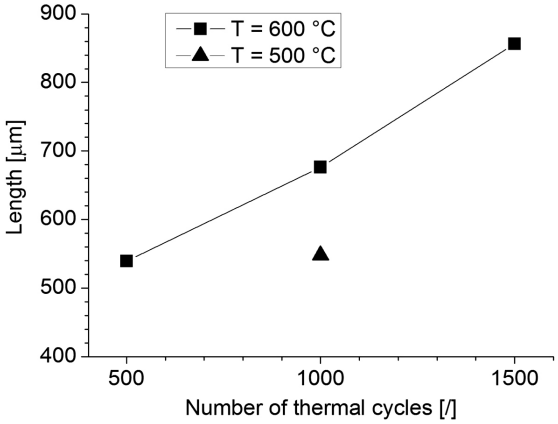

Figure 7: Average lengths of five longest cracks in dependence of the number of thermal cycles and test temperature

Slika 7: Povprečna velikost petih najdaljših razpok kot funkcija števila termičnih ciklov in temperature testiranja

cycles. For comparison, this value at the temperature of 500 °C and 1000 cycles was expectedly lower and is about 540 µm.

3.3 Microstructural characteristics of cracks

Cracks were predominately initiated at spots on the tested surface where the carbides are present (**Figures 8a** to **8b**). This process, which is a consequence of tensile stresses on surface layer, begins with cracking and spalling of the carbides, where cracks grow along the carbides, i.e., they use the carbides path. **Figure 8b** shows an empty area as a consequence of the carbides spalling at the crack's origin. Namely, the carbides have a lower temperature expansion coefficient and are also more brittle in comparison to the matrix. Thus during heating and cooling they cannot fully follow the dilatation of the base material and consequently they represent a notch effect, i.e., stress concentration. Furthermore, from **Figure 8b** it is also clear that the crack ends at the carbide–matrix interface. Note that crack growth within the matrix is hindered. In **Figure 8b** micro-cracks are visible that do not originate from the cooled surface but are internal in nature and are oriented in radial as well as in axial directions. EDS analyses revealed oxidation that expands on both sides of the crack.

In **Figure 8a** it can be also seen the transition of cracks growth from carbide to graphite and again to carbide, where crack again finishes at the carbide–matrix interface. This case illustrates alternating of carbide and graphite at crack growth that is also presented in **Figures 8c** to **8d**. It should be emphasized here that the shape of the carbides plays an important role since cracks usually grow in the direction of the flattened shaped graphite where the stress intensity is increased. Thus, nodularity (in this case 0.34) of the graphite should be increased in order to decrease the growth rates of the cracks. Similar results were also obtained by X. Tong et al.,[18] i.e., the thermal fatigue resistance of samples made from cast iron were sorted as nodular graphite iron > vermicular graphite iron > flake graphite iron. Furthermore, since cracks grow through carbide–graphite paths, their growth would be decreased by the interruption of these paths. This can be done by adding rare-earth elements. Note that in this way Wang et al.[31] achieved coagulation of the carbides and graphite and consequently also better thermal fatigue resistance of the roll steel. It can be assumed that a similar approach could also contribute to improved fatigue resistance for our type of roll cast iron. Also, slight hot deformation of the working layer of rolls would probably act in similar way, i.e., interruption of carbides paths by crushing of carbides.

Figure 9a shows the growth of cracks using the carbide and graphite path, while in **Figure 9b** the distribution of oxygen is presented. From both figures it is clear that during crack growth oxidation has taken place. This is also visible at the crack tip that decreases the local strength properties of the matrix and consequently also accelerates the growth rate of the cracks. Furthermore, it is also clear that the cracks in the graphite do not grow through its central part but along both lateral sides.

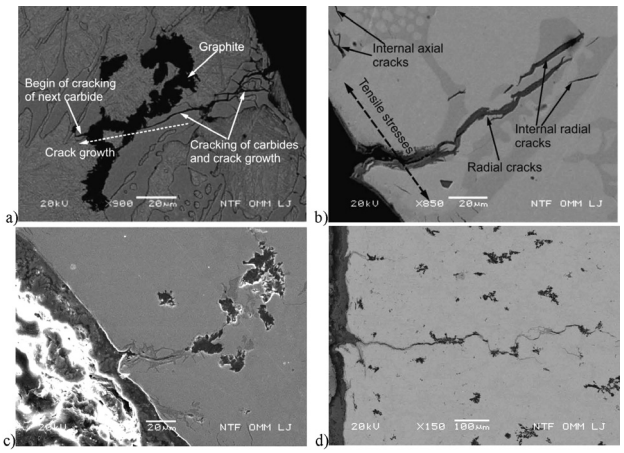

Figure 8: a) Initiation of cracks and cracking of carbides and b) growth of cracks using carbides (cementite) path, (c–d) growth of cracks using carbides and graphite particles

Slika 8: a) Nukleacija razpok ter pokanje karbidov in b) rast razpok po karbidnih (cementitnih) poteh, (c–d) rast razpok preko karbidov in grafitnih delcev

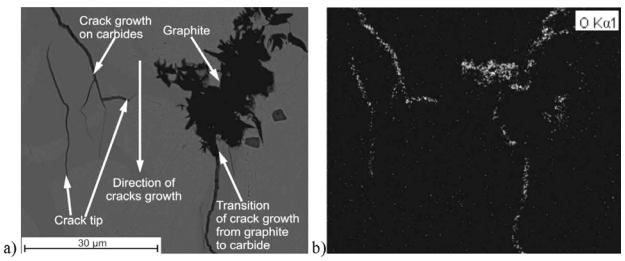

Figure 9: a) Crack growth in carbides (cementite) and graphite and oxidation of cracks, b) distribution of oxygen in cracks internal and on crack tip

Slika 9: a) Rast razpok v karbidih (cementitu) in grafitu ter oksidacija razpok, b) porazdelitev kisika v notranjosti razpok ter v njenih konicah

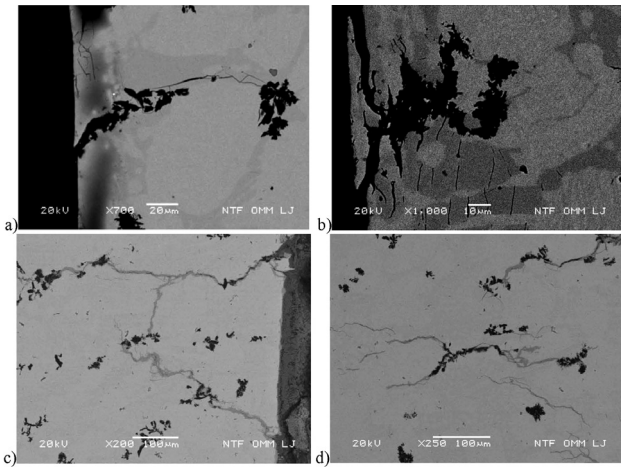

Figure 10: a) Initiation of cracks at sharp shaped (formed) graphite, b) spalling of small sized part of matrix at graphite, c) unification (linking) of cracks originate from different initial spots at surface, d) internal crack extending carbides and graphite particles

Slika 10: a) Nukleacija razpok na ostri obliki grafita, b) drobljenje majhnih delov grafitne matrike, c) združevanje razpok, ki izvirajo iz različnih začetnih točk na površini, d) širjenje notranje razpoke med karbidi in grafitnimi delci

Further crack growth from the graphite to carbides is characterized by crack oxidation of the main crack and by the occurrence of new micro-cracks on both sides. Note that improvement of oxidation resistance also leads to an improvement of the thermal fatigue resistance.[6,16,32]

As already mentioned, cracks are usually initiated at the carbides on cooled surfaces, which is shown in **Figure 10a**. But in very limited cases they are also initiated at the sharp graphite particles that are elongated in the longitudinal direction, i.e., flattened graphite particles. Furthermore, since the graphite is softer than the matrix, this can also leads to a notch effect at such spots. Otherwise, it was found that for the more equiaxied graphite that precipitated at the cooled surface, cracks does not occur, since only spalling of the small-sized base material takes place, as presented in **Figure 10b**. From this figure it is also visible the occurrence of microcracks in the axial direction in carbides close to the graphite. This behaviour was very frequently observed and can be attributed to the differences in the thermal extensions of all the main constituents (i.e., matrix, carbides and graphite) leading to local bending of carbides as a consequence of the occurrence of the temperature gradient and the different thermal dilatation, i.e., outer regions are subjected to higher thermal dilatation. Moreover, in this case the carbides are oriented perpendicular to the cooled surface and the cracks appeared approximately in length area of the graphite particle.

Spalling of the material occurs also when cracks, which originate from different initial spots on cooled surface, unify (link) in one crack. Consequently, no adhesion between the base and the crack limited part of base material exists (**Figure 10c**). It was also observed that not only internal micro-cracks for which extension is limited inside the carbides, but also connected internal cracks extend across several carbides and graphite particles (**Figure 10d**). Furthermore, in some cases graphite can hinder the crack growth when it is located far enough from the cooled surface and if its shape is approaching spherical.

4 CONCLUSIONS

Using a specially developed test rig, the resistance against thermal fatigue for ICDP cast iron roll was investigated. Tests were carried out at 500 °C and 600 °C and characteristics related to cracks at 500, 1000 and 1500 cycles were obtained. The average length of all the cracks, crack density, average length of five longest cracks and microstructure characteristics related to cracks were determined. From the results the following conclusions can be derived:

- Microstructure of tested cast iron consists of carbides (cementite), graphite particles, MnS inclusions which are inserted in the martensite matrix. Percentage of graphite with value for nodularity of 0.34 amounted 4.9 %, while percentage for carbides amounted 29.5 %.
- The initiation of cracks is predominately on spots of precipitated carbides on the cooled surface.
- In a very few cases also the initiation of cracks at graphite particles with thin (flattened) and elongated shape, was observed. In the case of location of spherical shaped graphite particles at cooled surface this results only in spalling of base material.
- Cracks grow using carbides (cementite) and graphite paths. Thin (flattened) and elongated shapes of graphite are more appropriate at cracks growth than spherical.
- Average length of all cracks as well as cracks density at test temperature of 600 °C increases almost linearly with an increasing of number of cycles.
- For 1000 cycles the density of the cracks at the test temperature of 500 °C was lower in comparison to the test temperature of 600 °C. The occurrence of oxidation within the cracks as well as at crack tips was revealed, which results in acceleration of crack growth.
- Decreasing the possibility of the connection of carbides and graphite cracks paths will decrease the growth rate of cracks. This could be achieved (i) by crushing of carbides cells, i.e., by imposing of hot plastic deformation, (ii) by refining of carbides by additional alloying by rare-earth elements[31], (iii) by increasing nodularity of graphite and (iv) by improving the heat treatment as well as rolls production procedures.

5 REFERENCES

[1] F. J. Belzunce, A. Ziadi, C. Rodriguez, Structural integrity of hot strip mill rolling rolls, Engineering Failure Analysis, 11 (**2004**), 789–797, doi:10.1016/j.engfailanal.2003.10.004

[2] R. Colas, J. Ramirez, I. Sandoval, J. C. Morales, L. A. Leduc, Damage in hot rolling work rolls, Wear 230 (**1999**), 56–60, doi:10.1016/S0043-1648(99)00081-2

[3] K. Goto, Y. Matsuda, K. Sakamoto, Y. Sugimoto, Basic Characteristics and Microstructure of High-carbon High Speed Steel Rolls for Hot Rolling Mill, ISIJ Int. 32 (**1992**), 1184–1189, doi:10.2355/isijinternational.32.1184

[4] N. F. G. Montes de Oca, R. Colas, W. M. Rainfort, On the damage of work roll grade high speed steel by thermal cycling, Engineering Failure analysis, 18 (**2011**), 1576–1583, doi:10.1016/j.engfailanal.2011.06.001

[5] G. K. Ahiale, W. D. Choi, Y. Suh, Y. K. Lee, Y. J. Oh, Effect of MC-Type Carbide Forming and Graphitizing Elements on Thermal Fatigue Behaviour of Indefinite Chield Cast Iron Rolls, Metalurgical and Materials Transactions A, 46A (**2015**), 4819–4827, doi:10.1007/s11661-015-3090-2

[6] M. Yong-an, J. Bergström, W. Xiao-chun, X. Luo-ping, Oxidation and Thermal Fatigue Behaviors of Two Type Hot Work Steels During Thermal Cycling, Journal of iron and steel research, 20 (**2013**) 11, 90–97, doi:10.1016/S1006-706X(13)60202-2

[7] B. Podgornik, V. Leskovšek, Wear mechanisms and surface engineering of forming tools, Mater. Tehnol., 49 (**2015**) 3, 313–324, doi:10.17222/mit.2015.005

[8] M. Sedlaček, B. Podgornik, S. Milanovič, A modified heat treatment to improve the properties of double layer cast rolls, Mater. Tehnol., 48 (**2014**) 6, 983–990

[9] C. K. Kim, J. I. Park, J. H. Ryu, S. Lee, Correlation of Microstructure and Thermal Fatigue Property of Centrifugaly Cast High-Speed Steel Rolls, Metallurgical and Materials Transactions A, 35 (**2004**), 481–492, doi:10.1007/s11661-004-0359-2

[10] V. Leskovšek, B. Podgornik, Multifunctional Kic test specimen for assessment of different tool and high speed steel properties, Mater. Tehnol., 47 (**2013**) 3, 273–283

[11] D. Mitrovič, P. Mrvar, M. Petrič, Characterization of cast-iron gradient castings, Mater. Tehnol., 49 (**2015**) 6, 871–875, doi:10.17222/mit.2014.102

[12] J. Gontarev, M. Doberšek, J. Medved, P. Mrvar, Solidification of hipereutectoid high speed steel for rolls, Metalurgija 50 (**2011**) 1, 29–32

[13] M. Stürmera, J. Dagnerb, P. Manstettena, H. Köstler, Real-time simulation of temperature in hot rolling rolls, Journal of Computational Science, 5 (**2014**), 732–742, doi:10.1016/j.jocs.2014.04.003

[14] D. Benasciuttia, E. Brusab, G. Bazzaroc, Finite elements prediction of thermal stresses in work roll of hot rolling mills, Procedia Engineering, 2 (**2010**), 707–716, doi:10.1016/j.proeng.2010.03.076

[15] M. Pellizzari, A. Molinari, G. Straffelini, Tribological behaviour of hot rolling rolls, Wear 259 (**2005**), 1281–1289, doi:10.1016/j.wear.2004.12.006

[16] A. Molinari, G. Straffelini, A. Tomasi, A. Biggi, G. Corbo, Oxidation behaviour of ledeburitic steels for hot rolls, Materials Science and Engineering A, 280 (**2000**) 255–262, doi:10.1016/S0921-5093(99)00693-0

[17] M. Pellizzari, A. Molinari, G. Straffelini, Thermal fatigue resistance of gas and plasma nitrided 41CrAlMo7 steel, Materials Science & Engineering A, 352 (**2003**) 186–194, doi:10.1016/S0921-5093(02)00867-5

[18] X. Tong, H. Zhou, L.-Q. Ren, Z.-H. Zhang, W. Zhang, R.-D. Cui, Effects of graphite shape on thermal fatigue resistance of cast iron with biomimetic non-smooth surface, International Journal of Fatigue, 31 (**2009**), 668–677, doi:10.1016/j.ijfatigue.2008.03.023

[19] A. Persson, S. Hogmark, J. Bergström, Simulation and evaluation of thermal fatigue cracking of hot work tool steel, International Journal of Fatigue, 26 (**2004**), 1095–1107, doi:10.1016/j.ijfatigue.2004.03.005

[20] M. Fazarinc, R. Turk, G. Kugler, P. Mrvar, M. Terčelj, Development of test rig for thermnal fatigue testing: preliminary results, RMZ - Materials and geoenvironment, 54 (**2007**) 1, 38–48

[21] S. Amiable, S. Chapuliot, A. Constantinescu, A. Fissolo, A comparison of life time prediction methods for a thermal fatigue experiment, International Journal of Fatigue, 28 (**2006**), 692–706, doi:10.1016/j.ijfatigue.2005.09.002

[22] A. Fissolo, S. Amiable, O. Ancelet, F. Mermaz, J. M. Stelmaszyk, A. Constantinescu Crack initiation under thermal fatigue: an overview of CEA experience. Part I: Thermal fatigue appears to be more damaging than uniaxial isothermal fatigue, Int. J. Fatigue, 31 (**2009**), 587–600, doi:10.1016/j.ijfatigue.2008.03.038

[23] D. Mellouli, N. Haddar, A. Köster, H. F. Ayedi, Hardness effect on thermal fatigue damage of hot-working tool steel, Engineering Failure Analysis, 45 (**2014**), 85–95, doi:10.1016/j.engfailanal.2014.06.007

[24] J. Absi, J.C. Glandus, Improved methods for severe thermal shocks testing of ceramics by water quenching, Journal of European Ceramic society, 24 (**2004**), 2835–2838, doi:10.1016/j.jeurceramsoc.2003.09.024

[25] D. Klobčar, J. Tušek, Thermal stresses in aluminium alloy die casting dies, Comp. Mater. Sci., 43 (**2008**), 1147–1154, doi:10.1016/j.commatsci.2008.03.009

[26] D. Klobčar, J. Tušek, B. Taljat, Thermal fatigue of materials for die-casting tooling. Mater. Sci. Eng. A, 472 (**2008**) 198–207, doi:10.1016/j.msea.2007.03.025

[27] Y. Birol, Effect of post-oxidation treatment on thermal fatigue behaviour of plasma nitrided hot work tool steel at elevated temperatures, Surf. Coat. Technol., 205 (**2010**), 597–602, doi:10.1016/j.surfcoat.2010.07.035

[28] Y. Birol, Response to thermal cycling of duplex-coated hot work tool steels at elevated temperatures, Mater. Sci. Eng. A, 528 (**2011**), 8402–8409, doi:10.1016/j.surfcoat.2010.07.035

[29] Y. Zhu, D. Schwam, J.F. Wallace, S. Birceanu, Evaluation of soldering, washout and thermal fatigue resistance of advanced metal materials for aluminum die-casting dies, Mater. Sci. Eng. A, 379 (**2004**), 420–31, doi:10.1016/j.msea.2004.03.020

[30] S. Le Roux, F. Medjedoub, G. Dour, F. Rézaï-Aria, Role of heat-flux density and mechanical loading on the microscopic heat-checking of high temperature tool steels under thermal fatigue experiments, International Journal of Fatigue, 51 (**2013**), 15–25, doi:10.1016/j.ijfatigue.2013.02.004

[31] M. Wang, Y. Li, Z. Wang, E. Bao, Effect of rare earth elements on the thermal cracking resistance of high speed steel rolls, Journal of Rare Earths, 29 (**2011**) 5, 489–439, doi:10.1016/S1002-0721(10)60485-1

[32] W. S. Dai, M. Ma, J. H. Chen, The thermal fatigue behavior and cracking characteristics of hot-rolling material, Materials Science and Engineering A, 448 (**2007**), 25–32, doi:10.1016/j.msea.2006.09.003

[33] Q. C. Jiang, H. L. Sui, Q. F. Guan, Thermal Fatigue Behavior of New Type High Cr Cast Hot Work Die Steel, ISIJ International, 44 (**2004**) 6, 1103–1112, doi:10.2355/isijinternational.44.1103

[34] Q. C. Jiang, H. Q. Liang, H. L. Sui, Effect of Y Ce Complex Modification on Thermal Fatigue Behavior of High Cr Cast Hot Working Die Steels, ISIJ International, 44 (**2004**) 6, 1762–1781, doi:10.2355/isijinternational.44.1762

[35] S. Lee, D. H. Kim, J. H. Ryu, K. Shin, Correlation of Microstructure and Thermal Fatigue Property of Three Work Rolls, Metallurgical and Materials Transaction A, 28 (**1997**), 2595–2608, doi:10.1007/s11661-997-0017-6

UDK 67.017:669.15-194.56:621.89.099
Original scientific article/Izvirni znanstveni članek

ISSN 1580-2949
MTAEC9, 51(3)523(2017)

MODIFICATION OF THE INCLUSIONS IN AUSTENITIC STAINLESS STEEL BY ADDING TELLURIUM AND ZIRCONIUM

MODIFIKACIJA VKLJUČKOV V AVSTENITNEM NERJAVNEM JEKLU Z DODAJANJEM TELURJA IN CIRKONIJA

Aida Mahmutović[1], Aleš Nagode[2], Milenko Rimac[3], Derviš Mujagić[4]

[1]University of Zenica, Faculty of Metallurgy and Materials Science, Travnička cesta 1, 72000 Zenica, Bosnia and Herzegovina
[2]University of Ljubljana, Faculty of Natural Sciences and Engineering, Aškerčeva 12, 1000 Ljubljana, Slovenia
[3]Defense Technologies Institute, Mije Kerošević Guje 3, 75000 Tuzla, Bosnia and Herzegovina
[4]University of Zenica, Metallurgical Institute Kemal Kapetanovic, Travnička cesta 7, 72000 Zenica, Bosnia and Herzegovina
aida.mahmutovic@famm.unze.ba

Prejem rokopisa – received: 2015-09-18; sprejem za objavo – accepted for publication: 2016-09-02

doi:10.17222/mit.2015.297

The control of the formation of non-metallic inclusions and the characterization represents the basis for the improvement of steel product properties and leads to sustainable development in the design of new steel grades. In order to produce steels with better machinability, such as AISI 303 grades, a modification of inclusions with a carefully designed chemical composition is presented. The aim of the research was to examine the possibility of increasing the effect of machinability of AISI 303 stainless-steel micro-alloying by tellurium and zirconium. In this work we present detailed SEM/EDS analyses of the modified non-metallic inclusions – manganese sulphides. In AISI 303 steel alloyed with Te and Zr the inclusions consisted of complex particles with more spherical shapes effectively acting as shaving breakers. For this reason the AISI 303 modified grades have better machinability compared to the standard AISI 303 grade and with mechanical properties within the limits prescribed for AISI 303 standard grade.

Keywords: stainless steel, machinability, inclusions, manganese sulphides, tellurium, zirconium

Kontrola tvorbe nekovinskih vključkov in njihova karakterizacija predstavljata osnovo za izboljšanje lastnosti jeklenih proizvodov in vodita k trajnostnemu razvoju novih vrst jekel. Predstavljena je modifikacija vključkov s skrbno načrtovano kemijsko sestavo z namenom izdelave jekel z boljšo obdelovalnostjo, kot je AISI 303. Namen raziskave je bil raziskati možnost izboljšanja obdelovalnosti nerjavnega jekla AISI 303, mikrolegiranega s telurjem in cirkonijem. V delu so predstavljene podrobne SEM/EDS analize modificiranih nekovinskih vključkov – manganovih sulfidov. V jeklu AISI 303, legiranem s Te in Zr, delujejo vključki, sestavljeni iz kompleksnih delcev sferične oblike, kot učinkoviti lomilci ostružkov. To je razlog, da ima modificirano jeklo AISI 303 boljšo obdelovalnost v primerjavi s standardnim jeklom AISI 303 in mehanske lastnosti v mejah, ki so predpisane za standardno jeklo AISI 303.

Ključne besede: nerjavno jeklo, obdelovalnost, vključki, manganovi sulfidi, telur, cirkonij

1 INTRODUCTION

Stainless steel plays an important role in all emerging technologies. Stainless steel type 1.4305 is popularly known as grade AISI 303 stainless steel. Grade AISI 303 is the most readily machineable of all the austenitic grades of stainless steel. The machineable nature of grade AISI 303 is due to the presence of sulphur in the steel composition.

The AISI 303 stainless steel referred to as "free-machining" stainless steel has the following nominal chemical composition, **Table 1**.[1]

Table 1: Chemical composition of standard AISI 303 austenitic stainless steel, in mass fractions (*w*/%)
Tabela 1: Kemijska sestava standardnih AISI 303 avstenitnih nerjavnih jekel, v masnih odstotkih (*w*/%)

C	Mn	Si	Cr	Ni	P	S
0.15	2.00	1.00	17.0-19.0	8.0-10.0	0.2	0.15 min

The MnS stringers help to promote the easy breakup of metal shavings during machining.[2,3] And while the sulphur improves the machining, it also causes a decrease in the corrosion resistance[4] and a slight lowering of the toughness and a general decrease of the mechanical properties.

The intention is to make higher machinability of this steel grade, but with good mechanical properties. The results show that after micro-alloying with tellurium or zirconium the modification of non-metallic inclusions – manganese sulphide of AISI 303 stainless steel – can be significantly changed. The machinability varies with the inclusion shape, which means that it is desirable that the manganese sulphide inclusions in steel must be as spherical as possible.[2]

The aim of the research was to examine the possibility of reducing the effect of sulphur on the mechanical properties of AISI 303 by micro-alloying with tellurium and zirconium, which can modify the MnS and improve the machinability, with mechanical properties within the limits prescribed for AISI 303 standard grade.

2 EXPERIMENTAL PART

The detrimental effects of inclusions in steel do not only depend on their sizes, shape, distribution, but also on their chemical composition and mechanical properties. For this reason, the control of the formation of non-metallic inclusions and the characterization represent the basis for the improvement of steel product properties and lead to sustainable development in the design of new steel grades.

The Thermo-Calc software package is used to show the temperature region where in theoretical way it is possible to form non-metallic inclusions. Also, it has to be taken into consideration that Thermo-Calc calculation is related to equilibrium state and is also related to global chemical steel composition, in this case of standard AISI 303.

The aim of the research was to examine the possibility of increasing the effect of machinability of AISI 303 stainless steel by micro-alloying with tellurium and zirconium. They seem to exert beneficial effects by promoting the retention of globular-shaped sulphide type inclusions.[5]

The intention is to make better machinability of AISI 303 stainless steel and to keep good mechanical properties. Tellurium or zirconium are considered to have a less deleterious effect than sulphur on the mechanical properties.

The production of AISI 303 stainless steel micro-alloyed by tellurium and zirconium was performed in a vacuum induction furnace with capacity of 20 kg at the Metallurgical Institute"Kemal Kapetanović" in Zenica. The ingots were processed by forging, hot rolling and heat treatment.

Two types of modified steel based on AISI 303 were used, the one modified by Te, and the other modified by Te and Zr, **Table 2**.

In order to prepare a sample, grinding and polishing of the testing samples were carried out. Then the analysis of the content, size and distribution of non-metallic inclusions in the unetched state was carried out at the Metallurgical Institute of Zenica, Bosnia and Herzegovina.

The detailed SEM/EDS analyses of modified non-metallic inclusions were performed by scanning electron microscope (SEM) Jeol JSM 5610 with attached energy-dispersive x-ray spectroscopy (EDS) system Gresham Scientific Instruments Ltd., Model Sirius 10/SUTW at an accelerating voltage of 15 kV at the Department of Materials and Metallurgy of Faculty of Natural Sciences and Engineering in Ljubljana, Slovenia.

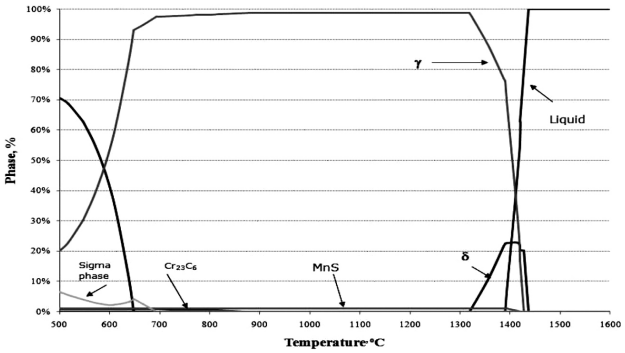

Figure 1: Thermo-Calc calculation of characteristically equilibrium phases for standard AISI 303 depending on temperature
Slika 1: Izračun karakterističnih ravnotežnih faz s programom ThermoCalc za standardno jeklo AISI 303 v odvisnosti od temperature

3 RESULTS AND DISCUSSION

3.1 Thermo-Calc calculation

Thermo-Calc calculation of the characteristic equilibrium phases for standard AISI 303 depending on the temperature is shown that characteristic non-metallic inclusions in these steels are manganese sulphides types, for which precipitation starts under the liquidus temperature, **Figure 1**.

3.2 Analysis of non-metallic inclusions modified by Te

The shape and composition of inclusions in the standard AISI 303 grade are typical MnS stringers (**Figure 2a**). **Figure 2b** shows the modified spherical shaped inclusions in the modified AISI 303 grade containing 0.033 % Te.[6]

Tellurium occurs in steels in the form of inclusions of manganese (sulpho) telluride ($MnTe_xS_{(1-x)}$), or a white coating of manganese sulphide, or in the form of globular inclusions, which are basically manganese sulphides. The shape of the formation depends on the content of tellurium in steel. It is necessary to take into account the ratio of Mn:S = 4 and Mn:Te = 20. Otherwise, during the hot processing characteristic cracks along the edges of semi-finished products appear.[7]

Figure 3 presents the elemental distribution of typical non-metallic inclusions for the stainless steel AISI 303 modified by Te performed by scanning electron microscope (SEM) Jeol JSM 5610 with attached

Table 2: Chemical composition of modified AISI 303 austenitic stainless steels, in mass fractions (*w*/%)
Tabela 2: Kemijska sestava spremenjenih AISI 303 avstenitnih nerjavnih jekel, v masnih odstotkih (*w*/%)

Type of AISI 303	C	Si	Mn	P	S	Cr	Ni	Te	Zr
by Te	0.05	0.40	0.80	0.010	0.16	18.9	9.3	0.033	–
by Te+Zr	0.03	0.47	0.72	0.012	0.18	18.5	8.9	0.040	0.007

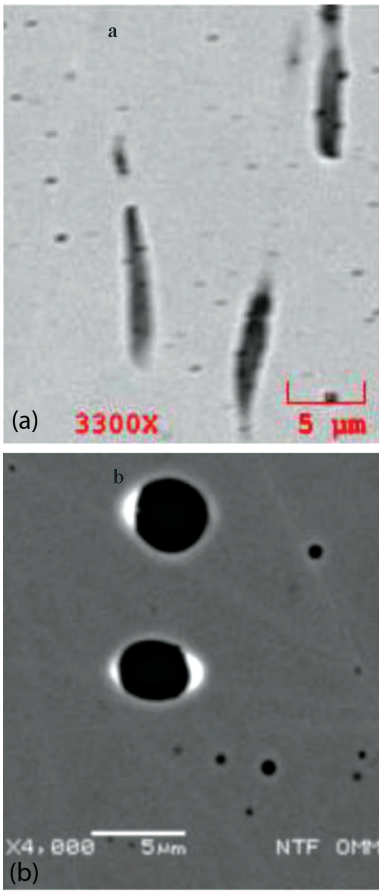

Figure 2: Typical shape of MnS inclusions: a) MnS stringers in standard AISI 303, b) spherical MnS inclusions by Te outlayer (bright colour) in modified AISI 303

Slika 2: Tipične oblike vključkov MnS (PSE): a) razpotegnjeni vključki MnS v standardnem jeklu AISI 303, b) sferični vključki s plastjo Te (svetla barva) v modificiranem jeklu AISI 303

energy-dispersive X-ray spectroscopy (EDS) system Gresham Scientific Instruments Ltd., Model No.: Sirius 10/SUTW at an accelerating voltage of 15 kV. EDS maps show an increase of the concentration of Mn and S, which means that these are manganese sulphides enriched around by Te. By means of additional research of sulphides it has been established that these are pure manganese sulphides with the atomic ratio Mn:S= 1:1.

Figure 4 presents a finding that there is a sharp change in composition at the interface of the MnS inclusion and matrix, with evidence of a Te-enriched zone (white color) around the MnS inclusion. There are tellurides based on Fe and Cr.

Table 3 shows the results of an energy-dispersive spectroscopy EDS analysis at site of interest 1 in **Fig-**

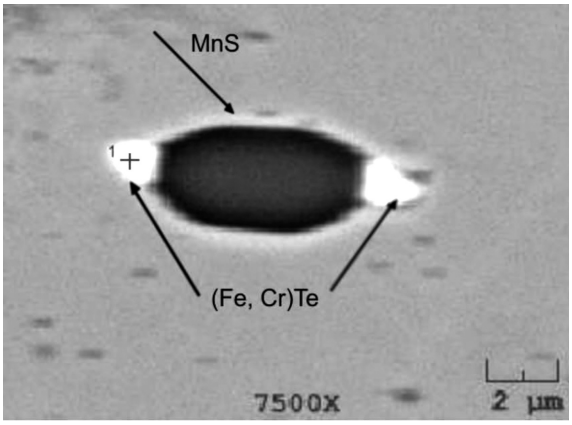

Figure 4: Modified spherical shaped MnS with Te-outer layer (white colour) in AISI 303 modified by Te

Slika 4: Modificiran sferičen vključek MnS obdan s plastjo Te (svetle barve) v jeklu AISI 303, modificiranem s Te

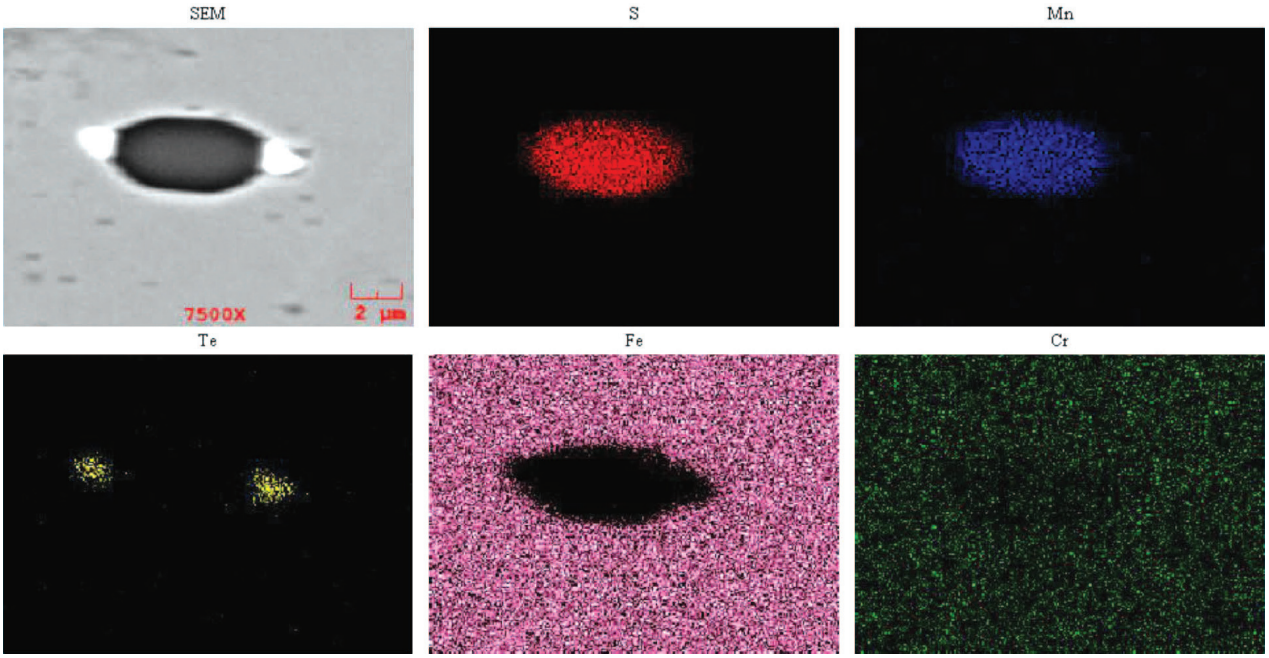

Figure 3: EDS maps of S, Mn, Te, Fe, Cr of non-metallic inclusion in AISI 303 stainless steel modified by Te

Slika 3: EDS-slike porazdelitve elementov S, Mn, Te, Fe Cr s PSE sliko nekovinskega vključka v jeklu AISI 303, modificiranem s Te

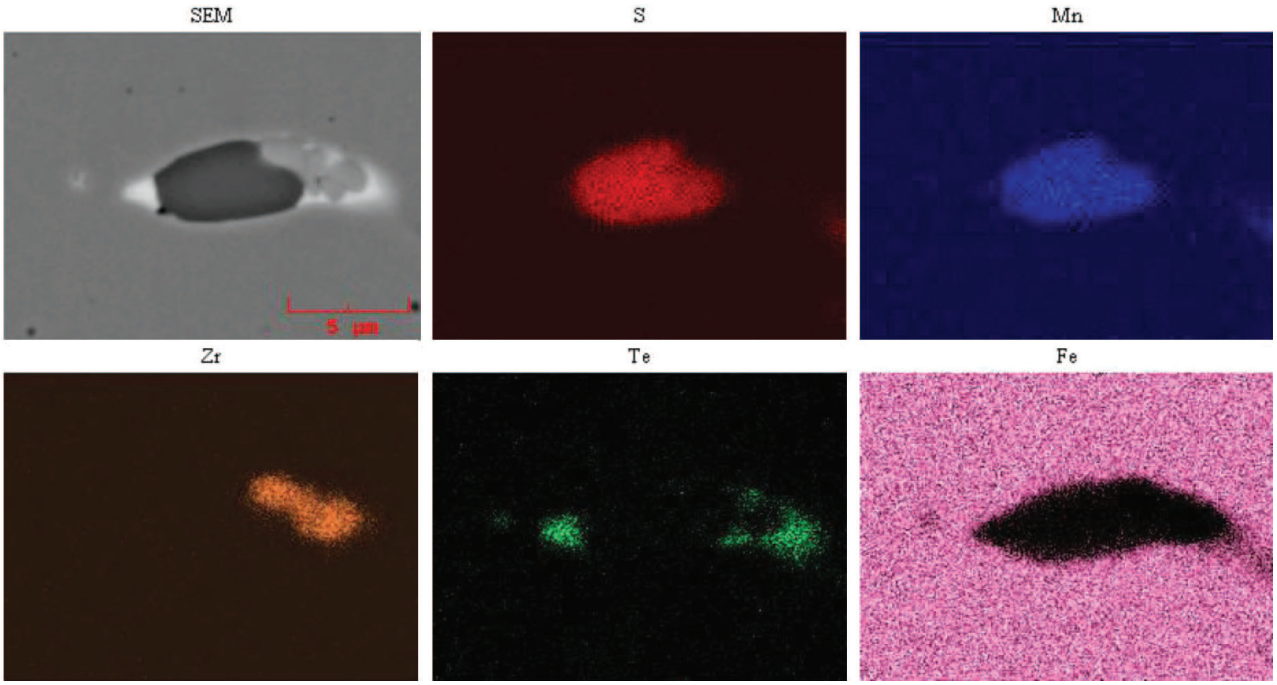

Figure 5: EDS maps of S, Mn, Te, Fe, Zr of non-metallic inclusion in AISI 303 stainless steel modified by Te and Zr
Slika 5: EDS-slike porazdelitve elementov Mn, S, Zr, Te, Fe s PSE sliko nekovinskega vključka v jeklu AISI 303 modificiranem s Te in Zr

ure 4, as well as the enrichment on Fe and Cr traversing the telluride

Table 3: Results of EDS analysis from the site of interest 1 in **Figure 4**, traversing the telluride
Tabela 3: Rezultati EDS-analize na mestu 1 na **Sliki 4**

Chemical element in site 1	Atomic %
Fe	33.31
Cr	30.44
Te	20.44
Mn	3.81
S	4.63
O	1.42
Cu	1.04
Ni	3.59
Si	0.72
Mo	0.57

3.3 Analysis of non-metallic inclusions modified by Te and Zr

In the case of stainless steel AISI303 modified by Zr and Te an investigation into the behaviour of transition metals like zirconium is carried out. Zirconium is used as a micro-alloying element, because it is strongly affined to sulphur and oxygen.[6]

Elemental distributions of typical non-metallic inclusions in modified AISI 303 by Te and Zr, are presented in **Figure 5**. There is also evidence of an enrichment of the elements S, Mn, Te and Zr.

Around sulphide inclusions MnS (black colour) can be noticed a sharp transition to the higher Te-ratio around the sulphide particle as well as a Zr-enriched zone connected to a sulphide inclusion.

Zirconium can affect the shape of manganese sulphide inclusions, causing the inclusions to be spherical rather than elongated. In high-chromium steel like AISI 303, zirconium can form complex precipitates that can occur in micro-segregation bands. The SEM micrograph (**Figure 6**) shows the multiple or connected inclusion in stainless steel AISI 303 modified by Te and Zr. These typical mixed inclusions consist usually of three constituents: manganese sulphide as main inclusion part with outer parts of zirconium sulphide/oxide particles and telluride based on Cr.

Table 4 shows an EDS results from the site of interest 1 (**Figure 6**) traversing the zirconium particles. By means of additional research of oxide/sulphides it has been established that those are based on zirconium with the atomic share Zr(S,O).

The modifications of non-metallic inclusions are considered to obtain a desired balance between mechanical properties and machinability. It should be pointed out that the total effect of different inclusions on the machinability and final mechanical properties depends on such characteristics of non-metallic inclusions as chemical composition, hardness, deformability, number, size, morphology and distribution in steel.[8]

The existence of MnS particles elongated during forging and hot-rolling in plastic mould steels is a cause of increasing the anisotropy of mechanical properties. The control of MnS particles with the additions of Ti, Cr, Zr, etc. has been studied to suppress the anisotropy of

mechanical properties and to ensure a uniform workability.[9–11] H.-H. Kim et al.[9] have investigated that the Zr addition controls the elongation of MnS particles by forming MnS-Zr_3S_4 compound in a steel containing a large amount of sulphur (0.25–0.35 %S). T. Sawai et al.[10,11] have reported that the coexistence of Mn-Si oxide particles and ZrO_2 particles can contribute to disperse fine MnS particles by acting as nucleation sites of MnS particles. The controlled MnS shape by the Zr addition improves the anisotropy of mechanical properties according to the distribution of MnS and Zr particles.[12]

Also, the shape and chemical change of MnS particles was observed by adding Te and Zr. Te and Zr addition controls the elongation of MnS particles by forming a complex compound in the stainless steel without significant reduction of mechanical properties. Both modified steel grades have mechanical properties (R_m 635–630 N/mm^2, KV 62–65 J) that are characteristic for AISI 303 standard grade. The modified machinability improved the steel grade with Te (cutting force 400 N) has up to 15 % better machinability compared to AISI 303 standard grade, and grade with Zr and Te (cutting force 360 N) has up to 25 % better machinability compared to AISI 303 standard grade (cutting force 459 N).

The modified machinability improved the steel grade with Te and Zr shows the structural and chemical changes of MnS according to the formation of complex inclusions.

Table 4: Results of EDS analysis from the site of interest 1 and 2 in **Figure 6**, traversing the zirconium particles (site 1) and telluride (site 2)

Tabela 4: Rezultati EDS-analize na mestu 1 na **Sliki 6**

Chemical element, atomic %	in site 1 (**Figure 6**)	in site 2 (**Figure 6**)
Zr	55.19	-
S	11.96	10.68
O	10.57	-
Mn	8.47	11.40
Cr	6.44	31.82
Fe	4.70	15.83
Te	0.94	28.44

4 CONCLUSIONS

In order to produce steels with better machinability, such as AISI 303 grade, the effects of Te and Zr on the modification of inclusions with carefully designed composition are presented.

Thermo-Calc calculation related to AISI 303 shows that the typical inclusions are the precipitates of manganese sulphides.

The manganese sulphide during the plastic deformation get thinner and longer, but by the formation of complex inclusions connected by Te and Zr particles their shape becomes more spherical.

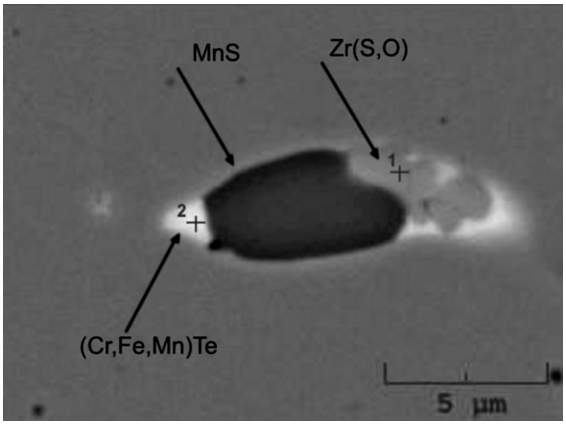

Figure 6: Mixed inclusions: spherical shaped MnS with telluride and zirconium particles in stainless steel AISI 303 modified by Te and Zr

Slika 6: Mešani vključki v nerjavnem jeklu AISI 303, modificiranem s Te in Zr: sferični vključek MnS s telurjevimi in cirkonijevimi delci

By chemical effects on the formation of non-metallic inclusion the nature of inclusions can be changed, thus the strength of the inclusion increases.

The results presented in this paper show that the micro-alloying by Te promoting the retention of spherical-shaped sulphide type inclusions and changing of their chemical composition.

In AISI 303 steel alloyed with Te and Zr the inclusions consist of complex inclusions – manganese sulphide connected on tellurium or that like Zr-oxide-sulphide.

The AISI 303 modified grades have better machinability compared to standard AISI 303 grade and with the mechanical properties in the limits prescribed for the AISI 303 standard grade.

5 REFERENCES

[1] http://www.northamericanstainless.com/wp-content/uploads/ 2010/10/Grade-303.pdf

[2] J. Grum, Quantitative analysis of sulphide inclusions in free cutting steels and their influence on machinability, Acta Stereologica, 18 (**1999**) 3, 319–331

[3] H. Shibata, T. Tanaka, K. Kimura, S.-Y. Kitamura: Composition change in oxide inclusions of stainless steel by heat treatment, Ironmaking and Steelmaking, 37 (**2010**) 7

[4] F. Bikić, D. Mujagić, Investigation of possibility for reducing AISI 303 stainless steel pitting corrosion by microalloying with boron or zirconium, Bulletin of the Chemists and Technologists of Bosnia and Herzegovina, 42 (**2014**), 41–46

[5] J. R. Davis, Alloying understanding the basics, ASM International, 2001

[6] A. Mahmutovic, M. Rimac: Modification of non-metallic inclusions by tellurium in austenitic stainless steel, 19th International Research/Expert Conference: Trends in the development of machinery and associated technology, TMT 2015, Barcelon, Spain

[7] K. Hribar, Vpliv kovinskih in nekovinskih dodatkov na obliko vključkov in tehnološke lastnosti jekel, Magistrsko delo, Jesenice, 1981

[8] N. Ånmark, A. Karasev, P. G. Jönsson, The Effect of Different Non-Metallic Inclusions on the Machinability of Steels, Materials, (**2015**) 8, 751–783

[9] H.-H. Kim, S.-J. Lee, O.-Y. Lee: Effect of Zr Addition on Mechanical Properties of Cr-Mo Plastic Mold Steels, World Academy of Science, Engineering and Technology International Journal of Chemical, Molecular, Nuclear, Materials and Metallurgical Engineering, 7 (**2013**) 10

[10] T. Sawai, M. Wakoh, S. Mizoguchi, Effect of Zr-oxide particles on the MnS precipitation in low S steels, Tetsu-to-hagané, 82 (**1996**), 587–592

[11] H. Hasegawa, K. Nakajima, S. Mizoguchi, The effects of inclusions in steel on MnS precipitation in Fe-Si alloys, Tetsu-to-hagané, 87 (2001), 700–706

[12] F. Chai, C. F. Yang, H. Su, Y. Q. Zhang, Effect of Zr addition to ti-killed steel on inclusion formation and microstructural evolution in welding induced coarse-grained heat affected zone, Acta Metall., 21 (**2008**) 3, 220–226

UDK 620.1:67.017:69
Professional article/Strokovni članek

ISSN 1580-2949
MTAEC9, 51(3)529(2017)

EXAMINATION METHODS FOR WATERPROOFING INJECTION SCREENS IN VARIOUS BUILDING MATERIALS

PREISKOVALNE METODE ZA VBRIZGANE HIDROIZOLACIJSKE MEMBRANE V RAZLIČNIH GRADBENIH MATERIALIH

Rostislav Drochytka, Vít Černý, Jindřich Melichar

Brno University of Technology, Faculty of Civil Engineering, Veveří 331/95, 602 00 Brno, Czech Republic
drochytka.r@fce.vutbr.cz,cerny.v@fce.vutbr.cz, melichar.j@fce.vutbr.cz

Prejem rokopisa – received: 2015-07-01; sprejem za objavo – accepted for publication: 2016-06-09

doi:10.17222/mit.2015.192

Practically all building structures are to some extent struck by wetness. Usually, there is no need to take measures, but when there finally are, the redevelopment method of wet masonry by additional creating a waterproofing injection screen in building structures is nowadays one of the most widespread methods for treating rising capillary wetness. The main advantages of this method are the relatively quick and easy application and the excellent final efficiency. Factors like wetness, temperature or type of building material have a large influence on the injection screens' functionality. The main focus of this paper is testing the specially created various types of injection gels' penetration abilities and their final efficiency in dependence on these factors.

Keywords: redevelopment of wet masonry, injection screens

Praktično vse zgrajene zgradbe prizadene vlaga. Običajno ni potrebe po ukrepih, kadar pa so potrebni, je dandanes najbolj razširjen postopek sanacije vlažnih zidov dodatno vbrizgavanje hidroizolacije v zidove za preprečevanje dviganja kapilarne vlage. Glavne prednosti te metode so relativno hitra in lahka izvedba ter odlična končna učnkovitost. Faktorji, kot: vlaga, temperature in vrsta gradbenega materiala, imajo velik vpliv na učinkovitost vbrizgane prepreke. Glavni poudarek tega članka je preizkušanje sposobnosti penetracije posebnih kreiranih gelov ter njihova končna učinkovitost, v odvisnosti od teh faktorjev.

Ključne besede: obnova vlažnih zidov, vbrizgane prepreke

1 INTRODUCTION

Every construction is affected by a number of negative factors, which are, for example, impacts of snow, wind or freezing, but the most significant influence on buildings usually comes from wetness. The disturbance of even one building material used in construction results in advancing the decrease of the durability in masonry. If this state of affairs occurs, then it is necessary to take a step to redevelopment of the building.[1]

Wetness in masonry used to be manually decreased only by mechanical methods in the past. These methods were based on additional cutting or breaking through masonry and applying various types of hydro-isolation. Obviously, the disadvantage of these procedures is that they have a big influence on buildings statics.[2,3]

One of the most widespread methods for treating rising wetness is the method of creating additional hydrophobic injection screen, which stops this event from happening. Substances used in order to create injection screen are called injection gels.

Many building constructions, especially those which are considerably old and fragile, would not withstand any other mechanical procedures which have usually a big impact on structure statics. Usually, it is just these types of buildings that are struck by rising wetness in lower levels and cellars. In that case the usage of injection gels is the ideal solution.[4]

The biggest advantages of using the injection screen method is the low mechanical impact of the treated building, because only a horizontal line of drill holes need to be applied in order to use this method. That allows the treatment of old or damaged structures, which would not withstand any other more invasive methods of treatment. The other advantage is the relatively quick application.[5,6]

2 EXPERIMENTAL PART

In cooperation with Betosan Co. six injection gels were developed. The main focus of the research was to create a series of laboratory testing methods, by which it would be possible to determine the properties of each gel, compare them with each other and afterwards choose one recapture with ideal properties for further testing. Each of the gels is silicate based and contains a share of secondary materials, which are in comparison with foreign materials much cheaper. Each of the tested materials contains a portion of silica fume, zeolite, bentonite, clay minerals and metakaolin.

Each recapture of injection gels had to be tested using laboratory methods. In that order reduced samples were created. Size of each sample was roughly the size of a half brick. It was (55 × 120 × 120) mm. In dependence on the requirements of each method, the tested

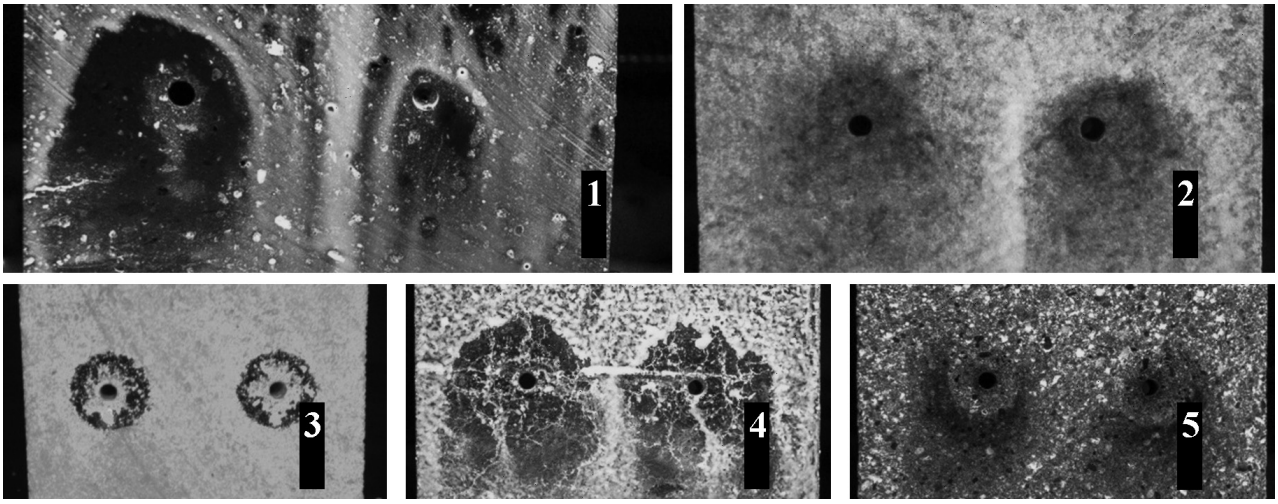

Figure 1: Samples with applied humidity indicator at temperature of 25 °C (1 – burnt brick, 2 – sandstone, 3 – aerated concrete, 4 – mason mortar 1, 5 – mason mortar 2)

Slika 1: Vzorci z nanosom indikatorja vlage pri temperaturi 25 °C (1 – žgana opeka, 2 – peščenjak, 3 – beton z zračnimi delci, 4 – malta 1, 5 – malta 2

materials were either applied on the surface or injected into the reduced drill holes.

Types of tested materials were chosen in order to cover the range of the most commonly used materials in building structures. It was burnt brick, sandstone, aerated concrete and two types of mason mortar.

In order to validate the properties of each injection material, a series of four testing methods was created. The first of these methods is measuring the surface permeability. In this case injection gels were applied on the tested surface of the test samples and the results are measured as the volume of water soaked up into the sample in given time through a certain surface.

The second laboratory method is a determination of the absorption power which is established by completely immersing the test samples in the water for a determined time and calculated as the difference between the weight of dry sample and sample entirely soaked with water. In this case the whole surface of the test sample was covered by a waterproofing gel. The results of the testing are pictured in two diagrams below. The results were split into two pictures, because of the significantly lower results of water absorption in both kinds of masonary mortar.

The next testing method was measuring the capillary attraction, which is carried out by treating the surface of the test samples, and placing their bottom part onto the plastic grate. In lower parts of samples two drill holes were created in which gels were injected. This testing method was executed by using only three gels, which showed the best results in the previous testing. It was gel B, C and D. The results are established as the ratio of the soaked up water in given time through a given surface of dried up sample.

The fourth testing method was observing the penetration rate of each injection gel in dependence on the temperature of the building materials. The tested temperatures were 5 °C, 10 °C, 25 °C and 30 °C. In this case two drill holes were created in the middle line of each sample in which each injection gel was applied. After maximum penetration of the sample it was cut in has perpendicularly to the line of the drill holes. Example specimens of each building material are shown in **Figure 1**.

The last research method was testing of injection gels in-situ. Based on the results of the laboratory testing mentioned before, the one gel with the most suitable properties was chosen. In order to test the gel in-situ, the brick wall which is a part of real building structure was chosen. First step was a determination of the wetness of building material 100 mm above the place, where drill holes were about to be created. The wetness was determined using a resistance moisture meter. The next step was creating a line of 10 drill holes with a diameter of 12 mm and a distance 110 mm with a depth of 310

Figure 2: Drill holes filled by waterproofing gel

Slika 2: Izvrtane luknje, napolnjene z hidroizolacijskim gelom

mm. This line of drill holes was created above the terrain level in the outside. The total thickness of the tested wall was 360 mm. After that the drill holes were cleaned by compressed air. In next step the drill holes were filled using waterproofing gel and left to penetrate for 30 d. Drill holes with injected gel can be seen in **Figure 2**.

3 RESULTS AND DISCUSSION

From the results of the water permeability measuring it is apparent that the presence of the injection gels significantly decreases the water volume absorbed through the treated surface compared to the reference samples. The most valuable decrease was observed for the samples treated by gels D and E, as observed in **Figure 3**.

From the results of the absorption power determination of first three building materials is apparent that the presence of all six types of gels decreases the volume of absorbed water through the surface. The most significant decrease was observed in samples treated by samples of injection gels B, C and D, as shown in **Figure 4**.

Practically the same trend was observed in both types of masonary mortar as in three previously tested building materials, which can be observed in **Figure 5**.

The testing results of the three gels applied into five building materials are pictured in the **Figure 6**.

It is again obvious that the presence of injection gels decreases the volume of absorbed water by capillary

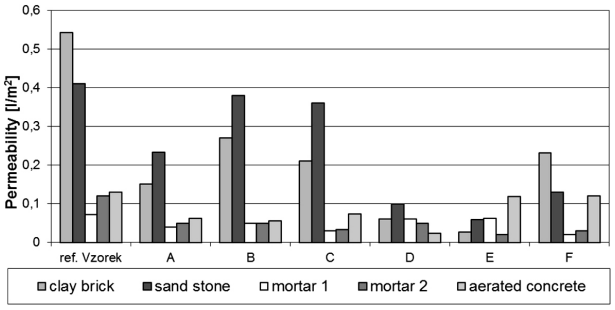

Figure 3: Results of measuring surface permeability of various building materials treated by six different waterproofing gels

Slika 3: Rezultati merjenja prepustnosti površine različnih gradbenih materialov, obdelanih s šestimi hidroizolacijskimi geli

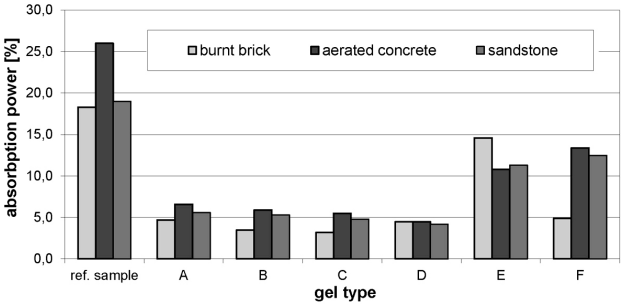

Figure 4: Results of burnt brick, aerated concrete and sandstone absorption power measurements

Slika 4: Rezultati merjenja moči absorpcije pri žgani opeki, porobetonu in peščenjaku

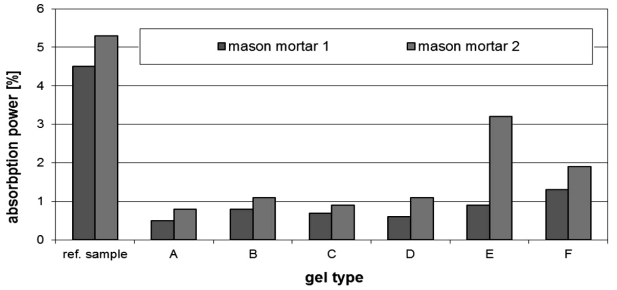

Figure 5: Results of masonary mortar 1 and masonary mortar 2 volume absorption measurements

Slika 5: Rezultati meritev volumske absorpcije zidarske malte 1 in zidarske malte 2

power in each tested material. The best results were observed in the samples treated by gel B.

In order to clearly observe the sector penetrated around each hole the UV humidity indicator was applied and the results were measured in millimeters. The results are displayed in **Table 1**.

Table 1: Results of penetration rate measurement in dependence on various temperatures

Tabela 1: Rezultati merjenja hitrosti penetracije v odvisnosti od različnih temperatur

	Penetration rate in dependence on temperature (mm)				
treatment	5 °C	10 °C	25 °C	35 °C	average
gel B	30.0	36.0	34.8	44.4	36.4
gel C	28.8	33.2	41.8	45.4	37.6
gel D	26.8	35.8	36.0	36.0	33.8

The results show that the largest penetration rate at all temperatures was achieved in the samples treated by injection gel C, closely after that is gel B and lowest penetration rate was observed in samples penetrated by gel D.

After this period of time the wetness was determined in same spots as before the application. The results are displayed in table below. The relative wetness of the surrounding environment was 45.5 % and the temperature of the air was 17.8 °C. The consumption of injection gel on one drill house was about 320–370 mL, which

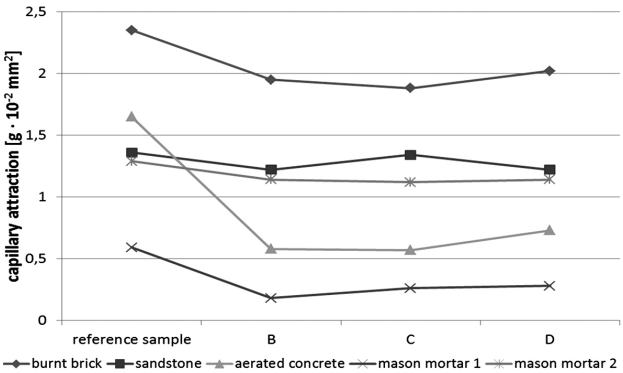

Figure 6: Results of capillary attraction measuring

Slika 6: Rezultati merjenja kapilarnosti

shows that all the drill holes were uniformly filled by the gel. The results are displayed in **Table 2**.

Table 2: Results of mass wetness determination before and after 30 d of application

Tabela 2: Rezultati določanja mase vlage pred in po 30 dneh uporabe

	Mass wetness (%)			
	Brick	Brick – average	Mason mortar	Mason mortar – average
Before application	7.9	**5.6**	6.7	**5.1**
	5.0		3.1	
	4.0		5.6	
30 days after application	1.2	**0.7**	1.7	**1.2**
	0.7		1.3	
	0.3		0.7	

From the results of the in-situ testing it is obvious that the presence of injection gels in the building structure distinctively decreases the reading of the mass moisture in the building materials by 80 %.

4 CONCLUSIONS

From all the results of the executed laboratory methods it is clear that it is possible to determine the properties of injection gels by their usage. By measuring the surface permeability, the absorption volume and the capillary attraction of reference samples and samples treated by six injection gels the results were obtained, by which comparison the specter of the tested gels was narrowed from six to three samples. Testing of the penetration rate under different temperatures of building materials that were injected by three types of gels is also an efficient method for comparing the properties of each gel.

There might also be other methods of examination, like testing the penetration rate of each gel in dependence on various moistures, creating bigger samples like columns and testing them or testing real damaged structures in-situ. But that is the object of further research.

Acknowledgements

This paper has been created under the project number LO1408 "AdMaS UP – Advanced Materials, Structures and Technologies".

5 REFERENCES

[1] R. Drochytka, J. Melichar, P. Dohnálek, Penetration Rate of Various Injection Gels in Dependence on Wetness of Building Materials, Applied Mechanics and materials, 752–753 (**2015**), 720–723, doi:10.4028/www.scientific.net/AMM.752-753.720

[2] R. Drochytka, J. Melichar, P. Dohnálek, Measuring of the Penetration Rate of Injection Gels during Remediation of Various Building Materials, Advanced Materials research, 103 (**2014**) 08, 219–222, doi:10.4028/www.scientific.net/AMR.1000.219

[3] J. Melichar, R. Drochytka, V. Cerny, Experimental Testing of Hydroinsulating Injection Screens, Advanced Materials research, 860-863 (**2014**), 2327–2330, doi:10.4028/www.scientific.net/AMR.860-863.2327

[4] J. Melichar, R. Drochytka, P. Dohnálek, Laboratory Verifying of Injection Screens Efficiency, Advanced Materials Research, 897 (**2014**), 325–328, doi:10.4028/www.scientific.net/AMR.897.325

[5] WTA directive 4-4-04/D: Injection of masonry against capillary wetness, Praha, Tauris, 2005

[6] J. Melichar, R. Drochytka, P. Dohnálek, Remediation of Old Sandstone Structures via Hydroinsulating Injection Gels, Advanced Materials Research, 1122 (**2015**), 51–54, doi:10.4028/www.scientific.net/AMR.1122.51

UDK 624.012.44:620.1:621.7.016
Professional article/Strokovni članek

ISSN 1580-2949
MTAEC9, 51(3)533(2017)

THE DEVELOPMENT OF NEW TYPES OF SECONDARY PROTECTION FOR CONCRETE STRUCTURES EXPOSED TO EXTREME CONDITIONS

RAZVOJ NOVIH VRST SEKUNDARNE ZAŠČITE BETONSKIH KONSTRUKCIJ IZPOSTAVLJENIH EKSTREMNIM POGOJEM

Amos Dufka, Tomáš Melichar, Jiří Bydžovský, Jan Vaněrek

Brno University of Technology, Faculty of Civil Engineering, Institute of Building Materials and Components, Veveří 95, 602 00 Brno, Czech Republic
dufka.a@fce.vutbr.cz

Prejem rokopisa – received: 2015-08-07; sprejem za objavo – accepted for publication: 2016-06-09

doi:10.17222/mit.2015.249

During their use reinforced concrete structures are exposed to external influences. Nowadays, the reducing effect of these influences is usually ensured by secondary (barrier) protection. At present, coatings based on organic substances are commonly used. However, these types of secondary protection show substantial limits under extreme conditions. A method that has considerable potential to eliminate these disadvantages includes the application of secondary protection based on alkali-activated materials or geopolymers. This paper is focused on the development and optimisation of secondary protection (coating, plaster) based on alkali-activated materials intended for reinforced concrete structures to be exposed to highly chemically aggressive environments.

Keywords: coatings, alkali-activated substances, extreme conditions, agressive environment, durability of structures

Med uporabo so armirane betonske konstrukcije izpostavljene zunanjim vplivom. Danes se zmanjšanje vpliva teh učinkov zagotovi z uporabo sekundarne zaščite (prepreka). Običajno se uporabljajo premazi na osnovi organskih snovi. Vendar pa so te vrste sekundarne zaščite precej omejene pri ekstremnih pogojih. Metoda s potencialom da odpravi te pomanjkljivosti, vključuje uporabo sekundarne zaščite na osnovi alkalno-aktiviranih materialov ali geopolimerov. Članek obravnava razvoj in optimiranje sekundarne zaščite (premaz, omet) na osnovi alkalno aktiviranega materiala, namenjenega za armirane betonske konstrukcije, ki bodo izpostavljene kemijsko močno agresivnemu okolju.

Ključne besede: premazi, alkalno-aktivirane snovi, ekstremni pogoji, agresivno okolje, zdržljivost konstrukcij

1 INTRODUCTION

The conditions of exploitation are a key factor that limits the service life of building structures. These include both physico-mechanical influences (especially the synergistic effect of moisture and frost, increased temperature, etc.) and physico-chemical influences (aggressive substances, biotic agents, etc.). In principle, the resistance of building structures to negative influences can be ensured by several approaches, i.e., by structural design and the resistance of the materials used (i.e., by primary protection) and, especially, by having the negative influences of external environment onto the structure eliminated by a barrier protection. In particular, this includes coatings, sheets, etc. (i.e., secondary protection). Presently, a wide range of coating materials to protect reinforced concrete structures is available. In general terms, it comprises high-quality materials that, under standard conditions and withadequate maintenance, contribute considerably to the increased service life of the structure. This, however, only applies to buildings exposed to normal conditions.

If, however, the building structures are exposed to extreme conditions, a different situation will occur. In some types of chemically aggressive environments, for example, the coating materials based on organic substances feature distinct limits. The situation is even more distinctive in the buildings exposed to increased temperatures. This primarily applies to cases when the temperature changes are associated with a conspicuous gradient. Under such conditions, stresses may occur in the coating-substrate interface due to the different thermal coefficients of expansion as well as due to changes in the microstructure of the polymer matrix, and result in the separation of the coating from the substrate, cracking, etc.

The development of coating materials with a matrix based on alkali-activated substances, or geopolymers, seems to be a very viable material basis making it possible to solve the above problems. The coating based on alkali-activated slag presented in this article shall hereinafter be referred to as AAM coating.

The unique properties of alkali-activated materials provide assumptions for the development of new secondary protections intended for reinforced concrete constructions operated in extreme conditions (for instance, in environments of synergistic actuation of higher temperature and chemically aggressive substances, etc.).

The alkali activated slag material being represented herein is intended as a secondary protection for reinforced concrete constructions. On that basis the properties of the developed AAM material are compared with an acrylate co-polymer-based coating intended just for the constructions exploited in chemically aggressive environments. In addition, the effect of the selected aggressive environment type is monitored on cement concrete without any secondary protection for comparison.

The developed material based on alkali-activated slag is not developed as repair mortar in this case but as secondary protection. Within this context the comparison of the properties of the secondary protection based on alkali-activated slag with a polymeric coating can therefore be considered as relevant.

2 SPECIFICATION OF THE COATINGS BEING DEVELOPED

In general terms, we can say that the coatings based on alkali-activated materials are made by the polycondensation of aluminosilicates at temperatures up to 100 °C. The polymerisation includes the chemical reactions of aluminosilicates (Al^{3+} in tetrahedral coordination) and alkaline polysilicates forming polymeric bindings Si–O–Al. As a result, a solid and compact structure forming a dominant component of the matrix of the composite, or coating system, is created.[1,2]

This paper deals with the development of a coating system based on alkali-activated substances to be used for the protection of reinforced concrete structures exposed to extreme conditions. A typical example representing such extreme conditions includes the joint effect of chemically aggressive environments and increased temperature. For example, the structures forming an integral part of process lines for the production of chemicals and the like may be subject to such exposure. Due to the specifics of the above productions, the reinforced concrete structures are frequently loaded by a cyclic effect of increased temperatures for long periods and exposed, on practically a continuous basis, to the effects of aggressive chemicals. The above-mentioned facts have been taken into account during the development of the coating system.

3 EXPERIMENTAL PART

The previous researches made in this field have been followed by the development of an alkali-activated coating. In terms of the service life and functionality of the coating system being developed, its adhesion to the substrate represents one of key parameters. With regard to this fact, the alkali-activated matrix was modified by a polymer dispersion. The coating composition obtained by the optimisation process is shown in **Table 1**. The optimisation process for AAM-based coating development follows the research presented in [1–4]. For instance, the effect of the water glass silicate module is examined in this case in relation to the slag chemical composition, further to the glass-phase content in it, etc. Optimizing the granulometry and the amount of filler used, for example, was based on data provided in [5,6].

Table 1: Composition of AAM coating
Tabela 1: Sestava AAM premaza

Coating component	Content of component (*w*/%)
Water glass	16
Polymer dispersion	2
Slag	31
Filler – silica sand, fraction of 0.45 mm	44
Water	7

For the water glass used, a silicate modulus of 1.7 was applied. Primarily, the water glass silicate module drew from the findings presented in [1,4,5]. The chemical composition of the water glass is shown in **Table 2**.

Table 2: Chemical composition of water glass
Tabela 2: Kemijska sestava vodnega stekla

Component of water glass	Content of component (*w*/%)
SiO_2	21.41 %
Na_2O	12.81 %
K_2O	0.62 %
CaO	0.02 %

The polymer dispersion used was based on vinyl acetate ethylene copolymer. For the chemical composition of the slag, please refer to **Table 3**.

Table 3: Chemical composition of slag
Tabela 3: Kemijska sestava žlindre

Component of slag	Content of component (*w*/%)
CaO	35.9
SiO_2	40.1
Fe_2O_3	6.9
Al_2O_3	8.2
Na_2O	2.1
K_2O	0.9
P_2O_5	1.4
MgO	2.1
MnO	0.3

The experiments were aimed at the development of a coating to be resistant as much as possible to extreme conditions, i.e., to the synergistic effect of highly chemically aggressive environments and increased temperature. In particular, the coating was exposed to the saturated solution of ammonium sulphate with a part of ammonia sulphate not already dissolved in the suspension. The solution temperature was 50 °C. The test samples were prepared so that the developed coating was applied to the concrete substrate using a roller (concrete class C30/37 was used). In order to assess the resistance

of the AAM coating in an impartial manner, a commercially available coating based on acrylate copolymer was exposed to the same type of aggressive environment. We used a coating designed by its manufacturer to protect the surface of the reinforced concrete structures exploited in chemically aggressive environments. Here again, test samples were prepared so that the coating was applied on the substrate consisting of concrete, class C30/37. The coating was applied in accordance with the applicable product's technical data sheet (i.e., especially in regard to the coating consumption and the method of application). Furthermore, the effect of the test environment was tested directly on the uncoated concrete; again, concrete class C30/37 was used. For both coating types (i.e., the developed AAM coating and the commercially available coating based on acrylate copolymer) as well as for the uncoated concrete, two sets of test specimens were prepared. The samples of the first set were kept under laboratory conditions for the entire period of the experiment (i.e., t = 20±2 °C, φ = 50±5 %). The values found in these specimens were considered as a reference. The test samples of the second set were exposed to the saturated solution of ammonium sulphate at increased temperature for periods of 3 months and 6 months. The test solution was prepared with an excessive amount of ammonium sulphate that remained unsolved. The solution temperature was maintained at 50 °C. Test samples aged for 28 d were placed in this aggressive environment.

In order to assess the effect of the test environment, individual test samples were then subject to the following determinations after the 3-month and 6-month exposures:

- Visual evaluation – the condition of coatings was primarily assessed in terms of the potential occurrence of cracks (ČSN EN ISO 4628-4) and blistering (ČSN EN ISO 4628-2). For the uncoated concrete, the appearance of the concrete surface layers was assessed;
- Determination of the coating thickness (ČSN EN ISO 2808);
- Determination of the coating adhesion to the substrate (ČSN EN ISO 4624). For the uncoated concrete, the tensile strength of the concrete surface layers was observed (ČSN 73 1318). During this test a disk with a 50-mm diameter is glued on the surface of the concrete being evaluated and it is cut to clearly define the loaded area. During this test the defined area is loaded by tensile force up to the breakage limit of the tested material;
- Determination of the water-tightness of coatings (ČSN 73 2578). This test proves the coating system's ability to hold water in the liquid state. The test result is expressed as the amount of water that passed through the coating in the screeding materials (without any actuation of the hydrostatic pressure) within 30 min; the unit is therefore 1 litre of water related to 1 m^2 of the tested surface;
- Analyses of the microstructure using a scanning electron microscope (methodological procedure No. 30-33/1 by Brno University of Technology, Faculty of Civil Engineering).

The mentioned complex of the experiments followed de facto the stipulations of the standards involved in questions of the rehabilitation of reinforced concrete constructions ČSN EN 1504-1 and ČSN EN 1504-2.

4 RESULTS

4.1 Visual evaluation

Attention was primarily paid to the evaluation of the condition of the surface layers of the tested samples. In the sample with the developed AAM coating, it was found that even the 6-month exposure to the test environment did not cause any changes to the coating that would prove its degradation due to aggressive substances. Even after the completion of the experiment, the coating structure remained practically identical. This

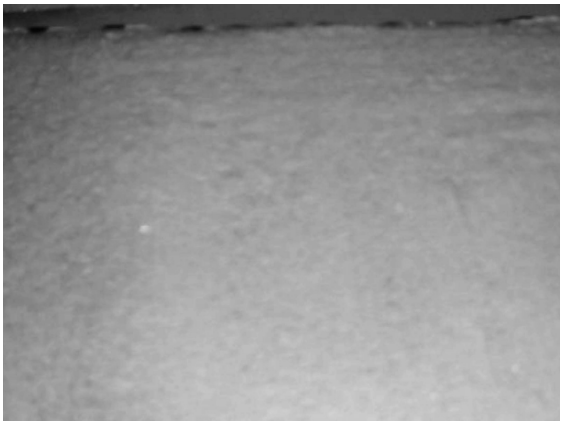

Figure 1: Macroscopic view of the structure of developed AMM coating prior to its exposure to aggressive environments

Slika 1: Makroskopski izgled konstrukcije z AMM-premazom pred izpostavitvijo agresivnemu okolju

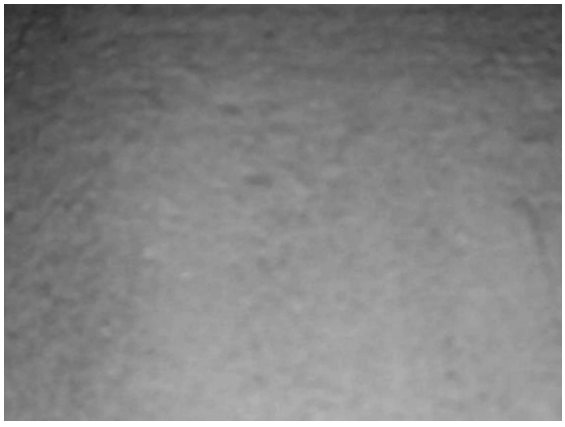

Figure 2: Macroscopic view of the structure of developed AMM coating after a 6-month exposure to ammonium sulphate

Slika 2: Makroskopski izgled konstrukcije z AMM premazom po šestih mesecih izpostavitve amonijevemu sulfatu

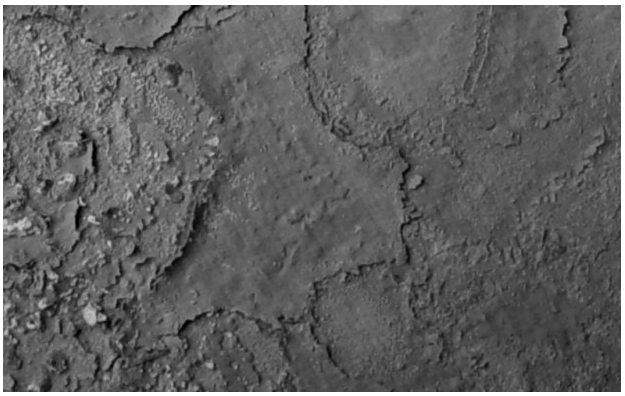

Figure 3: View of the macrostructure of coating based on acrylate copolymer after a 6-month exposure to the test environment
Slika 3: Izgled makrostrukture premaza na osnovi akrilatnega polimera po šestih mesecih izpostavljenosti preizkusnemu okolju

situation is documented in the following photographs (**Figures 1** and **2**):

It was concluded that even a 6-month exposure of the AAM coating would not cause any significant change in the structure of the surface layers of the AAM coating. In addition, the visual evaluation did not reveal any evident presence of cracks or any other defects. Yet, a different situation was found in the coating based on acrylate copolymer. In this case, a 6-month exposure to the solution of ammonium sulphate and an increased temperature resulted in the coating's degradation. This fact is documented in the following photographs (**Figures 3** and **4**). The evident destruction of the surface layers of the coating is shown in **Figure 3**. The destroyed surface layers of the coating film (i.e., flaking of the coating) and cracks are shown in **Figure 4**.

Furthermore, it was proven that the effect of the test environment on the concrete without secondary protection caused a significant degradation of the cement matrix. The visual evaluation revealed a change in the colour of surface layers, and especially the occurrence of cracks and local separations of surfaces layers (i.e., of concrete up to a depth of approx. 5 mm) from the substrate (**Figure 5**).

Figure 4: A 6-month exposure to the test environment caused the degradation of the coating based on copolymer acrylate
Slika 4: Šestmesečna izpostavljenost preizkusnemu okolju je povzročila degradacijo premaza na osnovi kopolimernega akrilata

Figure 5: A 6-month exposure to the test environment caused a massive degradation of surface layers of uncoated concrete
Slika 5: Šestmesečna izpostavljenost preizkusnemu okolju je povzročila močno degradacijo površine betona brez premaza

4.2 Determination of coating thickness

Coating thickness is one of the key factors determining the protective function of the coating. Besides, it is a parameter, the monitoring of which, or monitoring of changes in coating thickness, makes it possible to carefully assess the development of the coating degradation due to the aggressive environment. The coating thickness was measured prior to placing the individual samples in the aggressive environment (the samples were 28 d old) and then after 3-month and 6-month exposures to aggressive environments. The coating thickness was measured using a cutting method and procedure according to the ČSN EN ISO 2808 standard. For the results of the coating thickness measurements, please refer to **Table 4**. The shown values represent an arithmetic mean of ten measurements.

Table 4: Coating thickness
Tabela 4: Debelina premaza

Type of coating	Placement	Exposure time		
		28 d	3 months	6 months
Developed AAM coating	Laboratory environment	520 μm	510 μm	515 μm
	Aggressive environment	—	500 μm	490 μm
Commercially available coating based on acrylate copolymer	Laboratory environment	410 μm	415 μm	410 μm
	Aggressive environment	—	350 μm	290 μm

Evaluation

It was proven that even a 6-month exposure would not cause any significant change of the thickness of the AMM coating. Yet, a different situation occurred in the commercially available coating. In this coating, the

effect of the aggressive environment resulted in a thickness reduction by approximately 30 %. This finding is in full compliance with the visual evaluation that revealed a degradation of the coating based on acrylate copolymer (i.e., especially fissures, separations of surface layers of the coating, etc.). This degradation of the surface layers of the coating film, in particular, has then become the dominant cause of thickness reduction for the commercially available coasting.

4.3 Determination of coating adhesion to a substrate

Adhesion to a substrate is another parameter that is quite critical in terms of the protective function and service life of the coating. Coating-substrate adhesion was determined in accordance with the applicable provisions of the ČSN EN ISO 4624 standard. In addition, the effect of concentrated ammonium sulphate and increased temperature was tested in the uncoated concrete. The concrete was subjected to pull-off testing, and the tensile strength of the surface layers was determined using the procedure according to the ČSN 73 1318 standard.

For the results of the determination of coasting-substrate adhesion, or a determination of the tensile strength of the concrete surface layers, please refer to **Table 5**. The values shown represent an arithmetic mean of five measurements.

Table 5: Determination of coating-substrate adhesion
Tabela 5: Določanje adhezije premaz-podlaga

Type of material	Placement	Exposure time		
		28 d	3 months	6 months
Developed AAM coating	Laboratory environment	2.1 MPa	2.4 MPa	2.6 MPa
	Aggressive environment	—	2.2 MPa	2.0 MPa
Commercially available coating based on acrylate copolymer	Laboratory environment	2.9 MPa	3.0 MPa	2.9 MPa
	Aggressive environment	—	1.6 MPa	0.9 MPa
Uncoated concrete	Laboratory environment	2.6 MPa	2.9 MPa	3.0 MPa
	Aggressive environment	—	0.9 MPa	0.2 MPa

Evaluation

It was concluded that the test environment caused a degradation of the uncoated concrete, which resulted, for example, in a distinct decrease in the tensile strength of the surface layers. A significant decrease in the coating-substrate adhesion after the exposure to the test environment was found for the coating based on acrylate copolymer. The coating material itself, not the coating-substrate interface, was the area in which the defects were mainly revealed after pull-off testing. The smallest decrease in adhesion to the substrate was detected in the AMM coating. In this type of coating, a 6-month exposure to the test environment caused only a decrease of approximately 25 %. The AAM coating-substrate interface was the area with the most frequent occurrence of defects.

4.4 Determination of coating water-tightness

The water-tightness of the coatings was determined using the procedure according to the ČSN 73 2578 standard. For the test results, please refer to **Table 6**; the values represent an arithmetic mean of five measurements.

Table 6: Coating water-tightness
Tabela 6: Vodotesnost premaza

Type of coating	Placement	Exposure time		
		28 d	3 months	6 months
Developed AAM coating	Laboratory environment	0.9 $l.m^{-2}$	0.9 $l.m^{-2}$	0.8 $l.m^{-2}$
	Aggressive environment	—	1.0 $l.m^{-2}$	1.1 $l.m^{-2}$
Commercially available coating based on acrylate copolymer	Laboratory environment	0.2 $l.m^{-2}$	0.2 $l.m^{-2}$	0.2 $l.m^{-2}$
	Aggressive environment	—	0.6 $l.m^{-2}$	0.9 $l.m^{-2}$

Evaluation

The testing shows that the water-tightness of the developed AAM coating is lower when compared to the acrylate coating. In terms of water-tightness, the AAM coating satisfied the requirements for vapour-permeable coatings, while the coating based on acrylate copolymer has, in terms of this parameter, satisfied the requirements for vapour-tight coatings. However, it was proven that the water-tightness of the coating based on acrylate copolymer rapidly decreased when exposed to the test environment. A 6-month exposure to the test environment caused a more than four times lower water-tightness of the coating based on the acrylate copolymer. In

Figure 6: View of the microstructure of AAM-based coating. The coating structure is compact. 100× magnification
Slika 6: Izgled makrostrukture premaza na osnovi AAM. Struktura premaza je kompaktna. Povečava 100×

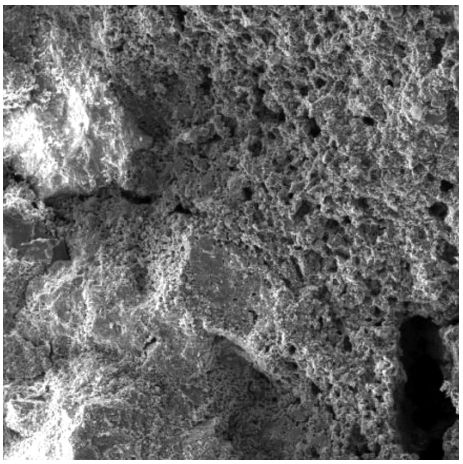

Figure 7: To increase the adhesion to the substrate, AAM coating was modified with polymer dispersion. 100× magnification
Slika 7: Za povečanje adhezije na podlago, je bil AAM premaz modificiran z disperzijo polimera. Povečava 100×

this case, the decrease in water-tightness is associated with the impaired compactness of the coating due to defects (occurrence of microcracks, etc.). In the AAM coating, the changes due to the test environment were not so distinct.

4.5 Analysis of microstructure with the electron microscope

Using the electron microscope, the microstructure of individual materials and, in particular, the changes caused by the effects of an aggressive environment were analysed. Hence, this method was primarily considered as comparative; it means that the samples were primarily compared prior to and after the exposure to laboratory conditions.

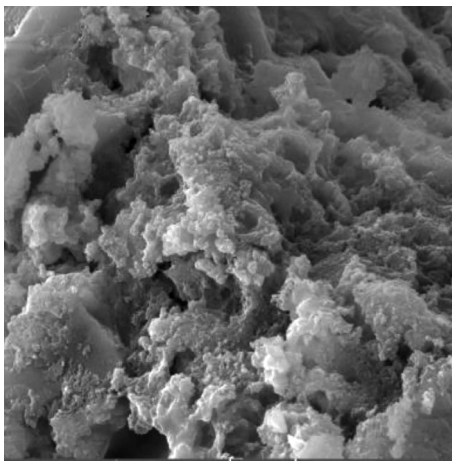

Figure 8: Pseudomorphs of calcium hydrosilicate gels in AAM-based coating – a sample placed at laboratory conditions. 5000× magnification
Slika 8: Psevdomorfija kalcijevega hidrosilikatnega gela v premazu na osnovi AAM – vzorec izpostavljen laboratorijskim pogojem. Povečava 5000×

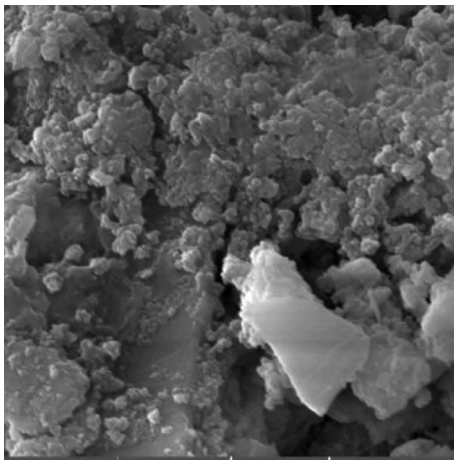

Figure 9: View of the microstructure of AAM-based coating after a 6-month exposure to the test environment. 5000× magnification
Slika 9: Izgled mikrostrukture premaza na osnovi AAM, po šest mesečni izpostavitvi preizkusnemu okolju. Povečava 5000×

Evaluation

The analysis of the microstructure with the electron microscope confirmed and further extended our knowledge obtained during the previous determinations. The resistance of the AAM coating to the effects of the test environment was confirmed. The fact that the structure of AAM coating is relatively compact is shown in **Figure 6**. To increase the adhesion to the substrate, AAM coating was modified with a polymer dispersion. This fact resulted in a partial increase in the porosity of the coating structure (**Figure 7**). Pseudomorphs of calcium hydrosilicate gels represent a dominant component of AAM-based coating (**Figure 8**). Calcium hydrosilicate phases are still dominant components of AAM-based coating also after a 6-month exposure to the test environment (**Figure 9**). Special attention was focused on the analysis of the interface AAM paint/con-

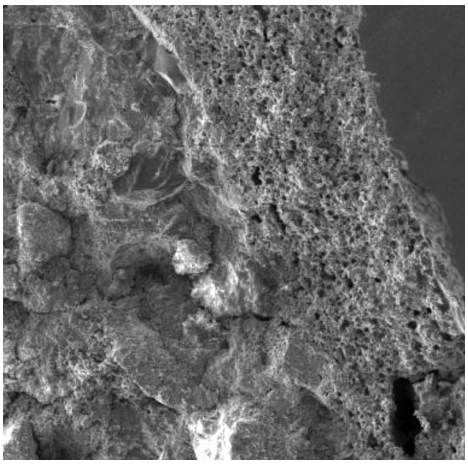

Figure 10: View of the AAM coating/concrete substrate interface after a 6-month exposure to the test environment. 600× magnification
Slika 10: Izgled stika AAM premaza/betonska podlaga po izpostavitvi šest mesecev preizkusnemu okolju. Povečava 600×

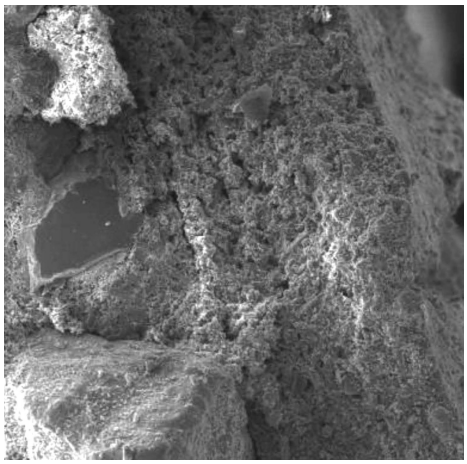

Figure 11: Detailed view of the AAM coating/concrete substrate interface after a 6-month exposure to the test environment. 1000× magnification

Slika 11: Detajl izgleda stika AAM premaz/betonska podlaga, po izpostavitvi šest mesecev preizkusnemu okolju. Povečava 1000×

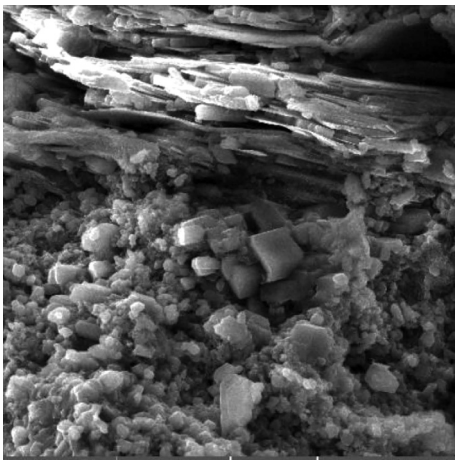

Figure 14: View of the structure of uncoated concrete after a three-month exposure to the test environment. The creation of corrosive products (gypsum pseudomorphs) in the microstructure is evident. 4200× magnification

Slika 14: Izgled zgradbe iz nezaščitenega betona po treh mesecih izpostavitve preizkusnemu okolju. Viden je nastanek korozijskih produktov (psevdomorfija mavca). Povečava 4200×

12)

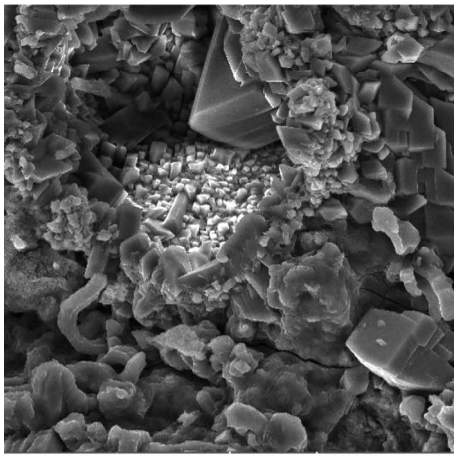

13)

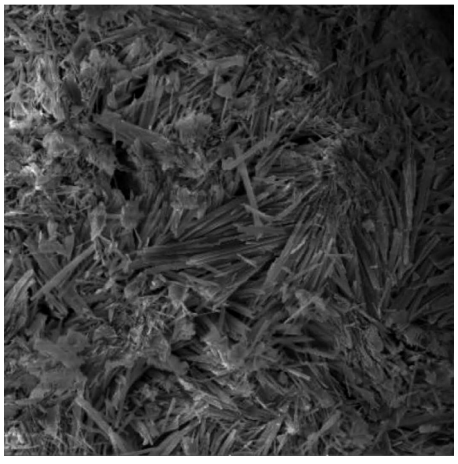

Figures 12 and 13: View of the structure of surface layers of the concrete that was protected with acrylate copolymer-based coating and exposed to an aggressive environment for a period of 6 months. 4200× magnification

Sliki 12 in 13: Izgled zgradbe površinske plasti betona, ki je bil zaščiten s prematom na osnovi akrilatnega polimera in izpostavljenega agresivnemu okolju za dobo šest mesecev. Povečava 4200×

crete. It was found that the interface structure is compact. The absence of any corrosive new formations both in the coating and in the substrate is evident (**Figures 10** and **11**).

Conversely, the surface layers of the concrete protected with the coating based on acrylate copolymer have proven that the exposure to an aggressive environment cause negative changes in the microstructure of the surface layers of the concrete substrate. It was found that the microstructure of this concrete has been subject to negative changes – new formations of ettringite and gypsum have been created (**Figures 12** and **13**).

The degradation due to the test environment has shown itself to an extreme degree in the concrete that was not protected with any coating during the exposure.

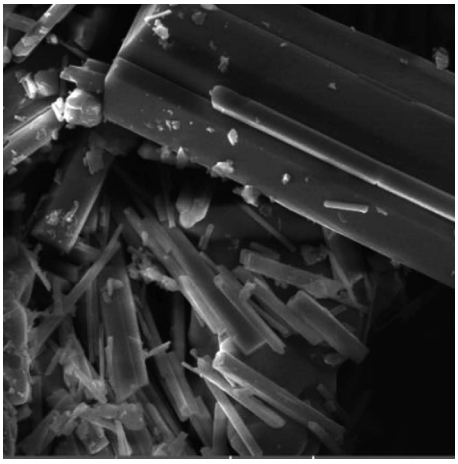

Figure 15: Detailed view of corrosive new formations (gypsum) in the microstructure of cement matrix after a 6-month exposure to the test environment. 4500× magnification

Slika 15: Detajl korozijskih produktov (mavec) v betonski osnovi po izpostavitvi šest mesecev preizkusnemu okolju. Povečava 4500×

In that case, the development of corrosive new formations (mainly of gypsum) was essential (**Figures 14** and **15**).

5 CONCLUSIONS

The performed experiments have confirmed that the synergistic effect of the concentrated solution of ammonium sulphate and the increased temperature results in a significant degradation of the coating based on acrylate copolymer. In this type of coating, the utility parameters have decreased despite the fact that the coating is designed for chemically aggressive environments. It is just the synergistic effect of chemicals and, in particular, of increased temperatures that can be designated as the primary cause of such a negative effect of the test environment.

In turn, positive results have been achieved with the coating based on alkali-activated slag using appropriate types of modifying additives. It has been confirmed that this type of coating is able to effectively withstand the joint effect of chemically aggressive substances and increased temperature. For any of the parameters observed, no decrease greater than 25 % has been found. The listed findings unambiguously confirm the potential for the use of material based on alkali-activated substances for the secondary protection of reinforced concrete structures exposed to extreme conditions. The development of this type of coating has not been completed yet, but it is still ongoing. In the following stages, attention will be paid, for example, to the possibility of having the autogenous shrinkage limited using nano-sized reinforcements, to the application of modifying additives; hence, the analysis of the AAM coating/concrete substrate interface, etc. will become an important research area.

Acknowledgements

This research was conducted with the financial help of project GAČR 14-25504S Research of Behaviour of Inorganic Matrix Composites Exposed to Extreme Conditions and the project No. LO1408 AdMaS UP – Advanced Materials, Structures and Technologies, supported by Ministry of Education, Youth and Sports under the National Sustainability Programme I.

6 REFERENCES

[1] P. Rovnanik, The influence of high temperatures on building materials based on alkali-activated binders, Habilitation thesis, 2012, Brno University of Technology, Faculty of Civil Engineering

[2] N. R. Rakhimova, Z. V. Rakhimov, Alkali-activated cements and mortars based on blast furnace slag and red clay brick waste, Materials and Design, 85 (**2015**), 324–331, doi:10.1016/j.matdes.2015.06.182

[3] B. Yuan, Q. L. Yu, H.J.H. Brouwers, Reaction kinetics, reaction products and compressive strength of ternary activators activated slag designed by Taguchi method, Materials and Design, 86 (**2015**), 878–886, doi:10.1016/j.matdes.2015.07.077

[4] A. Dufka, J. Kosikova, L. Meszarosova, The use of Geopolymers in Rehabilitation of Reinforced Concrete structures, Advanced Materials Research, 785–786 (**2013**), 224–230, doi:10.40288/www.scientific.net/amr.785-786.224

[5] P. Thometzek, A. Ludwig, A. Karbach, K. Kohler, Effects of morphology and surface treatment of inorganic pigments on waterborne coating properties, Progress in Organic Coatings. 36 (**1999**) 4, 201–209, doi:10.1016/S0300-9440(99)00037-5

[6] K. Dvořak, M. Fridrichova, P. Dobrovolny, Influence of different grinding types on granulometry of recycled glass, Construction Materials and Structures, 2014, 305–310, doi:10.3233/978-1-61499-466-4-305

[7] J.A. Golczewski, H.J. Seifert, F. A Aldinger, Thermodynamic model of amorphous silicates, 22 (**1998**) 3, 381–396, doi:10.1016/S0364-5916(98)00038-8

UDK 621.6.031:66.081.63:628.16:66.067.1
Professional article/Strokovni članek

ISSN 1580-2949
MTAEC9, 51(3)541(2017)

PERFORMANCE OF NANO-FILTRATION AND REVERSE OSMOSIS PROCESSES FOR WASTEWATER TREATMENT

OCENA ZMOGLJIVOSTI POSTOPKOV NANOFILTRACIJE IN POVRATNE OSMOZE PRI OBDELAVI ODPADNE VODE

Saad Al-Jlil

National Center for Membrane Technology (NCMT), King Abdulaziz City for Science and Technology (KACST),
P. O. Box 6086 Riyadh, Saudi Arabia
saljlil@kacst.edu.sa

Prejem rokopisa – received: 2015-08-09; sprejem za objavo – accepted for publication: 2016-06-30

doi:10.17222/mit.2015.250

This study was carried out to evaluate the performance of nano-filtration (NF) and reverse osmosis (RO) technology for reducing the total salt concentration from waste water. The nano-filtration proved very effective in removing the polyvalent cations and anions, such as SO_4^-, whereas the removal efficiency was 97.22 %. It is well known that a RO water-treatment process removes all the cations and anions from waste water or brine or sea water, especially removing the monovalent ions such as Cl^- where the removal efficiency was 94.4 %. The performance efficiency of RO and NF water-treatment processes declined significantly during the first 3 years of operation due to fouling and biofouling of the membrane. The research findings provided a concrete clue for the important issue of water treatment as an alternative to existing water use methods on a cost-effective basis. The research also highlighted the potential to replace the NF and RO membranes used in these two water-treatment techniques.

Keywords: desalination of waste water, reverse osmosis, nano-filtration

Izvedena je bila študija ocene zmogljivosti tehnologije nanofiltracije (angl. NF) in povratne osmoze (angl. RO) za zmanjšanje skupne vsebnosti soli v odpadni vodi. Nanofiltracija je zelo učinkovita pri odpravljanju polivalentnih kationov in anionov, kot so SO_4^-, kjer je bila učinkovitost odstranitve 97,22 %. Dobro je poznano, da RO postopek obdelave vode odstrani vse katione in anione iz odpadne vode, slanice ali morske vode, še posebno monovalentni Cl^-, kjer je bila učinkovitost odstranitve 94,4 %. Zmogljivost RO in NF procesov pri obdelavi vode se občutno zmanjša med prvim 3-letnim obratovanjem zaradi mašenja in biološkega nalaganja na membrane. Ugotovitve raziskave omogočajo konkreten namig za pomembno vprašanje obdelave vode, kot cenovno učinkovita alternativa sedanjim metodam. Raziskava je pokazala tudi možnost za zamenjavo NF in RO membran, ki se jih uporablja v teh dveh načinih obdelave vode.

Ključne besede: razsoljevanje odpadne vode, povratna osmoza, nanofiltracija

1 INTRODUCTION

Water uses are manifold, ranging from domestic, agriculture to industries. Among these, the chemical industry uses water as a coolant and to generate steam from boilers for use in different industrial processes for the production of different types of products. In boilers, water evaporates continuously and the dissolved salts precipitate after reaching the saturation stage at equilibrium, thus forming a hard scale that deposits on the inner walls of the boiler. There are several disadvantages of these deposits. Among them, the most important is corrosion, which decreases the efficiency of the boiler unit through the clogging of pipes, valves and condensers, decreases the heat-transfer rate, causes the excessive use of fuel and a danger of explosion. Therefore, wastewater treatment is important for the safe operation of boilers. Among the traditional methods of water softening, the addition of lime-soda is one process. But this process has some disadvantages i.e., it leaves more sodium chloride as residue in the raw water and the need for reaction tanks equipped with mechanical stirrers in addition of course to the main chemicals used by the process and the coagulant to facilitate filtration of the formed precipitates.

Presently, among the various techniques for softening high-hardness waters, membrane separation is a new approach. The membrane-separation processes have the unique advantage of not requiring energy to affect phase changes compared to distillation or crystallization. Hence, it is an economically attractive alternative as compared to costly methods due to low energy requirements.

The objective of this work was to investigate the possibility of using reverse osmosis and nano-filtration processes to improve the water quality by removing the major cations and anions, such as calcium, magnesium and chloride, from wastewater. We also wanted to determine the decline in the performance of RO and NF processes due to membrane fouling.

2 REVIEW OF LITERATURE

2.1 RO – Technology application

Membrane technology is playing an important role in the reclamation of municipal wastewater. In particular, high-quality reclaimed wastewater can be used by

industrial customers. Currently, many large-scale commercial membrane plants are in use for the treatment of municipal wastewater. These plants include the 270,000 m^3/day plant in Orange County, California and the 380,000 m^3/day plant for Sulayabia, Kuwait.[1]

A typical municipal wastewater treatment process consists of primary, secondary and tertiary treatments. When tertiary effluent from a conventional treatment process is supplied to a RO system, it encounters all forms of fouling, i.e., colloidal, biological, scaling and organic fouling. The coatings of foulant will impede the water transport through the membranes, thus resulting in short membrane life and increased operational cost.

Since the development of practical cellulose acetate membranes in the early 1960s and the subsequent development of thin-film, composite membranes, the use of reverse osmosis technology expanded to include not only the traditional desalination process but also a wide range of wastewater treatment applications. Several advantages of the RO process that make it particularly attractive for dilute aqueous wastewater treatment have been widely advocated by many investigators.[2–4] The applications reported for RO processes include the treatment of organic-containing wastewater, wastewater from electroplating and metal finishing, pulp and paper, mining and petrochemical, textile, and food processing industries, radioactive wastewater, municipal wastewater, and contaminated groundwater.[2,4,5]

2.2 Contaminated drinking water

Reverse osmosis processes can simultaneously remove hardness, color, many kinds of bacteria and viruses, and organic contaminants such as agricultural chemicals and trihalomethane precursors. T. Eisenberg and E. Middle Brooks[6] reviewed the RO treatment of drinking-water sources, and they indicated that RO can successfully remove a wide variety of contaminants. E. Chian et al.[7] studied several agricultural chemicals contaminating water supplies and found their removal was good by adsorption on the membranes. H. Odegaard and S. Koottatep[8] reported that humic and fulvic materials, which are THM precursors, were largely removed by RO membranes. T. Clair et al.[9] found the excellent removal (>95 %) of dissolved organic carbon from natural waters using FT30 membranes. T. Sorg et al.[10] showed that the RO system can effectively remove radium from contaminated water. J. Baier et al.[11] reported the removal of several agricultural chemicals from groundwater from 0 % to >94 % using different membranes. J. Taylor et al.[12] found that RO membranes could be used to remove 96 % of DOC, 97 % of color, 97 % of trihalomethane formation potential (THMFP), and 96 % of total hardness. L. Tan and R. Sudak[13] examined several RO membranes and found that all were capable of acceptably removing color from groundwater, even over long operating periods.

2. 3 Municipal wastewater

Reverse osmosis (RO) can remove dissolved solids from municipal wastewaters, which cannot be removed by biological or other conventional water-treatment processes. However, extensive pretreatment and periodic cleaning are usually needed to maintain acceptable membrane water fluxes. Early studies[14,15] showed that the high removal of TDS and the moderate removal of organics can be achieved. H. Tsuge and R. Mori[16] showed that tubular membranes (with a substantial pretreatment system) can remove both the inorganic and organic pollutants from municipal secondary effluent and produce water that meets drinking-water standards. Previously, N. Richardson and D. Argo[17], P. Allen and G. Elser[18] and I. Nusbaum and D. Argo[19] discussed municipal wastewater treatment at a large scale plant (Water Factory 21, Orange County, California). The feed water to the plant consisted of secondary effluent, and the process was composed of a variety of treatment systems, including RO membranes (several different types) with a 5 MGD capacity. The process reduced TDS and organics to levels that allowed the effluent to be injected into groundwater aquifers used for water supplies.

E. Cséfalvay et al.[20] stated that membrane separations are gaining increasing interest in wastewater treatment due to their efficiency. Nano-filtration and reverse-osmosis membranes were tested under different conditions to reduce the chemical oxygen demands (COD) of wastewaters. However, none of the membranes decreased the COD to the release limit in one step. Gholami et al. found that the range of rejection was 73.52 % to 99.36 % and 75.1 % to 98.8 %, for amoxicillin and ampicillin, respectively. Also, the application of the RO membrane was recommended for the removal of selected antibiotics up to 95 % from synthetic waste effluent.[21] In addition pressure-driven membrane processes, particularly nano-filtration (NF) and reverse osmosis (RO) have also been gaining attention in the past decade and their application in drinking-water treatment has been the focus of many researchers.[22]

2.4 Nano-filtration applications

Recently, nano-filtration membranes, having high water fluxes at low pressures, were developed as new applications in wastewater treatment. These membranes also reject organic compounds with molecular weights above 200 to 500. These properties have made possible some interesting new applications in wastewater treatment, such as selective separation and the recovery of pollutants that have charge differences, the separation of hazardous organics from monovalent salt solutions, and membrane softening to reduce hardness and trihalomethane precursors in drinking-water sources.[23, 24]

2.5 Contaminated drinking-water supplies

Nano-filtration membranes have attracted a great deal of attention for use in water softening and the removal of

various contaminants from drinking-water sources. Nano-filtration (NF) processes can reduce or remove TDS, hardness, color, agricultural chemicals, and high-molecular-weight humic and fulvic materials (which can form trihalomethanes when chlorinated). In addition, NF membranes typically have much higher water fluxes at low pressures than traditional RO membranes used for this application. W. Conlon [25] reported that FilmTec NF50 membranes can effectively remove color (96 %) and TOC (84 %), reduce hardness and TDS, and lower trihalomethane formation potential (THMFP) to below regulatory levels. P. Eriksson[23] and J. Cadotte et al.[24] also indicated that NF membranes (such as FilmTec NF40, NF50, and NF70) can be used to reduce TDS, hardness, color, and organics. B. Watson and C. Hornburg[26], and W. Conlon et al.[27] have also identified NF as an emerging technology for compliance with THM regulations and for the control of TDS, TOC, color, and THM precursors. P. Lange et al.[28] also suggested that NF treatment would be a reliable method of meeting existing and future THM limits compared to chemical treatment alternatives. G. Amy et al.[29] used NF70 membranes to remove dissolved organic matter from both groundwater (recharged from secondary effluent) and surface water in order to reduce THM precursors. They found that the process was effective in reducing the organics as well as the conductivity in both water sources. S. Duranceau et al.[30] also reported on the use of NF70 membrane separation for several agricultural chemicals spiked in groundwater. Ethylene dibromide and dibromochloropropane removals averaged 0 % and 32 %, respectively, while the remaining organics (chlordane, heptachlor, methoxychlor, and alachlor) were 100 % removed. Rejections of TDS were 85 % and THMFP were 95 %. However, it was also indicated that some of the organics adsorbed on the membrane.

2.6 Wastewater

Nano-filtration is also used to remove both the organics and inorganics from different wastewaters. A. Bindoff et al.[31] reported that using NF membranes, the color removal was >98 % at water recoveries up to 95 %, while the in-organics were poorly rejected. K. Ikeda et al.[32] indicated NF could give high separations of color-causing compounds such as lignin sulphonates in paper pulping wastewaters. M. Afonso et al.[33] found NF removal (>95 %) of chlorinated organic compounds from alkaline pulp and paper bleaching effluents with high water fluxes. M. Simpson et al.[34] reported the use of NF membranes to remove hardness and organics in textile mill effluents. S. Gaeta and U. Fedele[35] also indicated high water recoveries (up to 90 %) from textile dye house effluent could be achieved with NF membranes. M. Perry and C. Linder[36] discussed the recovery of low-molecular-weight dyes from high salt concentration effluent. K. Ikeda et al.[32] and J. Cadotte et al.[24] reported the use of NF membranes in the treatment of food-processing wastewaters. Some specific uses included the desalting of whey and the reduction of high BOD and nitrate levels in potato processing waters (Anonymous, 1988b). D. Bhattacharyya et al.[37] used NF40 membranes to selectively separate mixtures of cadmium and nickel. M. Williams et al.[38] examined NF40 membranes with and without pretreatment by feed preozonation to study the removal of various chlorophenols and chloroethanes. TOC rejections up to 90 % were possible with ozonation pretreatment. R. Rautenbach and A. Gröschl[39] discussed the separation results of several organics (ranging from methanol to ethylene glycol) by various NF membranes. M. Chu et al.[40] detailed the use of NF in a process for treating uranium wastewater; NF40 uranium rejections were 97 % to 99.9 %. C. Dyke and Bartels[41] discussed the use of NF membranes to replace activated carbon filters for the removal of organics from off-shore produced water containing residual oils. The produced waters contained ~1000 mg L^{-1} soluble organics (mostly carboxylic acids) and high inorganic concentrations (~15,000 mg L^{-1} Na^+ and ~25,000 mg L^{-1} Cl^- as well as other dissolved ions). Organic rejections were suitable to meet discharge standards, while inorganic rejections were low (<20 %), allowing operation at low pressures.

Andrade et al. observed that the MBR efficiently removed the organic matter and color of the feed effluent followed by nano-filtration as a polishing step for the removal of high contents of solids.[42] While the membrane separation systems and the combination of these systems with other technologies, such as membrane bioreactors (MBR), are the most promising treatment technologies for effluent reuse.[43] Also, studies show that NF is an efficient treatment system for secondary or tertiary effluents aiming at the generation of water for industrial, agricultural, or indirect potable reuse.[44,45]

3 MATERIALS AND METHODS

The experiment was carried at the Wastewater Treatment Plant (WTP), National Center for Water technology (NCWT), King Abdulaziz City for Science and Technology (KACST) during 2012-2013.

3.1 Analysis of wastewater samples

The water samples were analyzed for pH, cations and anions. Cations and anions such as chloride, sulphate were determined by using Dionex 300 Ion chromatography. The requirements for this analysis are Dionex ion chromatography with column As-14 (4mm), guard column AS-12, suppressor-ASR-1, fluent mixture of carbonate and bicarbonate, deionized water and nitrogen gas. The total dissolved solids (TDS) were estimated using Oven Heraeus Instruments. The pH was measured by using Hach HQ D40.

3.2 Experimental set-up

3.2.1 Advanced waste water treatment units (AWWTU)

The AWWTU at KACST consists of two parts representing two different water treatment technologies such as a Reverse Osmosis Unit (RO-Unit) and Nano-filtration (NF).

3.2.2 RO-Unit

The pre-treated water from the biological unit is desalinized using the RO-technology. Its water production capacity is 0.12 m^3/h (**Figure 1**).

3.2.3 NF-Unit

The pre-treated water from the biological unit is desalinized by applying NF technology. Its water production capacity is 0.12 m^3/h (**Figure 2**).

4 RESULTS AND DISCUSSION

The results of the RO and NF wastewater treatment technologies containing cations and anions are presented in **Figure 3**. Only moderate rejection was observed for the monovalent species, as expected with NF. However, the rejection of polyvalent cations and anions was high.

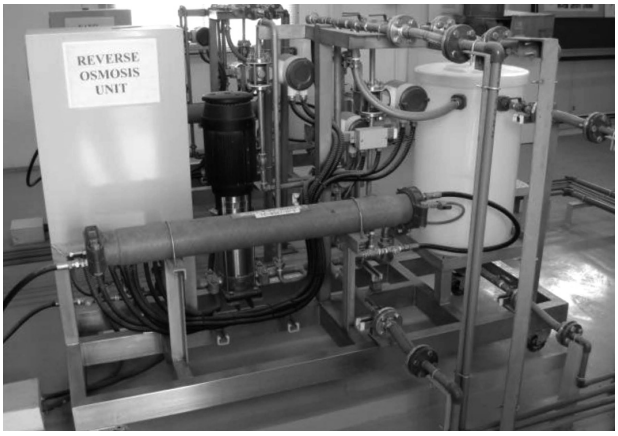

Figure 1: Layout of reverse osmosis (RO) unit
Slika 1: Postavitev naprave za reverzibilno osmozo (RO)

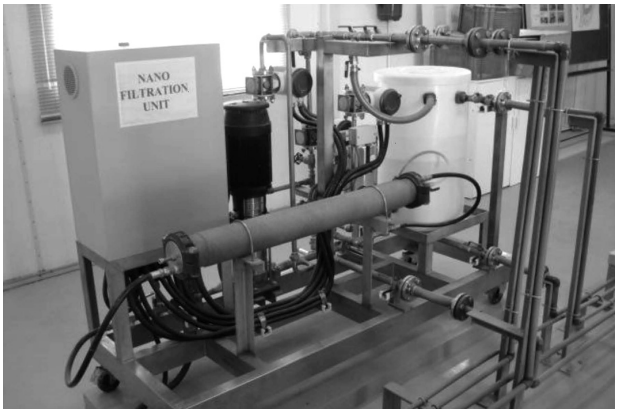

Figure 2: Layout of nano-filtration unit
Slika 2: Postavitev nanofiltracijske naprave

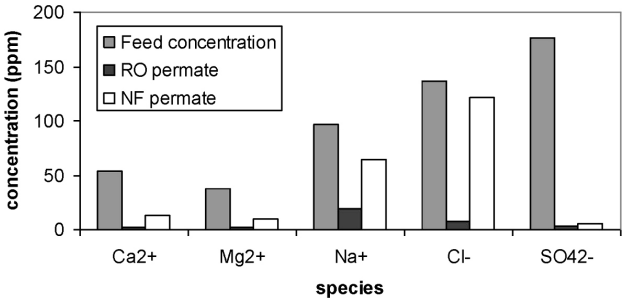

Figure 3: Comparison of the performance of new RO and NF membranes
Slika 3: Primerjava zmogljivosti novih RO in NF membran

On the other hand, strong rejection was observed for monovalent cations and anions by RO.[46] The percentage rejection of species ions (rej. %) was calculated as follows in Equation (1):

$$\text{rej } \% = \frac{a-b}{a} \times 100 \quad (1)$$

a – concentration of species in the feed,
b – concentration of species in the permate.

The data in **Figure 4** shows the results of the advanced treatment RO and NF of waste water containing cations and anions using old RO and NF membranes (worked for 3 years). It was found that the rejection of the cations and anions decreased for monovalent species. This behavior is expected with old membranes. Also, modest rejection was observed for polyvalent cations and anions. On the other hand, moderate rejection was observed for monovalent cations and anions by RO due to membrane fouling and biofouling. This reason is definitely right, because the wastewater has different types of bacteria and pathogens and organic material. The organic material adsorbed onto the membrane surface and increased the fouling problem.

Figure 5 shows the performance of NF and RO for the rejection of TDS. In general, the TDS rejection decreases with an increase in the feed concentration due to increased concentration polarization at the membrane solution interface.[47] It was observed that TDS rejection was less by NF than RO membrane. This could be attributed to the monovalent ions such as Na^+, which

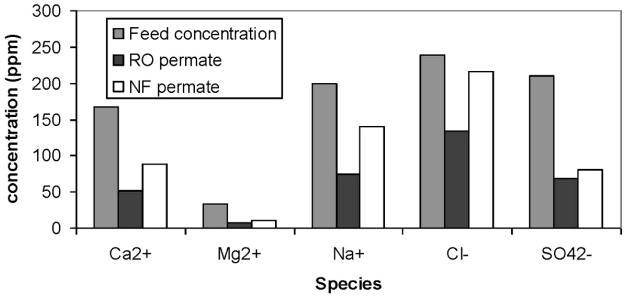

Figure 4: Comparison of the performance of old RO and NF membranes
Slika 4: Primerjava zmogljivosti starih RO in NF membran

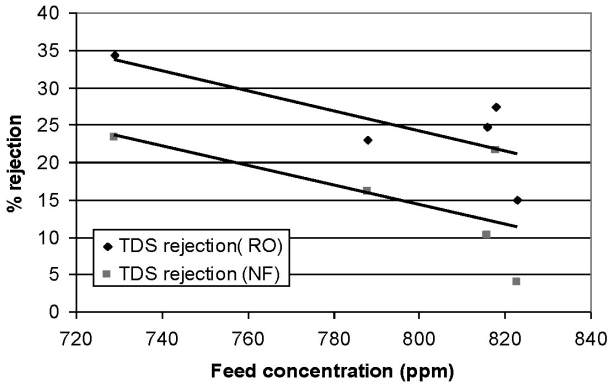

Figure 5: Percentage rejection of TDS versus feed concentration for RO and NF membranes

Slika 5: Odstotek zavrnitev TDS v odvisnosti od vstopne koncentracije pri RO- in NF-membranah

represents the main component in the feed water; therefore, the ability of NF in rejection of the monovalent ions is weak.

Figure 6 shows the performance of the NF and RO membranes for the rejection of TDS at the same pH of feed water. The percentage rejection of the Na^+ ion by RO membrane was higher than the NF membrane. This could be attributed to the fact that the rejection of monovalent ions such as Na^+ by NF is weak.[42,43] In addition, the pH did not affect the membrane rejection when the polyamide membrane pH operating range is 4–11.

Figure 7 shows the results of RO for waste water treatment containing cations and anions using the old RO and new RO membranes. The old membrane was 3 years old. It was found that the percent rejection decreased for all the ion species. For example, the percent rejection of Cl^- ion was 94.4 % using the new membranes and the membrane percent rejection was 43.9 after three years. This would mean that the membrane performance declined due to fouling and biofouling. The study results agree with those of Gholami et al., and Sahar et al. who reported the significant rejection of pollutants from waste effluents.[21,22]

Figure 8 shows the results of NF for wastewater treatment containing cations and anions using the old NF and new NF membranes. The old membrane worked for

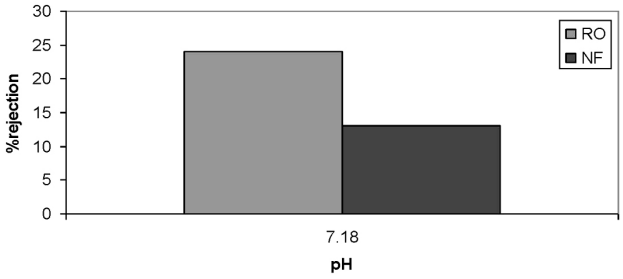

Figure 6: Effect of pH on removing sodium ions using RO and NF membranes

Slika 6: Vpliv pH na odstranitev ionov natrija, z uporabo RO in NF membran

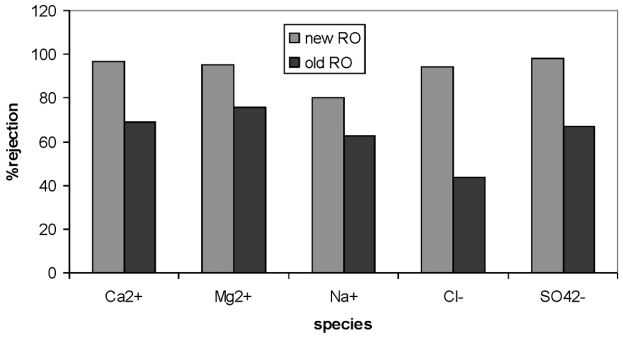

Figure 7: Comparison of the performance of RO membranes during 3 years of operation

Slika 7: Primerjava zmogljivosti RO-membran med triletnim obratovanjem

3 years. It was found that the rejection decreased for polyvalent cations and anions. This behavior was expected with the old membranes. On the other hand, the percent rejection of monovalent cations and anions by NF was not affected. For example, the percentage rejection of Cl^- ion was 11.6 %, while after three years, the membrane rejection was 9.62 %. The rejection of SO_4^- ions was 97.22 % with the new membrane, while after 3 years the membrane rejection was 61.43 %. A strong rejection was observed for polyvalent cations and anions by NF.[46]

Figure 9 and **Table 1** show the percent decline of RO for the treatment of waste water containing cations and anions. It is clear that the decline in the performance of RO was higher during 3 years operation. This decline in performance could be attributed to fouling and biofouling on the surface of the membrane. In conclusion, this promising method, based on these results, suggests replacing the old membrane by a new product. Where the % decline of performance of membrane (decline %) can be calculate as follows in Equation (2):

$$\text{decline } \% = \frac{c-d}{c} \times 100 \qquad (2)$$

c – rejection of new membrane, d – rejection of old membrane

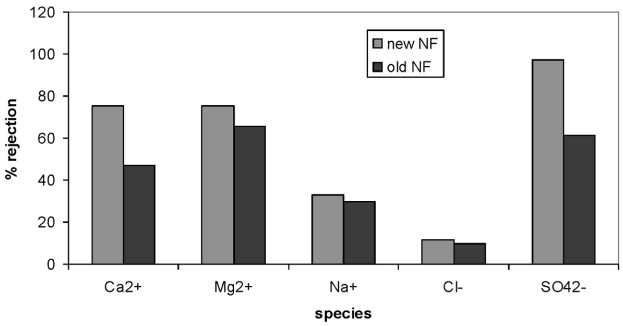

Figure 8: Comparison of the performance of NF membranes during 3 years operation

Slika 8: Primerjava zmogljivosti NF membrane med triletnim obratovanjem

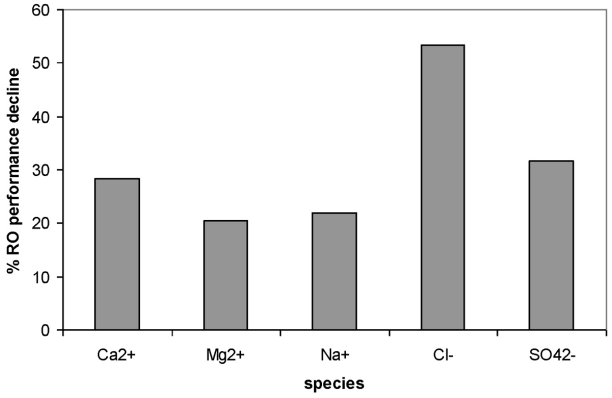

Figure 9: Percentage decline of the performance of RO during 3 years operation
Slika 9: Odstotek zmanjšanja zmogljivosti RO med triletnim obratovanjem

Table 1: Percentage decline of the performance of RO
Tabela 1: Odstotek zmanjšanja zmogljivosti RO

Species	% decline of performance of RO
Ca^{2+}	28.38
Mg^{2+}	20.39
Na^{+}	21.98
Cl^{-}	53.45
$SO4^{2-}$	31.73

Figure 10 and **Table 2** show the percent decline in the performance of NF for the treatment of wastewater containing cations and anions. It is clear that the decline in the performance of NF was higher during 3 years operation, which might be due to fouling and biofouling on the surface of the membrane. The results of this investigation suggest that the old membrane should be replaced with the new product.

Table 2: Percentage decline of the performance of NF
Tabela 2: Odstotek padanja zmogljivosti pri NF

Species	% decline of performance of NF
Ca^{2+}	37.67
Mg^{2+}	12.72
Na^{+}	9.37
Cl^{-}	16.97
$SO4^{2-}$	36.81

4.1 Factors affecting the decline performance of the membrane

There are many factors that affect the performance of membranes, such as membrane fouling and biofouling, membrane degradation by oxidation and hydrolysis, mechanical damage, inorganic colloids, adsorbed organics, coagulants, silica scale and other inorganic scale and fouling with waste water. In general, biofouling and fouling are the major constraints that cause a decline in the performance of membranes. In order to find the possible reasons causing a decline in membrane performance, membrane autopsy was conducted to collect

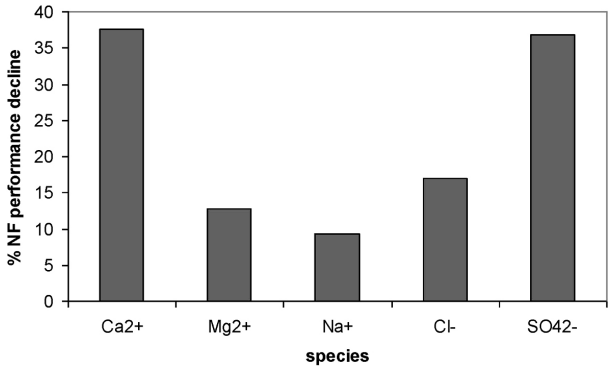

Figure 10: Percentage decline of the performance of NF during 3 years operation
Slika 10: Odstotek padanja zmogljivosti NF med triletnim obratovanjem

sheet membrane samples for examination by using energy-dispersive x-ray to analyze the fouling deposit. Also, Fourier-transform infrared spectroscopy was used to identify the components of the deposition that deposit on the membrane. In addition, SEM can be used with the membrane samples to show the advanced fouling on the membrane surface

4.2 Factors to control membrane fouling

Many factors can be used to control the membrane fouling, these are:

1. Pretreatment for the water.
2. Membrane cleaning in the early stages of fouling.
3. Control of bacterial growth by depriving bacteria from nutrition by controlling the organic content in the feed water.
4. Efficient control of membrane fouling by proper sanitization of membrane system by using chlorination or UV.

5 CONCLUSIONS

Nano-filtration (NF) is very effective in removing polyvalent cations and anions such as SO_4^- (where the percent rejection of SO_4^- ions was 97.22 %). While the RO membrane is very effective in removing all ions, especially the monovalent cations and anions such as Cl^-, where the percent rejection of Cl^- ions was 94.4 %. The decline in the performance of RO and NF was very significant after 3 years of operation, attributed mainly to fouling and biofouling on the surface of the membrane. The study results suggested strongly to replace the old membranes with new ones to improve the system performance and efficiency for wastewater treatment on a cost-effective basis.

5.1 Recommendations and suggestions

1. Change the membrane for a new one.

2. Observe the performance after fixing a new membrane and backwash after 10 % of decline in performance.
3. Conduct training for the technicians in RO and NF systems maintenance, including the backwash and fouling problems.
4. Regular cleaning of the membrane to improve recovery of the membrane.
5. Conduct autopsy of the membrane to know the exact reason for the decline of performance.
6. Use an alternate membrane, such as a ceramic membrane.

6 REFERENCES

[1] M. Al-Shammiri, A. Al-Saffar, S. Bohamad, M. Ahmed, Waste water quality and reuse in irrigation in Kuwait using microfiltration technology in treatment, Desalination, 185 (**2005**) 1–3, 213–225, doi:10.1016/j.desal.2005.02.078

[2] P. S. Cartwright, Membranes separations technology for industrial effluent treatment, Desalination, 56 (**1985**), 17–35, doi:10.1016/0011-9164(85)85012-8

[3] P. S. Cartwright, Zero Discharge/Water Reuse - The opportunities for membrane technologies in pollution control, Desalination, 83 (**1991**) 225, 225–241, doi:10.1016/0011-9164(91)85097-E

[4] C. S. Slater, R. C. Ahlert, C. G. Uchrin, Applications of reverse osmosis to complex industrial wastewater treatment, Desalination, 48 (**1983**) 2, 171–187, doi:10.1016/0011-9164(83)80015-0

[5] A. H. Ghabris, M. Abdel-Jawad, G. S. Aly, Municipal wastewater renovation by reverse osmosis state of the art, Desalination, 75 (**1989**), 213–240 , doi:10.1016/0011-9164(89)85015-5

[6] T. Eisenberg, E. Middlebrooks, Reverse osmosis treatment of drinking water, (**1986**), 1–271, doi:10.1016/B978-0-250-40617-3.50004-4

[7] E. Chian, W. Bruce, H. Fang, Removal of pesticides by reverse osmosis, Environmental Science and Technology, 364 (**1975**) 9, 52–59, doi:10.1021/es60099a009

[8] H. Odegaard, S. Koottatep, Removal of humic substances from natural waters by reverse osmosis, Water Research, 16 (**1982**) 5, 613–620, doi:10.1016/0043-1354(82)90082-3

[9] T. Clair, J. Kramer, M. Sydo, D. Eaton, Concentration of aquatic dissolved organic matter by reverse osmosis, Water Research, 25 (**1991**) 9, 1033–1037, doi:10.1016/0043-1354(91)90196-w

[10] T. Sorg, R. Forbes, D. Chambers, Removal of radium-226 from sarasota county, fla., drinking water by reverse osmosis, Journal AWWA, 72, (**1980**) 4, 230–237, doi: JAW-0003802 2

[11] J. Baier, B. Lykins, C. Fronk, S. Kramer, Using reverse osmosis to remove agricultural chemicals from groundwater, Journal AWWA, 79 (**1987**) 8, 55–60, doi: JAW-0021235

[12] J. Taylor, D. Thompson, J. Carswell, Applying membrane processes to groundwater sources for Trihalomethane precursors, Journal AWWA, 79 (**1987**) 8, 72–82 doi: JAW-0021238

[13] L. Tan, R. Sudak, Removing color from a groundwater source, Journal AWWA, 84 (**1992**) 1, 79–87, doi:JAW-0031493

[14] J. Cruver, Waste-treatment applications of reverse osmosis, Transactions ASME, 97 (**1976**) 1, 246–251, doi:10.1115/1.3438546

[15] H. Fang, E. Chian, Reverse osmosis separation of polar organic compounds in aqueous solution, Environmental Science & Technology, 10 (**1976**) 4, 364–369, doi:10.1021/es60115a011

[16] H. Tsuge, R. Mori, Reclamation of municipal sewage by reverse osmosis, Desalination, 23 (**1977**) 1, 123–132, doi:10.1016/S0011-9164(00)82515-1

[17] N. Richardson, D. Argo, Orange county's 5 MGD reverse osmosis plant, Desalination, 23 (**1977**) 1, 563–573, doi:10.1016/S0011-9164(00)82555-2

[18] P. Allen, G. Elser, They said it couldn't be done-the orange County, California experience, Desalination, 30 (**1979**) 1, 23–38, doi:10.1016/S0011-9164(00)88430-1

[19] I. Nusbaum, D. Argo, Design, operation, and maintenance of a 5-mgd wastewater reclamation reverse osmosis plant. in Synthetic Membrane Processes: Fundamentals and Water Applications, Academic Press, Orlando, FL, (**1984**), 377–436, doi:10.1016/B978-0-12-085480-6.50016-5

[20] E. Csefalvay, P. M. Imre, P. Mizsey , Applicability of nanofiltration and reverse osmosis for the treatment of wastewater of different origin, Central European Journal of Chemistry, 6 (**2008**) 2, 277–283, doi:10.2478/s11532-008-0026-3

[21] M. Gholami, R. Mirzaej, R. R. Kalantary, A. Sabzali, F. Gatei, Performance evaluation of reverse osmosis technology for selected antibiotics removal from synthetic pharmaceutical wastewater, Iranian J Environ Health Sci. Eng, 9 (**2012**) 1, 9–19, doi:10.1186/1735-2746-9-19

[22] E. Sahar, I. David, Y. Gelman, H. Chikurel, A. Aharoni, R. Messalem, A. Brenner, The use of RO to remove emerging micropollutants following CAS/UF or MBR treatment of municipal wastewater, Desalination, 273 (**2011**), 142–147, doi:10.1016/j.desal.2010.11.004

[23] P. Eriksson, Nanofiltration extends the range of membrane filtration, Environmental Progress, 7 (**1988**) 1, 58–62, doi:10.1002/ep.3300070116

[24] J. Cadotte, Forester, R. Kim, M. Petersen, R. T. Stocker, Nanofiltration membranes broaden the use of membrane separation technology, Desalination, 70 (**1988**) 1–3, 77–88, doi:10.1016/0011-9164(88)85045-8

[25] W. Conlon, Pilot field test data for prototype ultra low pressure reverse osmosis elements, Desalination, 56 (**1985**), 203–226, doi:10.1016/0011-9164(85)85026-8

[26] B. Watson, C. Homburg, Low-energy membrane nanofiltration for removal of color, organics and hardness from drinking water supplies, Desalination, 72 (**1989**) 1/2, 11–22, doi:10.1016/0011-9164(89)80024-4

[27] W. Conlon, C. Homburg, B. Watson, C. Kiefer, Membrane softening: the concept and its application to municipal water supply, Desalination, 78 (**1990**) 2, 157–175, doi:10.1016/0011-9164(90)80040-1

[28] P. Lange, P. Laverty, E. Edwards, I. Watson, THM precursor removal and softening – ft. myers 12 mgd ro membrane plant, Florida USA, Desalination, 76 (**1989**), 39–52, doi:10.1016/0011-9164(89)87037-7

[29] G. Amy, B. Alleman, C. Cluff, Removal of dissolved organic matter by nanofiltration, Journal of Environmental Engineering, 116 (**1990**) 1, 200–205, doi:10.1061/(ASCE)0733-9372

[30] S. Duranceau, J. Taylor, L. Mulford, SOC Removal in a membrane softening process, Journal AWWA, 84 (**1992**) 1, 68–78

[31] A. Bindoff, C. Davies, C. Kerr, C. Buckley, The nanofiltration and reuse of effluent from the caustic extraction stage of wood pulping, Desalination, 67 (**1987**), 455–465, doi:10.1016/0011-9164(87)90262-1

[32] K. Ikeda, T. Nakano, H. Ito, T. Kubota, S. Yamamoto, New composite charged reverse osmosis membrane, Desalination, 68 (**1988**) 2, 109–119, doi:10.1016/0011-9164(88)80048-1

[33] M. Afonso, V. Geraldes, M. Rosa, M. De Pinho, Nanofiltration removal of chlorinated organic compounds from alkaline bleaching effluents in a pulp and paper plant, Water Research, 26 (**1992**) 12, 1639–1643, doi:10.1016/0043-1354(92)90163-X

[34] M. Simpson, C. Kerr, C. Buckley, The effect of ph on the nanofiltration of the carbonate system in solution, Desalination, 64 (**1987**), 305–319, doi:10.1016/0011-9164(87)90104-4

[35] S. Gaeta, U. Fedele, Recovery of water and auxiliary chemicals from effluents of textile dye houses, Institution of Chemical Engineers Symposium Series, 83 (**1991**) 1/3, 183–194, doi:10.1016/0011-9164(91)85094-B

[36] M. Perry, C. Linder, Intermediate reverse osmosis ultrafiltration (ROUF) membranes for concentration and desalting of low molecular weight organic solutes, Desalination, 71 (**1989**) 3, 233–245, doi:10.1016/0011-9164(89)85026-X

[37] D. Bhattacharyya, R. Adams, M. Williams, Separation of selected organics and inorganic solutes by low pressure reverse osmosis membranes, in biological and synthetic membranes, D. Butterfield, ed., Alan R. Liss, New York. 292 (**1989**) 1–2, 153–67, doi:10.1002/pi.4980230130

[38] M. Williams, R. Deshmukh, D. Bhattacharyya, Separation of hazardous organics by reverse osmosis membranes, Environmental Progress, 9 (**1990**) 2, 118–125, doi: 10.1002/ep.670090220

[39] R. Rautenbach, A. Gröschl, Separation potential of nanofiltration membranes, Desalination, 77 (**1990**), 73–84, doi:10.1016/0011-9164(90)85021-2

[40] M. Chu, C. Tung, M. Shieh, A study on triple-membrane-separator (TMS) process to treat aqueous effluents containing uranium, Separation Science and Technology, 25 (**1990**) 13–15, 1339–1348, doi:10.1080/01496399008050395

[41] C. Dyke, C. Bartels, Removal of organics from offshore produced waters using nanofiltration membrane technology, Environmental Progress, 9 (**1990**) 3, 183–186, doi:10.1002/ep.670090320

[42] L. H. Andrade, F. D. S. Mendes, J. C. Espindola, M. C. S. Amaral, Reuse of dairy wastewater treated by membrane bioreactor and nanofiltration: technical and economic feasibility, Braz. J. Chem. Eng., 32 (**2015**) 3, 735–747, doi:10.1590/0104-6632.20150323-s00003133

[43] E. L. Subtil, J. C. Mierzwa, I Hespanhol, Comparison between a conventional membrane bioreactor (C-MBR) and a biofilm membrane bioreactor (BF-MBR) for domestic wastewater treatment, Braz. J. Chem. Eng.,31 (**2014**) 3, 683–691, doi:10.1590/0104-6632.20140313s00002890

[44] F. A. Riera, A. Suárez, C. Muro, Nanofiltration of UHT flash cooler condensates from a dairy factory: Characterisation and water reuse potential, Desalination, 309 (**2013**), 52–63, doi:10.1016/j.desal.2012.09.016

[45] L. H. Andrade, G. E. Motta, M. C. S. Amaral, Treatment of dairy wastewater with a membrane bioreactor. Braz. J. Chem. Eng., 30 (**2013**) 4,759–770, doi:10.1590/S0104-66322013000400008

[46] M. G. Khedr, Nanofiltration and low energy reverse osmosis for rejection of radioactive isotopes and heavy metal cations from drinking water sources, Desalination and Water Treatment, 2 (**2009**), 342–350, doi:10.5004/dwt.2009.333

[47] M. Einar, S. Bjorn, Concentration polarization and fouling, Desalination, 35 (**1980**), 59–103, doi:10.1016/s0011-9164(00)88604-x

UDK 67.017:620.172:620.173.24
Professional article/Strokovni članek

ISSN 1580-2949
MTAEC9, 51(3)549(2017)

TENSILE BEHAVIOUR AND FRACTOGRAPHY ANALYSES OF LM6/ZrO_2 COMPOSITES

OBNAŠANJE IN ANALIZA PRI NATEZNI OBREMENITVI PRELOMA KOMPOZITOV LM6/ZrO_2

Govindan Karthikeyan[1], Gowthanithankachi Raghuvaran Jinu[2]

[1]University College of Engineering Pattukottai, A Constituent College of Anna University Chennai, Department of Mechanical Engineering, Rajamadam, Pattukottai-614701, Tamilnadu, India
[2]University College of Engineering, Department of Mechanical Engineering, Nagercoil-629004, Tamilnadu, India
p_gkarthikeyan@yahoo.co.in, gr_jinu1980@yahoo.com

Prejem rokopisa – received: 2015-10-21; sprejem za objavo – accepted for publication: 2016-06-15

doi:10.17222/mit.2015.319

Aluminium-based metal matrix (LM6) composite materials were prepared using various percentages of 0 %, 3 %, 6 %, 9 % and 12 % of zirconia by the weight fraction method and fabricated by the stir casting method. Five samples were prepared as per the ASTM B-557-M-94 standard, and then the prepared sample was subjected to an energy-dispersive spectrometry (EDS), hardness and tensile tests. The hardness and tensile test results revealed that the maximum hardness, maximum ultimate strength, yield strength was obtained for the composite containing 12 % of mass fractions of ZrO_2. The percentage of increase in zirconia increases the hardness, ultimate strength, yield strength. The minimum percentage of zirconia gives the minimum hardness and ultimate strength. Then EDS test was conducted on prepared samples. It was confirmed that aluminium and zirconia particles are present in the metal matrix composites. Fractography analysis was also employed in this work to understand the fracture mechanics of the surface. The fractography analysis was conducted with a scanning electron microscope (SEM). From the fractography analysis it was revealed that the nature of the fracture surface was changed from ductile with a large dimple surface to brittle fracture.

Keywords: metal matrix composites, aluminium LM6 alloy, zirconia (ZrO_2), tensile test, fractography

Kovinski kompoziti na osnovi aluminija (LM6) so bili pripravljeni z različnimi masnimi deleži 0 %, 3 %, 6 %, 9 % in 12 % cirkonijevega dioksida, z metodo ulivanja z mešanjem taline. Pet vzorcev je bilo pripravljenih skladno s standardom ASTM B-557-M-94 in nato pregledanih z energijsko disperzijsko spektrometrijo (EDS), izmerjena je bila trdota in izvedeni so bili natezni preizkusi. Iz meritve trdote in nateznih preizkusov sledi, da je bila največja trdota in najvišja natezna trdnost dosežena pri kompozitu z 12 masnimi % ZrO_2. Naraščajoča vsebnost cirkonijevega dioksida povišuje trdoto, natezno trdnost in mejo plastičnosti. Najmanjša vsebnost cirkonijevega dioksida daje najmanjšo trdoto in najnižjo natezno trdnost. Na pripravljenih vzorcih je bila izvedena tudi EDS analiza, ki je potrdila, da sta aluminij in delci iz cirkonijevega dioksida prisotna v kovinski osnovi kompozita. Analiza prelomov je bila tudi uporabljena v tem delu, da bi razumeli mehaniko preloma površine. Analiza prelomov je bila izvedena z vrstičnim elektronskim mikroskopom. Analiza prelomov je odkrila, da se narava površine preloma spreminja iz duktilnega z velikimi jamicami, v krhek prelom.

Ključne besede: kompoziti s kovinsko osnovo, aluminijeva LM6 zlitina, cirkonijev dioksid (ZrO_2), natezni preizkus, analiza preloma

1 INTRODUCTION

Metal matrix composites offer various advantages in applications where high specific strength, stiffness, and resistance are required.[1] Aluminium-based composites containing ceramic whiskers, fibers and particles have been used for automobile parts such as pistons and cylinder liners in engines due to their superior wear properties.[2] Stir casting techniques are the conventional and economic way of producing AMC. But with the conventional stir casting techniques, it is difficult to produce a particulate reinforced composite.[3] They are usually reinforced by Al_2O_3, SiC, C, and in addition SiO_2, B, BN, B_4C may also be considered.[4] In this field, aluminium is the most popular matrix for the metal matrix composites. Most of the research works deal with aluminium matrix because of their lightweight nature. The Al alloys are quite attractive due to their low density, good corrosion resistance, processing flexibility, high thermal and electrical conductivity, improved elastic modulus, strength and their high damping capacity. Different processing techniques are used for the production of aluminium metal matrix composites. A lot of researchers have concentrated on developing new composites such as Al 6061, LM25, reinforcing with various elements such as TiB_2, SiC, TiC, ZrB_2, AIN, Si_3N_4, Al_2O_3 and their tensile properties were analyzed in earlier researchers.[3-6] Very few works were identified in analyzing the effect of ZrO_2 on the tensile behavior. Zirconia is a refractory material with a melting point of about 2680 °C. ZrO_2 possesses good properties, such as a low coefficient of thermal expansion, good thermal shock resistance, high melting point, low thermal conductivity and excellent thermal stability. Its density, Young's modulus, and hardness are 5.71 g/cm^3, 190 GPa and 1200 HV, respectively.

Table 1: Chemical composition of aluminum LM6 alloy, in mass fractions (*w*/%)
Tabela 1: Kemijska sestava aluminijeve zlitine LM6 v masnih odstotkih (*w*/%)

Cu	Mg	Si	Fe	Mn	Ni	Zn	Pb	Sn	Ti	Al
0.1	0.10	10-13	0.6	0.5	0.1	0.1	0.1	0.05	0.2	Bal

No works have been identified in analyzing the effect of ZrO_2 on LM6 base material while subjected to tensile and fractography analysis. Hence, the works mainly concentrated on developing new composite material by taking LM6 as the base material and varying the percentage of ZrO_2 to identify the influence of ZrO_2 on the tensile and fracture behavior. The tensile strength and fractography analysis of these materials were also studied. The present research is an attempt to test and analyze the mechanical properties of LM6 reinforced with (0, 3, 6, 9 and 12) % various by weight fractions of ZrO_2 particulate produced by the stir casting method.

2 MATERIALS AND METHODS

2.1 Experimental part

The LM6 aluminium alloy was taken as the base material and ZrO_2 powder (particle size 1–10 μm) was chosen as the reinforcement material. The corresponding chemical compositions are given in **Table 1**. In this work, five cast samples were prepared by keeping LM6 as the base material at varying weight percentage of ZrO_2, such as 0 %, 3 %, 6 %, 9 %, and 12 %. The casting was carried out using the stir casting process, as shown in **Figure 1**. Initially, the aluminum LM6 alloy was melted in a pot by heating in a blower furnace at 850 °C for 15 min. The ZrO_2 powder was preheated at 575 °C in a separate muffle furnace. The furnace temperature was raised above the liquid temperature of LM 6 at about 850 °C to melt the LM6 completely and then it is slowly added to the preheated ZrO_2 powder. The stirring was carried out with the help of the drilling machine for about 15 min and the stirring rate maintained a speed of about 950 min^{-1}. This combination was then transferred into the mould cavity, and it is cooled to a room temperature. This procedure was followed for the preparation of five specimens with different compositions of ZrO_2 as shown in **Figure 1**.

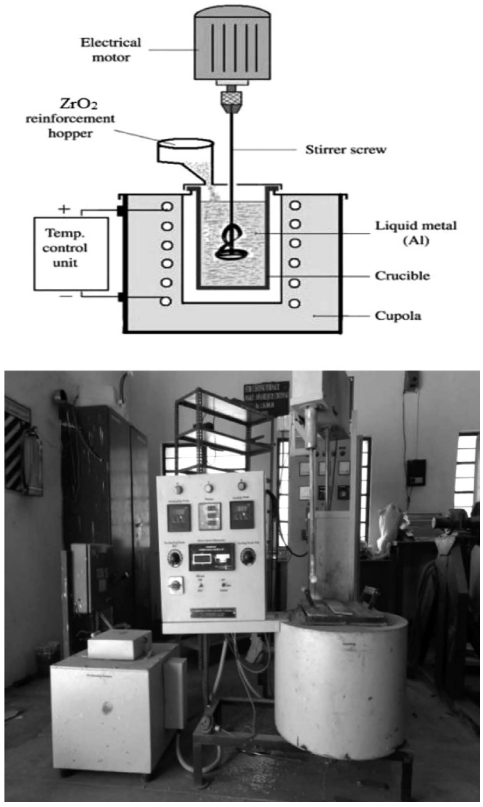

Figure 1: a) Schematic view of stir casting setup, casting of MMC by using stir casting method, b) image of stir casting setup, casting of MMC using the stir casting method

Slika 1: a) Shematski prikaz sestava za ulivanje z mešanjem, ulivanje MMC z uporabo metode mešanje-ulivanje, posnetek sestava za ulivanje z mešanjem, ulivanje MMC z uporabo metode mešanje-vlivanje

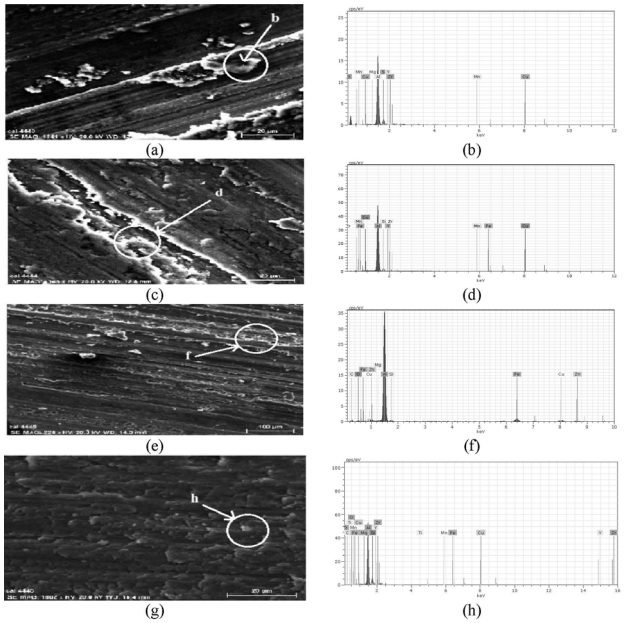

Figure 2: SEM images and EDS patterns of various composites: a) SEM image of LM6, b) EDS pattern of LM6, c) SEM image of LM6-3% ZrO_2 composites, d) EDS pattern of LM6-3% ZrO_2 composites, e) SEM image of LM6-6% ZrO_2 Composites, f) EDS pattern of LM6-6% ZrO_2 composites, g) SEM image of LM6-9% ZrO_2 composites, h) EDS pattern of LM6-9% ZrO_2 composites

Slika 2: SEM-posnetki in EDS-analiza različnih sestav: a) SEM-posnetek LM6, b) EDS-analiza LM6, c) SEM-posnetek kompozita LM6 – 3 % ZrO_2, d) EDS-analiza kompozita LM6 – 3 % ZrO_2, e) SEM-posnetek kompozita LM6 – 6 % ZrO_2, f) EDS-analiza kompozita LM6 – 6 % ZrO_2, g) SEM-posnetek kompozita z 9 % ZrO_2, h) EDS-analiza kompozita LM6 – 9 % ZrO_2

2.2. SEM-EDS analysis of LM6/ZrO_2 composite specimen

Energy-dispersive spectrometry analyses are applied in the present work, which helps to find out information of the type of element present in the samples. From the above **Figures 2b, 2d, 2f** and **2h** indicate the energy-dispersive spectrum of aluminium LM6 with their elements. The **Figures 2a, 2c, 2e** and **2g** indicates the topographical scanning electron microscope (SEM). The microstructure and EDS analysis of ZrO_2 particles are shown in **Figures 2e, 2f, 2g** and **2h**. From the graph after finishing EDS test, results are confirmed that the chemical composition of LM6/ZrO_2 composites like aluminium, zirconium, iron, copper, magnesium, zinc, silicon, and others all the elements are present in the prepared composites as shown in **Figures 2f** and **2h**. The shrinkage and porosity were not identified in the micrograph. This is evidence of the good quality of the casting. Finally, EDS analyses confirmed the presence of aluminium, ZrO_2 particles, which showed in **Figures 2f** and **2h**. The areas or points of the EDS analyses were taken from the SEM images given in **Figures 2a, 2c, 2e** and **2g**.

3 RESULTS AND DISCUSSION

3.1 Hardness measurements

Microhardness tests were conducted on the polished samples of aluminium LM6 alloy and its composites by adopting a standard testing procedure. The hardness of the composite was measured using a Vickers microhardness tester as per ASTM: E384-10. All the samples were applied with a load of 300 g for a period of 10 s. The test was carried out at three different locations to avoid the possible effect of the indenter resting on the hard reinforcement particles. The averages of all the five readings were reported. The hardness of the composite depends on the reinforcement of the matrix material. As the coefficient of thermal expansion of zirconia is less than the aluminium alloy, an enormous amount of dislocations are generated at the particle-matrix interface during the solidification process. This makes a further increase in the hardness of the matrix.[5] The results are graphically shown in **Figure 3**. It is observed that the hardness values of the material are directly proportional to the presence of ZrO_2, and with the increase in ZrO_2, the hardness increases.

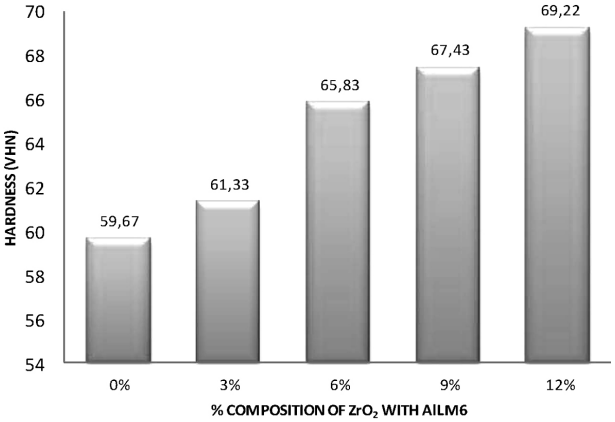

Figure 3: Vickers hardness values of various LM6/ZrO_2 composites
Slika 3: Vrednosti za Vickers trdoto različnih kompozitov LM6/ZrO_2

Figure 4: Photograph of tensile-tested specimen
Slika 4: Posnetek izgleda nateznih preizkušancev

3.2 Tensile test

The 15 tensile test sample specimens were prepared as per the ASTM standard (ASTM B-557-M-94) as shown in **Figure 4**, and they were tested in a Universal Testing Machine (FIE Pvt.Ltd., model: unitek 94100). Before measuring the tensile strength, the 15 samples were machined into a cylindrical shape. Three samples were tested for each composition to obtain the best tensile test result. The tensile tested sample of the five specimens LM6 reinforced with 0 %, 3 %, 6 %, 9 %, and 12 %, respectively, are given in **Figure 4**. From **Figure 5** it is clear that the maximum ultimate tensile strength is obtained for the sample 5, which contains 12 % of ZrO_2. Therefore, this clearly reveals that the ultimate tensile strength increases with an increasing percentage of ZrO_2, as shown in **Figure 5**. Similar trends have been observed by many other researchers.[6–8]

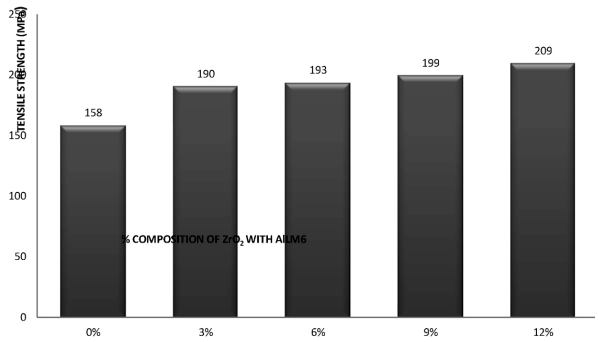

Figure 5: Tensile strength of various LM6/ZrO_2 composites
Slika 5: Natezna trdnost različnih kompozitov LM6/ZrO_2

3.3 SEM and fractography analysis of tensile specimen

From these SEM images (**Figures 6** to **8**) it is clear that the distribution of particles throughout the matrix was found to be fairly uniform as a dark region. It is also observed that as the weight percentage of reinforcement of ZrO_2 increases the area fraction also increases as shown in **Figures 7** and **8** as a dark region. It can also be noticed that the average grain size of the aluminium LM6 matrix decreases with an increase in the weight fraction of ZrO_2 reinforcement.

From these **Figures 7** and **8** it is clear that the homogeneous distributions of ZrO_2 reinforced particles with aluminium alloy occurred. Further, these figures reveal the homogeneity of the cast composites. The properties of the aluminium MMCs depend not only on the matrix particle and the weight fraction but also on the distribution of the reinforcing particles and the interface bonding between the particle and the matrix.

Fracture surface analysis revealed different topographies for the composites containing different weight percentages of zirconia particles. The results of the fracture surface analyses conducted on fracture toughness specimens of FCC structured LM6 alloy samples revealed large dimples, along with a large amount of plastic deformation, indicating a ductile fracture. The fracture surfaces also exhibit fine and shallow dimples, indicating that the fracture is ductile, as shown in **Figure 9**.

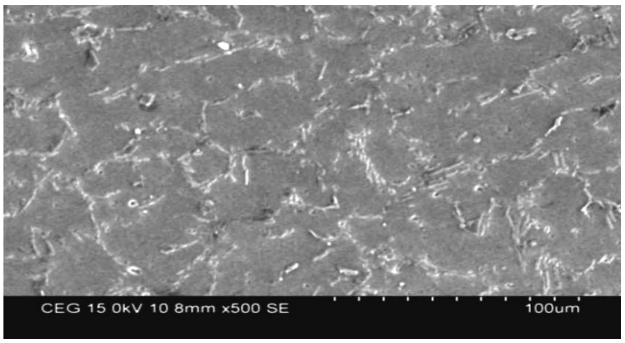

Figure 6: SEM image of LM6 alloy
Slika 6: SEM-posnetek zlitine LM6

Figure 7: SEM image of LM6–6% of ZrO_2
Slika 7: SEM-posnetek LM6 – 6 % ZrO_2

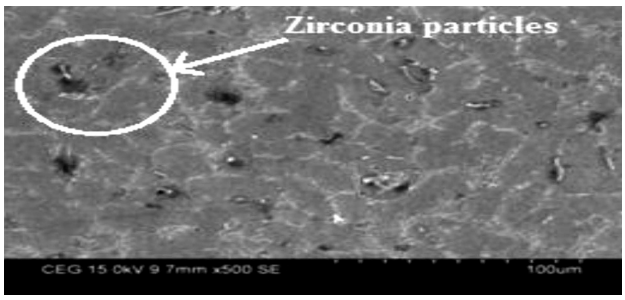

Figure 8: SEM image of LM6–12% of ZrO_2
Slika 8: SEM-posnetek LM6 – 12 % ZrO_2

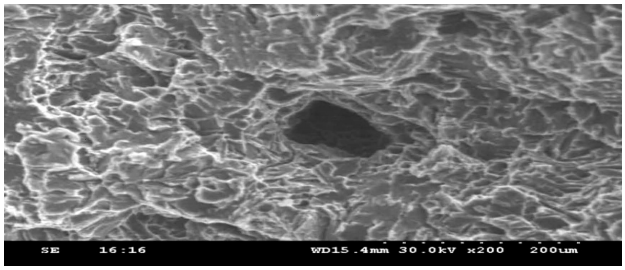

Figure 9: Fractured surface of 0% zirconia and 100% LM6
Slika 9: Slika preloma pri 0 % ZrO_2 in 100 % LM6

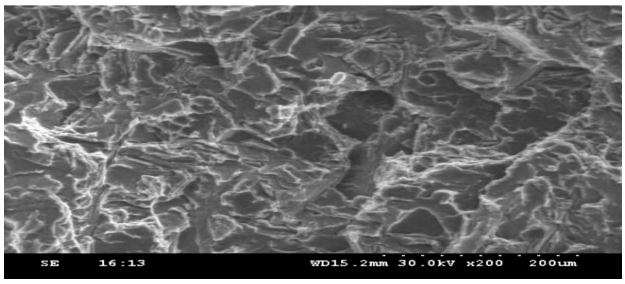

Figure 10: Fractured surface of composite with 6 % zirconia and 94 % LM6
Slika 10: Površina preloma kompozita z 6 % ZrO_2 in 94 % LM6

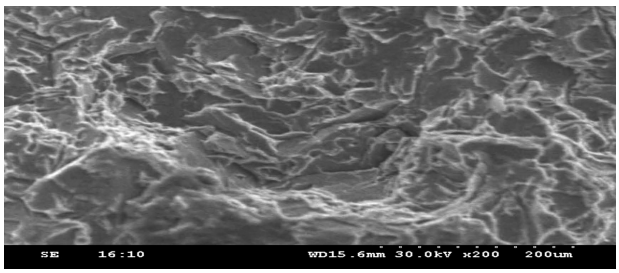

Figure 11: Fractured surface of composite with 12 % of zirconia and 88 % LM6
Slika 11: Površina preloma kompozita z 12 % ZrO_2 in 88 % LM6

Fracture surfaces of the MMCs tested are shown in **Figures 9** to **11**. An examination of these fracture surface features in the SEM at high magnification is to identify the fatigue and final fracture region, to identify areas of micro-crack initiation and early crack growth, and the over-loaded region to identify the fine scale fracture features.

Fracture surfaces revealed different topographies for the composites containing a different weight percentage of zirconia particles. The fracture surface in the case of MMCs containing 12 % of mass fractions reinforcement revealed a cleavage type of fracture (**Figure 11**) due to the presence of excessive zirconia particulates. It can also be seen that regions of clustered particles for reinforcement above 6 % of mass fractions (**Figure 10**) are sensitive to premature damage in the composites and the large particles seem to be prone to fracture and hence registered a reduction in the fracture-toughness value. The fracture mode of the matrix alloy which changed from ductile to cleavage type (in the case of MMCs) was dominated with microcrack nucleation and propagation, as shown in **Figures 9** to **11**. Scanning electron microscope observations of MMCs suggest that, at higher reinforcement content (12 % of mass fractions, **Figure 11**), void nucleation may also take place at large participates in addition to the matrix/particle interface, while at lower reinforcement (0, 6 % of mass fractions, **Figures 9** and **10**) rates the fracture seems to occur through the breakage of the particles.

Fracture surface analysis of MMCs containing 12 % of mass fractions dispersoid (**Figure 11**) exhibit predominantly that fractured particles (dispersoid) and the matrix material with coarse dimples, suggests that fracture is of mixed mode type. Close examination of the fractured surface indicates that most dimples were associated with the matrix material (**Figure 11**). Massive separations of the particle indicate that failure of the material is initiated by the fracture of the particles rather than debonding between the matrix and the reinforcements. The microstructural features are shown in **Figures 10** and **11**, which are a sample containing 12 % of mass fractions dispersion casting of 10 mm thick, which indicates that zirconia particles have fractured during straining and fracture could have occurred in a brittle manner as a result of stress concentrations and the propagation of the cracks. Finally, a composite containing 12 % of mass fractions dispersoid showed cleavage indicating that the fracture is towards brittle.

4 CONCLUSIONS

The aluminium-based composite was successfully fabricated by the stir casting method with a uniform distribution of ZrO_2 particles.

EDX studies confirmed the presence of aluminium, zirconium, iron, magnesium, silicon in the prepared composite material.

The hardness of the reinforced composites was improved compared with the unreinforced alloy and 12 % of mass fractions of ZrO_2 combination achieves the high hardness value.

There is an improvement in the tensile strength, ultimate tensile strength with the addition of ZrO_2 particle.

The SEM images of various weight percentage of ZrO_2 reinforcement reveal that the SEM image for 12 % of mass fractions of ZrO_2 contains more presence of ZrO_2 particles. It was clearly seen as a dark region.

The fractography results show that the increase in weight percentage of the ZrO_2 changes the mode of failure from ductile to brittle, which is revealed from the occurrence of large dimple tiny particles with a large amount of plastic deformation present in the low weight percentages of ZrO_2 reinforced composites.

Fracture surface observation of the samples shows that the failure of the LM6 /zirconia composite is similar to the unreinforced LM6 alloy one, which was controlled by inter-dendrite cracking of the matrix. In addition, a number of dimples were observed on the fracture surface of all the samples, which could be the result of the void nucleation and self-subsequent coalescence during the fracture process.

5 REFERENCES

[1] R. Kumar, S. Chauhan, Study on surface roughness measurement for turning of Al 7075/10/SiCp and Al7075 hybrid composites by using Response Surface Methodology and Artificial Neural Networking, Measurement, 65 (**2015**), 166–180, doi:10.1016/j.measurement.2015.01.003

[2] H. J. Choi, S. M. Lee, D. H. Bae, Wear characteristic of aluminum-based composites containing multi-walled carbon nanotubes, Wear, 270 (**2010**), 1–2, 12–18, doi:10.1016/j.wear.2010.08.024

[3] S. Gopalakrishnan, N. Murugan, Production and wear characterization of AA6061 matrix titanium carbide particulate reinforced composite by enhanced stir casting method, Composites Part B: Engineering, 43 (**2012**) 2, 302–308, doi:10.1016/j.compositesb.2011.08.049

[4] M. Hayajneh, A. M. Hassan, A. Alrashdan, A. T. Mayyas, Prediction of tribological of aluminum-copper based composite using Artificial neural network, Journal of Alloys and Compounds, 470 (**2009**) 1–2, 584–588, doi:10.1016/j.jallcom.2008.03.035

[5] S. Das, S. Das, K. Das, Abrasive wear of zircon sand and alumina reinforced Al–4.5 wt% Cu alloy matrix composites—A comparative study, Composites Science and Technology, 67 (**2007**) 3–4, 746–751, doi:10.1016/j.compscitech.2006.05.001

[6] M. Balasubramanian, V. Jayabalan, V. Balasubramanian, Developing mathematical models to predict tensile properties of pulsed current gas tungsten arc welded Ti–6Al–4V alloy, Materials & Design, 29 (**2008**) 1, 92–97, doi:10.1016/j.matdes.2006.12.001

[7] Li Pengting, Li Yunguo, Wu Yuying, Ma Guolong, Liu Xiangfa, Distribution of TiB_2 particles and its effect on the mechanical properties of A390 alloy, Materials Science and Engineering: A, 546 (**2012**) 1, 146–152, doi:10.1016/j.msea.2012.03.042

[8] S. C. Tjong, K. C. Lau, Abrasive wear behavior of TiB_2 particle-reinforced copper matrix composites, Material Science and Engineering: A, 282 (**2000**) 1–2, 183–186, doi:10.1016/S0921-5093(99)00752-2

Erratum

In Materiali in tehnologije/Materials and Technology 51 (2017) 2, 229-236, doi: 10.17222/mit.2015.211 in the article entitled PREPARATION OF BIO-POLYMERIC MATERIALS, THEIR MICROSTRUCTURES AND PHYSICAL FUNCTIONALITIES, by Xin-Li Chen, Ai-Juan Zhao, Hai-Jie Sun and Xian-Ru Pei, the name of the first author was written incorrectly. The correct name is Xiu-Li Chen. The MIT (Materials and Technology) Editorial Office apologizes to the authors for any inconvenience relating to the mistake.

MIT Editorial

ELECTRONIC ACCESS

http://mit.imt.si

ISSN 1580-2949